Physics of the Solid State, Vol. 47, No. 4, 2005, pp. 599–603. Translated from Fizika Tverdogo Tela, Vol. 47, No. 4, 2005, pp. 577–580.
Original Russian Text Copyright © 2005 by Shein, Ivanovskiĭ.

METALS AND SUPERCONDUCTORS

Effect of Lattice Vacancies on the Band Structure of the $Ag_5Pb_2O_6$ Ternary Oxide

I. R. Shein and A. L. Ivanovskiĭ
Institute of Solid-State Chemistry, Ural Division, Russian Academy of Sciences,
Pervomaĭskaya ul. 91, Yekaterinburg, 620219 Russia
e-mail: shein@ihim.uran.ru

Received September 22, 2004

Abstract—The effect of structural vacancies in the silver sublattice on the band structure and on the nature of interatomic interactions in the ternary oxide $Ag_5Pb_2O_6$ is discussed in terms of the results of self-consistent full-potential linearized muffin-tin orbital (LMTO) calculations. © *2005 Pleiades Publishing, Inc.*

1. INTRODUCTION

Djurek *et al.* [1] studied the conducting properties of Ag–Pb–C–O polycrystalline ceramics and assumed that a new high-temperature superconductor can be revealed in this system. More comprehensive investigations have demonstrated that the electrical characteristics of the samples studied in [1] are predominantly determined by the ternary oxide $Ag_5Pb_2O_6$, the so-called Bystrom–Evers phase described earlier in [2]. This oxide is characterized by extended homogeneity regions for the silver and oxygen sublattices. The nominal compositions of the samples synthesized by Iwasaki *et al.* [3] correspond to compounds of the general formula $Ag_{5-x}Pb_2O_{6-y}$ ($0.25 \le x \le 0.5$; $y \sim 0.13$), which possess metallic conductivity, negative Seebeck coefficients, and weak diamagnetism. In a recent work [4], it was found that annealed samples of the Bystrom–Evers compound $Ag_5Pb_2O_6$ exhibit a colossal (anisotropic) electrical conductivity ($>10^9$ Ω^{-1} cm^{-1}) in the temperature range 210–525 K. This effect is associated with the formation of ordered (along the *c* axis) channels of silver vacancies.

The qualitative interpretation of the electrical properties of the $Ag_5Pb_2O_6$ compound is based on the semiempirical calculation performed by Brennan and Burdett [5]. According to this calculation, the energy at the Fermi level E_F coincides with the local peak of the density of Ag*s* states and the extended Ag states, which form both chains and layers in the structure of the $Ag_5Pb_2O_6$ compound (see below), are assumed to make a dominant contribution to the conductivity effects. It is also assumed that, upon electron doping, the $Ag_5Pb_2O_6$ oxide can undergo a transition to the semiconducting state.

In this paper, we report the results of *ab initio* band structure calculations for the ternary oxide $Ag_5Pb_2O_6$ and discuss the possible effect exerted by vacancies in the silver sublattice on the electronic properties of this compound.

2. OBJECTS OF INVESTIGATION AND CALCULATION TECHNIQUE

The structure of the ternary oxide $Ag_5Pb_2O_6$ (space group $P\text{–}31m$) with the unit cell parameters $a = 0.5932$ nm and $c = 0.6411$ nm [6] consists of alternating networks of silver atoms (Ag^2), the so-called (3,6,3,6) Kagome lattices, and molecular layers, which, in turn, are formed by PbO_6 trigonal prisms and chain motifs of silver atoms (Ag^1). The Ag^2 and Ag^1 atoms are twofold- and threefold-coordinated by oxygen atoms, respectively (Fig. 1). The $Ag_5Pb_2O_6$ oxide was modeled by a 13-atom cell $[Ag^1_2(Ag^2_3Pb_2O_6)]$. The nonstoichiometric oxide (with defects in the Ag sublattice) of the formal composition $Ag_4Pb_2O_6$ was modeled by a 12-atom

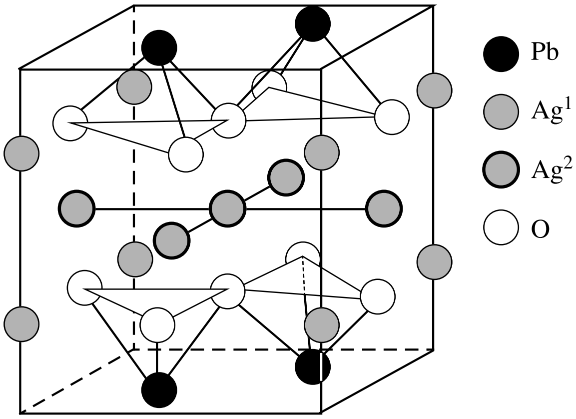

Fig. 1. Crystal structure of the $Ag_5Pb_2O_6$ ternary oxide [4]. The nonequivalent silver positions Ag^1 and Ag^2 are shown.

1063-7834/05/4704-0599$26.00 © 2005 Pleiades Publishing, Inc.

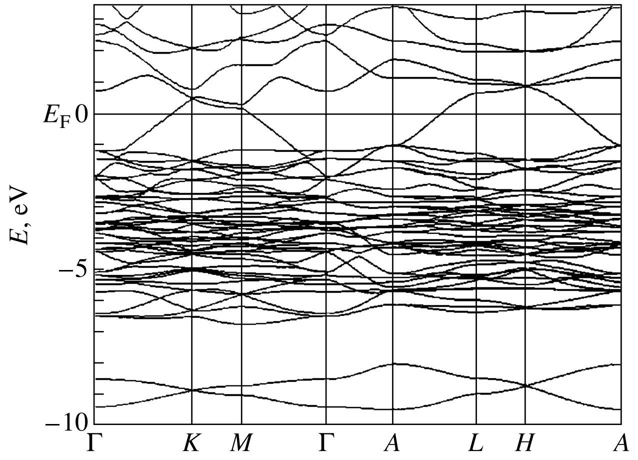

Fig. 2. Energy bands of the $Ag_5Pb_2O_6$ ternary oxide.

cell $[Ag^1\square(Ag_3^2Pb_2O_6)]$, where □ is a vacancy in the Ag^1 position. The band structure calculations were carried out using the scalar relativistic self-consistent full-potential linearized muffin-tin orbital (LMTO) method [7] in the framework of the generalized gradient approximation with inclusion of the exchange–correlation effects [8].

3. RESULTS AND DISCUSSION

Figures 2 and 3 show the dispersion curves $E(k)$ and the total and partial densities of states for the stoichiometric ($Ag_5Pb_2O_6$) and nonstoichiometric ($Ag_4Pb_2O_6$) oxides. The valence band of the $Ag_5Pb_2O_6$ compound has a total width of 9.42 eV (without regard for the low-energy quasi-core O2*s* bands located ~ 15 eV below the Fermi level E_F) and consists of two groups of energy bands located in the ranges –(9.6–8.0) and –(6.7–1.0) eV. These groups are separated by an indirect (*A*–*M* transition) band gap of ~1.3 eV. The lower group includes two bands of O2*p*–Pb6*s* states, whereas the upper group includes a compact group of bands of the mixed Ag4*d*–O2*p*–Pb5*d*, 6*p* type. The near-Fermi bands of the O2*p*–Pb6*s* antibonding states are characterized by a considerable dispersion $E(k)$ and form a density-of-states plateau. Earlier [5], it was assumed that the Ag *s* states play a decisive role in the conductivity effects. However, according to our calculations, their contribution to the near-Fermi bands is negligible and the occupied Ag5*s* states are substantially admixed to the group of energy bands of the Ag4*d*–O2*p*–Pb5*d*, 6*p* type (Figs. 2, 3). The dominant contribution (~70%) to the total density of states at the Fermi level [$N(E_F)$ = 1.298 states/(eV formula units)] is made by the O2*p* and Pb6*s* states (see table).

Depending on the type of atomic (twofold- or threefold-coordinated) position, the energy distributions of

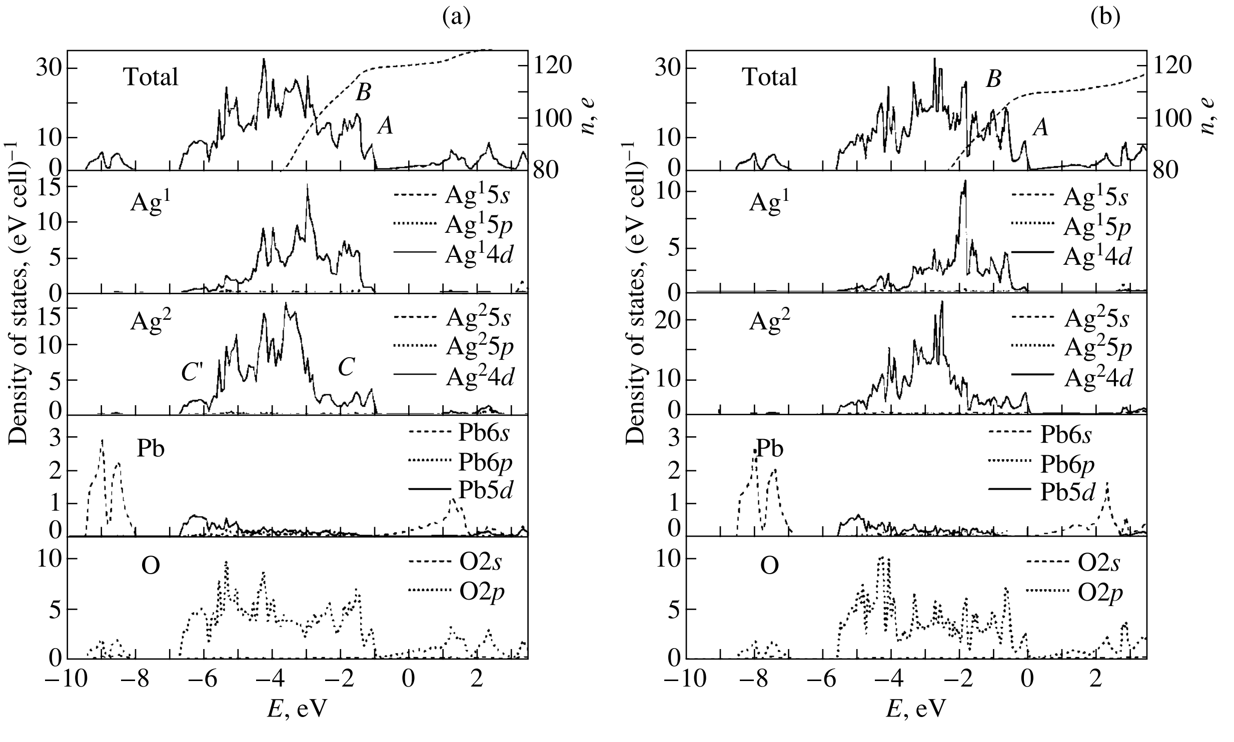

Fig. 3. Total and partial densities of states of (a) the stoichiometric $Ag_5Pb_2O_6$ oxide and (b) the nonstoichiometric $Ag_{5-x}Pb_2O_6$ oxide containing 50% Ag^1 vacancies. Dashed lines in the upper part show the number of electrons *n* in the cell.

Total and partial densities of states at the Fermi level $N(E_F)$ [states/(eV formula units)] and at the peaks *A* and *B* for the stoichiometric $Ag_5Pb_2O_6$ and nonstoichiometric $Ag_4Pb_2O_6$ (with defects in the silver sublattice) oxides

Oxide	Spectral region*	Total densities of states	Partial densities of states							
			Ag^15s Ag^25s	Ag^15p Ag^25p	Ag^14d Ag^24d	Pb6*s*	Pb6*p*	Pb5*d*	O2*s*	O2*p*
$Ag_5Pb_2O_6$	$N(E_F)$	1.298	0.040	0.023	0.078	0.201	0.009	0.004	0.086	0.675
			0.024	0.009	0.109					
	Peak *A*	8.150	0.018	0.032	0.775	0.024	0.025	0.048	0.046	3.037
			0.284	0.012	3.806					
	Peak *B*	17.129	0.056	0.216	5.878	0.079	0.089	0.135	0.110	6.839
			0.268	0.060	3.230					
$Ag_4Pb_2O_6$	$N(E_F)$	3.547	0.010	0.006	0.156	0.030	0.010	0.024	0.037	1.255
			0.127	0.005	1.676					
	Peak *A*	8.863	0.012	0.016	0.429	0.028	0.028	0.048	0.052	3.077
			0.358	0.016	4.317					
	Peak *B*	18.684	0.008	0.146	4.210	0.039	0.076	0.198	0.093	8.257
			0.238	0.051	3.448					

* Peaks *A* and *B* are shown in Fig. 3.

the Ag^1 and Ag^2 atoms differ significantly. In particular, the center of the energy band of the Ag^2d states is located ~ 1.2 eV deeper than that in the case of the Ag^1 atoms (Fig. 3). Moreover, noticeable density-of-states peaks are observed in the vicinity of the upper and lower edges of the Ag^24d band (peaks *C* and *C'* in Fig. 3). The above peaks indicate hybrid interactions of these states with the surrounding oxygen atoms. As a consequence, the Ag*d* bands, which are nearest to the Fermi level E_F (peak *A* of the total density of states for the oxide in Fig. 3), are predominantly formed by the states of the twofold-coordinated Ag^2 atoms comprising the Kagome lattices, whereas the states of the threefold-coordinated Ag^1 atoms make a significant contribution to the peak *B* (which is next in energy to the peak *A*) (see table). This feature can be explained in terms of the difference between the interatomic interactions of these centers with their nearest environment. The interatomic interactions depend on both the coordination number of the atoms and the Ag–O distances, which are equal to 0.2122 and 0.2286 nm for atoms in the (Ag^2) network and in the (Ag^1) layer, respectively [6].

The map of the charge density ρ is shown in Fig. 4. It can be seen from this figure that the Ag^2–O bond is stronger than the Ag^1–O bond. The silver–oxygen and lead–oxygen bonds are the strongest bonds in the oxide. By contrast, the silver–silver bonds, which, according to the assumption made in [5], should play a dominant role in the oxide, are very weak. The overlap of the contours of the charge density ρ for individual atoms Ag^2–Ag^2 (in the network) is insignificant. For centers of different types (Ag^1–Ag^2), the corresponding overlap is entirely absent.

The introduction of vacancies into the Ag^1 positions only slightly affects the density-of-states distribution in the stoichiometric $Ag_5Pb_2O_6$ oxide (see Fig. 3, table). The main effect exerted by vacancies is reduced to the depletion of the O2*p*–Pb6*s* antibonding bands. The Fermi level shifts to lower energies and coincides with the low-energy wing of the peak *A*. The system of interatomic interactions in the oxide also remains virtually unperturbed. Judging from the distributions of the charge density ρ (Fig. 4), no new bonds are formed in the nonstoichiometric oxide of the formal composition $Ag_4Pb_2O_6$ (except for the insignificant overlap of the contours of the charge density ρ along the Ag^1–Ag^2 directions). The degree of localization of the charge density in the region of vacancies is relatively small. According to our estimates, the charge of the empty muffin-tin (MT) sphere does not exceed 0.3 e. The fundamental changes in the electronic properties of the nonstoichiometric (defect-containing) oxide are associated with the enhancement of its “metallization” due to a sharp increase (by a factor of ~ 2.7) in the density of states at the Fermi level $N(E_F)$, as well as with the radical change in the structure of the near-Fermi bands containing comparable (in magnitude) contributions from the Ag^24d (47%) and O2*p* (35%) states.

To the best of our knowledge, there are no reliable experimental data on the change in the properties of the ternary oxide in the homogeneity region (except for the dependences of the lattice parameters on the silver content in $Ag_{5-x}Pb_2O_{6-y}$ samples [3]). Reasoning from the results obtained, we believe that, in the oxide under investigation, the nonstoichiometric effects are most pronounced for the properties governed by the system

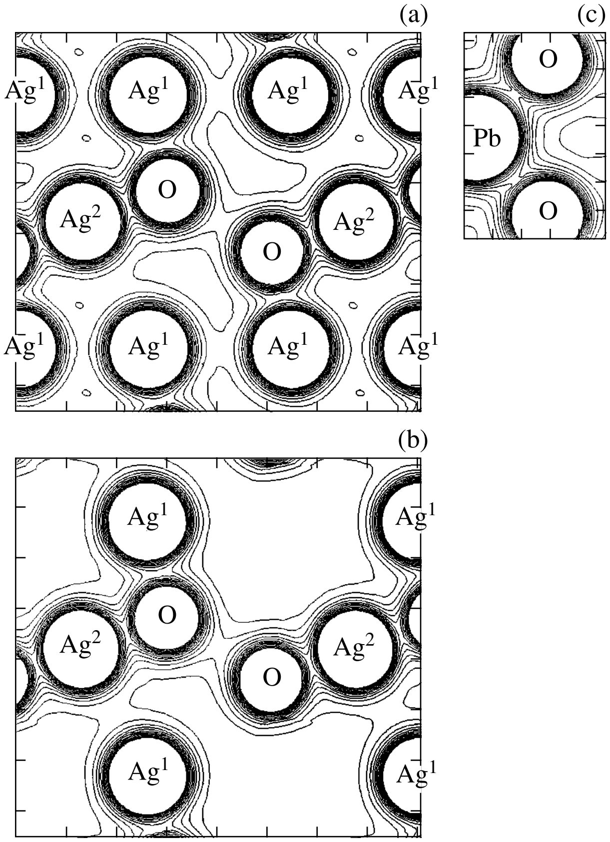

Fig. 4. Charge density maps in the cross-sectional plane of (a) the stoichiometric $Ag_5Pb_2O_6$ oxide and (b) the nonstoichiometric $Ag_{5-x}Pb_2O_6$ oxide containing 50% Ag^1 vacancies and (c) the charge density map in the cross-sectional plane of the PbO_6 prism in the structure of the $Ag_5Pb_2O_6$ oxide. Contours of the charge density distribution $\Delta\rho$ are drawn at intervals of 0.075 e/Å^3.

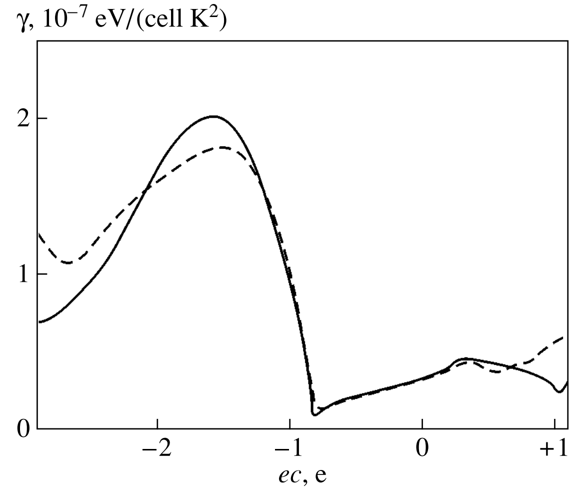

Fig. 5. Estimates of the low-temperature electronic heat capacity coefficient γ as a function of the electron concentration *ec* in the homogeneity region of the Bystrom–Evers phase according to the calculated data for the stoichiometric $Ag_5Pb_2O_6$ oxide (dashed line) and the nonstoichiometric oxide (with defects in the Ag^1 sublattice) of the nominal composition $Ag_4Pb_2O_6$ (solid line). The zero value corresponds to the electron concentration *ec* in the cell of the stoichiometric oxide.

of delocalized (near-Fermi) electrons. Moreover, the calculations performed demonstrate that the lattice defects in the stoichiometric $Ag_5Pb_2O_6$ oxide, unlike some oxides of Group III–VI transition metals with a partially filled *d* shell, do not contribute to the formation of new vacancy states in the electronic spectrum. Consequently, the effect of vacancies on the electronic spectrum of the ternary oxide can be reduced to a change in the degree of occupation of the energy bands due to a variation in the electron concentration (*ec*) in the system. Therefore, to a first approximation, this effect can be described within the rigid-band model. In this case, for example, the low-temperature electronic heat capacity coefficient, which is estimated in the framework of the free-electron model as $\gamma = (\pi^2/3)N(E_F)k_B^2$, varies in the homogeneity region in a nonmonotonic manner. More precisely, this coefficient decreases to a minimum at an electron concentration *ec* ~ 108.15 e in the cell and increases abruptly with further deviation of the oxide composition from stoichiometry (Fig. 5). As is seen from Fig. 5, the estimates obtained for both the magnitude and the general behavior of γ as a function of *ec* on the basis of the rigorous band calculations performed for the stoichiometric and defect-containing oxides appear to be close to each other. It can be assumed that these estimates will also be valid for the ternary oxide with a “double” imperfection (in the silver and oxygen sublattices), as is the case in $Ag_{5-x}Pb_2O_{6-y}$ samples [3].

4. CONCLUSIONS

Thus, the calculations performed allowed us to establish the main features in the structure of the energy spectrum of the ternary oxide $Ag_5Pb_2O_6$ and, for the first time, to investigate the effect of vacancies on the band structure of this compound. It was found that the interatomic interactions in the ternary oxide (which was described earlier in [5, 6] as an ionic metal) have a covalent component due to the hybridization of the (Ag,Pb)–O states. For the stoichiometric oxide, the states forming the O2*p*–Pb6*s* antibonding bands play a key role in the conductivity effects. The presence of silver vacancies in the structure brings about both an increase in the magnitude and a change in the composition of the density of states at the Fermi level $N(E_F)$. As a result, the contributions from the O2*p* states and 4*d* states, as well as from the silver atoms, which form Kagome lattices (of the Ag^2 type), become dominant. It should also be noted that, in contrast to the results of the semiempirical calculation performed in [5], our data indicate that neither electron nor hole doping will lead to a crossover of the system from the metal-like state to the semiconducting state.

ACKNOWLEDGMENTS

This study was performed as part of the program for support of leading scientific schools of the Russian Federation, project nos. NSh-829.2003.3 and NSh-1046.2003.3.

REFERENCES

1. D. Djurek, Z. Medunic, A. Tonejc, and M. Paljevic, Physica C (Amsterdam) **351** (1), 78 (2001).
2. A. Bystrom and L. Evers, Acta Chem. Scand. **4** (4), 613 (1950).
3. K. Iwasaki, H. Yamane, S. Kubota, J. Takahashi, Y. Miyazaki, T. Kajitani, K. Nakajima, T. Yamashita, and M. Shimada, Physica C (Amsterdam) **382** (2–3), 263 (2002).
4. D. Djurek, Z. Medunic, M. Paljevic, and A. Tonejc, cond-mat/0310011.
5. T. D. Brennan and J. K. Burdett, Inorg. Chem. **33** (21), 4794 (1994).
6. M. Jansen, M. Bortz, and K. Heidebrecht, J. Less-Common Met. **161** (1), 17 (1990).
7. S. Y. Savrasov, Phys. Rev. B **54** (23), 16470 (1996).
8. J. P. Perdew, K. Burke, and Y. Wang, Phys. Rev. B **54** (23), 16533 (1996).

Translated by N. Korovin

Physics of the Solid State, Vol. 47, No. 4, 2005, pp. 604–605. Translated from Fizika Tverdogo Tela, Vol. 47, No. 4, 2005, pp. 581–582.
Original Russian Text Copyright © 2005 by Haroutunian.

An Interpolation Formula for the Coulomb Gap in Lightly Doped and Compensated Semiconductors

S. L. Haroutunian

State Engineering University of Armenia, Gyumri Educational Complex, Gyumri, 377503 Armenia
e-mail: sashar@rambler.ru

Received March 24, 2003

Abstract—An interpolation formula is proposed for the density-of-states function of charge carriers in the impurity band of a lightly doped semiconductor. This formula involves two parameters and holds for an arbitrary energy. These parameters—the energy at the Fermi level and the parameter characterizing the width of the peaks in the density-of-states function—are determined from the conditions of normalization and electrical neutrality. *© 2005 Pleiades Publishing, Inc.*

The existence of a Coulomb gap in the density of states of charge carriers near the Fermi level in lightly doped semiconductors in both two-dimensional and three-dimensional systems has been proved in numerous theoretical studies and directly (or indirectly) confirmed by experimental data (see, for example, [1–8] and references therein).

In particular, Efros and Shklovskii [3] demonstrated that, owing to the long-range Coulomb potential, the density of states $g(\varepsilon)$ near the Fermi level μ in three-dimensional systems goes to zero according to the universal law

$$g(\varepsilon) = \frac{3}{\pi}\frac{\kappa^3}{a^6}(\varepsilon-\mu)^2 = \frac{4n_D(\varepsilon-\mu)^2}{\varepsilon_D^3}, \qquad (1)$$

where n_D is the concentration of majority donor impurities, $\varepsilon_D = e^2/\kappa R_D$ is the energy of the Coulomb interaction at the average donor impurity separation $R_D = (4\pi n_D/3)^{-\frac{1}{3}}$, and κ is the permittivity of the sample.

Analytical treatment of the density-of-states function $g(\varepsilon)$ over a wide range of variations in the energy ε involves a complicated many-electron problem that cannot be reduced to a single-electron problem (see, for example, [4]). Consequently, the structure of the impurity band in semiconductors, as a rule, has been investigated using numerical simulation (see review [5]).

In their review [5], Shklovskii and Efros presented the results of investigations of the impurity band and the plots of the density-of-states function $g(\varepsilon)$ obtained using numerical simulation at different degrees of compensation $K = n_A/n_D$ (where n_A is the concentration of compensating impurities, for example, acceptor impurities in an electron semiconductor).

According to the results reported in [1–3, 5, 6], it can be stated that numerical investigations of the structure of the impurity band have revealed and proved the following features of the density of states.

(i) The density of states always exhibits two peaks. The high-energy peak is assigned to the ionized donor states, whereas the low-energy peak is attributed to the occupied donor states.

(ii) The Coulomb gap is located between these peaks, and the density-of-states function $g(\varepsilon)$ near the Fermi level tends to zero according to the universal law (1).

(iii) In the limiting cases of weak ($K \longrightarrow 0$) and strong ($K \longrightarrow 1$) compensations, the width of the Coulomb gap tends to zero.

Due to the lack of a rigorous theory regarding the structure of the impurity band in semiconductor materials, the physical properties determined by the structure of this band have often been investigated using different numerical methods (see, for example, [9]). Analysis of the available experimental data has been performed for the most part in the framework of three approaches.

Within the first approach, the density-of-states functions are determined for the cases of ultimately weak and strong compensations (see, for example, [4, 10]). The second approach is based on relationship (1), which holds in the vicinity of the Fermi level (see, for example, [5]). In the third approach (away from the Fermi level), depending on the conditions of the problem, one function or another can be chosen that is satisfied in a narrow interval (see, for example, [11, 12]).

Therefore, in order to analyze the experimental data under these conditions, it is expedient to use a formula that will adequately reproduce the aforementioned properties of the density-of-states function $g(\varepsilon)$ over a wide range of variations in the energy ε.

In this paper, a similar interpolation formula is proposed for the density-of-states function $g(\varepsilon)$.

Numerical values of parameters c (the Fermi energy expressed in units of ε_D), a (characterizing the width of the secondary maxima), and Δ_0 (characterizing the width of the Coulomb gap) for different degrees of compensation

K	0.1	0.2	0.3	0.4	0.5	0.6	0.7	0.8	0.9
c	0.258	0.184	0.119	0.058	0	–0.058	–0.119	–0.184	–0.258
a	0.285	0.36	0.402	0.423	0.43	0.423	0.402	0.36	0.285
Δ_0	1.099	1.214	1.273	1.303	1.312	1.303	1.273	1.214	1.099

It is easy to verify that a function of the type

$$g(\varepsilon) = \frac{4n_D(\varepsilon-\mu)^2}{\varepsilon_D^3}\exp\frac{\mu^2-\varepsilon^2}{\gamma^2} \qquad (2)$$

with the adjustable parameters μ and γ satisfies all the requirements given in items (i)–(iii) (see below). In this case, the parameter μ is the energy at the Fermi level and the parameter γ characterizes the widths of the peaks mentioned in item (i).

In order to determine the adjustable parameters, it is necessary to use the normalization condition $\int_{-\infty}^{\infty} g(\varepsilon)d\varepsilon = n_D$ and the condition of electrical neutrality, which, at absolute zero temperature, has the form $\int_{\mu}^{\infty} g(\varepsilon)d\varepsilon = n_A$.

Taking into account these conditions and relationship (2) for the dimensionless parameters $c = \mu/\varepsilon_D$ (where c is the Fermi energy expressed in units of ε_D) and $a = \left(\frac{\gamma}{\varepsilon_D}\right)^2$, we obtain the system of transcendental equations

$$\begin{gathered} 1+\frac{2c^2}{a} = \frac{1}{2\sqrt{\pi a^3}}\exp\left(-\frac{c^2}{a}\right), \\ \operatorname{erfc}\left(\frac{c}{\sqrt{a}}\right) = 2K+\frac{4c}{a}, \end{gathered} \qquad (3)$$

where erfc(x) is an error function.

Numerical solutions to the systems of transcendental equations for different degrees of compensation are presented in the table.

It can be seen from the table that, in the range $K <$ 0.5, the Fermi energy satisfies the inequality $\mu > 0$ (the energy is reckoned from the energy level of the isolated donor state E_D). In this range, the parameter μ monotonically decreases with an increase in the parameter K and becomes zero ($\mu = 0$) at $K = 0.5$. In the range $1 > K > 0.5$, the parameter μ is negative in sign ($\mu < 0$) and again monotonically decreases as the parameter K increases.

Let us assume that the width of the Coulomb gap is the energy separation between the peaks. Hence, it follows from relationship (2) that the width of the Coulomb gap expressed in units of ε_D is determined by the formula

$$\Delta_0 = \sqrt{c^2+4a}. \qquad (4)$$

According to the numerical estimates given in the table, the width of the Coulomb gap Δ_0 has a maximum at $K = 0.5$ and decreases in the limiting cases of weak ($K \longrightarrow 0$) and strong ($K \longrightarrow 1$) compensations. Moreover, taking into account the fact that, at the limiting compensations, the height of one of the peaks tends to zero, we can argue that, under these conditions, the Coulomb gap can be ignored.

All the above results fully coincide with the data obtained by numerical simulation in [4, 5]. Therefore, these results can be used in analyzing experimental data on the kinetic and optical properties of the aforementioned systems.

REFERENCES

1. M. L. Knotek and M. Pollak, Phys. Rev. B **9**, 664 (1974).
2. T. Kurosava and H. Sugimoto, Prog. Theor. Phys. Suppl. **57**, 217 (1975).
3. A. L. Efros and B. I. Shklovskii, J. Phys. C: Solid State Phys. **8**, L49 (1975).
4. B. I. Shklovskii and A. L. Efros, *Electronic Properties of Doped Semiconductors* (Nauka, Moscow, 1979; Springer, New York, 1984).
5. B. I. Shklovskii and A. L. Efros, Fiz. Tekh. Poluprovodn. (Leningrad) **14**, 825 (1980) [Sov. Phys. Semicond. **14**, 487 (1980)].
6. É. V. Devyatov, A. A. Shashkin, V. T. Dolgopolov, W. Hansen, and M. Holland, Usp. Fiz. Nauk **170** (3), 327 (2000) [Phys. Usp. **43**, 285 (2000)].
7. A. G. Andreev, A. G. Zabrodskiĭ, I. P. Zvyagin, and S. V. Egorov, Fiz. Tekh. Poluprovodn. (St. Petersburg) **31** (10), 1174 (1997) [Semiconductors **31**, 1008 (1997)].
8. A. G. Zabrodskiĭ, Usp. Fiz. Nauk **168** (7), 804 (1998) [Phys. Usp. **41**, 722 (1998)].
9. V. M. Barzdov and T. A. Petrovich, Fiz. Tekh. Poluprovodn. (St. Petersburg) **31** (1), 89 (1997) [Semiconductors **31**, 72 (1997)].
10. S. L. Haroutunian, V. A. Haroutunian, H. A. Jivanian, and G. O. Demirjian, Thin Solid Films **258**, 347 (1995).
11. N. A. Poklonskiĭ, S. Yu. Lopatin, and A. G. Zabrodskiĭ, Fiz. Tverd. Tela (St. Petersburg) **42** (3), 432 (2000) [Phys. Solid State **42**, 441 (2000)].
12. D. V. Nikolaenkov, V. N. Arkhipov, and V. R. Nikitenko, Fiz. Tekh. Poluprovodn. (St. Petersburg) **34** (6), 682 (2000) [Semiconductors **34**, 655 (2000)].

Translated by O. Moskalev

Physics of the Solid State, Vol. 47, No. 4, 2005, pp. 606–613. Translated from Fizika Tverdogo Tela, Vol. 47, No. 4, 2005, pp. 583–590.
Original Russian Text Copyright © 2005 by Bagaev, Klevkov, Zaĭtsev, Krivobok.

SEMICONDUCTORS AND DIELECTRICS

Photoluminescence of ZnTe Crystals Grown under Deviation from Thermodynamic Equilibrium

V. S. Bagaev, Yu. V. Klevkov, V. V. Zaĭtsev, and V. S. Krivobok
Lebedev Physical Institute, Russian Academy of Sciences, Leninskiĭ pr. 53, Moscow, 119991 Russia
e-mail: bagaev@lebedev.ru

Received June 29, 2004

Abstract—Crystalline textured and columnar structures, as well as needlelike ZnTe single crystals, were grown from the vapor phase and in a tellurium melt under deviation of the growth conditions from equilibrium. Low-temperature photoluminescence and x-ray structural studies showed the samples thus grown to exhibit high structural perfection, a uniform impurity distribution, and weak interaction between impurities and defects of the crystal structure. Polariton scattering from neutral donors was detected in structures having a noticeable residual concentration of donors in the substituted state. It is shown that the spectrum of samples grown under nonequilibrium conditions exhibits transitions that are not typical of equilibrium crystals. Measurements of the luminescence spectra as a function of temperature, excitation level, and annealing conditions made it possible to draw tentative conclusions about the nature of these transitions. *© 2005 Pleiades Publishing, Inc.*

1. INTRODUCTION

ZnTe is a material that holds considerable promise for modern optoelectronics. However, its device potential is limited because of the so-called problem of self-compensation, which prevents the development of an *n*-type material even under moderate doping. More than one model has thus far been proposed for self-compensation [1–4]. These models are based, as a rule, on the interaction of a native lattice defect with a donor impurity, culminating in the formation of complexes of a nontrivial nature during the crystal growth. In the first stage, the formation of such a complex consists naturally in the creation of a spaced donor–compensating-defect pair, which subsequently transforms into a complex due to diffusion (as the internal equilibrium is established in the long time taken by the growth of the crystal and its cooling down to room temperature). The models proposed for the compensation suggest that, at high enough growth rates, the diffusion of the components making up the complex becomes inefficient. In this case, the donor and the compensating defect will remain predominantly in a separated state. The realization of nonequilibrium conditions conducive to such effects is also of interest from another respect. As shown in [5–7], if a crystal is grown from the vapor phase, a sufficiently high supersaturation may give rise to a change in morphology, e.g., to a change of the growth planes, which may result, in turn, in a crossover to another mechanism of impurity incorporation into the lattice and a change in the type of "leading" structural lattice defect. Thus, investigation of ZnTe obtained in nonequilibrium conditions could prove useful both for shedding light on the mechanism of self-compensation and from the standpoint of developing technologies for the production of materials exhibiting novel properties.

We report here on a low-temperature photoluminescence (PL) study of undoped ZnTe crystals obtained by free crystallization from the vapor phase and liquid tellurium through the vapor–liquid–crystal mechanism [8] under growth conditions deviating from equilibrium. Furthermore, the effect of various annealing conditions on the PL spectra of the polycrystals thus obtained was also investigated. This culminated in the detection of a number of remarkable features characteristic of nonequilibrium growth conditions.

The paper is organized as follows. Section 2 describes the technology of crystal growth and the experimental techniques used. Section 3 presents a general analysis of PL spectra of series *Z*6*V* and *Z*6*L*. Section 4 discusses the results obtained and the effects associated with the influence of the donor impurity and outlines the results of a study of a doubly charged acceptor in *Z*6*L*.

2. TECHNOLOGY AND EXPERIMENTAL TECHNIQUES

Undoped ZnTe crystallites of different shape and orientation were grown in liquid tellurium at a temperature of ~700°C through the vapor–liquid–crystal mechanism (series *Z*6*L*). A continuous zinc vapor flow from a cell, which was maintained at ~720°C (P_{Zn} ~ 80 Torr), was admitted to a cylindrical quartz cell with liquid tellurium 150 g in mass held at ~700°C (P_{Te} ~ 30–35 Torr). Both cells were mounted in a quartz reactor, with the growth proceeding in dynamic vacuum. The starting components used in this process were preliminarily purified by vacuum distillation. The crystallite growth procedure took about 50–60 min until no components remained. We believe that the changes observed in the structure of growing ZnTe (the free-growth direction and growth rate of crystallites) are associated with the supersaturation varying as the tellurium volume phase is expended in the course of ZnTe formation, as well as with violation of the liquid-phase stability initiated by concentration and temperature fluctuations immediately before the crystallization front. Because the cross-sectional thickness of the tellurium melt in the cell of the above design represents a segment with a maximum height of up to 5 mm, the formation of the ZnTe structure in different cross sections has specific features.

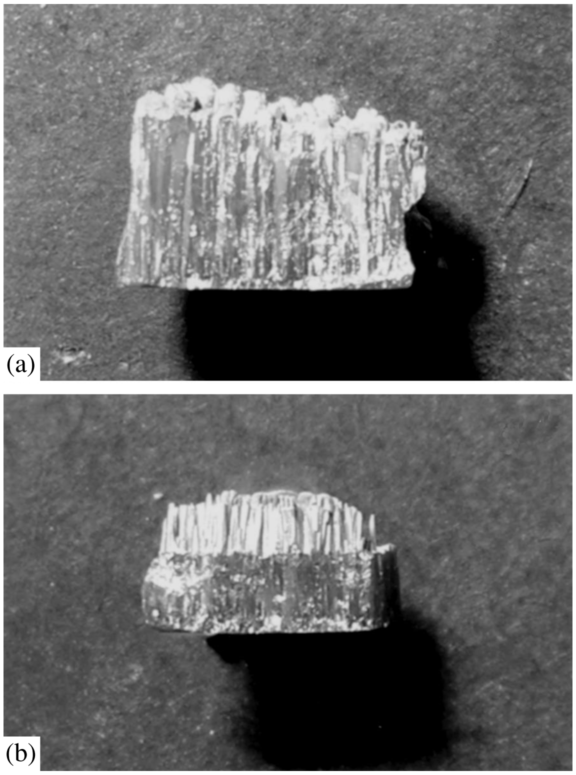

Fig. 1. Photographs (a) of a *Z6L* texture along the [111] growth direction, which terminates in outgrowths of smaller crystallites, and (b) of a *Z6L* structure with a morphological transition associated with a change in supersaturation at the crystallization front.

Figure 1 shows photographs of fragments of the ZnTe structure taken from different parts of the segment. Preliminary studies of the growth direction (by using x-ray diffraction) and luminescent properties of ZnTe were carried out on the fragment presented in Fig. 1a. The diffractogram exhibits reflections of one series ([111], [222], [333]) from ZnTe and a weak [003] reflection due to Te. This suggests that the central part of the segment consists only of [111] fibers, which may slightly deflect from the normal to the growth surface toward the Zn flow. The presence of a small amount of Te with the basal plane oriented parallel to the film surface and the absence of other reflections indicate directed penetration of tellurium over the ZnTe grain boundaries. Our attempt to accurately determine the epitaxial relation between ZnTe and Te did not meet with success because of the low tellurium concentration. In the same process, needlelike ZnTe crystals (*Z6V* series), produced from the vapor phase in the chemical reaction between the components, grew on the end wall of the tellurium cell.

PL spectra were measured in He vapor in the temperature interval from 5 to 45 K. Optical pumping was provided by an argon laser with excitation lines at 5145 Å (2.41 eV) and 4880 Å (2.54 eV). The excitation spot was ~100 μm in size. The spectra were analyzed with a DFS-24 double monochromator with a resolution of at least 0.1 meV. The PM tube output was processed in the photon counting mode.

3. RESULTS OF THE EXPERIMENT

3.1. Photoluminescence of Samples Grown from the Vapor Phase (Z6V Series)

Figure 2a presents for illustration a PL spectrum of a crystal from the *Z6V* series. Samples of this series have a high PL quantum yield, and their PL spectra demonstrate extremely high reproducibility for different crystallites.

We will now dwell briefly on the notation of the transitions observed in the spectrum. The transitions can be conveniently divided into intrinsic radiation, radiation associated with substitutional impurities, radiation originating from complex defects, and LO-phonon replicas of the luminescence lines. The complex structure observed in the free-exciton region can be accounted for in terms of the polariton concept taking into account valence band degeneracy. It is known that, in this case, the spectrum derives from radiation produced by the lower (LP), upper (UP), and middle (MP) polariton branches [9]. The splitting observed in the radiation deriving from the lower polariton branch is due to a neutral donor.

The radiation deriving from isolated substitutional impurities in samples of the *Z6V* series is due to band–impurity (*e*–*A*) transitions, donor–acceptor (DA) pairs, and exciton–impurity complexes. The strongest PL line in *Z6V* samples (A^0X) is produced in an optical transition in which the localized hole left after annihilation of an exciton that was bound to a neutral acceptor remains in the ground state. The two-hole (TH) transitions seen at longer wavelengths occur in processes in which the localized hole left after exciton annihilation is in one of the excited states. Such states are denoted in what follows by $|F\rangle A$, where F identifies an excited hole state and A stands for a substitutional impurity (for example, $3S_A$ Li). The excited states are classified in accordance with a theoretical paper [10]. The exciton localized on a neutral donor can be treated in a similar manner;

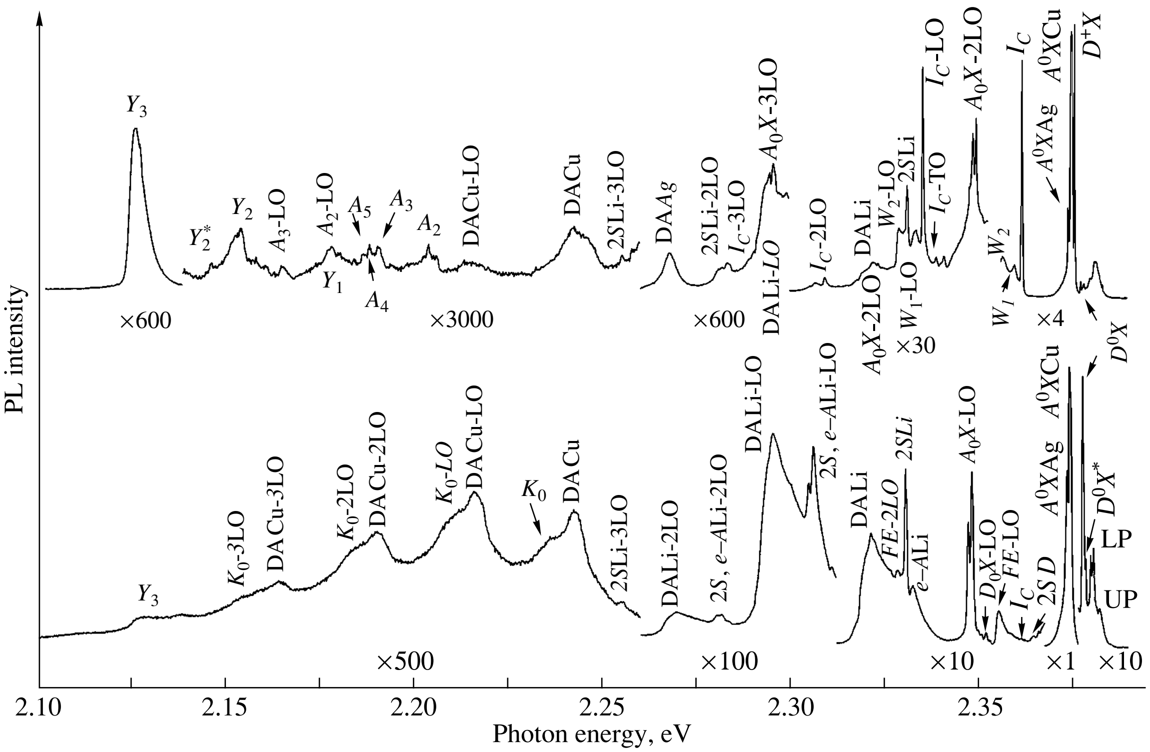

Fig. 2. PL spectra of samples of (a) *Z*6*V* and (b) *Z*6*L* series.

namely, there is a ground-state line D^0X and a series of two-electron (TE) transitions, whose notation is similar to that employed for two-hole transitions, with the only difference being that $|F\rangle$ is understood now to be an excited electron state.

The *Z*6*V* PL spectrum clearly reveals two main acceptors in the substitutional state, Li and Cu. The A^0X line, however, has a doublet structure, whose strongest peak (~2.3749 eV) coincides in position, to within experimental error, with the A^0X lines for Li and Cu. The second, weaker peak (~2.3740 eV) coincides in position with the A^0X for Ag and the so-called *k* acceptor [11]. Other indications of the presence of Ag and the *k* acceptor (the corresponding TH or DA transitions) were not detected.

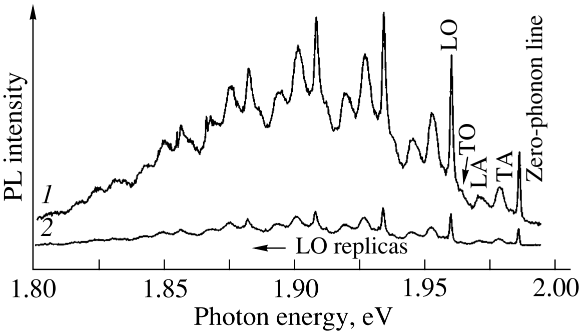

Fig. 3. PL spectra of (*1*) *Z*6*V* and (*2*) *Z*6*L* samples in the oxygen region.

The presence of a donor impurity (tentatively identified with Cl_{Te}) in the substitutional state is suggested by the D^0X (2.3779 eV) and D^0X^* (2.3785 eV) lines [12] and the TE and DA transitions. The noticeable concentration of the donor in the substitutional state and the fairly good quality of the crystal lattice permitted detection of a number of remarkable features caused by polariton interaction with a neutral donor. These features are discussed in Subsection 4.1.

The weak transition (I_C) at around 2.3619 eV corresponds to the ground-state line of the exciton localized at a doubly charged acceptor [13]. Observation of this transition is typical of crystals grown in conditions deviating from equilibrium. In the long-wavelength part of the *Z*6*V* spectrum (Fig. 3), there is radiation associated with the isoelectronic impurity O_{Te} and the K_0 complex, which includes a Zn vacancy [14] (Fig. 2a). Note also that the *Z*6*V* spectra have no lines characteristic of ZnTe that are associated with extended defects. The only exception is possibly a weak Y_3 line, which is discussed in detail in Subsection 3.2.

3.2. Photoluminescence of Samples Grown in Liquid Te through the Vapor–Liquid–Crystal Mechanism (Z6L Series)

Spectra of these polycrystals exhibit variations in the integrated PL intensity through the height of the structure, as well as slight changes in the relative intensity of some lines. Note that the PL intensity at the edge of the spectra of *Z*6*L* crystals is, on the average, one-fourth of that of the *Z*6*V* crystals.

Figure 2b presents a spectrum of a *Z*6*L* polycrystal. Of major interest in this case is the appearance of a nonstandard structure in the region of the A^0X and D^0X lines. The two long-wavelength components (~2.3740 and ~2.3750 eV) are the A^0X lines for Ag and a band of spectrally unresolved A^0X lines for Cu and Li. The presence of these impurities is corroborated by the detection of the corresponding DA transitions and, in addition, of the TH transitions for Li. The two short-wavelength components (~2.3779 and ~2.3785 eV), just as in the *Z*6*V* spectra, are actually the D^0X and D^0X^* lines. The presence of a neutral donor is also supported by the appearance of a weak TE transition and a dip in the polariton luminescence spectrum (in some places, when the D^0X line is weak, the dip transforms into a structural feature), which derives from the polariton scattering on a neutral donor.

Of major interest is the fairly strong narrow line at ~2.3760 eV. We assigned it to a transition corresponding to recombination of an exciton localized on a charged donor. The specific features of the PL spectra and arguments for this interpretation are considered in detail in Subsection 4.2.

The strong line (I_C) in the region of 2.3619 eV, the two broad bands W_1 and W_2, and a series of long-wavelength satellites A_2–A_5 originate from recombination of an exciton bound to a doubly charged acceptor, which is typical of nonequilibrium growth processes occurring at an excess of Te.

Note that, in contrast to *Z*6*V*, the spectra of *Z*6*L* crystals contain broad bands Y_1 and Y_2. The corresponding transitions were shown in [15–17] to be associated with extended defects, such as dislocations. The Y_1 and Y_2 bands in these samples may originate from grain boundaries (which are absent in *Z*6*V* single crystals). Let us consider the Y_3 line (~2.126 eV) in more detail; this line was observed by us, although in a less pronounced form, in other nonequilibrium crystals and was not detected in crystals obtained in quasi-equilibrium conditions. The intensity of the PL associated with this transition reveals a tendency toward rapid decay with time (the PL intensity drops by a few times in a few minutes). This process is reversible, with the signal recovering rapidly after the excitation is removed. This line also exhibits fairly rapid quenching as the temperature increases (there is practically no signal at $T \sim 30$ K). In crystals grown under deviation from equilibrium, this line is practically insensitive to vacuum annealings and low-temperature heating (at ~400°C) in a zinc atmosphere; this line disappears completely, however, in *Z*6*L* crystals annealed in Zn vapor at $T = 820$°C. We believe that the Y_3 line is associated with the formation of a compound of another phase (primarily on the natural growth surface, which accounts for the high quantum yield of this band in *Z*6*L* samples); further studies would, however, be needed to ascertain the nature of this transition. Note that the Y_1, Y_2, and Y_3 lines have a zero Huang–Rhys factor, which is not characteristic of states produced by point defects.

4. DISCUSSION OF THE RESULTS

4.1. Scattering of a Slow Polariton from a Neutral Donor

As already mentioned, nonequilibrium growth of a crystal from the vapor phase (*Z*6*V* series) permits one to reach a noticeable residual concentration of neutral donors in the substituted state. This feature, combined with the high structural perfection of the crystal lattice, made it possible to observe interaction of the so-called slow exciton-like polaritons with neutral donors. Such effects have been seen in the luminescence of undoped GaAs epitaxial films containing different residual concentrations of donors [18]. The situation with GaAs is known to be analogous to that with ZnTe in that the values of $E_{\rm EX}$ are similar: $E_{\rm D} \ll E_{\rm A}$, $m_{hh}/m_e \sim 5$, and $R_{\rm EX} \sim R_{\rm D} \gg R_{\rm A}$, where $E_{\rm A}$ and $R_{\rm A}$ are the binding energy and localization length of the hole at an acceptor, respectively; $E_{\rm D}$ and $R_{\rm D}$ are the binding energy and localization length of the electron at a donor; and $R_{\rm EX}$ is the Bohr radius of the exciton. Thus, the mechanisms of elastic scattering of excitons from neutral impurities proposed in [18] may be similar in character in ZnTe and GaAs. As shown for GaAs, the elastic scattering cross section of a slow exciton (kinetic energy, ~0.1 meV) from a donor exceeds that on an acceptor by more than an order of magnitude. If the donor concentration is high enough, the diffusion length of a slow exciton-like polariton decreases strongly and a dip appears in the intrinsic PL spectrum near the exciton band bottom.

Figure 4 displays fragments of PL spectra of different ZnTe crystals in the polaritonic emission region. Crystals with a low donor concentration (curve *1*) reveal a triplet structure of radiation associated with three polariton branches [9]. The intrinsic radiation of a *Z*6*V* crystal excited by 2.54-eV photons (curve *2*) also consists of three polaritonic branches, but with a dip in the region of the lower branch emission. This structure of intrinsic PL cannot be related to a manifestation of additional features in the dispersion curves of *Z*6*V*, because the dip also appears in the emission from nonthermalized polaritons. Curve *3* plots the radiation spectrum of a fine-grained structure excited by 2.41-eV photons, which is above the exciton band bottom by about the LO phonon energy. Also, we estimated the crystallite size (a few micrometers) to be comparable to the diffusion length corresponding to polariton thermalization due to acoustic phonons. Thus, the populations of polariton states are not thermalized in this case, and this becomes manifest in the polaritonic PL.

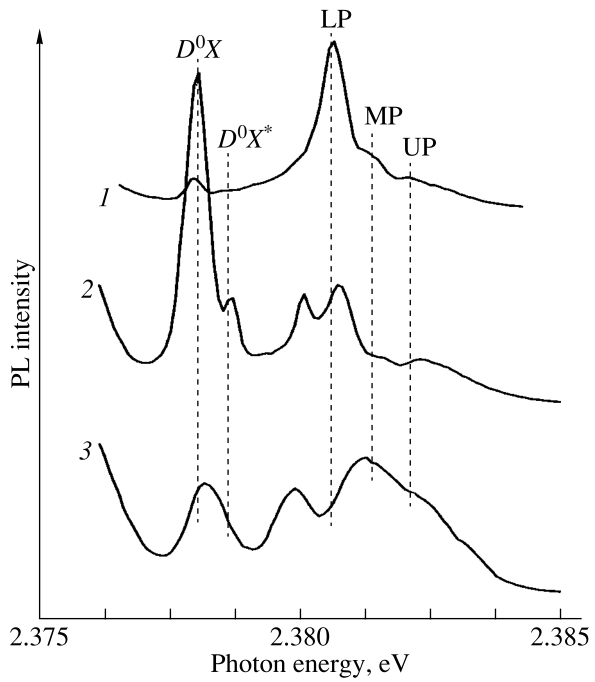

Fig. 4. PL spectra of (*1*) a crystal with a low donor concentration (pumped at 4880 Å), (*2*) a *Z*6*V* crystal (pumped at 4880 Å), and (*3*) a fine-grained structure with grains a few μm in size (pumped at 5145 Å).

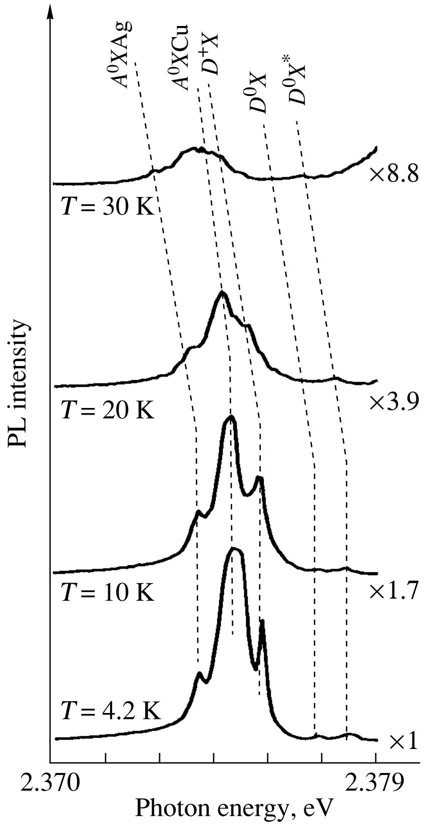

Fig. 5. Temperature dependence of the D^+X line.

Note that the feature observed in the structureless line is not seen in the LO replica of polaritonic radiation. This implies that the dip is absent in the real population of polariton states inside the crystal. This observation supports the elastic character of polariton scattering. The small mean free path of slow polaritons due to such scattering reduces their diffusion length and increases their localization probability inside the crystal. The strong correlation of the dip with the concentration of the neutral donor impurity (the latter is derived in a straightforward manner from the line intensities of the D^0X and TE transitions) in all the crystals studied and the absence of such effects for any other lattice irregularity (acceptor impurities, complex defects, etc.) suggest that this scattering takes place, as in the GaAs case, from neutral donors.

The above spectra can be used to estimate the polariton scattering cross section from a donor near the minimum of the group velocity of the polariton. It is known that the radiation from spaced donor–acceptor pairs (in our case, the zero-phonon lines at ~2.243 eV for Cu and at ~2.322 eV for Li) offers the possibility of estimating the impurity concentration [19]. The results given in [19] permit an upper estimate of the neutral donor concentration of $\sim 2 \times 10^{16}$ cm^{-3}. In terms of our model, a dip will appear in the PL spectrum if the polariton mean free path L_P near the minimum of its group velocity is comparable to the absorption depth of the pump light (4880 Å) or less. Thus, for a lower estimate of the cross section σ, we obtain

$$L_P \sim 1/n\sigma \sim 0.3\ \mu\text{m},$$

$$\sigma \sim 1/nL_P \sim 1.6 \times 10^{-12}\ \text{cm}^2 \sim \pi R_{\text{EX}}^2.$$

4.2. Exciton Localized on a Charged Donor

The strong D^+X line observed in the *Z*6*L* crystal near ~2.3760 eV may be of potential interest for establishing the presence of a donor impurity. Near this energy position are known to be the h–D transition (the hole from the valence band annihilates with a donor-bound electron) and the transition associated with the excited state of the exciton localized on the copper atom, A^0X^*Cu [11]. In our case, however, this assignment comes into conflict with some features of this line (a small halfwidth, ~0.3 meV, and a high intensity) and its temperature dependence (Fig. 5). The intensity of the excited-state line A^0X^*Cu as compared to the intensity of A^0XCu should grow exponentially with increasing temperature [11]. This line is discussed in [20], which reports on a study of Cl-doped epitaxial films grown on ZnTe substrates. In the case of *Z*6*L*, apparently, this line can also be related to Cl_{Te} on account of Cl atoms being present in the starting components; furthermore, chlorine was shown in [21] to enter the lattice more efficiently in the presence of excess tellurium. The specific relation of this impurity with the tellurium sublattice is also supported by the effect of annealing on the above transition. Figure 6a displays spectra of *Z6L* crystals in the corresponding spectral region before annealing, after annealing at $T = 820°C$ in Zn vapor for 72 h, and after vacuum annealing at 500°C for ~5 h. We can see that annealing in Zn vapor has almost no influence on this transition, whereas short annealing in vacuum brings about the disappearance of the line under study while not noticeably influencing the spectrum of the sample with the impurity present on the zinc sublattice (A^0X, TH transition).

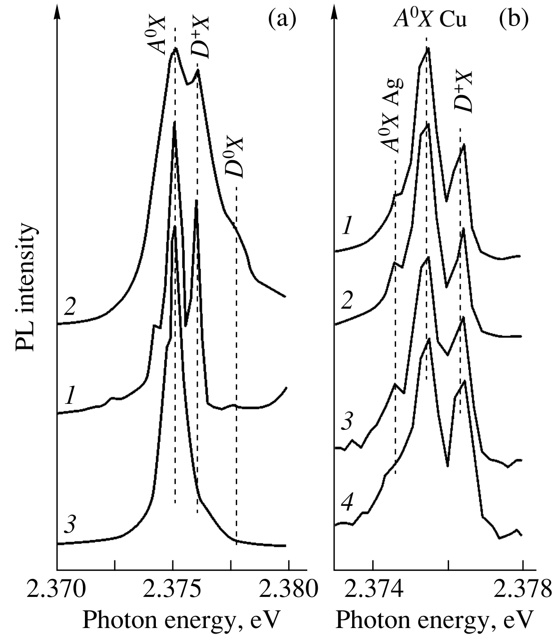

Fig. 6. (a) Effect of annealing on PL line D^+X: (*1*) starting crystal, (*2*) annealing in Zn vapor at $T = 820°C$ for 72 h, and (*3*) annealing in vacuum at $T = 500°C$ for 5 h. (b) Relative intensity of the D^+X and A^0X lines for various values of the pump power: (*1*) 400, (*2*) 55, (*3*) 15, and (*4*) 1 W/cm^2.

It is known that Cl_{Te} in ZnTe is a shallow donor [22]. The temperature dependence of the above transition illustrated in Fig. 5 suggests that the corresponding center should be a bound exciton. For this reason, this transition was tentatively interpreted in [21] as D^0X[Cl]. We assign this transition to D^+X[Cl] (exciton localized on a charged donor). In contrast to excitons localized on charged acceptors, the donor-localized exciton should be stable in ZnTe, because $\nu = m_{hh}/m_e \sim 5$, which is in excess of the available theoretical estimates of ν at which the corresponding complex becomes unstable. Furthermore, the D^+X line has been reliably detected in the related compound CdTe [23]. The following observations may be considered indirect evidence supporting this hypothesis.

(1) There is an absence of any new satellites belonging to this center, for instance, of TE transitions related to the line under consideration.

(2) The dependence of the intensity of this line on pump power (Fig. 6b). The intensities of the A^0X and D^0X lines decay faster with decreasing pump power than does the D^+X intensity, because the donors and shallow acceptors (Li) are primarily in the charged state in the absence of excitation and the exciton–impurity complex, unlike the complex associated with D^+X, forms in two stages.

(3) The fact that the D^+X line does not influence the polariton luminescence is, as already mentioned, not characteristic of shallow donors in the neutral state.

One of the problems arising in the assignment of this line is the involvement of a deep compensating acceptor level. This level may be related to a doubly charged acceptor (see Subsection 4.3), which, like D^+X, manifests itself strongly in *Z6L*.

4.3. Doubly Charged Acceptor

The PL spectrum of practically all our samples prepared under substantial deviation from equilibrium contains a more or less pronounced series of transitions originating from a doubly charged acceptor [13]. The strong line I_C at 2.3619 eV, which is seen in both the PL and absorption spectra, derives from annihilation of the exciton bound to such an acceptor. Annihilation of the holes localized at acceptors leaves them in the ground state and is accompanied, as a rule, by two fairly broad satellites, W_1 and W_2. It was shown in [13] that the $n = 1$ state of a system splits in J into two sublevels with $J = 0$ (Γ_1) and $J = 2$, with the latter being crystal-field-split into the Γ_3 and Γ_5 states (Γ_i are irreducible representations of the point group of the crystal). Thus, the triplet structure given by I_C, W_1, and W_2 is due to the presence of three sublevels in the final state of the system, the lowest of them being Γ_3. In the long-wavelength region of the spectrum, there is also a series of satellites (A_2–A_5), which allows interpretation in terms of the two-hole transition concept. This series allows one to estimate the acceptor ground-state energy as $E = 180 \pm 2$ meV.

The above center was observed to produce PL after prolonged annealing (~5 days) of undoped samples in Zn vapor at $T = 750–950°C$ [24]. Also, the acceptor state with $E_A \sim 180$ meV (revealed in electrical measurements of annealed samples) affected the Fermi level in some cases.

Let us sum up the main properties of the doubly charged acceptor as applied to the samples under study. First, we note that this transition is never present in crystals grown from the vapor phase at close-to-equilibrium conditions. The I_C band of varying intensity almost always appears when the growth conditions deviate from equilibrium; this band becomes quite strong under nonequilibrium growth in the presence of excess tellurium (exactly what is observed in *Z6L* samples). All of the annealings conducted here (in Zn vapor for 72 h at $T = 820°C$ or for 48 h at $T = 400°C$; in

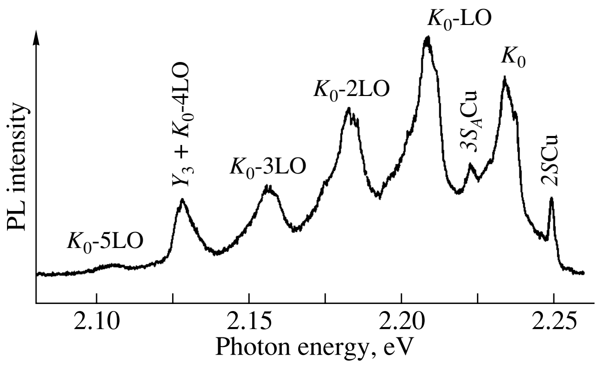

Fig. 7. Radiation associated with the K_0 complex and observed after annealing of *Z*6*L* in vacuum at $T = 500°C$ for 5 h.

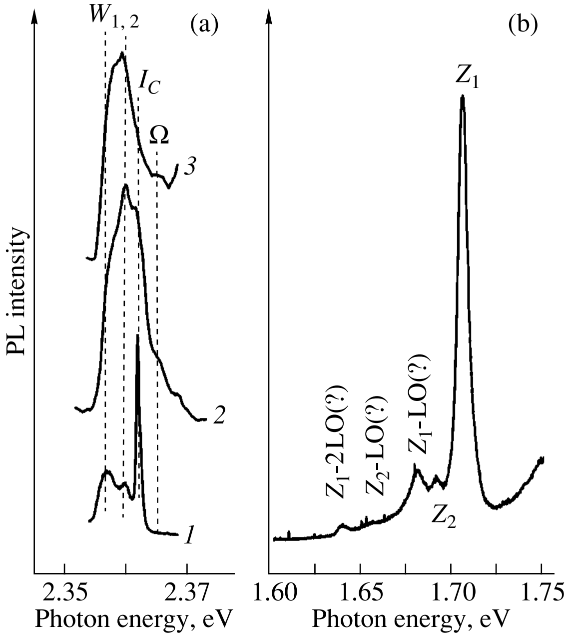

Fig. 8. (a) PL spectrum in the region of the I_C line: (*1*) starting *Z*6*L* sample at $T = 5$ K, (*2*) starting *Z*6*L* sample at $T = 30$ K (with inclusion of the band shift), and (*3*) *Z*6*L* after annealing in Zn vapor at $T = 820°C$ for 72 h. (b) PL spectrum in the region of *Z* lines.

dynamic vacuum for 5 h at 500°C) brought about a disappearance of the I_C band from the spectrum.

Short annealing in vacuum brought about, in addition, the formation of a binary complex (Fig. 7) including the V_{Zn} vacancy [14]; the second component of this complex is most probably Cl_{Te}. The formation of this vacancy may be traced to zinc depletion of the ZnTe surface layer occurring in dynamic vacuum. In review [25], the I_C band was also related to isolated V_{Zn} vacancies. This concept suggests another mechanism of the formation of the above complex involving the diffusion of Cl_{Te} and V_{Zn}, which were originally present in the crystal (in the case of the charged vacancy state V_{Zn}^-, Coulomb interaction should favor this mechanism of complex formation). In view of the large vacancy diffusion coefficients, this model offers a straightforward explanation of the effect of low-temperature (~400°C) annealing in Zn.

As already mentioned, the I_C line was observed after prolonged annealing in Zn vapor at temperatures $T \sim$ 750–950°C [24]. While *Z*6*L* samples annealed in Zn vapor for 72 h at $T = 820°C$ do not exhibit the I_C line, a shorter wavelength band Ω peaking at ~2.365 eV (Fig. 8a) appears in the spectrum. This controversy in the interpretation of V_{Zn} could be associated with the fact that, due to the fairly strong compensation resulting from the noticeable concentration of Cl_{Te}, the doubly charged acceptor in annealed *Z*6*L* crystals may reside primarily in the charged state (by capturing one electron). In the case where the doubly charged acceptor is in the neutral state, the process of emission can be divided into two stages, namely, capture of a nonequilibrium hole followed by localization of the exciton. Relaxation among the Γ_1, Γ_3, and Γ_5 states (responsible for the I_C, W_1, and W_2 emission) in a one-step process is *J* forbidden, so the corresponding relaxation times should be fairly long. Thus, in this case, it may be conjectured that the I_C, W_1, and W_2 bands are emitted in the absence of thermalization (i.e., without dominant population of Γ_3) among the Γ_1, Γ_3, and Γ_5 sublevels in an annealed crystal. As the temperature increases to 30 K (where $kT \sim 2.5$ meV is comparable to the splitting between Γ_1, Γ_3, and Γ_5 and, hence, the population of Γ_3 likewise should not dominate), long-wavelength components are indeed observed in the spectra of unannealed *Z*6*L* samples, one of which coincides with the Ω band, provided the temperature-induced shift is taken into account. Another interesting feature associated with the Ω band is its correlation with a number of long-wavelength lines (*Z*), which also appear in the PL spectrum after prolonged annealing in Zn vapor (Fig. 8b). These lines may also derive from the doubly charged acceptor, for instance, from the DA or *e*–*A* transitions in a deep charged center. Further studies would be needed to ascertain the nature of the *Z* and Ω lines.

5. CONCLUSIONS

Textured and columnar structures and needlelike single crystals have been obtained in a single process based on a modification of nonequilibrium low-temperature synthesis of crystalline ZnTe in a liquid layer of tellurium and from the vapor phase. The high luminescence quantum yield, the small spectral width of the exciton–impurity complex lines (~0.3 meV), and the observation of TH transitions and strong exciton-polariton emission indicate a high structural perfection of these samples.

The samples prepared in the nonequilibrium growth regime are characterized by a close-to-uniform distribution of impurity atoms (donors and acceptors) over the crystal lattice and weak interaction between impurities and lattice defects, which is signaled by the absence of bands typical of such a process in the spectrum.

The PL spectrum of *Z*6*V* samples is the most instructive in this sense. This spectrum consists essentially of an intense polariton band; clearly resolved D^0X and A^0X lines; TH, TE, and *e–A* transitions; separated DA pairs; and phonon replicas of the above luminescence lines. The appearance of the strong D^0X line in the spectrum and observation of the TE and DA transitions imply a noticeable concentration of neutral donors, which accounts for the specific feature in the polariton spectrum deriving from polariton scattering on neutral donors.

The PL spectrum of ZnTe samples obtained in the same process by chemical synthesis from liquid tellurium is largely similar to that of *Z*6*V*. However, the enhanced Te content and the existence of grain boundaries give rise to the appearance of a nonstandard bound-exciton line located at 2.3762 eV in the PL spectrum, a noticeably increased intensity of the structured line belonging to the exciton localized at a doubly charged acceptor, weak Y_1 and Y_2 lines, and the observation of a previously unreported intense line Y_3 exhibiting a nonstandard dependence on excitation duration.

The measured dependences of the luminescence spectra on the temperature and pumping level, as well as on the different annealing conditions for *Z*6*L* samples, have made it possible to identify the 2.3762-eV line as being due to the exciton localized at a charged donor, D^+X [Cl] and to consider the zinc vacancy V_{Zn} a doubly charged acceptor accounting for the formation of the exciton–impurity complex I_C.

ACKNOWLEDGMENTS

The authors are indebted to V.P. Martovitskiĭ for performing the x-ray structural measurements and for helpful discussions.

This study was supported by the Russian Foundation for Basic Research (project nos. 02-02-17392, 03-02-16854, 04-02-17078) and the Foundation for Support of Leading Scientific Schools (project no. 1923.2003.2).

REFERENCES

1. S. I. Cheyas, S. Hirano, M. Nishio, and H. Ogawa, Appl. Surf. Sci. **100/101**, 634 (1996).
2. J. A. Garcfa, A. Remon, V. Munoz, and R. Triboulet, Jpn. J. Appl. Phys. **38**, 5123 (1999).
3. S. Lee and K. J. Chang, Phys. Rev. B **57** (11), 6239 (1998).
4. J. Bittebierre and R. T. Cox, Phys. Rev. B **34** (4), 2360 (1986).
5. A. Hill, Nature **348**, 426 (1990).
6. P. Galenko and S. Sobolev, Phys. Rev. E **55**, 343 (1997).
7. I. Prigogine and D. Kondepudi, *Modern Thermodynamics* (Wiley, Chichester, 1998; Mir, Moscow, 2002).
8. A. A. Chernov, E. I. Givargizov, Kh. S. Bagdasarov, V. A. Kuznetsov, Ya. N. Dem'yanets, and A. N. Lobachev, *Modern Crystallography,* Vol. 3: *Crystal Growth*, Ed. by B. K. Vaĭnshteĭn, A. A. Chernov, and L. A. Shuvalov (Nauka, Moscow, 1980; Springer, Berlin, 1984).
9. V. S. Bagaev, V. V. Zaĭtsev, Yu. V. Klevkov, V. S. Krivobok, and E. E. Onishchenko, Fiz. Tekh. Poluprovodn. (St. Petersburg) **37** (3), 299 (2003) [Semiconductors **37**, 283 (2003)].
10. M. Said and M. A. Kanehisa, J. Cryst. Growth **101**, 488 (1990).
11. P. J. Dean and H. Venghaus, Phys. Rev. B **21** (4), 1596 (1980).
12. P. J. Dean, D. C. Herbert, and A. M. Lahee, J. Phys. C **13**, 5071 (1980).
13. P. J. Dean, M. J. Kane, N. Magnea, F. de Maigret, L. S. Dang, A. Nahmani, R. Romestain, and M. S. Skolnick, J. Phys. C **18**, 6185 (1985).
14. B. A. Wilson, C. E. Bonner, R. D. Feldman, R. F. Austin, D. W. Kisker, J. J. Krajewski, and P. M. Bridenbaugh, J. Appl. Phys. **64** (6), 3210 (1988).
15. A. Naumov, K. Wolf, T. Reisinger, H. Stanzl, and W. Gebhardt, J. Appl. Phys. **73** (5), 2581 (1993).
16. S. I. Gheays, S. Hirano, M. Nishio, and H. Ogawa, Appl. Surf. Sci. **100/101**, 647 (1996).
17. K. Wolf, A. Naumov, T. Reisinger, M. Kastner, H. Stanzl, W. Kuhn, and W. Gebhardt, J. Cryst. Growth **135**, 113 (1994).
18. S. Koteles, J. Lee, J. P. Salerno, and M. O. Vassell, Phys. Rev. Lett. **55** (8), 867 (1985).
19. L. S. Dang and R. Romestain, Solid State Commun. **43** (11), 829 (1982).
20. T. Tanaka, K. Hayashida, M. Nisho, Q. Guo, and H. Ogawa, J. Appl. Phys. **94** (3), 1527 (2003).
21. Y. Hishida, T. Toda, and T. Yamaguchi, J. Cryst. Growth **117**, 396 (1992).
22. J. H. Chang, T. Takai, B. H. Koo, J. S. Song, T. Handa, and T. Yao, Appl. Phys. Lett. **79** (6), 785 (2001).
23. Q. Kim and D. W. Langer, Phys. Status Solidi B **122**, 263 (1984).
24. M. Magnea, J. L. Pautrat, L. S. Dang, R. Romestain, and P. J. Dean, Solid State Commun. **47** (9), 703 (1983).
25. W. S. Kuhn, A. Lusson, B. Quhen, C. Grattepain, H. Dumont, O. Gorochov, S. Bauer, K. Wolf, M. Morz, T. Reisinger, A. Rosenauer, H. P. Wagner, H. Stanzl, and W. Gebhardt, Prog. Cryst. Growth Charact. Mater. **31**, 119 (1995).

Translated by G. Skrebtsov

Physics of the Solid State, Vol. 47, No. 4, 2005, pp. 614–621. Translated from Fizika Tverdogo Tela, Vol. 47, No. 4, 2005, pp. 591–597.
Original Russian Text Copyright © 2005 by Dymnikov.

SEMICONDUCTORS AND DIELECTRICS

Sum Rules for Reduced Matrix Elements of the Generalized Momentum Operator in III–V Semiconductors

V. D. Dymnikov
Ioffe Physicotechnical Institute, Russian Academy of Sciences, Politekhnicheskaya ul. 26, St. Petersburg, 194021 Russia
e-mail: Dymnik@pop.ioffe.rssi.ru

Received July 5, 2004

Abstract—The band structure of III–V semiconductors near the Γ point is studied with full account of the spin–orbit interaction, which results not only in band splitting but also in spin–orbit mixing of wave functions of different spatial symmetry. In view of the last circumstance, a new version of the $\mathbf{k} \cdot \mathbf{p}$ method of perturbation theory is developed and strict symmetry relations are derived for the first time in which sums containing optical matrix elements and energy denominators are related to intrinsic electron characteristics (masses, *g* factors). These relations (sum rules) appear to be informative in analyzing the spatial symmetry of electronic states near the Γ point and are useful for quantitative estimation of the most important optical matrix elements. © *2005 Pleiades Publishing, Inc.*

1. INTRODUCTION

Recently, there has been a growing interest in studying spin-dependent phenomena in semiconductors. A new direction has appeared in electronics called spintronics. In spintronics, the electron spin, in addition to its charge, is an active element for storing and transmitting information [1]. Spintronics is believed to be prospective for the development of new scientific fields, such as quantum computing and quantum information transmission [2, 3]. However, when speaking about the electron spin in semiconductors, one usually implies its magnetic moment, which is actually formed not only by the spin but also, to a large degree, by interatomic orbital motion inside the wave packet that is associated with the quasiparticle; this has been shown by Herring [4]. In the effective-mass method, an electron is represented as a wave packet, and it is the structure of the wave packet that forms the intrinsic characteristics of the quasiparticle (mass, *g* factor).

It is known [5] that, in III–V semiconductors, the currents in an electron wave packet are induced by spin–orbit interaction. Therefore, a more detailed study of spin–orbit interaction in semiconductors and of its role in forming the intrinsic electron structure is of importance.

Usually, when calculating the effective masses and *g* factors of charge carriers, the Kane band model [6] is used, in which the spin–orbit interaction is taken into account only when calculating band splitting of orbital states at the Γ point. However, it is known [7] that spin–orbit interaction also allows for mixing of wave functions of different spatial symmetries. The last circumstance is usually disregarded because the mixing is assumed to be negligible. Nevertheless, there are situations where mixing plays a crucial role [8–10].

In this study, we consider the intrinsic structure of particles with full inclusion of the spin–orbit interaction at the Γ point. Based on the results of [10], where general selection rules are obtained for the generalized momentum operator $\boldsymbol{\pi}$ at the center of the Brillouin zone, we develop a new version of the $\mathbf{k} \cdot \boldsymbol{\pi}$ method, in which the spin–orbit interaction is taken into account correctly in zeroth approximation and only the operator $\mathbf{k} \cdot \boldsymbol{\pi}$ is treated as a perturbation. This approach allowed us to obtain, for the first time, strict symmetry relations between, on the one hand, the electron effective masses and *g* factors for all energy bands and, on the other hand, dimensionless sums of terms associated with optical transitions to energy bands with different symmetries of the T_d group. The terms in these sums coincide, up to a constant factor, with the corresponding oscillator strengths. It appeared that the number of such sums in each band coincides with the number of characteristics of the electron intrinsic structure. This fact allowed us to invert the relations and express the sums in terms of masses and *g* factors. The expressions obtained for the sums are called the sum rules for the reduced matrix elements of the generalized momentum operator. The theoretical novelty of these rules induced us to bring them into the title of this article. These sum rules appear to be informative in analyzing the spatial symmetry of electronic states at the Γ point and allow one to make quantitative estimations of the optical matrix elements.

In this study, using known masses and *g* factors, we analyze the spatial symmetry of the Γ_6 conduction bands and the Γ_7 and Γ_8 valence bands and compare the experimental values of the optical matrix element between the Γ_6 and Γ_8 bands with the theoretical values obtained from the sum rules for a number of III–V compounds. The experimental value of the optical matrix element is found to agree well with the known band parameters and g factors for all materials considered. We also indicate the compounds (InSb, GaSb) in which the spin–orbit mixing can be strong. Experimental data are given to corroborate this statement.

2. WAVE FUNCTIONS

Disregarding the spin, the electron states at the Γ point in III–V compounds are described by wave functions $|\Gamma_\alpha\rangle$ that transform according to the representations Γ_α ($\alpha = 1, 2, 3, 4, 5$) [7]. With allowance for spin, the electron energy levels correspond to the Γ_n spinor representations ($n = 6, 7, 8$) and their wave functions form from the $|\Gamma_\alpha\rangle$ coordinate functions and the spin functions $\begin{pmatrix}1\\0\end{pmatrix}$ and $\begin{pmatrix}0\\1\end{pmatrix}$ [7, 11].

Generally, the electron wave functions in the Γ_n band can be written as

$$|\Gamma_n;\, M\rangle = \sum_{\Gamma_\alpha} C_{\Gamma_n\Gamma_\alpha}|\Gamma_n(\Gamma_\alpha);\, M\rangle, \tag{1}$$

where M specifies the degenerate states and $|\Gamma_n(\Gamma_\alpha);\, M)\rangle$ are the wave functions that transform according to the Γ_n representation and are constructed from coordinate functions $|\Gamma_\alpha\rangle$. Summation in Eq. (1) is performed over all representations Γ_α involved in the Γ_n state. The phase factors of the $|\Gamma_n(\Gamma_\alpha);\, M)\rangle$ functions are chosen so that the mixing coefficients $C_{\Gamma_n\Gamma_\alpha}$ are real. Functions of the form of Eq. (1) are assumed to be normalized to unity; i.e., the coefficients $C_{\Gamma_n\Gamma_\alpha}$ satisfy the condition

$$\sum_{\Gamma_\alpha} C^2_{\Gamma_n\Gamma_\alpha} = 1. \tag{2}$$

In general, the $|\Gamma_n;\, M\rangle$ functions in all Γ_6, Γ_7, and Γ_8 bands can be represented in the form

$$|\Gamma_6;\, M\rangle = \sum_{\Gamma_1} C_{\Gamma_6\Gamma_1}|\Gamma_6(\Gamma_1);\, M\rangle + \sum_{\Gamma_5} C_{\Gamma_6\Gamma_5}|\Gamma_6(\Gamma_5);\, M\rangle, \quad M = \pm\frac{1}{2}, \tag{3}$$

$$|\Gamma_7;\, M\rangle = \sum_{\Gamma_2} C_{\Gamma_7\Gamma_2}|\Gamma_7(\Gamma_2);\, M\rangle + \sum_{\Gamma_4} C_{\Gamma_7\Gamma_4}|\Gamma_7(\Gamma_4);\, M\rangle, \quad M = \pm\frac{1}{2}, \tag{4}$$

$$|\Gamma_8;\, M\rangle = \sum_{\Gamma_3} C_{\Gamma_8\Gamma_3}|\Gamma_8(\Gamma_3);\, M\rangle + \sum_{\Gamma_4} C_{\Gamma_8\Gamma_4}|\Gamma_8(\Gamma_4);\, M\rangle + \sum_{\Gamma_5} C_{\Gamma_8\Gamma_5}|\Gamma_8(\Gamma_5);\, M\rangle, \quad M = \pm\frac{3}{2}, \pm\frac{1}{2}. \tag{5}$$

The coordinate system in Eqs. (3)–(5) is assumed to be associated with the [100], [010], and [001] directions. The quantization z axis is directed along [001]. The explicit form of the $|\Gamma_n(\Gamma_\alpha);\, M\rangle$ spin–orbit harmonics is given in [10].

3. SELECTION RULES

In this section, we write out the selection rules for the $\mathbf{k}\cdot\boldsymbol{\pi}$ operator, where $\mathbf{k}$ is the quasimomentum and $\boldsymbol{\pi}$ is the generalized momentum operator

$$\boldsymbol{\pi} = \mathbf{p} + \mu(\boldsymbol{\sigma}\times\nabla V), \quad \mu = \frac{\hbar}{4mc^2}. \tag{6}$$

In Eq. (6), $\mathbf{p}$ is the momentum operator, $\boldsymbol{\sigma}$ are the Pauli matrices, V is a periodic potential, m is the free electron mass, c is the velocity of light, and $\hbar$ is the Planck constant. Matrix elements of the $\mathbf{k}\cdot\boldsymbol{\pi}$ operator are calculated between all states at the Γ point. Selection rules are formulated in terms of the Clebsch–Gordan coefficients and the reduced matrix elements.

In [10], wave functions (3)–(5) were used to calculate the matrix elements

$$\langle\Gamma_6;\, M|\mathbf{k}\boldsymbol{\pi}|\Gamma_8;\, M'\rangle = k_{M'-M}C^{\frac{3}{2}M'}_{1M'-M\frac{1}{2}M}A^{\Gamma_6\Gamma_8}, \quad M = \pm\frac{1}{2}, \quad M' = \pm\frac{3}{2}, \pm\frac{1}{2}, \tag{7}$$

for the $\Gamma_6 \rightleftarrows \Gamma_8$ transitions,

$$\langle\Gamma_6;\, M|\mathbf{k}\boldsymbol{\pi}|\Gamma_7;\, M'\rangle = k_{M'-M}C^{\frac{1}{2}M'}_{1M'-M\frac{1}{2}M}B^{\Gamma_6\Gamma_7}, \quad M, M' = \pm\frac{1}{2}, \tag{8}$$

for the $\Gamma_6 \rightleftarrows \Gamma_7$ transitions, and

$$\langle\Gamma_7;\, M_1|\mathbf{k}\boldsymbol{\pi}|\Gamma_8;\, M_2\rangle = \left[-\sqrt{\frac{10}{3}}k_{+1}C^{\frac{1}{2}M_1}_{\frac{3}{2}M_2 21} + \sqrt{\frac{5}{3}}k_0\left(C^{\frac{1}{2}M_1}_{\frac{3}{2}M_2 2-2} - C^{\frac{1}{2}M_1}_{\frac{3}{2}M_2 22}\right) + \sqrt{\frac{10}{3}}k_{-1}C^{\frac{1}{2}M_1}_{\frac{1}{2}M_2 2-1}\right]C^{\Gamma_7\Gamma_8} \tag{9}$$

($M_1 = \pm\frac{1}{2}$, $M_2 = \pm\frac{3}{2}, \pm\frac{1}{2}$) for the $\Gamma_7 \rightleftarrows \Gamma_8$ transitions,.

In Eqs. (7)–(9), k_α ($\alpha = -1, 0, 1$) are the circular components of the vector **k** [12]; $C^{JM}_{j_1m_1j_2m_2}$ are Clebsch–Gordan coefficients; and $A^{\Gamma_6\Gamma_8}$, $B^{\Gamma_6\Gamma_7}$, and $C^{\Gamma_7\Gamma_8}$ are the real reduced matrix elements.

The selection rules for $\Gamma_8 \longleftrightarrow \Gamma_{8'}$ transitions are written as [10]

$$\langle\Gamma_8; M|\mathbf{k}\boldsymbol{\pi}|\Gamma_{8'}; M'\rangle = \frac{1}{3}D_s^{\Gamma_8\Gamma_{8'}}(I^s)_{MM'} + \frac{1}{3}D_A^{\Gamma_8\Gamma_{8'}}(I^A)_{MM'}, \tag{10}$$

$$M, M' = \pm\frac{3}{2}, \pm\frac{1}{2}.$$

Here, I^s and I^A are hermitian and antihermitian 4×4 matrices, which can be expressed in terms of the matrices J_x, J_y, and J_z of the angular momentum $J = 3/2$ as

$$\begin{aligned} I^s = {} & k_x\{J_x, J_y^2 - J_z^2\} + k_y\{J_y, J_z^2 - J_x^2\} \\ & + k_z\{J_z, J_x^2 - J_y^2\}, \end{aligned} \tag{11}$$

$$I^A = i(k_x\{J_y, J_z\} + k_y\{J_z, J_x\} + k_z\{J_x, J_y\}), \tag{12}$$

where

$$J_x = \begin{pmatrix} 0 & \frac{\sqrt{3}}{2} & 0 & 0 \\ \frac{\sqrt{3}}{2} & 0 & 1 & 0 \\ 0 & 1 & 0 & \frac{\sqrt{3}}{2} \\ 0 & 0 & \frac{\sqrt{3}}{2} & 0 \end{pmatrix},$$

$$J_y = \begin{pmatrix} 0 & -i\frac{\sqrt{3}}{2} & 0 & 0 \\ i\frac{\sqrt{3}}{2} & 0 & -i & 0 \\ 0 & i & 0 & -i\frac{\sqrt{3}}{2} \\ 0 & 0 & i\frac{\sqrt{3}}{2} & 0 \end{pmatrix}, \tag{13}$$

$$J_z = \begin{pmatrix} \frac{3}{2} & 0 & 0 & 0 \\ 0 & \frac{1}{2} & 0 & 0 \\ 0 & 0 & -\frac{1}{2} & 0 \\ 0 & 0 & 0 & -\frac{3}{2} \end{pmatrix}.$$

In Eqs. (11) and (12), the symbol {…} denotes an anticommutator: $\{A, B\} = AB + BA$. The quantities $D_s^{\Gamma_8\Gamma_{8'}}$ and $D_A^{\Gamma_8\Gamma_{8'}}$ in Eq. (10) are real reduced matrix elements satisfying the conditions

$$D_s^{\Gamma_8\Gamma_{8'}} = D_s^{\Gamma_{8'}\Gamma_8}, \quad D_A^{\Gamma_8\Gamma_{8'}} = -D_A^{\Gamma_{8'}\Gamma_8}. \tag{14}$$

All reduced matrix elements in Eqs. (7)–(10) can be expressed in terms of the mixing coefficients and are explicitly written out in [10].

4. EXPRESSIONS FOR THE EFFECTIVE MASSES IN A NEW VERSION OF THE $\mathbf{k} \cdot \boldsymbol{\pi}$ METHOD

The above selection rules make it possible to formulate a new version of the $\mathbf{k} \cdot \boldsymbol{\pi}$ method in which the spin–orbit interaction is taken into account exactly in zeroth approximation and only the operator $\mathbf{k} \cdot \boldsymbol{\pi}$ is considered a perturbation. In this version, exact symmetry expressions can be derived for the effective masses at the Γ point in all bands. Let us consider the electron kinetic energy in quadratic approximation in **k**. The spectrum of charge carriers in the degenerate Γ_n bands (n = 6, 7, 8) can be found in terms of the standard approach of perturbation theory [13] by diagonalizing the effective kinetic-energy Hamiltonian $H_{\text{eff, kin}}$ whose matrix elements are defined as [11, 13]

$$\begin{aligned} \langle\Gamma_n; M|H_{\text{eff, kin}}|\Gamma_n; M'\rangle = {} & \langle\Gamma_n; M|V_{\mathbf{k}}|\Gamma_n; M'\rangle \\ & + \sum_{\Gamma_{m, M''}} \frac{\langle\Gamma_n; M|V_{\mathbf{k}}|\Gamma_m; M''\rangle\langle\Gamma_m; M''|V_{\mathbf{k}}|\Gamma_n; M'\rangle}{E_{\Gamma_n} - E_{\Gamma_m}}, \end{aligned} \tag{15}$$

$$V_{\mathbf{k}} = \frac{\hbar^2k^2}{2m} + \frac{\hbar}{m}\mathbf{k} \cdot \boldsymbol{\pi}. \tag{16}$$

In Eq. (15), E_{Γ_n} is the energy eigenvalue in the Γ_n band and M'' specifies the degenerate states in the Γ_m band. Summation in Eq. (15) is performed over all states other than Γ_n.

First, we consider the electron spectrum in the Γ_6 band. Using selection rules (7) and (8), we obtain

$$\langle\Gamma_6; M|H_{\text{eff, kin}}|\Gamma_6; M'\rangle = \frac{\hbar^2k^2}{2m_{\Gamma_6}}\delta_{MM'}, \tag{17}$$

where $\delta_{MM'}$ is the Kronecker delta and m_{Γ_6} is the electron effective mass in the Γ_6 band, which is given by

$$\frac{m}{m_{\Gamma_6}} = 1 + \frac{4}{3}A_{\Gamma_6} + \frac{2}{3}B_{\Gamma_6}, \tag{18}$$

$$A_{\Gamma_6} = \frac{1}{m}\sum_{\Gamma_8}\frac{(A^{\Gamma_6\Gamma_8})^2}{E_{\Gamma_6} - E_{\Gamma_8}}, \quad B_{\Gamma_6} = \frac{1}{m}\sum_{\Gamma_7}\frac{(B^{\Gamma_6\Gamma_7})^2}{E_{\Gamma_6} - E_{\Gamma_7}}. \tag{19}$$

The difference between the effective mass and the free electron mass is due to the interaction of the Γ_6 band with all Γ_7 and Γ_8 bands.

Analogous calculations can be performed for the Γ_7 band using selection rules (8) and (9). The result is

$$\langle \Gamma_7 : M | H_{\text{eff, kin}} | \Gamma_7; M' \rangle = \frac{\hbar^2 k^2}{2 m_{\Gamma_7}} \delta_{MM'}, \tag{20}$$

where m_{Γ_7} is the electron effective mass in the Γ_7 band, which is determined by

$$\frac{m}{m_{\Gamma_7}} = 1 + \frac{2}{3} B_{\Gamma_7} + \frac{4}{3} C_{\Gamma_7}, \tag{21}$$

$$B_{\Gamma_7} = \frac{1}{m} \sum_{\Gamma_6} \frac{(B^{\Gamma_6 \Gamma_7})^2}{E_{\Gamma_7} - E_{\Gamma_6}}, \quad C_{\Gamma_7} = \frac{1}{m} \sum_{\Gamma_8} \frac{(C^{\Gamma_7 \Gamma_8})^2}{E_{\Gamma_7} - E_{\Gamma_8}}. \tag{22}$$

The quantities defined by Eqs. (22) characterize the interaction of the Γ_7 band with all Γ_6 and Γ_8 bands and determine the effective mass m_{Γ_7}.

In contrast to the Γ_6 and Γ_7 bands, the energy spectrum in the Γ_8 band is anisotropic and $H_{\text{eff, kin}}$ contains not only quadratic but also linear terms in $\mathbf{k}$:

$$\begin{aligned} &\langle \Gamma_8; M | H_{\text{eff, kin}} | \Gamma_{8'}; M' \rangle \\ &= (H^{(1)}_{\text{eff, kin}})_{MM'} + (H^{(2)}_{\text{eff, kin}})_{MM'}. \end{aligned} \tag{23}$$

First, we find the matrix $H^{(2)}_{\text{eff, kin}}$. This matrix describes the part of the spectrum in the Γ_8 band that is quadratic in $\mathbf{k}$. Using Eq. (15) and selection rules (7), (9), and (10), we arrive at the conclusion that this part of the spectrum is due to the interaction of the Γ_8 band with all Γ_6, Γ_7, and other Γ_8 bands and involves the sums

$$A_{\Gamma_8} = \frac{1}{m} \sum_{\Gamma_6} \frac{(A^{\Gamma_6 \Gamma_8})^2}{E_{\Gamma_8} - E_{\Gamma_6}}, \quad C_{\Gamma_8} = \frac{1}{m} \sum_{\Gamma_7} \frac{(C^{\Gamma_7 \Gamma_8})^2}{E_{\Gamma_8} - E_{\Gamma_7}}, \tag{24}$$

$$\begin{gathered} D^{(1)}_{\Gamma_8} = \frac{1}{m} {\sum_{\Gamma_{8'}}}' \frac{(D_s^{\Gamma_8 \Gamma_{8'}})^2}{E_{\Gamma_8} - E_{\Gamma_{8'}}}, \quad D^{(2)}_{\Gamma_8} = \frac{1}{m} {\sum_{\Gamma_{8'}}}' \frac{(D_A^{\Gamma_8 \Gamma_{8'}})^2}{E_{\Gamma_8} - E_{\Gamma_{8'}}}, \\ D^{(3)}_{\Gamma_8} = \frac{1}{m} {\sum_{\Gamma_{8'}}}' \frac{D_s^{\Gamma_8 \Gamma_{8'}} D_A^{\Gamma_8 \Gamma_{8'}}}{E_{\Gamma_8} - E_{\Gamma_{8'}}}. \end{gathered} \tag{25}$$

With the notation

$$\begin{aligned} \gamma_1 &= -1 - \frac{2}{3} A_{\Gamma_8} - \frac{2}{3} C_{\Gamma_8} - \frac{2}{3} D^{(1)}_{\Gamma_8} - \frac{2}{3} D^{(2)}_{\Gamma_8}, \\ \gamma_2 &= -\frac{1}{3} A_{\Gamma_8} + \frac{1}{3} C_{\Gamma_8} + \frac{2}{3} D^{(3)}_{\Gamma_8}, \\ \gamma_3 &= -\frac{1}{3} A_{\Gamma_8} - \frac{1}{3} C_{\Gamma_8} + \frac{1}{3} D^{(1)}_{\Gamma_8}, \end{aligned} \tag{26}$$

the matrix $H^{(2)}_{\text{eff, kin}}$ can be written as

$$\begin{aligned} H^{(2)}_{\text{eff, kin}} &= \frac{\hbar^2 k^2}{2m} \Big[-\left(\gamma_1 + \frac{5}{2} \gamma_2 \right) I \\ &+ 2\gamma_2 (\nu_x^2 J_x^2 + \nu_y^2 J_y^2 + \nu_z^2 J_z^2) + 2\gamma_3 (\nu_x \nu_y \{J_x, J_y\} \\ &+ \nu_y \nu_z \{J_y, J_z\} + \nu_z \nu_x \{J_z, J_x\}) \Big], \end{aligned} \tag{27}$$

$$\mathbf{v} = \frac{\mathbf{k}}{k}.$$

Here, I is the unit 4 × 4 matrix; and the matrices J_x, J_y, and J_z are given by Eqs. (13). Expression (27) coincides exactly with the Luttinger Hamiltonian [14]; therefore, the quantities γ_1, γ_2, and γ_3 are the Luttinger parameters. We omitted the subscript Γ_8 at the parameters γ_1, γ_2, and γ_3 in (26) for ease of reading. Clearly, each Γ_8 band has its own set of Luttinger parameters. Relations (26) reveal the origin of the spectrum in the Γ_8 band.

In practice, a spherical model is frequently used for the valence band by putting $\gamma_2 = \gamma_3$. From Eq. (26), we see that this assumption corresponds to disregarding the interaction of the Γ_8 band with the Γ_7 and $\Gamma_{8'}$ bands. Below, it will be shown that this assumption is reasonable for many III–V compounds, since the Luttinger parameters are mainly due to the interaction with the Γ_6 bands.

The linear term in $\mathbf{k}$ in $H^{(1)}_{\text{eff, kin}}$ in Eq. (23) comes from the term in Eq. (15) that is linear in $V_{\mathbf{k}}$ and is due to the absence of an inversion center. For symmetry reasons [11, 15], the former term can be written as

$$\begin{aligned} H^{(1)}_{\text{eff, kin}} &= \frac{1}{\sqrt{3}} c_k (k_x \{J_x, J_y^2 - J_z^2\} \\ &+ k_y \{J_y, J_z^2 - J_x^2\} + k_z \{J_x, J_y^2 - J_z^2\}). \end{aligned} \tag{28}$$

It follows from selection rules (10) that the parameter c_k [15] can be expressed in terms of the coefficient $D_s^{\Gamma_8 \Gamma_8}$ [10] as

$$c_k = \frac{\hbar}{m} \sqrt{3} D_s^{\Gamma_8 \Gamma_8}. \tag{29}$$

For III–V compounds, Eqs. (18), (21), (26), and (29) provide a complete set of characteristics of the electron energy spectrum near the Γ point in the quadratic approximation in $\mathbf{k}$.

5. *g* FACTORS OF ELECTRONS

The new version of the $\mathbf{k} \cdot \boldsymbol{\pi}$ method allows us to derive exact symmetry expressions for the g factors of electrons in all energy bands. According to the effective-mass method [11], the Zeeman term H'_{Γ_n} in the effective Hamiltonian describing the interaction of an electron in the Γ_n band with a magnetic field can be written in the matrix form as [11]

$$(H'_{\Gamma_n})_{MM'} = \frac{1}{2}\mu_0\sum_{\gamma}H_{\gamma}\Bigg[g_0\langle\Gamma_n;\,M|\sigma_{\gamma}|\Gamma_n;\,M'\rangle - \frac{i2}{m}\sum_{\Gamma_m,\,M''}{}^{'}\frac{\langle\Gamma_n;\,M|\pi_{\alpha}|\Gamma_m;\,M''\rangle\langle\Gamma_m;\,M''|\pi_{\beta}|\Gamma_n;\,M'\rangle}{E_{\Gamma_n}-E_{\Gamma_m}}\varepsilon_{\alpha\beta\gamma}\Bigg]. \quad (30)$$

Here, the subscripts α, β, and γ denote the Cartesian projections of the vectors; H_{γ} is the magnetic field; $\varepsilon_{\alpha\beta\gamma}$ is the unit antisymmetric tensor of order 3; M'' specifies the degenerate states of the Γ_m band; μ_0 is the Bohr magneton; g_0 is the free-electron g factor; and σ_{γ} are the Pauli matrices.

In the Γ_6 band, an electron is described by a two-component spinor. Using the method of invariants [11], we can write Hamiltonian (30) in the form

$$(H'_{\Gamma_6})_{MM'} = \frac{1}{2}g_{\Gamma_6}\mu_0(\boldsymbol{\sigma}\cdot\mathbf{H})_{MM'}. \quad (31)$$

Here, g_{Γ_6} is the effective g factor of an electron in the Γ_6 band.

Using Eqs. (30) and (31) and selection rules (7) and (8) and taking into account that $g_0 = 2$, we can obtain the following expression for the effective g factor of an electron in the Γ_6 band:

$$g_{\Gamma_6} = 2\left(1-\frac{4}{3}\alpha^2\right)-\frac{4}{3}A_{\Gamma_6}+\frac{4}{3}B_{\Gamma_6}, \quad (32)$$

$$\alpha^2 = \sum_{\Gamma_5}(C_{\Gamma_6\Gamma_5})^2. \quad (33)$$

The quantities A_{Γ_6} and B_{Γ_6} in Eq. (32) are given by Eqs. (19). In Eq. (32), the first term is associated with the average electron spin in the Γ_6 state and the other terms are related to the intrinsic orbital angular momentum of an electron. When deriving Eq. (32), we used normalization condition (2).

Analogous calculations can be performed for the Γ_7 band using selection rules (8) and (9). In this way, the effective g factor of an electron in the Γ_7 band can be found to be

$$g_{\Gamma_7} = 2\left(-\frac{1}{3}+\frac{4}{3}\beta^2\right)+\frac{4}{3}B_{\Gamma_7}-\frac{4}{3}C_{\Gamma_7}, \quad (34)$$

$$\beta^2 = \sum_{\Gamma_2}(C_{\Gamma_7\Gamma_2})^2. \quad (35)$$

Here, the quantities B_{Γ_7} and C_{Γ_7} are given by Eqs. (22). The appearance of sum (35) in Eq. (34) is related to normalization condition (2).

In the Γ_8 band, the electrons are described by four-component wave functions and the Zeeman term H'_{Γ_8} in Eq. (30) is a 4 × 4 matrix. According to Luttinger [14], this matrix can be expressed in terms of the $J = 3/2$ angular momentum matrices (13) as

$$(H'_{\Gamma_8})_{MM'} = -2\mu_0[\kappa\mathbf{J}\cdot\mathbf{H} + q(J_x^3H_x+J_y^3H_y+J_z^3H_z)]_{MM'}. \quad (36)$$

In Eq. (36), the dimensionless Luttinger parameters κ and q characterize the intrinsic magnetic moment of an electron in the Γ_8 band.

Using Eqs. (30) and (36) and selection rules (7), (9), and (10), the parameters κ and q can be found to be

$$\kappa = -\frac{1}{3}-\frac{5}{6}s^2+\frac{13}{9}t^2-\frac{1}{3}A_{\Gamma_8}+\frac{10}{9}C_{\Gamma_8} + \frac{7}{18}D^{(1)}_{\Gamma_8}-\frac{7}{9}D^{(2)}_{\Gamma_8}-\frac{13}{18}D^{(3)}_{\Gamma_8}, \quad (37)$$

$$q = \frac{2}{3}s^2-\frac{4}{9}t^2-\frac{4}{9}C_{\Gamma_8}-\frac{2}{9}D^{(1)}_{\Gamma_8}+\frac{4}{9}D^{(2)}_{\Gamma_8}+\frac{2}{9}D^{(3)}_{\Gamma_8}, \quad (38)$$

$$s^2 = \sum_{\Gamma_3}(C_{\Gamma_8\Gamma_3})^2, \quad t^2 = \sum_{\Gamma_5}(C_{\Gamma_8\Gamma_5})^2. \quad (39)$$

When deriving Eqs. (37) and (38), we used the relation

$$\sum_{\Gamma_4}(C_{\Gamma_8\Gamma_4})^2 = 1-s^2-t^2, \quad (40)$$

which follows from normalization condition (2) for the wave functions.

Expressions (32), (34), (37), and (38) provide complete information on electron g factors near the Γ point in III–V compound crystals. They are exact symmetry relations correctly taking into account the spin–orbit interaction.

6. SUM RULES FOR REDUCED MATRIX ELEMENTS

Equations (18), (21), (26), (32), (34), (37), and (38) express observable physical quantities through sums that involve optical matrix elements. It can be seen that the number of sums in each band coincides with the number of intrinsic characteristics of an electron (masses, g factors). To analyze the matrix elements, it is convenient to invert the above relations and to express the sums in terms of the observable quantities. The inverse relations have the form

$$A_{\Gamma_6} = \frac{1}{2}\frac{m}{m_{\Gamma_6}} - \frac{1}{4}g_{\Gamma_6} - \frac{2}{3}\alpha^2, \tag{41}$$

$$B_{\Gamma_6} = \frac{1}{2}\left(\frac{m}{m_{\Gamma_6}} + g_{\Gamma_6}\right) - \frac{3}{2} + \frac{4}{3}\alpha^2, \tag{42}$$

$$B_{\Gamma_7} = \frac{1}{2}\left(\frac{m}{m_{\Gamma_7}} + g_{\Gamma_7}\right) - \frac{1}{6} - \frac{4}{3}\beta^2, \tag{43}$$

$$C_{\Gamma_7} = \frac{1}{2}\frac{m}{m_{\Gamma_7}} - \frac{1}{4}g_{\Gamma_7} - \frac{2}{3} + \frac{2}{3}\beta^2, \tag{44}$$

$$\begin{aligned} A_{\Gamma_8} &= -\frac{1}{4}(\gamma_1 + 2\gamma_2 + 3\gamma_3) \\ &\quad - \frac{5}{4}\kappa - \frac{41}{16}q - \frac{2}{3}(1 - s^2 - t^2), \end{aligned} \tag{45}$$

$$C_{\Gamma_8} = -\frac{1}{4}(\gamma_1 - 2\gamma_2 + 3\gamma_3) + \frac{3}{4}\kappa + \frac{15}{16}q - \frac{2}{3}t^2, \tag{46}$$

$$D^{(1)}_{\Gamma_8} = -\frac{1}{2}\gamma_1 + \frac{3}{2}\gamma_3 - \frac{1}{2}\kappa - \frac{13}{18}q - \frac{2}{3}(1 - s^2), \tag{47}$$

$$D^{(2)}_{\Gamma_8} = -\frac{1}{2}\gamma_1 + \kappa + \frac{13}{4}q - \frac{1}{6} - \frac{4}{3}s^2, \tag{48}$$

$$D^{(3)}_{\Gamma_8} = \gamma_2 - \kappa - \frac{7}{4}q - \frac{1}{3} + \frac{1}{3}s^2 + \frac{2}{3}t^2. \tag{49}$$

7. CONCLUSIONS

Sum rules (41)–(49) for matrix elements allow one to obtain useful information on III–V semiconductors. In particular, from these sum rules, one can draw conclusions on the space symmetry of electronic states near the Γ point and quantitatively estimate certain optical matrix elements.

In this section, we draw conclusions about the spatial symmetry of the conduction and valence bands and estimate the optical matrix element for transitions between the conduction and the valence bands. In what follows, we use the band diagram shown in the figure.

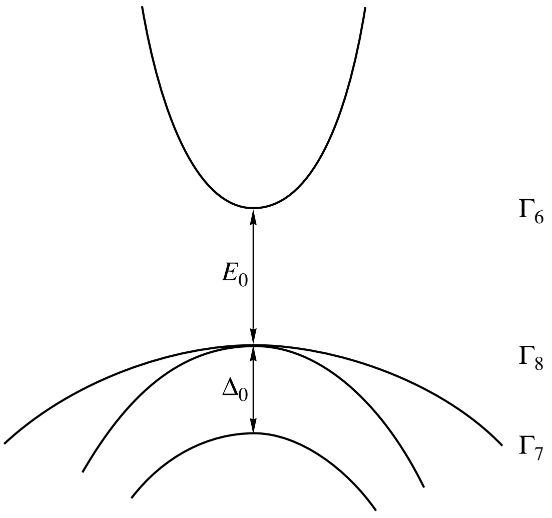

Three-band model of III–V semiconductors near the Γ point. Γ_6 is the conduction band, Γ_8 and Γ_7 are the valence bands, $E_0 = E_{\Gamma_6} - E_{\Gamma_8}$ is the band gap, and $\Delta_0 = E_{\Gamma_8} - E_{\Gamma_7}$ is the spin–orbit splitting.

Table 1 lists the band parameters, effective masses, and *g* factors for the Γ_6 conduction band and the Γ_8 and Γ_7 valence bands of a number of III–V compounds. The data listed in Table 1 are taken from [15–17].

For the same compounds, Table 2 gives the quantities A_{Γ_6}, A_{Γ_8}, B_{Γ_6}, and B_{Γ_7} calculated from Eqs. (41), (45), (42), and (43), respectively, and from the data in Table 1. With these quantities, one can estimate the matrix elements $|A^{\Gamma_6\Gamma_8}|$ and $|B^{\Gamma_6\Gamma_7}|$ (which are responsible for the $\Gamma_8 \longrightarrow \Gamma_6$ and $\Gamma_7 \longrightarrow \Gamma_6$ optical transitions) without any assumptions on the spatial symmetry of the wave functions at the Γ point. This conclusion follows from the fact that the parameters α^2 in Eq. (33), β^2 in Eq. (35), and s^2 and t^2 in Eqs. (39) (characterizing the mixing of the wave functions) do not exceed unity and, therefore, one can assume, to a good accuracy, that the numerical values listed in Table 2 refer directly to the quantities A_{Γ_6}, A_{Γ_8}, B_{Γ_6}, and B_{Γ_7}, whose absolute values are much greater than unity. Furthermore, by analyzing Eqs. (19), (22), and (24), which give these quantities in the form of sums, and taking into account that the quantities A_{Γ_6} and B_{Γ_6} are close in value to $|A_{\Gamma_8}|$ and $|B_{\Gamma_7}|$, respectively, we can conclude that the contributions to these sums are mainly due to the interactions between the nearest neighbor bands Γ_6 and Γ_8 and between the nearest neighbor bands Γ_6 and Γ_7. Therefore, in order to estimate the matrix elements $|A^{\Gamma_6\Gamma_8}|$ and $|B^{\Gamma_6\Gamma_7}|$, it is reasonable to use the relations

$$\frac{1}{m}\frac{(A^{\Gamma_6\Gamma_8})^2}{E_{\Gamma_6} - E_{\Gamma_8}} \cong \frac{1}{2}(A_{\Gamma_6} - A_{\Gamma_8}), \tag{50}$$

$$\frac{1}{m}\frac{(B^{\Gamma_6\Gamma_7})^2}{E_{\Gamma_6} - E_{\Gamma_7}} \cong \frac{1}{2}(B_{\Gamma_6} - B_{\Gamma_7}). \tag{51}$$

Table 2 gives the values of the matrix elements $\frac{\hbar}{m}|A^{\Gamma_6\Gamma_8}|$ and $\frac{\hbar}{m}|B^{\Gamma_6\Gamma_7}|$ (in atomic units) calculated using formulas (50) and (51) and the data from Tables 1 and 2. The values of the matrix elements $\frac{\hbar}{m}|A^{\Gamma_6\Gamma_8}|$ obtained from magneto-optical experiments are listed

Table 1. Band parameters and g factors in III–V semiconductors

Parameter	Compound				
	InSb	InAs	InP	GaSb	GaAs
E_0 (eV)	0.235	0.42	1.424	0.813	1.519
Δ_0 (eV)	0.803	0.38	0.108	0.76	0.340
$\frac{m_{\Gamma_6}}{m}$	0.014	0.025	0.08	0.0412	0.067
$\frac{m_{\Gamma_7}}{m}$	–0.1	–0.089	–0.121	–0.15	–0.15
g_{Γ_6}	–51.3	–14.8	1.48	–9.1	–0.44
g_{Γ_7}	–10	–13.0	–1.95	–6.2	–4.9
κ	17	7.86	1.47	3.5	1.72
q	0.39	0.04	0.02	0.13	0.04
γ_1	40.1	19.67	5.05	13.2	6.85
γ_2	18.1	8.37	1.6	4.4	2.10
γ_3	19.2	9.29	1.73	5.7	2.90

Table 2. Sums of the reduced matrix elements and the main matrix elements for III–V semiconductors

Sums and matrix elements	Compound				
	InSb	InAs	InP	GaSb	GaAs
$A_{\Gamma_6} + \frac{2}{3}\alpha^2$	48.54	23.7	5.88	14.41	7.57
$B_{\Gamma_6} - \frac{4}{3}\alpha^2$	8.56	11.1	5.49	6.09	5.74
$B_{\Gamma_7} + \frac{4}{3}\beta^2$	–10.17	–12.28	–5.27	–6.60	–5.95
$A_{\Gamma_8} - \frac{2}{3}(s^2 + t^2)$	–56.39	–26.44	–5.92	–15.15	–7.86
$\frac{\hbar}{m}\lvert A^{\Gamma_6\Gamma_8}\rvert$ (a.u.)	0.675	0.623	0.557	0.666	0.658
	(0.694)	(0.618)	(0.560)	(0.691)	(0.660)
$\frac{\hbar}{m}\lvert B^{\Gamma_6\Gamma_7}\rvert$ (a.u.)	0.600	0.588	0.552	0.559	0.663

in Table 2 in parentheses. These values are taken from the review paper by Hermann and Weisbuch published in [18]. In this review, one can also find references to the original papers. The closeness of the calculated and experimental values indicates that the matrix element $A^{\Gamma_6\Gamma_8}$ agrees well with the band parameters and g factors.

From the data in Table 2, one can draw conclusions about the spatial symmetry of the conduction and the valence bands. We see that, in three out of five materials, the matrix elements $\lvert A^{\Gamma_6\Gamma_8}\rvert$ and $\lvert B^{\Gamma_6\Gamma_7}\rvert$ are close in value. Once the spin–orbit mixing is disregarded, the equality $A^{\Gamma_6\Gamma_8} = A^{\Gamma_6\Gamma_7} = -i\langle s|p_x|x\rangle$ is satisfied [10]; therefore, one may assume that, in these compounds, the wave functions in the Γ_6 and Γ_8 bands are mainly functions of the s and p types, respectively, as is assumed in the Kane model [6]. The small difference between these matrix elements suggests that mixing effects in the Γ_6, Γ_7, and Γ_8 bands are small, i.e., that α^2, β^2, s^2, $t^2 \ll 1$.

In the InSb and GaSb compounds, there is a certain difference between the matrix elements. We may assume that, in these materials, the mixing effects are stronger. This conclusion is supported by the experiment reported in [16], in which strong absorption due to "forbidden" $\Gamma_7 \longrightarrow \Gamma_8$ transitions was observed in p-GaSb ($\alpha \cong 2 \times 10^3$ cm^{-1}, where α is the absorption factor). It is known that the $\Gamma_7 \longrightarrow \Gamma_8$ transitions at $k = 0$ are possible only in the presence of mixing (see, e.g., [8]).

ACKNOWLEDGMENTS

The author thanks E.L. Ivchenko for stimulating discussions, V.I. Perel' and his colleagues for their discussion at a seminar, and O.V. Konstantinov for useful discussions and remarks.

REFERENCES

1. G. A. Prinz, Science **282**, 1660 (1998).
2. D. P. Di Vincenzo, Science **270**, 255 (1995).
3. K. A. Valiev and A. A. Kokin, *Quantum Computers: Hope and Reality* (Regul. Khaot. Din., Izhevsk, 2001) [in Russian].
4. Y. Yafet, in *Solid State Physics*, Ed. by F. Seitz and D. Turnbull (Academic, New York, 1963), Vol. 14, p. 93.
5. L. M. Roth, B. Lax, and S. Zwerdling, Phys. Rev. **114**, 90 (1959).
6. E. O. Kane, J. Phys. Chem. Solids **1**, 249 (1957).
7. G. Dresselhaus, Phys. Rev. **100** (2), 580 (1955).
8. V. D. Dymnikov, in *Abstracts of III All-Russian Conference on the Physics of Semiconductors* (Moscow, 1997), p. 211.
9. X. Marie, T. Amand, P. Le Jeune, M. Paillard, P. Renucci, L. E. Golub, V. D. Dymnikov, and E. L. Ivchenko, Phys. Rev. B **60** (8), 5811 (1999).
10. V. D. Dymnikov, Fiz. Tverd. Tela (St. Petersburg) **43** (11), 1957 (2001) [Phys. Solid State **43**, 2037 (2001)].
11. G. L. Bir and G. E. Pikus, *Symmetry and Strain-Induced Effects in Semiconductors* (Nauka, Moscow, 1972; Wiley, New York, 1975).
12. D. A. Varshalovich, A. N. Moskalev, and V. K. Khersonskiĭ, *Quantum Theory of Angular Momentum* (Nauka, Leningrad, 1975; World Sci., Singapore, 1988).
13. L. D. Landau and E. M. Lifshitz, *Course of Theoretical Physics*, Vol. 3: *Quantum Mechanics: Non-Relativistic Theory*, 4th ed. (Nauka, Moscow, 1989; Pergamon, New York, 1977).
14. J. M. Luttinger, Phys. Rev. **102** (4), 1030 (1956).
15. M. Cardona, N. E. Christensen, and G. Fasol, Phys. Rev. B **38** (3), 1806 (1988).
16. G. N. Iluridze, A. N. Titkov, and E. M. Chaĭkina, Fiz. Tekh. Poluprovodn. (Leningrad) **21** (1), 80 (1987) [Sov. Phys. Semicond. **21**, 48 (1987)].
17. *Landolt–Börnstein Tables*, Ed. by O. Madelung, M. Shulz, and H. Weiss (Springer, Berlin, 1982), Vol. 17a.
18. *Optical Orientation*, Ed. by F. Meier and B. P. Zakharchenya (North-Holland, Amsterdam, 1984; Nauka, Leningrad, 1989).

Translated by I. Zvyagin

Physics of the Solid State, Vol. 47, No. 4, 2005, pp. 622–626. Translated from Fizika Tverdogo Tela, Vol. 47, No. 4, 2005, pp. 598–602.
Original Russian Text Copyright © 2005 by Sharenkova, Kaminskiĭ, Golubkov, Vasil'ev, Kamenskaya.

SEMICONDUCTORS AND DIELECTRICS

The Structure of a Metallic-Phase Film Produced by Mechanical Polishing of Polycrystalline SmS

N. V. Sharenkova, V. V. Kaminskiĭ, A. V. Golubkov, L. N. Vasil'ev, and G. A. Kamenskaya
Ioffe Physicotechnical Institute, Russian Academy of Sciences, Politekhnicheskaya ul. 26, St. Petersburg, 194021 Russia
e-mail: Vladimir.Kaminski@mail.ioffe.ru

Received August 31, 2004

Abstract—X-ray diffraction is used to study the structure of a metallic-phase film that forms during controlled polishing of homogeneous polycrystalline semiconducting $Sm_{1+x}S$ samples. Structural changes that appear in the semiconducting phase under these conditions were studied. The x dependence of the thickness of the metallic layer forming on the sample surface is analyzed to explain the effect of excess samarium ions on the transformation parameters. The cause of the stabilization of the metallic modification of SmS after polishing is terminated is explained using estimates based on the measured sizes of coherent domains in samples of different compositions. The appearance and stabilization of the metallic phase are related to a decrease in and subsequent conservation of the coherent-domain size, respectively. *© 2005 Pleiades Publishing, Inc.*

1. INTRODUCTION

One of the unique properties of samarium sulfide (SmS) is its ability to be transformed from a semiconductor into a metallic state through mechanical polishing of the sample surface [1]. The semiconductor–metal phase transformation occurs in the surface layer of the sample, and the metallic phase can exist for an infinitely long time. The formation of the metallic phase is related to the pressure of abrasive particles put on the sample surface; this pressure results in a complex strained state in the bulk of the sample and in compression of the SmS surface layer [2]. As a result, the effect reduces to the well-known reversible (isomorphous to NaCl–NaCl) semiconductor–metal phase transformation that occurs in uniformly compressed SmS under a pressure of ~6.5 kbar [3] and that is caused by the transition of samarium ions from the divalent to trivalent state. The mechanism of stabilization of the metallic phase at the surface of the semiconducting phase is less well understood. For single-crystal SmS, the stabilization is related to a network of misfit dislocations that forms at the semiconductor–metallic phase interface due to the difference in their lattice parameters (a = 5.97 and 5.7 Å, respectively) and stabilizes the strained state of the metallic film [4, 5]. However, this model does not tie in well with the long-time (many-year) and high-temperature (up to 400°C) stability of the SmS metallic phase, which was observed in both single-crystal and polycrystalline samples.

According to [6], thin polycrystalline SmS films contain excess samarium ions with respect to the stoichiometric composition and these ions are in the trivalent state. The fact that they are trivalent follows from an analysis of the results of [6]. Figure 1 shows the amount of excess samarium ions (curve *1*) and the amount of Sm^{3+} ions (curve *2*) (reduced to the total amount of samarium ions in a film) as a function of the film lattice parameter. If we take into account that, according to [6], part of the Sm^{3+} ions belongs to samarium oxysulfide (whose fraction in a film is ~4%) rather than to SmS, then the true amount of Sm^{3+} ions in SmS can be given by curve *3*. Curves *3* and *1* are seen to agree well, which indicates that all excess samarium ions in SmS are trivalent. It is believed that the additional Sm^{3+} ions should affect the parameters of the phase transformation upon mechanical polishing.

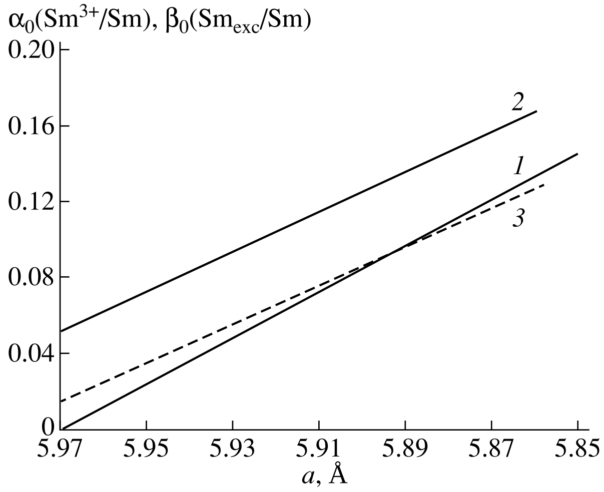

Fig. 1. Characteristics of thin polycrystalline SmS films as a function of the lattice parameter: (*1*) fraction of excess samarium ions in a SmS film [6], (*2*) Sm^{3+} ion fraction of the total amount of samarium ions without regard for oxysulfide impurity in a film [6], and (*3*) Sm^{3+} ion fraction of the total amount of samarium ions with allowance for the presence of ~4% oxysulfide impurity in SmS.

Thus, the mechanism of the stabilization of the SmS metallic phase has not been convincingly explained. Moreover, the effect of the excess samarium ions on the parameters of the phase transformation upon polishing has not been studied. In this work, in order to solve these problems, we examine the structure of SmS polycrystals in the region of homogeneity of this semiconductor compound using x-ray diffraction. These problems are also of practical interest, since partial transition of SmS into its metallic phase during polishing is used to control the electrical resistance of polycrystalline thin-film resistive-strain sensors [7].

2. EXPERIMENTAL

We prepared nine polycrystalline samples of samarium monosulfide, with their compositions falling in the region of homogeneity ($Sm_{1+x}S$, with x = 0–0.17). The samples were (4–9) × 3 × 20 mm in size. The method used for their preparation was described in [8]. The samples were synthesized in three stages. In the first stage, SmS was synthesized from simple elements (samarium and sulfur) in quartz ampoules and then briquetted. In the second stage, the samples were subjected to homogenizing annealing at 1000–1200°C. In the third stage, they were subjected to high-temperature annealing at T = 1600–1700°C.

To form the metallic phase, the samples were polished with diamond pastes under the same conditions. They were first polished with coarse diamond pastes and then gently polished with a micron-sized paste (to an equal degree); the treatment time was 30 min.

X-ray diffraction data were obtained with a DRON-2 apparatus using CuK_α radiation. The sample lattice parameters were measured before polishing by extrapolating the data on reflections lying in the angular range θ = 30°–75°. After polishing, it is difficult to determine the lattice parameter of the semiconducting phase in samples with high values of x in the angular range θ = 30°–75°, since the intensities of the reflections of this phase are low as compared to those of the metallic phase. Therefore, in this x range, the values of a of the semiconducting and metallic phases were determined by averaging the values calculated from reflections lying in the angular range θ = 15°–75°.

From the difference in the lattice parameters of the semiconducting and metallic phases with the same crystal structure, we calculated the relative amount of the forming metallic phase with respect to the total amount of SmS by measuring the reflection peak heights. For this purpose, we used the (111), (200), and (220) reflections of the semiconducting phase and their counterpart reflections of the metallic phase. The calculated amounts of the metallic phase were averaged.

The crystallite size (i.e., the size of coherent-scattering domains) was determined approximately by assuming that the broadening of the reflection peaks is due to the small size of coherent-scattering domains. As a standard, we used a Ge powder, and we chose $y = 1/(1 + \gamma x^2)$ as an approximating function. For calculation, we used the Scherrer formula

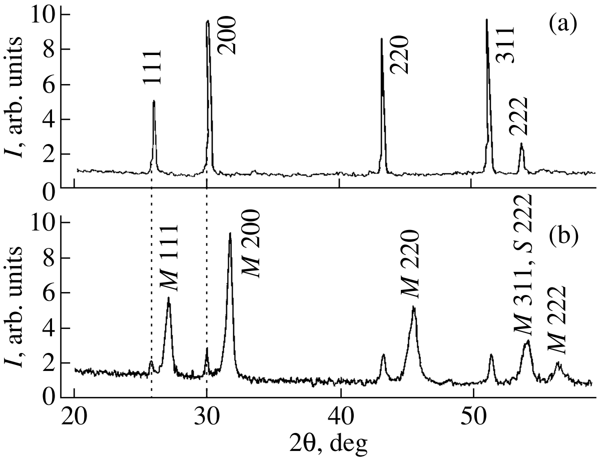

Fig. 2. X-ray diffraction patterns of a polycrystalline $Sm_{1.08}S$ sample (a) before and (b) after polishing (M stands for the metal phase, S stands for the semiconducting phase).

$$D = \frac{0.9\lambda}{\cos\theta_0\Delta'(2\theta)}.$$

Here, D is the effective coherent-scattering domain size, λ is the x-ray radiation wavelength, θ_0 is the Bragg angle (chosen for calculations), and $\Delta'(2\theta)$ is the half-width at half-maximum (HWHM), which was determined from the formula $\Delta' = \sqrt{\Delta_1'^2 - \Delta_0'^2}$, where Δ_1' is the measured HWHM of the (111) reflection of SmS and Δ_0' is the measured HWHM of the (200) reflection of the standard. The conditions for recording the x-ray diffraction patterns of samples and the standard were identical. As an example, Fig. 2 shows x-ray diffraction patterns of a polycrystalline $Sm_{1.08}S$ sample before (Fig. 2a) and after polishing (Fig. 2b).

3. RESULTS AND DISCUSSION

Figure 3 shows the concentration dependences of the SmS lattice parameter in the region of homogeneity in the semiconducting phase (curve *1*) and in the metallic phase produced by polishing (curve *2*). A sharp decrease in a is observed in the semiconducting phase at $x > 1.06$. Figure 4 shows the experimental concentration dependence of the relationship between the reflection intensities of CuK_α radiation for the metallic phase (I_m) and the semiconducting phase (I_s) after polishing. At $x > 1.06$, the relative reflection intensity of the metallic phase, $S = I_m/(I_m + I_s)$, begins to increase sharply. The table gives the measured coherent-scattering domain sizes in polycrystals in the initial state (D_0) and after polishing (D_s for the semiconducting phase and D_m for the metallic phase). It can be seen that, in all

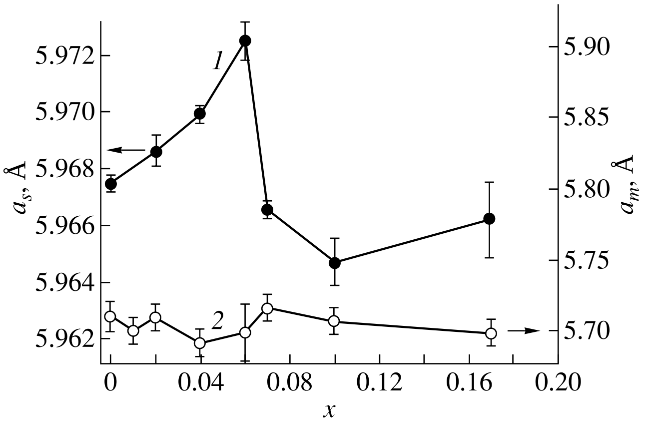

Fig. 3. Concentration dependence of the lattice parameter of homogeneous polycrystalline $Sm_{1+x}S$ in (*1*) the semiconducting phase and (*2*) the metallic phase produced by polishing.

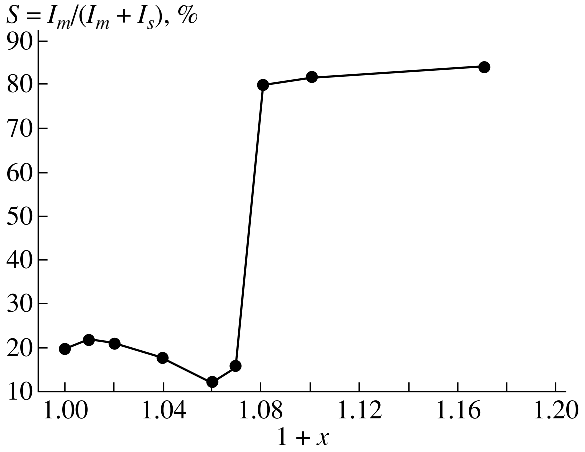

Fig. 4. Concentration dependence of the relative x-ray diffraction intensity for the reflections of the metallic (I_m) and semiconducting (I_s) phases after controlled polishing.

samples after polishing, the coherent-scattering domain sizes decrease and these sizes for the semiconducting state are always larger than those for the metallic state ($D_0 > D_s > D_m$ for all compositions).

X-ray coherent-scattering domain sizes in the semiconducting (before and after polishing) and metallic phases of $Sm_{1+x}S$ samples

x	D_0, Å	D_s, Å	D_m, Å
0	550	350	190
0.02	750	320	151
0.04	700	370	190
0.06	570	360	184
0.07	600	375	182
0.08	550	370	215
0.10	–	400	176
0.17	500	300	190

The experimental results given in Fig. 3 make it possible to calculate the thicknesses of the metallic layers that form at the surface of SmS semiconducting samples with different compositions during polishing. To calculate the relative intensity of x-ray diffraction reflections for $Sm_{1+x}S$ polycrystalline samples, we used conventional relations for the x-ray diffraction intensities in the Debye–Scherrer method with inclusion of absorption, which depends on the sample shape, the absorption coefficient, and the Bragg angle θ [9]. We assume that the crystallite orientation distribution is isotropic and that each crystallite is sufficiently small. In this case, extinction can be neglected and the energy scattered by a small volume dV per unit time in the direction of a ring with indices (hkl) is given by

$$I = I_0\frac{e^4}{m^2c^4}\frac{1+\cos^2(2\theta)}{2} \times \frac{1}{16\pi r\sin^2\theta\cos\theta}\lambda^3F_{hkl}^2 n\frac{1}{V_c^2}WdV, \qquad (1)$$

where I is the power scattered per unit length of the diffraction line at a distance r from the sample, I_0 is the intensity of the primary beam per unit area of its cross section, θ is the Bragg angle ($\lambda = 2d_{hkl}\sin\theta$), F_{hkl} is the structure factor of the (hkl) plane, n is the multiplicity factor of the (hkl) plane, V_c is the unit cell volume, and W is the Debye–Waller temperature factor. To take into account the absorption of x-ray radiation, we assume that, at a depth x, the intensity of the primary beam decreases to $I_0\exp(-\mu\rho x)$, where μ and ρ are the mass absorption factor and the density of a sample, respectively. We also take into account that the semiconductor–metal phase transformation in SmS is isostructural and that the measurements were performed at the same temperature. Then, for the case of a thin h-thick metallic SmS film located on the semiconducting-phase surface, Eq. (1) gives the following expression for the relative intensity of the reflection x-ray diffraction from the metallic and semiconducting phases:

$$S = \frac{I_m(h)}{I_m(h) + I_s(h)}, \qquad (2)$$

where

$$I_m(h) = \frac{\left(1 - \exp\left(-2\mu\rho_m\frac{h}{\sin\theta_m}\right)\right)\Phi(\theta_m)}{\rho_m a_m^6},$$

$$I_s(h) = \exp\left(-2\mu\rho_s\frac{h}{\sin\theta_s}\right)\frac{\Phi(\theta_s)}{\rho_s a_s^6}$$

are the reflection intensities for the metallic and semiconducting phases, respectively, with allowance for absorption; $\Phi(\theta) = (1+\cos^2 2\theta)/\sin^2\theta\cos\theta$ is an angular factor; and a is the lattice parameter. The results of calculations from Eq. (2) are shown in Fig. 5. Direct measurements of the thickness of the metallic layer forming on the surface of a thin-film SmS sample of stoichiometric composition during polishing agree reasonably well with Fig. 5a.[1]

The jumplike increase in the thickness of the metallic layer with increasing x (Fig. 5b) can be explained using a concentration model of the semiconductor–metal phase transformation in SmS. According to this model, the transformation occurs when a critical value of the electron concentration in the conduction band ($n_{\rm cr} \sim 10^{20}$ cm^{-3}) is reached. At this concentration, first the Coulomb potential of impurity (defect) samarium ions and then the Coulomb potential of the ions located on the lattice sites are completely screened. In the region of homogeneity of SmS, these impurity ions are excess samarium ions with respect to the stoichiometric composition. In [10], it was shown that, in the region of homogeneity, there is a certain value of x above which all impurity samarium ions are ionized to the trivalent state ($\mathrm{Sm}^{2+} \longrightarrow \mathrm{Sm}^{3+} + \bar{e}$). For the polycrystalline samples considered here, this value is $x \sim 0.06$, which is consistent with the behavior of the lattice parameter in the homogeneity region for the samples in the semiconductor state (Fig. 3). As shown in [11], the transition from the semiconducting $\mathrm{Sm}^{2+}\mathrm{S}$ phase to the metallic $\mathrm{Sm}^{3+}\mathrm{S}$ phase is accompanied by a change in the lattice parameter, which is proportional to the change in the valence of samarium ions. Thus, by knowing the lattice parameters of $\mathrm{Sm}^{2+}\mathrm{S}$ (a_n = 5.97 Å), $\mathrm{Sm}^{3+}\mathrm{S}$ (a_{n+1} = 5.62 Å), and the compound with an intermediate samarium valence ($a_{n+\varepsilon}$), we can find the addition to the valence of +2 (in our case, $n = 2$) for a samarium ion from the formula $\varepsilon = (a_n - a_{n+\varepsilon})/(a_n - a_{n+1})$. According to the data in Fig. 2, this addition is $\varepsilon \sim 0.02$, which can correspond to a jumplike complete or partial transition into the trivalent state of the excess (impurity) samarium ions (whose concentration is two orders of magnitude lower than that of the host ions located on the lattice sites [10]). When a sample is polished, $n_{\rm cr}$ is reached in the surface layer that transforms into the metallic phase. According to [2], $n_{\rm cr}$ is reached when the relative decrease in volume of SmS under the polishing-induced pressure, $\Delta = \varepsilon_{xx} + \varepsilon_{yy} + \varepsilon_{zz}$ reaches the value corresponding to $n_{\rm cr}$. Upon compression, the concentration of conduction electrons in SmS increases, so $n_{\rm cr} = n_0 + n_\Delta$, where n_Δ is the compression-induced addition to the electron concentration. Since Δ decreases monotonically with distance from the sample surface [2], a jumplike increase in n_0 with increasing x leads to a jumplike increase in the thickness of the metallic layer; it is this behavior that is seen in Fig. 5b.

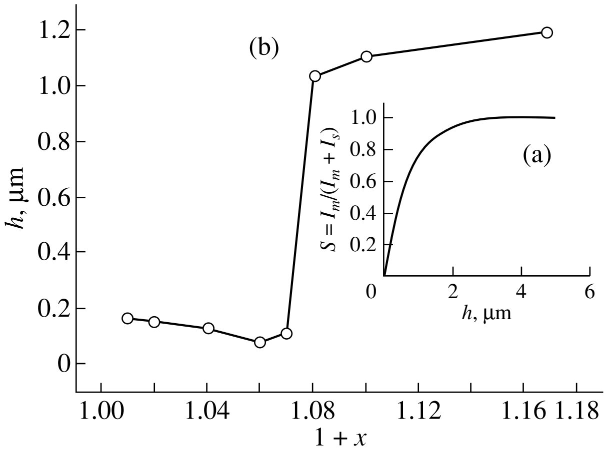

Fig. 5. (a) Dependence of the relative diffraction intensity on the thickness of the metallic film calculated from Eq. (2) and (b) the concentration dependence of the thickness of a metallic film (produced by polishing of $\mathrm{Sm}_{1+x}\mathrm{S}$), calculated from the data on the relative intensity of x-ray reflections (CuK_α radiation).

The data given in the table allow us to understand the cause of the stabilization of the metallic SmS modification after the termination of polishing. When a polycrystal is polished, many defects form in its surface layer, which results in a decrease in the sizes of coherent-scattering domains (single-crystal domains with an ordered arrangement of ion sites).[2] The formation of defects is related to the change in the volume of SmS due to the phase transformation (~14%). The boundaries of single-crystal domains are defect-containing SmS layers whose thickness is generally accepted to be equal to about one lattice parameter. Using this fact and the values of D_s, D_m, and D_0, we can estimate the volume fraction V of the defect-containing material in each specific case from the formula

$$V = 1 - \frac{(D-2a)^3}{D^3}. \qquad (3)$$

The minimum value of V for the metallic phase (D_m = 215 Å, see table) can be calculated to be 0.15. The maximum value of V for the semiconducting phase (D_s = 300 Å) is 0.115. Thus, in homogeneous polycrystalline $\mathrm{Sm}_{1+x}\mathrm{S}$ samples, the fraction of defect samarium ions

---

[1] With a MII-4 microinterferometer, we measured the thicknesses of a SmS film before and after chemical etching of the metallic layer formed on its surface. The thickness of the metallic layer determined as the difference of these two thicknesses was found to be ~0.1 µm.

[2] It should be noted that the coherent-scattering domain sizes do not coincide with the crystallite sizes in a polycrystal but rather are much smaller. According to our data, the coherent-scattering domain sizes do not exceed 2500 Å even in the most perfect single-crystal SmS samples.

is always higher than 0.15 in the metallic phase and is always lower than 0.12 in the semiconducting phase.

It is known [12] that, in $Sm_{1-x}Ln_xS$ substitutional solid solutions of samarium monosulfide with monosulfides of trivalent elements (Ln = Cd, Y), hysteresis takes place as an applied hydrostatic pressure is removed. The hysteresis consists in the fact that, when the concentration of these elements is higher than a certain critical value lying in the range $0.12 < x < 0.15$, the samples retain their metallic state after the pressure is removed and again become semiconductors only after heating. A similar situation is likely to take place in our case. The only difference is that the role of the foreign trivalent ions is played by the samarium ions in the "defect" (trivalent) state. Their critical concentration $V = 0.12$–0.15 is in good agreement with the critical value of x for Gd and Y. After the polishing is terminated, i.e., once the action of pressure is removed, D becomes small and the sample accumulates an amount of Sm^{3+} ions for which the number of electrons in the conduction band exceeds n_{cr}; therefore, the sample is in the metallic phase. This phase can exist for an infinitely long time until the amount of defect samarium ions is decreased by any means (e.g., by annealing). This conclusion is corroborated experimentally. The surface of a SmS sample was transformed into the metallic state through polishing and had the following parameters: $S = 13\%$, $D_s = 350$ Å ($V = 0.10$), and $D_m = 200$ Å ($V = 0.16$). After vacuum annealing at $T = 500°C$, the metallic phase disappeared ($S < 1\%$), which was accompanied by an increase in the coherent-scattering domain size to $D = 530$ Å. This value corresponds to $V = 0.07$, which is sufficiently small (below the critical value $V = 0.12$) for the transformation into the semiconducting state to occur. A decrease in the relative amount of defects is seen to result in transformation of the metallic SmS phase into the semiconducting phase.

4. CONCLUSIONS

We have studied the structures of the semiconducting and metallic modifications of polycrystalline samarium sulfide in the region of its homogeneity ($Sm_{1+x}S$ with $x = 0$–0.17) and revealed the following features.

(1) The metallic phase forms upon polishing because of an increase in the amount of defects in the surface layer, which manifests itself in a decrease in the x-ray coherent-scattering domain size. The excess samarium ions (with respect to the stoichiometric composition) decrease the critical values of the external influences for the transformation into the metallic phase because these ions transfer to the trivalent state at $x \geq 0.06$.

(2) The metallic modification is retained on the surface of a semiconductor sample because the coherent-scattering domain size remains sufficiently small (less than the critical value of ≤ 200 Å) after polishing has terminated; mechanical residual stresses do not play an important role in this stabilization.

ACKNOWLEDGMENTS

This work was supported by the Dial Engineering Closed Company.

REFERENCES

1. A. V. Golubkov, E. V. Goncharova, V. P. Zhuze, G. M. Loginov, V. M. Sergeeva, and I. A. Smirnov, *Physical Properties of Chalcogenides of Rare-Earth Elements* (Nauka, Leningrad, 1973) [in Russian].
2. L. N. Vasil'ev, V. V. Kaminskiĭ, and Sh. Lani, Fiz. Tverd. Tela (St. Petersburg) **39** (3), 577 (1997) [Phys. Solid State **39**, 502 (1997)].
3. V. V. Kaminskiĭ, V. A. Kapustin, and I. A. Smirnov, Fiz. Tverd. Tela (Leningrad) **22** (12), 3568 (1980) [Sov. Phys. Solid State **22**, 2091 (1980)].
4. A. V. Ryabov, B. I. Smirnov, S. G. Shul'man, T. B. Zhukova, and I. A. Smirnov, Fiz. Tverd. Tela (Leningrad) **19** (9), 2694 (1977) [Sov. Phys. Solid State **19**, 1580 (1977)].
5. T. B. Zhukova, V. M. Sergeeva, S. G. Shul'man, and I. A. Smirnov, Fiz. Tverd. Tela (Leningrad) **20** (1), 236 (1978) [Sov. Phys. Solid State **20**, 131 (1978)].
6. S. V. Pogarev, I. N. Kulikova, E. V. Goncharova, M. V. Romanova, L. D. Finkel'shteĭn, N. N. Efremova, T. B. Zhukova, K. G. Gartsman, and I. A. Smirnov, Fiz. Tverd. Tela (Leningrad) **23** (2), 434 (1981) [Sov. Phys. Solid State **23**, 245 (1981)].
7. N. M. Volodin and V. V. Kaminskiĭ, USSR Inventor's Certificate No. 1,311,357.
8. A. V. Golubkov, T. B. Zhukova, and V. M. Sergeeva, Neorg. Mater. **2** (1), 77 (1966).
9. A. Guinier, *Theorie et Technique de la Radiocristallographie* (Dunod, Paris, 1956; Fizmatgiz, Moscow, 1961).
10. V. V. Kaminskiĭ, A. V. Golubkov, and L. N. Vasil'ev, Fiz. Tverd. Tela (St. Petersburg) **44** (8), 1501 (2002) [Phys. Solid State **44**, 1574 (2002)].
11. M. B. Maple and D. Wohlleben, Phys. Rev. Lett. **27**, 511 (1971).
12. A. Jayaraman, P. D. Dernier, and L. D. Longinotti, High Temp. High Press. **7** (1), 1 (1975).

Translated by K. Shakhlevich

Physics of the Solid State, Vol. 47, No. 4, 2005, pp. 627–631. Translated from Fizika Tverdogo Tela, Vol. 47, No. 4, 2005, pp. 603–607.

SEMICONDUCTORS AND DIELECTRICS

Excitation of Self-Trapped-Exciton Luminescence in the Recombination of Frenkel Defects in BeO

S. V. Gorbunov* and V. Yu. Yakovlev**

**Ural State Technical University, ul. Mira 19, Yekaterinburg, 620002 Russia*
e-mail: zats@dpt.ustu.ru
***Tomsk Polytechnic University, pr. Lenina 30, Tomsk, 634034 Russia*

Received April 14, 2004; in final form, August 6, 2004

Abstract—Polarized luminescence and transient optical absorption (TOA) induced by pulsed electron irradiation in beryllium oxide crystals were studied. Exponential stages with decay times $\tau = 6.5$ ms were observed to exist in luminescence bands at 4.0, 5.0, and 6.7 eV, which coincide in spectral composition and polarization characteristics with the luminescence of self-trapped excitons (STEs) of two types. The formation efficiency of centers with a 6.5-ms decay time is comparable to that of triplet STEs. The general characteristics of the kinetics and the decay times of the TOA of these centers do not depend on electron fluence and are governed by the monomolecular recombination process. The spectra of TOA centers with a decay time of 6.5 ms were found to be similar to those of *V*-type hole centers and STE hole components. The mechanism by which recombination of closely spaced, spatially correlated Frenkel pairs, Be^+ and V^- centers, brings about an exponential component with a 6.5-ms decay time in the luminescence of STEs of two types in BeO is discussed. *© 2005 Pleiades Publishing, Inc.*

1. INTRODUCTION

Earlier luminescence studies revealed the existence of two different types of self-trapped excitons (STEs) in beryllium oxide [1, 2]. The two STE types originate from bonds of two types in the BeO wurtzite lattice, namely, $Be–O_{axial}$ and $Be–O_{nonaxial}$ bonds, which are oriented parallel and at an angle of 109° to the optical *C* axis of the crystal, respectively. The luminescence, decay times, and polarization parameters permitted assignment of the bands at 6.7 and 4.0 eV to the triplet and singlet "axial" STEs (referred to subsequently as STE I). The luminescence at 4.9 eV was attributed to triplet "nonaxial" STEs (STE II in what follows).

The structure of triplet STEs of both types in BeO has been subsequently studied using time-resolved pulsed absorption spectroscopy with nanosecond-range electron beam excitation [1, 3]. A band at 1.7 eV, associated with optical transitions in the electronic exciton component, has been detected in the transient optical absorption (TOA) spectrum of STE I and STE II. The data from [3] permitted the conclusion that the electronic components of both triplet STE types have a similar structure. Recent studies of STEs in BeO conducted using optically detected magnetic resonance [4] revealed that the electronic component of the STEs is partially localized at the *s* states of beryllium. An analysis of the STE TOA spectrum at energies $E > 2$ eV revealed transitions in the hole core, whose structure is different in STE I and STE II. The TOA decay kinetics studied in the region of the STE-I hole component exhibits, in addition to the stage governed by the STE-I lifetime, an exponential stage with a relaxation time $\tau = 6.5$ ms. This component was attributed to the formation and decay of self-trapped holes [5]. The same exponential component with $\tau = 6.5$ ms was revealed in the decay kinetics of luminescence in the 4.0-eV region [6] and was assigned to radiative transitions from the STE-II triplet state split by the low-symmetry crystal field. Thus, the controversial data obtained in [5, 6] on the centers associated with the 6.5-ms component did not establish their nature reliably.

The present study deals with a search for the decay component with $\tau = 6.5$ ms in the STE luminescence. An analysis of luminescence and TOA data establishes the main characteristics of luminescence excitation of the two STE types related to the formation and recombination of closely spaced, spatially correlated cation Frenkel pairs of BeO defects.

2. EXPERIMENTAL TECHNIQUES

The studies were carried out on nominally pure BeO crystals grown, using the Czochralski–Kyropoulos technique, from a beryllium oxide solution in a sodium tungstate melt [7]. The content of the characteristic impurities Li, B, Mg, Al, and Zn did not exceed 10 ppm. Optical measurements in the range 1.0–6.0 eV were carried out at temperatures of 80–300 K using pulsed absorption and luminescence spectroscopy with nanosecond-range time resolution [8]. Luminescence was excited using a GIN-600 pulsed electron accelerator with beam parameters $E_e = 0.25$ MeV, $W = 0.02$–0.50 J/cm^2, and $t_{pulse} = 10^{-8}$ s. Additional studies of opti-

Spectral response, decay kinetics, and polarization of STE luminescence in BeO

STE type	Luminescence peak position E_m, eV	Decay time τ, s	Degree of polarization P
Singlet STE I	4.0	2×10^{-9}	+0.67
Triplet STE I	6.7	340×10^{-6}	–0.75
Triplet STE II	4.9	36×10^{-6}	–0.60

cal absorption spectra in polarized light and of polarized luminescence were conducted with a Rochon prism. The degree of polarization of luminescence was determined as

$$P = (I_{\parallel} - I_{\perp})/(I_{\parallel} + I_{\perp}),$$

where $I_{\parallel}$ and $I_{\perp}$ are the luminescence intensities with the electric vector parallel and perpendicular to the C axis of the BeO crystal, respectively.

3. EXPERIMENTAL RESULTS AND DISCUSSION

Our study of the luminescence decay kinetics in the range 3.0–6.0 eV revealed, in addition to the components deriving from radiative relaxation of the two types of STEs (see table), an exponential stage with a decay time $\tau = 6.5$ ms. Figure 1 displays a cathodoluminescence (CL) spectrum of BeO induced by an electron beam pulse at 80 K and measured with a time delay $t_d = 15$ ms to exclude the effect of the STE luminescence, which is a few orders of magnitude stronger. As seen from the deconvolution into Gaussian constituents, the CL spectrum of the component with $\tau = 6.5$ ms consists of three bands. The band at 4.0 eV, for which the degree of polarization is $P = +0.64 \pm 0.03$, coincides with the luminescence of singlet STE I in terms of its spectral and polarization characteristics (see table). In the spectral region $E > 5.5$ eV, one observes a steep growth in the luminescence intensity. As is evident from Fig. 1, the spectral behavior of the "slow" luminescence stage in this region fits well with that of the long-wavelength decay of the 6.7-eV band of triplet STE I. Also, the degree of polarization (–0.70 ± 0.05) of the luminescence with a relaxation time of 6.5 ms at 6.0 eV is practically identical to that of triplet STE I (see table). It should be pointed out that, using Gaussian extrapolation to the region of the maximum of the 6.7-eV band, the luminescence intensity of the slow component is found to be two orders of magnitude greater than the luminescence intensity at 4.0 eV.

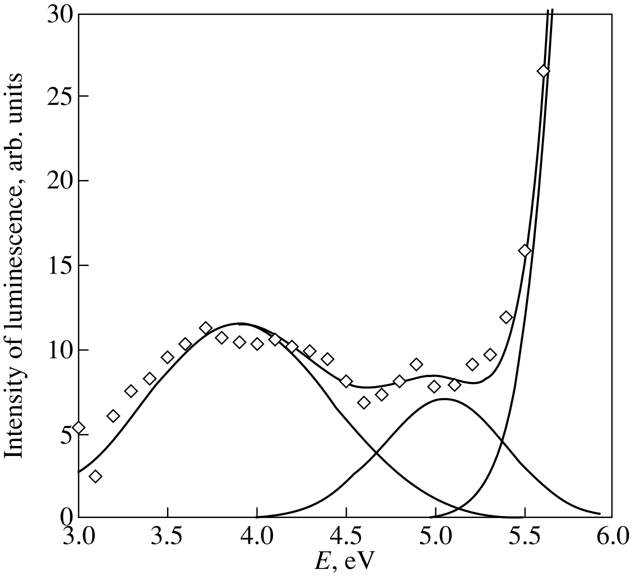

Fig. 1. Luminescence spectrum obtained at 80 K with a gate delay of 15 ms after termination of an electron beam pulse.

In addition to the luminescence bands at 4.0 and 6.7 eV attributed to the singlet and triplet STE I, the spectrum of the CL component with $\tau = 6.5$ ms contains a band peaking at 5.0 eV. The degree of polarization at about 4.7 eV was found to be $P = –0.30 \pm 0.10$. This figure differs slightly from the luminescence polarization of triplet STE II (see table) because of the contribution due to the positively polarized luminescence at 4.0 eV in this region. The spectral and polarization characteristics of the 5.0-eV luminescence band with a decay time of 6.5 ms suggest that it is related to the luminescence of triplet STE II.

The above conclusions are supported by the temperature dependences of the relaxation times and of the initial luminescence band intensity of the component with $\tau = 6.5$ ms (Fig. 2). We see that the main features in the behavior of these dependences coincide; indeed, for $T > 100$ K, one observes a shortening of the decay time paralleled by an increase in the initial intensity with the same activation energy $E_a = 120 \pm 10$ meV. This temperature dependence suggests that the component with $\tau = 6.5$ ms provides a constant contribution to the integrated intensity of the luminescence bands at 4.0, 5.0, and 6.7 eV. Thus, our luminescence studies of BeO crystals revealed the existence of centers whose destruction with a 6.5-ms time constant gives rise to the formation of luminescence states of both types of STEs.

To probe the nature of these centers, we carried out a comprehensive study of the decay kinetics and spectra of the TOA induced by an electron pulse at 80 K. In the 3.6-eV region, the decay of optical absorption can be described by a sum of three exponential components with decay times $\tau_1 = 340$ μs, $\tau_2 = 6.5$ ms, and $\tau_3 = 450$ ms (Fig. 3). This indicates the existence of three different centers of nonsteady absorption, among which triplet STE I is the first to undergo radiative relaxation with a decay time of 340 μs. An investigation of the temperature dependence of the decay times and initial optical density of the component with $\tau_2 = 6.5$ ms showed that, at $T > 100$ K, the lifetime of the centers responsible for this component shortens with the same activation energy $E_a = 120 \pm 10$ meV with which the relaxation of the STE-I and STE-II luminescence component with $\tau_2 = 6.5$ ms is accelerated (Fig. 2). Note that the initial optical absorption amplitude of these centers is temperature-independent. The efficiency of creation of the centers responsible for the $\tau_2 = 6.5$-ms component, as estimated from the initial optical absorption density, turned out comparable (70–80% of the initial optical density of the component with $\tau_1 = 340$ μs) to that of triplet STE I.

To comprehensively analyze the relaxation processes, we investigated the dependence of the decay kinetics and of the initial TOA optical density on the electron beam fluence. The results obtained reveal the following features of centers of metastable optical absorption.

(1) The electron pulse–induced optical absorption density of STE I and of centers with a characteristic decay time of 6.5 ms increases in proportion to the electron fluence (Fig. 3). This observation indicates the intrinsic nature of the absorption centers.

(2) The amplitude of the optical absorption density of centers with a characteristic lifetime of 450 ms tends to a constant value with increasing electron fluence (Fig. 3). This suggests that these centers are lattice defects or impurities.

(3) Increasing the electron fluence has no effect on the exponential pattern of the kinetics or the decay time of the component with $\tau = 6.5$ ms. This feature of the kinetic behavior should be attributed to the monomolecular character of recombination in genetic pairs [9]. As an illustration, we may recall the recombination brought about by Coulomb or elastic interaction of charged or neutral defects. Such relaxation processes are known to occur, in particular, with spatially correlated anion Frenkel pairs in alkali halide crystals (α–I and *F*–*H* centers) [10].

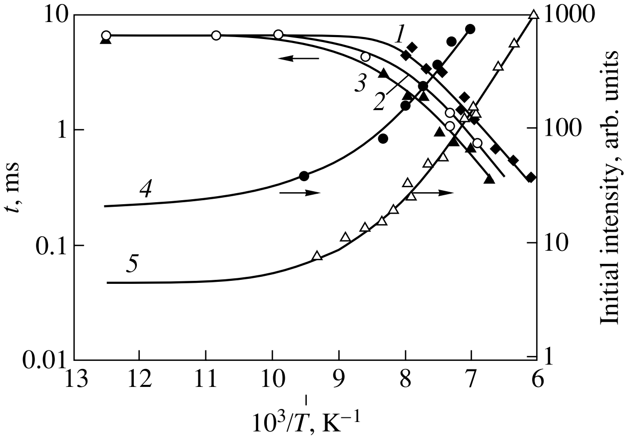

Fig. 2. Temperature dependence of the decay times of (*1*, *3*) luminescence, (*2*) TOA, and (*4*, *5*) initial luminescence intensity at (*1*, *5*) 4.0 and (*3*, *4*) 6.0 eV.

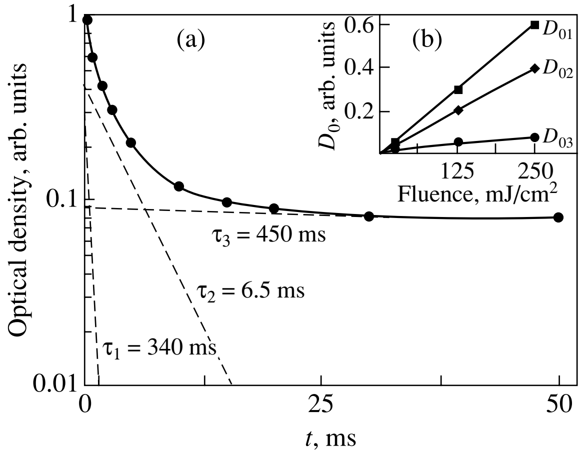

Fig. 3. (a) Relaxation kinetics of transient optical absorption at 3.6 eV induced by an electron beam pulse in BeO crystals at 80 K. Dashed curves are deconvolution of the kinetics curve into exponential functions. (b) Optical-density amplitudes of optical absorption decay kinetics components plotted versus electron fluence.

A specific feature of the hexagonal (wurtzite) structure of BeO is the close-packed arrangement of oxygen ions, in which one-half of the tetrahedral voids is occupied by beryllium ions, while the other half of the tetrahedral voids ($r_t = 0.34$ Å) and all octahedral voids ($r_{\text{oct}} = 0.55$ Å) form interstitial space [11]. Comparing the effective ionic radii of O^{2-} (1.36 Å) and Be^{2+} (0.34 Å) suggests that the most probable process for BeO would be the formation of close-spaced cation Frenkel pair defects (CFPD). In an attempt to find support for this hypothesis, we studied TOA spectra obtained at 80 K with different time delays after termination of the electron pulse (Fig. 4). As follows from a comparison of induced-absorption spectra, centers with a relaxation time of 6.5 ms do not produce a band at 1.7 eV, which is due to optical transitions in the STE electronic component. Because the electronic component is actually an electron localized at the *s* states of beryllium [4], this observation may be due to the Be^+ ion being displaced from a lattice site into an interstice. At $E > 2$ eV, the TOA spectrum of centers with a 6.5-ms decay time lies in the region of optical transitions in the STE hole core in BeO. Furthermore, the absorption spectrum of these centers correlates well with that of the V^- and V_B stable hole centers, which are a hole trapped by an oxygen ion (O^- center) near an isolated cation vacancy or near a cation vacancy associated with a Be^{2+} ion, acting here as a charge compensator (Fig. 4).

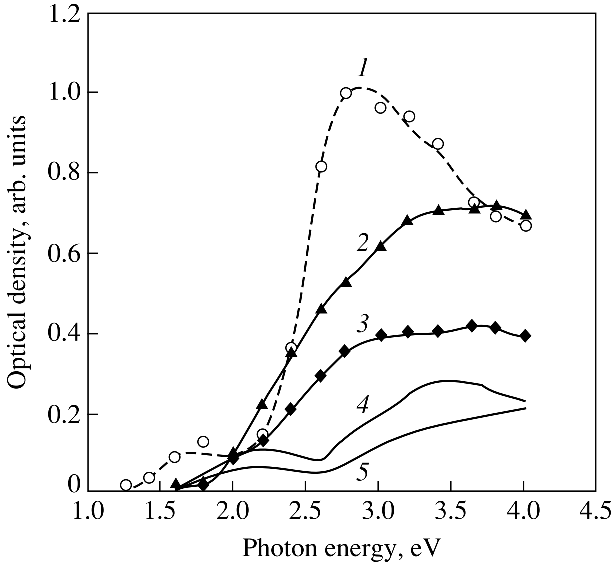

Fig. 4. (*1–3*) TOA spectra measured (*1*) at the end of electron irradiation and (*2, 3*) with a gate delay of 5 ms. (*4, 5*) Spectra of steady-state optical absorption of hole V_B centers measured for polarized light with (*1, 3, 5*) $\mathbf{E} \perp \mathbf{C}$ and (*2, 4*) $\mathbf{E} \parallel \mathbf{C}$.

Based on all of the above observations, we put forward the following mechanism for the formation of centers whose recombination is accompanied by the luminescence of both STE types in BeO with a decay time of 6.5 ms.

(1) In the first stage, an electron beam initiates the formation of excitons and their relaxation to the self-trapped state, which is accompanied by localization of the electron at the *s* states of a beryllium ion in the form of a Be^+ center and localization of the hole at the *p* states of an oxygen ion in the form of an O^- center.

(2) Fast vibrational relaxation of the electronic STE subsystem to the lowest luminescing state imparts an energy to the Be^+ ion that is high enough to displace the ion to an interstitial site with the formation of a charged, spatially correlated CFPD, namely, a Be^+ center and a V^- center.

(3) Coulomb interaction stimulates recombination of close-spaced CFPDs, which occurs with a relaxation time of 6.5 ms at 80 K. This brings about lattice recovery and the formation of excited states of STEs of both types in BeO. Radiative relaxation from these states manifests itself as an exponential component with monomolecular decay kinetics in the luminescence bands of the STE-I singlet and triplet at 4.0 and 6.7 eV, as well as in the luminescence band at 5.0 eV of the STE-II triplet. An increase in temperature gives rise to an increase in the recombination rate of close-spaced CFPDs characterized by an activation energy of 120 meV, but the contribution of this mechanism to the integrated luminescence intensity of both STE types in BeO remains constant.

The possibility of spatial separation of the CFPD components in BeO remains an open problem. The kinetics of electron beam pulse–induced absorption contains a stage with a decay time $\tau_3 = 450$ ms (Fig. 3). The above characteristics of the centers responsible for this stage suggests their relation to defects. We believe that these metastable defects could be spatially separated components of cation Frenkel pairs (Be^+ and V^- centers) forming in the dissociation, as it were, of spatially correlated CFPDs. Indeed, the TOA spectrum of the stage characterized by a 450-ms decay time is similar to the absorption spectrum of stable *V*-type hole color centers. The long relaxation times of these centers are signatures of the localization and migration of interstitials (Be^+ ions) separated by a considerable distance from the *V* centers. For $T > 120$ K, these processes undergo thermally stimulated acceleration with an activation energy of 190 ± 10 meV, which brings about a decrease in the decay time of the $\tau = 450$-ms component in the recombination of spatially separated Be^+–V^- Frenkel pairs. The activation energy (190 meV) of thermally stimulated recombination of spatially separated CFPDs is higher than that of spatially correlated CFPDs (120 meV).

The activation energy of 190 meV is close to the average activation energy of ~200 meV in the region of the peak of thermally stimulated luminescence (TSL) at 100 K, which is characteristic of all BeO crystals [12]. The spectral composition of the TSL peak at 100 K (which contains STE luminescence bands at 4.9 and 6.7 eV) may be governed by the recombination of spatially separated CFPD components.

ACKNOWLEDGMENTS

The authors are grateful to A.F. Zatsepin, S.O. Cholakh, and A.I. Kukharenko for discussions and assistance in the work.

REFERENCES

1. S. V. Gorbunov, S. V. Kudyakov, B. V. Shulgin, and V. Yu. Yakovlev, Radiat. Eff. Defects Solids **135**, 269 (1995).
2. V. A. Pustovarov, V. Yu. Ivanov, M. Kirm, A. V. Kruzhalov, A. V. Korotaev, and G. Zimmerer, Fiz. Tverd. Tela (St. Petersburg) **43** (7), 1189 (2001) [Phys. Solid State **43**, 1233 (2001)].
3. S. V. Gorbunov, S. V. Kudyakov, V. Yu. Yakovlev, and A. V. Kruzhalov, Fiz. Tverd. Tela (St. Petersburg) **38** (4), 1298 (1996) [Phys. Solid State **38**, 719 (1996)].
4. U. Rogulis, S. V. Gorbunov, and J.-M. Spaeth, in *Proceedings of 12th International Conference on Radiation Physics and Chemistry of Inorganic Materials* (Tomsk, Russia, 2003), p. 38.
5. S. V. Gorbunov, S. V. Kudyakov, V. Yu. Yakovlev, and A. V. Kruzhalov, Fiz. Tverd. Tela (St. Petersburg) **38** (1), 214 (1996) [Phys. Solid State **38**, 119 (1996)].

6. S. V. Gorbunov, K. V. Bautin, A. V. Kruzhalov, and V. Yu. Yakovlev, in *Abstracts of the 5th International Conference on Inorganic Scintillators and Their Applications, SCINT99* (Moscow, 1999), p. 73.
7. Yu. V. Shurupov, A. V. Kruzhalov, and S. V. Gorbunov, in *Abstracts of XV Congress of the International Union of Crystallography* (Bordeaux, France, 1990), PS-13.03.22.
8. B. P. Gritsenko, V. Yu. Yakovlev, G. D. Lyakh, and Yu. N. Safonov, in *Abstracts of All-Union Conference on Metrology of High-Speed Processes* (Moscow, 1978), p. 61.
9. Yu. R. Zakis, L. N. Kantorovich, E. A. Kotomin, V. N. Kuzovkov, I. A. Tale, and A. L. Shlyuger, *Models of Processes in Wide-Gap Solids with Defects* (Zinatne, Riga, 1991) [in Russian].
10. Ch. B. Lushchik and A. Ch. Lushchik, *Decay of Electron Excitations with Defect Formation in Solids* (Nauka, Moscow, 1989) [in Russian].
11. R. A. Belyaev, *Beryllium Oxide* (Atomizdat, Moscow, 1980) [in Russian].
12. I. N. Ogorodnikov, V. Yu. Ivanov, and A. V. Kruzhalov, Fiz. Tverd. Tela (St. Petersburg) **36** (11), 3287 (1994) [Phys. Solid State **36**, 1748 (1994)].

Translated by G. Skrebtsov

Physics of the Solid State, Vol. 47, No. 4, 2005, pp. 632–637. Translated from Fizika Tverdogo Tela, Vol. 47, No. 4, 2005, pp. 608–613.

Temperature Dependence of the Permittivity of $PbWO_4$ Crystals in the Range 290–550 K

V. N. Shevchuk and I. V. Kayun
Lviv Franko National University, Lviv, 79005 Ukraine
e-mail: shevchuk@wups.lviv.ua

Received May 11, 2004; in final form, July 14, 2004

Abstract—The temperature dependence of the permittivity ε of $PbWO_4$ crystals is studied in the range T = 290–550 K at a frequency of 1 kHz. The ε(T) dependences measured on heating and cooling are different. On heating, groups of narrow maxima at 290–330 K and 330–400 K are observed in the ε(T) curves. The first group of peaks is dominant. High-temperature polarization produces an additional broad peak in the ε(T) curve at 400 K. A linear ε(T) dependence is observed in the range 400–470 K. Above 470 K, the variation in ε(T) closely follows an exponential law. Restoring relaxation of ε in the range 25–30 at 290 K after high-temperature sample heating proceeds exponentially in a few stages. The features of ε(T) curves are determined by the dipole polarization and the hopping mechanism of charge exchange between complex dipole associates. Such structural defects may be pairs of doubly charged lead and oxygen vacancies (diplons). These defects also form a basis for more complicated defect complexes with localized holes (or electrons) at the corresponding vacancies. *© 2005 Pleiades Publishing, Inc.*

1. INTRODUCTION

Scheelite-structure crystals of lead tungstate $PbWO_4$ (PWO) have been intensively studied in view of their use as effective self-activated scintillation materials with short afterglow times [1]. The luminescent properties of PWO and its time characteristics depend on structural defects. However, points of view on the nature of these defects vary. The electrical and dielectric properties of this compound have not been studied sufficiently, despite the fact that they are informative in revealing point defects and monitoring the changes in the state of these defects during heat treatment.

We have performed a series of studies on the electrical properties of PWO crystals in an external ac electric field and on thermally stimulated polarization–depolarization currents in the temperature range 290–600 K [2–4]. The permittivity and dielectric loss of doped PWO crystals were considered in [5–11] in order to establish the features of impurity defect formation.

The first of those studies [5] deals with some dielectric characteristics of lead molybdate and tungstate at temperatures above 540 K. In [6–10], the methods of dielectric response in the frequency range 10–10^6 Hz were used to clarify the laws of incorporation of Nb, Y, La, Gd, and F atoms into the PWO matrix at temperatures of 413–673 K. When interpreting the results, it was assumed that impurity ion–lead vacancy dipole complexes formed. Complicated vacancy dipole complexes in PWO crystals were considered in [11] using the frequency dependence of the dielectric loss. The temperature dependence of the dielectric characteristics of $CuWO_4$ was measured after various heat treatments in [12]. The permittivity and dielectric loss of some polycrystalline tungstates at a frequency of 1 kHz are given in [13].

In this study, we consider the experimental temperature and isothermal dependences of the permittivity ε in order to obtain information on the dielectric properties of PWO crystals in the range 290–550 K; isothermal variations in the permittivity were measured on samples relaxing to the quasi-equilibrium state.

2. EXPERIMENTAL

Undoped PWO crystals obtained using the Czochralski technique were studied. Samples in the form of plane-parallel plates $10 \times 10 \times 0.4$ mm in size were cut normally to the growth axis [001]. Aquadag electrodes were deposited onto the polished and cleaned surfaces of samples. A quartz temperature-controlled measuring cell was used in the experiments (with an accuracy of temperature control of better than ±1 K). The values of ε were calculated assuming that the edge effects were small and using the well-known relation for a flat capacitor [14],

$$\varepsilon = Cd/\varepsilon_0 S, \tag{1}$$

where C is the measured capacitance of the sample; d and S are its thickness and area, respectively; and ε_0 is the permittivity of free space. The capacitance of a sample was recorded using a CLR E7-13 measuring unit (operating frequency, 1 kHz). The root-mean-square value of the voltage drop on a measured object did not exceed 0.2 V. To obtain correct results, the capacitance of the connecting system was taken into account. All other experimental details were the same as those described earlier in [15]. The temperature was measured with a standard chromel–alumel thermocouple.

Measurements were performed in the regime of linear heating or cooling at a rate of 0.1 K/s in the range 290–550 K. Relaxation of a sample to the quasi-equilibrium state at room temperature after high-temperature heating was controlled by measuring the sample capacitance in certain time intervals *t*. In order to study the effect of preliminary excitation in an external dc electric field, we applied a dc voltage (up to 50 V) to a crystal over a time t_p = 5–15 min at different fixed temperatures T_p. Using the standard Origin software package, we processed the experimental data and decomposed the complex-structure maxima of the measured curves into Gaussians.

3. RESULTS

Figures 1a–1d show the temperature dependences of the permittivity of PWO crystals for different maximum sample heating temperatures T_h in each experiment. Curves are plotted both for heating and for cooling with one or several successive heating–cooling cycles. The temperature T_h was chosen in accordance with earlier studies on thermally stimulated currents for the same samples [2–4]. Using the thermal-depolarization method, under certain conditions, we observed series of maxima of depolarization currents in the temperature ranges 290–350 K (range *A*), 350–380 K (*B*), and 400–600 K (*C*). We assumed that these maxima are related to dipole polarization (ranges *A*, *B*) or to space charges produced by equilibrium carriers in a sample (range *C*) [2–4].

In Fig. 1, we see that, in ranges *A* and *B*, polarization effects strongly affect the ε(*T*) curves. In the range 400–520 K, a conventional shape of the ε(*T*) curves is observed (curve *1* in Fig. 1d). A nonlinear increase in ε at high temperatures is caused by an exponential increase in conductivity with activation energies of 0.7–0.9 eV [2–4] in the corresponding temperature intervals. In the range 290–400 K, the ε(*T*) curves measured in the heating mode exhibit closely spaced complicated maxima grouped in two rather narrow temperature regions (290–330, 330–400 K) (curve *3* in Fig. 1a; curves *1* in Figs. 1c, 1d).

The ε(*T*) curves measured on heating and cooling differ in shape. Thermal hysteresis appears for $T_h \geq$ 400 K, where the values of ε measured on heating are higher than those on cooling. In the cooling mode, no maxima are observed in the ε(*T*) curve. In repeated experiments, the ε(*T*) curves measured on heating remain nonlinear irrespective of T_h or of the duration of exposure of a sample to normal conditions prior to measurements. At $T_h \geq$ 400 K (Figs. 1a, 1b), the values of ε measured on cooling are greater than on heating for the same temperatures.

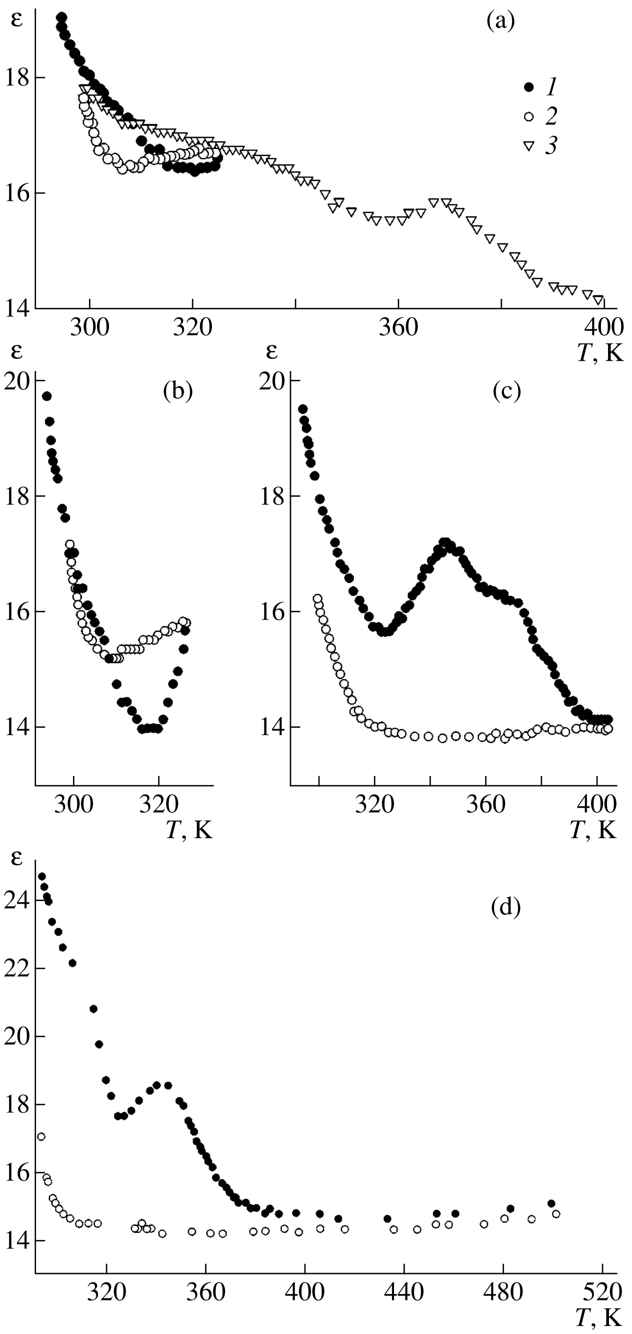

Fig. 1. Temperature dependences of the permittivity of $PbWO_4$ crystals on (*1*) heating and (*2*) cooling for different maximum measurement temperatures T_h in one heating–cooling cycle. (*3*) Heating of the sample after the first measurement cycle represented by curves *1* and *2*. T_h values: (a) 325, (b) 335, (c) 405, and (d) 515 K. Measurements in each cycle in (a–d) were performed after keeping the sample under normal conditions for longer than 24 h.

At room temperature, the values of ε usually lie in the interval 25–30. These values agree with the data obtained for PWO in [7, 16]. For quasi-equilibrium values of ε to be established after high-temperature heat-

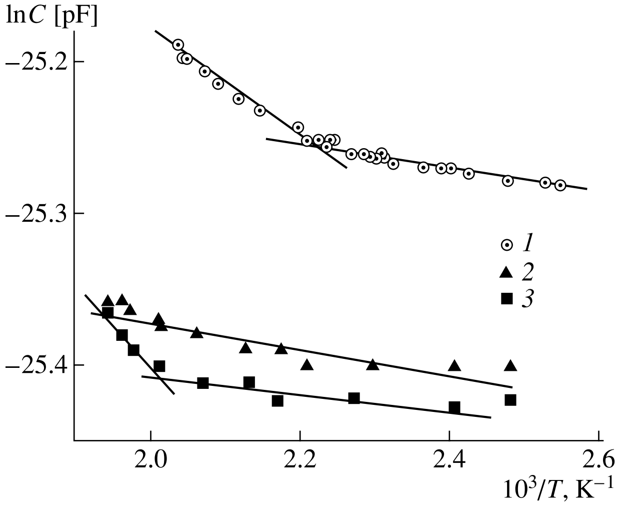

Fig. 2. Dependence of the capacitance on the inverse temperature in the case of (*1*) heating of a polarized $PbWO_4$ sample (T_p = 500 K, t_p = 5 min) and (*2*) heating and (*3*) cooling of a nonpolarized sample.

ing, a sample must be kept for about 24 h under normal conditions. The initial conductivity of the crystal is recovered in the same time period [4].

When measured on heating in the range 400–470 K, the function $\varepsilon(T)$ is linear and can be approximated by

$$\varepsilon = 10.72 + 1.67 \times 10^{-3} T. \quad (2)$$

On cooling in the range 470–320 K, ε also depends linearly on T:

$$\varepsilon = 10.71 + 9.07 \times 10^{-4} T. \quad (3)$$

For temperatures $T > 470$ K, the experimental $\varepsilon(T)$ curve deviates from a linear dependence. This deviation was observed practically in all materials (see, e.g., [12, 13, 16, 17]). The authors of [12] fitted the high-temperature segment of the $\varepsilon(T)$ curve with an exponential function. In [17], the nonlinear segment of the ε curve was described by a quadratic law. In our case, in the range 470–550 K, the best agreement between the experimental $\varepsilon(T)$ curve measured on heating and the calculated curve was obtained using an exponential function of the form

$$\varepsilon \cong 29.87 \exp(-\Delta H/kT), \quad (4)$$

where k is the Boltzmann constant. When measured on cooling, the preexponential factor in Eq. (4) was equal to ~28.70. Thus, in the $\ln C$–T^{-1} coordinates, we can fit the experimental $C(T)$ curve for $T > 470$ K with one or two straight lines (Fig. 2), whose slopes determine the activation energies ΔH. The activation energy is found to be ~0.014 eV in the case of heating for $T > 400$ K, ~0.033 eV for cooling in the region $T > 500$ K, and ~0.011 eV for cooling in the region $T < 500$ K.

The results of studies of the effect of an external dc electric field on the $\varepsilon(T)$ dependence in PWO are shown in Fig. 3 (curves *1*, *2*). For comparison, Fig. 3 also shows data for a nonpolarized sample (curves *3*, *4*). As the field was switched off at 290 K, fast relaxation processes were observed corresponding to C decreasing with time. The $C(T)$ function was measured after the end of the fast relaxation. The experiments show that, in the range 290–430 K, several maxima are observed in the $\varepsilon(T)$ curve in the case of polarized samples (peaks I–V at 305, 314, 332, 362, and 400 K, respectively; curves *1*, *2* in Fig. 3). Maxima I–III near 320 K form a dominant, rather narrow peak. During the first measurement in the heating mode, this peak was found to be a few times higher than the corresponding peak in the case of a nonpolarized sample. The intensities of peaks I–IV decrease after several heating–cooling cycles and free relaxation of the sample under normal conditions over 4–5 days. A sample polarized at T_p = 300 K and not heated retains high values of ε = 150–200 at room temperature for a long time. In the $\ln C$–T^{-1} coordinates, the increase in the capacitance of polarized samples at $T > 400$ K can be fitted by two straight lines with a kink at $T = 450$ K (curve *1* in Fig. 2). The activation energies are also low: 0.008 eV in the range $400 < T < 450$ K and 0.027 eV at $T > 450$ K.

A broad low maximum V on the $\varepsilon(T)$ dependence (curve *2* in inset to Fig. 3) is observed only for samples polarized at T_p = 400–500 K. The intensities of peaks I–III in this case are low. For nonpolarized samples at $T \geq 420$ K, ε slowly increases with T. The polarization of a sample leads to a faster increase in ε in the range 400–550 K as compared to that for a nonpolarized sample (see inset to Fig. 3).

After one or two cycles of heating to $T > 400$ K and subsequent cooling to room temperature, a nonpolarized sample returns to the quasi-equilibrium state with the initial value of ε. The kinetics of relaxation of the sample to the initial state is shown in Fig. 4. The results of measurements are plotted in the $\ln[\Delta C/(C_\infty - C)]$ versus t coordinates, where $\Delta C = C_\infty - C_0$ is the difference between the quasi-stationary value of the capacitance at $t \longrightarrow \infty$ and the initial capacitance C_0. At $t = 0$, the capacitance of the sample is $C = C_0$. To describe the time dependence of the capacitance, we used the relation

$$C = C_0 + \Delta C(1 - e^{-t/\tau}).$$

Here, τ is the time constant in the model of a homogeneous electrically neutral insulator with deep energy levels [18]. In the case of several exponential relaxation processes, a few linear segments are observed in the $\ln[\Delta C/(C_\infty - C)] = f(t)$ curve, and the slopes of these segments determine the corresponding values of τ. It is seen in Fig. 4 (curve *1*) that the $C(t)$ curve in the $\ln[\Delta C/(C_\infty - C)]$ versus t coordinates contains at least two linear segments (I, II) with a small transition region

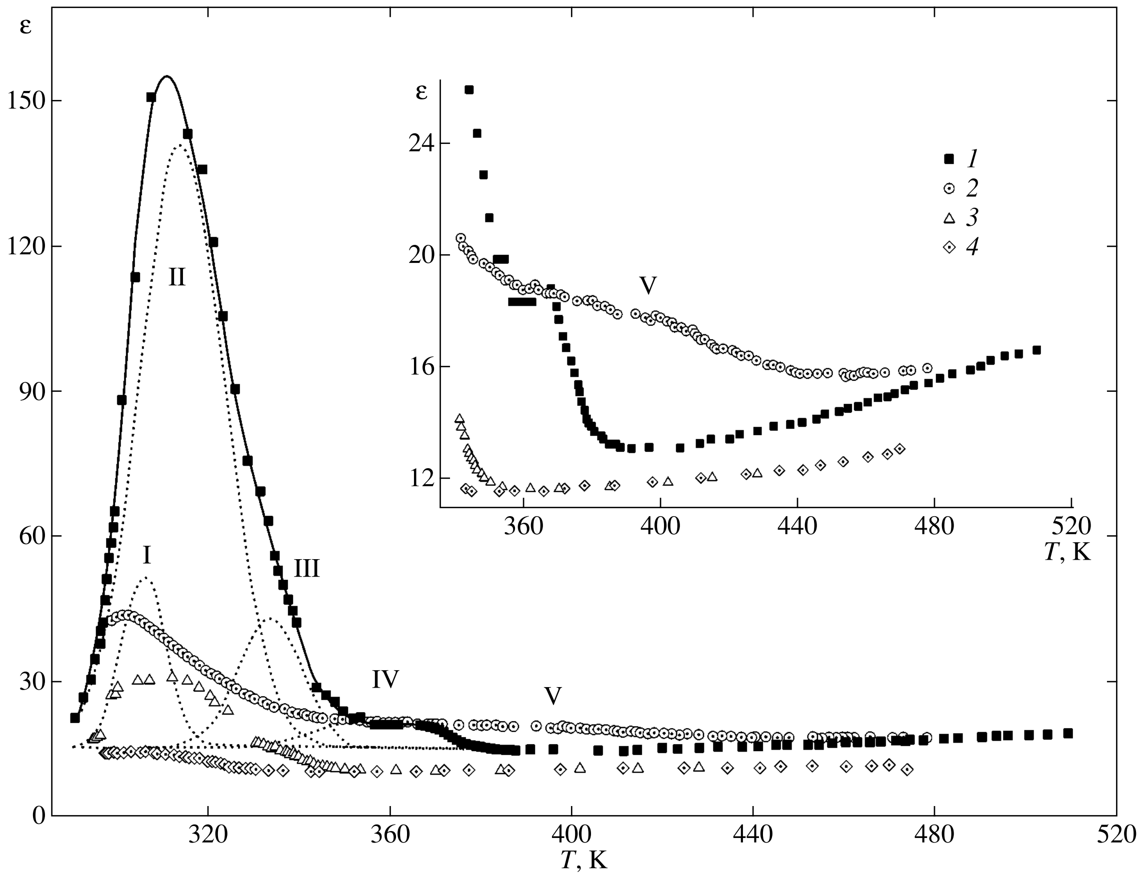

Fig. 3. Temperature dependences of the permittivity of (*1*) an initially polarized $PbWO_4$ crystal (T_p = 300 K, t_p = 10 min) and (*2*) the same sample during subsequent heating (T_p = 500 K, t_p = 5 min). (*3*, *4*) Measurements for a nonpolarized sample during two successive heating cycles, respectively. The dotted line shows elementary components (I–IV) obtained by decomposing curve *1* into Gaussians. Points correspond to the experiment, and the solid line is the sum of components I–IV. The inset shows the ε(*T*) dependence near high-temperature shoulder V.

between them. At the final stage of the relaxation, processes with large values of τ are observed (Fig. 4). As $t \longrightarrow 24$ h, quasi-equilibrium is established and the *C*(*t*) curve becomes a straight line parallel to the *t* axis. The time constants for the first and second components of the kinetics of relaxation of *C* at the initial stage (curve *1* in Fig. 4) are τ_1 = 4.3 h and τ_2 = 6.8 h.

Repeated heating–cooling cycles produce irreversible changes in the sample that are equivalent to its annealing at elevated temperatures; namely, the values of ε at 290 K decrease and, on the whole, the duration of the relaxation process in the sample shortens. The fast component is eliminated. After repeated heating–cooling cycles, only one linear segment dominates in the plot of relaxation recovery of *C*(*T*) (curves *2*, *3* in Fig. 4). The time constants corresponding to curves *2* and *3* in Fig. 4 are ~6.9 and ~24.5 h, respectively.

4. DISCUSSION

The results of the measurements show that, after cooling at a rate of ~0.1 K/s from an elevated tempera-

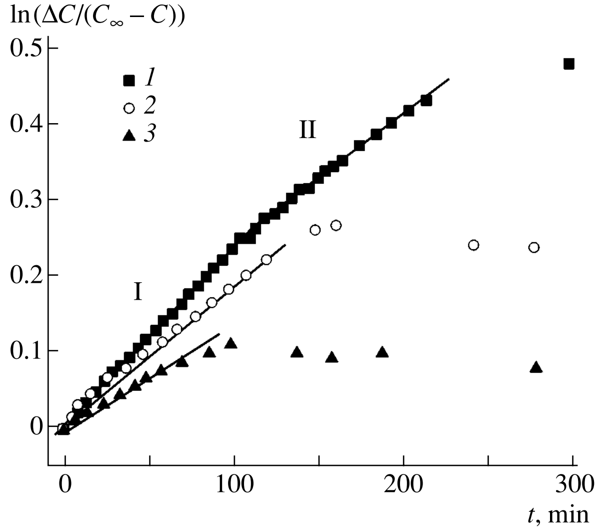

Fig. 4. Relaxation of the $PbWO_4$ sample capacitance at 290 K (*1*) after the first heating to 550 K, (*2*) after three or four subsequent measurements of ε(*T*) in the range 290–550 K, and (*3*) after many repeated heating–cooling cycles for the same sample.

ture ($T > 500$ K) to room temperature, the PWO samples under study can stay in a nonequilibrium state for a long time. This feature of the crystals is the cause of hysteresis phenomena (Fig. 1), which are known to be explained by the difference in the evolution of electrically active defects during heating and cooling [19]. For example, the dissociation energy of complicated neutral defect complexes can differ from their energy of association. Therefore, even at low cooling rates, the crystal has no time to reach quasi-equilibrium (the initial state of the defects), since the initial concentrations of defect complexes are not recovered instantaneously and the return of the sample to the equilibrium state requires long relaxation at room temperature. These processes occur in the case of a predominance of Schottky defects [19, 20]. In PWO, which is a typical system with deviation from stoichiometry, the defects are usually doubly charged lead vacancies V_{Pb}^{2-} and oxygen vacancies V_{O}^{2+}. Energy minimization and electrostatic interaction between V_{O}^{2+} and V_{Pb}^{2-} lead to the formation of neutral associates of such vacancies (bivacancies, or diplons). These associates serve as a basis for the formation of more complicated dipole defect complexes with localized electrons (holes) at oxygen (lead) vacancies. The localization of holes (p) on V_{Pb}^{2-} vacancies and the capture of electrons (e) by V_{O}^{2+} vacancies weaken the electrostatic interaction between the components of diplons and can result in bond breaking. Therefore, defect centers can arise whose formation can be simply represented by the processes

$$V_{\mathrm{Pb}}^{2-} + p = V_{\mathrm{Pb}}^{-}, \quad V_{\mathrm{O}}^{2+} + e = V_{\mathrm{O}}^{+}. \tag{5}$$

At the measurement temperatures, the existence of electrically neutral associates $V_{\mathrm{Pb}}^{2-} + 2p$ and $V_{\mathrm{O}}^{2+} + 2e$ are improbable from the energy point of view. The relations between the concentrations of vacancy pairs (diplons), isolated vacancies, charged centers of type (6), and ($V_{\mathrm{Pb}}^{-} + V_{\mathrm{O}}^{+}$) associates with a zero effective charge are dictated by the electrical neutrality condition and the completeness of the corresponding quasi-chemical reactions. We assume that the concentration of uncontrollable impurities is negligible.

The above schemes of dominant disordering in PWO crystals can also be used to consistently consider the electrical conductivity and thermal depolarization currents [2–4]. These defect models were also substantiated by PWO studies using other methods, in particular, with optical measurements [21, 22], ESR [23], and using theoretical calculations [24].

The change in the charge state of defect associates with a variation in the crystal temperature in the presence of an applied field is accompanied by hopping of holes (electrons) from one defect site to another. This process is equivalent to a change in the orientational state and/or dipole moment of the associate and provides an additional contribution to the $\varepsilon(T)$ dependence due to dipole polarization. In solids, polarization and other dipole effects in hopping transport over defect lattice sites are quite common [25]. For example, these processes determine certain dielectric properties of the complex oxides studied in [12, 26]. A significant increase in ε with temperature and maxima in the $\varepsilon(T)$ curve related to these phenomena have been observed in semiconductor materials [27, 28]. Localization of nonequilibrium charge carriers on vacancy dipole associates in gadolinium gallium garnet single crystals [29] leads to photoinduced reorientation of these dipoles under illumination by nonpolarized light at $T_p = 80$ K and to dipole polarization (peaks observed in thermal depolarization currents at ~320 K and ~450 K).

The discussed hopping mechanism of recharging of centers can be induced by ionizing radiation [22, 23] and probably causes thermal luminescence, which was experimentally studied, for example, in [21, 23]. We note that the number of maxima of thermal luminescence and their temperature positions, half-widths, and relative intensities are close to the respective parameters of the maxima of thermal depolarization currents (in the region 290–470 K) [2–4]) and of the maxima in $\varepsilon(T)$ curves studied in this work.

5. CONCLUSIONS

Thus, in the temperature interval 290–550 K, there are three regions (290–380 K, 400–470 K, 470–550 K) over which the changes in ε (or C) of PWO crystals are determined by different components that dominate the temperature and/or isothermal evolution of ionic and electronic processes. The weak $\varepsilon(T)$ dependence for PWO crystals observed in the range 400–470 K follows linear laws (2) and (3) on heating and cooling, respectively, and indicates mainly electronic polarization with characteristic times in the range 10^{-15}–10^{-13} s. This type of $\varepsilon(T)$ dependence is observed against a background of a small contribution to ε related to a weak growth of the crystal conductivity. A substantial increase in the electrical conductivity of PWO was observed only at $T > 470$ K [2–4]. The difference between the $\varepsilon(T)$ curves measured on heating and cooling is minimum in the range 400–470 K (Figs. 1–3).

The experiments show that, in the range 290–380 K, the temperature variation in $\varepsilon(T)$ is strongly affected by the relaxation polarization related to the hopping displacement of charge carriers and possible reorientation and association–dissociation of dipole defect complexes in the PWO crystal lattice. At $T > 470$ K, as the conductivity increases, the increase in ε follows an approximately exponential law with low activation energies (~0.010–0.033 eV).

We may assume that the high values of ε of PWO crystals at room temperature are substantially determined by intrinsic electrically active structural defects (vacancies and vacancy associates). Thermal excitation of the crystal induces hopping exchange of charges between the structural defects, which produces an increase in ε at $T < 400$ K. Likewise, the temperature dependence of the permittivity is affected by thermal polarization and annealing at elevated temperatures ($T > 500$ K). By heating samples in air, we can influence the long-time relaxation of PWO crystals at room temperature that takes place after high-temperature treatment; namely, we can reduce the relaxation time of the process of restoration of the quasi-equilibrium values of ε. Heating of PWO crystals to elevated temperatures stimulates dissociation of dipole clusters of point defects and increases the concentration of free vacancies. The vacancies migrate to dislocations or other imperfections of the crystal structure and are fixed there. Therefore, these vacancies cease to participate in active processes, which causes irreversible changes in the samples.

REFERENCES

1. M. Nikl, Phys. Status Solidi A **178** (2), 595 (2000).
2. V. N. Shevchuk and I. V. Kayun, Fiz. Tverd. Tela (St. Petersburg) **45** (10), 1807 (2003) [Phys. Solid State **45**, 1898 (2003)].
3. V. N. Shevchuk and I. V. Kayun, Funct. Mater. **10** (2), 229 (2003).
4. V. N. Shevchuk and I. V. Kayun, Visn. L'viv. Derzh. Univ., Ser. Fiz. **35**, 60 (2002).
5. J. A. Groenink and H. Binsma, J. Solid State Chem. **29** (2), 227 (1979).
6. B. Han, X. Feng, G. Hu, P. Wang, and Z. Yin, J. Appl. Phys. **84** (5), 2831 (1998).
7. H. Huang, W. Li, X. Feng, and P. Wang, Phys. Status Solidi A **187** (2), 563 (2001).
8. W.-S. Li, T.-B. Tang, H.-W. Huang, and X.-Q. Feng, Jpn. J. Appl. Phys., Part 1 **40** (12), 6893 (2001).
9. H.-W. Huang, Z.-G. Ye, M. Dong, W.-L. Zhu, and X.-Q. Feng, Jpn. J. Appl. Phys., Part 2 **41** (6B), L713 (2002).
10. H.-W. Huang, X. Feng, T.-B. Tang, M. Dong, and Z.-G. Ye, Phys. Status Solidi A **196** (2), R7 (2003).
11. W. Li, T.-B. Tang, and X. Feng, J. Appl. Phys. **87** (11), 7692 (2000).
12. S. K. Arora and T. Mathew, Phys. Status Solidi A **116** (1), 405 (1989).
13. O. V. Ivanov, A. P. Nakhodnova, and V. N. Krivobok, Zh. Neorg. Khim. **27** (3), 587 (1982).
14. A. A. Potapov, *Dielectric Method for Studying Substances* (Irkut. Gos. Univ., Irkutsk, 1990) [in Russian].
15. A. E. Nosenko and V. N. Shevchuk, Fiz. Tverd. Tela (St. Petersburg) **39** (5), 871 (1997) [Phys. Solid State **39**, 775 (1997)].
16. M. V. Mokhosoev and Zh. G. Bazarova, *Complex Oxides of Molybdenum and Tungsten with Elements of Groups I–IV* (Nauka, Moscow, 1990) [in Russian].
17. Y. R. Reddy and L. Sirdeshmukh, Phys. Status Solidi A **103** (2), K157 (1987).
18. J. Bourgoin and M. Lannoo, *Point Defects in Semiconductors*, Vol. 2: *Experimental Aspects* (Springer, New York, 1983; Mir, Moscow, 1985).
19. A. B. Lidiard, *Ionic Conductivity* (Springer, Berlin, 1957; Inostrannaya Literatura, Moscow, 1963).
20. E. A. Ukshe and N. G. Bukun, *Solid Electrolytes* (Nauka, Moscow, 1977) [in Russian].
21. M. Nikl, K. Nitsch, S. Baccaro, A. Cecilia, M. Montecchi, B. Borgia, Dafinei, I. M. Diemoz, M. Martini, E. Rosetta, G. Spinolo, A. Vedda, M. Kobayashi, M. Ishii, Y. Usuki, O. Yarolimek, and P. Reiche, J. Appl. Phys. **82** (11), 5758 (1997).
22. Q. Zhang, T. Liu, J. Chen, and X. Feng, Phys. Rev. B **68**, 064101 (2003).
23. V. V. Laguta, M. Martini, A. Vedda, E. Rosetta, M. Nikl, E. Mihokova, J. Rosa, and Y. Usuki, Phys. Rev. B **67**, 205102 (2003).
24. Y. B. Abraham, A. W. Holzwarth, R. T. Williams, G. E. Matthews, and A. R. Tackett, Phys. Rev. B **64**, 245109 (2001).
25. A. K. Jonscher, *Universal Relaxation Law. Dielectric Relaxation in Solids* (Chelsea Dielectric, London, 1996).
26. T. V. Panchenko, L. M. Karpova, and V. M. Duda, Fiz. Tverd. Tela (St. Petersburg) **42** (4), 671 (2000) [Phys. Solid State **42**, 689 (2000)].
27. P. V. Zhukovskiĭ, Ya. Partyka, P. Vengerék, Yu. Shostak, Yu. Sidorenko, and A. Rodzik, Fiz. Tekh. Poluprovodn. (St. Petersburg) **34** (10), 1174 (2000) [Semiconductors **34**, 1124 (2000)].
28. L. E. Soshnikov, V. M. Trukhan, and S. F. Marenkin, Neorg. Mater. **39** (4), 395 (2003).
29. A. E. Nosenko and V. N. Shevchuk, Radiat. Eff. Defects Solids **134** (1–4), 251 (1995).

Translated by I. Zvyagin

Physics of the Solid State, Vol. 47, No. 4, 2005, pp. 638–645. Translated from Fizika Tverdogo Tela, Vol. 47, No. 4, 2005, pp. 614–621.
Original Russian Text Copyright © 2005 by Golyandin, Sapozhnikov, Kustov.

DEFECTS, DISLOCATIONS, AND PHYSICS OF STRENGTH

Acoustic Study of Martensitic-Phase Aging in Copper-Based Shape Memory Alloys

S. N. Golyandin[1], K. V. Sapozhnikov[1], and S. B. Kustov[1, 2]
[1]*Ioffe Physicotechnical Institute, Russian Academy of Sciences, Politekhnicheskaya ul. 26, St. Petersburg, 194021 Russia*
e-mail: k.sapozhnikov@mail.ioffe.ru
[2]*Departamento de Fisica, Universitat de les Illes Balears, Palma de Mallorca, E-07122 Spain*

Received July 27, 2004

Abstract—An acoustic technique was applied to study aging of the β'_1 martensitic phase in a number of copper-based shape memory alloys (Cu–Zn–Al, Cu–Al–Ni, Cu–Al–Be) characterized by various degrees of martensitic-phase stabilization. The nonlinear anelasticity of the martensitic phase was studied in wide ranges of temperature (7–300 K) and vibrational strain amplitude (2×10^{-7}–2×10^{-4}) at vibrational-loading frequencies of ~100 kHz. It was shown that aging effects of the martensitic phase can have homogeneous and heterogeneous components. The homogeneous component is associated with a change in the degree of atomic order in the crystal volume. The basic heterogeneous mechanisms of martensitic-phase aging are associated with the formation of atmospheres of point defects and local changes (which are greater than those in the crystal volume) in the degree of atomic order in the vicinity of partial dislocations and the boundaries between martensite variants. It is concluded that various stabilization properties of the alloys at hand result not only from the different diffusion properties of quenching point defects but also from the different influence of these defects on the degree of atomic order and the different features of their interaction with partial dislocations and intervariant boundaries. *© 2005 Pleiades Publishing, Inc.*

1. INTRODUCTION

In general, the parameters of shape memory alloys (in particular, the phase transformation temperatures) have to be stable in order for them to be used in application. However, martensitic-phase aging in copper-based shape memory alloys results in the so-called martensitic-phase stabilization, which manifests itself in an increase in the temperature of the reverse martensitic transformation. There can occur low-temperature stabilization of the homogeneous martensitic phase and high-temperature martensite decomposition into a heterogeneous mixture of phases [1–4]. It is believed that martensitic-phase stabilization occurs through several mechanisms simultaneously [2, 4–7]. In general, the following basic mechanisms are considered: (i) a change in the atomic long-range (and/or short-range) order [1–9], (ii) pinning of boundaries of martensite variants [2, 4–6, 8], and (iii) changes in the martensite defect structure (stacking faults) [2, 5, 7, 8, 10]. However, the relative role of each mechanism of martensitic-phase stabilization remains uncertain to a large degree.

Acoustic techniques, in particular, those based on internal friction (IF), are a very sensitive tool for studying structural defects in solids. We can distinguish two essential aspects of the stabilization phenomenon that facilitate efficient application of acoustic techniques for studying the evolution of the martensitic-phase microstructure during aging. First, an important role in stabilization is played by diffusion, which is significantly enhanced at high concentrations of quenching vacancies. IF-based techniques allow detailed studies of the diffusion of point defects and their interaction with other defects (see, e.g., [11]).The effects associated with diffusion mobility of point defects (which pin linear or planar defects in the martensitic phase) can be studied using IF measurements over a wide temperature range, where point defects change state from immobile to highly mobile. Second, the proposed mechanisms for martensite stabilization presuppose different spatial distributions of active zones, i.e., regions subject to changes during aging. Changes in the degree of atomic order occur throughout the entire crystal volume, whereas the active zones of pinning of boundaries and changes in the martensite defect structure are located near intervariant boundaries and partial dislocations (which limit stacking faults). Thus, in terms of active-zone localization in the crystal volume, stabilization mechanisms can be classified as homogeneous or heterogeneous. Measurements of nonlinear IF in a wide range of inelastic strains (amplitudes of vibrational displacements of linear/planar defects) allow the study of both homogeneous and heterogeneous stabilization components.

In this work, the acoustic technique is applied to study the heterogeneous and homogeneous structural changes due to aging of the β'_1 martensitic phase in a number of copper-based shape memory alloys (Cu–Zn–Al, Cu–Al–Ni, Cu–Al–Be) characterized by various degrees of martensitic-phase stabilization. The results obtained for samples subjected to aging in the martensitic phase are compared with data on samples aged in the high-temperature β phase. Aging in the high-temperature β phase makes it possible to anneal excess quenching vacancies and thereby suppress stabilization of the martensitic phase in alloys prone to stabilization. As indicators of structural changes, we used amplitude-dependent IF (ADIF) δ_h and the amplitude-dependent Young modulus defect $(\Delta E/E)_h$, which are caused by nonlinear vibrational motion of linear and planar defects in the martensitic phase.

2. EXPERIMENTAL TECHNIQUE

We studied single crystals of Cu–26.4 wt % Zn–3.8 wt % Al, Cu–13.2 wt % Al–4.0 wt % Ni, and Cu–10.5 wt % Al–0.5 wt % Be alloys in the β'_1 martensitic phase (the temperature M_s of the onset of martensitic transformation is 308, 360, and 372 K, respectively). Samples were homogenized for 1800 s at 1073 K (Cu–Zn–Al), 900 s at 1173 K (Cu–Al–Ni), and 900 s at 1123 K (Cu–Al–Be) and then quenched, followed by aging in the martensitic or high-temperature β phase. Aging in the martensitic phase was carried out at room temperature. The Cu–Al–Ni alloy samples were quenched in water at room temperature, after which they were subjected to long-term aging in the martensitic phase or were annealed for 14 400 s in an oil bath at 473 K. The Cu–Zn–Al alloy samples were quenched in ice water and then subjected to aging in the martensitic phase or placed in boiling water immediately after quenching, where they were annealed for 5400 s at 373 K (upquenching). The Cu–Al–Be alloy samples were subjected to direct quenching in water at room temperature followed by aging of the martensitic phase or to step quenching (quenching in oil at 438 K with subsequent annealing for 2700 s followed by room-temperature quenching in water).

An ultrasonic resonant technique and a computer-controlled system based on a compound piezoelectric oscillator [12] were used to excite longitudinal vibrations in rod-shaped samples and to measure the temperature and amplitude dependences of the IF and the dynamic Young modulus at ultrasonic frequencies of ~100 kHz. Measurements were carried out under thermal cycling at a rate of ~0.03 K/s in the temperature range 7–300 K. The temperature dependences were measured simultaneously for two values of the vibrational strain amplitude, which were within the amplitude-independent and amplitude-dependent ranges, respectively, of the amplitude dependences of the IF and dynamic Young modulus. These measurements made it possible to construct the ADIF temperature spectrum as the difference between two measured IF spectra. In the same thermal cycle, it was possible to measure (at any temperature) the dependences of the IF and dynamic Young modulus on the vibrational strain amplitude in the range 2×10^{-7}–2×10^{-4}. The amplitude dependences were measured for increasing and subsequent decreasing vibration amplitudes.

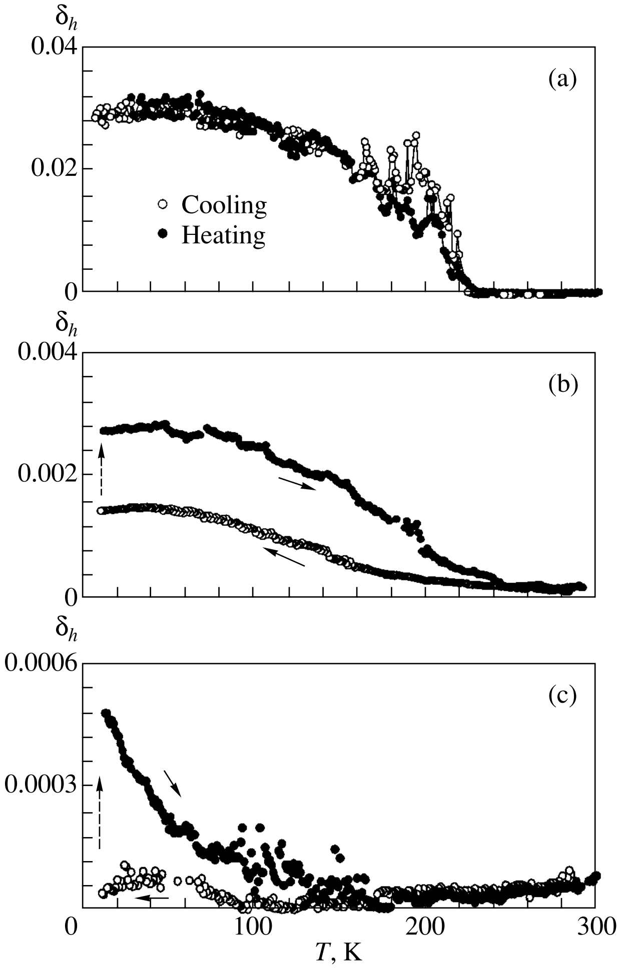

Fig. 1. Temperature dependences of the amplitude-dependent component of the vibration decrement of (a) Cu–Al–Ni, (b) Cu–Zn–Al, and (c) Cu–Al–Be alloy samples subjected (after quenching) to aging in the martensite state for (a) 1 year, (b) 7.5 days, and (c) 48 days. The amplitude-dependent decrement of vibrations is measured upon cooling and subsequent heating for different vibrational strain amplitudes: (a) 3×10^{-5}, (b) 5×10^{-5}, and (c) 2×10^{-5}. Vertical dashed arrows in panels (b, c) at low temperatures indicate the value of the increase in the amplitude-dependent internal friction when the amplitude dependence of internal friction is measured for vibrational strain amplitudes of up to 2×10^{-4}.

3. EXPERIMENTAL RESULTS

Figure 1 shows the ADIF temperature spectra (measured in the cooling–heating thermal cycle) for samples of three alloys under study subjected to aging in the martensitic state. In the thermal cycle (both upon heating and cooling) shown in Fig. 1a for the Cu–Al–Ni alloy, the amplitude dependence of IF was measured. For the other alloys, we show thermal cycles in which the amplitude dependence of IF upon cooling was not

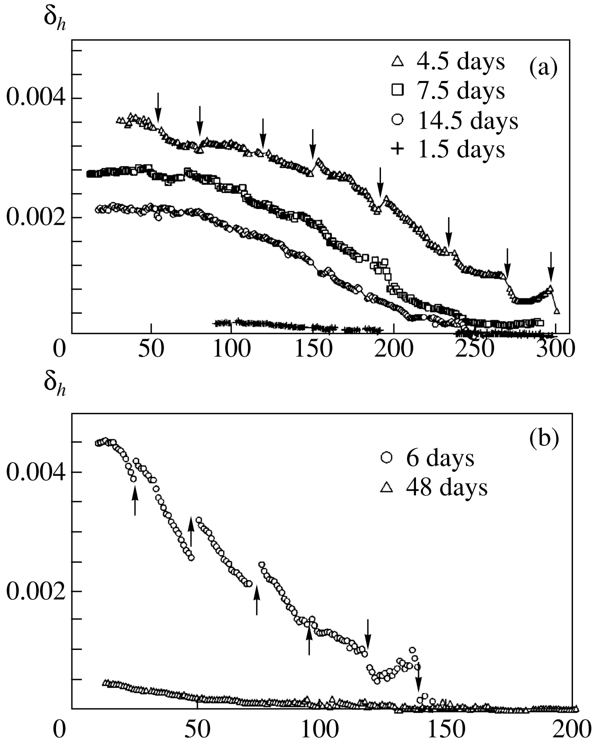

Fig. 2. Influence of aging duration in the martensite state on the temperature dependences of the amplitude-dependent component of the vibration decrement of (a) Cu–Zn–Al and (b) Cu–Al–Be alloy samples measured upon heating. The amplitude-dependent decrement of vibrations is measured for vibrational strain amplitudes of (a) 5×10^{-5} and (b) 2×10^{-5}. Arrows indicate the value of the change in the amplitude-dependent internal friction when the amplitude dependence of internal friction is measured for vibrational strain amplitudes of up to 2×10^{-4}.

measured and high-amplitude acoustic excitation of samples at low temperature (~10 K) caused an increase in the ADIF value during measurements of the amplitude dependence of IF. The reason for this increase is that the largest vibrational strain amplitude exceeded the value stabilized when measuring the ADIF temperature spectrum upon cooling. This effect is indicated in Figs. 1b and 1c by vertical arrows. We note that high-amplitude excitation of the Cu–Zn–Al alloy at low temperatures changed the ADIF value but did not change the temperature dependence of ADIF. A slightly different behavior was observed for the Cu–Al–Be alloy, where high-amplitude excitation at low temperatures resulted not only in an increase in the ADIF value but also in a change in the character of the temperature dependence of ADIF measured upon subsequent heating. The ADIF of the Cu–Al–Be alloy decreased rapidly upon heating beginning from temperatures of ~15 K, which demonstrates the low-temperature recovery stage after high-amplitude excitation (this stage is absent in the Cu–Zn–Al and Cu–Al–Ni alloys). The temperature dependences of ADIF of Cu–Zn–Al and Cu–Al–Ni alloys exhibit identical features: the athermal behavior at low temperatures switches to a negative temperature dependence (a decrease in ADIF with an increase in the temperature, $d\delta_h(T)/dT < 0$) at temperatures above 70 K. We note that, despite the qualitative similarity of the observed temperature dependences, the ADIF levels differ significantly. As shown below, this difference is caused by aging of the Cu–Zn–Al and Cu–Al–Be alloys in the martensitic phase.

The influence of the duration of aging in the martensitic state on the temperature dependences of ADIF for the Cu–Zn–Al and Cu–Al–Be alloys is shown in Figs. 2a and 2b, respectively. We can see that aging in the martensitic state results in ADIF suppression over a wide temperature range. Each measurement of the amplitude dependence of IF during thermal cycling has an effect on the ADIF value in the temperature range where a negative temperature dependence of ADIF is observed. This effect is indicated by arrows in Fig. 2. We note that, in the low-temperature range of athermal ADIF behavior, only the first measurement of the amplitude dependence of IF has an effect on the ADIF values.

Figure 3 shows the amplitude dependences of IF at various temperatures measured upon heating (simultaneously with the ADIF temperature spectra shown above) for Cu–Al–Ni (Fig. 1a), Cu–Zn–Al (Fig. 2a, 4.5 days of aging), and Cu–Al–Be alloys (Fig. 2b, 6 days of aging). We can see that the amplitude dependences of IF measured for increasing and then decreasing vibration amplitudes are identical at low temperatures in the range of athermal ADIF behavior. At temperatures corresponding to a negative temperature dependence of ADIF, hysteresis of IF as a function of vibration amplitude is observed (i.e., a difference between the amplitude dependences of IF measured for increasing and decreasing vibration amplitude is observed). This hysteresis increases with temperature.

Figure 4 shows the amplitude dependences of IF measured at low temperatures (in the range of athermal ADIF behavior) for alloys subjected to heat treatments under various conditions. These results are obtained for subsequent rather than the first measurement cycle; therefore, the influence of high-amplitude excitation on the ADIF value (IF amplitude hysteresis) is absent. We note that the amplitude-independent background of IF is not detected in the entire range of vibration amplitudes covered at low temperatures and that the total measured decrement is almost identical to its amplitude-dependent component: $\delta \cong \delta_h$. It is of particular interest to compare the data for samples subjected to aging in the martensitic phase and the data for samples aged in the high-temperature β phase. All the dependences can be subdivided into two groups. The Cu–Al–Ni alloy (independent of heat treatment) and Cu–Zn–Al and Cu–Al–Be alloys aged in the high-temperature β phase comprise a group of materials with a high low-temperature ADIF level, which is almost independent

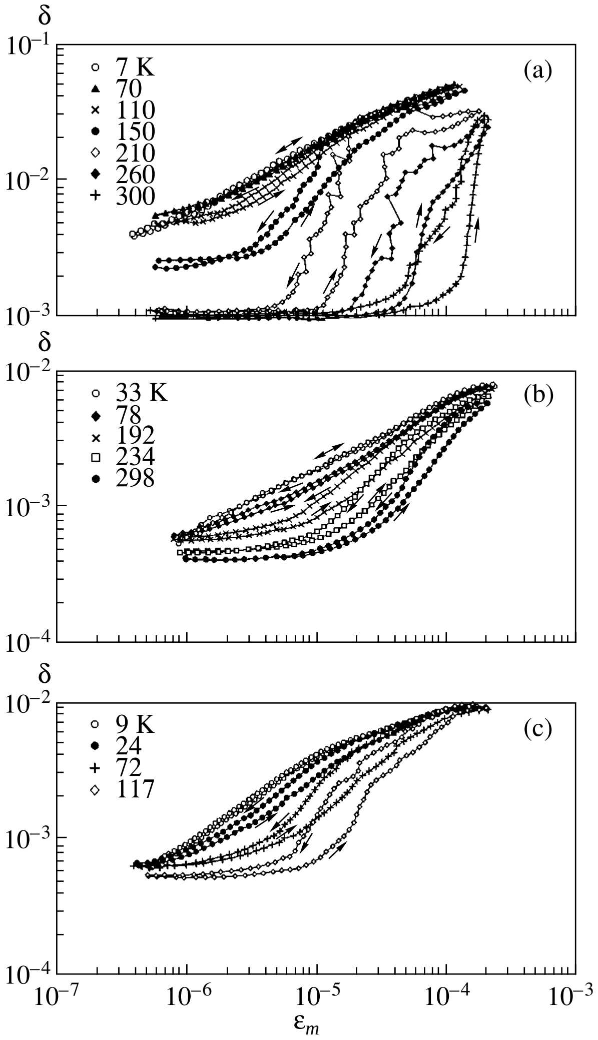

Fig. 3. Dependences of the vibration decrement on the vibrational strain amplitude measured at various temperatures upon heating for (a) Cu–Al–Ni, (b) Cu–Zn–Al, and (c) Cu–Al–Be alloy samples subjected (after quenching) to aging in the martensite state for (a) 1 year, (b) 4.5 days, and (c) 6 days. Arrows indicate the direction of variation in the vibration amplitude during measurements.

of the material type (curves *1*, *2*, *6*, *9* in Fig. 4). The other group includes the Cu–Zn–Al and Cu–Al–Be alloys subjected to aging in the martensitic phase at low temperatures, which are characterized by a much lower value of the ADIF and by a dependence on the duration of aging in the martensitic phase (curves *3*–*5* for Cu–Zn–Al and curves *7*, *8* for Cu–Al–Be). All the dependences can be fitted fairly well by power-law functions, $\delta_h \propto \varepsilon_m^n$, with the exponent *n* being almost independent of the alloy type and heat treatment and lying in the range 0.45–0.55. Thus, aging of Cu–Zn–Al and Cu–Al–Be alloys in the martensitic phase results in significant (approximately proportional to the duration of aging) suppression of low-temperature ADIF in the entire vibration amplitude range under study.

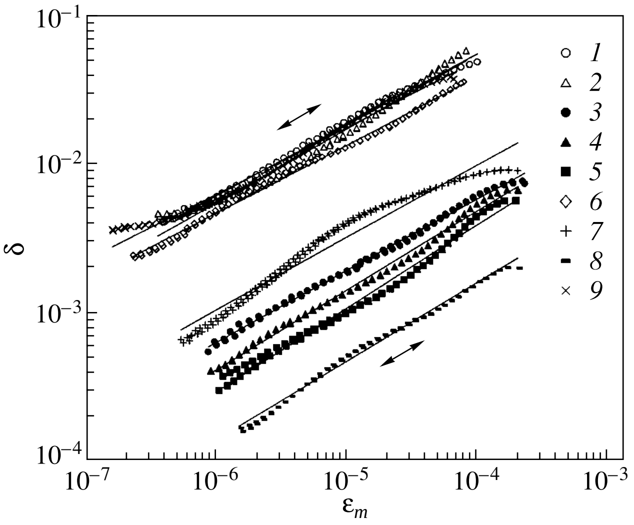

Fig. 4. Dependences of the vibration decrement on the vibrational strain amplitude measured at low temperatures for Cu–Al–Ni, Cu–Zn–Al, and Cu–Al–Be alloy samples subjected to various heat treatments. The data are obtained from repeated measurements, for which the dependences measured for increasing and subsequent decreasing vibration amplitudes are identical. The dependences are fitted by power-law functions. (*1*) Cu–Al–Ni, 1 year of aging in the β_1' phase, $T = 7$ K; (*2*) Cu–Al–Ni aged in the β phase, $T = 7$ K; (*3*) Cu–Zn–Al, 4.5 days of aging in the β_1' phase, $T = 33$ K; (*4*) Cu–Zn–Al, 7.5 days of aging in the β_1' phase, $T = 10$ K; (*5*) Cu–Zn–Al, 14.5 days of aging in the β_1' phase, $T = 14$ K; (*6*) Cu–Zn–Al aged in the β phase, $T = 8$ K; (*7*) Cu–Al–Be, 6 days of aging in the β_1' phase, $T = 9$ K; (*8*) Cu–Al–Be, 48 days of aging in the β_1' phase, $T = 10$ K; and (*9*) Cu–Al–Be aged in the β phase, $T = 9$ K.

The behavior of the amplitude-dependent component of the IF of Cu–Al–Ni and Cu–Zn–Al alloys aged in the martensitic state upon heating at 140–300 K is shown in Fig. 5. For the Cu–Zn–Al alloy (Fig. 5b), a single stage of the amplitude dependence of IF is observed, with the slope in the log–log coordinates being almost independent of temperature. The influence of temperature manifests itself in continuous proportional suppression of ADIF of the Cu–Zn–Al alloy in the entire vibration amplitude range under study. The decrease in the ADIF of the Cu–Al–Ni alloy with an increase in temperature is more complicated; this decrease first takes place at low vibration amplitudes and then gradually extends to the high-amplitude range (Fig. 5a). Here, three stages are observed in the amplitude dependence of IF: a moderate increase in IF at low vibration amplitudes, a sharp increase at intermediate amplitudes, and switching to a weak amplitude dependence at high vibration amplitudes. It is noteworthy that, after the formation of the low-amplitude stage of the amplitude dependence of IF, the ADIF value at this stage remains unchanged as the temperature increases

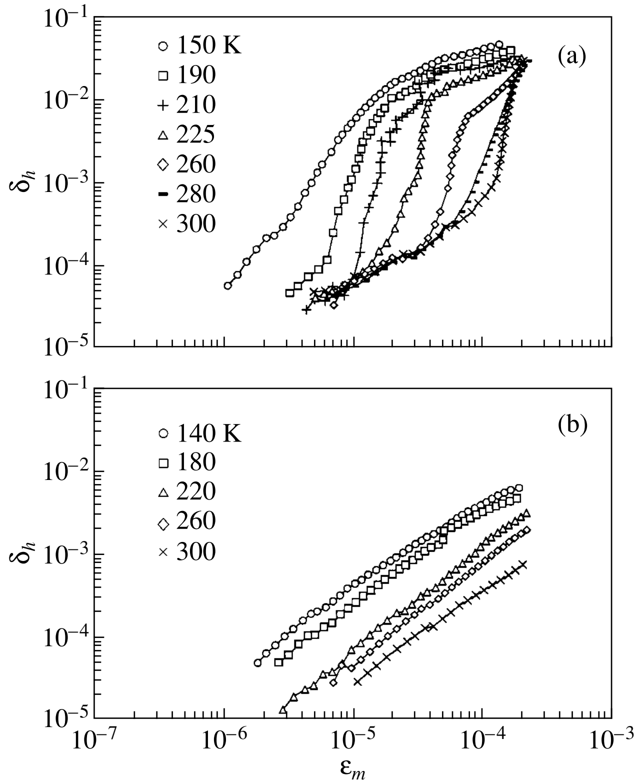

Fig. 5. Amplitude-dependent component of the vibration decrement measured at various temperatures upon heating from ~10 K for (a) Cu–Al–Ni and (b) Cu–Zn–Al alloy samples subjected (after quenching) to aging in the martensitic state for (a) 1 year and (b) 7.5 days. The amplitude dependences of internal friction are measured for increasing vibration amplitudes.

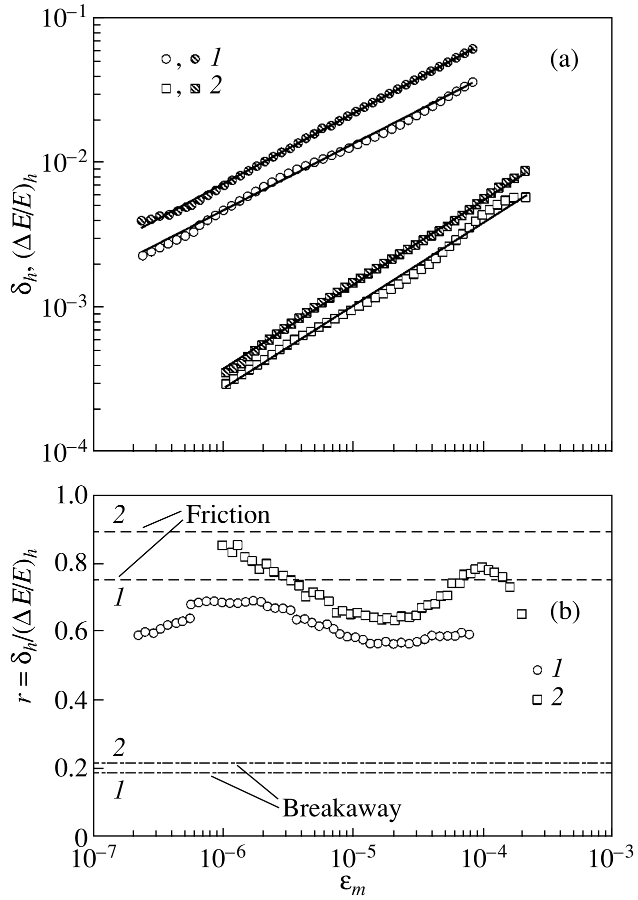

Fig. 6. (a) Amplitude-dependent components of the vibration decrement (open symbols) and the Young modulus defect (closed symbols) and (b) their ratio $r = \delta_h/(\Delta E/E)_h$ measured at ~10 K for Cu–Zn–Al alloy samples subjected (after quenching) to aging in (*1*) the β phase and (*2*) martensitic phase for 14.5 days. The amplitude dependences are measured for increasing vibration amplitudes. The dependences of the vibration decrement and the Young modulus defect are fitted by power-law functions. Dash-dotted and dashed lines in panel (b) indicate the ratios *r* calculated using these power-law functions and the relations from the breakaway and friction models, respectively.

further; only the range of the low-amplitude stage extends to higher vibrational strain amplitudes.

4. RESULTS AND DISCUSSION

The nonlinear anelasticity of the β_1' martensitic phase can be caused by partial dislocations bounding stacking faults in the basal plane and by the boundaries of martensite variants. Since the conclusions on the mechanisms of martensitic phase aging drawn in this paper (see below) are related to both types of structural defects, there is no need to determine more exactly the type of defects responsible for the nonlinear anelasticity. We only note that there is some evidence in favor of the dislocation mechanism of anelasticity [13–15].

The alloys under study have various stabilization properties. The Cu–Al–Ni alloy is not prone to room-temperature martensite stabilization [16], whereas martensitic-phase aging in Cu–Zn–Al and Cu–Al–Be alloys causes pronounced stabilization after direct quenching of the alloys into martensite [1, 2, 4–9, 15, 17], which can be suppressed using special heat treatments with annealing in the high-temperature β phase. The cause of this difference is still a subject of study. It is believed that this difference arises as a result of different intensities of diffusion processes [16], in particular, different diffusion mobilities of quenching vacancies [8, 18]. The authors of [19] also believe that different stabilization properties are caused by different concentrations of quenching vacancies. The results from acoustic studies allow comparison of diffusion properties of point defects in the alloys under study.

4.1. The Temperature Range of Mobility of Quenching Point Defects in the Martensitic Phase

A distinguishing feature of the ADIF behavior in all the alloys under study, which characterizes the temperature range of point defect mobility, is the existence of a range with a negative temperature dependence of ADIF. This behavior was also observed previously [15, 20–23] and can be explained as follows. Thermal cycling of polyvariant samples of copper alloys in the β_1' martensitic phase results in the generation of significant thermal stresses due to an anisotropic thermal expansion of martensite variants. Therefore, the temperature dependence of ADIF in the martensitic phase is controlled by the competition of microplastic deformation and dynamic strain aging. The negative temperature dependence of ADIF (Figs. 1, 2) is observed in the temperature range in which quenching point defects diffuse to partial dislocations and the boundaries between variants, thereby decreasing their mobility more strongly, the higher the temperature [15, 21–23]. The diffusion mobility of point defects also causes the time dependence of IF, which gives rise to hysteresis of IF as a function of vibration amplitude in the temperature range where $d\delta_h(T)/dT < 0$, when measuring the amplitude dependence of IF (Fig. 3). A local perturbation of atmospheres of mobile point defects caused by measuring the amplitude dependence of IF also results in a change in the ADIF value, which manifests itself in the ADIF temperature dependences at a fixed amplitude (Fig. 2). At low temperatures, when quenching point defects are immobile, the ADIF of the martensitic β_1' phase exhibits athermal behavior (Fig. 1), which we observed previously [15, 21]. It is important that the temperature ranges of the athermal behavior and of the negative temperature dependence of ADIF are identical in the Cu–Zn–Al and Cu–Al–Ni alloys (Figs. 1a, 1b). Hence, the temperature range of diffusion mobility of quenching point defects in these alloys is the same, despite their different stabilization properties. Thus, the data obtained indicate the absence of a unique relation between the diffusion mobility of quenching point defects and martensite stabilization. In the Cu–Al–Be alloy, the diffusion mobility of point defects is detected at significantly lower temperatures (Figs. 1–3) than that in the Cu–Zn–Al and Cu–Al–Ni alloys. The low-temperature diffusion mobility of point defects in the Cu–Al–Be alloy will be considered in a later paper.

4.2. Homogeneous Processes of Martensitic-Phase Aging

As noted above, the negative temperature dependence of ADIF indicates unpinning of partial dislocations and intervariant boundaries from point defect atmospheres under thermal stresses. At low temperatures (in the range of athermal ADIF behavior), point defects are immobile. Under these conditions, measurements of the amplitude dependence of IF allow one to study the influence of homogeneous processes of aging of the martensitic phase on the mobility of partial dislocations and intervariant boundaries. To this end, it is necessary to ensure that linear or planar defects, whose motion causes ADIF at low temperatures, are indeed not pinned by point defect atmospheres.

First, this fact is indicated by the behavior of the IF amplitude hysteresis at low temperatures. The first-cycle measurement of the amplitude dependence of IF at low temperatures is accompanied by amplitude hysteresis of IF, since superposition of thermal and strong vibrational stresses results in additional unpinning of partial dislocations and intervariant boundaries from point defect atmospheres [15]. Repeated measurements in the same range of vibration amplitudes are completely reproducible (Fig. 4), which indicates defect structure stability at low temperatures.

Second, information on the motion of carriers of the amplitude-dependent anelasticity can be obtained by simultaneously studying the ADIF and the Young modulus defect and determining the ratio of the amplitude-dependent decrement and the Young modulus defect, $r = \delta_h/(\Delta E/E)_h$. This quantity takes on various values in various models of the amplitude-dependent anelasticity. It is believed that the anelasticity can be described by the model of nonlocal friction if point defects are immobile and are not segregated at dislocations and by the model of dislocation breakaway from a single row of pinning points in the case of dislocation pinning by point defects [11]. Figure 6a shows simultaneously measured amplitude-dependent components of the IF and Young modulus defect for Cu–Zn–Al alloy samples in the stabilized state and after annealing in the β phase, which suppresses stabilization. As mentioned above, the martensitic-phase anelasticity at low temperatures remains, for the most part, amplitude-dependent at the lowest amplitudes covered. This fact complicates direct determination of the amplitude-independent Young modulus. When constructing the amplitude dependence of the Young modulus defect shown in Fig. 6, the values of the amplitude-independent modulus were chosen such that, in the low amplitude region, the Young modulus defect exhibits a power-law dependence similar to the amplitude dependence of the decrement. In the basic models of the dislocation amplitude-dependent anelasticity, the quantity r is independent of the vibration amplitude in the case of power-law amplitude dependences of the IF and Young modulus defect and is determined only by the exponent n; more specifically, $r = 4n/(n + 2)$ [24–26] for the friction model and $r = n/(n + 2)$ [26] for the breakaway model. (We note that acoustic measurements make it possible to find the values of the “actual” elastic modulus for which the relations between r and n are more complex than the relations indicated above for the “secant” elastic modulus. However, at small n, those relations yield almost the same values of r [26].) Figure 6b shows the experimental amplitude dependences of r and the values of r calculated for the power-law functions fitting the experimental amplitude dependences of the IF and Young modulus defect for stabilized and non-stabilized states of the Cu–Zn–Al alloy. As in theoretical models, the experimental values of r remain basically unchanged over a wide range of vibration amplitudes. We can see that the experimental value of r agrees well with the value calculated in the friction model but disagrees with the value calculated in the breakaway model, irrespective of the alloy state. Thus, despite the significant difference between ADIF levels in stabilized and nonstabilized alloys, the amplitude dependences of the IF and Young modulus defect measured at low temperatures are consistent with the friction model, i.e., are caused by motion of linear or planar defects through elastic fields of point defects, which are uniformly distributed over the crystal volume. Hence, the carriers of the amplitude-dependent anelasticity break away from point defect atmospheres in both the stabilized and nonstabilized alloy at low temperatures.

Figure 4 shows that the low-temperature ADIF is high and is almost independent of the material type when the martensitic phase stabilization is suppressed (curves *1*, *2*, *6*, *9* in Fig. 4). Aging of the martensitic phase in alloys subjected to martensite stabilization results in suppression of the low-temperature ADIF, which is stronger, the longer the duration of aging (curves *3*–*5* for Cu–Zn–Al and curves *7*, *8* for Cu–Al–Be in Fig. 4). In this case, the power-law shape of the amplitude dependences of IF remains almost unchanged; i.e., aging causes proportional suppression of ADIF over a wide range of vibration amplitudes (displacements of linear or planar defects). This fact suggests that the process resulting in suppression of the low-temperature ADIF is homogeneous over the crystal volume. This homogeneous process can be a change in the degree of atomic long-range and/or short-range order. Various mechanisms of changes in the short-range atomic order, which increases the stress required to change the orientation of martensite variants, are considered in the literature [3, 4, 27, 28]. It seems that the detected homogeneous suppression of low-temperature ADIF during aging of the martensitic phase is caused by one of these mechanisms. We note that homogeneous suppression of the mobility of inelastic-deformation carriers is not observed in the Cu–Al–Ni alloy, in contrast to the Cu–Zn–Al and Cu–Al–Be alloys. This fact allows us to conclude that a homogeneous change in the degree of atomic order due to room-temperature aging does not take place in the Cu–Al–Ni alloy.

4.3. Heterogeneous Aging of the Martensitic Phase

The transition of partial dislocations and intervariant boundaries from the unpinned state (at temperatures below 70 K) to a pinned state upon heating makes it possible to study heterogeneous structural changes associated with the interaction of these defects with mobile point defects. The data shown in Fig. 5 demonstrate a significant difference in the mechanisms of formation of pinning atmospheres of point defects between the Cu–Zn–Al and Cu–Al–Ni alloys.

The three-stage amplitude dependence of IF that takes place upon heating in the Cu–Al–Ni alloy (Fig. 5a) has also been observed for the β_1' martensitic phase of various copper-based alloys [15, 22, 23, 29] and was explained as follows. The low-amplitude stage of the gradual IF increase arises as a result of partial-dislocation motion inside extended atmospheres of point defects. As the vibration amplitude increases further, partial dislocations break through the atmospheres and their vibrations outside the atmospheres result in a stage of a sharp increase in IF, which is followed by a stage of a weak amplitude dependence of IF at high vibration amplitudes. An analysis carried out in [15] allowed the conclusion that the ADIF level at the low-amplitude stage is controlled by the point defect concentration in atmospheres at a constant density of carriers of inelastic deformation: the higher the atmosphere density, the lower the ADIF level at a constant amplitude. The fact that ADIF remains unchanged in the low-amplitude stage in the Cu–Al–Ni alloy (after the formation of this stage upon heating) suggests that atmospheres with a saturated concentration of point defects arise in this alloy [22]. Further aging entails only an increase of the atmospheres in size (the shift of the second and third stages of the amplitude dependence of IF to higher vibration amplitudes).

The one-stage amplitude dependence of IF observed in the Cu–Zn–Al alloy (Fig. 5b) is indicative of partial dislocation motion inside extended atmospheres of point defects without breaking beyond the atmospheres (see [15] for more details). A continuous decrease in the partial dislocation mobility with increasing temperature at the stage of motion inside atmospheres indicates a continuous increase in the concentration of point defects in the atmospheres. It can be assumed that this process is also associated with the degree of atomic order near partial dislocations changing more greatly than does the homogeneous degree of atomic order in the crystal volume [15]. The causes of this greater change in the degree of atomic order can be the higher concentration of mobile quenching defects in atmospheres and faster diffusion near partial dislocations and intervariant boundaries [29]. Thus, heterogeneous processes of the martensitic-phase aging can include the formation of point defect atmospheres and a local change (greater than that in the crystal volume) in the degree of atomic order near partial dislocations and intervariant boundaries.

Density saturation of point defect atmospheres in the Cu–Al–Ni alloy can be explained if it is assumed that atmospheres are formed not by quenching vacancies but rather by point defect complexes (including quenching vacancies) that repel each other [22]. In this case, coagulation and annihilation of vacancies due to their interaction with partial dislocations and intervariant boundaries do not occur and vacancies are retained in the atmospheres. This assumption makes it possible to explain the stability of quenching vacancies in the martensitic phase of the Cu–Al–Ni alloy and the difference in behavior between the Cu–Al–Ni and Cu–Zn–Al alloys observed in measurements of the resistivity and positron annihilation [18].

5. CONCLUSIONS

(1) The processes that accompany the aging of the martensitic phase can be analyzed in terms of their localization in the crystal volume. The homogeneous aging component is caused by a change in the atomic order in the crystal volume. Heterogeneous aging processes are associated with linear and planar defects in the martensitic phases and can include both pinning of these defects by mobile point defects and a local change (greater than the homogeneous change) in the atomic order near linear or planar defects.

(2) The difference in the stabilization properties of the alloys in question results not only from the different diffusion properties of quenching point defects but also from the different influence of these defects on the degree of atomic order and from their different interactions with partial dislocations and the boundaries between martensite variants.

ACKNOWLEDGMENTS

This study was supported by the Department of Physical Sciences of the Russian Academy of Sciences (the program “Coherent Acoustic Fields and Signals”).

REFERENCES

1. A. Abu Arab and M. Ahlers, Acta Metall. **36**, 2627 (1988).
2. M. H. Wu and C. M. Wayman, Mater. Sci. Forum **56–58**, 553 (1990).
3. K. Otsuka and X. Ren, Mater. Sci. Eng. A **312**, 207 (2001).
4. M. Ahlers and J. L. Pelegrina, Mater. Sci. Eng. A **356**, 298 (2003).
5. G. Scarsbrook, J. M. Cook, and W. M. Stobbs, Metall. Trans. A **15**, 1977 (1984).
6. T. Suzuki, R. Kojima, Y. Fujii, and A. Nagasawa, Acta Metall. **37** (1), 163 (1989).
7. Y. Nakata, O. Yamamoto, and K. Shimizu, Mater. Trans., JIM **34** (5), 429 (1993).
8. M. Chandrasekaran, E. Cesari, J. Wolska, I. Hurtado, R. Stalmans, and J. Dutkiewicz, J. Phys. IV **5** (C2), C2-143 (1995).
9. K. Marukawa, K. Tsuchiya, and Y. Arai, J. Phys. IV **5** (C8), C8-841 (1995).
10. M. Zhu, D. Z. Yang, and C. L. Jia, Metall. Trans. A **20**, 1631 (1989).
11. G. Gremaud, Mater. Sci. Forum **366–368**, 178 (2001).
12. G. Gremaud, S. Kustov, and Ö. Bremnes, Mater. Sci. Forum **366–368**, 652 (2001).
13. S. B. Kustov, S. N. Golyandin, I. Hurtado, J. Van Humbeeck, and R. De Batist, J. Phys. IV **5** (C8), C8-943 (1995).
14. S. B. Kustov, J. Van Humbeeck, I. Hurtado, S. N. Golyandin, and R. De Batist, in *M*^{3}*D III: Mechanics and Mechanisms of Material Damping*, Ed. by A. Wolfenden and V. K. Kinra (ASTM, Philadelphia, 1997), Spec. Tech. Publ., No. 1304, p. 94.
15. S. Kustov, S. Golyandin, K. Sapozhnikov, E. Cesari, J. Van Humbeeck, and R. De Batist, Acta Mater. **50**, 3025 (2002).
16. E. Cingolani, J. Van Humbeeck, and M. Ahlers, Metall. Mater. Trans. A **30**, 493 (1999).
17. S. Kustov, J. Pons, E. Cesari, and M. Morin, Scr. Mater. **46**, 817 (2002).
18. Y. Kong, B. Jiang, T. Y. Hsu, B. Wang, and T. Wang, Phys. Status Solidi A **133**, 269 (1992).
19. B. Kostrubiec, J. Rasek, R. Wiśniewski, and H. Morawiec, Solid State Phenom. **89**, 287 (2003).
20. M. Morin and G. Guénin, Mater. Sci. Forum **56–58**, 499 (1990).
21. S. Kustov, S. Golyandin, K. Sapozhnikov, J. Van Humbeeck, and R. De Batist, Acta Mater. **46**, 5117 (1998).
22. K. Sapozhnikov, S. Golyandin, S. Kustov, J. Van Humbeeck, and R. De Batist, Acta Mater. **48**, 1141 (2000).
23. S. Kustov, S. Golyandin, K. Sapozhnikov, and M. Morin, Scr. Mater. **43**, 905 (2000).
24. S. B. Kustov, Candidate’s Dissertation (Ioffe Physicotechnical Inst., USSR Academy of Sciences, Leningrad, 1989).
25. A. B. Lebedev and S. B. Kustov, Phys. Status Solidi A **136**, K85 (1993).
26. A. B. Lebedev, Fiz. Tverd. Tela (St. Petersburg) **41**, 1214 (1999) [Phys. Solid State **41**, 1105 (1999)].
27. K. Marukawa and K. Tsuchiya, Scr. Metall. Mater. **32**, 77 (1995).
28. J. A. Giampaoli, J. L. Pelegrina, and M. Ahlers, Acta Mater. **46** (10), 3333 (1998).
29. K. Sapozhnikov, S. Golyandin, S. Kustov, J. Pons, E. Cesari, and M. Morin, J. Phys. IV **112**, 557 (2003).

Translated by A. Kazantsev

Physics of the Solid State, Vol. 47, No. 4, 2005, pp. 646–651. Translated from Fizika Tverdogo Tela, Vol. 47, No. 4, 2005, pp. 622–627.
Original Russian Text Copyright © 2005 by Bugaĭ, Sazonov.

DEFECTS, DISLOCATIONS, AND PHYSICS OF STRENGTH

Effects of Transverse Perturbations on the Motion of an Edge Dislocation

A. N. Bugaĭ and S. V. Sazonov
Kaliningrad State University, Kaliningrad, 236041 Russia
e-mail: foton1@baltnet.ru

Received April 13, 2004; in final form June 21, 2004

Abstract—The influence of transverse perturbations on the motion of an edge dislocation is studied using the averaged Lagrangian of the Ritz–Whitham type. The dislocation is described by the Frenkel–Kontorova model with inclusion of elastic anharmonicity and lattice discreteness (acoustic dispersion). The quadratic anharmonicity and acoustic dispersion are shown to promote self-focusing of the dislocation and microcrack formation. Under certain conditions, cubic anharmonicity can stabilize transverse compression of the dislocation, which can bring about the development of "crowdion droplets." *© 2005 Pleiades Publishing, Inc.*

1. INTRODUCTION

The motion of the edge dislocation core in a crystal is described reasonably well by the one-dimensional Frenkel–Kontorova model [1]. However, the one-dimensional model fails as the transverse boundary of the dislocation core is approached and the front of the dislocation is distorted. In motion, the dislocation core can undergo dynamic transformations; for example, its transverse edges can be bended forward in the propagation direction, which leads to self-focusing of the dislocation and the development of a crack. If the transverse edges are bended backward, the internal stresses in the dislocation gradually loosen and the dislocation finally dissolves and disappears in the bulk. On the contrary, the self-focusing increases the internal stresses and decreases the characteristic dimensions of the dislocation. Consequently, the lattice discreteness and anharmonic vibrations should be taken into account. Appropriate considerations were made in [2, 3] with a number of simplifying assumptions. The main approximation used was that the cubic anharmonicity and lattice discreteness (acoustic dispersion) are linked to each other by a certain relation. This restriction made it possible to obtain an analytical expression for the dislocation field [2] and reduce the problem to integrable equations [3]. By including cubic anharmonicity and acoustic dispersion, the authors of [2] came to the conclusion that the supersonic motion of dislocations is possible. It turned out that it is much more difficult to develop a theory with inclusion of quadratic anharmonicity than with inclusion of cubic anharmonicity [2]. Meanwhile, in most cases, quadratic acoustic nonlinearity dominates in crystals and is the main reason behind the thermal expansion.

The goal of this paper is to study the effects of transverse perturbations on the edge dislocation motion in the case where elastic anharmonicity of the second and third orders and acoustic dispersion are important.

2. MODEL

Let us consider propagation of a crowdion-like edge dislocation in a cubic crystal along the z axis chosen in the direction of one of the fourfold symmetry axes. The transverse dynamics is taken into account in the paraxial approximation [4], which corresponds to distortion of the dislocation front that is not too strong. This approximation greatly simplifies computations and, at the same time, describes reasonably well the well-known results from the wave theory, among them self-focusing [5]. The acoustic dispersion is also assumed to be small and is taken into account in the first order. The contributions of the transverse dynamics, acoustic dispersion, and elastic anharmonicity are considered to be of the same order. Summarizing, we write the Hamiltonian of the plastic deformation displacement field in the crystal:

$$H = \int \mathcal{H} d^3\mathbf{r}, \tag{1}$$

where the Hamiltonian density is

$$\begin{aligned}\mathcal{H} = {} & \frac{p^2}{2nm} + \frac{\lambda_{11}}{2}\left(\frac{\partial u}{\partial z}\right)^2 + nU_0\sin^2\frac{\pi u}{h} + \frac{\lambda_{11}}{2}(\nabla_\perp u)^2 \\ & - \frac{\lambda_{11}h^2}{24}\left(\frac{\partial^2 u}{\partial z^2}\right)^2 + \left(\lambda_{11} + \frac{\lambda_{111}}{3}\right)\left(\frac{\partial u}{\partial z}\right)^3 \\ & + \left(\lambda_{11} + \frac{\lambda_{111}}{3} + \frac{\lambda_{1111}}{4}\right)\left(\frac{\partial u}{\partial z}\right)^4.\end{aligned} \tag{2}$$

Here, ρ is the momentum density corresponding to the displacement u of lattice sites along the z axis; λ_{11}, λ_{111}, and λ_{1111} are the adiabatic elastic moduli of the second,

1063-7834/05/4704-0646$26.00 © 2005 Pleiades Publishing, Inc.

third and forth orders, respectively; h is the lattice constant; m is the mass of atoms that are displaced in the crystal during plastic deformation; n is the atomic concentration; and U_0 is the Frenkel–Kontorova barrier formed by the "substrate," which is considered to be fixed. The fourth and fifth terms in Hamiltonian (2) describe the transverse perturbations and acoustic dispersion, respectively, and the sixth and seventh correspond to the quadratic and cubic anharmonicity, respectively. The first three terms correspond to the one-dimensional Frenkel–Kontorova model.

Hamilton's equations for the displacement field have the form

$$\frac{\partial p}{\partial t} = -\frac{\delta H}{\delta u}, \quad \frac{\partial u}{\partial t} = \frac{\delta H}{\delta p}. \tag{3}$$

Combining Eqs. (1)–(3) gives the equation

$$\begin{aligned}\frac{\partial^2\theta}{\partial z^2} - \frac{1}{v_0^2}\frac{\partial^2\theta}{\partial t^2} &= a\sin\theta + b_2\frac{\partial\theta}{\partial z}\frac{\partial^2\theta}{\partial z^2} \\ &\quad - b_3\left(\frac{\partial\theta}{\partial z}\right)^2\frac{\partial^2\theta}{\partial z^2} - b\frac{\partial^4\theta}{\partial z^4} - \Delta_\perp\theta,\end{aligned} \tag{4}$$

where

$$\theta = \frac{2\pi u}{h}, \quad a = \frac{2\pi^2 n^2 m U_0}{\lambda_{11}h^2}, \quad b = \frac{h^2}{12}, \quad b_2 = \frac{h\Gamma}{\pi},$$

$$b_3 = \frac{2h^2}{\pi^2}\left(\frac{3\lambda_{1111}}{8\lambda_{11}} - \Gamma\right),$$

$\Gamma = -(3/2)(1 + \lambda_{111}/3\lambda_{11})$ is the Grüneisen constant, and $v_0 = \sqrt{\lambda_{11}/nm}$ is the speed of sound in linear theory.

In Eq. (4), the terms involving the constants a, b, b_2, and b_3 are associated with the Frenkel–Kontorova potential, acoustic dispersion, and quadratic and cubic anharmonicity, respectively.

We employ the paraxial approximation $\partial^2\theta/\partial z^2 \gg \Delta_\perp\theta$; therefore, in the right-hand side of Eq. (4), all terms other than $\sin\theta$ are small as compared to the terms in the left-hand side and we can solve Eq. (4) using the convergence method. In the zero approximation, we have $\theta = \theta(z - v_0 t)$, which describes a dislocation propagating along the z direction. Now, we introduce a "slow time" $\tau = \delta t$ and consider it to be a small correction, $\delta \ll 1$. Then, the solution takes the form $\theta = \theta(\zeta, \tau)$, where $\zeta = z - v_0 t$. Neglecting terms of the order of $\sim\delta^2$, we get

$$\frac{\partial^2}{\partial z^2} = \frac{\partial^2}{\partial \zeta^2}, \quad \frac{\partial^2}{\partial t^2} \cong v_0^2\frac{\partial^2}{\partial\tau^2} - 2\delta v_0\frac{\partial^2}{\partial\zeta\partial\tau}.$$

Substituting these relations into Eq. (4) and returning to the variable t, we obtain

$$\begin{aligned}\frac{\partial^2\theta}{\partial\zeta\partial t} &= \alpha\sin\theta + \beta_2\frac{\partial\theta}{\partial\zeta}\frac{\partial^2\theta}{\partial\zeta^2} - \beta_3\left(\frac{\partial\theta}{\partial\zeta}\right)^2\frac{\partial^2\theta}{\partial\zeta^2} \\ &\quad - \beta\frac{\partial^4\theta}{\partial\zeta^4} - \frac{v_0}{2}\Delta_\perp\theta,\end{aligned} \tag{5}$$

where

$$\alpha = a v_0/2, \quad \beta = b v_0/2, \quad \beta_{2,3} = b_{2,3} v_0/2.$$

The equation obtained was studied in [3] for the special case of the Kosevich–Kovalev constraints $\beta_2 = 0$ and $\beta_3 = 3\beta/2$ in the absence of transverse perturbations ($\Delta_\perp\theta = 0$). It was proven that this equation is integrable under the above conditions, and its multisoliton solution was found.

3. INCLUSION OF TRANSVERSE PERTURBATIONS IN THE GEOMETRIC APPROXIMATION

We perform further analysis of Eq. (5) using the variational method of the averaged Lagrangian [6–8]. The Lagrangian corresponding to Eq. (5) can be written as

$$\begin{aligned}L &= \frac{1}{2}\frac{\partial\theta}{\partial t}\frac{\partial\theta}{\partial\zeta} + \alpha(1 - \cos\theta) - \frac{\beta_2}{6}\left(\frac{\partial\theta}{\partial\zeta}\right)^3 \\ &\quad + \frac{\beta_3}{12}\left(\frac{\partial\theta}{\partial\zeta}\right)^4 - \frac{\beta}{2}\left(\frac{\partial^2\theta}{\partial\zeta^2}\right)^2 + \frac{v_0}{4}(\nabla_\perp\theta)^2.\end{aligned} \tag{6}$$

Let us chose a trial function in the form of a crowdion considered in [2, 3]:

$$\theta = 4\arctan\exp(\rho(\zeta - \Phi)). \tag{7}$$

In the one-dimensional case, we have $\rho = 1/l = \text{const}$ and $\Phi = (v - v_0)t$, where v is the dislocation velocity, which is dependent on the dislocation length l. Taking into account inhomogeneities in the paraxial approximation, we conclude that $\rho = \rho(t, \mathbf{r}_\perp)$ and $\Phi = \Phi(t, \mathbf{r}_\perp)$ are slow and fast functions of their parameters, respectively.

Substituting Eq. (7) into Eq. (6) and integrating over the fast variable ζ, we get the averaged Lagrangian

$$\begin{aligned}\Lambda \equiv \frac{1}{4}\int_{-\infty}^{+\infty} L d\zeta &= \rho\frac{\partial\Phi}{\partial t} - \frac{\alpha}{\rho} + \frac{\pi}{6}\beta_2\rho^2 - \left(\frac{4}{3}\beta_3 - \beta\right)\frac{\rho^3}{3} \\ &\quad - \frac{\pi^2}{6}v_0\frac{(\nabla_\perp\rho)^2}{\rho^3} - \frac{1}{2}v_0\rho(\nabla_\perp\Phi)^2.\end{aligned} \tag{8}$$

Varying Λ with respect to ρ and Φ, we obtain the Euler–Lagrange equations

$$\frac{\partial\rho}{\partial t} + \nabla_\perp(\rho\mathbf{V}_\perp) = 0, \tag{9}$$

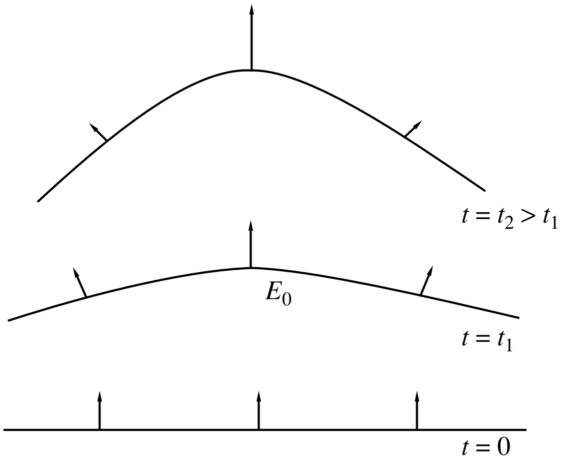

Fig. 1. Bending of the transverse fronts of an edge dislocation during defocusing.

$$\frac{\partial\varphi}{\partial t} + \frac{\mathbf{V}_\perp^2}{2} + \int\frac{dP}{\rho} = F(t, \mathbf{r}_\perp), \tag{10}$$

where $\varphi = -v_0\Phi$, $\mathbf{V}_\perp = \nabla_\perp\varphi$,

$$\frac{dP}{d\rho} = 2v_0\left(\frac{\alpha}{\rho^2} - \frac{\pi}{6}\beta_2\rho + \left(\frac{4}{3}\beta_3 - \beta\right)\rho^2\right), \tag{11}$$

$$F(t, \mathbf{r}_\perp) = \frac{\pi^2}{12}v_0^2\rho^{-3}\left(\Delta_\perp\rho - \frac{3}{2}\frac{(\nabla_\perp\rho)^2}{\rho}\right). \tag{12}$$

In the one-coordinate case ($\nabla_\perp = 0$), the set of equations (9) and (10) in combination with Eq. (11) can be easily integrated. In this case, the velocity of a one-dimensional crowdion can be found to be

$$v = v_0\left[1 - \frac{al^2}{2} - \frac{\pi b_2}{6l} + \left(\frac{4}{3}b_3 - b\right)\frac{1}{2l^2}\right]. \tag{13}$$

Under the Kosevich–Kovalev constraints ($b_2 = 0$, $b_3 = 3b/2$), the velocity v is given by

$$v = v_0\left(1 - \frac{al^2}{2} + \frac{b}{2l^2}\right),$$

which coincides with the result obtained in [3] to within the notation for the factors a and b. This fact is an important argument in favor of the averaged-Lagrangian approach adopted in this paper.

The right-hand side of Eq. (10) contains derivatives of the slow variable ρ with respect to the transverse coordinates. To draw an analogy with optics [4, 9], we can say that $F(t, \mathbf{r}_\perp)$ describes the wave properties of the dislocation and includes diffraction of the dislocation on its own inhomogeneities. At the initial stage of distortion of the dislocation front, the wave properties can be neglected and the consideration can be limited to the eikonal (geometric) approximation, which corresponds to $F = 0$. In this case, the set of equations (9) and (10) coincides with the equations of potential flow of an ideal liquid (the continuity equation and the Cauchy integral for non-steady-state flow, respectively). Here, φ acts as the velocity potential $\mathbf{V}_\perp$ and P and ρ are analogs of the pressure and density, respectively. Equation (11) plays the part of the thermodynamic equation for the isoentropic liquid flow (the adiabatic equation). In this case, the condition of stable liquid flow described by Eqs. (9)–(11)

$$dP/d\rho > 0 \tag{14}$$

corresponds to the stability condition of the solution to Eq. (7) relative to self-focusing [10–12]. In our case, this condition means that the dislocation will spread over the crystal, thereby preventing the formation of cracks because local stresses will diminish. Combined with Eq. (11), inequality (14) takes the form

$$\frac{a}{\rho^2} + \frac{4}{3}b_3\rho^2 - \frac{\pi}{6}b_2\rho - b\rho^2 > 0. \tag{15}$$

This condition has a clear physical meaning. Indeed, using the relation $l = 1/\rho$ and Eq. (13), Eq. (15) can be shown to coincide with the condition $dv/d\rho > 0$. From the definition of θ, it follows that $\partial\theta/\partial\zeta \sim \partial u/\partial z \sim \varepsilon$, where ε is the local relative deformation. Using Eq. (7), we get

$$\frac{\partial\theta}{\partial\zeta} = 2\rho\,\mathrm{sech}[\rho(\zeta - \Phi)].$$

Thus, $\rho \sim \varepsilon_m$, where ε_m is the maximum value of ε.

The quantity ε_m is maximum in the center of the dislocation cross section. If the velocity v grows with increasing ε_m (i.e., $dv/d\rho > 0$), then the dislocation front is bent such that its central part propagates faster than the peripheral sections (Fig. 1), which leads to defocusing of the dislocation. Otherwise, the dislocation becomes unstable with respect to self-focusing.

It follows from Eq. (15) that the stability of a crowdion with respect to self-focusing depends on several competing effects. The Frenkel–Kontorova crystal potential U_0 causes defocusing. The quadratic anharmonicity (which is the main factor governing the thermal expansion) and acoustic dispersion promote the self-focusing. The cubic anharmonicity can play on either side: it impedes the self-focusing if $\lambda_{1111} > 8\Gamma\lambda_{11}/3 \equiv 8\Gamma nm v_0^2/3$ and facilitates it otherwise.

4. DIFFRACTION EFFECTS

Let $F \neq 0$ in Eq. (10), which means that we take into account diffraction of the crowdion on the crystal inhomogeneities created by the crowdion itself. In this case, we will employ the methods of optics and general wave theory [4, 5]. We assume that the dislocation field is axisymmetric. Following [4, 5], we write ρ in the self-similar form

$$\rho = \rho_0\frac{R_0^2}{R^2}\exp\left(-\frac{r^2}{R^2}\right), \tag{16}$$

where R_0 and $R(t)$ are the initial and current transverse radii of the crowdion. We expand ρ into a power series in r and keep only the zero- and first-order terms limiting ourselves to the paraxial approximation ($r^2/R^2 \ll 1$) [4, 5]:

$$\varphi = f_1(t) + f_2(t)\frac{r^2}{2} + \ldots. \tag{17}$$

Substituting Eqs. (16) and (17) into Eq. (9), we get

$$f_2 = \frac{\dot{R}}{R}. \tag{18}$$

Substituting Eqs. (16) and (17) into Eq. (10) and equating the coefficients of the zero and first powers of r/R, we obtain the following set of equations:

$$\begin{aligned} \dot{f}_1 = \frac{v_0^2}{2}\biggl(&\frac{aR^4}{\rho_0^2 R_0^4} + \frac{\pi}{6}b_2\rho_0\frac{R_0^2}{R^2} \\ &-\left(\frac{4}{3}b_3 - b\right)\rho_0^2\frac{R_0^4}{R^4} - \frac{2\pi^2}{3}\frac{R^2}{\rho_0^2 R_0^4}\biggr), \end{aligned} \tag{19}$$

$$\begin{aligned} \dot{f}_2 + f_2^2 = 2v_0^2\biggl(&\frac{aR^2}{\rho_0^2 R_0^4} + \frac{\pi}{6}b_2\rho_0\frac{R_0^2}{R^4} \\ &+\left(\frac{4}{3}b_3 - b\right)\rho_0^2\frac{R_0^4}{R^6} - \frac{5\pi^2}{6}\frac{1}{\rho_0^2 R_0^4}\biggr). \end{aligned} \tag{20}$$

Substituting Eq. (18) into Eq. (20), we get the differential equation for the dislocation radius,

$$\ddot{R} = -\frac{\partial U}{\partial R}, \tag{21}$$

which coincides in form with the equation of motion of a Newtonian particle of unit mass in a potential field given by

$$\begin{aligned} U(R) = \frac{v_0^2}{2}\biggl[&\left(\frac{4}{3}b_3 - b\right)\rho_0^2\frac{R_0^4}{R^4} - \frac{\pi}{3}b_2\rho_0\frac{R_0^2}{R^2} \\ &- \frac{a}{\rho_0^2}\frac{R^4}{R_0^4} + \frac{5\pi^2}{3}\frac{R^2}{\rho_0^2 R_0^4}\biggr]. \end{aligned} \tag{22}$$

The first and second terms in the square brackets in Eq. (22) correspond to the cubic and quadratic lattice anharmonicity, respectively, and the third term describes the influence of the periodic crystal potential of the substrate in the Frenkel–Kontorova model.

It is clear that the effects of these terms precisely match the influences of the corresponding physical phenomena on the crowdion transverse dynamics, as considered in the previous section in the geometric approximation.

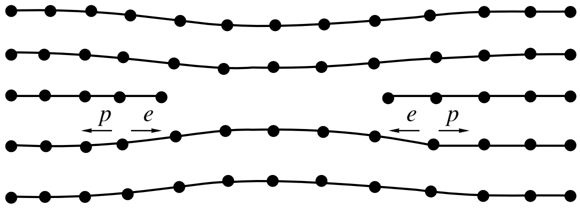

Fig. 2. Competing influences of (e) elastic and (p) plastic deformations on the transverse structure of an edge dislocation.

The diffraction is taken into account by the last term in the square brackets in Eq. (22), which formally coincides with the potential energy of a harmonic oscillator with the single difference that $R > 0$ in our case. Note that, in the geometric approximation ($R_0, R \longrightarrow \infty$), the diffraction term in Eq. (22) vanishes, unlike the other terms. This term is favorable for self-focusing of the crowdion, i.e., for the attraction of its portions to the regions of maximum local deformation. This happens because the diffraction effects correspond to elastic deformation in the cross-sectional planes of the crowdion. The plastic deformation acting in these directions expands the crowdion to free atom vacancies (Fig. 2), whereas the elastic strain, as usual, confronts the plastic deformation and restores the crystal symmetry.

It is convenient to trace the crowdion dynamics during its propagation using an analogy with the equation of motion. If $R \longrightarrow 0$, the dislocation is self-focusing and this will finally lead to the formation of a crack in the crystal. If $R \longrightarrow \infty$, the dislocation spreads over the crystal and finally disappears. Qualitative conclusions about $R(t)$ can be made by studying $U(\dot{R})$ in the form of Eq. (22).

Let us consider the important special case of the classical Frenkel–Kontorova model by setting $b = b_2 = b_3 = 0$ in Eq. (22).

The $U(R)$ dependence calculated for this case (Fig. 3) shows that the dislocation either collapses (if $R_0 < R_c$) or spreads if $R_0 > R_c$, where

$$R_c = \sqrt{\frac{5}{6}}\pi l_s \approx 2.9 l_s. \tag{23}$$

Here, $l_s = 1/\sqrt{a}$ is the size of the static Frenkel–Kontorova dislocation and $l_0 = 1/\rho_0$. In this case, v is close to v_0 and we can write $v = v_0\sqrt{1 - al^2} \equiv v_0\sqrt{1 - l^2/l_s^2} \cong v_0(1 - l^2/2l_s^2)$, which coincides with Eq. (13) if $b = b_2 = b_3 = 0$.

The quadratic anharmonicity and acoustic dispersion shift R_c to higher values. Moreover, $U(R) \longrightarrow -\infty$ if $R \longrightarrow 0$ (Fig. 4). Therefore, these factors promote self-focusing, i.e., increase the probability of formation of microcracks. The influence of the cubic anharmonic-

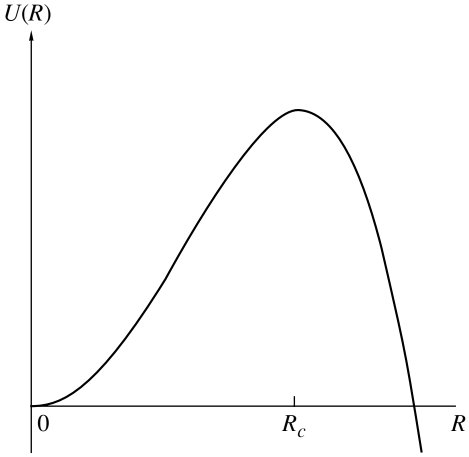

Fig. 3. $U(R)$ according to the Frenkel–Kontorova model.

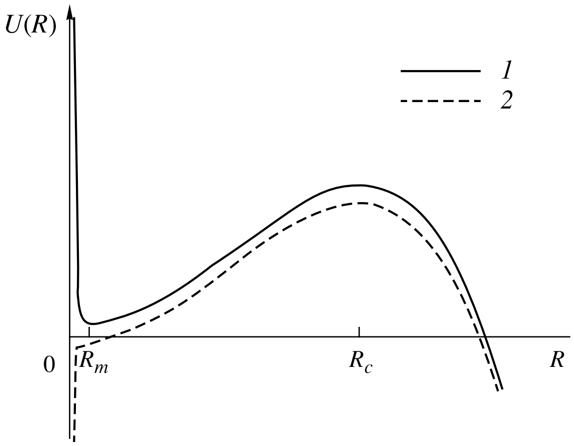

Fig. 4. U(R) in the presence of quadratic and cubic anharmonicity (*1*) for the case of $b_3 > 3b/4$, where the formation of crowdion droplets is possible, and (*2*) for the case of $b_3 < 3b/4$.

ity is opposite. If $b_3 < 3b/4$, this anharmonicity is unable to prevent cracks. However, if $b_3 > 3b/4$, the cubic nonlinearity can avert self-focusing. In this case, there are two possibilities: either the dislocation spreads away or its radius oscillates around an equilibrium value R_m (Fig. 4). The latter can be interpreted as a propagation of a crowdion droplet.

Let us study the requirements for this mode in detail. We start from Eq. (22) for the "potential energy." The extremum condition $\partial U/\partial R|_{R = R_m} = 0$ can be written as

$$Q(q_m) = q_m^4 - Dq_m^3 - B_2 q_m + B_3 = 0, \qquad (24)$$

where $q_m = (R_m/R_0)^2$, $D = R_c^2/R_0^2$, $B_2 = \pi b_2 l_s^2/6l_0^3$, and $B_3 = (4b_3/3 - b)l_s^2/l_0^4 > 0$.

For a crowdion droplet to form, the extremum has to be a minimum of U; i.e., the condition $\partial^2 U/\partial R^2|_{R = R_m} > 0$ has to be satisfied. Taking into account Eq. (24), this condition can be written as

$$S(q_m) = Dq_m^3 + 3B_2 q_m - 4B_3 < 0. \qquad (25)$$

Note that a droplet forms under several opposing influences. One of them is cubic anharmonicity, whose contribution is given by the last terms in Eqs. (24) and (25). The others are diffraction and quadratic anharmonicity, the second and third terms in Eq. (24), respectively.

Let us calculate the propagation velocity of a crowdion droplet. Note that $\zeta - \Phi = z - v_0 t - \Phi = z - (v_0 + \dot{\Phi})t$. Hence, the velocity relative to the laboratory reference frame is given by $v = v_0(1 - \dot{\varphi}/v_0^2)$. Using Eqs. (19) and (24), we obtain

$$v = v_0\left(1 - \frac{l_0^2}{10 l_s^2 q_m^2}(Dq_m^3 + 10B_2 q_m - 10B_3)\right). \qquad (26)$$

It follows from Eqs. (25) and (26) that the crowdion droplet can propagate at supersonic speed if there is no quadratic anharmonicity.

In general, Eqs. (24) and (25) are quite cumbersome and too complex to be analyzed. Therefore, we limit ourselves to studying several important limiting cases illustrating the main features.

Let us assume that the diffraction contribution is small. Setting $D = 0$ in Eqs. (24) and (25), we can find the initial parameters of the dislocation required for the creation of a droplet. The polynomial $Q(q_m)$ has real roots if its coefficients satisfy certain conditions. In analyzing Eq. (24), we conclude that $q_m = (B_2/4)^{1/3}$ corresponds to a minimum of $Q(q_m)$ and to an inflection point of the potential energy. In order for Eq. (24) to have at least two roots, one of which is a minimum of $U(R)$, the inequality $Q((B_2/4)^{1/3}) < 0$ has to be satisfied. Hence, the parameters of the medium have to be subject to the condition

$$B_3 < 0.47 B_2^{4/3},$$

in order for the formation of crowdion droplets to be possible. The range of possible dimensions of a droplet can be found from Eqs. (24) and (25) to be

$$R_m < 0.87 B_3^{1/8} R_0.$$

Let us study now the case where the quadratic anharmonicity is small and the diffraction is substantial. Setting $B_2 = 0$ in Eqs. (24) and (25) and proceeding as above, we obtain the condition for the droplet formation:

$$R_0 < 0.87 B_3^{1/8} R_c.$$

In this case, the droplet dimensions lie in the range

$$R_m < 1.15 B_3^{1/8} R_0$$

and the crowdion droplet moves at supersonic speed.

Let us study the possible realization of a crowdion droplet in crystals. For this purpose, we use the Morse potential [13]

$$W = W_0(e^{-2\xi/r_0} - 2e^{-\xi/r_0}),$$

where $\xi \equiv u_{j+1} - u_j$ is the site relative displacement, r_0 is the parameter describing the scope of the potential, and W_0 is its magnitude.

In the vicinity of the minimum, the potential can be expanded as

$$W = W_0\left\{\frac{h^2}{r_0^2}\left(\frac{\partial u}{\partial z}\right)^2 - \frac{h^3}{r_0^3}\left(\frac{\partial u}{\partial z}\right)^3 + \frac{7h^4}{12r_0^4}\left(\frac{\partial u}{\partial z}\right)^4\right\}.$$

Through comparison with Eq. (2), we get $\lambda_{111}/\lambda_{11} = -3h/2r_0$ and $\lambda_{1111}/\lambda_{11} = 7h^2/6r_0^2$. The values of the elastic moduli of the second and third order are well-known, so we can estimate the fourth-order constant λ_{1111}.

We take as an example NaCl crystals. For this compound, $h = 5.63$ Å, $\lambda_{11} = 49$ GPa [14], and $\lambda_{111} = -8.5 \times 10^2$ GPa [15]. Hence, $b_2 = 3.7$ Å, $b_3 = 48.3$ Å^2, and $b = 2.6$ Å^2. The condition $b_3 > 4b/3$ (Fig. 4) is satisfied. Assuming the dislocation parameters to be $l_0 \sim 10h$ and $l_s \sim 100h$, we get $B_2 = 3.5$ and $B_3 = 2$. For $R_0 = 0.5R_c = 145h$, from Eqs. (24) and (25) we obtain $R_m = 0.68R_0 = 99h$. The cross section of such a dislocation starts to collapse, and later, in the course of propagation, it will oscillate near the equilibrium size R_m. The peak value of the plastic strain inside the crowdion droplet is $\varepsilon_m \cong h/\pi l_0 = 0.03$. The droplet velocity practically coincides with the speed of sound, exceeding it by just a few hundredths of one percent.

5. CONCLUSIONS

In contrast to studies employing one-dimensional models of atomic chains, the influence of transverse perturbations on the motion of edge dislocations has been considered in the present paper with inclusion of elastic anharmonicity of the second and third orders and the acoustic dispersion. The effects of each of these factors on the dislocation dynamics have been found.

The stability of an edge dislocation of the crowdion type with respect to self-focusing depends on several competing contributions. The Frenkel–Kontorova crystal potential causes defocusing. However, the quadratic anharmonicity (which is the main factor governing the thermal expansion) and acoustic dispersion promote self-focusing. The cubic anharmonicity plays a dual role: if the cubic nonlinearity exceeds the acoustic dispersion, it can impede the self-focusing; otherwise, it facilitates the focusing effect.

There is a range of parameters where the dislocation radius oscillates around an equilibrium value. In this case, we have a crowdion droplet, which can propagate at supersonic speed. For the formation of a crowdion droplet, it is important to have several competing contributions. In our case, these are the cubic anharmonicity exceeding the acoustic dispersion (which corresponds to $b_3 > 3b/4$) providing a defocusing effect on the one hand and the quadratic anharmonicity and diffraction promoting self-focusing on the other hand.

A trial solution to Eq. (7) has been chosen to coincide with the single-soliton solution of the Frenkel–Kontorova model in the absence of elastic anharmonicity. As was shown in [16], the quadratic anharmonicity in the one-dimensional case can give rise to fundamentally new dislocation-type solutions that cannot be reduced to the Frenkel–Kontorova soliton. We believe it will be of interest to study the influence of transverse perturbations on such dislocations.

REFERENCES

1. Ya. I. Frenkel’ and T. A. Kontorova, Zh. Éksp. Teor. Fiz. **8** (12), 1340 (1938).
2. A. M. Kosevich and A. S. Kovalev, Solid State Commun. **12**, 763 (1973).
3. K. Konno, W. Kemeyama, and H. Sanuki, J. Phys. Soc. Jpn. **37**, 171 (1974).
4. N. V. Karlov and N. A. Kirichenko, *Oscillations, Waves, and Structures* (Fizmatlit, Moscow, 2003) [in Russian].
5. M. B. Vinogradova, O. V. Rudenko, and A. P. Sukhorukov, *The Theory of Waves*, 2nd ed. (Nauka, Moscow, 1990) [in Russian].
6. D. Anderson, Phys. Rev. A **27**, 3135 (1983).
7. S. K. Zhdanov and B. A. Trubnikov, Zh. Éksp. Teor. Fiz. **92**, 1612 (1987) [Sov. Phys. JETP **65**, 904 (1987)].
8. S. K. Zhdanov and B. A. Trubnikov, *Quasi-Gaseous Unstable Media* (Nauka, Moscow, 1991) [in Russian].
9. S. V. Nesterov and S. V. Sazonov, Kvantovaya Élektron. (Moscow) **34** (2), 151 (2004).
10. S. V. Sazonov, Zh. Éksp. Teor. Fiz. **119** (3), 419 (2001) [JETP **92**, 361 (2001)].
11. S. V. Sazonov, Usp. Fiz. Nauk **171** (6), 663 (2001) [Phys. Usp. **44**, 631 (2001)].
12. S. V. Sazonov and A. F. Sobolevskiĭ, Zh. Éksp. Teor. Fiz. **123** (6), 1160 (2003) [JETP **96**, 1019 (2003)].
13. A. N. Orlov, *Introduction to the Defect Theory in Crystals* (Vysshaya Shkola, Moscow, 1983) [in Russian].
14. C. Kittel, *Introduction to Solid State Physics*, 3rd ed. (Wiley, New York, 1966; Fizmatlit, Moscow, 1963).
15. L. K. Zarembo and V. A. Krasil’nikov, Usp. Fiz. Nauk **102** (4), 549 (1970) [Sov. Phys. Usp. **13**, 778 (1971)].
16. S. A. Beklemishev and V. L. Klochikhin, Fiz. Tverd. Tela (St. Petersburg) **37** (1), 152 (1995) [Phys. Solid State **37**, 81 (1995)].

Translated by G. Tsydynzhapov

Physics of the Solid State, Vol. 47, No. 4, 2005, pp. 652–655. Translated from Fizika Tverdogo Tela, Vol. 47, No. 4, 2005, pp. 628–631.
Original Russian Text Copyright © 2005 by Zhoga, Shil'nikov, Shpeĭzman.

DEFECTS, DISLOCATIONS, AND PHYSICS OF STRENGTH

Effect of an Electric Field on the Fracture of Ferroelectric Ceramic Materials

L. V. Zhoga*, A. V. Shil'nikov†*, and V. V. Shpeĭzman**

** Volgograd State Architecture and Building Academy, Akademicheskaya ul. 1, Volgograd, 400074 Russia*
e-mail: postmaster@vgasa.ru
*** Ioffe Physicotechnical Institute, Russian Academy of Sciences, Politekhnicheskaya ul. 26, St. Petersburg, 194021 Russia*
e-mail: shpeizm.v@mail.ioffe.ru

Received July 6, 2004

Abstract—This paper reports on the experimental results of measuring the time elapsed between the loading and the fracture of ferroelectric ceramic specimens under the action of a static electric field and mechanical stresses that differ in magnitude. The dependence of the durability of the specimens on the applied stress is determined for electric fields in the range from 0 to 5 MV/m. It is shown that, in the time range 1–10^3 s, the durability of the ferroelectric ceramic material substantially increases in weak electric fields (the hardening effect) and significantly decreases in strong electric fields. The results obtained can be explained in terms of the fact that the load and the electric field affect the same defects (fracture nuclei) in the ferroelectric ceramics.

1. INTRODUCTION

In solving problems regarding the strength of ferroelectric ceramic materials, an important question arises as to how an external electric field affects the development of their fracture. There are virtually no experimental works concerned with the fracture kinetics of ferroelectric ceramic materials in the presence of an electric field. The fracture of these materials under the action of an electric field was investigated earlier in [1–4]. The nature of mechanical stresses generated by the inverse piezoelectric effect in the $BaTiO_3$ piezoelectric ceramic material was theoretically considered by Bondarenko *et al.* [5, 6]. However, those authors assumed that the fracture is critical; i.e., it occurs only when the electric field reaches a critical value. The purpose of the present work was to investigate the regularities of the fracture of ferroelectric ceramic materials for various combinations of electric fields and mechanical stresses and to compare the obtained kinetic parameters of the fracture.

2. SPECIMENS AND EXPERIMENTAL TECHNIQUE

The experiments were performed with ferroelectric ceramics of the PZT type (PZT-19) based on lead zirconate titanate $Pb(Zr,Ti)O_3$. Specimens were prepared in the form of disks with a diameter $2c = 20$ mm and a thickness $h = 0.7$ mm and had attached electrodes. The mean grain size in the specimens was equal to 4 μm, and the porosity varied in the range 17–20%. The voltage measurements were carried out in an ethylsiloxane liquid. A dc voltage was applied to the electrodes until the specimen was fractured. Mechanical loading was accomplished using axisymmetrical bending. The diameters of the supporting and loading rings were chosen to be $2b = 13$ mm and $2a = 7$ mm, respectively. The load was applied in steps $\Delta P = 1.5$ N, which corresponded to $\Delta\sigma = 1.7$ MPa. During loading, the specimen was held at a constant load for a time $\Delta t = 900$ s. The maximum tensile stresses were calculated according to the formula for the bending of round plates with an undistorted neutral plane [7]:

$$\sigma = \frac{3(1+\nu)}{2\pi h^2}\left(\ln\frac{b}{a} + \frac{(1+\nu)(b^2-a^2)}{2(1-\nu)c^2}\right)Q. \qquad (1)$$

Here, Q is the load and ν is the Poisson ratio of the piezoelectric ceramic material. The durability τ was taken as the time elapsed between the last loading and the fracture of the specimen.

In our experiments, the electric field E was equal to 0, 1, 2, 3, 4, and 5 MV/m.

3. EXPERIMENTAL RESULTS AND DISCUSSION

The experiments demonstrated that the fracture of the ferroelectric ceramic specimens under the action of mechanical stresses has a kinetic character. The fracture was observed at various constant mechanical stresses applied over different periods of time. In this case, the spread of times elapsed between the loading and the fracture of the specimens was very large: for a chosen testing time Δt, the specimen under the load

---

[†] Deceased.

Results of the statistical processing of the obtained data on the fracture kinetics of ferroelectric ceramic materials in an electric field

	σ, MPa													
	7.5	10	12.5	15		17.5		20		22.5	25	27.5	30	35
E, MV/m	4	4	4	4	1	4	1	4	1	1	1	1	1	1
$n\downarrow$	0	1	7	20	0	33	0	41	3	8	15	27	32	37
n_i	0	5	12	12	0	7	2	0	5	7	12	5	4	0
$n\uparrow$	41	35	22	9	37	0	35	0	29	22	10	5	1	0
n_i/n	0	0.12	0.29	0.29	0	0.17	0.05	0	0.14	0.19	0.32	0.14	0.11	0
$n\downarrow/n$	0	0.02	0.20	0.51	0	0.83	0	1	0.08	0.22	0.41	0.73	0.86	0.97

Note: $n\downarrow$ is the number of specimens fractured under stepwise loading up to the stress σ, n_i is the number of specimens fractured in the time range from $\tau_{\min}$ to $\tau_{\max}$, and $n\uparrow$ is the number of specimens not fractured under loading at the stress σ.

could be both fractured at the instant of loading and not fractured. Figures 1a and 1b present the results of measuring the durability of ferroelectric ceramic specimens under different stresses for electric fields of 1 and 4 MV/m.

Earlier [8], we showed that the time elapsed between the loading and the fracture of the specimen under stepwise loading (i.e., the durability of the specimen) can be described by the expression

$$\tau = \tau_0 \exp\frac{U_0 - V_{\text{eff}}\sigma}{kT}. \qquad (2)$$

Here, V_{eff} is the effective activation volume, U_0 is the activation energy of fracture, T is the measurement temperature, k is the Boltzmann constant, and τ_0 is a constant. At a constant temperature, expression (2) takes the form $\tau = Ae^{-B\sigma}$, where A characterizes the activation energy and B determines the effective activation volume of fracture. In [8], we also developed a procedure for calculating the parameters A and B from the average mechanical strength $\bar{\sigma}$ and the fracture probability W at a constant stress σ in a specified time range from $\tau_{\min}$ to $\tau_{\max}$:

$$\log\frac{A}{\tau_{\min}} = \frac{\bar{\sigma}\log\tau_{\max}/\tau_{\min}}{\int\limits_{-\infty}^{\infty} W d\sigma}, \quad B = \frac{\log A/\tau_{\min}}{\bar{\sigma}}. \qquad (3)$$

In our experiment, the fracture probability W was taken as the ratio of the number of specimens (n_i) fractured at a given stress σ_i in the time range from $\tau_{\min}$ to $\tau_{\max}$ to the total number of tested specimens (n). The average mechanical strength was determined from the integral curve of the mechanical strength distribution, which involves the data obtained for the specimens fractured at all previous stages and at the instant of last loading, i.e., before the onset of loading at the given stress (their number is denoted as $n\downarrow$).

The table summarizes the results of the statistical processing of the data presented in Figs 1. The probability function $W(\sigma)$ and the strength distribution function from which the quantity $\bar{\sigma}$ was determined for electric fields of 1 and 4 MV/m are shown in Fig. 2. These data and the corresponding results obtained for other electric fields were used to calculate the coefficients A and B (Fig. 3) from expression (3). As can be

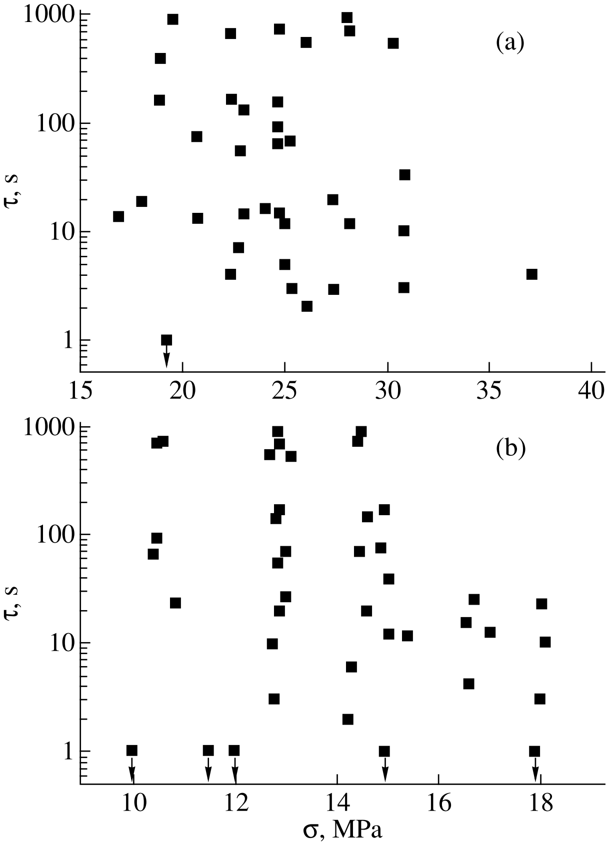

Fig. 1. Time τ elapsed between the loading and the fracture of the specimens under simultaneous action of a static electric field with strengths of (a) 1 and (b) 4 MV/m and a stepwise increasing mechanical load as a function of the stress σ.

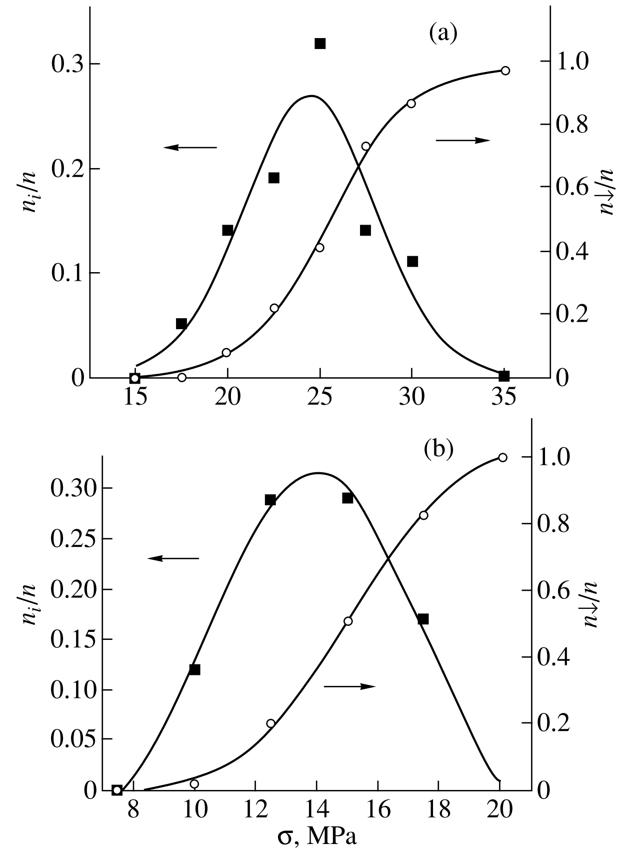

Fig. 2. Dependences of the fracture probability W in the time range 1–10^3 s on the stress σ and the integral curve of the mechanical strength distribution for electric fields E = (a) 1 and (b) 4 MV/m.

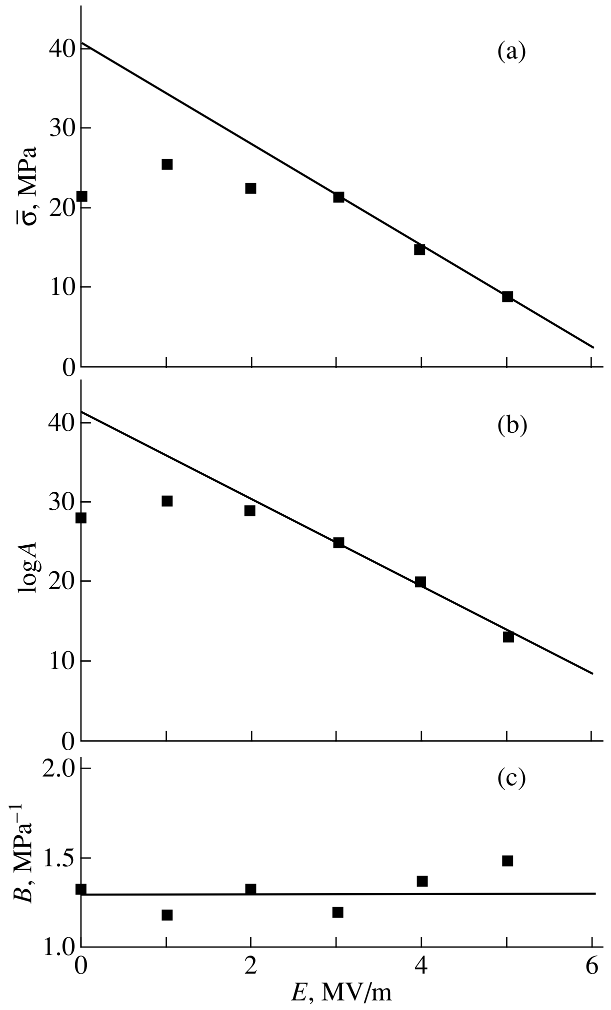

Fig. 3. Dependences of (a) the average strength $\bar{\sigma}$ and the parameters (b) A and (c) B on the electric field E.

seen from Fig. 3, the dependences of log$A$ and $\bar{\sigma}$ on the electric field have a similar behavior and, as a first approximation, the coefficient B can be assumed to be constant. The decrease in the average mechanical strength $\bar{\sigma}$ with an increase in the electric field E according to a nearly linear law with a slope of 6.4 N/Vm is observed only at $E \geq 3$ MV/m. In weaker electric fields E, the average mechanical strength first slightly increases and then again becomes close to the mechanical strength in the absence of an electric field. A similar result was obtained earlier in [8]. However, in [8], this inference holds only for the mechanical strength corresponding to $\tau = 1$ s. In the present work, we can extend this inference to times (or loading rates) up to 10^3 s. The mean value of $B = 1.3$ MPa^{-1} allows us to determine the effective activation volume $V_{\text{eff}} = 12 \times 10^{-27}$ m^{-3}, which is in close agreement with the results published in our recent paper [9].

A comparison of the results obtained in this work with the data reported in [8, 9] allows the conclusion that, upon fracture of the specimens under the action of an electric field and mechanical loading, the time effects manifest themselves in a similar manner. This confirms the assumption made earlier in [8] that the observed processes are affected by the same structural defects.

Thus, the results of our experiments indicate that the mechanical fracture of ferroelectric ceramic specimens in an electric field has a kinetic character. In this case, the fracture probability in a specified time range [i.e., the quantity proportional to the effective activation volume V_{eff}, as follows from expression (3)] does not depend on the electric field. An insignificant hardening in weak electric fields is observed in the time range 1–10^3 s. Most likely, this hardening can be associated with the relaxation processes proceeding in the structure of the ferroelectric ceramics. By assuming that the preexponential factor τ_0 in expression (2) is equal to 10^{-13} s in the studied ranges of E and σ, we can estimate the activation energy of fracture. For $E \leq 3$ MV/m, the activation energy of fracture is almost constant and is equal to 2.3 eV. For $E \geq 3$ MV/m, the activation energy decreases with an increase in the electric field. The large spread in the values of the mechanical strength and the durability for several ferroelectric ceramic specimens is caused by both the structural inhomogeneity and the large number of defects of different nature. In [8], we thoroughly investigated the mechanical strength distribution for a similar ferroelectric ceramic material. In particular, it was shown that the Weibull strength distribution exhibits a kink. This suggests that there exist two types of defects. The results obtained in this study on the fracture kinetics in a static electric field have demonstrated that the initial defects are fracture nuclei (at least, for times up to 10^3 s) and that the average mechanical strength and durability are related by expression (2).

ACKNOWLEDGMENTS

This work was supported by the Russian Foundation for Basic Research (project no. 02-02-16232), the Competition Center of the Ministry of Education of the Russian Federation (project no. E02-3.4-424), and the Ministry of Education of the Russian Federation within the program “Ceramics and Ferroelectric Ceramics” (project no. 202-03-02-04).

REFERENCES

1. A. D. Feronov and V. A. Servuli, *Physics of Dielectrics and Semiconductors* (Volgogr. Politekh. Inst., Volgograd, 1981) [in Russian].
2. S. N. Koĭkov and A. I. Tsikin, *Electrical Ageing of Solid Dielectrics* (Énergiya, Leningrad, 1968) [in Russian].
3. M. A. Bagirov, Ya. T. Razimov, T. F. Abbasov, and S. A. Abbasov, Fiz. Tverd. Tela (Leningrad) **15** (5), 1579 (1973) [Sov. Phys. Solid State **15**, 1055 (1973)].
4. M. S. Dakhiya, V. A. Zakrevskiĭ, and A. I. Slutsker, Fiz. Tverd. Tela (Leningrad) **26** (9), 2716 (1984) [Sov. Phys. Solid State **26**, 1645 (1984)].
5. E. I. Bondarenko, V. Yu. Topolov, and A. V. Turik, Zh. Tekh. Fiz. **57** (7), 1416 (1987) [Sov. Phys. Tech. Phys. **32**, 841 (1987)].
6. E. I. Bondarenko, V. Yu. Topolov, and A. V. Turik, Zh. Tekh. Fiz. **62** (12), 155 (1992) [Sov. Phys. Tech. Phys. **37**, 1206 (1992)].
7. F. F. Vitman, Ya. S. Uflyand, and B. S. Ioffe, Prikl. Mekh. **5** (6), 122 (1970).
8. L. V. Zhoga and V. V. Shpeĭzman, Fiz. Tverd. Tela (St. Petersburg) **34** (8), 2578 (1992) [Sov. Phys. Solid State **34**, 1382 (1992)].
9. L. V. Zhoga, A. V. Shil’nikov, and V. V. Shpeĭzman, Izv. Ross. Akad. Nauk, Ser. Fiz. **67** (8), 1207 (2003).

Translated by I. Volkov

Physics of the Solid State, Vol. 47, No. 4, 2005, pp. 656–662. Translated from Fizika Tverdogo Tela, Vol. 47, No. 4, 2005, pp. 632–638.
Original Russian Text Copyright © 2005 by Malygin.

DEFECTS, DISLOCATIONS, AND PHYSICS OF STRENGTH

Analysis of the Factors That Cause Unstable Deformation and Loss of Plasticity in Neutron-Irradiated Copper

G. A. Malygin

Ioffe Physicotechnical Institute, Russian Academy of Sciences, Politekhnicheskaya ul. 26, St. Petersburg, 194021 Russia
e-mail: malygin.ga@mail.ioffe.ru

Received July 7, 2004

Abstract—Copper is used as an example to analyze the effect of radiation on the stress–strain curves and deformation stability of radiation-hardened metals. The analysis is based on an equation that describes the evolution of the dislocation density with deformation in a plastically deformed material. Deformation instability in the initial stage of the stress–strain curve is caused by strong deformation localization at the microscopic level as a result of the transformation of immobile radiation defects (vacancy and interstitial loops) into mobile dislocations. The channeling of a large number of dislocations along slip planes causes the appearance of a yield drop and a yield plateau in the stress–strain curves. The critical conditions for their appearance, as well as the theoretical irradiation-dose dependences of the yield-plateau length and the uniform strain to necking, are found. *© 2005 Pleiades Publishing, Inc.*

1. INTRODUCTION

Neutron irradiation of metals at doses higher than 10^{17} cm^{-2} at temperatures $T < 0.3T_m$, where T_m is the melting temperature, is accompanied by a number of specific features. The main features are the formation of clusters of radiation defects (vacancy or interstitial loops and stacking-fault tetrahedra) with a density of 10^{16}–10^{18} cm^{-3}, which cause a sharp increase in the critical shear stress and the appearance of a yield drop and a yield plateau in the stress–strain curve of an irradiated metal, and a strong decrease in the uniform strain to necking. The latter two circumstances indicate a low resistance of plastic deformation of a radiation-hardened metal to deformation localization and fracture. At high radiation doses (higher than 10^{23} cm^{-2}, or 1 dpa), the metal completely loses its plasticity; in other words, it becomes brittle. All these phenomena occur in both pure fcc and bcc metals and structural austenitic and ferritic alloys used in nuclear engineering [1].

Structural studies of metals plastically deformed after irradiation, performed using optical and electron-microscopic methods, have revealed that deformation localization during radiation-induced hardening takes place not only at the macroscopic level but also at the meso- and microscopic levels. At the mesoscopic level, this phenomenon manifests itself in the appearance of nonuniform deformation and its propagation as the Lüders front along the gage portion of a tensile specimen [2]. At the microscopic level, this phenomenon manifests itself in dislocation channeling. The latter effect signifies the formation of radiation defect–free "channels" 0.1- to 0.5-μm wide along slip planes in an irradiated metal during plastic deformation as a result of dislocation motion on these planes and the "sweeping" of defects [3, 4]. Materials with such channels can carry large local plastic shears of about 1–10, whereas the macroscopic strain of a sample under these conditions is only several percent. Large local shears indicate that many dislocations pass through the channels. The related steps on a crystal surface can reach a few microns [3], which can be dangerous for a polycrystalline material if the grain boundaries become brittle as a result of irradiation.

The mechanism of formation of the defectless channels and dislocation channeling was theoretically considered in [5, 6] using a kinetic equation for the density of dislocations that form as a result of the transformation of radiation-induced prismatic Frank loops and stacking-fault tetrahedra into glide dislocations followed by annihilation of the screw segments of the dislocations, which causes the disappearance of both loops and dislocations in the channels. In this work, these results are used to analyze the factors that have an effect on the instability of plastic deformation in irradiated fcc metals in the initial stage of their deformation (the appearance of a yield drop and a yield plateau) and on the uniform deformation up to deformation localization in the form of necking.

Like in [7, 8], our analysis of the effect of structural factors (radiation defects in the form of point-defect clusters) on the parameters of the stress–strain curve of an irradiated metal is based on the equation for the evolution of the mean dislocation density with strain. To illustrate and verify the theoretical results obtained, we use the data reported on plastic deformation and the defect structure of radiation-hardened copper [1, 9–12]. In Sections 2 and 3, we generalize and analyze the experimental and theoretical results regarding the variations in the radiation-defect density and the critical shear stress in copper with irradiation dose. Sections 4 and 5 give a theoretical consideration of the effect of radiation defects on the stability of plastic deformation and on the parameters and shape of the stress–strain curve of neutron-irradiated copper.

2. DEFECT DENSITY AND THE CRITICAL SHEAR STRESS

As an example, Fig. 1 shows stress–strain curves of polycrystalline copper after neutron irradiation to various doses [1, 9]. The yield strength (for a single crystal, the critical shear stress τ_i) is seen to increase strongly with irradiation dose. It has been reliably established that, in the case where dislocations interact with radiation defects with a volume density N and a transverse size d, the critical shear stress is given by [1, 10, 12]

$$\tau_i = \alpha_i(T, \dot{\varepsilon})\mu b(dN)^{1/2}, \quad (1)$$

where μ is the shear modulus, b is the Burgers vector, and α_i is a coefficient determining the interaction of a dislocation with a defect (this coefficient depends on the temperature T and strain rate $\dot{\varepsilon}$ if dislocations overcome defects via thermal activation). In Eq. (1), the quantities that can be dependent on the irradiation dose are the mean defect size d and the volume density of defects N [10, 11]. As was shown in [11], the mean defect size in copper changes only weakly with the irradiation dose, whereas the dislocation loop density increases by a few orders of magnitude and reaches saturation at irradiation doses $D > 10^{-2}$ dpa. The dependence of N on the irradiation dose for copper is described by the formula [11]

$$N = N_m\left[1 - \exp\left(-\frac{D}{D_0}\right)\right], \quad (2)$$

where $N_m = 7 \times 10^{17}$ cm^{-3} and $D_0 = 1.25 \times 10^{-2}$ dpa. If the irradiation dose is characterized by a fluence ϕ, i.e., the number of neutrons per unit area of an irradiated object, rather than by displacements per atom (dpa), then, taking into account that, in the case of $N \ll N_m$, the defect density in copper increases as $N \sim \phi^{2/3}$ [5, 10], we obtain the following dependence of the volume defect density on the fluence ϕ, which is alternative to Eq. (2):

$$N = N_m\left[1 - \exp\left(-\left(\frac{\phi}{\phi_0}\right)^{2/3}\right)\right]. \quad (3)$$

Substituting Eqs. (2) and (3) into Eq. (1), we obtain the following dependence of the critical shear stress on the irradiation dose measured in the corresponding units:

$$\tau_i = \tau_{im}\left[1 - \exp\left(-\frac{D}{D_0}\right)\right]^{1/2}, \quad (4a)$$

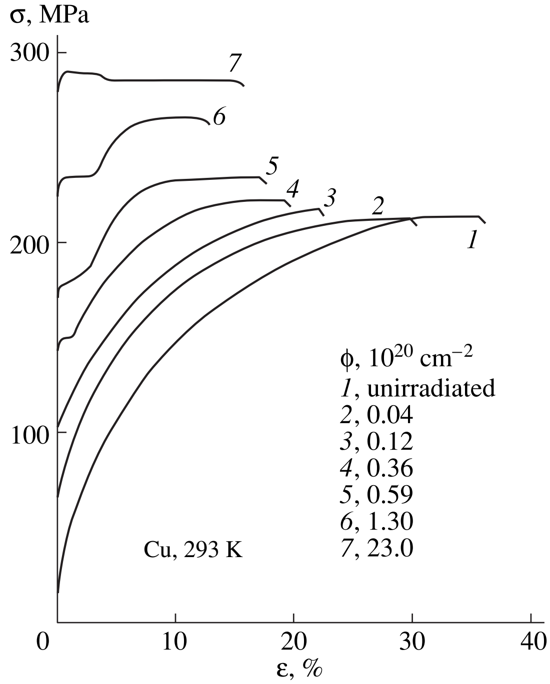

Fig. 1. Stress–strain curves of polycrystalline copper irradiated by neutrons to different doses ϕ [1, 9].

$$\tau_i = \tau_{im}\left[1 - \exp\left(-\left(\frac{\phi}{\phi_0}\right)^{2/3}\right)\right]^{1/2},$$
$$\tau_{im} = \alpha_i(T, \dot{\varepsilon})\mu b(dN_m)^{1/2}. \quad (4b)$$

The dependence of the yield strength on the irradiation dose described by Eq. (4a) is valid for a wide range of austenitic steels [13]. At $\phi \ll \phi_0$, it follows from Eq. (4b) that $\tau_i \sim \phi^{1/3}$. Dependences of this type were observed in copper in [14–16]. In Fig. 2, the experimental dependence of the yield strength of polycrystalline copper $\sigma_i = m\tau_i$ on the irradiation dose (shown in Fig. 1) is given in the $\log\sigma_i$ versus $\log\phi$ coordinates (points). The solid curve in Fig. 2 is plotted according to Eq. (4b) at $\sigma_{im} = m\tau_{im} = 370$ MPa and $\phi_0 = 5 \times 10^{20}$ cm^{-2} (m is the Taylor factor). The dotted line in Fig. 2 corresponds to the dependence $\sigma_i \sim \phi^{1/3}$.

The thermal-activation analysis of the interaction of dislocations with radiation defects performed in [14, 17] indicates that the coefficient α_i that specifies the interaction of a dislocation with a defect varies with temperature T and strain rate $\dot{\varepsilon}$ as

$$\alpha_i = \alpha_{0i} + \alpha_{i0}\left[1 - \left(\frac{T}{T_i}\right)^q\right]^{1/q}, \quad T_i = \frac{H_0}{k\ln\frac{\dot{\varepsilon}_0}{\dot{\varepsilon}}}, \quad (5)$$

where α_{0i} is the athermal component of this interaction, α_{i0} is the thermal component at $T = 0$, $q = 2/3$ [14] or 1/2 [17], H_0 is the full potential barrier that is overcome

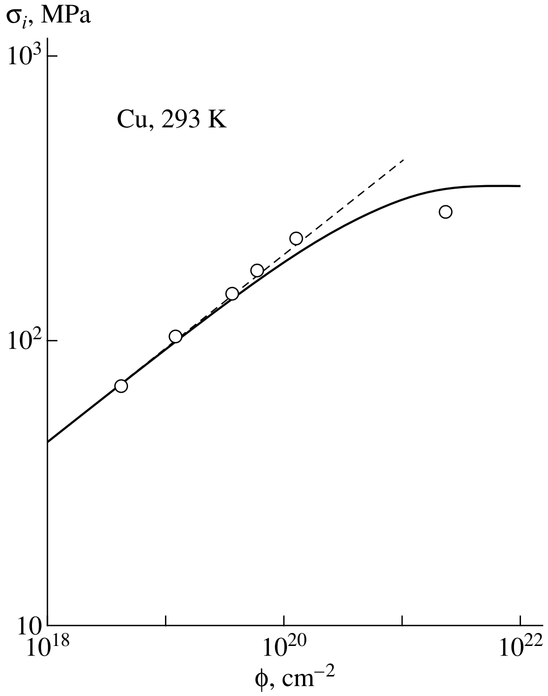

Fig. 2. Dependence of the yield strength of copper on the irradiation dose (see Fig. 1). The solid line illustrates Eq. (4b), and the dotted line is plotted according to the dependence $\sigma_i \sim \phi^{1/3}$.

by a dislocation, $\dot{\varepsilon}_0$ is the preexponential factor in the expression for the plastic strain rate, and k is the Boltzmann constant. According to experimental data [17], in neutron-irradiated copper, we have $\alpha_{0i} = 0.05$, $\alpha_{i0} = 1$, $T_i \approx 10^3$ K, and $q = 1/2$. In this case, from Eq. (5) at 293 K, we obtain $\alpha_i = 0.26$, which is close to the experimental value given in [12].

3. STRAIN DEPENDENCE OF THE RADIATION-DEFECT DENSITY

The formation of defectless channels at the initial stage of deformation of an irradiated metal and the high local shear strains due to these channels indicate the channeling of a large number of dislocations along the corresponding slip planes. Indeed, if we assume that all radiation defects in the form of prismatic Frank loops or stacking-fault tetrahedra transform into mobile dislocations as a result of interaction and reaction with glide dislocations, then the initial density of these defects in the material is $\rho_{i0} = \pi dN$. For example, for copper at d = 2 nm and $N = 10^{16}$–10^{18} cm^{-3} [11], we obtain $\rho_{i0} \approx 6 \times (10^9$–$10^{11})$ cm^{-2}. This dislocation density is characteristic of large plastic strains and late (third, fourth, etc.) stages of the stress–strain curve, where the processes of dynamic recovery and annihilation of screw dislocations develop in a dislocation ensemble at temperatures $T < 0.3T_m$.

The transformation of prismatic loops into mobile dislocations and the formation of defectless channels occur nonuniformly throughout the crystal. According to [5, 6], these processes are described by the following kinetic equation for the density of radiation-induced dislocations ρ_i:

$$\frac{\partial\rho_i}{\partial t} + u_x\frac{\partial\rho_i}{\partial x} + D_y\frac{\partial^2\rho_i}{\partial y^2} = nu + (1-\beta_{im})\frac{u}{\lambda_m}\rho_i - h_a u\rho_i^2. \qquad (6)$$

Here, $\rho_i = \rho_i(x, y, t)$ is the density of mobile dislocations in the crystal (in a grain of a polycrystal) at the instant t; u_x is the dislocation velocity along the x axis in a slip plane; $D_y > 0$ is the diffusion coefficient of dislocations along the y axis, which is transverse to the plane of dislocation motion with allowance for the inversion of the sign of the dislocation flux due to strain hardening [18]; $n = n(\rho_{i0})$ is the volume density of the dislocation sources that appear as a result of the transformation of Frank loops and stacking-fault tetrahedra into glide dislocations; β_{im} is the coefficient of immobilization of dislocations at obstacles not associated with deformation; λ_m is the mean free path of dislocations between these obstacles; h_a is the characteristic annihilation distance of the screw segments of dislocation loops; and u is the average dislocation velocity in the crystal.

Equation (6) describes both the dislocation annihilation front motion along an individual channel [6] and the formation of new channels as the Lüders front moves in the crystal in the direction transverse to the plane of dislocation motion. In the case of a polycrystalline sample, the y axis, along which the Lüders front moves, coincides with the sample axis. In this case, the diffusion coefficient D_y of dislocations has the meaning of the diffusion coefficient averaged over all grains. Unfortunately, Eq. (6) cannot be solved in the general case. In [5], we could only find the solution to this equation in the steady-state case, where the motion of the Lüders front ceased and a system of defectless channels with a width $\Delta\Lambda$ and a spacing Λ between them formed.

Obviously, the disappearance of part of the radiation defects as a result of the formation of channels with a high local plastic shear in them should cause a decrease in the flow stress and the occurrence of a yield drop. When the Lüders front moves in a sample, this disappearance should result in a yield plateau in the stress–strain curve of an irradiated material, which is observed experimentally (Fig. 1). To demonstrate this behavior theoretically, we consider the solution to Eq. (6) in the uniform approximation. To this end, we drop the second and third terms in the left-hand side of Eq. (6) and take into account that $\partial\rho_i/\partial t = (\partial\rho_i/\partial\gamma_i)\dot{\gamma}_i$, where $\dot{\gamma}_i = b\rho_i u$ is the local plastic strain rate in a channel. As a result, we obtain the following equation for the radiation-induced dislocation density ρ_i as a function of strain:

$$\rho_i \frac{\partial \rho_i}{\partial \gamma_i} = \frac{n}{b} + (1 - \beta_{im}) k_m \rho_i - k_a \rho_i^2, \tag{7a}$$

where $k_m = 1/b\lambda_m$ and $k_a = h_a/b$ is the dislocation annihilation coefficient. The estimates made in [5] show that, in pure metals, the second term in the right-hand side of Eq. (7a) can be neglected as compared to the other two.[1] In this case, we obtain

$$\rho_i \frac{d\rho_i}{\partial \gamma_i} = \frac{n}{b} - k_a \rho_i^2. \tag{7b}$$

By integrating this equation under the initial condition $\rho_i(0) = \rho_{i0}$, we find the dependence of the radiation-dislocation density on the local strain γ_i,

$$\rho_i = \rho_{i0}[\eta_i + (1 - \eta_i)\exp(-2k_a \gamma_i)]^{1/2}, \tag{8}$$

where $\eta_i = n/bk_a\rho_{i0}^2$. The volume density of the dislocation sources is equal to $n = \delta_0 l_i^{-3}$, where $l_i = \rho_{i0}^{-1/2}$ is the average length of the dislocation segments that form Frank–Read dislocation sources and $\delta_0 < 1$ is the relative fraction of effective sources. Thus, we find that $\eta_i = \delta_0/bk_a\rho_{i0}^{1/2}$.

Taking into account Eq. (3), we obtain the following dependence of the parameter η_i on the irradiation dose:

$$\eta_i(\phi) = \eta_{im}\left[1 - \exp\left(-\left(\frac{\phi}{\phi_0}\right)^{2/3}\right)\right]^{-1/2},$$
$$\eta_{im} = \frac{\delta_0}{bk_a(dN_m)^{1/2}}. \tag{9}$$

For copper at $\delta_0 = 1.4 \times 10^{-2}$ [5], $T = 293$ K, $k_a = 3.5$ [18], and the values of d, N_m, and ϕ_0 given above, we have $\eta_{im} = 0.24$. Thus, it follows from Eq. (9) that $\eta_i = \eta_{im} < 1$ at high irradiation doses and $\eta_i \sim \phi^{-1/3} > 1$ at low irradiation doses ($\phi \ll \phi_0$). Figure 3 shows the variation in the radiation-dislocation density ρ_i with the local strain γ_i with respect to the initial value of ρ_{i0} plotted according to Eq. (8) at different values of the parameter η_i. It can be seen that the dislocation density increases with the local strain at low doses, where $\eta_i > 1$ (curve *1*), and decreases at high doses, where $\eta_i < 1$ (curve *2*). In the latter case, dislocation annihilation dominates over dislocation generation from dislocation sources. At $\eta_i = 1$, these two processes are balanced and the dislocation density remains unchanged (Fig. 3, dashed line). The criterion $\eta_i < 1$ for the dominance of dislocation annihilation over dislocation generation from dislocation sources coincides with the criterion for the appearance of defectless channels in irradiated metals [5].

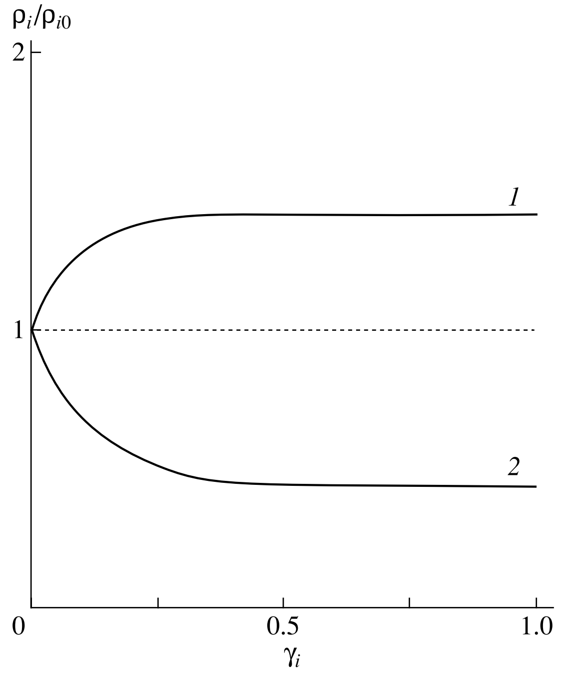

Fig. 3. Dependence of the relative change in the radiation-induced dislocation density on the local strain γ_i plotted according to Eq. (8) at $k_a = 5$ and for various values of the parameter η_i: (*1*) 2, (*2*) 0.2, and (dotted line) 1.

Since the density of radiation-induced defects in the form of prismatic Frank loops and the radiation-induced dislocation density are connected by the relation $\rho_i = \pi dN$, we substitute this relation into Eq. (7b) and obtain the following kinetic equation for the radiation-defect density:

$$N\frac{dN}{d\gamma_i} = \frac{n}{\pi^2 bd^2} - k_a N^2. \tag{10}$$

The solution $N(\gamma_i, \phi)$ to Eq. (10) is similar to Eq. (8) and describes the density of the initial radiation defects in an irradiated material as a function of plastic strain. An equation for the radiation-defect density of the same type as Eq. (10) for the particular case of $n = 0$ was analyzed earlier in [19].

4. YIELD DROP AND YIELD PLATEAU

It follows from Eqs. (1), (8), and (9) that a decrease in the radiation-defect density due to the formation of defectless channels causes the flow stress to decrease according to the expression

$$\tau_i(\gamma_i, \phi) = \alpha_i' \mu b \rho_i^{1/2}(\gamma_i, \phi), \tag{11}$$

where $\alpha_i' = \pi^{-1/2}\alpha_i$, since $\rho_i = \pi dN$. By making allowance for the fact that the strain of the material upon the

---

[1] This term, however, has a substantial effect on the formation of defectless channels in alloys with a sufficiently high volume fraction of precipitates or other disperse particles. This problem requires separate discussion.

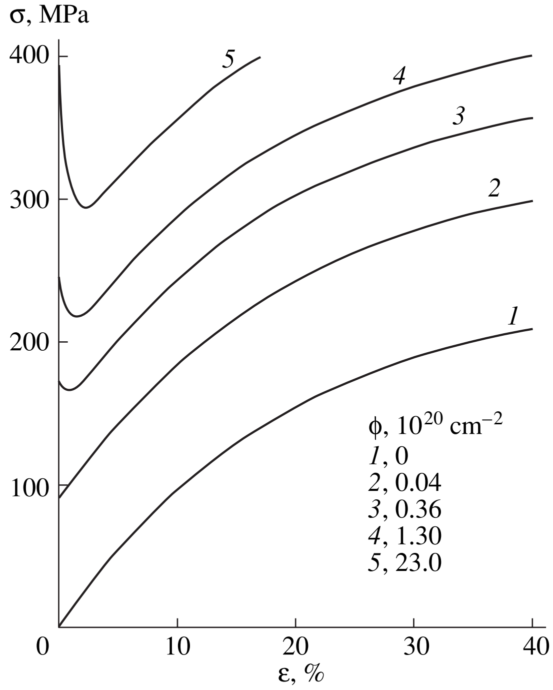

Fig. 4. Stress–strain curves calculated from Eq. (15) for copper irradiated by neutrons to different doses ϕ.

formation of channels is $\varepsilon = f_i\gamma_i/m$ (where $f_i = \Delta\Lambda/\Lambda$ is the relative fraction of the material occupied by the channels), we can obtain the following dependence of the stress $\sigma_i = m\tau_i$ on the plastic strain and irradiation dose for a polycrystalline material:

$$\sigma_i(\varepsilon, \phi) = \sigma_{i0}(\phi)[\eta_i(\phi) + (1 - \eta_i(\phi)) \times \exp(-2mf_i^{-1}k_a\varepsilon)]^{1/4}, \tag{12a}$$

$$\sigma_{i0}(\phi) = m\alpha_i'\mu b\rho_{i0}^{1/2}(\phi). \tag{12b}$$

In the absence of radiation defects and other structural defects, the kinetic equation for the dislocation density ρ_d under conditions of multiple slip has the form [18, 20]

$$\frac{d\rho_d}{d\gamma} = k_f\rho_d^{1/2} - k_a\rho_d, \tag{13}$$

where k_f is a coefficient that specifies the intensity of dislocation multiplication at forest dislocations. By integrating Eq. (13) and taking into account that the flow stress in this case is determined by the relation $\sigma_d = m\alpha\mu b\rho_d^{1/2}$, we obtain the strain-hardening curve for an unirradiated material:

$$\sigma_d(\varepsilon) = \sigma_3\left[1 - \exp\left(-\frac{1}{2}mk_a\varepsilon\right)\right], \quad \sigma_3 = m\alpha\mu b\rho_3^{1/2}, \quad \rho_3 = (k_f/k_a)^2, \tag{14}$$

where σ_3 is the flow stress at the end of the third stage of the stress–strain curve (the stage of dynamic recovery), ρ_3 is the dislocation density at the end of this stage, and α is the dislocation interaction constant for multiple slip. Thus, with allowance for Eqs. (12) for the stress, which specifies the radiation-induced hardening of the material, the full flow stress of the material is

$$\sigma(\varepsilon, \phi) = \sigma_i(\varepsilon, \phi) + \sigma_d(\varepsilon). \tag{15}$$

Equation (15) implies linear summation of the stresses upon radiation hardening and strain hardening of the material. Quadratic summation of these stresses is also possible. However, an analysis shows that, in our case, linear summation fits experiment better.

Figure 4 shows the strain-hardening curves of copper irradiated at various neutron doses and calculated from Eqs. (12)–(15). The doses given in Fig. 4 are the same as those in Fig. 1. When calculating the stress σ_i, we assumed that $f_i = 0.1$ [5], $k_a = 3.4$, and $m = 3$. In calculating the stress σ_d, we assumed that $\alpha = 0.5$, $bk_f = 1.1 \times 10^{-2}$, $b = 0.256$ nm, and $\mu = 48.5$ GPa. The values of the other parameters were given above. Although we failed to achieve complete quantitative agreement between the strain-hardening curves shown in Figs. 1 and 4, there is, in general, reasonable agreement between theory and experiment. As can be seen from Fig. 4, a yield drop appears in strain-hardening curves *3*–*5*, just as in the corresponding curves in Fig. 1, at irradiation doses higher than 10^{19} cm^{-2}; this drop is caused by the appearance of a large number of mobile dislocations during channel formation. Since new channels form as a result of the motion of the Lüders front, the yield drop in the σ–ε curves in Fig. 1 is followed by a yield plateau and the corresponding stress (the lower yield stress σ_L).

To find the length of the yield plateau (the Lüders strain ε_L) and the stress σ_L, we use the equal-area rule. As an example, let us consider the dashed line in Fig. 5, which corresponds to curve *5* in Fig. 4. The letters *b* and *c* designate the points of intersection of straight line *ac* with the σ(ε) curve at the level of the lower yield strength. The equal-area rule means equality of the areas between this curve and straight line *ac* above and below it. This rule can be written as

$$\int_0^{\varepsilon_b}[\sigma(\varepsilon, \phi) - \sigma_L(\phi)]d\varepsilon = -\int_{\varepsilon_b}^{\varepsilon_c}[\sigma(\varepsilon, \phi) - \sigma_L(\phi)]d\varepsilon \tag{16a}$$

or, after certain manipulations,

$$\int_0^{\varepsilon_c}\sigma(\varepsilon, \phi)d\varepsilon = \sigma_L\varepsilon_c, \tag{16b}$$

where ε_b and ε_c are the strains corresponding to points *b* and *c* in Fig. 5. Another condition for the determination of the strains ε_b and ε_c is also the condition specifying both the lower yield strength

$$\sigma_L(\phi) = \sigma(\varepsilon_b, \phi) = \sigma(\varepsilon_c, \phi), \tag{17}$$

and the Lüders strain $\varepsilon_L(\phi) = \varepsilon_c(\phi)$. The set of equations (16) and (17) for the strains ε_b and ε_c was solved numerically for each value of the irradiation dose ϕ. Figure 6 shows the dependence of the strain ε_L on the irradiation dose obtained by solving these equations and the experimental $\varepsilon_L(\phi)$ dependence for copper derived from the data in Fig. 1. A yield plateau is seen to form at irradiation doses above 10^{19} cm^{-2}, where the effect of dislocation channeling appears in the material.

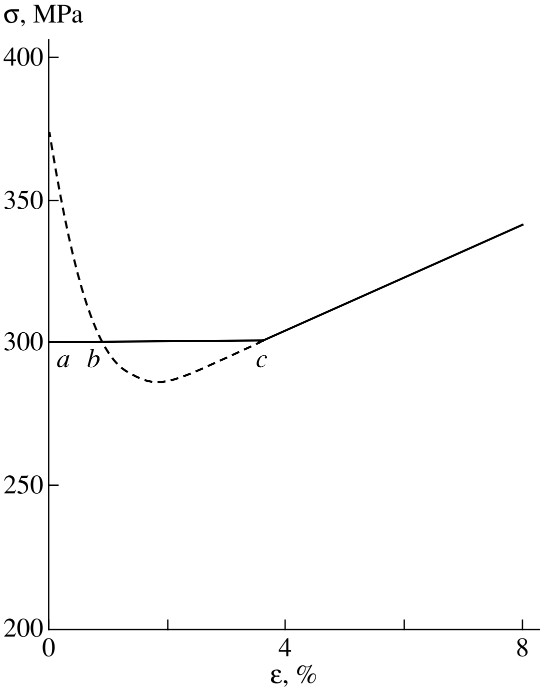

Fig. 5. Schematic diagram for the determination of the Lüders strain and the lower yield strength (see text).

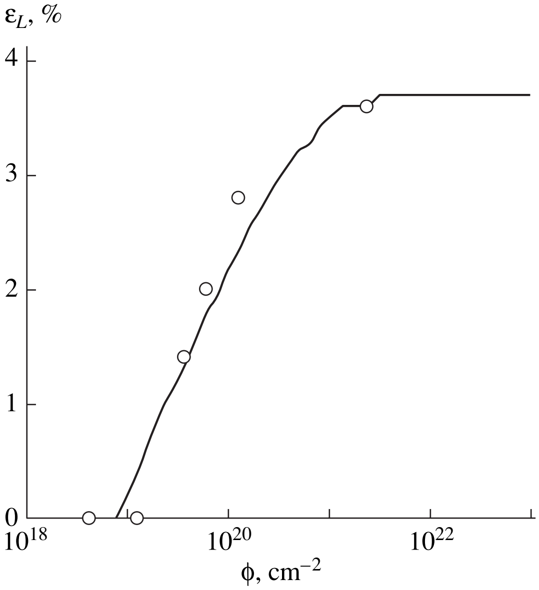

Fig. 6. Dependence of the yield-plateau length ε_L in copper on the irradiation dose ϕ constructed according to Eqs. (16) and (17). Experimental points correspond to the data in Fig. 1.

5. UNIFORM STRAIN

One more phenomenon related to irradiation is the strong decrease in the uniform strain ε_u when a radiation-hardened material is under tension. The uniform straining lasts until the appearance of plastic instability in the form of a “neck,” which results in fracture of a material via plastic shearing (Fig. 1). The appearance of this instability is determined by the well-known Considére criterion $d\sigma/d\varepsilon \le \sigma$. According to this criterion, deformation loses its stability when the strain-hardening coefficient $d\sigma/d\varepsilon$ becomes lower than the flow stress σ. It is obvious from Eq. (15) that the higher the stress of radiation-induced hardening $\sigma_i(\phi)$, the lower the strain ε_u at which this criterion begins to be satisfied. Equations (12)–(15) allow us to obtain the theoretical dependences of the uniform strain ε_u and the corresponding flow stress σ_u (ultimate tensile strength) on the stress $\sigma_i(\phi)$ and, hence, on the irradiation dose.

It is seen in Fig. 1 that deformation loses its stability in the irradiated copper at strains exceeding the Lüders strain ($\varepsilon_u > \varepsilon_L$). At these strains, it follows from Eq. (12a) that the stress of radiation hardening is $\sigma_i(\phi) = \eta_i^{1/4}\sigma_{i0}(\phi)$. This stress is strain-independent and, hence, does not contribute to the left-hand side of the Considére condition. After substituting Eq. (15) into this condition and taking into account Eq. (14), we find that

$$\varepsilon_u = \frac{2}{mk_a}\ln\frac{1+\frac{1}{2}mk_a}{1+\xi\frac{\sigma_i(\phi)}{\sigma_3}}, \tag{18a}$$

$$\sigma_u = \frac{\frac{1}{2}mk_a}{1+\frac{1}{2}mk_a}(\sigma_i(\phi)+\sigma_3), \tag{18b}$$

where ξ is a certain correction factor. Figure 7 illustrates the theoretical dependence of the strain ε_u on the irradiation dose (curve *1*) obtained according to Eq. (18a) at $\xi = 2$. The experimental points (circles) in Fig. 7 demonstrate the variation in the uniform strain in copper irradiated to different doses (Fig. 1). The irradiation to a dose of 2.3×10^{21} cm^{-2} is seen to decrease the uniform strain to necking by a factor of more than 2.

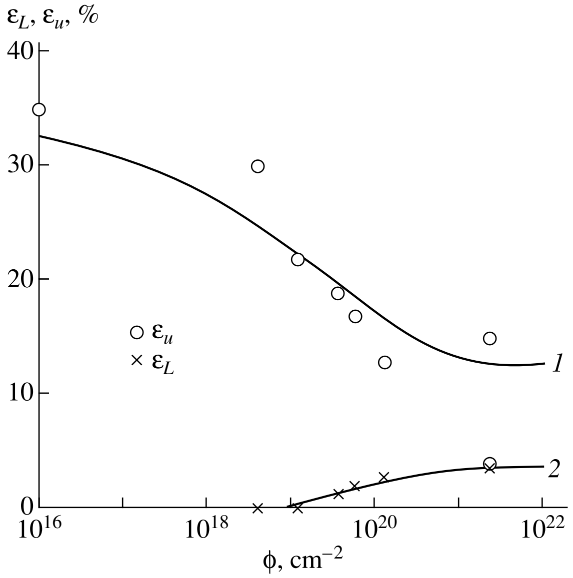

Fig. 7. Dependences of the uniform strain ε_u and the Lüders strain ε_L in copper on the irradiation dose corresponding to the data from Fig. 1. Theoretical curves: (*1*) calculated from Eq. (18a) and (*2*) obtained by solving Eqs. (16) and (17).

This decrease will be even more pronounced if the beginning of necking is taken to be the first decrease in the stress in curve *7* in Fig. 1 immediately after the end of the yield plateau. The corresponding strain (4%) is also shown in Fig. 7. For comparison, Fig. 7 also shows the dependence of the Lüders strain on the irradiation dose (Fig. 6). It is seen that, at high doses, ε_u and ε_L approach each other, which indicates a significant loss and the absence of a plasticity margin in the radiation-hardened metal. A similar result was obtained in [21] for neutron-irradiated nickel. Since the appearance of a yield plateau and the Lüders strain is related to the formation of defectless channels, the authors of [21] considered this strain to be the critical strain required for the appearance of these channels at a given irradiation dose. It should be noted that, at high irradiation doses, the theoretical $\varepsilon_u(\phi)$ dependence for copper (Fig. 7, curve *1*) deviates strongly from the experimental dependence at a dose of 2.3×10^{21} cm^{-2} if the strain ε_u is taken to be the Lüders strain. This discrepancy is likely caused by the fact that, at high irradiation doses, the law of quadratic summation of the radiation hardening and the strain hardening fits experiment better than does the linear law.

In conclusion, we would like to note that the approach to analyzing the effect of radiation on deformation stability and the plasticity of radiation-hardened materials that is based on the dislocation kinetics equations makes it possible, first, to adequately describe the character and specific features of the strain-hardening curves of these materials and, second, to find a quantitative relationship between these features and the irradiation dose.

REFERENCES

1. L. I. Ivanov and Yu. M. Platov, *Radiation Physics of Metals and Its Applications* (Nauka, Moscow, 2002) [in Russian].
2. H. Neuhäuser, in *Dislocation in Solids*, Ed. by F. R. N. Nabarro (North-Holland, Amsterdam, 1983), Vol. 6, p. 319.
3. L. V. Sharp, Radiat. Eff. **14** (1), 71 (1972).
4. Z. Yao, R. Schaublin, and M. Victoria, J. Nucl. Mater. **307/311**, 374 (2002).
5. G. A. Malygin, Fiz. Tverd. Tela (Leningrad) **33** (4), 1069 (1991) [Sov. Phys. Solid State **33**, 606 (1991)].
6. G. A. Malygin, Fiz. Tverd. Tela (Leningrad) **33** (6), 1855 (1991) [Sov. Phys. Solid State **33**, 1042 (1991)].
7. G. A. Malygin, Fiz. Tverd. Tela (St. Petersburg) **47** (2), 236 (2005) [Phys. Solid State **47**, 246 (2005)].
8. G. A. Malygin, Fiz. Tverd. Tela (St. Petersburg) **47** (5) (2005) (in press).
9. M. J. Makin, *Radiation Effects* (Gordon and Breach, New York, 1967), p. 627.
10. M. J. Makin, A. D. Whampham, and F. J. Minter, Philos. Mag. **7** (74), 285 (1962).
11. M. Victoria, N. Baluc, C. Bailat, Y. Dai, M. I. Luppo, R. Schaublin, and B. N. Singh, J. Nucl. Mater. **276**, 114 (2000).
12. S. Kojiama, S. J. Zinkle, and H. L. Heinish, J. Nucl. Mater. **179/181**, 982 (1991).
13. G. R. Odetta and G. E. Lucas, J. Nucl. Mater. **179/181**, 572 (1991).
14. M. J. Makin and F. J. Minter, Acta Metall. **8** (10), 691 (1960).
15. T. A. Blewitt, R. R. Coltman, and R. E. Jamisson, J. Nucl. Mater. **2** (4), 277 (1960).
16. F. W. Young, J. Phys. Soc. Jpn. **17** (Suppl. 1), 1 (1963).
17. T. J. Koppenaal and R. J. Arsenault, Philos. Mag. **12** (119), 951 (1965).
18. G. A. Malygin, Usp. Fiz. Nauk **169** (9), 979 (1999) [Phys. Usp. **42**, 887 (1999)].
19. C. Pokor, X. Averty, Y. Brechet, P. Dubusson, and J. P. Massoud, Scr. Mater. **50** (5), 597 (2004).
20. U. F. Kocks, A. S. Argon, and M. F. Ashby, *Thermodynamics and Kinetics of Slip* (Pergamon, New York, 1975).
21. A. Okada, K. Kanao, T. Y. Yoshii, *et al.*, Trans. Jpn. Inst. Met. **30** (4), 265 (1989).

Translated by K. Shakhlevich

Physics of the Solid State, Vol. 47, No. 4, 2005, pp. 663–669. Translated from Fizika Tverdogo Tela, Vol. 47, No. 4, 2005, pp. 639–645.
Original Russian Text Copyright © 2005 by Razorenov, Savinykh, Zaretsky, Kanel, Kolobov.

DEFECTS, DISLOCATIONS, AND PHYSICS OF STRENGTH

Effect of Preliminary Strain Hardening on the Flow Stress of Titanium and a Titanium Alloy during Shock Compression

S. V. Razorenov*, A. S. Savinykh*, E. B. Zaretsky, G. I. Kanel***, and Yu. R. Kolobov******
** Institute of Problems of Chemical Physics, Russian Academy of Sciences,*
Institutskiĭ pr. 18, Chernogolovka, Moscow oblast, 142432 Russia
e-mail: razsv@ficp.ac.ru
*** Ben-Gurion University of the Negev, Beer-Sheva, 84105 Israel*
**** Institute for High Energy Densities, Associated Institute for High Temperatures, Russian Academy of Sciences,*
ul. Izhorskaya 13/19, Moscow, 125412 Russia
e-mail: kanel@ficp.ac.ru
***** Institute of Strength Physics and Materials Science, Siberian Division, Russian Academy of Sciences,*
Akademicheskiĭ pr. 2/1, Tomsk, 634021 Russia

Received April 20, 2004; in final form, July 7, 2004

Abstract—The effect of preliminary strain hardening of VT1-0 titanium and a Ti–6 wt % Al–4 wt % V alloy on their mechanical properties under quasi-static and high-rate (>10^5 s^{-1}) loading is studied. Preliminary hardening is accomplished using equal-channel angular pressing (which results in a significant decrease in the grain size and a twofold increase in the quasi-static yield strength) and shock waves. High-rate deformation is attained via shock-wave loading of samples. The experimental results show that structural defects weaken the dependence of the yield strength on the strain rate. The difference in the rate dependences can be so high that the effect of these defects on the flow stress can change sign when going from quasi-static to high-rate loading.

1. INTRODUCTION

The physical mechanisms of plastic deformation of crystalline bodies are known to be based on dislocation motion. Dislocation motion is hindered by different types of structural inhomogeneities (dislocation pile-ups, grain boundaries, inclusions, etc.). The relative contributions of different-level defects to the hardening of a material can be revealed experimentally by varying the strain rate. The point is that the flow stress of crystalline solids increases with the loading rate. At a sufficiently high strain rate, the operating stresses become so high that dislocations can overcome some obstacles that are insurmountable under conditions of low-rate deformation.

In other words, not all of the structural factors that exert a hardening effect at low strain rates can be effective under conditions of high-rate deformation. In this work, we compare the effects exerted on the quasi-static-deformation resistance of titanium and a titanium alloy by defects that appear during preliminary severe plastic deformation or during a shock-wave compression.

The mechanical properties of materials at a strain rate above 10^4 s^{-1} are studied upon shock-wave loading of samples. The use of shock waves makes it possible to effectively investigate the properties of materials at extremely high strain rates under controlled conditions of loading. Shock waves are known to harden a material due to intense dislocation multiplication [1], which occurs even at low total strains. Severe deformation causes grain refinement, which results in an increase in the yield strength (Hall–Petch effect). These two methods of mechanical treatment are effective for increasing the quasi-static strength of metals and alloys. However, their effects on the strength properties under high-rate deformation have not been studied yet.

2. EXPERIMENTAL

Shock-wave experiments were performed on samples 2–6 mm thick, in which plane compression waves were excited by impact with a flyer plate. Flyer plates made of aluminum, titanium, or copper 0.4–2.0 mm thick were launched at velocities of 0.1–1.25 km/s with explosive devices [2] and light-gas gun-barrel devices [3]. In the experiments, we recorded the velocity profiles of the free back surfaces of the samples with VISAR laser Doppler interferometric velocimeters [4]. The frequency bandwidth of the signal path was no less than 0–350 MHz. The output signals of the velocimeters were recorded with digital oscilloscopes, and the time intervals between measurement points were 0.4 or 2.0 ns.

Samples were made of commercial-purity (type-1) titanium containing the following impurities (wt %): 0.15 O; 0.10 Fe; 0.018 Cr; 0.015 Ni; 0.026 C; less than 0.02 Al; and less than 0.01 Cu, Zr, V, and Mn. The sam-

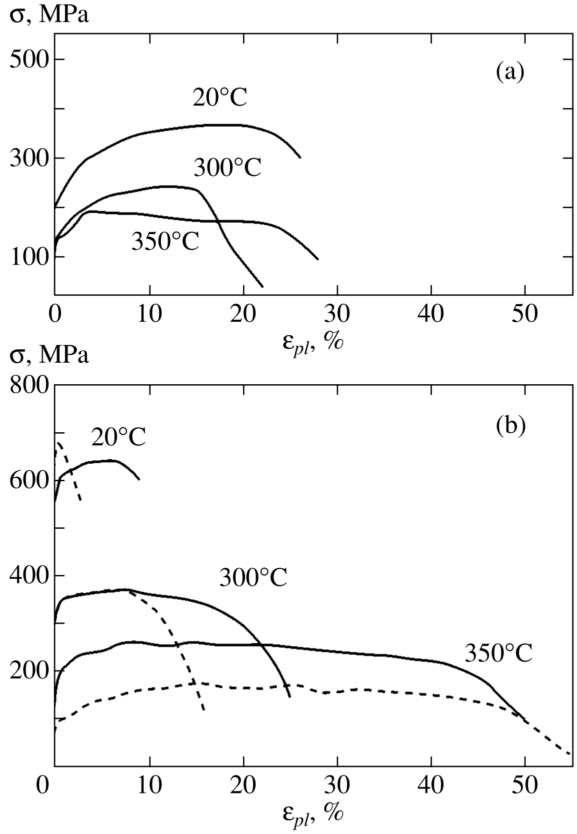

Fig. 1. Stress–strain diagrams of (a) the coarse-grained and (b) submicrocrystalline titanium in the longitudinal (solid lines) and transverse directions (dashed lines) with respect to the ECAP axis plotted at 20, 300, and 350°C. The strain rate is 3×10^{-5} s^{-1}.

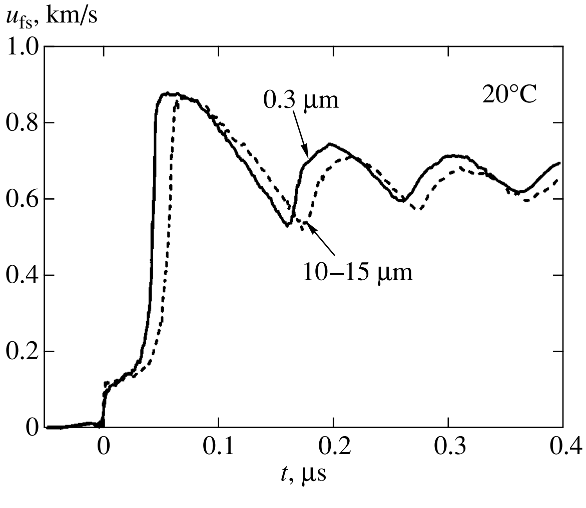

Fig. 2. Free surface velocity history of a 2.23-mm-thick VT1-0 titanium plate and 2.02-mm-thick submicrocrystalline titanium at room temperature. Impact with an aluminum plate 0.4-mm thick at a velocity of 1250 ± 50 m/s.

ples were cut off from a 4.98-mm-thick sheet. We also studied rod-shaped samples made from VT1-0 titanium containing 0.12 O, 0.18 Fe, 0.10 Si, 0.07 C, 0.010 H, and 0.04 N or from a Ti–6 wt % Al–4 wt % V alloy (hereafter, the Ti–6Al–4V alloy) containing 5.62 Al, 4.1 V, 0.2 O, 0.05 N, 0.08 C, 0.05 Fe, and 0.013 H. The density and longitudinal and transverse (normal to the loading direction) velocities of sound for the type-1 titanium were measured to be ρ = 4.53 g/cm^3, c_l = 6.195 km/s, and c_s = 3.26 km/s, respectively; the corresponding values for the Ti–6Al–4V alloy were ρ = 4.41 g/cm^3, c_l = 6.153 km/s, and c_s = 3.149 km/s. The VT1-0 titanium was tested in two states: in the initial state with a grain size of 10–15 μm and in a submicrocrystalline state. The grain size was decreased to a submicron level via severe plastic deformation by equal-channel angular pressing (ECAP); more specifically, a billet was repeatedly extruded through two channels having the same cross section and intersecting at an angle of 90° in an instrument designed specially for this purpose [5]. The grain size in the VT1-0 titanium subjected to ECAP was 0.3 μm, and grains as large as 1 μm were also present. However, large grains were divided predominantly into 0.3-μm fragments having low-angle boundaries with misorientations less than 5°. After ECAP, the longitudinal sound velocity remained virtually unchanged (5.87 ± 0.05 km/s).

Figure 1 shows diagrams of low-rate deformation of the coarse-grained and submicrocrystalline titanium at various temperatures. Severe plastic deformation is seen to increase the strength of the material by more than twofold. The high yield strength is retained upon heating to 300°C; a further increase in the temperature leads to recrystallization and a loss of the hardening effect of ECAP.

We compared the behaviors of the sheet titanium and the Ti–6Al–4V alloy in their initial state after the action of a shock wave slightly above the dynamic elastic limit. The shock-wave hardening of the materials was determined by measuring their hardness.

3. EXPERIMENTAL RESULTS

Figures 2 and 3 show the free surface velocity history $u_{fs}(t)$ of the VT1-0 titanium with a fine- or coarse-grained structure at room temperature and elevated temperatures. The wave profiles clearly exhibit splitting of the shock wave into an elastic precursor and a plastic compression wave. The velocity jump at the precursor front is proportional to the dynamic yield strength of the material [2]. After the circulation of the shock wave, a rarefaction wave forms in the flyer plate and propagates into the sample after the shock wave. When the rarefaction wave reaches the sample surface, the surface velocity decreases. As a result of the reflection of the compression pulse from the free surface of the sample, tensile stresses are generated inside the sample. The fracture of the material (spall fracture) is accompanied by the disappearance of tension resistance and results in a compression wave, which reaches the surface in the form of a so-called spall pulse and again increases the surface velocity.

The longitudinal stress at the elastic-precursor front (the dynamic elastic limit) is

$$\sigma_{xe} = 0.5u_{\mathrm{fs}e}\rho_0 c_l,$$

where $u_{\mathrm{fs}e}$ is the velocity jump of the free surface in the precursor, ρ_0 is the initial material density, and c_l is the longitudinal sound velocity in the material. Compression stresses are taken to be positive. Unexpectedly, for the submicrocrystalline titanium at room temperature, the value of σ_{xe} behind the elastic-precursor front was found to be 1.4 GPa, which is somewhat lower than that for the initial material (σ_{xe} = 1.6 GPa).

For one-dimensional deformation, the elastic limit is connected with the conventional yield strength σ_Y by the relation [2]

$$\sigma_Y = \frac{3}{2}\sigma_{xe}(1 - c_b^2/c_l^2),$$

where $c_b = \sqrt{K/\rho}$ is the bulk sound velocity and K is the bulk modulus of elasticity. The value of c_b = 4.78 km/s for the titanium and the alloy was determined from their shock compressibilities measured with allowance for the possible effect of texture on the sound velocities. The values of the dynamic yield strength at room temperature thus found were σ_Y = 0.81 GPa for the VT1-0 titanium in the initial state and 0.71 GPa for the titanium subjected to ECAP. Thus, as the strain rate increases, the effect of the grain size on the yield strength of titanium decreases such that the hardening effect of severe plastic deformation virtually disappears. In our experiments, the average rate of shock-wave deformation (which was estimated as the degree of compression divided by the compression time) was calculated to be $\sim 4 \times 10^5$–10^6 s^{-1}.

With allowance for the temperature dependences of the elastic moduli (and, therefore, the sound velocities) [6], the stress at the precursor front is found to be 1.77 GPa for the VT1-0 titanium in the initial state at 600°C and 1.15 GPa for the submicrocrystalline titanium at 300°C. It is seen that the surface velocity at the elastic-precursor front for the VT1-0 titanium in the initial state increases upon heating. However, in our case, this effect is a consequence of the decreased shear modulus: the dynamic yield strength decreases with increasing temperature (0.76 GPa for the initial material at 600°C and 0.59 GPa for the submicrocrystalline titanium at 300°C). Thus, at a strain rate of above 10^5 s^{-1}, the softening effect of temperature on the flow stress greatly depends on the structure of the material.

The spall strength σ^* of a material is determined from the decrease in the velocity Δu_{fs} from its maximum value to the value ahead of a spall-pulse front using the formula [2, 7]

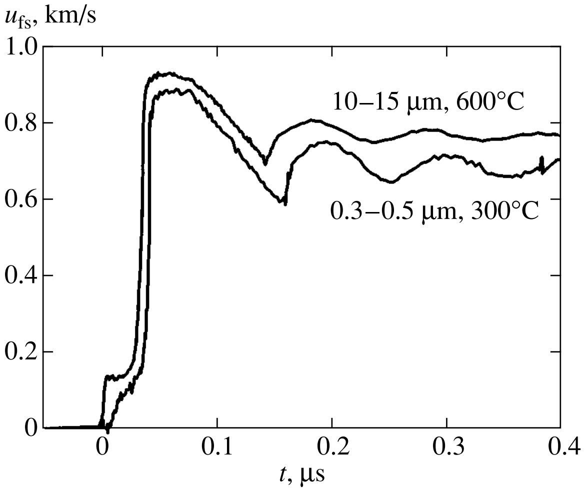

Fig. 3. Free surface velocity history of 2.02-mm-thick VT1-0 titanium plates in the initial and submicrocrystalline states at elevated temperatures.

$$\sigma^* = \frac{1}{2}\rho_0 c_b(\Delta u_{\mathrm{fs}} + \delta),$$

where δ is the correction for the distortion of the velocity profile caused by the difference between the velocity c_l of the spall-pulse front propagating in the tensioned material and the velocity c_b of the plastic portion of the incident unloading wave in front of this pulse [7, 8]. The spall strength of the titanium at room temperature increases insignificantly with decreasing grain size, namely, from 4.05 GPa in the initial state to 4.25 GPa after ECAP. The dynamic breaking strength of the material is likely to depend mainly on the presence of impurities in the material rather than on its granular structure.

Apart from information on the yield strength, the wave profiles also give information on the $\sigma(\varepsilon)$ dependence during compression and, hence, on the strain hardening of the material. The stress–strain diagram was plotted using the measured profile of an elastoplastic compression wave in terms of the simple centered-wave approximation [2]. For such a wave, which is described by a fan of straight-line characteristics, the increments in the longitudinal stress ($d\sigma$) and in the strain ($d\varepsilon_x = -dV/V_0$) are connected by the relation

$$d\sigma = \rho_0 a_\sigma^2 d\varepsilon_x,$$

where a_σ is the phase velocity of the portion of the wave with a compression stress σ in the Lagrangian coordinates. For one-dimensional deformation, the maximum shear stress τ in a shock wave is determined by the dif-

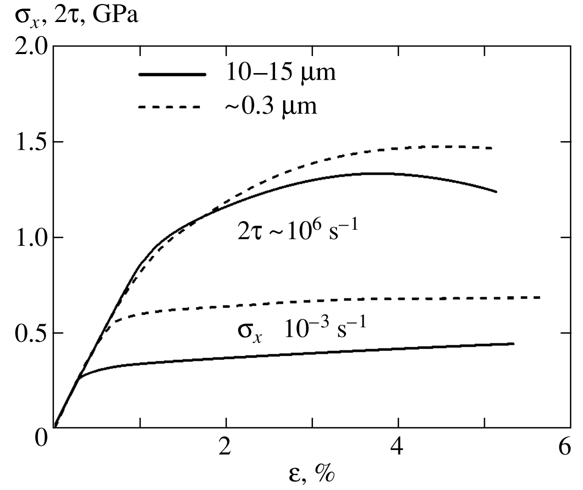

Fig. 4. Stress–strain diagrams for the VT1-0 titanium calculated from the measured free surface velocity history shown in Fig. 2 and measured using a standard procedure during quasi-static deformation.

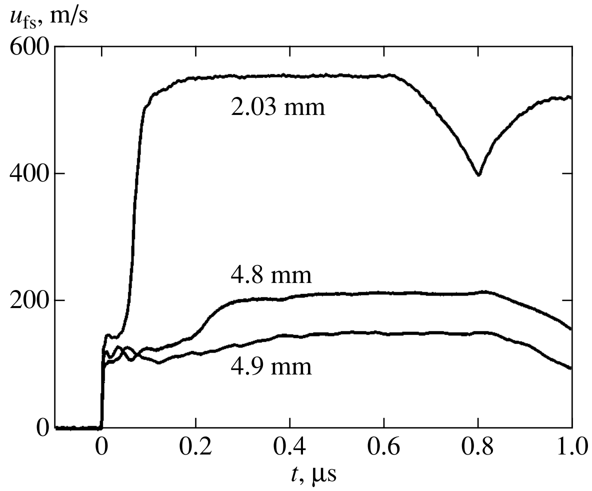

Fig. 5. Free surface velocity history determined from experimental data for sheet titanium samples of different thicknesses. Loading by impact with a 1.97-mm-thick titanium plate at a velocity of 550 m/s and with a 2-mm-thick copper plate at velocities of 191 and 132 m/s. The numerals on the curves are the sample thicknesses.

ference between the longitudinal stress σ and the pressure p:

$$\tau = \frac{3}{4}(\sigma - p).$$

For a simple centered wave, the phase velocity a_σ is defined as

$$a_\sigma = -\frac{h}{h/c_l + t(\sigma)},$$

where h is the distance between the impact surface (the pole of the fan of centered wave characteristics) and the section in the sample in which the $\sigma(t)$ profile is analyzed and t is the time counted off from the instant of the elastic-precursor front. In our case, instead of the $\sigma(t)$ profile, we analyzed the free-surface velocity profile $u_{\text{fs}}(t)$ using the empirical law of velocity doubling

$$u_{\text{fs}}(t) = 2u_p(t), \quad d\sigma(t) = \rho a_\sigma du_p(t).$$

A more detailed analysis with inclusion of the interaction between the incident and reflected waves near the sample surface gives the following expression for a_σ:

$$a_\sigma = c_l\frac{2h - c_l t(\sigma)}{2h + c_l t(\sigma)}.$$

The simple-wave approximation is inaccurate. The sources of error in it are related to the relaxation of deviator stresses, the assumption that the mass velocity and the free-surface velocity are interrelated, errors in the volume-compressibility data, and the specific features of the reflection of elastoplastic waves from the sample surface.

In Fig. 4, the calculated stress–strain diagrams of the VT1-0 titanium in the initial and submicrocrystalline states for shock compression are compared with the corresponding quasi-static stress–strain diagrams. The comparison shows that, although the grain refinement results in a small decrease in the dynamic yield strength, the strain hardening of the submicrocrystalline titanium is higher than that of the initial titanium. At a plastic strain of higher than 0.6%, the flow stress of the former material is higher than that of the initial titanium.

Figure 5 shows the velocity profiles of the free surface of sheet (type-1) titanium samples at various impact velocities. The dependence of the precursor amplitude on the distance traveled and on the shock-wave intensity, as well as the increase in the plastic-wave steepness with increasing maximum compression stress, is the consequence of the dependence of the flow stress on the strain rate. At low impact velocities, the wave profiles contain irregular oscillations, which indicate that the process of plastic deformation is substantially inhomogeneous. As shown in [3], the shock compression of this material is accompanied by intense twinning. We may assume that the stress oscillations are related to the development of individual twins, as is the case during low-rate deformation. As the shock-compression pressure increases, the wave profiles become more regular. According to the measurements, the compression stress σ_{xe} at the elastic-precursor front in the sheet titanium reaches as high as 1.8–2.1 GPa, which corresponds to a yield strength σ_y = 1.13–1.30 GPa.

Figure 6 shows the experimental results for the samples preliminarily subjected to shock waves. The hardness of the sheet titanium subjected to single shock loading is slightly higher in the central part of the sam-

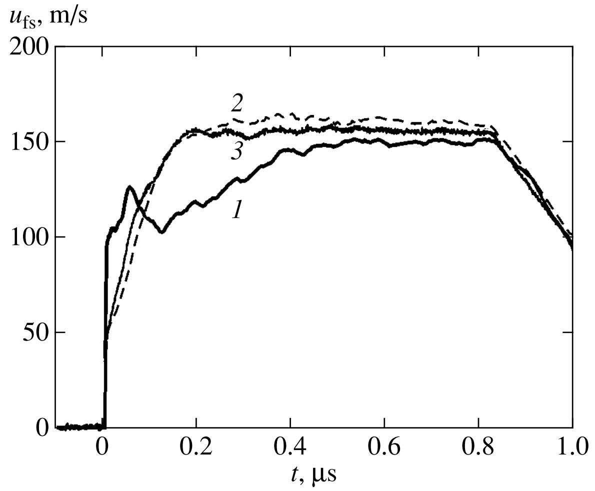

Fig. 6. Effect of preliminary exposure to a shock wave on the compression-wave profile in a 4.9-mm-thick sheet titanium sample: (*1*) the free surface velocity history for the initial material loaded by a 2-mm-thick copper plate at a velocity of 132 m/s, (*2*) the free surface velocity history for repeated shock loading at a velocity of 141.5 m/s, and (*3*) experimental results for the sample subjected to triple exposure to a shock wave at an impact velocity of 134 m/s.

ple (it increases from 2.05 ± 0.05 GPa in the initial state to 2.20 ± 0.05 GPa after loading). Upon repeated loading, however, σ_{xe} decreases more than twofold. The difference in sign between the effects of a shock wave on the resistance to quasi-static and high-rate deformation suggests that the main mechanisms of high-rate deformation and fracture and, correspondingly, the structural factors that determine the yield strength and the ultimate strength of the material need not be coincident with those in the case of low-rate deformation.

Figure 7 shows the shock-wave stress–strain curves calculated from the experimental data for the sheet titanium in the initial state and after exposure to a shock wave at an average compression rate of (3–6) × 10^4 s^{-1}. The shock wave is seen to change the initial segment of the stress–strain curve. The decrease in the elastic limit is related to the appearance of intense strain hardening.

Figure 8 shows the free surface velocity history of the Ti–6Al–4V alloy samples at various impact velocities. The compression stress behind the elastic-precursor front is 2.65 GPa and varies only slightly with the sample thickness and the maximum pressure of shock compression. Unlike titanium, the alloy exhibits no signs of inhomogeneous plastic deformation in the wave profiles.

Figure 9 shows the experimental results for the Ti–6Al–4V alloy samples preliminarily subjected to a shock wave. After the experiment represented by curve *1b*, the hardness of the material in the central part of the sample increased from ~3.05 GPa (in the initial material) to ~3.20–3.25 GPa. Nevertheless, just as in the previous case, the stress behind the front of the elastic compression wave decreased from 2.65 to 1.95 GPa, which corresponds to a decrease in the yield strength from 1.45 to 1.05 GPa. Virtually the same stress behind the precursor front was obtained in the experiment represented by curve *2a*, although, during the preliminary shock action, the compression stress exceeded the dynamic elastic limit only insignificantly.

Figure 10 shows the stress–strain diagrams for the alloy in the initial state and after exposure to a shock wave calculated from the experimental data obtained at a low-velocity shock. It is seen that, just as in the exper-

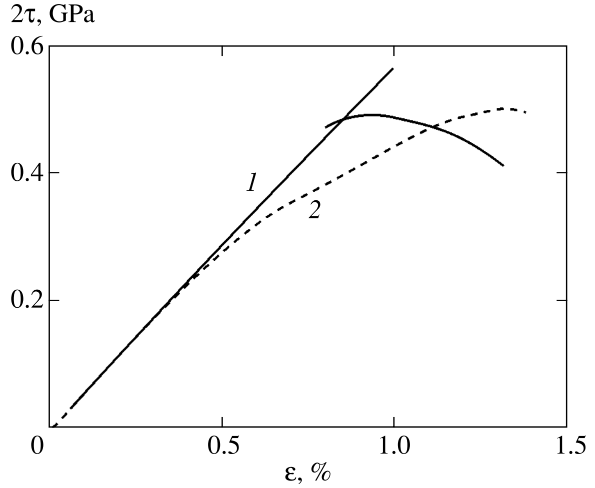

Fig. 7. Stress–strain diagrams for sheet titanium calculated in the simple-wave approximation from the measured velocity profiles of the free surface shown by curves *1* and *2* in Fig. 6.

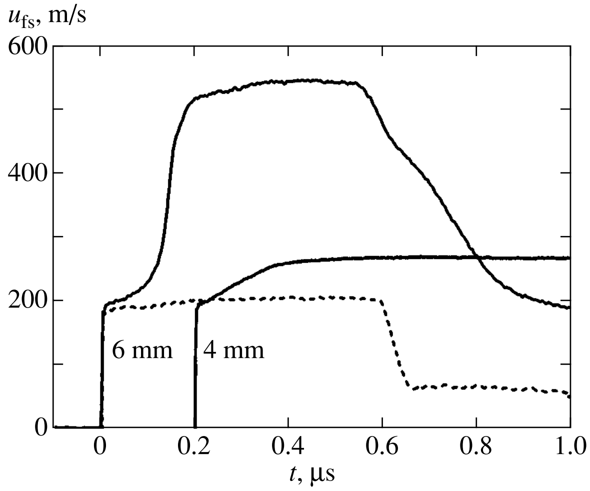

Fig. 8. Free surface velocity history of the Ti–6Al–4V alloy. Loading by impact with a 2-mm-thick titanium plate at velocities of 206 and 538 m/s (sample thickness, 6 mm) and with a 2-mm-thick copper plate at a velocity of 223 m/s (sample thickness, 4 mm).

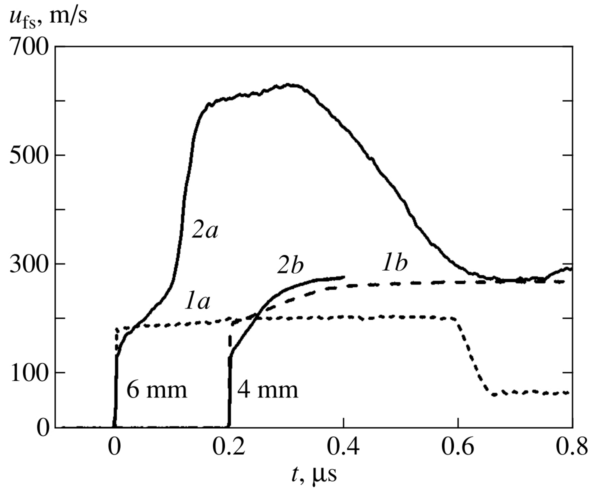

Fig. 9. Effect of preliminary exposure to a shock wave on the compression-wave profile in the Ti–6Al–4V alloy. Profiles *1a* and *1b* are plotted for the initial material, and profiles *2a* and *2b* correspond to repeated loading.

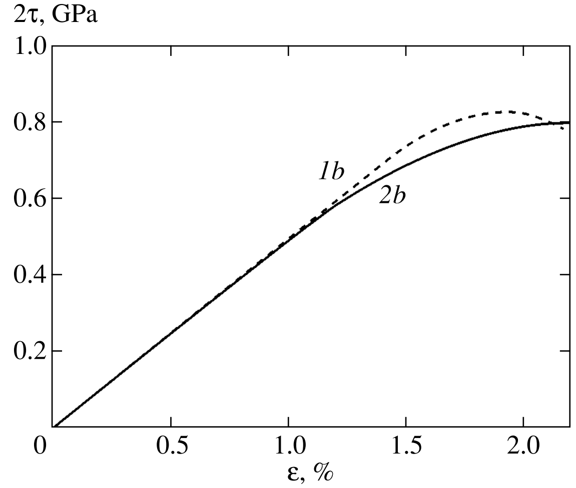

Fig. 10. Stress–strain diagrams for the Ti–6Al–4V alloy calculated in the simple-wave approximation from the measured free surface velocity history shown by curves *1b* and *2b* in Fig. 9.

iments with titanium, the decrease in the elastic limit of the alloy is related to the increased strain hardening. As a result, the flow stresses in the shock-compressed state in these two experiments are found to be virtually identical.

4. DISCUSSION OF THE RESULTS

The results of this experimental study unambiguously demonstrate an anomalous effect of hardening mechanical treatment on the resistance to high-rate deformation and fracture. Phenomenologically, the decrease in the dynamic elastic limit after exposure to a shock wave could be interpreted as a manifestation of the Bauschinger effect. According to this effect, a certain fraction of plastic deformation is reversible and does not contribute to the strain hardening [9]. This interpretation is supported by the fact that, despite the significantly decreased elastic limit, preliminary exposure to a shock wave does not affect the flow stress in the shock-compressed state of the titanium and titanium alloy. The manifestation of the Bauschinger effect is also indicated by numerous results obtained in recording full stress pulses [2]. These pulses show that the process of deformation during unloading after shock-induced compression deviates from an elastoplastic process toward low deviator stresses and that plastic deformation often begins immediately behind the unloading-wave front without a finite elastic region. The authors of [10] found that, when metals and alloys were loaded by two sequential shock-compression pulses, an elastic precursor with a finite amplitude was not detected in the second shock wave. However, the Bauschinger effect cannot explain why the mechanical treatment that increases the resistance to low-rate deformation can cause the reverse effect at high strain rates.

The experimental data obtained indicate that structural defects weaken the dependence of the yield strength on the strain rate. The change in the rate dependence can be so high that the effect of these defects on the flow stress can change sign when going from quasi-static to high-rate loading. The effect of high stresses is likely to change the relative contributions from thermal fluctuations, structural microdefects, grain boundaries, inclusions, and other inhomogeneities to the processes of plastic flow.

To interpret the experimental results obtained, we have to take into account that applied shear stresses induce not only dislocation motion but also dislocation generation and multiplication. Dislocations are generated near stress concentrators in the form of disturbances in long-range order. On the one hand, structural defects are hardening factors, but on the other, they are sources of plastic-deformation carriers (dislocations). In other words, the same defects can both increase the deformation resistance under quasi-static conditions and be sources of plastic-deformation carriers (dislocations) at high strain rates and high stresses, thus decreasing the resistance to plastic deformation.

It seems instructive to formalize the experimental results by classifying defects in terms of the stresses required to overcome them. Depending on the operating stress, one part of the defects is involved in the process of plastic deformation while the other part hinders deformation. In the course of plastic deformation, the parameters of the defect spectrum change. This approach is thought to provide more a detailed description of the properties of a material and to be more informative for studies at high strain rates.

ACKNOWLEDGMENTS

This work was supported by the program of basic research of the Presidium of the Russian Academy of Sciences "Thermal Physics and Mechanics of Intense Energy Actions" and the program of the Department of Energy, Mechanics, Science of Machines, and Control Problems of the Russian Academy of Sciences "Structural Mechanics of Materials and Construction Members: Interaction of Nano-, Micro-, Meso-, and Macroscales during Deformation and Fracture."

REFERENCES

1. G. N. Épshteĭn, *Structure of Metals Deformed by Explosion* (Metallurgiya, Moscow, 1980) [in Russian].
2. G. I. Kanel, S. V. Razorenov, A. V. Utkin, and V. E. Fortov, *Shock-Wave Phenomena in Condensed Media* (Yanus-K, Moscow, 1996) [in Russian].
3. B. Herrmann, A. Venkert, G. Kimmel, A. Landau, D. Shvarts, and E. Zaretsky, AIP Conf. Proc. **620**, 623 (2002).
4. J. R. Asay and L. M. Barker, J. Appl. Phys. **45** (6), 2540 (1974).
5. Yu. R. Kolobov, R. Z. Valiev, I. P. Grabovetskaya, A. P. Zhilyaev, E. F. Dudarev, K. V. Ivanov, M. B. Ivanov, O. A. Kashin, and E. V. Naĭdenkin, *Grain-Boundary Diffusion and Properties of Nanostructural Materials* (Nauka, Novosibirsk, 2001) [in Russian].
6. M. W. Guinan and D. J. Steinberg, J. Phys. Chem. Solids **35**, 1501 (1974).
7. T. Antoun, L. Seaman, D. R. Curran, G. I. Kanel, S. V. Razorenov, and A. V. Utkin, *Spall Fracture* (Springer, New York, 2003).
8. G. I. Kanel, Prikl. Mekh. Tekh. Fiz. **42** (2), 194 (2001).
9. F. A. McClintock and A. S. Argon, *Mechanical Behavior of Materials* (Addison-Wesley, Reading, Mass, 1966; Mir, Moscow, 1970).
10. G. I. Kanel, A. M. Molodets, and A. N. Dremin, Fiz. Met. Metalloved. **46** (1), 201 (1978).

Translated by K. Shakhlevich

Physics of the Solid State, Vol. 47, No. 4, 2005, pp. 670–673. Translated from Fizika Tverdogo Tela, Vol. 47, No. 4, 2005, pp. 646–649.
Original Russian Text Copyright © 2005 by Kobelev, Kolyvanov, Khonik.

Effect of Deformation and Heat Treatment on the Damping Constant and Shear Modulus of a Bulk Zr–Cu–Ni–Al–Ti Metallic Glass

N. P. Kobelev*, E. L. Kolyvanov*, and V. A. Khonik**
** Institute of Solid State Physics, Russian Academy of Sciences, Chernogolovka, Moscow oblast, 142432 Russia*
e-mail: kobelev@issp.ac.ru
*** Voronezh State Pedagogical University, ul. Lenina 86, Voronezh, 394043 Russia*

Received June 1, 2004; in final form, July 7, 2004

Abstract—The effect of deformation by rolling or quenching from temperatures close to the glass transition temperature on the damping constant and the shear modulus of preliminarily annealed bulk samples of a $Zr_{52.5}Ti_5Cu_{17.9}Ni_{14.6}Al_{10}$ metallic glass was studied. These treatments are found to result in recovery of the “irreversible” contributions to the damping constant and the shear modulus, and the deformation treatment is shown to lead to an increase in the amplitude-dependent internal friction. *© 2005 Pleiades Publishing, Inc.*

1. INTRODUCTION

Metallic glasses are in a nonequilibrium structural state; therefore, irreversible changes in their structure (so-called irreversible structural relaxation) can occur and substantially influence their physical properties. The processes of irreversible structural relaxation that take place at temperatures below the glass transition temperature T_g are still less well understood. However, study of these processes can yield important information on the character and nature of energy excitations in glasses above the glass transition temperature.

In [1–3], by using low-frequency internal friction, we studied the temperature and time dependences of the irreversible structural relaxation of a bulk $Zr_{52.5}Ti_5Cu_{17.9}Ni_{14.6}Al_{10}$ metallic glass. It was found that irreversible changes in the shear modulus and acoustic damping due to structural relaxation begin approximately 100 K below the glass transition temperature and terminate mainly at about T_g. Based on an analysis of the temperature, time, and frequency dependences of the damping constant and the shear modulus, we proposed a phenomenological model for these processes; this model implies the presence of relaxation centers that are like elastic dipoles with an asymmetric double-well energy potential. It was assumed that irreversible changes in the damping constant and the shear modulus are related to the relaxation of the nonequilibrium high-energy states of these centers, which are “frozen” due to quenching of the glass. We estimated the activation-energy spectrum of irreversible relaxation. The characteristic energies in this spectrum for the alloy in question (~2 eV) were found to be only slightly lower (by 0.2–0.3 eV) than the activation energies for reversible relaxation (whose parameters are reproduced during thermal cycling), which occurs at temperatures above the glass transition temperature [1, 2]. Therefore, we assumed that the reversible and irreversible portions of the relaxation spectrum are related to the same centers and that the process of reversible structural relaxation is caused by thermally activated transitions between their high- and low-energy states. In this case, at temperatures above T_g, the high-energy states of the relaxation centers should again be filled; when the alloy is rapidly quenched from these temperatures, one should expect partial recovery of the “irreversible” contributions to the damping constant and the shear modulus. One of the purposes of this work was to verify this assumption.

If we assume that, during irreversible relaxation, the centers that are involved in this process fail only incompletely and pass to their low-energy state, then the irreversible relaxation can be recovered by a high-energy action at room temperature. One type of such an action is plastic deformation. Since the stresses at which bulk metallic glasses begin to deform are rather high, one can expect mechanical activation of the high-energy states of the centers in question during this action. Therefore, another purpose of this work was to check the possibility of recovering irreversible structural relaxation through deformation treatment.

2. EXPERIMENTAL

As in [1–3], the logarithmic decrement and the shear modulus were measured with an inverse torsional pendulum; the measurement frequency was 10–20 Hz. All measurements were performed on bulk samples of a $Zr_{52.5}Ti_5Cu_{17.9}Ni_{14.6}Al_{10}$ metallic glass. The starting alloy was melted using vacuum induction melting under levitation conditions; then, in order to obtain a

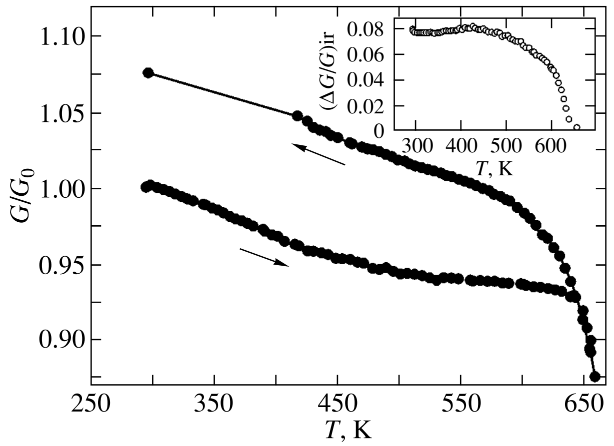

Fig. 1. Temperature dependences of the relative change in the shear modulus of a bulk $Zr_{52.5}Ti_5Cu_{17.9}Ni_{14.6}Al_{10}$ metallic glass quenched from 690 K, obtained in cycles of heating and cooling at a rate of 2 K/min. The inset shows the temperature dependence of the irreversible contribution to the shear modulus.

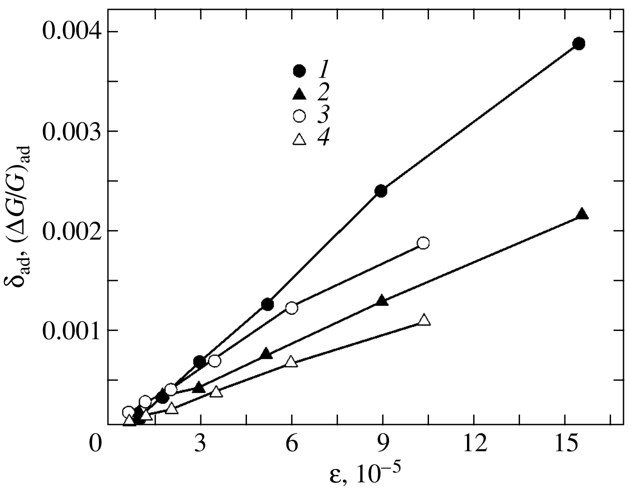

Fig. 2. Amplitude-dependent contributions to (*1*, *2*) the shear modulus and (*3*, *4*) the damping constant of a Zr–Cu–Ni–Al–Ti alloy measured at room temperature after (*1*, *3*) quenching from 690 K followed by (*2*, *4*) heating to 670 K.

metallic glass, the melt was quenched by pressing it out onto an evacuated copper mold held at room temperature. The quenching rate in the vicinity of the glass transition temperature was about 10^2 K/s [1–4]. The characteristic dimensions of the samples (with a ~2-mm^2 cross section and a length of 25- to 40-mm) and the method used to prepare them (spark cutting followed by mechanical polishing) were identical to those used in [1–3]. The structural (amorphous) state of the samples was controlled by x-ray diffraction. The glass transition temperature and the crystallization temperature (for a heating rate of 2 K/min) were approximately 650 and 700 K, respectively.

All the samples on which the effect of heat or deformation treatment was studied were preliminarily annealed to eliminate irreversible changes in the damping constant and the shear modulus in them. To this end, they were heated to 650–660 K according to a procedure described in [1, 2] and the damping constant and the shear modulus were measured during heating and cooling at a rate of 2 K/min. After this treatment, the irreversible change in the shear modulus in the samples under study (its increment at room temperature) was 7–15%. During repeated thermal cycling (up to 650–680 K), we failed to detect any irreversible changes in the damping constant and the shear modulus. Then, the samples were subjected to heat or deformation treatment.

The heat treatment (quenching) of the samples was conducted as follows: the samples were placed in a bath with molten tin for 5 min (the melt temperature was 660–690 K) and then water-quenched. The deformation treatment of the samples was performed via rolling at room temperature to a strain of 4–25%. After the samples were subjected to the heat or deformation treatment, the temperature dependences of the damping constant and the shear modulus G were measured repeatedly. The rate of temperature variation was about 2 K/min.

3. RESULTS AND DISCUSSION

Figure 1 shows the temperature dependences of the shear modulus measured in heating and cooling cycles for a sample after heat treatment (quenching). The shear modulus is seen to change irreversibly. The temperature dependence of the irreversible contribution is shown in the inset to Fig. 1; its character is identical to that observed in as-quenched (from the melt) Zr–Cu–Ni–Al–Ti samples [1, 2]. Like in [1, 2], an irreversible contribution to the damping constant is detected at temperatures above 500 K. In these experiments, the temperature from which quenching was performed had only an insignificant effect on the recovered irreversible contribution to the shear modulus. The observed variations (from 7% for quenching from 660 K to approximately 8.5% for 690 K) are too small for this effect to be discussed. To this end, additional experiments are required to obtain much more statistical data over a wider range of temperatures from which quenching is performed.

In the samples subjected to heat treatment, the damping constant and the shear modulus are found to depend on the strain amplitude ε (Fig. 2); the amplitude-dependent contribution is approximately the same as that in as-quenched samples [3]. Annealing at temperatures above 600 K somewhat weakens the amplitude dependences but cannot eliminate them completely.

Deformation treatment also causes irreversible changes in the damping constant and shear modulus

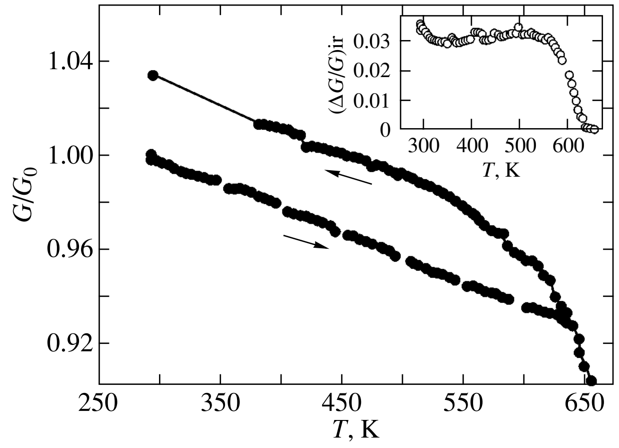

Fig. 3. Temperature dependences of the relative change in the shear modulus of a $Zr_{52.5}Ti_5Cu_{17.9}Ni_{14.6}Al_{10}$ alloy deformed by rolling to 15%, obtained in cycles of heating and cooling at a rate of 2 K/min. The inset shows the temperature dependence of the irreversible contribution to the shear modulus.

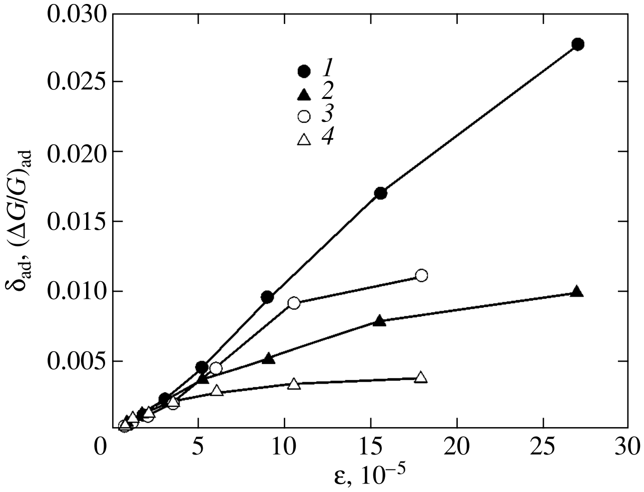

Fig. 4. Amplitude-dependent contributions to (*1*, *2*) the shear modulus and (*3*, *4*) the damping constant of a Zr–Cu–Ni–Al–Ti alloy measured at room temperature after (*1*, *3*) 4% deformation by rolling followed by (*2*, *4*) heating to 660 K.

(Fig. 3). However, the effect in this case is much lower than that induced by heat treatment (a ~2.5% change in the modulus at a 4% strain and a ~4.5% change upon rolling to a 25% strain). The amplitude dependences in deformed samples were found to be almost one order of magnitude stronger than those of heat-treated and as-quenched samples (Fig. 4). Annealing of deformed samples at high temperatures results in a more pronounced relative decrease in the amplitude-dependent contributions (Fig. 3) but also does not eliminate them completely. The deformation treatment induces two additional internal-friction peaks at about 300 and 500 K (Fig. 5). As a result of heating to ~670 K, the high-temperature peak is completely removed and the low-temperature peak decreases significantly but does not disappear. We did not study the characteristics of these peaks in more detail. However, it should be noted that deformation-induced peaks similar to the peak at 300 K have been observed earlier in conventional metallic glasses (see, e.g., [5]). In many parameters, such peaks resemble Hasiguti peaks in crystals; therefore, it seems natural to relate the former peaks to defects that are analogous to dislocations in crystals. However, since the existence of dislocations in amorphous materials is still disputable, the question regarding the mechanism of the appearance of these peaks remains open. The same is true of the variations in the damping constant and shear modulus with strain amplitude. Obviously, these variations are of a deformational nature and such amplitude-dependent friction in crystalline materials is usually related to dislocations (e.g., to the breakaway of dislocations from pinning points [6, 7]).

It should be noted that amplitude-dependent (hysteretic) internal friction can be described in terms of the model of relaxation centers with a double-well energy potential. At $\omega\tau \gg 1$ (where ω is the circular frequency, $\tau = \tau_0\exp(E/T)$, τ_0^{-1} is the characteristic attempt frequency, and E is the activation energy for transition from one energy minimum to the other) and low strain amplitudes, the relaxation contributions to the damping constant and shear modulus are small. As the strain amplitude increases to $\varepsilon_0 \approx E/GV$ at 0 K or $\varepsilon \approx \varepsilon_0\left[1-\left(T/E\ln\frac{1}{\omega\tau_0}\right)^m\right] = \varepsilon_0[1-(1-T/E\ln\omega\tau)^m]$ at a finite temperature (here, V is the activation volume and

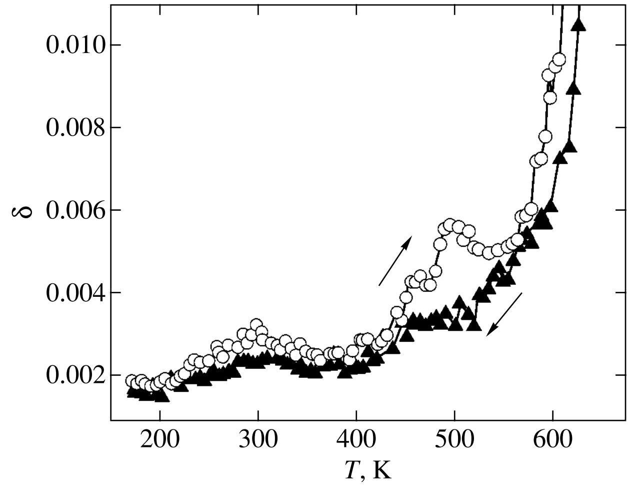

Fig. 5. Temperature dependences of the damping constant (measured at a frequency of 15 Hz) of a Zr–Cu–Ni–Al–Ti alloy deformed by rolling to 25%, obtained in heating and cooling cycles.

m is a numerical coefficient dependent barrier shape), a relaxation center switches from one energy minimum to the other during load cycling. This switching results in additional hysteretic internal friction. However, in any case, such centers cannot consist of a small number of atoms. As follows from the above formulas for the strain amplitude at which amplitude-dependent internal friction appears, the value of $VG\varepsilon$ should be higher than T. From this condition, we can easily find that the amplitude dependences will become observable at the strain amplitudes realized experimentally if the activation volume of such a relaxation center is at least a few cubic nanometers. Therefore, the only possible candidates for such relaxation centers are likely to be clusters. Note that this estimate of the activation volume is consistent with the dislocation model of amplitude-dependent internal friction.

4. CONCLUSIONS

Our experiments have shown that special-purpose heat or deformation treatment can, at least partly, recover the irreversible contributions to the internal friction and to the shear modulus of a bulk metallic glass; that is, so-called irreversible structural relaxation is reversible under certain conditions. This finding can be of fundamental importance in understanding the structural evolution of amorphous materials under external influences. Moreover, this finding makes it possible to study irreversible structural relaxation (and its relation to reversible structural processes) in more detail, since there are methods for repeatedly recovering this relaxation in the same samples in a sufficiently controlled manner.

ACKNOWLEDGMENTS

The authors thank A.S. Aronin and M.I. Karpov for treating the sample.

This work was supported by the Civilian Research and Development Foundation (project no. RP1-2320-VO-02) and the Ministry of Industry, Science, and Technology of the Russian Federation (project no. NSh-2169.2003.2).

REFERENCES

1. N. P. Kobelev, E. L. Kolyvanov, and V. A. Khonik, Fiz. Tverd. Tela (St. Petersburg) **45** (12), 2124 (2003) [Phys. Solid State **45**, 2225 (2003)].
2. N. P. Kobelev, E. L. Kolyvanov, and V. A. Khonik, Vest. Tambov. Univ. **8** (4), 545 (2003).
3. N. P. Kobelev, E. L. Kolyvanov, and V. A. Khonik, Fiz. Tverd. Tela (St. Petersburg) **47** (3), 400 (2005) [Phys. Solid State **47**, 411 (2005)].
4. A. E. Berlev, O. P. Bobrov, V. A. Khonik, K. Csach, A. Juríková, J. Miŝkuf, H. Neuhäser, and M. Yu. Yazvitsky, Phys. Rev. B **68**, 132 203-1 (2003).
5. V. A. Khonik and L. V. Spivak, Acta Mater. **44** (1), 367 (1996).
6. A. Granato and K. Lücke, J. Appl. Phys. **27**, 583 (1956).
7. L. J. Teutonico, A. V. Granato, and K. Lücke, J. Appl. Phys. **35**, 220 (1964).

Translated by K. Shakhlevich

Physics of the Solid State, Vol. 47, No. 4, 2005, pp. 674–677. Translated from Fizika Tverdogo Tela, Vol. 47, No. 4, 2005, pp. 650–653.
Original Russian Text Copyright © 2005 by Guseva, Zatsepin, Vazhenin, Schmidt, Gavrilov, Cholakh.

Magnetic Resonance of Metallic Nanoparticles in Vitreous Silicon Dioxide Implanted with Iron Ions

V. B. Guseva*, A. F. Zatsepin*, V. A. Vazhenin, B. Schmidt***,
N. V. Gavrilov****, and S. O. Cholakh***

** Ural State Technical University, ul. Mira 19, Yekaterinburg, 620002 Russia*
e-mail: valentina.guseva@usu.ru
*** Research Institute of Physics and Applied Mathematics, Ural State University,*
pr. Lenina 51, Yekaterinburg, 620083 Russia
**** Research Center Rossendorf, Institute of Ion Beam Physics and Materials Research, Dresden, D-01314 Germany*
***** Institute of Electrophysics, Ural Division, Russian Academy of Sciences,*
ul. Komsomol'skaya 34, Yekaterinburg, 620216 Russia

Received June 15, 2004

Abstract—Silica glasses exposed to steady-state and pulsed irradiation with Fe^+ ions are studied using magnetic resonance. The irradiation doses used in experiments are equal to 1×10^{15}, 1×10^{16}, and 1×10^{17} cm^{-2}. It is found that, under both steady-state and pulsed irradiation conditions, glass samples exposed at a dose of 1×10^{17} cm^{-2} exhibit a broadband orientation-dependent signal. The shape of inclusions is evaluated under the assumption that the observed spectrum is caused by the ferromagnetic resonance induced in a new phase of metallic iron. *© 2005 Pleiades Publishing, Inc.*

1. INTRODUCTION

At present, one of the most promising trends in solid-state physics is the design of nanoobjects and research into their structures and properties. Nanomaterials play an important role in many fields of modern science and engineering (physics, chemistry, materials science, medicine, biology, etc.). The main advantages of nanotechnologies are associated primarily with the fact that radically new functional properties can be imparted to materials by varying the sizes and shape of nanostructures. However, considerable progress in the design of nanostructures can be achieved only with a clear understanding of the factors responsible for the physicochemical properties of nanomaterials and the fundamental principles underlying the methods used for their preparation.

Isolated nanostructures have often been prepared according to techniques based on either chemical synthesis or layer-by-layer growth. Moreover, the possibility exists of producing nanoobjects in surface layers of the already prepared material. This can be accomplished through implantation of accelerated ions into the material.

Upon irradiation of optical oxide glasses with a beam of accelerated metal ions under specific conditions, colloidal metallic particles whose size can reach a few nanometers and which provide nonlinear effects in transmission of light are formed in a surface layer of the irradiated material [1–6]. Dielectric glasses implanted with paramagnetic ions have been used as magnetic materials [7, 8].

The purpose of this work was to investigate how exposure of silica glasses to irradiation with magnetic ions under various conditions and at different doses affects the glass structure. Furthermore, we analyzed the potentialities of magnetic resonance as a tool for detecting the possible aggregates of implanted particles and evaluating their shape. The magnetic measurements of silica glass samples were performed using ferromagnetic resonance (FMR) and electron paramagnetic resonance (EPR).

2. SAMPLE PREPARATION AND EXPERIMENTAL TECHNIQUE

For our experiments, samples of type I silica glasses in the form of polished disks 10 mm in diameter with a surface of optical quality were exposed to irradiation with Fe^+ ions. The fluences (i.e., the integrated fluxes of accelerated ions under irradiation) were equal to 1×10^{15}, 1×10^{16}, and 1×10^{17} cm^{-2}.

Pulsed irradiation of the samples was accomplished with an ion source developed at the Institute of Electrophysics (Ural Division, Russian Academy of Sciences, Yekaterinburg, Russia) with a design similar to that described in [9]. The irradiation conditions were as follows: ion energy, $E = 30$ keV; pulse width, 400 μs; and beam current density, 2–7 mA/cm^2. In the course of irradiation, the temperature of the sample surface did not exceed 400 K.

Steady-state irradiation was performed using a DANFYSIC high-current implanter operating at a voltage of 200 V at the Research Center Rossendorf (Institute of Ion Beam Physics and Materials Research, Dresden, Germany). The implantation was carried out with a natural iron isotope and ^{57}Fe ions (the isotope content in the beam was no less than 90%). The ion energy was equal to 100 keV, the beam current density was 8–10 mA/cm^2, and the temperature of the sample surface during implantation did not exceed 350 K.

The FMR spectra were measured, for the most part, on a setup that consisted of a modified RÉ1301 spectrometer operating in the 3-cm band with high-frequency magnetic-field modulation and providing measurements in magnetic fields up to 7.5 kG; devices used for varying, stabilizing, and measuring the temperature; and a system intended for computer recording of the spectra.

3. RESULTS AND DISCUSSION

For the samples exposed to pulsed irradiation, the magnetic resonance spectrum was observed at room and low temperatures only in the case of the maximum irradiation dose (1×10^{17} cm^{-2}). It turned out that the amorphous material exhibits an unexpected dependence of the position of the magnetic resonance signal on the angle θ between the magnetic field vector **H** and the normal **n** to the sample surface (Fig. 1). At a temperature of 133 K, the signal measured in the magnetic field $\mathbf{H} \parallel \mathbf{n}$ is shifted to the high-field range (Fig. 2). We failed to measure a signal in the magnetic field $\mathbf{H} \perp \mathbf{n}$, because the possible resonance signal was masked by a broadband spurious signal from the resonator.

The magnetic resonance measurements of the samples exposed to steady-state irradiation also revealed a broadband signal at a dose of 1×10^{17} cm^{-2}. The dependence of the position of this signal on the direction of the magnetic field (Fig. 3) appeared to be more pronounced than that in the above case. The observed signals were slightly asymmetric in shape.

It should be noted that neither FMR nor EPR signals were revealed for the samples irradiated at lower doses. The absence of an FMR spectrum for the samples exposed to ion irradiation at low doses can be explained by the decrease in the size and number of ferromagnetic grains. At the same time, the EPR spectrum of clusters or individual paramagnetic iron ions can be not observable because of both the very low concentration of these centers and the orientational averaging of the spectra of individual ions in the amorphous material.

In order to explain the orientation dependence of the resonance signal from the samples irradiated with Fe$^+$ ions at the maximum dose, we initially assumed that there is a preferred direction (strictly connected with the sample surface) of the principal axes of the paramagnetic centers generated upon ion implantation. However, this assumption did not provide a satisfactory explanation of the anomalously large width of the observed signal, which, in addition, changes only

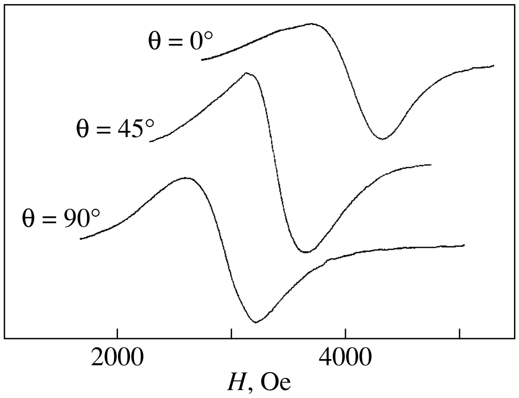

Fig. 1. FMR spectra of the silica glass implanted with Fe$^+$ ions (energy, 30 keV; fluence, 1×10^{17} cm^{-2}) for different angles θ between the normal to the sample surface and the magnetic field vector **H**. T = 297 K.

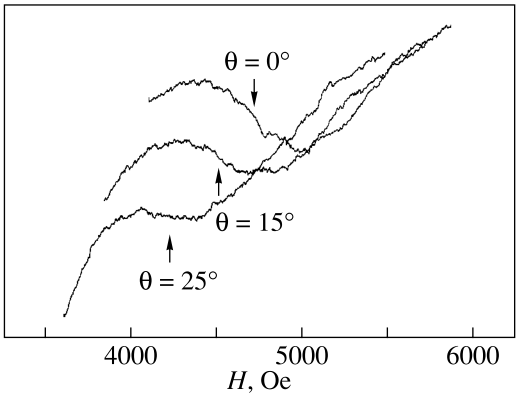

Fig. 2. FMR spectra of the silica glass implanted with Fe$^+$ ions (energy, 30 keV; fluence, 1×10^{17} cm^{-2}) for different angles θ between the normal to the sample surface and the magnetic field vector **H**. T = 133 K.

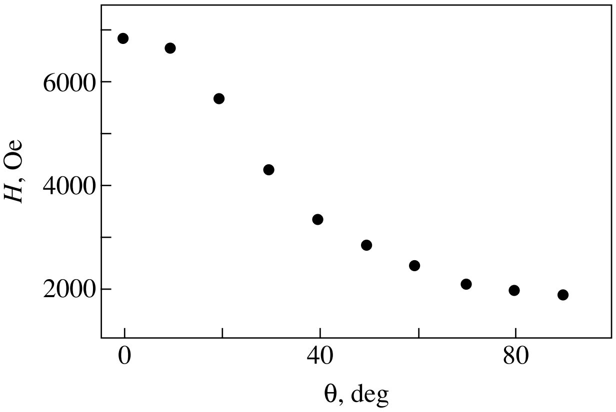

Fig. 3. Dependence of the position of the FMR signal on the angle θ between the normal to the sample surface and the magnetic field vector **H** for the silica glass implanted with Fe$^+$ ions (energy, 100 keV; fluence, 1×10^{17} cm^{-2}).

Evaluation of the shape of ferromagnetic inclusions from the results of measurements performed in this work

E, keV	ν_{res}, MHz	T, K	Direction of the magnetic field	**H**, Oe	$\Delta\mathbf{H}^{*}_{pp}$, Oe	ΔN	$l/l_{\perp}$	R_p^{**}, nm	d_{max}, nm
30	9380	295	$\mathbf{H} \parallel \mathbf{n}$	4046	600	0.49	0.91	27	57
			$\mathbf{H} \perp \mathbf{n}$	2994	600	0.27	0.95		
		133	$\mathbf{H} \parallel \mathbf{n}$	4700	650	0.67	0.88		
100	9400	295	$\mathbf{H} \parallel \mathbf{n}$	6850	800	2.13	0.68	68	200
			$\mathbf{H} \perp \mathbf{n}$	1890	1000	2.11	0.67		

* ΔH_{pp} is the peak-to-peak derivative width of the signal caused by the absorption of the ac electromagnetic field.

** R_p is the projective range (the mean projection of the ion trajectory onto the normal to the irradiated surface) calculated with the TRIM software package. For steady-state irradiation at an energy of 100 keV, the sputtering of a SiO_2 surface layer approximately 15 nm thick is taken into account.

slightly with a variation in the direction of the magnetic field. Comparison with the results obtained in [1, 8, 10] counts in favor of another mechanism. The broadband orientation-dependent signal measured for the silica glass implanted with iron ions can be caused by the ferromagnetic resonance induced in the iron microphase formed upon implantation (as is the case with silicate glasses [8]). Therefore, the change observed in the position of the resonance signal with a decrease in the temperature can be associated with the temperature dependence of the saturation magnetization.

As was shown in [11], the ferromagnetic resonance frequency for an ellipsoidal sample subjected to a magnetic field **H** aligned parallel to the axis of revolution of the ellipsoid (**H** ‖ **n**) can be written in the form

$$\omega_{res} = 2\pi\nu_{res} = \gamma(H - \Delta N M_S). \qquad (1)$$

Here, M_S is the saturation magnetization; $\Delta N = N_{\parallel} - N_{\perp}$ is the difference between the demagnetizing form factors, which are oriented parallel and perpendicular to the axis of revolution; β is the Bohr magneton; $\hbar$ is the Planck constant; and $\gamma = g\beta/\hbar$ is the gyromagnetic ratio. In the magnetic field directed perpendicular to the axis of revolution of the ellipsoid (**H** ⊥ **n**), the relationship for the ferromagnetic resonance frequency takes the form

$$\omega_{res} = 2\pi\nu_{res} = \gamma(H^2 + \Delta N M_S H). \qquad (2)$$

The table presents the estimates obtained from relationships (1) and (2) under the assumption that the saturation magnetization M_S for individual iron inclusions is equal to 1700 Oe [8] and that the g factor is 2.084 ± 0.004 (the averaged value for polycrystalline α-Fe [12, 13]). Knowing the values of ΔN, we can estimate the semiaxial ratio of the ellipsoid of revolution $l/l_{\perp}$ (this ratio and the quantity $\Delta N/4\pi$ are related by the Osborn formula [11]) and determine the maximum diameter d_{max} of the inclusions of the metallic phase with due regard for the projective range R_p. For low temperatures, the quantity ΔN was determined from the saturation magnetization M_S, which, in turn, was estimated from the dependence $M_S(T)$ obtained earlier by Gengalgen and Hoffman [14].

It can be seen from the table that metallic inclusions formed upon steady-state irradiation have a more distorted spherical shape than those formed upon pulsed irradiation. This difference can be associated with the difference between the degrees of local melting of the glass under the conditions of steady-state and pulsed irradiation.

Bukharev *et al.* [8] established that, for α-Fe precipitates with a semiaxial ratio of 0.44, the changeover from the parallel orientation to the perpendicular orientation of the magnetic field (with respect to the normal to the sample surface) leads to a severalfold increase in the width of the FMR signal. In our case, the widths of the resonance signals from the sample irradiated with iron ions at an energy of 30 keV and characterized by a semiaxial ratio close to unity turned out to be virtually identical for both directions of the magnetic field, whereas the width of the resonance signal from the sample exposed to steady-state irradiation somewhat increased upon changing over from the parallel orientation to the perpendicular orientation.

According to Griscom *et al.* [13], the range covered by the FMR spectrum of spherically symmetric inclusions of the α-Fe phase, in which the crystallographic axes are randomly oriented with respect to the nonmagnetic matrix, can be determined from the relationship $5/3H_a = 5/3 \times 2K_1/M_S$, where K_1 is the first constant of crystalline magnetic anisotropy and H_a is the magnetic-anisotropy field. By assuming that the width of the FMR signal from the sample exposed to pulsed irradiation (with a nearly spherical precipitates) is governed by the spatial spread in the orientations of the crystallographic axes, the constant K_1 is determined to be 540×10^3 erg/cm^3 ($H_a \approx 10^3$ Oe), which is close to the values obtained in [13, 14].

As can be seen from the results presented in the table, the maximum sizes of the metallic particles implanted at energies of 30 and 100 keV do not exceed 57 and 200 nm, respectively. The number of implanted metallic particles per unit area can be estimated from the known density and molar mass of iron. As a result, we find that, for an irradiation dose of 1×10^{17} cm^{-2}, the number of implanted metallic particles per square centimeter is of the order of unity. However, it is evident that the implanted metallic particles are characterized by a size distribution. Therefore, we can assume that, for the greater part, implanted particles are inclusions with a characteristic size of the order of 10 nm. The change in the magnetization and the corresponding spread in the saturation magnetizations due to the presence of small-sized particles in the material can be responsible for the additional broadening of the magnetic resonance signal.

4. CONCLUSIONS

Thus, silica glasses irradiated with Fe$^+$ ions at doses of 1×10^{15}, 1×10^{16}, and 1×10^{17} cm^{-2} were studied using magnetic resonance. It was found that glass samples irradiated at a dose of 1×10^{17} cm^{-2} contain the ferromagnetic iron phase. The above analysis of the angular dependence of the resonance signal demonstrated that metallic inclusions are isolated and have a nearly spherical shape. The threshold dose (1×10^{17} Fe$^+$ ions per square centimeter) required to observe ferromagnetic resonance does not depend on the irradiation conditions. However, the irradiation conditions themselves substantially affect the shape of metallic inclusions. The implantation of silica glasses with iron ions at low doses ($\leq 2 \times 10^{16}$ cm^{-2}) does not lead to the formation of paramagnetic centers in detectable amounts.

ACKNOWLEDGMENTS

We would like to thank D.R. Emlin, M.Yu. Artemov, and V.V. Ovchinnikov for their assistance in performing the experiments.

This work was performed as part of the Russian federal program “Integration” (project no. LO135) and under the program “Advanced Materials” of the Ural Research and Education Center (award nos. REC-005, EK-005-X1, CRDF) and was supported by the International Association of Assistance for the Promotion of Cooperation with Scientists from the New Independent States of the Former Soviet Union (project INTAS no. 01-0458).

REFERENCES

1. L. D. Bogomolova and V. A. Jachkin, Fiz. Khim. Stekla **24** (1), 3 (1998) [Glass Phys. Chem. **24** (1), 1 (1998)].
2. H. Hosono and R. A. Zuhr, J. Non-Cryst. Solids **178**, 160 (1994).
3. K. Fukumi, A. Chayahara, N. Kitamara, T. Akai, J. Hayakawa, K. Fujii, and M. Satou, J. Non-Cryst. Solids **178**, 155 (1994).
4. T. S. Anderson, R. H. Magruder, R. A. Weeks, and R. A. Zuhr, J. Non-Cryst. Solids **203**, 155 (1996).
5. O. Mariuyata, Y. Senda, and S. Omi, J. Non-Cryst. Solids **259**, 100 (1999).
6. A. Nakajima, H. Nakao, T. Futatsugi, and N. Yokoyama, J. Vac. Sci. Technol. B **14** (4), 1317 (1999).
7. A. L. Stepanov, V. N. Popok, and D. E. Hole, Fiz. Khim. Stekla **28** (2), 131 (2002) [Glass Phys. Chem. **28** (2), 90 (2002)].
8. A. A. Bukharev, A. V. Kazakov, R. A. Manapov, I. B. Khaĭbullin, and N. R. Yafaev, Fiz. Khim. Stekla **12** (3), 376 (1986).
9. I. G. Brawn, Rev. Sci. Instrum. **68** (10), 30 (1994).
10. G. Wichard, R. A. Weeks, and R. A. Zuhr, in *Proceedings of XIV International Congress on Glass* (Nauka, Leningrad, 1989), Vol. 26, p. 271.
11. *Ferromagnetic Resonance*, Ed. by S. V. Vonsovskiĭ (Fizmatgiz, Moscow, 1961) [in Russian].
12. Z. Frait, Czech. J. Phys., Sect. B **27** (2), 185 (1977).
13. D. L. Griscom, E. J. Friebele, and D. B. Shinn, J. Appl. Phys. **50** (3), 2402 (1979).
14. H. Gengalgen and U. Hoffman, Phys. Status Solidi **29**, 91 (1968).

Translated by O. Borovik-Romanova

Physics of the Solid State, Vol. 47, No. 4, 2005, pp. 678–683. Translated from Fizika Tverdogo Tela, Vol. 47, No. 4, 2005, pp. 654–659.
Original Russian Text Copyright © 2005 by Martynov.

MAGNETISM AND FERROELECTRICITY

Transition between Incommensurate Phases Accompanied by Reversal of the Magnetic Structure Vector in CuB_2O_4

S. N. Martynov
Kirensky Institute of Physics, Siberian Division, Russian Academy of Sciences,
Akademgorodok, Krasnoyarsk, 660036 Russia
e-mail: unonav@iph.krasn.ru

Received June 22, 2004

Abstract—The incommensurate magnetic state of copper metaborate CuB_2O_4 is studied in the temperature range $2 < T < 12$ K. Competition between frustrated and non-frustrated antisymmetric exchange interactions is shown to cause the magnetic structure vector to reverse at $T = 10$ K. *© 2005 Pleiades Publishing, Inc.*

1. INTRODUCTION

Recent intensive studies on the magnetic structure of CuB_2O_4 have revealed several different types of magnetic ordering, with phase transitions between them occurring under variation of either the temperature or magnetic field [1–5]. The variety of magnetic structures is due to the fact that, in copper metaborate, there are two distinct subsystems of magnetic Cu^{2+} ions in which the ions occupy different crystallographic positions and interact differently both within a subsystem and between them. The exchange interaction between the copper ions occupying the 4*b* sites with S_4 symmetry forms a three-dimensional magnetic subsystem *A* with a Néel temperature $T_{N1} = 20$ K, below which the average magnetic moment at *A* sites grows rapidly and reaches $0.94\mu_B$ at $T = 2$ K. The magnetic moments of subsystem *B* in the 8*d* sites with C_2 symmetry reach only $0.54\mu_B$ at the above temperature. The low magnitude of the magnetic moment at $T \longrightarrow 0$ K indicates quasi-low-dimensionality [6, 7] and/or a frustrated nature [8] of the main exchange interactions. Analysis of the exchange interactions in subsystem *B* has shown that there are two distinct competing AFM interactions between nearest and next-to-nearest neighbors and that these interactions create zigzag ladder chains along the tetragonal axis (a quasi one-dimensional magnetic structure) [9]. The existence of quasi-one-dimensional fluctuations caused by short-range correlations in CuB_2O_4 is also supported by strong diffuse neutron scattering observed both above and below the Néel temperature [3]. Therefore, the main distinction between the magnetic subsystems is the difference in the magnetic dimensionality of the main interactions within the subsystems. Analysis of the spin excitation spectra of each subsystem with inclusion of these interactions leads to the conclusion that the interactions between the subsystems have little effect on the dynamic properties of copper metaborate at $T = 12$ K [9, 10]. The reason for the interactions between the two subsystems being weak is the geometry of the intersubsystem exchange bonds. All paths of the indirect exchange interactions link an ion of one subsystem to two ions of another subsystem that belong to different antiferromagnetic (AFM) sublattices. This leads to fully frustrated exchange interaction between the subsystems when there is an AFM ordering within them. Ladder chains interact in a similar fashion, so the subsystem *B* becomes quasi-low-dimensional. An incommensurate magnetic structure is observed in CuB_2O_4 below $T_s \approx 10$ K with the wave vector directed along the tetragonal axis [3, 4]. The magnitude of the wave vector grows steadily with decreasing temperature and reaches 0.15 relative lattice units (rlu) at $T = 2$ K. According to a phenomenological analysis of the transition into the incommensurate phase, the Lifshitz invariant plays an important part in its formation [3, 4, 11]. From the field dependence and resonance properties of CuB_2O_4, it follows that a long-period incommensurate magnetic structure also exists in the high-temperature phase in the range $10 < T < 20$ K [4, 5]. In this paper, we analyze the magnetic structure of copper metaborate using a simple-helix model in the range $2 \text{ K} < T < 12$ K in order to determine the microscopic mechanism and type of transition between these two phases.

2. CRYSTAL STRUCTURE AND EXCHANGE INTERACTIONS

The crystal structure of CuB_2O_4 (Fig. 1) has been studied in detail in several papers [3, 4, 12]. The exchange interactions are due to hybrid *s*–*p* orbitals of tetrahedrons formed by oxygen atoms around boron atoms (the indirect superexchange chains Cu–O–B–O–Cu). Aside from the AFM exchange interactions within each subsystem, which were considered in [9, 10], we take into account the following: (i) the AFM exchange interaction between the subsystems (Fig. 1, solid lines), (ii) the exchange interaction between the ladders of subsystem *B* (dashed lines), and (iii) antisymmetric exchange interactions both between the subsystems and within them. In case (i), the AFM exchange interaction between the subsystems J_{ab}^m is realized along three different paths connecting Cu^{2+} ions separated by $\Delta z = c/8$, $3c/8$, and $5c/8$ along the tetragonal *c* axis. The exchange interaction between neighbors that are the most closely spaced along *z* and are remote in the *ab* plane is realized via the single Cu–O–B–O–Cu chain shown by single solid lines in Fig. 1. Two other exchange interactions are realized via the "one-and-a-half" chain shown by double solid lines in Fig. 1. The latter chain is displayed separately in Fig. 1. In case (iii), the exchange interaction between the ladder chains of subsystem *B* is realized via similar one-and-a-half chains and the local environment of interacting Cu^{2+} ions roughly comprises the mutually orthogonal squares formed by oxygen ions, similar to the case of the exchange between the subsystems. All exchange interactions of types (i) and (ii) are fully frustrated when the magnetic moments within the subsystems have AFM ordering. Symmetry analysis of the structure of CuB_2O_4 [11] shows that two distinct types of antisymmetric exchange interaction are possible in case (ii) [13, 14]. One type causes the magnetic moments of the AFM sublattices to be tilted and results in a weak ferromagnetic moment. This type of interaction occurs between the nearest neighbors in subsystem *A* (D_a). The other type of antisymmetric exchange interaction results in a turn in the interacting moments, which leads to the appearance of a helical structure. This type of interaction can occur between the subsystems (D_{ab}) and between the nearest and next-to -nearest neighbors within the ladders (D_{b1}, D_{b2}). The D_{b2} interaction only results in inessential renormalization of the analogous exchange interaction D_{b1}, so it is ignored below. Therefore, the exchange Hamiltonian in CuB_2O_4 can be written as

$$H = \sum_a \sum_{ii'} J_a^\alpha S_i^\alpha S_{i'}^\alpha + J_{b1}\sum_j \mathbf{S}_j \mathbf{S}_{j+1} + J_{b2}\sum_j \mathbf{S}_j \mathbf{S}_{j+2}$$

$$+ \sum_m \sum_{ij} J_{ab}^m \mathbf{S}_i \mathbf{S}_j + J_{b3}\sum_{jj'} \mathbf{S}_j \mathbf{S}_{j'} + D_a^z \sum_{ii'} (-1)^i [\mathbf{S}_i \times \mathbf{S}_{i'}]_z \tag{1}$$

$$+ D_{b1}^z \sum_j [\mathbf{S}_j \times \mathbf{S}_{j+1}]_z + \sum_m \sum_{ij} D_{ab}^{m,z} [\mathbf{S}_i \times \mathbf{S}_j]_z.$$

The first term in Eq. (1) describes easy-plane anisotropy in subsystem *A* [10]. Since all interactions occur between the magnetic moments positioned in various tetragonal planes ($\Delta z \neq 0$), the interacting spins are numbered along the tetragonal axis.

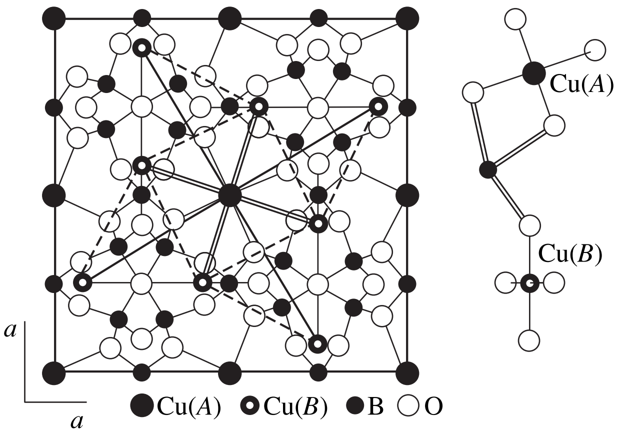

Fig. 1. CuB_2O_4 crystal structure (projection onto the tetragonal plane). The intersubsystem exchange interaction $J_{ab}^{2,3}$ is shown to the right.

3. LOCAL EXCHANGE FIELDS

If the transition of an antiferromagnet to an ordered phase is not accompanied by doubling of the elastic neutron scattering reflections, the number of possible orientations of magnetic moments of the antiferromagnet coincides with the number of magnetic ions in its unit cell. The unit cell of CuB_2O_4 has six magnetic ions: two ions in subsystem *A* and four ions in subsystem *B*. In order to describe a simple helix, we need to introduce the angle 2δ corresponding to the rotation of magnetic moments in passing from one unit cell to the next along the direction of the incommensurability vector. Since the Hamiltonian is invariant under rotation of the crystal in the tetragonal plane, the origin for the angles in the plane can be chosen arbitrarily. Consequently, we need six variables to describe the simple helix structure in CuB_2O_4. Among them, five angular variables for one unit cell can be found from the condition that the components of the total average field that are normal to the equilibrium orientation of each of the moments must be zero. The sixth variable, the helix angle, can be found by minimizing the total free energy of the unit cell with respect to this variable. A simplified diagram of the exchange interactions is shown in Fig. 2.

We choose a local coordinate frame for each of the moments such that its **Z** axis is along the tetragonal axis. The direction of the projection of the equilibrium moment $\mathbf{S}_i$ onto the tetragonal *xy* plane is chosen to be another coordinate axis, $\mathbf{X}_i$. Now, we express the Hamiltonian in terms of the orientation angles of the local coordinate axes. For each pair of interacting spins, we get

$$S_i^x S_j^x + S_i^y S_j^y = (S_{xi}S_{xj} + S_{yi}S_{yj})\cos(\alpha_i - \alpha_j)$$
$$+ (S_{xi}S_{yj} - S_{yi}S_{xj})\sin(\alpha_i - \alpha_j),$$

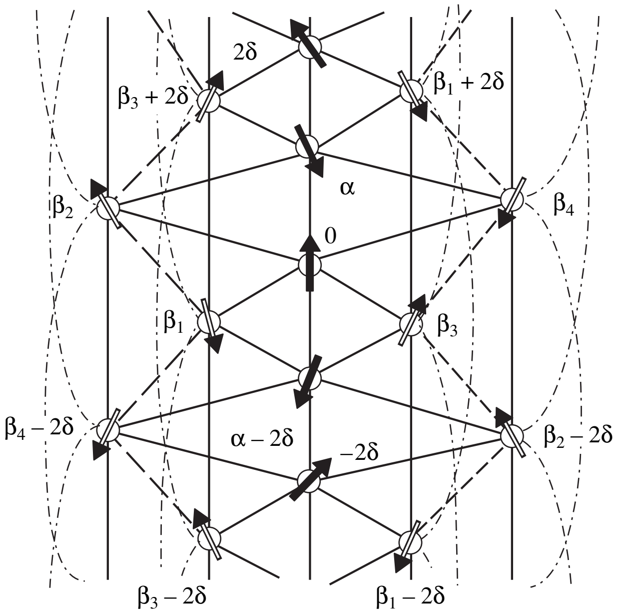

Fig. 2. Simplified diagram of the exchange interactions. Vertical lines represent the J_a exchange interaction in subsystem A with the coordination number $z_a = 4$ (the central line) and the J_{b1} exchange interaction in four ladders passing through all unit cells of the crystal (coordination number $z_b = 2$). Slanting lines represent the J_{ab}^1 exchange interaction between the subsystems and half of the J_{b3} exchange interactions between ladders (dashed lines). Dash-dotted lines represent the J_{b2} exchange interaction. The $J_{ab}^{2,3}$ exchange interactions are not shown. Arrows in the chart represent the directions of magnetic moments projected onto the tetragonal plane. Each arrow corresponds to a layer of moments (z = const) changing its orientation along the tetragonal (z) axis, which coincides with the vertical axis of the chart. An arbitrary spin of subsystem A $\alpha_0 = 0$ is chosen as a reference for the angles (the central spin in the chart).

$$S_i^xS_j^y - S_i^yS_j^x = -(S_{xi}S_{xj} + S_{yi}S_{yj})\sin(\alpha_i - \alpha_j) + (S_{xi}S_{yj} - S_{yi}S_{xj})\cos(\alpha_i - \alpha_j).$$

In the local reference frame, we have $\langle S_{yi}\rangle \equiv 0$. In the mean-field approximation, coefficients h_y^i of the transverse components S_{yi} must vanish after summing the contributions from nonzero components of the average spins $\langle S_{xi}\rangle$ over interactions included in Eq. (1) [15]:

$$h_y^0 = -2S_{ax}\cos\delta(J_a\sin(\gamma-\delta) - D_a\cos(\gamma-\delta)) - S_{bx}\left(f_1\cos\frac{\beta_1-\beta_3}{2} + f_2\cos\frac{\beta_2-\beta_4}{2}\right) \equiv 0,$$

$$h_y^{\beta1} = -S_{bx}[\sin(\beta_1-\beta_3)(J_{b1}\cos2\delta + D_{b1}\sin2\delta) + 2J_{b3}\cos\delta(\sin(\beta_1-\beta_2+\delta) + \sin(\beta_1-\beta_4+\delta))] + S_{ax}\cos(\beta_1 - 0.5\gamma + \delta)f_3(\gamma,\delta) \equiv 0,$$

$$h_y^{\beta2} = -S_{bx}[\sin(\beta_2-\beta_4)(J_{b1}\cos2\delta + D_{b1}\sin2\delta) + 2J_{b3}\cos\delta(\sin(\beta_2-\beta_1-\delta) + \sin(\beta_2-\beta_3-\delta))] + S_{ax}\cos(\beta_2 - 0.5\gamma + \delta)f_4(\gamma,\delta) \equiv 0,$$

$$h_y^{\beta3} = h_y^{\beta1}(\beta_1 \longleftrightarrow \beta_3),$$

$$h_y^{\beta4} = h_y^{\beta2}(\beta_2 \longleftrightarrow \beta_4),$$

$$f_1(\gamma,\delta) = J_{ab}^1\cos(0.5\gamma-\delta) + J_{ab}^2\cos(0.5\gamma+\delta) + J_{ab}^3\cos(0.5\gamma-3\delta) - D_{ab}^1\sin(0.5\gamma-\delta) + D_{ab}^2\sin(0.5\gamma+\delta) - D_{ab}^3\sin(0.5\gamma-3\delta),$$

$$f_2(\gamma,\delta) = J_{ab}^1\cos(0.5\gamma) + J_{ab}^2\cos(0.5\gamma-2\delta) + J_{ab}^3\cos(0.5\gamma+2\delta) + D_{ab}^1\sin(0.5\gamma) - D_{ab}^2\sin(0.5\gamma-2\delta) + D_{ab}^3\sin(0.5\gamma+2\delta),$$

$$f_3(\gamma,\delta) = -J_{ab}^1\sin(0.5\gamma-\delta) - J_{ab}^2\sin(0.5\gamma+\delta) - J_{ab}^3\sin(0.5\gamma-3\delta) - D_{ab}^1\cos(0.5\gamma-\delta) + D_{ab}^2\cos(0.5\gamma+\delta) - D_{ab}^3\cos(0.5\gamma-3\delta),$$

$$f_4(\gamma,\delta) = J_{ab}^1\sin(0.5\gamma) + J_{ab}^2\sin(0.5\gamma-2\delta) + J_{ab}^3\sin(0.5\gamma+2\delta) - D_{ab}^1\cos(0.5\gamma) + D_{ab}^2\cos(0.5\gamma-2\delta) - D_{ab}^3\cos(0.5\gamma+2\delta),$$

where $\gamma = \alpha - \pi$ is the angle of deviation of the magnetic moments of subsystem A from the AFM orientation within each unit cell. Here and henceforth, $S_{ax,\,bx}$ denote the average x components of the spins of the subsystem. Therefore, all angles in the basic unit cell are expressed in terms of δ. The mean fields acting on the x components of the spins of each subsystem are given by

$$h_{ax} = -\frac{S_{ax}}{2}\left[4\cos(\gamma-\delta)(J_a\cos\delta + D_a\sin\delta) + \frac{(J_{b1}\cos2\delta + D_{b1}\sin2\delta)(f_3^2 + f_4^2) + 2J_{b3}\cos\delta f_3f_4}{(J_{b1}\cos2\delta + D_{b1}\sin2\delta)^2 - (J_{b3}\cos\delta)^2}\right], \tag{2}$$

$$h_{bx} = -S_{bx}(J_{b1}\cos2\delta + D_{b1}\sin2\delta - J_{b2}\cos4\delta),$$

because of the condition imposed on γ:

$$2\cos\delta(J_a\sin(\gamma-\delta) - D_a\cos(\gamma-\delta))((J_{b1}\cos2\delta + D_{b1}\sin2\delta)^2 - (J_{b3}\cos\delta)^2) - (J_{b1}\cos2\delta + D_{b1}\sin2\delta)(f_1f_3 - f_2f_4) - J_{b3}\cos\delta(f_1f_4 - f_2f_3) = 0.$$

Thus, in the mean-field approximation, the intersubsystem interaction in the simple-helix model results in an additional longitudinal field acting on spins of subsystem A (the second term in Eq. (2)) and, furthermore, the decrease in the intrasubsystem exchange field is compensated for by a tilt of the magnetic moments in subsystem B ($\beta_1 - \beta_3 \neq \pi \neq \beta_2 - \beta_4$). The subsystems remain quasi-independent, because the additional effective fields within each subsystem do not depend directly on the magnetization of the other subsystem.

4. FREE ENERGY

In the mean-field approximation, the minimum of the free energy

$$F = -k_{\mathrm{B}}T\ln \mathrm{Sp}\{\exp(-\beta H)\}$$

can be easily found by fixing the magnitude of the average spin at sites of each subsystem and varying the total energy with respect to the helix pitch. Possible influence of the pitch variation on the spin magnitude is disregarded. This simplification is equivalent to the approximation of the fixed magnitude of the order parameter, which is widely used for phenomenological analysis of incommensurate structures [16]. In the temperature range of interest, the magnetic moments of subsystem A are oriented approximately in the tetragonal plane; their magnitude varies between $0.86\mu_{\mathrm{B}}$ and $0.94\mu_{\mathrm{B}}$ and will be assumed to be constant and equal to $0.9\mu_{\mathrm{B}}$. The magnitude of the magnetic moments of subsystem B varies from $0.2\mu_{\mathrm{B}}$ at $T = 12$ K to $0.54\mu_{\mathrm{B}}$ at $T = 2$ K. In order to describe its variation with temperature between these limits, we consider subsystem B as a set of two-level single-site spin $S = 1/2$ states. The corresponding wave functions for the ground and excited states are given by

$$\Psi_{0i} = C_0^+|+\rangle_i\Psi^+_{0,\,N-1} + C_0^-|-\rangle_i\Psi^-_{0,\,N-1},$$

$$\Psi_{ei} = C_e^+|+\rangle_i\Psi^+_{e,\,N-1} + C_e^-|-\rangle_i\Psi^-_{e,\,N-1}$$

for each spin subjected to the mean field of all other spins. Here, $C^{+,-}_{0,\,e}$ are the probability amplitudes of the ground and excited states of the spin S_i with "+" and "–" projection to the local axis, respectively, and $\Psi^{+,-}_{0,\,e,\,N-1}$ are the corresponding normalized wave functions of the states of all other $N - 1$ spins. The average values of the spin at a site in each of the states are

$$S_0 = S_b(T \longrightarrow 0) = \frac{1}{2}(|C_0^+|^2 - |C_0^-|^2),$$

$$S_e = \frac{1}{2}(|C_e^+|^2 - |C_e^-|^2)$$

and differ from the values for the free ion $S = \pm 1/2$. The temperature dependence of the spin can be found to be

$$S_b(T) = \frac{S_0\exp(\Delta E/2k_{\mathrm{B}}T) + S_e\exp(-\Delta E/2k_{\mathrm{B}}T)}{\exp(\Delta E/2k_{\mathrm{B}}T) + \exp(-\Delta E/2k_{\mathrm{B}}T)},$$

where ΔE is the level splitting in the mean field. From the condition $\lim S_b\,(T \longrightarrow \infty) = 0$, we get $S_0 = -S_e$ and the energy is $\Delta E/2 = S_0h_b$. Finally, we arrive at the well-known expression for a two-level system in the mean field h_b:

$$S_b = S_0\tanh\frac{S_0h_b}{k_{\mathrm{B}}T}.$$

For an experimentally observed long-period helix [4], the difference in the temperature dependence between the mean field h_b and the average spin due to the helical in-plane rotation of the moments (the term in parentheses in the second of equations (2) depends on δ) is small and can be neglected. Thus, the temperature dependence of the average magnetization at sites in subsystem B can be described with sufficient accuracy in terms of the temperature of the onset of macroscopic magnetization in subsystem B [15]:

$$m_b = m_b^0\tanh\frac{m_bT_{N2}}{m_b^0T}, \tag{3}$$

$$k_{\mathrm{B}}T_{N2} = S_0^2(J_{b1} - J_{b2}). \tag{4}$$

For the magnetization values cited above, we get $m_b^0 = 0.54\mu_{\mathrm{B}}$ and $T_{N2} = 12.6$ K.

The angle the magnetic moments of the subsystem B make with the tetragonal axis increases from a small value to $\Theta_0 \approx \pi/2.7$ as the temperature decreases to $T = 2$ K [3]. We do not consider the mechanism behind this change in direction because, in this paper, we disregard anisotropy of subsystem B for the sake of simplicity. The variation in the orientation of the moments in system B with temperature is described by a power law,

$$\Theta = \Theta_0(1 - T/T^*)^n \tag{5}$$

with $n = 1$ (linear dependence) or $n = 0.5$ (which corresponds to the variation in the order parameter for the second-order orientation phase transition in a three-dimensional system [17]). In both cases, the temperature of the onset of reorientation, according to experiment [3], is close to T_{N2}: $T^* = 12.4$ K ($n = 1$) and 12.3 K ($n = 0.5$). This simple approximation gives only a qualitative description of $k(T)$ for intermediate temperatures.

Varying the free energy with respect to the helix pitch in one unit cell of the crystal reduces to varying the longitudinal mean fields

$$\delta F_1 = 2S_{ax}\delta h_{ax} + 4S_b\delta h_b.$$

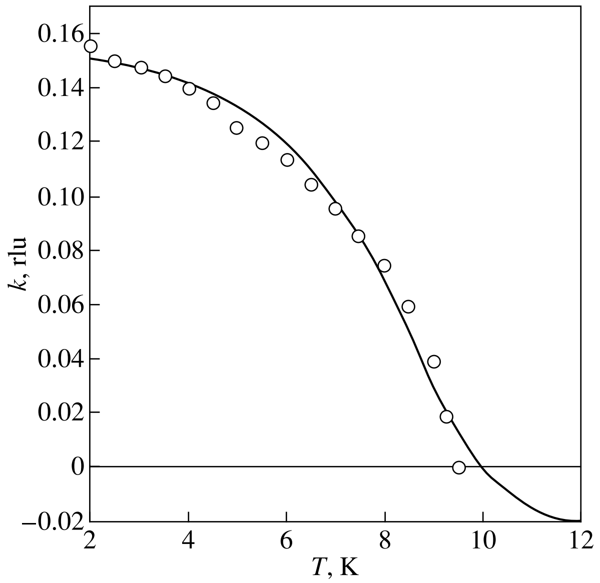

Fig. 3. Temperature dependence of the incommensurability vector $k(T)$. Dots are experimental data [4] and the solid line is the mean-field approximation in the simple-helix model with a linear temperature dependence of the moment direction in subsystem B: $\Theta = \Theta_0(1 - T/T^*)$. Parameter values: $J_{b1} = 234$ K, $J_{b2} = 59.4$ K, $J_{ab} = 67.5$ K, $D_{b1} = 21.1$ K, $D_{ab} = 5.6$ K, $D_a = 1.1$ K, and $J_{b3} = 0$ K.

The component h_{bz} is invariant relative to helical rotation of the moments in the tetragonal plane:

$$h_b = \sqrt{h_{bx}^2 + h_{bz}^2}, \quad \delta h_b = \frac{h_{bx}\delta h_{bx}}{\sqrt{h_{bx}^2 + h_{bz}^2}} = \sin\Theta\delta h_{bx}, \tag{6}$$
$$S_{bx} = S_b\sin\Theta, \quad \Delta F_1 = 2S_{ax}\delta h_{ax} + 4S_{bx}\delta h_{bx}.$$

Within our approximations, the part of the free energy that changes with the helix pitch depends only on the x components of spins of the subsystems and its variation with temperature is determined by the temperature dependence of the x component of subsystem B.

Using Eqs. (2) for the fields and Eqs. (3) and (5) for the temperature dependences of the magnitude and direction of the magnetic moment, we numerically minimize the part of the free energy that depends on the helix angle,

$$F_1(\delta) = 2S_{ax}h_{ax}(\delta) + 4S_{bx}h_{bx}(\delta), \tag{7}$$

and obtain the temperature dependence of the simple-helix vector $k(T)$.

5. RESULTS AND DISCUSSION

The best agreement between the calculated temperature dependence of the incommensurate structure vector and elastic neutron scattering data is obtained for $n = 1$ and

$$2J_{ab}^1 = J_{ab}^2 = J_{ab}^3 = J_{ab}, \quad 2D_{ab}^1 = D_{ab}^2 = D_{ab}^3 = D_{ab}$$

(Fig. 3). The J_{b3} interaction between ladders has almost no effect on $k(T)$, so it was assumed to be zero in calculations. The main feature of the temperature dependence of the helix vector is the reversal of the vector sign at $T_s \approx 10$ K; i.e., the left-handed helix is replaced by a right-handed one. This transition can be either continuous or discontinuous, depending on the relationship between the next-to-nearest neighbor exchange interaction in subsystem B (which is responsible for the potential with two minima as a function of δ) and the Dzyaloshinskiĭ interaction. The exchange constant of subsystem A in the Hamiltonian was assumed to be equal to $J_a = 45$ K, a value obtained from analyzing the spin-wave spectrum and the Néel temperature T_{N1} [10]. The magnitudes of exchange interactions in subsystem B were varied in a wide range subject to Eq. (7). For the ratio of the next-to-nearest and nearest neighbor exchange interactions, we obtained $J_{b2}/J_{b1} = 0.25$, which is close to the value of 0.26 obtained in [9]. However, the magnitudes of each of the interactions are almost one order of magnitude greater than the results from [9], because the linear theory of spin waves employed in [9] does not take into account the decrease in the saturation value of the moment due to quasi-low-dimensionality of the system. Consequently, the exchange interactions that were derived through comparison with the spin excitation energy given by inelastic neutron scattering measurements are underestimated. The saturation value of the site moment of $S = 1/2$ chains in the mean field of interchain interaction is related to the ratio of the intrachain interaction and the Néel temperature [6, 7]. This relation shows how much the Néel temperature of a quasi-one-dimensional system differs from the Néel temperature of the corresponding three-dimensional system. In our case, it is convenient to compare subsystems A and B, for which we obtain

$$K = \frac{z_a J_a T_{N2}}{z_b(J_{b1} - J_{b2})T_{N1}} \approx 0.33.$$

This value is in good quantitative agreement with the theoretical result from [6] for $m_b^0 = 0.54\mu_B$ [7]. The maximum value of the incommensurability vector $k = 0.15$ rlu at $T = 2$ K is determined by the combined effect of the next-to-nearest-neighbor AFM exchange interaction J_{b2} and the Dzyaloshinskiĭ nearest neighbor interaction D_{b1} in subsystem B. As the temperature increases, the contribution from subsystem B to the free energy decreases as $(m_b^0)^2$ [10] and the incommensurability vector reverses at the point where the interactions D_{b1} and D_{ab} are balanced. Although these antisymmetric exchange interactions are of the same sign, the contributions from them are different because the former interaction couples the moments of different AFM sublattices, while the latter couples the moments of a subsystem to the moments of both sublattices of the other subsystem, i.e., with the weak ferromagnetic moment. The ratios of these interactions to the corresponding AFM exchange interactions are similar, 0.9×10^{-1} and 0.8×10^{-1}. The sign of the Dzyaloshinskiĭ exchange interaction between spins of subsystem A is unknown. If $D_a < 0$, this interaction promotes the $k < 0$ phase and the agreement with the experimental data is achieved at a lower value of D_{ab}.

Note that, near the temperature where k changes sign, the simple-helix model is inadequate and cannot describe a longitudinal modulation of magnetization [11] or a complex magnetic structure of the soliton-lattice type. The existence of such a structure is indicated by the satellite peaks observed in neutron scattering near T_s [2]. Clearly, the approximation of the magnetization by the Brillouin function, Eq. (6), is well-founded only for $T < 12$ K, where the magnetization of subsystem B is mainly determined by the intrasubsystem exchange interactions J_{b1} and J_{b2}. At $T > 12$ K, the intersubsystem exchange interaction plays an important part and the magnetization of subsystem B does not vanish until the long-range order disappears in subsystem A at $T_{N1} = 20$ K. For small values of m_b, there is a solution for the unit cell angles that gives a longitudinal field differing from Eq. (2). Therefore, the structure vector found by us, $k(T = 12\text{ K}) \sim 0.02$ rlu, is only an upper bound estimation. However, the growth of the wave vector in magnitude with the temperature increasing from T_s is indirectly supported by the temperature–field phase diagram [4, 5]. The fact that the field destroying the incommensurate structure increases with temperature indicates that k at $H = 0$ also increases.

6. CONCLUSIONS

We can draw two main conclusions from the results obtained in this paper. (1) The magnitudes of exchange interactions, the temperature of the onset of macroscopic magnetization, and the saturation moment of subsystem B correspond to the quasi-one-dimensional type of interactions in this subsystem. (2) The competition between the frustrated and nonfrustrated antisymmetric exchange interactions causes the magnetic structure vector to reverse sign at $T_s \approx 10$ K.

6. ACKNOWLEDGMENTS

The author is grateful to V.I. Zinenko, M.A. Popov, G.A. Petrakovkiĭ, and A.I. Pankrats for helpful discussions.

This work was supported by the Russian Foundation for Basic Research, project no. 03-02-16701.

REFERENCES

1. G. Petrakovskii, D. Velikanov, A. Vorotinov, *et al.*, J. Magn. Magn. Mater. **205** (1), 105 (1999).
2. B. Roessli, J. Schefer, G. Petrakovskii, *et al.*, Phys. Rev. Lett. **86** (9), 1885 (2001).
3. M. Boehm, B. Roessli, and J. Schefer, Phys. Rev. B **68**, 024405 (2003).
4. G. A. Petrakovskii, A. I. Pankrats, M. A. Popov, *et al.*, Low Temp. Phys. **28** (8–9), 606 (2002).
5. A. I. Pankrats, G. A. Petrakovskiĭ, M. A. Popov, *et al.*, Pis'ma Zh. Éksp. Teor. Fiz. **78** (9–10), 1058 (2003) [JETP Lett. **78**, 569 (2003)].
6. H. J. Schultz, Phys. Rev. Lett. **77** (13), 2790 (1996).
7. K. M. Kojima, Y. Fudamoto, M. Larkin, *et al.*, Phys. Rev. Lett. **78** (9), 1787 (1997).
8. E. M. Lifshitz and L. P. Pitaevskiĭ, *Statistical Physics* (Fizmatlit, Moscow, 2001; Butterworth, Oxford, 1998), Part 2.
9. S. Martynov, G. Petrakovskii, B. Roessli, *et al.*, J. Magn. Magn. Mater. **269**, 106 (2004).
10. M. Boehm, S. Martynov, B. Roessli, *et al.*, J. Magn. Magn. Mater. **250**, 313 (2002).
11. M. A. Popov, G. A. Petrakovskiĭ, and V. I. Zinenko, Fiz. Tverd. Tela (St. Petersburg) **46** (3), 478 (2004) [Phys. Solid State **46**, 491 (2004)].
12. M. Martinez-Ripoli, S. Martinez-Carrera, and S. Carcia-Blanco, Acta Crystallogr. B **27**, 677 (1971).
13. I. E. Dzyaloshinskiĭ, Zh. Éksp. Teor. Fiz. **47** (3), 992 (1964) [Sov. Phys. JETP **20**, 573 (1964)].
14. T. Moriya, Phys. Rev. **120**, 91 (1960).
15. J. S. Smart, *Effective Field Theories of Magnetism* (Saunders, London, 1966; Mir, Moscow, 1968).
16. Yu. A. Izyumov, *Diffraction of Neutrons on Long-Period Structures* (Énergoatomizdat, Moscow, 1987) [in Russian].
17. K. P. Belov, A. K. Zvezdin, A. M. Kadomtseva, and R. Z. Levitin, *Orientation Transitions in Rare-Earth Magnets* (Nauka, Moscow, 1979) [in Russian].

Translated by G. Tsydynzhapov

Physics of the Solid State, Vol. 47, No. 4, 2005, pp. 684–689. Translated from Fizika Tverdogo Tela, Vol. 47, No. 4, 2005, pp. 660–665.
Original Russian Text Copyright © 2005 by Shalygina, Kozlovskiĭ, Abrosimova, Mukasheva.

MAGNETISM AND FERROELECTRICITY

Effect of Annealing on the Magnetic and Magnetooptical Properties of Ni Films

E. E. Shalygina, L. V. Kozlovskiĭ, N. M. Abrosimova, and M. A. Mukasheva

Moscow State University, Vorob'evy gory, Moscow, 119992 Russia

e-mail: shal@magn.ru

Received March 9, 2004; in final form, July 7, 2004

Abstract—The magnetic and magnetooptical properties of 50- to 200-nm-thick Ni films, both as-deposited and annealed at T_{ann} = 300, 400, or 500°C, were studied. Volume and near-surface hysteresis loops were measured with a vibrating-sample magnetometer (VSM) and with the use of the transverse Kerr effect (TKE). The annealing temperature was found to exert a strong effect on the magnetic characteristics of the samples under study. It was established, in particular, that the coercivity H_C of Ni films increases and the remanent magnetization decreases with increasing annealing temperature. The observed dependences of the magnetic properties of the films on film thickness and annealing temperature are explained as being due to microstructural characteristics of the samples. It was found that, while TKE spectra obtained in the incident-photon energy region from 1.5 to 6 eV have the same shape for all the Ni films studied, the magnitude of the TKE decreases with increasing T_{ann}. This experimental observation is accounted for by the decreased saturation magnetization of the annealed films.

1. INTRODUCTION

In recent years, there has been an increasing interest in the investigation of low-dimensional magnetic systems, one or two dimensions of which lie in the micro- or nanometer range. Thin magnetic films (TMFs) with a thickness considerably smaller than the other two dimensions are only one illustration of solid-state low-dimensional systems. TMFs exhibit unique magnetic, magnetooptical, kinetic, and dynamic properties, which accounts for their broad application. TMFs are used, in particular, as miniature components in modern microelectronic devices [1–3] and magnetic storage cells [4–6], as interference filters, as reflecting and antireflection coatings [7, 8], etc.

Considerable progress was achieved in the 1990s in the technology of TMF fabrication, which spurred studies on TMFs to a considerable extent. Some of the results obtained have already stimulated the solution of a number of problems in the physics of thin magnetic films. In particular, a deeper understanding of the effect of the interface between a magnetic film and the substrate on the kinetic, magnetic, and magnetooptical properties has been gained. The influence of morphology, the size, and crystallographic orientation of grains in the nonmagnetic layer deposited between a magnetic film and a substrate on the magnetic properties of thin-film magnetic systems has been studied in considerable detail (see, e.g., [9]). A wealth of experimental data have been obtained on the effect of the microstructure and thickness of nonmagnetic layers (Zr, Ta, Al, Mo, Pt, Pd) on the magnetic characteristics of Fe and Co films that vary in thickness over a broad range (from 2 to 200 nm) [10–13]. By contrast, the magnetic characteristics of Ni films have been investigated less extensively (see, e.g., [14–17]), while the effect of annealing on their magnetic and magnetooptical properties has not been considered at all.

In this paper, we report the results of a study of the magnetic and magnetooptical properties of Ni films in the original state and after annealing at a temperature of 300, 400, or 500°C.

2. SAMPLES AND EXPERIMENTAL TECHNIQUES

Several series of Ni films were fabricated by magnetron sputtering in an USU-4 ultrahigh vacuum setup. Films were deposited on glass substrates at a base pressure of 10^{-8} Torr in the operating chamber. An in-plane magnetic field H_{sub} = 70 Oe was applied in the process of film deposition. The films were deposited on room-temperature substrates. Ultrahigh vacuum was attained with a magnetic discharge pump after heating of the operating vacuum chamber at 200°C for 8 h. The operating inert gas was xenon. The inert gas pressure was about 10^{-3} Torr. The film thickness in each series was varied from 50 to 200 nm. To prevent oxidation, the films were coated by a 10-nm-thick carbon layer. Ni films with the above thicknesses were annealed at T_{ann} = 300, 400, or 500°C for 1 h in vacuum.

The microstructure of the samples for study was characterized using x-ray diffraction. The volume mag-

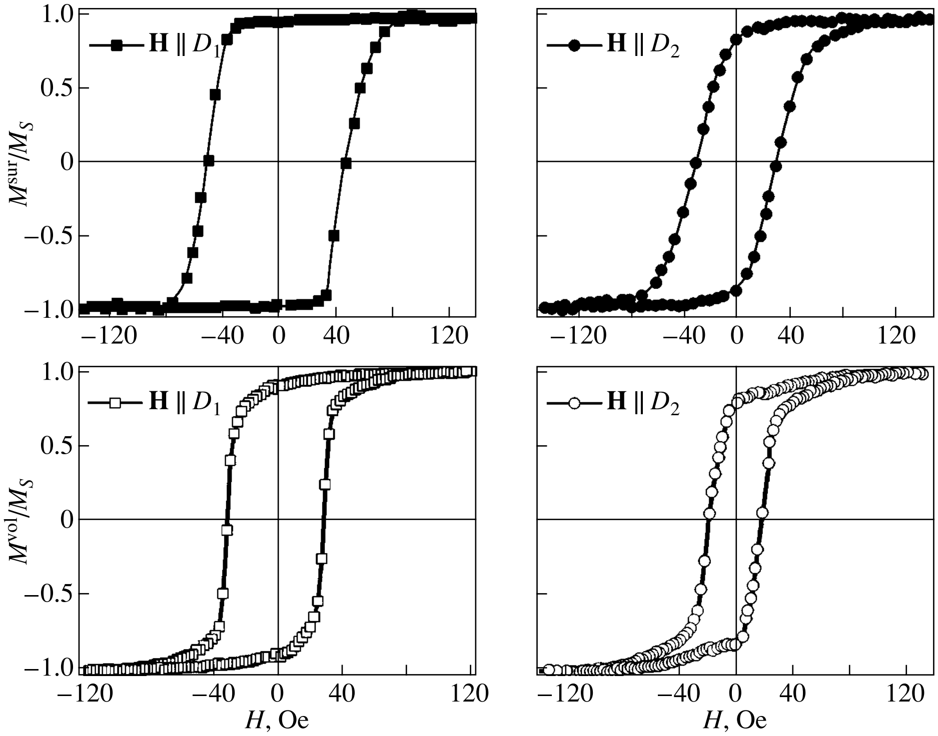

Fig. 1. Hysteresis loops obtained with a vibrating-sample magnetometer (VSM) and the magnetooptical transverse Kerr effect (MOKE) for an as-deposited 200-nm-thick Ni film in a magnetic field applied in directions D_1 and D_2, parallel and perpendicular, respectively, to the field H_{sub} applied parallel to the substrate in the process of film deposition.

netic characteristics of the nickel films were measured with a vibrating-sample magnetometer. Information on the near-surface magnetic characteristics of the samples was obtained using a magnetooptical magnetometer, which is described in detail in [18]. The magnetooptical Kerr effect (MOKE) is known to be sensitive to the magnetization of a near-surface layer with a thickness equal to the light penetration depth t_{pen}. This thickness is derived from the relation $t_{pen} = \lambda/4\pi k$, where λ is the incident light wavelength and k is the absorption coefficient of the medium. Available experimental information [13] suggests that t_{pen} for metallic ferromagnets does not exceed 10–30 nm within the incident-photon energy range $0.5 < \hbar\omega < 5$ eV. In our case, t_{pen} was of the order of 15 nm. Near-surface hysteresis loops were found by measuring the value of the transverse Kerr effect (TKE) $\delta = (I - I_0)/I_0$, where I and I_0 are the intensities of light reflected from the magnetized and demagnetized samples, respectively. Actually, the ratio $\delta(H)/\delta_S \propto M(H)/M_S$ was measured (δ_S is the value of TKE at $M = M_S$, where M_S is the saturation magnetization) under cyclic variation of the external magnetic field (from $+H$ to $-H$ and from $-H$ to $+H$), which was applied parallel to the sample surface and perpendicular to the plane of incidence of light. The spectral response of TKE was measured in the range of incident-photon energies 1.5 eV $< \hbar\omega <$ 6.0 eV. The angle of incidence of light on the sample was 65°. All measurements were performed at room temperature.

3. EXPERIMENTAL RESULTS AND DISCUSSION

Volume and near-surface hysteresis loops for all Ni films to be studied were measured with a vibrating-sample and magnetooptical magnetometer. The measurements were performed for the case where an external in-plane magnetic field **H** was directed either parallel or perpendicular (these two directions will be referred to as D_1 and D_2, respectively) to the direction in which a magnetic field was applied during the film deposition.

It was found that both surface and volume hysteresis loops of as-deposited nickel films and of films annealed at 300°C are close to rectangular in shape when measured in a field applied along the direction D_1 and are inclined when measured in a field applied along the direction D_2. No such difference in the magnetic properties was observed for films annealed at 400 and 500°C. Figures 1 and 2 illustrate the case with hysteresis loops obtained for an as-deposited nickel film and a film annealed at T_{ann} = 400°C (the film thicknesses are 200 nm). The near-surface and volume values of the coercivity H_C and of the reduced remanent magnetization M_R/M_S of Ni films are plotted in Figs. 3 and 4 as a function of film thickness.

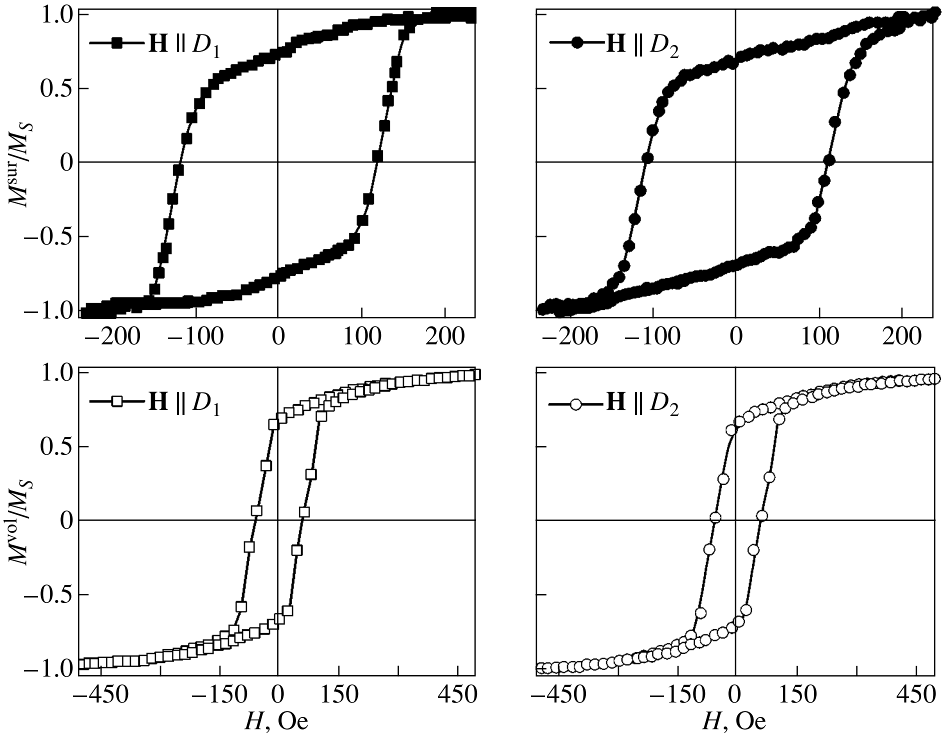

Fig. 2. Same as in Fig. 1 but for a 200-nm-thick Ni film annealed at T_{ann} = 400°C.

The difference in the shape of the hysteresis loops observed for as-deposited nickel films and films annealed at 300°C demonstrates the presence of in-plane magnetic anisotropy, which is presently believed (see, e.g., [19]) to be induced by the application of a magnetic field H_{sub} in the process of film deposition. It is known [19] that, for thin single-domain magnetic films with the easy magnetization axis (EMA) lying in the film plane, square hysteresis loops are observed in a field parallel to the EMA, whereas in a perpendicular field hysteresis is absent and the coercivity and remanent magnetization are zero. Bitter-pattern microscopy established the Ni films under study to be multidomain type. As a result, for as-deposited nickel films and films annealed at 300°C, hysteresis loops in a field along the direction D_1 (parallel to H_{sub}) are close to rectangular in shape (the reduced remanent magnetization is $M_R^{\mathrm{sur}}/M_S \sim 0.94$–$0.97$, $M_R^{\mathrm{vol}}/M_S \sim 0.9$), while in the case where the field is applied along the direction D_2 the loops are inclined and have a nonzero coercivity. An analysis of the dependences of the near-surface and volume coercivity H_C and of the reduced remanent magnetization M_R/M_S on the Ni film thickness revealed that, for all the films under study, the coercivity increases with the Ni film thickness t_{Ni}. When measured in a field applied along the direction D_1, the reduced remanent magnetization of the as-deposited films and films annealed at 300°C is practically independent of t_{Ni}. For a series of Ni samples annealed at 400 and 500°C, both the near-surface and volume reduced remanent magnetizations decrease with increasing film thickness and the volume values M_R^{vol}/M_S measured along the directions D_1 and D_2 are the same, while the surface values are different. Thus, annealing of nickel films at T_{ann} = 400 and 500°C makes them isotropic and magnetically harder. Finally, Figs. 3 and 4 suggest that the near-surface and volume values of H_C and M_R/M_S are different for all samples, with $H_C^{\mathrm{sur}} > H_C^{\mathrm{vol}}$ and $M_R^{\mathrm{sur}}/M_S > M_R^{\mathrm{vol}}/M_S$. These relations between the near-surface and volume values of H_C and M_R/M_S are known [19] to be characteristic of 50- to 200-nm-thick magnetic films. By analogy with available data [19], this observation may be attributed to the domain structures of the near-surface layer and of the film volume being different.

Microstructural studies of Ni films can be used to explain the observed increase in coercivity H_C with an increase in the thickness t_{Ni} and in the annealing temperature. It is currently known that the behavior of thin films with the application of a magnetic field depends primarily on the size of the crystallites making up the film and on their crystallographic orientation. It was found that all the films studied have a polycrystalline structure with crystallites comparable in size to the film thickness. X-ray diffraction patterns obtained for our films revealed only {111} lines, which shows the grains to be predominantly (111) oriented parallel to the sample surface. It was also observed that the {111} line

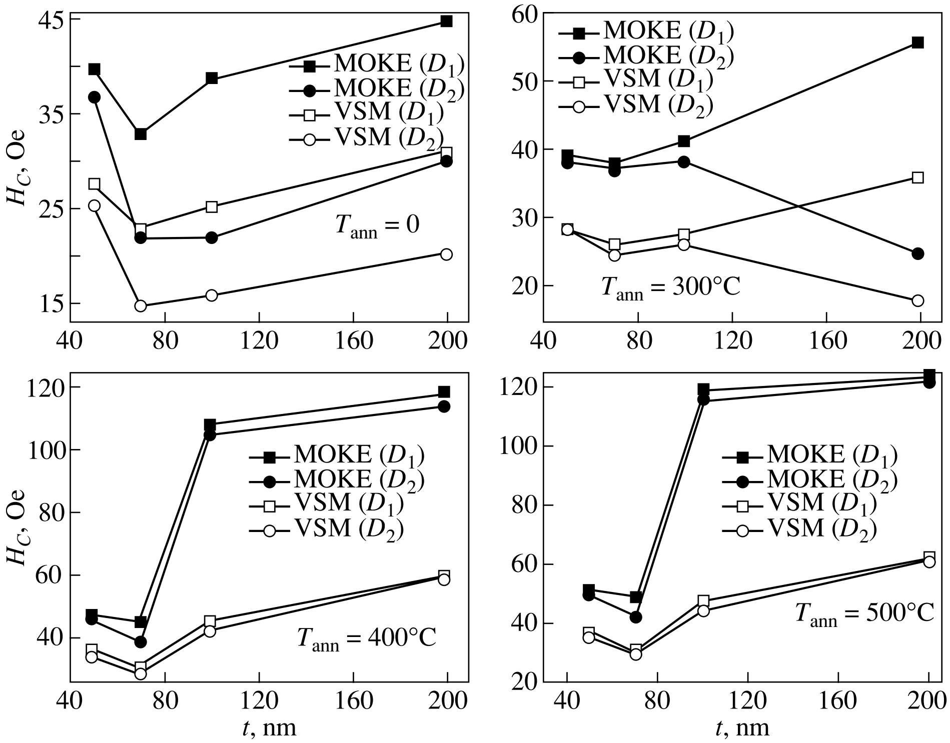

Fig. 3. Near-surface and volume coercivity H_C plotted as a function of film thickness for as-deposited and annealed Ni films.

intensity increases with annealing temperature (see table), which should be assigned [20] to the sample texture becoming more pronounced.

It was shown in [20] that, in more strongly (111)-textured samples (with other conditions, for example, the thickness and composition, being equal), the coercivity increases. Furthermore, in accordance with the data from [12, 13], the coercivity H_C increases as the thickness of the magnetic films increases, which was attributed to the growth in grain size in the film volume. We did indeed observe such a correlation between the magnetic and microstructural properties of Ni films.

The increase in the near-surface values H_C^{sur} and, hence, in the volume values H_C^{vol} with an increase in the annealing temperature can also be accounted for by the increased surface roughness of the annealed samples, which is supported by our atomic-force microscope data. For example, the average roughness of an as-deposited film and films annealed at 300, 400, and 500°C (film thickness 70 nm) is 0.45, 0.53, 0.68, and 0.72 nm, respectively, and the maximum roughness is 0.65, 1.00, 1.07, and 1.12 nm, respectively.

Figure 5 displays the dependence of TKE on the incident-photon energy $\hbar\omega$ measured for our nickel films at $H > H_S$, where H_S is the saturation field for the sample under study. We readily see that the $\delta(\hbar\omega)$ curves are similar in shape for all the films under investigation; for films of the same series, the magnitude of the TKE does not depend on the sample thickness, which (considering the above description of the magnetooptical techniques used) is due to the fact that the thickness of our films is $t_{\text{Ni}} > t_{\text{pen}}$. The maximum value of TKE, $\delta^{\max}$, is observed at around $\hbar\omega = 3.7$ eV for all samples. The values of $\delta^{\max}$ are 4.6×10^{-3}, 3.9×10^{-3}, 3.6×10^{-3}, and 3.2×10^{-3} for as-deposited nickel films and films annealed at 300, 400, and 500°C, respectively. The value of TKE is seen to decrease with increasing annealing temperature. The following explanation can be given for this observation. According to the measurements made with the vibrating-sample magnetometer, the saturation magnetization M_S of nickel films annealed at 300, 400, and 500°C decreases by a factor of approximately 1.2, 1.3, and 1.4, respectively, as compared to M_S of the as-deposited films. The ratio of the maximum values of TKE, $\delta^{\max}$, for the

{111} line intensity observed with as-deposited and annealed films

t_{Ni}, nm	T_{ann}, °C			
	0	300	400	500
50	48	152	2130	3040
70	180	2280	2400	3488
100	260	3600	3680	3980
200	1808	3760	4800	5640

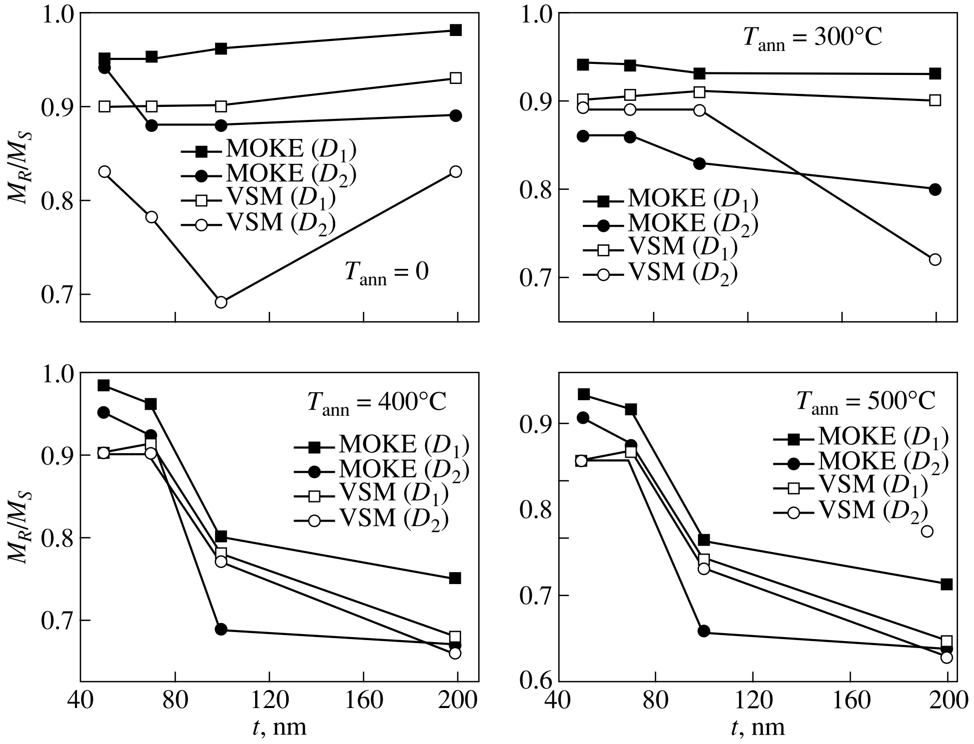

Fig. 4. Near-surface and volume remanence plotted as a function of film thickness for as-deposited and annealed Ni films.

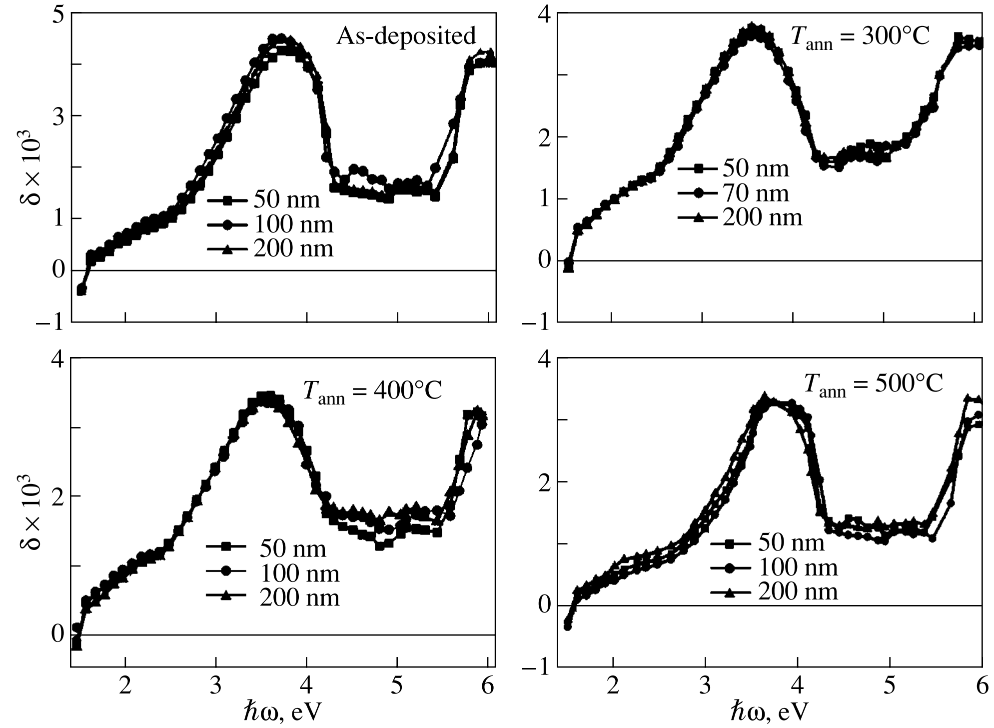

Fig. 5. Dependences of TKE on the incident-photon energy obtained for as-deposited and annealed Ni films.

annealed and as-deposited films is practically the same. It is known that the magnetooptical effects scale linearly, in a first approximation, with magnetization ($\delta \propto M$). Thus, it may be conjectured that the decrease in TKE in annealed samples is caused by the decrease in M_S.

4. CONCLUSIONS

We have studied the effect of annealing temperature on the magnetic and magnetooptical properties of 50- to 200-nm-thick Ni films. We observed a noticeable increase in coercivity in the films with increasing annealing temperature. The observed variations in the magnetic properties with the film thickness and annealing temperature correlate well with the microstructural changes in the samples. The magnitude of the TKE has been found to decrease with increasing annealing temperature. This change in the TKE was shown to be due to the decrease in the saturation magnetization M_S in annealed films. The experimental data obtained can be applied to advantage in the development of multilayer systems for spintronic devices.

ACKNOWLEDGMENTS

This study was supported by the Russian Foundation for Basic Research, project no. 02-02-16627.

REFERENCES

1. M. Xu, T. M. Liakopoulos, C. H. Ahn, S. H. Han, and H. J. Kim, IEEE Trans. Magn. **34** (4), 1369 (1998).
2. K. H. Shin, M. Inoue, and K. I. Arai, Smart Mater. Struct. **9**, 357 (2000).
3. I. Fergen, K. Seemann, A. V. D. Weth, and A. Schüppen, J. Magn. Magn. Mater. **242–245**, 146 (2002).
4. Y. M. H. Kryder, Thin Solid Films **216** (1), 174 (1992).
5. H. Kanai, K. Yamada, K. Aoshima, Y. Ohtsuka, J. Kane, M. Kanamine, J. Toda, and Y. Mizoshita, IEEE Trans. Magn. **32** (5), 3368 (1996).
6. Z. Wang and Y. Nakamura, J. Appl. Phys. **79** (8), 6639 (1996).
7. H. Lessoff and D. C. Webb, Thin Solid Films **39**, 185 (1976).
8. H. D. Buckley, Prog. Surf. Sci. **12**, 1 (1982).
9. *Proceedings of International Magnetic Conference*; IEEE Trans. Magn. **35**, 2517 (1999); **35**, 2520 (1999); **35**, 2628 (1999); **35**, 2643 (1999); **35**, 2661 (1999); **35**, 2667 (1999).
10. E. E. Shalygina, A. A. Korendyasev, and L. V. Kozlovskiĭ, Pis’ma Zh. Tekh. Fiz. **22** (3), 63 (1996) [Tech. Phys. Lett. **22**, 120 (1996)].
11. E. E. Shalyguina, N. I. Tsidaeva, S. Khudaykova, R. Iskhakov, and J. Moroz, J. Magn. Soc. Jpn. **21** (Suppl. S2), 181 (1997).
12. J. A. Barnard, M. Tan, A. Waknis, and E. Haftek, J. Appl. Phys. **69**, 5298 (1991).
13. E. E. Shalyguina and K. H. Shin, J. Magn. Magn. Mater. **220**, 167 (2000).
14. C. Y. Shin, C. L. Bauer, and J. O. Artman, J. Appl. Phys. **64** (10), 5428 (1988).
15. T. Otiti, G. A. Niklasson, P. Svedlindh, and C. G. Granqvist, Thin Solid Films **307**, 247 (1997).
16. Y. V. Kudryavtsev, V. V. Nemoshkalenko, Y. P. Lee, K. W. Kim, C. G. Kim, and B. Szymanski, J. Appl. Phys. **88** (5), 2430 (2000).
17. O. Kohmoto, N. Mineji, Y. Isagawa, F. Ono, and O. Kubo, J. Magn. Magn. Mater. **239**, 36 (2000).
18. E. E. Shalygina, V. V. Molokanov, and M. A. Komarova, Zh. Éksp. Teor. Fiz. **122** (3), 593 (2002) [Sov. Phys. JETP **95**, 511 (2002)].
19. G. S. Krinchik, *Physics of Magnetic Phenomena* (Mosk. Gos. Univ., Moscow, 1985) [in Russian].
20. C. J. Lin, G. L. Gorman, C. H. Lee, R. F. C. Farrow, E. E. Marinero, H. V. Do, and H. Notarys, J. Magn. Magn. Mater. **93**, 194 (1991).

Translated by G. Skrebtsov

Physics of the Solid State, Vol. 47, No. 4, 2005, pp. 690–696. Translated from Fizika Tverdogo Tela, Vol. 47, No. 4, 2005, pp. 666–672.
Original Russian Text Copyright © 2005 by Kalita, Loktev.

MAGNETISM AND FERROELECTRICITY

Temperature-Induced Magnetic Phase Transitions in Crystals with Competing Single-Ion and Interionic Magnetic Anisotropies

V. M. Kalita* and V. M. Loktev**
**Institute of Physics, National Academy of Sciences of Ukraine, pr. Nauki 144, Kiev, 03028 Ukraine*
***Institute of Theoretical Physics, National Academy of Sciences of Ukraine, Kiev, 03143 Ukraine*
e-mail: vloktev@bitp.kiev.ua

Received August 28, 2004

Abstract—Temperature-induced phase transitions in a uniaxial ferromagnetic system of spins $S = 1$ with competing one-particle and two-particle anisotropies are studied. It is shown that, in the case where easy-plane single-ion anisotropy dominates over easy-axis two-particle anisotropy, the transition from the paramagnetic state to a ferromagnetic state with magnetization perpendicular to the anisotropy axis is a second-order displacive magnetic phase transition. In the opposite case, where two-particle anisotropy dominates over single-particle anisotropy, the transition to a ferromagnetic state with magnetization perpendicular to the anisotropy axis is also continuous but of the order–disorder type. In a system with competing second-order one- and two-particle anisotropies, the orientational first-order phase transition can occur to a state with the magnetization directed along or perpendicular to the anisotropy axis. *© 2005 Pleiades Publishing, Inc.*

1. INTRODUCTION

Orientational magnetic phase transitions (PTs) can be induced by an external magnetic field or temperature. An example is the Morin transition in hematite α-Fe_2O_3, during which, as the temperature lowers, the Fe^{3+} spins switch from the orientation along the easy axis (the symmetry axis of the uniaxial crystal) to the orientation in the easy plane perpendicular to this axis (which becomes the hard axis) [1, 2]. It is this type of orientational PT that is discussed in this paper. Phenomenologically, this transition is explained by the fact that, at a certain temperature T_M (the Morin temperature), the anisotropy constant changes sign.

The mechanism of an orientational PT will be different if the anisotropy is a sum of anisotropies having different order and constants that differ in sign. Taking into account the fact that the temperature dependences of the anisotropy constants are different [3], we find that there is one temperature range over which the anisotropy of one order dominates over the anisotropy of the other order and a second temperature range over which the reverse is true.

This phenomenological approach ignores the fact that there are different types and mechanisms of formation of anisotropy. In monograph [4], two fundamentally different types of anisotropy are discussed in detail: the spin–spin interaction anisotropy and single-particle (single-ion) anisotropy (SIA) due to the combined effect of the crystal field exerted on the magnetic ions and the spin–orbit coupling. The thermodynamic average of the product of spin-operator projections of two neighbor ions and the thermodynamic average of the product of spin-operator projections of the same order but taken for one ion vary differently with temperature [4]. Therefore, it may be suggested that an orientational PT can occur even in a model that includes only second-order anisotropic interactions but properly takes into account the difference between the single-ion and interionic-interaction anisotropies. We note that, phenomenologically, this change in the orientation of magnetization is analogous to that caused by a change in the sign of the anisotropy constant.

Competing anisotropies are also of importance for another reason. It was shown in [5] that, in a uniaxial ferromagnet with easy-axis SIA, the transition from the paramagnetic (singlet) state to a ferromagnetic (FM) state is a displacive magnetic PT. The main distinction of this transition from conventional order–disorder PTs is that the magnetization occurs due to the nondegenerate ionic states being polarized spontaneously at the PT point.

Note that easy-plane magnets with an integer spin and SIA are typically Van Vleck systems [6]; the ionic states in them have no spin projection in the easy plane, with the consequence that magnetic ordering with magnetization in this plane can occur only due to admixture (polarization) of the ground state of the ions. In the case where, in addition to easy-plane SIA, there is interionic-interaction anisotropy competing with the easy-plane SIA and dominating over it, the transition from the paramagnetic to FM phase will be an order–disorder phase transition, with the magnetization directed along the easy axis. This transition is possible because the ionic-spin projection onto the easy axis has its maximum value rather than being zero.

Therefore, depending on the relationship between the constants of competing easy-plane SIA and easy-axis interionic anisotropy, the PT from the paramagnetic to a FM state can be either an order–disorder or displacive magnetic PT. In addition, an orientational PT can occur in the FM phase (the temperature of this transition will be designated as $T_{\text{EA–EP}}$).

It should be noted that the effect of competing single-ion and interionic-interaction anisotropies on the magnetization has been considered in the literature, but only in the Ising model [7, 8]. In this model (without isotropic exchange) with competing easy-plane SIA and easy-axis interionic anisotropy, magnetic ordering with spins lying in the easy plane cannot occur. However, the application of this model to the problems considered in [7, 8] is well justified.

If SIA is weak, its effect can be treated [9] using the semiclassical approximation, in which the average of the SIA operator is replaced by the corresponding combination of the spin averages. In this approximation, however, competition between anisotropies reduces to competition between the anisotropy constants; therefore, there will be no difference between the effects of single-ion and interionic anisotropies in terms of their temperature dependence. To the best of our knowledge, the above-mentioned problems involving competition between anisotropies have not been considered in the literature, although Hamiltonians with two types of anisotropy (which are experimentally observed in certain magnets) are frequently used.

In what follows, we consider a simple model of temperature-induced orientational PTs in an initially easy-axis ferromagnet with spins $S = 1$. This model includes isotropic exchange interactions and two competing (single-ion and interionic) second-order anisotropies.

2. THE MODEL HAMILTONIAN AND ITS GROUND STATE

The model Hamiltonian of an anisotropic ferromagnet is taken in the form

$$H = -\frac{J}{2}\sum_{\mathbf{n},\mathbf{m}} \mathbf{S}_{\mathbf{n}}\mathbf{S}_{\mathbf{m}} - \frac{\Delta J}{2}\sum_{\mathbf{n},\mathbf{m}} S_{\mathbf{n}}^Z S_{\mathbf{m}}^Z + D\sum_{\mathbf{n}} (S_{\mathbf{n}}^Z)^2, \quad (1)$$

where **n** and **m** label the positions of the spins and the Z axis is taken to be along the easy axis. In Eq. (1), the first term describes anisotropic exchange and the second and third terms allow for interionic and single-ion anisotropies, respectively. The SIA is assumed to be of the easy-plane type, and the interionic anisotropy, of the easy-axis type; therefore, both anisotropy constants in Eq. (1) are positive ($\Delta J > 0$, $D > 0$).

We analyze the ground state of Hamiltonian (1) in the mean-field approximation using the variational principle. Ignoring interspin fluctuations, we write the ground-state energy per magnetic ion E_{gr} in the form

$$E_{\text{gr}} = -\frac{1}{2}Jz\mathbf{s}^2 - \frac{1}{2}\Delta Jz(s^Z)^2 + DQ^{ZZ}, \quad (2)$$

where **s** is the average ionic spin in the ground state, z is the number of nearest neighbors (the pairwise interaction constants are proportional to this number, so the constants J and ΔJ are assumed to include this number), and Q^{ZZ} is the quantum-mechanical average of the square of the Z projection of the spin operator (a component of the quadrupole spin moment [10–12]).

For each spin, we introduce a local coordinate system (ξ, η, ζ), where the ζ axis is taken along the direction of the average spin and the ξ axis lies in the $Z\zeta$ plane. In this coordinate frame, as shown in [13], the wave function of the spin ground state has the form

$$\psi_{\mathbf{n}}^{(0)} = \cos\phi|1\rangle_{\mathbf{n}} + \sin\phi|-1\rangle_{\mathbf{n}}, \quad (3)$$

where $|\pm1\rangle$ and $|0\rangle$ are the eigenfunctions of the operator $S_{\mathbf{n}}^{\zeta}$ (in the bra-and-ket notation). Using Eq. (3), the average values of the spin and the components of the quadrupole moment can be calculated to be

$$s_0 = \cos 2\phi, \quad Q_0^{\zeta\zeta} = 1, \quad Q_0^{\zeta\zeta} = \frac{1}{2}(1 + \sin 2\phi), \quad (4)$$

where the subscript "0" denotes the average for a spin with wave function (3).

With Eqs. (4), energy (2) can be written as

$$\begin{aligned} E_{\text{gr}} &= -\frac{1}{2}J\cos^2 2\phi - \frac{1}{2}\Delta J\cos^2 2\phi\cos^2\theta \\ &+ D\left[\cos^2\theta + \frac{\sin^2\theta}{2}(1 + \sin 2\phi)\right], \end{aligned} \quad (5)$$

where θ is the angle between the spins and the crystallographic Z axis (or between the ζ and Z axes). Note that the wave functions that are defined in the crystallographic rather than the local coordinate system involve parameters associated with rotation of the eigenvectors $|\pm1\rangle_{\mathbf{n}}$ and $|0\rangle_{\mathbf{n}}$ in Hilbert space, which leads to a complicated relation between the observed and sought (variational) parameters.

In our approach, the orientation of the spins in different phases (depending on the values of the parameters of the Hamiltonian) at $T = 0$ can be found by minimizing energy (5) with respect to ϕ and θ, which gives the equations

$$\cos 2\phi[2(J + \Delta J\cos^2\theta)\sin 2\phi + D\sin^2\theta] = 0, \quad (6)$$

$$\cos\theta\sin\theta[\Delta J\cos^2 2\phi - D(1 - \sin 2\phi)] = 0. \quad (7)$$

Let us analyze the solutions to this set of equations. One solution is $\sin\theta = 0$ and $\sin 2\phi = 0$. In this case, the average spins are directed along the Z axis and have a maximum value of $s_0 = S = 1$. In this state, energy (2) is given by

$$E_{\rm gr}^{(\rm EA)} = -\frac{1}{2}(J + \Delta J) + D. \tag{8}$$

The other solution is $\cos\theta = 0$ and $\sin 2\phi = -D/2J$, which corresponds to the case where the spins are perpendicular to the Z axis and their value is $s_0 = \sqrt{1-(D/2J)^2}$ [9–13] (this value is less than the limiting value $S = 1$). The energy of this state is independent of ΔJ and differs substantially from Eq. (8):

$$E_{\rm gr}^{(\rm EP)} = \frac{1}{2}(-J + D) - \frac{D^2}{8J}. \tag{9}$$

There is also a third solution, $\cos 2\phi = 0$. The average spins in this state are minimum, $s_0 = 0$. This is a Van Vleck singlet (paramagnetic) state with a zero magnetization [6]. In [10–12], this phase is called the quadrupole spin state, because the difference $Q^{\xi\xi} - Q^{\eta\eta} \neq 0$ is nonzero in this state and is a limiting value. In [14], this phase is called the nematic spin state. In our opinion, the name "Van Vleck singlet magnet" is preferable. The values of the parameters of Hamiltonian (1) for which the singlet state arises are not determined in this paper.

It can be seen from Eq. (8) that, in the case where the magnetization in the ground state is parallel to the Z axis, the energy is a linear combination of the model parameters and corresponds to the semiclassical approximation. In the case where the magnetization vector in the ground state lies in the easy plane, the energy does not correspond to the semiclassical approximation, because the average spin is less than its limiting value. In this case, the energy is given by Eq. (9) and contains two terms with D. These terms in $E_{\rm gr}^{(\rm EP)}$ are opposite in sign, and one of them is a quadratic function of the SIA constant. At $T = 0$, the actual magnetic structure corresponds to the minimum value of the energy given by Eqs. (8) and (9). In the case of $T \neq 0$, the equilibrium states are determined by the free energy and the behavior of the system can be more complicated.

3. THE FREE ENERGY OF A UNIAXIAL FERROMAGNET

In order to find the thermodynamically equilibrium states of Hamiltonian (1) at $T \neq 0$, we have to take into account the populations of all single-ion states. At $T = 0$, we chose the quantization axis to be along the direction of the average spin in the ground state of ions. Now, it is convenient to take the quantization axis to be along the magnetization vector of the ferromagnet. In this case, according to [13], the wave function of the ground state of the uniaxial ferromagnet is given by Eq. (3) and the wave functions of excited single-ion states are

$$\psi_{\mathbf{n}}^{(1)} = |0\rangle_{\mathbf{n}}; \quad \psi_{\mathbf{n}}^{(2)} = -\sin\phi|1\rangle_{\mathbf{n}} + \cos\phi|-1\rangle_{\mathbf{n}}. \tag{10}$$

Using Eqs. (3) and (10), we can calculate the expectation values in the single-ion states denoted by superscripts 0, 1, and 2: the partial values of the spin projection onto the quantization axis are $s^{(0)} = -s^{(2)} = \cos 2\phi$ and $s^{(1)} = 0$; the partial averages of the operator $(S^\zeta)^2$ are 1, 0, and 1, respectively; and the averages of the operator $(S^\xi)^2$ are $(1 + \sin 2\phi)/2$, 1, and $(1 - \sin 2\phi)/2$, respectively.

The thermodynamic average of the spin (the magnitude of the average magnetization **m**) and the average $\langle S^Z\rangle_T^2$ can be found to be

$$m = 2\Delta p\cos 2\phi, \tag{11}$$

$$\langle S^Z\rangle_T^2 = 2p\cos^2\theta + (1 - p + \Delta p\sin 2\phi)\sin^2\theta. \tag{12}$$

Here, $\Delta p = (p^{(0)} - p^{(2)})/2$ and $p = (p^{(0)} + p^{(2)})/2$, where $p^{(0)}$ and $p^{(2)}$ are the probabilities of an ion being in states (10) with a nonzero projection of the spin onto the quantization axis.

By definition, the free energy is $F = E - TS_{\rm en}$, where E is the internal energy and $S_{\rm en}$ is the entropy, which is configurational if intersite fluctuations are neglected.

The internal energy per particle of the system with Hamiltonian (1) can be written as

$$E = -\frac{1}{2}J\mathbf{m}^2 - \frac{1}{2}\Delta J(m^Z)^2 + D\langle S^Z\rangle^2, \tag{13}$$

and the entropy is given by

$$S_{\rm en} = -\sum_{j=0,1,2} p^{(j)}\ln p^{(j)}, \tag{14}$$

where $p^{(j)}$ are the probabilities of an ion being in states (10), which satisfy the obvious condition $\sum_{j=0,1,2} p^{(j)} = 1$.

Using the notation introduced in Eqs. (11) and (12), the entropy can be written as

$$\begin{aligned} S_{\rm en} &= -(p + \Delta p)\ln(p + \Delta p) \\ &- (p - \Delta p)\ln(p - \Delta p) - (1 - 2p)\ln(1 - 2p) \end{aligned} \tag{15}$$

and the free energy of the system with Hamiltonian (1) takes the form

$$\begin{aligned} F &= -2(J + \Delta J\cos^2\theta)(\Delta p)^2\cos^2 2\phi \\ &+ D[2p\cos^2\theta + (1 - p + \Delta p\sin 2\phi)\sin^2\theta] \\ &+ T[(p + \Delta p)\ln(p + \Delta p) - (p - \Delta p)\ln(p - \Delta p) \\ &- (1 - 2p)\ln(1 - 2p)]. \end{aligned} \tag{16}$$

Thermodynamically equilibrium states can be found by minimizing the free energy (16). The variational parameters are the angle ϕ, which defines the value of the polarization of the single-ion states; the angle θ, which defines the direction of the average magnetization; and p and Δp, which determine the populations of the polarized states. By equating the derivatives of expression (16) with respect to these parameters to zero, we obtain the equations of state

$$\frac{\partial F}{\partial \phi} = 2\cos 2\phi[4(J+\Delta J\cos^2\theta)\Delta p\sin 2\phi + D\sin^2\theta]\Delta p = 0, \tag{17}$$

$$\frac{\partial F}{\partial \theta} = 2\cos\theta\sin\theta[2\Delta J(\Delta p)^2\cos^2 2\phi + D(1-3p+\Delta p\sin 2\phi)] = 0, \tag{18}$$

$$\frac{\partial F}{\partial \Delta p} = -4(J+\Delta J\cos^2\theta)\Delta p\sin^2 2\phi + D\sin 2\phi\sin^2\theta + T\ln\frac{p+\Delta p}{p-\Delta p} = 0, \tag{19}$$

$$\frac{\partial F}{\partial p} = D(2\cos^2\theta - \sin^2\theta) + T\ln\frac{p^2-(\Delta p)^2}{(1-2p)^2} = 0. \tag{20}$$

Thus, in contrast to the results obtained in [4, 7, 8], Eq. (16) for the free energy and equations of state (17) and (18) make it possible to determine the polarization of the ionic states in singlet magnets.

4. PHASE TRANSITIONS AT $T \neq 0$

At finite temperatures, as well as at $T = 0$, the state with the magnetization directed along the Z axis corresponds to the solution $\sin\theta = 0$ and $\sin 2\phi = 0$ and the parameters Δp and p are determined from the equations

$$-4(J+\Delta J)\Delta p + T\ln\frac{p+\Delta p}{p-\Delta p} = 0, \tag{21}$$

$$2D + T\ln\frac{p^2-(\Delta p)^2}{(1-2p)^2} = 0. \tag{22}$$

In this case, the spin polarization in the single-ion states is maximum and the spin projections have their extreme values ±1. The magnetization vector is directed along the easy axis, and its magnitude is determined only by the difference between the populations of the energy levels, $m = 2\Delta p$. Therefore, during the PT from the paramagnetic phase to a FM state with the magnetization directed along the easy axis, a spontaneously arising exchange field causes only a change in the populations of the single-ion levels. This PT is of the order–disorder type.

In the paramagnetic phase, the population of the lowest singlet state (with a zero average spin projection onto the quantization axis) is higher than the populations of the single-ion states with the extreme values of the average spin projection. At the PT point, the doublet splits spontaneously, whereas the energy of the singlet state remains unchanged; near $T_C^{(\mathrm{EA})}$, the singlet state remains the ground state of the ions. Only as one goes away from $T_C^{(\mathrm{EA})}$ does a crossing of single-ion states occur.

In the easy-plane FM state, we have $\cos\theta = 0$ and $\sin 2\phi = -D/4J\Delta p$ and the parameters p and Δp satisfy the equations

$$-4J\Delta p + T\ln\frac{p+\Delta p}{p-\Delta p} = 0, \tag{23}$$

$$-D + T\ln\frac{p^2-(\Delta p)^2}{(1-2p)^2} = 0. \tag{24}$$

In this phase, the average spin projection is $s = \cos 2\phi = \sqrt{1-D^2/(4J\Delta p)^2}$ (which is not the maximum possible value). As the temperature increases, Δp decreases and, therefore, the polarization of the single-ion states decreases. The PT to a paramagnetic state occurs at a temperature $T = T_C^{(\mathrm{EP})}$ at which the polarization is zero in all single-ion states, i.e., $s(T_C^{(\mathrm{EP})}) = 0$. Note that now the quantization axis lies in the easy plane and, in contrast to the case of an easy-axis ferromagnet, the spin projection onto the quantization axis perpendicular to the crystal axis is considered.

Thus, the formation of the easy-plane FM phase is associated with an exchange field that arises in the plane perpendicular to the crystal axis and polarizes the single-ion states. Therefore, the PT from the paramagnetic to an easy-plane FM state is a displacive magnetic PT [5]. In this case, only the lowest ionic energy level is polarized and, hence, no crossing of the single-ion levels occurs in the easy-plane ferromagnet.

The polarization causes a change in the magnetization. In the easy-plane FM phase, the magnetization is $m = 2\sqrt{\Delta p^2 - D^2/(4J)^2}$, where Δp satisfies Eqs. (23) and (24).

The temperature $T_C^{(\mathrm{EA})}$ of the transition from the paramagnetic to the easy-axis FM phase can be found from the transcendent equation

$$2T_C^{(\mathrm{EA})} - 2(J+\Delta J) + T_C^{(\mathrm{EA})}\exp(D/T_C^{(\mathrm{EA})}) = 0, \tag{25}$$

and the temperature $T_C^{(\mathrm{EP})}$ of the transition from the paramagnetic to the easy-plane FM phase is given by [4]

$$T_C^{(\mathrm{EP})} = \frac{D}{\ln(1+D/J) - \ln(1-D/2J)}. \tag{26}$$

The transition from the paramagnetic to the easy-axis FM state occurs if $T_C^{(\mathrm{EA})} > T_C^{(\mathrm{EP})}$. Otherwise, the system undergoes a transition from the paramagnetic to the easy-plane FM state. However, in the case where

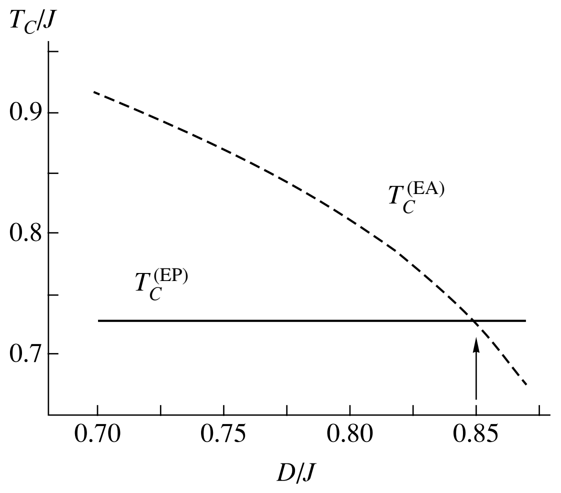

Fig. 1. Dependences of the critical temperatures $T_C^{(\mathrm{EP})}$ and $T_C^{(\mathrm{EA})}$ for the transitions from the paramagnetic to the easy-plane and easy-axis FM phases, respectively, on the ratio between the single-ion anisotropy and exchange constants, D/J.

$T_C^{(\mathrm{EA})} > T_C^{(\mathrm{EP})}$, the easy-axis phase may become unstable as $T \longrightarrow 0$.

Indeed, in the case of weak anisotropies, $D/J \ll 1$ and $\Delta J/J \ll 1$, the critical temperatures are given by

$$T_C^{(\mathrm{EA})} = \frac{2}{3}J\left(1 + \frac{\Delta J}{J} - \frac{D}{2J} - \frac{3}{8}\frac{D^2}{J^2}\right), \tag{27}$$

$$T_C^{(\mathrm{EP})} = \frac{2}{3}J\left(1 + \frac{D}{4J} - \frac{3}{16}\frac{D^2}{J^2}\right). \tag{28}$$

It follows that $T_C^{(\mathrm{EA})} > T_C^{(\mathrm{EP})}$ if $\Delta J > \frac{3}{4}D\left(1 + \frac{D}{4J}\right)$. However, according to Eqs. (8) and (9) for the energies of the ground state, the easy-axis FM phase is stable at larger values of the interionic anisotropy constant, $\Delta J > D\left(1 + \frac{D}{4J}\right)$. Therefore, for values of the interionic anisotropy constant lying in the range

$$\frac{3}{4} + \frac{3D}{16J} < \frac{\Delta J}{D} < 1 + \frac{D}{4J} \tag{29}$$

the critical temperature for the transition to the easy-axis FM phase is higher than that for the transition to the easy-plane FM phase but the latter phase is more stable at $T = 0$. It follows that, if the anisotropy constants satisfy inequalities (29), then, at a certain finite temperature $T_{\mathrm{EA-EP}}$, the orientational PT will occur from the easy-axis FM phase to the easy-plane FM phase. Since it is very difficult to calculate this temperature analytically, we determine $T_{\mathrm{EA-EP}}$ for certain fixed (not small) values of the anisotropy constants in what follows.

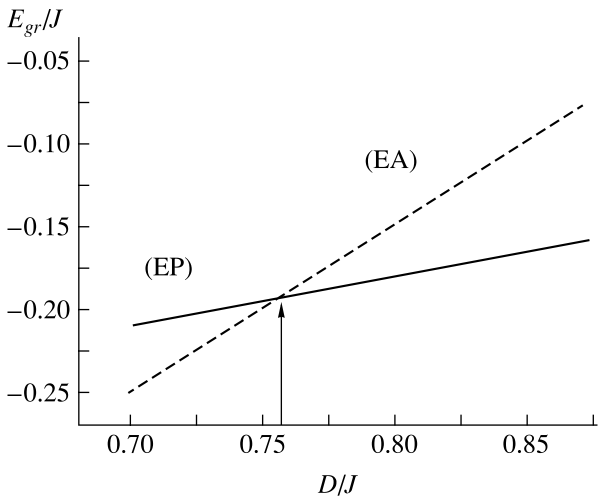

Fig. 2. Dependence of the ground-state energy E_{gr}/J of a ferromagnet on the ratio between the single-ion anisotropy and exchange constants, D/J, for the case where the magnetization vector either lies in the easy plane (solid line) or is directed along the easy axis (dashed line).

Figure 1 shows the dependences of $T_C^{(\mathrm{EA})}$ and $T_C^{(\mathrm{EP})}$ on the SIA constant. It can be seen that the temperature $T_C^{(\mathrm{EP})}$ (solid line) is almost constant in the region of $D/J \approx 0.8$. This behavior can be explained as follows. For an isotropic ferromagnet, we have $T_C = 2J/3$. With inclusion of SIA with $D > 0$, as can be seen from Eq. (28), the temperature $T_C^{(\mathrm{EP})}$ first increases insignificantly (up to $T_C^{(\mathrm{EP})} \sim 0.728J$) with increasing D up to $D/J \approx 0.8$. As the quantity D/J increases further, $T_C^{(\mathrm{EP})}$ begins to decrease slowly and then, as $D/2J \longrightarrow 2$, the temperature $T_C^{(\mathrm{EP})}$ falls off sharply to zero. This behavior is due to the logarithmic dependence of expression (26). In Fig. 1, $T_C^{(\mathrm{EP})}$ is plotted near the maximum in a small range of D/J values, so it remains almost unchanged.

The temperature $T_C^{(\mathrm{EA})}$ of the transition to the easy-axis FM phase is shown by the dashed line in Fig. 1 for the interionic anisotropy constant $\Delta J/J = 0.9$. Up to $D/J \approx 0.85$, we have $T_C^{(\mathrm{EA})} > T_C^{(\mathrm{EP})}$, and then the inequality is reversed.

Figure 2 shows the energy of the ground state (at $T = 0$) as a function of the SIA constant for the easy-plane FM phase (solid line) and the easy-axis FM phase (dashed line) for $\Delta J = 0.9J$. It can be seen that, at $D/J < 0.75$, the energy of the latter phase is lower than the

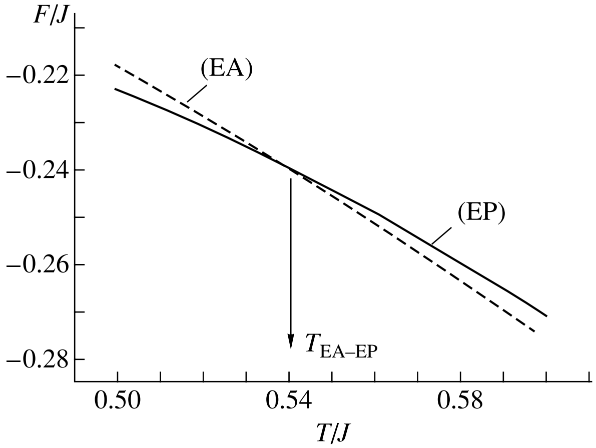

Fig. 3. Dependences of the free energy F/J on temperature T/J for the easy-axis and easy-plane FM phases.

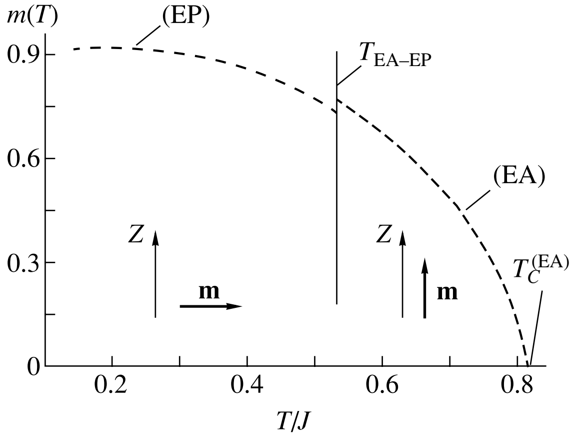

Fig. 4. Temperature dependence of the magnetization $m(T)$ near the orientational phase transition point.

energy of the former phase; in the range $0.75 < D/J < 0.85$, the easy-axis FM phase becomes unstable.

The temperature $T_{\text{EA–EP}}$ can be determined by equating the free energies of these phases. The temperature dependences of the free energies can be found by substituting the solutions to Eqs. (21)–(24) into Eq. (16) and are shown in Fig. 3 in the region in which their plots intersect. The model parameters are taken to be $\Delta J = 0.9J$ and $D = 0.8J$. The plots for the easy-axis FM phase (dashed line) and the easy-plane FM phase (solid line) in Fig. 3 cross at the point corresponding to $T_{\text{EA–EP}} \approx 0.54J$. At $T < T_{\text{EA–EP}}$, the easy-axis FM phase with the magnetization directed along the Z axis has a higher free energy. At $T > T_{\text{EA–EP}}$, on the contrary, the free energy of the easy-axis FM phase is lower than that of the easy-plane FM phase. Thus, for the model parameters indicated above, the order–disorder PT of the second order from the paramagnetic to the easy-axis FM phase occurs at the point $T_C^{(\text{EA})} = 0.825J$ and the orientational PT from the easy-axis to easy-plane FM phase occurs at $T_{\text{EA–EP}} = 0.54J$. This orientational PT is of the order–disorder type.

In the example considered above, the temperature of the orientational PT $T_{\text{EA–EP}}$ is much less than $T_C^{(\text{EA})}$. Therefore, although the direction of the magnetization vector is switched, its magnitude varies insignificantly. Figure 4 shows the temperature dependence of the magnetization in both FM phases calculated for the same parameters as those in Fig. 3. The temperature dependence for the high-temperature easy-axis phase (with the magnetization directed along the Z axis) is shown by the dashed curve, and the temperature dependence for the easy-plane phase (arising after the orientational PT) is shown by the dotted curve. It can be seen from Fig. 4 that the change in the magnitude of the magnetization caused by the PT is very small. Obviously, this is due to the fact that the change in the free energy of these phases near $T_{\text{EA–EP}}$ is also small (a few percent).

5. CONCLUSIONS

It has been shown that, in a magnetic system with competing easy-plane single-ion anisotropy and easy-axis interionic interaction anisotropy, two types of PTs to the ordered FM state can occur. A magnetic order–disorder PT occurs in the case where easy-axis anisotropy dominates over single-ion anisotropy. In this case, the single-ion spin states have the extreme values of the spin projection onto the direction of the spontaneous magnetization, which coincides with the anisotropy axis. If single-ion anisotropy dominates over interionic anisotropy, the spontaneous magnetization vector lies in the easy plane. In this direction in the paramagnetic state, the single-ion spin states are unpolarized (the spin projections of all ionic states are zero); spontaneous magnetization will arise if the single-ion states become polarized at the PT point. This PT to the FM phase with the magnetization perpendicular to the anisotropy axis is a displacive magnetic PT.

It has also been shown that, in a ferromagnet with competing interionic-interaction and single-ion anisotropies, a first-order orientational PT from the easy-axis to the easy-plane FM phase can occur with a variation in temperature. In this case, both anisotropies are second-order and the anisotropy constants are temperature-independent. The anisotropies cancel each other at the PT point, because the temperature dependences of their contributions to the free energy are different. Phenomenologically, this orientational PT in a uniaxial ferromagnet is due to the second-order anisotropy constant changing sign at a certain temperature and is closely analogous to the Morin transition. However, it should be noted that, in the case of two competing anisotropies, the easy-axis FM phase forms through conventional ordering, whereas in the easy-plane phase quantum processes of polarization of the single-ion states occur.

ACKNOWLEDGMENTS

The authors are grateful to S.M. Ryabchenko and those who participated in the seminar organized by him for discussions and helpful remarks.

This study was supported in part by the Ministry of Education and Science of Ukraine, grant no. F7/514-2001.

REFERENCES

1. V. I. Ozhogin, Zh. Éksp. Teor. Fiz. **54** (1), 96 (1968) [Sov. Phys. JETP **27**, 54 (1968)].
2. V. I. Ozhogin, Zh. Éksp. Teor. Fiz. **55** (5), 1735 (1968) [Sov. Phys. JETP **28**, 915 (1969)].
3. K. P. Belov, M. A. Belyanchikova, R. Z. Levitin, and S. A. Nikitin, *Rare-Earth Ferro- and Antiferromagnets* (Nauka, Moscow, 1965) [in Russian].
4. A. K. Zvezdin, V. M. Matveev, A. A. Mukhin, and A. I. Popov, *Rare-Earth Ions in Magnetically Ordered Crystals* (Nauka, Moscow, 1985) [in Russian].
5. V. M. Kalita and V. M. Loktev, Fiz. Tverd. Tela (St. Petersburg) **45** (8), 1450 (2003) [Phys. Solid State **45**, 1523 (2003)].
6. J. H. van Vleck, *Theory of Electric and Magnetic Susceptibilities* (Oxford Univ. Press, Oxford, 1932).
7. H. W. Capiel, Physica (Amsterdam) **32** (5), 966 (1966); Physica (Amsterdam) **33** (2), 295 (1967).
8. M. Blume, V. J. Emery, and R. B. Griffiths, Phys. Rev. A **4**, 1071 (1971).
9. V. S. Ostrovskii and E. Petrov, Phys. Status Solidi B **71**, 369 (1975).
10. F. P. Onufrieva, Zh. Éksp. Teor. Fiz. **89** (12), 2270 (1985) [Sov. Phys. JETP **62**, 1311 (1985)].
11. Yu. N. Mitsaĭ, A. N. Maĭorova, and Yu. A. Fridman, Fiz. Tverd. Tela (St. Petersburg) **34** (1), 66 (1992) [Sov. Phys. Solid State **34**, 34 (1992)].
12. V. V. Val'kov and G. N. Matsuleva, Preprint No. 645F, IF SO AN SSSR (Inst. of Physics, Siberian Division, USSR Academy of Sciences, Novosibirsk, 1987).
13. V. M. Loktev and V. S. Ostrovskiĭ, Fiz. Nizk. Temp. **20** (10), 983 (1994) [Low Temp. Phys. **20**, 775 (1994)].
14. A. F. Andreev and I. A. Grishchuk, Zh. Éksp. Teor. Fiz. **87** (8), 467 (1984) [Sov. Phys. JETP **60**, 267 (1984)].

Translated by Yu. Epifanov

Physics of the Solid State, Vol. 47, No. 4, 2005, pp. 697–702. Translated from Fizika Tverdogo Tela, Vol. 47, No. 4, 2005, pp. 673–678.
Original Russian Text Copyright © 2005 by Zakharov, Kukushkin, Osipov.

MAGNETISM AND FERROELECTRICITY

Theory of Switching of Multiaxial Ferroelectrics (the Main Stages)

M. A. Zakharov*, S. A. Kukushkin, and A. V. Osipov****

**Novgorod State University, ul. Sankt-Peterburgskaya 41, Novgorod, 173003 Russia*
***Institute of Problems of Mechanical Engineering, Russian Academy of Sciences,*
Vasil'evskiĭ Ostrov, Bol'shoĭ pr. 61, St. Petersburg, 199178 Russia
e-mail: ksa@phase.ipme.ru

Received May 17, 2004

Abstract—The kinetics of switching of multiaxial ferroelectric crystals with 180° and 90° domains under conditions of normal and layer-by-layer domain growth is studied using the multidimensional theory of first-order phase transitions. The main stages of the process of switching of a multiaxial ferroelectric are considered under the assumption that repolarized cylinder-shaped domains grow three-dimensionally. A closed set of equations describing the kinetics of switching is derived with allowance for a change in repolarization in the course of the phase transition. Equations for the time-dependent switching current are derived. The main characteristics of switching are compared qualitatively with the experimental data on barium titanate. *© 2005 Pleiades Publishing, Inc.*

1. INTRODUCTION

In this work, we continue the theoretical study made in [1] on the switching of multiaxial ferroelectric crystals. As indicated in [2, 3], the switching of ferroelectrics and related materials can be conventionally divided into three characteristic stages, as can any other first-order phase transition. The initial stage of switching of multiaxial ferroelectrics was analyzed in [1]. In this paper, we consider the main stages of switching of these ferroelectrics. It should be noted that the theory developed below is characterized by the following three important features. First, this theory is equally applicable to the formation of 180° and 90° domains. Second, we consider the general case of the three-dimensional growth of repolarized domains having two degrees of freedom, which is made possible by using the multidimensional kinetic theory [4–6]. Finally, our theory takes into account various mechanisms of domain growth, in particular, the normal and layer-by-layer mechanisms.

The paper is organized as follows. In Section 2, we consider the stage of large-scale switching of a multiaxial ferroelectric and derive the corresponding set of kinetic equations. Section 3 deals with the switching current in ferroelectric crystals. Section 4 is devoted to a comparison of theory with experimental data on barium titanate, which is a well-studied multiaxial ferroelectric.

2. KINETICS OF LARGE-SCALE SWITCHING

The kinetics of switching of multiaxial ferroelectrics under the condition of three-dimensional growth of repolarized domains is described by the two-dimensional kinetic equation [1]

$$\frac{\partial f(n,\alpha,t)}{\partial t}+\frac{\partial}{\partial n}[V_n f(n,\alpha,t)]+\frac{\partial}{\partial\alpha}[V_\alpha f(n,\alpha,t)] = \frac{\partial}{\partial n}\left[D_n\frac{\partial f(n,\alpha,t)}{\partial n}\right]+\frac{\partial}{\partial\alpha}\left[D_\alpha\frac{\partial f(n,\alpha,t)}{\partial\alpha}\right], \quad (1)$$

where $f(n, \alpha, t)$ is the two-dimensional nonequilibrium distribution function of repolarized domains over the number of unit cells and shapes of domains; n is the number of unit cells in a cylindrical domain with height H and base radius R; $\alpha = H/R$ is the characteristic ratio of the linear dimensions of a domain; $V_n = dn/dt$ and $V_\alpha = d\alpha/dt$ are growth velocities of domains in the space of the sizes and shapes of domains, respectively; and D_n and D_α are the coefficients of diffusion of repolarization nuclei in the space of the sizes and shapes of domains, respectively.

Following [1], it can be shown that the two-dimensional distribution function $f(n, \alpha, t)$ can be written in the form

$$f(n,\alpha,t) = C\exp\left(-\frac{B(\alpha-\alpha_c)^2}{k_\mathrm{B}T}\right)\varphi(n,t),$$

where $\alpha_c = 2$ is the critical value of the characteristic ratio α, k_B is the Boltzmann constant, and T is the temperature. The constant B is given by $B = 2\pi\sigma^3\omega^2/3|\Delta f|^2$, where σ is the surface tension of a domain wall, ω is the unit cell volume, and Δf is the difference between the free energies per unit cell of the medium and of a repolarization nucleus. The normalization factor C is chosen such that the distribution function $\varphi(n, t)$ is normalized to the number of domains per unit volume $N(t)$ of the crystal; i.e., $\int_0^\infty \varphi(n, t)dn = N(t)$.

In this case, the two-dimensional kinetic equation (1) reduces to the Zel'dovich one-dimensional equation for the function $\varphi(n, t)$,

$$\frac{\partial\varphi(n,t)}{\partial t} + \frac{\partial}{\partial n}[V_n\varphi(n,t)] = \frac{\partial}{\partial n}\left[D_n\frac{\partial\varphi(n,t)}{\partial n}\right] \quad (2)$$

with the initial and boundary conditions

$$\varphi(n, 0) = 0, \quad \left.\frac{\varphi(n,t)}{\varphi_{\text{eq}}(n)}\right|_{n\to 0} \longrightarrow 1,$$

$$\left.\frac{\varphi(n,t)}{\varphi_{\text{eq}}(n)}\right|_{n\to\infty} \longrightarrow 0,$$

where $\varphi_{\text{eq}}(n)$ is the known equilibrium distribution function.

Equation (2) is the continuity equation in the space of domain sizes; the corresponding flux $J(n, t)$ is the sum of two components, namely, the "hydrodynamic" flux $V_n\varphi(n, t)$ and the "fluctuation" flux $D_n\partial\varphi(n, t)/\partial n$. The former component corresponds to the change in the distribution function of repolarized domains due to their growth at a rate V_n, and the latter component describes the fluctuation change in the domain sizes.

It should be noted that, at the stage of large-scale switching, the equation of evolution (2) can be simplified, because the hydrodynamic component of the flux is dominant at this stage [2]. Therefore, we neglect the fluctuation flux and rewrite Eq. (2) in the form

$$\frac{\partial\varphi(n,t)}{\partial t} + \frac{\partial}{\partial n}[V_n\varphi(n,t)] = 0. \quad (3)$$

The repolarization of the crystal varies due to the formation of a large number of repolarization nuclei, which influence the internal electric field of the parent medium. However, the total number of unit cells, which are carriers of elementary polarization (dipole moment) p, is conserved. Therefore, following [2], kinetic equation (3) should be supplemented by the balance equation

$$J(E_0)\frac{p}{P_{10}} = \frac{d\xi}{dt} + \frac{p}{P_{10}}\int_0^\infty V_n\varphi(n,t)dn, \quad (4)$$

where P_{10} is the equilibrium polarization, $J(E_0)(p/P_{10})$ is the source of repolarization produced by an electric field E_0, $\xi(t)$ is the relative repolarization [1], and $(p/P_{10})\int_0^\infty V_n\varphi(n, t)dn$ is the rate of transformation of polarization into the new phase.

Kinetic equation (3) and balance equation (4) constitute a closed set of equations describing the stage of large-scale switching of a multiaxial ferroelectric where most of the repolarization nuclei reach the critical size.

To solve the Fokker–Planck equation (3), we need to find the growth velocity V_n in the space of domain sizes, which depends substantially on the domain growth mechanism. For the sake of definiteness, we assume that the low-symmetry phase of the ferroelectric under study belongs to the tetragonal point group 4*mm*. This symmetry is typical of the pyroelectric phases of certain multiaxial ferroelectrics, e.g., barium titanate. It is also assumed that spontaneous polarization arises along the z axis in the absence of an external electric field. Using the method developed in [1, 2] for calculating the growth rate of nuclei in the space of their sizes, we find

$$V_n = 3\frac{\xi(t)}{t_0}n^{2/3}, \quad (5)$$

where t_0 is a time constant dependent on the specific mechanism of domain growth.

In particular, for the growth of 180° domains, we have

$$\begin{aligned} t_0^{(1)} &= \left(\frac{2\pi}{\omega}\right)^{2/3}\frac{\varepsilon_0\chi_{zz}k_BT}{2\pi\beta_0P_{10}p}, \\ t_0^{(2)} &= \left(\frac{2\pi}{\omega}\right)^{2/3}\frac{\varepsilon_0\chi_{zz}k_BT\sigma_{\text{st}}}{4\pi\beta_{\text{st}0}P_{10}p\sigma}, \end{aligned} \quad (6)$$

where superscripts "1" and "2" refer to the normal and layer-by-layer mechanisms of domain growth, respectively; ε_0 is the permittivity of free space; k_B is the Boltzmann constant; T is the temperature; χ_{zz} is the zz component of the dielectric susceptibility tensor; β_0 is a kinetic coefficient; and σ_{st} and $\beta_{\text{st}0}$ are the surface tension and kinetic coefficient related to a step, respectively.

For the growth of 90° domains, the time constant t_0 is given by

$$\begin{aligned} t_0^{(1)} &= \left(\frac{2\pi}{\omega}\right)^{2/3}\frac{\varepsilon_0\chi_{yy}k_BT}{2\pi\beta_0P_{10}p}, \\ t_0^{(2)} &= \left(\frac{2\pi}{\omega}\right)^{2/3}\frac{\varepsilon_0\chi_{yy}k_BT\sigma_{\text{st}}}{4\pi\beta_{\text{st}0}P_{10}p\sigma}. \end{aligned} \quad (7)$$

It should be stressed that Eq. (5) for the growth velocity in the space of domain sizes is derived, following [1], under the assumption of three-dimensional growth of cylindrical nuclei having two degrees of freedom. The specific features of the domain growth mechanism are determined by the constant t_0.

Let us introduce the dimensionless nucleus radius $\rho = n^{1/3}$ and pass over from the distribution function of domains over the number of unit cells in them $\varphi(n, t)$ to the distribution function of domains over dimensionless radii $g(\rho, t)$. With this function, kinetic equation (3) takes the form

$$\frac{\partial g(\rho, t)}{\partial t} + \frac{\xi(t)}{t_0}\frac{\partial}{\partial \rho}[g(\rho, t)] = 0. \quad (8)$$

According to [2], we can neglect the derivative $d\xi/dt$ in balance equation (4) at the stage of large-scale switching. In this case, we obtain

$$\frac{\xi_0}{\xi(t)} - 1 = \frac{3p\tau}{P_{10}t_0}\int_0^{\infty} \rho^2 g(\rho, t)d\rho, \quad (9)$$

where ξ_0 is the repolarization of the ferroelectric at the initial instant of time and τ is a parameter dependent on the operative mechanism of domain growth and the type of repolarized domains. In particular,

$$\tau^{(1)} = \frac{\varepsilon_0 \chi_{zz} k_B T}{2\beta'_0 p^2}, \quad \tau^{(2)} = \frac{\varepsilon_0 \chi_{zz} k_B T \sigma_{st}}{4\beta'_{st0} p^2 \sigma}, \quad (10)$$

for 180° domains and

$$\begin{aligned} \tau^{(1)} &= \frac{\varepsilon_0 \chi_{yy} k_B T}{2\beta'_0 p^2}, \\ \tau^{(2)} &= \frac{\varepsilon_0 \chi_{yy} k_B T \sigma_{st}}{4\beta'_{st0} p^2 \sigma}, \end{aligned} \quad (11)$$

for 90° domains. Here, $\beta'_0 = N_V \nu \exp(-V_0/k_B T)$ is a kinetic coefficient, V_0 is the height of the energy barrier to switching of the unit-cell dipole moment p in the absence of an external field, N_V is the number of unit cells per unit volume of the crystal, ν is the vibration frequency of atoms in a unit cell, and β_{st0} is the analogous kinetic coefficient for a step in the case where the layer-by-layer mechanism of domain growth dominates.

Following [2], the set of equations (8) and (9) is supplemented by initial and boundary conditions of the form $g(\rho, 0) = 0$ (for $\rho > \rho_c$) and $g(0, t) = I(\xi(t))t_0/\xi(t)$, where $I(\xi(t))$ is the repolarization flux.

This set of equations can be solved analytically. A method for solving these equations as applied to uniaxial ferroelectrics is proposed in [2]. The formulas derived in [2] (not presented here) can be used to calculate all main kinetic characteristics of the process of switching of multiaxial ferroelectric crystals at the stage of large-scale switching with inclusion of various mechanisms of domain growth and different types of repolarized domains (corresponding to appropriately chosen parameters t_0 and τ).

The final stage of switching of ferroelectric crystals in an external field (as well as of other first-order phase transitions) is the Ostwald ripening, also known as coalescence. In this stage, coarse nuclei grow by merging with fine nuclei. This thermodynamically favorable process causes the total area of interphase boundaries to decrease, and the average size of repolarized domains increases with time. The interaction between repolarized domains is characterized by a self-consistent field produced by the entire ensemble of domains. As a result of the Ostwald ripening, the relative repolarization of the crystal decreases to zero; the initially metastable system reaches complete thermodynamic equilibrium, at which the ferroelectric is a single domain with polarization directed along the external electric field.

The kinetics of switching of ferroelectric crystals at the stage of the Ostwald ripening was studied in detail in [2, 3] with allowance for the normal and layer-by-layer mechanisms of domain growth. It was shown in those papers that the basic kinetic equations describing first-order phase transitions at the stage of the Ostwald ripening are similar in structure and, therefore, have similar solutions. For this reason, we do not write out the explicit expressions for the distribution function of nuclei over sizes, the average nucleus size, the nucleus density, the relative repolarization at the stage of the Ostwald ripening, or other kinetic characteristics of switching, which can be found in the papers mentioned above.

3. SWITCHING CURRENT

The time dependence of the switching current density in a multiaxial ferroelectric crystal is defined as [7]

$$J = -2P_{10}\frac{dQ}{dt}, \quad (12)$$

where Q is the fraction of the crystal that has not yet been repolarized and P_{10} is the initial value of the spontaneous polarization of the ferroelectric.

In the initial stage of switching, the system is not influenced by new-phase nuclei and its thermodynamic parameters remain virtually unchanged. The relative volume of the crystal involved in the phase transition is very small, and the rate of its change is almost zero. Therefore, there is no polarization current in the initial stage of switching. This current arises only at the second stage of the phase transformation, where large-scale switching occurs. To calculate the polarization current, let us consider kinetic equations (1)–(9).

We introduce the fraction of the repolarized volume of the crystal $Z = 1 - Q$ and, following [2], rewrite balance equation (4) in the form

$$\frac{d\xi}{dt} = \frac{\xi_0}{\tau} - \frac{\xi}{\tau} - \frac{(\xi_0 - \xi)}{(1 - Z)}\frac{dZ}{dt}, \quad (13)$$

where ξ_0 is the relative repolarization at the initial instant of time and τ is a time constant that is dependent on the operative mechanism of domain growth and the type of repolarized domains and is given by Eqs. (10) and (11).

All the main characteristics of switching can be found by solving kinetic equation (3) in combination with balance equation (13). For this purpose, we express Z in terms of ρ and t using the relations $\rho = n^{1/3}$ and $\varphi(n, t)dn = g(\rho, t)d\rho$. By differentiating Z with respect to time and using Eqs. (5) and (8) and the boundary condition $g(\rho, t)|_{\rho \to \infty} = 0$, we obtain

$$\left(\frac{1}{\xi}\left(\frac{Z'}{\xi}\right)'\right)' = \frac{6\omega\xi}{t_0^3}N, \tag{14}$$

where N is the number of domains. From Eq. (14), it follows that

$$\left[\frac{1}{\xi}\left(\frac{1}{\xi}\left(\frac{Z'}{\xi}\right)'\right)'\right]' = \frac{6\omega}{t_0^3}I(\xi), \tag{15}$$

where $I(\xi)$ is the flux of nuclei.

Using Eq. (12), we find that the polarization current satisfies the equation

$$\left[\frac{1}{\xi}\left(\frac{1}{\xi}\left(\frac{J}{\xi}\right)'\right)'\right]' = \frac{12\omega P_{10}}{t_0^3}I(\xi). \tag{16}$$

Thus, Eq. (16) in combination with balance equation (13) makes it possible to calculate the polarization current as a function of time and external field.

From Eqs. (12), (13), and (16), we obtain

$$\left[\frac{1}{\xi}\left(\frac{1}{\xi}\left(\frac{\left(\frac{\xi_0}{\tau} - \xi' - \frac{\xi}{\tau}\right)(1 - Z)}{(\xi_0 - \xi)\xi}\right)'\right)'\right]' = \frac{6\omega}{t_0^3}I(\xi). \tag{17}$$

From Eq. (17), subject to the condition that the polarization current, its time derivatives, and the repolarization be zero at the initial instant of time, we can find the time dependence of the relative repolarization.

The dependence of the nucleus flux on the relative repolarization is found in [1] and can be written in the form

$$\begin{aligned} I^{(1)}(\xi) &= I_0^{(1)}\exp(-\alpha/\xi^2), \\ I^{(2)}(\xi) &= I_0^{(2)}\exp(-\alpha/\xi^2), \end{aligned} \tag{18}$$

where

$$I_0^{(1)} = \beta_0 N_V \omega\sqrt{\frac{6\sigma}{k_B T}},$$

$$I_0^{(2)} = 2\beta_{st0}N_V\omega\frac{\sigma}{\sigma_{st}}\sqrt{\frac{6\sigma}{k_B T}}.$$

Here, N_V is the number of unit cells per unit volume of the crystal, which can be estimated as $N_V \sim 1/\omega$, and superscripts “1” and “2” refer to the normal and layer-by-layer mechanisms of domain growth, respectively.

The parameter α depends on the type of nuclei. In particular,

$$\alpha = \frac{2\pi\sigma^3}{k_B T}\left(\frac{\varepsilon_0\chi_c\omega}{pP_{10}}\right)^2,$$

for 180° domains and

$$\alpha = \frac{8\pi\sigma^3}{k_B T}\left(\frac{\varepsilon_0\chi_a\omega}{pP_{10}}\right)^2,$$

for 90° domains, where χ_c and χ_a are the dielectric susceptibilities of the ferroelectric along the c and a axes, respectively.

Equations (3) and (13)–(18), subject to appropriate initial and boundary conditions, constitute a closed set. By solving these equations, we can find the main kinetic characteristics of switching of a multiaxial ferroelectric crystal, namely, the switching current density, relative repolarization, nucleus flux, etc.

4. DISCUSSION OF THE RESULTS AND COMPARISON WITH EXPERIMENT

Now, we make estimates using the theoretical dependences obtained above and the experimental data on barium titanate, a classical multiaxial ferroelectric. According to [8–10], the Curie temperature of barium titanate is $T_C \sim 393$ K; the equilibrium spontaneous polarization at $T \sim 373$ K is $P_{x10} \sim 1.2 \times 10^{-1}$ C m^{-2}; the dielectric susceptibilities along and perpendicular to the polar axis are $\chi_c \sim 60$ and $\chi_a \sim 300$, respectively; the molar mass is $M \sim 0.233$ kg mol^{-1}; and the density is $\rho \sim 6.02 \times 10^3$ kg m^{-3}. The unit cell volume of crystal barium titanate can be estimated as $\omega \sim M/\rho N_A = 0.64 \times 10^{-28}$ m^3 (where N_A is the Avogadro constant); therefore, $N_V \sim \omega^{-1} = 1.6 \times 10^{28}$ m^{-3}. The kinetic coefficient β_0 depends on the activation energy for atomic displacements in the ferroelectric and, according to [2], can be estimated as $\beta_0 \sim 10^{31}$ m^{-2} s^{-1}.

As indicated in [1], there is a wide scatter in the experimental, as well as theoretical, estimates of the surface tension of a domain wall. According to [11–15], the surface tension σ of a domain wall in barium titanate lies within the range from $\sim 0.1 \times 10^{-3}$ to $\sim 10 \times 10^{-3}$ J m^{-2}. Due to this wide scatter in the experimental data on surface tension, we can make only qualitative estimates.

We assume the surface tension of a domain wall to be $\sigma \sim 0.7 \times 10^{-3}$ J m^{-2}, which is intermediate between the calculated values of Miller and Weinreich and estimates made by Zhirnov. In the case of the layer-by-layer mechanism of domain growth, we also need to know the surface tension of a step. For this reason, we restrict our consideration to the normal mechanism of domain growth. For the formation of 180° domains, we have $t_0 \sim 10^{-12}$ s, $\tau \sim 10^{-7}$ s, and $\alpha \sim 5.7 \times 10^{-4}$. Figure 1 shows the time dependences of the relative repolarization $\xi(t)$, nucleation rate $I(t)$, repolarized-domain den-

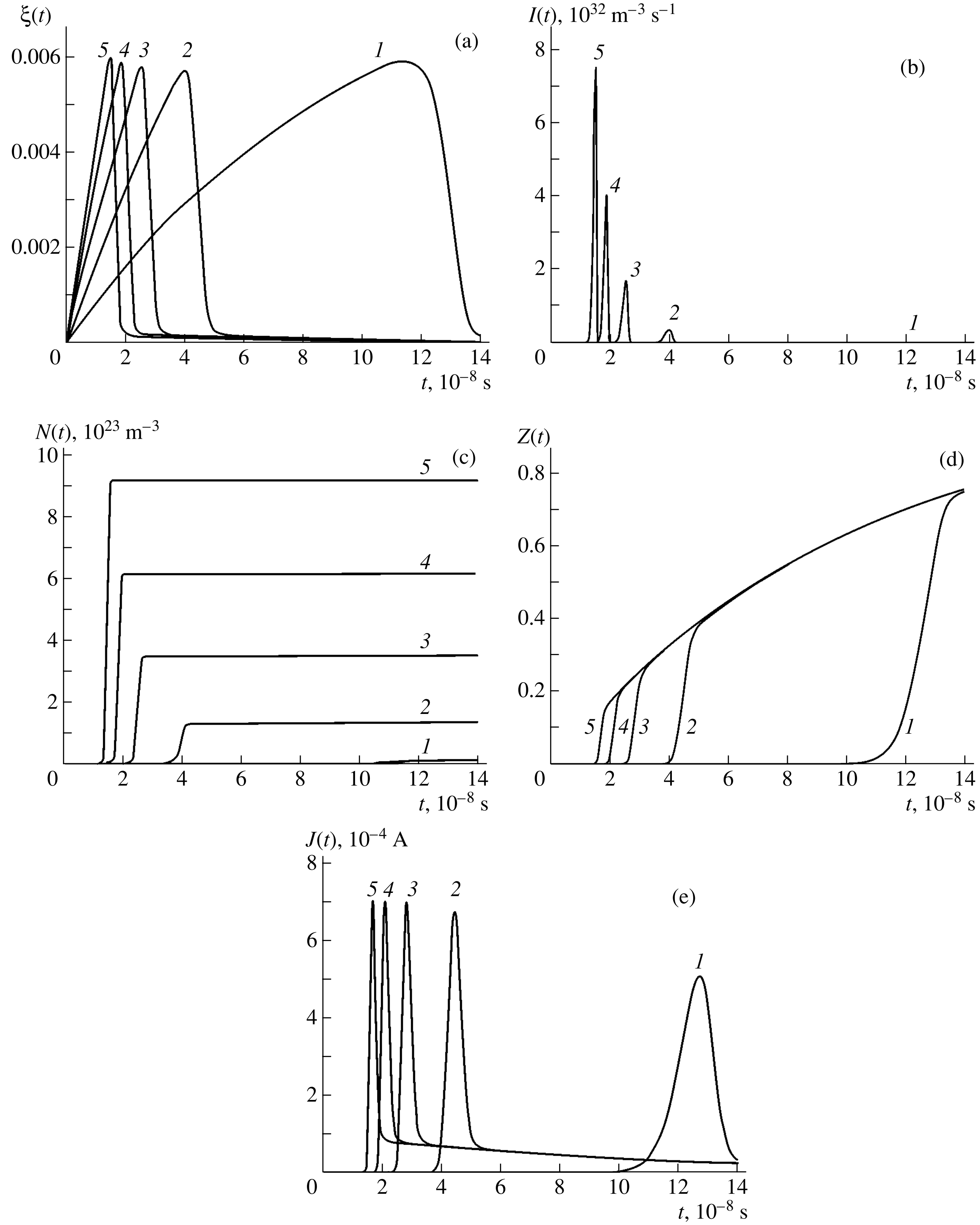

Fig. 1. Time dependences of (a) the relative repolarization $\xi(t)$, (b) nucleation rate $I(t)$, (c) repolarized-domain density $N(t)$, (d) fraction of the repolarized volume of the crystal $Z(t)$, and (e) switching of the current density $J(t)$ at various values of the external field E: (*1*) 2, (*2*) 4, (*3*) 6, (*4*) 8, and (*5*) 10 MV m^{-1}. The area of the sample is $S \sim 10^{-9}$ m^2.

sity $N(t)$, fraction of the repolarized volume $Z(t)$, and switching current density $J(t)$ at various values of the external field found by solving Eqs. (13)–(18). The corresponding switching times t_s are shown in Fig. 2 as a function of external field. It should be noted that the plots of the switching current are so-called “affine” curves and agree qualitatively with the experimental time dependence of switching of currents in ferroelec-

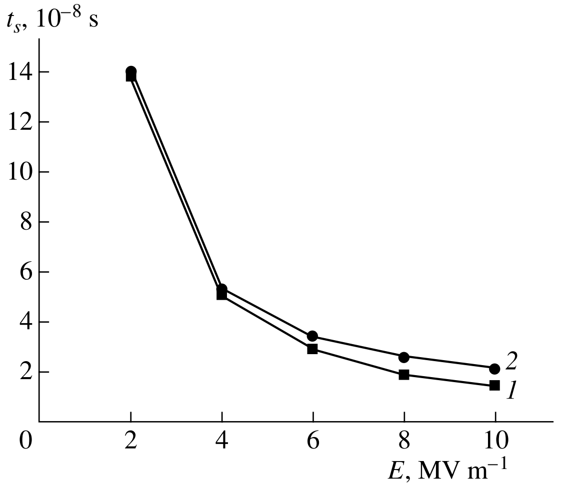

Fig. 2. (*1*) Experimental (after Stadler [17]) and (*2*) theoretical dependences of the switching time t_s on external field.

trics [8, 9, 16]. Furthermore, it can be seen from Fig. 2 that the switching times are consistent with the experimental data of Stadler [17].

In closing, we note that application of the theory developed here is hampered by the fact that calculations of the constants I_0, t_0, τ, and α involve parameters (such as the surface tension of a domain wall and kinetic coefficients) that are not well determined. It is more reasonable to solve the inverse problem; namely, by comparing the theoretical dependences of the switching current with experimental data, one can estimate the parameters of ferroelectrics that cannot be determined directly from experimental measurements. It should also be stressed that the theory developed here is applicable solely to weakly metastable systems; otherwise, one has to use approximations of the Ginzburg–Landau type rather than the classical Fokker–Planck equations. The case of strongly metastable uniaxial ferroelectrics was considered in [2].

ACKNOWLEDGMENTS

This study was supported in part by the Russian Foundation for Basic Research (project nos. 03-01-00574, 03-03-32503); the Russian federal research center “Integration” (project nos. A0151, B0056); the program “Control of Nonlinear Mechanical Systems under Conditions of Uncertainty and Chaos” (project no. 19); the Ministry of Industry, Science, and Technology of the Russian Federation (project no. 40.010.11.1195); state contract nos. NFM-1/03 and NSh-2288.2003.1; the RFBR–NWO program (project no. 047.011.2001.011); and the government of Mexico (grant “CONACYT” no. 35460-U).

REFERENCES

1. M. A. Zakharov, S. A. Kukushkin, and A. V. Osipov, Fiz. Tverd. Tela (St. Petersburg) **46** (7), 1238 (2004) [Phys. Solid State **46**, 1277 (2004)].
2. S. A. Kukushkin and A. V. Osipov, Fiz. Tverd. Tela (St. Petersburg) **43** (1), 80 (2001) [Phys. Solid State **43**, 82 (2001)]; Fiz. Tverd. Tela (St. Petersburg) **43** (1), 88 (2001) [Phys. Solid State **43**, 90 (2001)]; Fiz. Tverd. Tela (St. Petersburg) **43** (2), 312 (2001) [Phys. Solid State **43**, 325 (2001)].
3. S. A. Kukushkin and M. A. Zakharov, Fiz. Tverd. Tela (St. Petersburg) **44** (2), 332 (2002) [Phys. Solid State **44**, 345 (2002)]; Fiz. Tverd. Tela (St. Petersburg) **44** (12), 2193 (2002) [Phys. Solid State **44**, 2298 (2002)].
4. V. A. Shneĭdman, Zh. Éksp. Teor. Fiz. **91** (2), 520 (1986) [Sov. Phys. JETP **64**, 306 (1986)].
5. F. M. Kuni and A. A. Melikhov, Teor. Mat. Fiz. **81** (2), 247 (1989).
6. S. A. Kukushkin and A. V. Osipov, Fiz. Tverd. Tela (St. Petersburg) **36** (5), 1258 (1994) [Phys. Solid State **36**, 687 (1994)].
7. Y. Ishibashi and Y. Takagi, J. Phys. Soc. Jpn. **31**, 506 (1971).
8. B. A. Strukov and A. P. Levanyuk, *Physical Principles of Ferroelectric Phenomena in Crystals* (Nauka, Moscow, 1995) [in Russian].
9. F. Jona and G. Shirane, *Ferroelectric Crystals* (Pergamon, Oxford, 1962; Mir, Moscow, 1965).
10. J. Burfoot, *Ferroelectrics: An Introduction to the Physical Principles* (Van Nostrand, London, 1967; Mir, Moscow, 1970).
11. M. Hayashi, J. Phys. Soc. Jpn. **33**, 616 (1972).
12. E. V. Burtsev and S. P. Chervonobrodov, Ferroelectrics **45**, 97 (1982).
13. M. Molotskii, R. Kris, and G. Rosenmann, J. Appl. Phys. **88** (9), 5318 (2000).
14. A. K. Tagantsev, I. Stolichnov, E. L. Colla, and N. Setter, J. Appl. Phys. **90** (3), 1387 (2001).
15. R. E. Nettleton, J. Appl. Phys. **38** (7), 2775 (1967).
16. W. J. Merz, J. Appl. Phys. **27**, 938 (1956).
17. H. L. Stadler, J. Appl. Phys. **33** (12), 3487 (1962).

Translated by Yu. Epifanov

Physics of the Solid State, Vol. 47, No. 4, 2005, pp. 703–709. Translated from Fizika Tverdogo Tela, Vol. 47, No. 4, 2005, pp. 679–685.
Original Russian Text Copyright © 2005 by Olekhnovich, Radyush, Vyshatko, Moroz, Pushkarev, Palatnikov.

MAGNETISM AND FERROELECTRICITY

Thermal Hysteresis of the Permittivity of $Li_{0.12}Na_{0.88}Ta_yNb_{1-y}O_3$ Solid Solutions ($y \geq 0.7$) Prepared under High or Normal Pressure

N. M. Olekhnovich*, Yu. V. Radyush*, N. P. Vyshatko*,
I. I. Moroz*, A. V. Pushkarev*, and M. N. Palatnikov**
**Institute of Solid State and Semiconductor Physics, National Academy of Sciences of Belarus,*
ul. P. Brovki 17, Minsk, 220072 Belarus
e-mail: olekhnov@ifttp.bas-net.by
***Institute of Rare-Element and Mineral Chemistry and Technology, Russian Academy of Sciences, ul. Fersmana 14, Apatity,*
Murmansk oblast, 184200 Russia

Received March 25, 2004; in final form, June 15, 2004

Abstract—The structural characteristics and dielectric properties (ε', $\tan\delta$) of $Li_{0.12}Na_{0.88}Ta_yNb_{1-y}O_3$ solid solutions ($y \geq 0.7$) synthesized under high or normal pressure (HP and NP ceramics, respectively) were studied. It was established that these solid solutions have an orthorhombic perovskite structure (space group *Pnma*) in the paraelectric state. The temperature and frequency dependences of the dielectric properties of the solid solutions are described in terms of microinhomogeneity of a system containing ferroelectric clusters with an enhanced Nb content as compared to that in the matrix. The characteristics of the cluster system depend on the method by which the ceramics were prepared. The HP ceramic is more homogeneous on the microscale. The permittivity ε' was found to undergo thermal hysteresis in the region from 200 to 400 K, the parameters of which strongly differ for the HP and NP ceramics. The temperature of the maximum ε' obtained in cooling runs for the NP and HP ceramics is 50–60 and 110 K lower, respectively, than that on the heating branch. The hysteresis may originate from interaction of the antipolar mode condensing under cooling with nonpolar ordered distortions, which drives the system to the state of global minimum. When the system residing in this state is heated, this mode undergoes decondensation at a higher temperature. © *2005 Pleiades Publishing, Inc.*

1. INTRODUCTION

Solid-solution systems of sodium and lithium niobate tantalates occupy a special place in the family of perovskite-type complex oxides. They undergo temperature- and concentration-driven phase transitions, including ferro- and antiferroelectric transformations. These transitions are accompanied by a change in the pattern of ordered lattice distortions associated with specific crystallochemical features of the starting compounds and interatomic bond stresses caused by misfits between the size of the cations and the volume of the polyhedra they occupy. A system worth mentioning in this family is the quasi-binary series of $Li_{0.12}Na_{0.88}Ta_yNb_{1-y}O_3$ solid solutions [1], one of whose extreme compositions ($Li_{0.12}Na_{0.88}NbO_3$) is located within the morphotropic region of coexistence of two phases with orthorhombic and rhombohedral structures [2, 3] and the other extreme composition, based on sodium tantalate, reveals anomalous dielectric properties with signs of a quantum paraelectric at low temperatures [4]. In this series of solid solutions, morphotropic regions with specific physical properties and a transition to the state with superionic conduction have been observed [1]. The characteristics of the morphotropic regions, the crystal structure of individual phases, their regions of existence, and their physical properties depend on the extent of microscopic inhomogeneity and cation ordering, as well as on stoichiometry, which is indicated by the structural and physical parameters being sensitive to the conditions of sample preparation and heat treatment. This makes it necessary to prepare and study solid solutions of this system with different, and, above all, with the highest possible, homogeneity on the microscale. It appears that the best way to reach this goal lies in carrying out the synthesis at high pressures and temperatures, i.e., under conditions conducive to attaining a higher degree of compositional order and microscopic homogeneity. Moreover, this type of synthesis provides a better preservation of sample composition, because the process is run in a closed volume.

Our goal in this work was to study the structural characteristics and dielectric properties of $Li_{0.12}Na_{0.88}Ta_yNb_{1-y}O_3$ solid solutions (LNTN) ($y \geq 0.7$) prepared in the form of ceramics at high pressure and temperature and to compare them with the properties of ceramics of the same composition but synthesized using standard technology at normal pressure.

2. EXPERIMENTAL TECHNIQUES

Ceramics of LNTN solid solutions were prepared in two stages. In the first stage, an oxide–carbonate powder mixture of the starting reagents (OSCh-grade nio-

Table 1. Lattice parameters of $Li_{0.12}Na_{0.88}Ta_yNb_{1-y}O_3$ solid solutions

Composition, *y*	$a \times 10$, nm	$b \times 10$, nm	$c \times 10$, nm
0.7	5.489	7.759	5.497
0.8	5.487	7.762	5.496
0.9	5.489	7.766	5.497

bium and tantalum oxides and sodium and lithium carbonates) were pressed into pellets, which were subsequently calcined at a temperature of 1100 to 1150 K. The calcined mixture was ground to a powder, which served as a starting batch for the second stage of solid-solution preparation. Samples of high-pressure LNTN ceramics were processed at 6 GPa and temperatures ranging from 1600 to 1800 K for three to five minutes and cooled subsequently under applied pressure. The ceramics prepared at high pressure were in the form of compacted pellets.

Normal-pressure samples were prepared from the above batch by sintering at 1400 K.

X-ray diffraction measurements of LNTN ceramics were performed in a diffracted beam of CuK_α radiation on DRON-3 and Rigaku D/Max-B computerized diffractometers. The diffraction spectra were scanned in the angular range $20° \le 2\Theta \le 90°$ in steps of 0.02° with an exposure time of up to 10 s at each point. The spectra were treated with the full-profile technique using the FullProf 2000 computer code.

The permittivity ε' and the loss tangent $\tan\delta$ were measured with an E7-12 and an E7-14 immitance meter on capacitor samples with silver electrodes at frequencies of 0.1, 1, and 10 kHz and 1 MHz and temperatures varied at a rate of 2 K/min in the range 77–600 K. The samples were preliminarily calcined in air at 700 K. Dielectric measurements for studying the thermal hysteresis of ε' and $\tan\delta$ were performed in a nitrogen environment in a cyclic mode including heating from room temperature to 500 K followed by cooling to 77 K and subsequent heating to 600 K. The measurement cycles were repeated several times. In another series, measurements were also conducted in the cyclic mode including heating to 500 K followed by quenching in liquid nitrogen and then heating to 600 K. The quenching was performed both without a dc electric field applied (ZFQ) and in a field (FQ) of up to 22 kV/cm. We also studied the evolution in time of the permittivity at temperatures in the region of the maximum, ε'_m.

3. EXPERIMENTAL DATA

An analysis of the x-ray diffraction spectra of LNTN solid solutions was performed in the approximation of a reduced pseudocubic perovskite lattice and revealed, irrespective of the technique by which they were prepared, weak superstructural reflections of the type (*h* + 1/2, *k* + 1/2, 0), (*h* + 1/2, *k* + 1/2, *l* + 1/2), and (*h* + 1/2, *k* + 1/2, *l*). This result suggests that the solid solutions under study have a regularly distorted crystal structure. A full-profile analysis of the diffraction spectra showed that ordered lattice distortions observed at temperatures above the phase transition to the antiferroelectric state are related to oxygen tetrahedron tilting of the $[a^-b^+a^-]$ type [5, 6], which results in an orthorhombic structure (space group *Pnma* (no. 62)).

The orthorhombic cell parameters (Table 1) are related to the parameters of the reduced cubic cell (a_p) as $a \simeq \sqrt{2}a_p$, $b = 2a_p$, and $c \simeq \sqrt{2}a_p$. The relative ordered displacements of the oxygen ions depend only weakly on composition.

The low intensity of the superstructural reflections and its weak variation with temperature in the range 77–700 K covered here prevented us from determining the actual type of antipolar ordered displacements of the Ta(Nb) cations.

The dielectric response of the LNTN solid solutions was found to have a complex pattern. The high- and normal-pressure ceramics reveal thermal hysteresis of the real part of the permittivity ε'(*T*). The ε'(*T*) relations measured on the cooling and heating branches within the same 500- to 77- to 600-K cycle behave differently (Figs. 1, 2). We readily see maxima of the permittivity (ε'_m) in the cooling and heating branches. The cooling branch has one maximum ε'_m at a temperature T'_{mc} for all solid-solution compositions. The pattern obtained in heating runs is, in general, more complex and dependent on composition. For the *y* = 0.9 and 0.8 compositions, this branch has one maximum ε'_m at a temperature T'_{mh1}, while for the *y* = 0.7 composition the high-pressure ceramic (Fig. 2) exhibits, in addition to the main maximum at T'_{mh1}, a second maximum at T'_{mh2}, which lies near the maximum obtained in cooling runs (T'_{mc}). Note that the heating curve obtained for the *y* = 0.7 normal-pressure ceramic also reveals a weakly pronounced maximum in the region of the temperatures corresponding to the maxima ε'_m (T'_{mh2}, T'_{mc}) in the cooling–heating runs of the high-pressure ceramic (Fig. 2). The temperature of the maximum ε'_m obtained in cooling runs (T'_{mc}) is lower than that of the main maximum on the heating branch (T'_{mh1}), irrespective of the composition of the ceramic and the method of its preparation. The values of the permittivity ε' on the cooling branches obtained in the region of the thermal hysteresis are higher than those measured in the heating runs. The magnitude of ε' on the cooling and heating branches decreases with increasing field frequency. The extent of this decrease depends on the actual composition and type of ceramic involved. The temperature

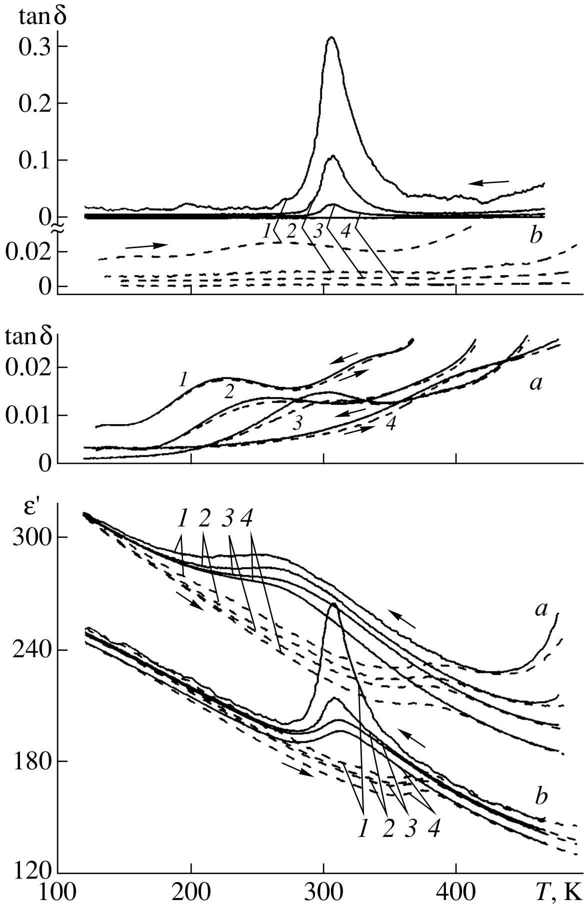

Fig. 1. Temperature dependence of ε' and tan δ of (*a*) high-pressure and (*b*) normal-pressure LNTN ceramics with $y = 0.9$ (the cooling and heating branches are specified by arrows) measured at various field frequencies: (*1*) 10^2, (*2*) 10^3, (*3*) 10^4, and (*4*) 10^6 Hz.

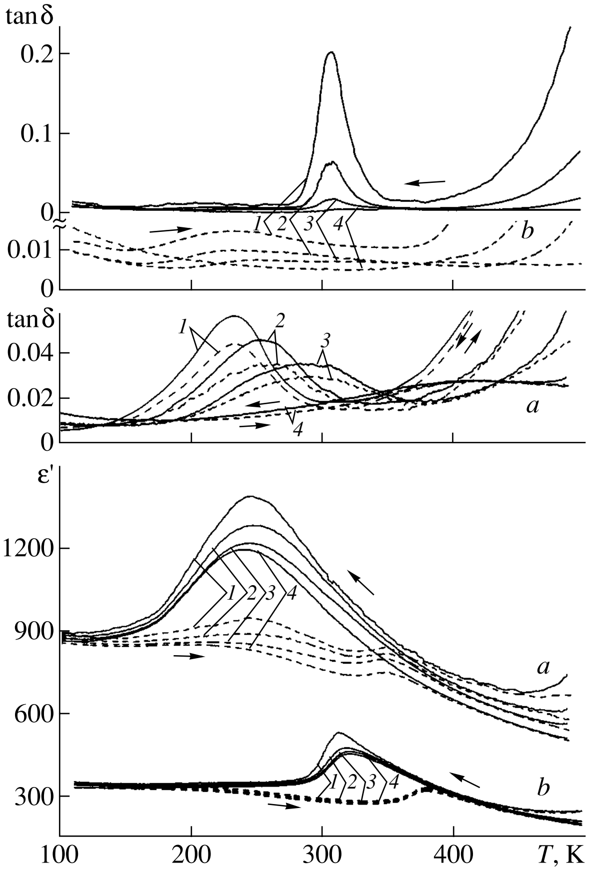

Fig. 2. Temperature dependence of ε' and tan δ of (*a*) high-pressure and (*b*) normal-pressure LNTN ceramics with $y = 0.7$ (the cooling and heating branches are specified by arrows) measured at various field frequencies: (*1*) 10^2, (*2*) 10^3, (*3*) 10^4, and (*4*) 10^6 Hz.

positions of the maxima in permittivity (T'_{mh1}, T'_{mc}) vary only weakly with the field frequency.

The characteristics of the behavior of ε' of the high-pressure ceramic with temperature measured both in the hysteresis region and beyond it differ substantially from those of the ceramic prepared under normal pressure (Tables 1, 2). The temperature position of the maximum ε'_m of the high-pressure ceramic on the cooling branch (T'_{mc}) is shifted toward lower temperatures as compared to T'_{mc} for the normal-pressure ceramic. The difference in the position of the main maximum ε'_m on the heating branch (T'_{mh1}) between the two types of ceramics is comparatively small. The width of the thermal hysteresis of ε' for the high-pressure ceramic is about 110 K for all compositions, while for the normal-pressure ceramic this width is 50 to 60 K. The values of ε' on the branches of the hysteresis and beyond it for the high-pressure ceramic are substantially larger than the respective values for the normal-pressure ceramic, and this difference increases with the Nb concentration in the system. Note that, at temperatures below the hysteresis region, the pattern of the variation in permittivity with temperature depends on the ceramic type. For y = 0.9 and 0.8, ε' increases with decreasing temperature

Table 2. Characteristics of the thermal hysteresis of ε' of high-pressure (HP) and normal-pressure (NP) $Li_{0.12}Na_{0.88}Ta_yNb_{1-y}O_3$ ceramics

y	0.7		0.8		0.9	
	HP	NP	HP	NP	HP	NP
T'_{mc}, K	250	320	280	350	280	320
T'_{mh}, K	360	380	390	400	390	380
ε'_{mc} (1kHz)	1290	490	570	320	285	220
ε'_{mh} (1MHz)	840	320	400	245	230	175

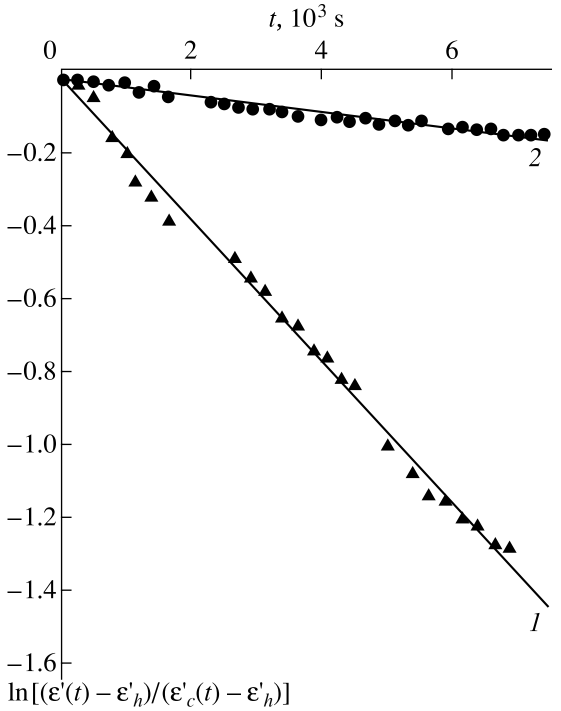

Fig. 3. Relative decrease in $\ln[(\varepsilon'(t) - \varepsilon'_h)/(\varepsilon'_c(0) - \varepsilon'_h)]$ with time for a high-pressure LNTN ceramic ($y = 0.7$) measured in a cooling run at a field frequency of 10^6 Hz and at a temperature of (*1*) 210 and (*2*) 282 K.

for both types of ceramic and this growth is steeper for the high-pressure ceramic. For the $y = 0.7$ composition, the $\varepsilon'(T)$ curves saturate in the low-temperature domain.

At high frequencies, the permittivity measured in the cooling and heating runs at temperatures 20 to 30 K above T'_{mc} and T'_{mh1}, respectively, falls off in accordance with the Curie–Weiss law. At low frequencies and high temperatures, ε' increases because of the contributions due to the microinhomogeneity of the system and hopping ion transport.

While the ε' behavior retains its pattern in repeated cycles on both branches, its magnitude exhibits a certain tendency to decrease. The high- and normal-pressure ceramics reveal a qualitatively different temperature dependence of $\tan\delta$ on both the cooling and heating runs (Figs. 1, 2). The normal-pressure ceramic exhibits a sharp maximum, $(\tan\delta)_m$, on the cooling branches at a temperature T''_{mc}. Its position is practically independent of the field frequency, but the magnitude of $(\tan\delta)_m$ decays rapidly with increasing frequency. The $\tan\delta$ measured in a heating run varies slowly with temperature. Its low-frequency value is approximately one order of magnitude smaller than that measured under cooling.

The magnitude of $\tan\delta$ of the high-pressure ceramic varies with temperature similarly under cooling and heating. In the region of the thermal hysteresis of ε', the $\tan\delta(T)$ relation exhibits a maximum. The main feature of the $\tan\delta(T)$ dependence is a large frequency dispersion of the temperature of the maximum in $\tan\delta$. It can be seen from Figs. 1 and 2 that, as the field frequency increases from 10^2 to 10^6 Hz, the maximum $(\tan\delta)_m$ shifts about 170 K toward higher temperatures for all the ceramic compositions studied.

In connection with the existence of the thermal hysteresis of ε' and of the relaxation-type dielectric properties of the LNTN ceramic, a question may arise concerning the stability of the system on the upper branch of the thermal hysteresis. To answer this, the variation in ε' with time was studied at different temperatures, from 500 to 77 K, in the region of the maximum on the cooling branch. The studies were conducted in the following manner. After heating to 500 K, a sample was cooled at a rate of 2 K/min to the preset temperature in the region of the maximum permittivity (Figs. 1, 2). Next, the variation in ε' with the duration t of exposure to a preset temperature was measured. These measurements showed that ε' decreases with increasing time t. The rate of this decrease depends on temperature and field frequency (Fig. 3). It was found that the observed $\varepsilon'(t)$ relation has an exponential character and can be fitted by the expression

$$\varepsilon'(t) = \varepsilon'_h + (\varepsilon'_c(0) - \varepsilon'_h)\exp(-t/\tau_f), \quad (1)$$

where $\varepsilon'_c(0)$ is the initial permittivity on the cooling branch at a given temperature, ε'_h is the value of permittivity corresponding to the heating branch of hysteresis at the same temperature, and τ_f is the characteristic time for the system to transfer to the steady state under the given conditions. It was found that τ_f decreases strongly as the temperature of the system decreases. For instance, for the $y = 0.7$ high-pressure ceramic studied at a field frequency of 10^2 Hz, we have $\tau_f \simeq 2.1 \times 10^4$ s at $T = 282$ K and $\tau_f \simeq 3.0 \times 10^3$ s at $T = 210$ K. As the frequency increases to 10^6 Hz, τ_f increases by about 1.6–2.1 times, depending on the temperature. The higher the temperature, the larger the frequency dispersion of τ_f. For the normal-pressure ceramic, τ_f is one order of magnitude larger. Because of the large magnitude of τ_f, the transfer of the system to a steady state, to which the lower branch of the thermal hysteresis of ε' corresponds, is very slow.

Measurements of the dielectric characteristics on quenched samples showed that the temperature dependences of ε' measured in heating from 77 K after quenching have two maxima (Fig. 4) at the temperatures T'_{m1} and T'_{m2}, respectively ($T'_{m1} < T'_{m2}$). The temperature T'_{m1} is practically the same for ceramics of

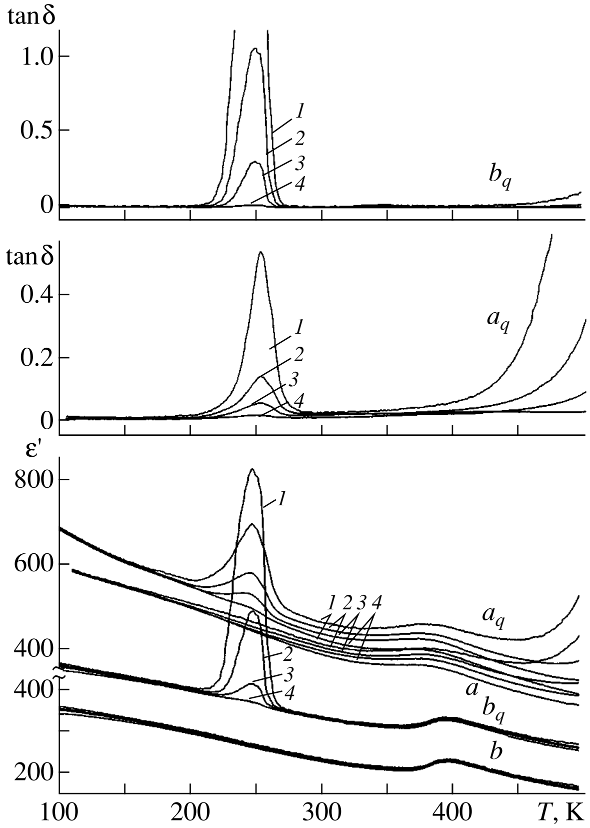

Fig. 4. Temperature dependence of ε' and tan δ (heating branch) for $y = 0.8$ LNTN ceramics from (a, a_q) high-pressure and (b, b_q) normal-pressure synthesis (a_q and b_q correspond to zero-field quenching) measured at various frequencies: (*1*) 10^2, (*2*) 10^3, (*3*) 10^4, and (*4*) 10^6 Hz.

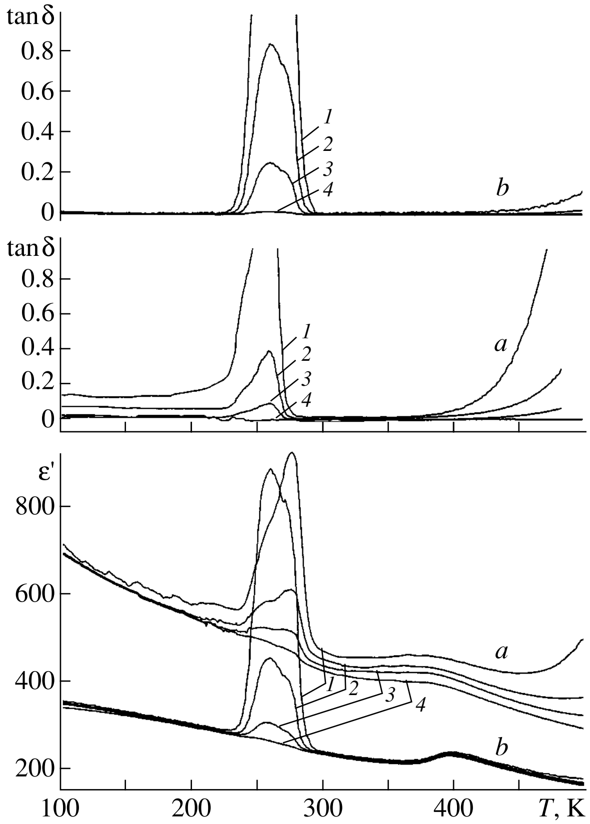

Fig. 5. Temperature dependence of ε' and tan δ (heating branch) for $y = 0.8$ LNTN ceramics from (a) high-pressure and (b) normal-pressure synthesis after field quenching measured at various frequencies: (*1*) 10^2, (*2*) 10^3, (*3*) 10^4, and (*4*) 10^6 Hz.

both types and is approximately equal to or slightly lower than the temperature T'_{mc} corresponding to ε'_m measured in cooling for the unquenched high-pressure ceramic (Figs. 1, 2). The position of the high-temperature maximum (T'_{m2}) coincides with that of ε'_m on the heating branch of the unquenched high- and normal-pressure ceramic, T'_{mh1}. In the subsequent measurement cycle, 600–77–600 K, the nature of the temperature dependence of ε' for both types of ceramic is recovered; i.e., it becomes the same as before quenching.

The existence of two maxima in the temperature dependence of ε' for quenched samples indicates that, in the course of heating, the quenched LNTN ceramic undergoes two phase transitions associated with a change in the character of dipole ordering. The temperature dependences of ε' and tan δ of quenched high- and normal-pressure ceramics exhibit common features in the region of the temperature T'_{m1} (Fig. 4). While the temperature T'_{m1} at which the maxima ε'_m and $(\tan\delta)_m$ are observed is practically independent of field frequency for both types of ceramic, the values of ε'_m and $(\tan\delta)_m$ undergo strong dispersion; more specifically, their values decrease strongly with increasing frequency. The effect of quenching on the values of ε' and tan δ in the region of T'_{m1} for the normal-pressure ceramic is far larger than that for the ceramic prepared under high pressure. The maximum ε'(T) obtained in this region for the quenched high-pressure ceramic is more diffuse, and the degree of broadening increases with the Nb content in the system.

The behavior of ε' and tan δ in the region of the second maximum in ε' (in the vicinity of T'_{m2}) for quenched samples of both types of ceramic remains practically the same as that for the unquenched ones.

Quenching of samples in dc electric fields of up to 22 kV/cm (FQ) in liquid nitrogen affects the temperature dependence of the dielectric response in the heating runs in a different way than does zero-field quenching (ZFQ) (Figs. 4, 5). However, the behavior of ε' and tan δ in the temperature region of the second maximum (T'_{m2}) remains practically unaffected under quenching both in the FQ and ZFQ conditions. This implies that the quenching-induced change in the state of the dipole system becomes annealed (relaxes) at temperatures lower than T'_{m2}.

4. DISCUSSION OF THE RESULTS

An analysis of the above experimental data showed that they can be adequately described if it is assumed that the solid solutions are compositionally inhomogeneous on the microscale, primarily in Ta and Nb. The microscopically inhomogeneous distribution of these cations over the octahedral lattice sites is due to their having practically equal ionic radii and differing in terms of the magnitude and character of the anisotropy in the covalent component of their bonding to the anions [7]. It may be conjectured that the crystalline matrix of the LNTN solid solutions contains clusters with a Nb-cation concentration higher than that in the matrix. The matrix behaves like a quantum paraelectric, which is indicated by the continuous growth or saturation of ε' in the temperature region below the temperatures of the thermal hysteresis (Figs. 1, 2). As the average concentration of cations in the system increases, so does their fraction in the matrix, which gives rise to an increase in ε'. Below a certain temperature, the dipole system of clusters transfers to an ordered state. This ordering may be assumed to be antipolar in the temperature region under study, as is the case with $NaNbO_3$.

The matrix and the clusters in the paraelectric state form an ordered distorted lattice of orthorhombic symmetry (space group *Pnma*, no. 62). The ordered distortions involve $[a^-b^+a^-]$ tilting of the oxygen octahedra. The cluster lattice symmetry lowers under dipole ordering.

The character of the dielectric response of such an inhomogeneous system is governed by the dimensions and concentration of the clusters depending on the actual conditions of preparation of the LNTN solid solutions. High pressures and temperatures favor a higher homogeneity of the system on the microscale. As a result, the concentration of the clusters and their size decrease, while the fraction of the Nb cations in the matrix increases, which manifests itself in an increase in permittivity. Because of the low cluster concentration in a high-pressure ceramic, the clusters are weakly bonded to one another. Their contribution to the dielectric response is practically independent, so the spectrum of relaxation times for such a dipole cluster system is narrow. This conclusion is supported by the observation that the frequency dependence of the temperature of the maximum in the loss tangent (T''_m) for a high-pressure ceramic (Figs. 1, 2) satisfies the relation

$$\ln\omega = -\ln\tau_0 - \Delta E/kT''_m, \tag{2}$$

which follows from the Debye relation for $\tan\delta$ of a system of independent dipoles combined with the Arrhenius expression for the relaxation time ($\tau = \tau_0\exp(\Delta E/kT)$):

$$\tan\delta = \frac{\varepsilon'_s - \varepsilon'_\infty}{\varepsilon'_s}\frac{\omega\tau_0\exp(\Delta E/kT)}{1+\omega^2\tau_0^2\exp(2\Delta E/kT)}. \tag{3}$$

The notation used here is standard. The activation energy ΔE is about 0.4 eV and depends only weakly on the actual composition of the LNTN system, and τ_0 is about 10^{-11} s.

The effect of the matrix on the dielectric response of clusters can manifest itself in the magnitudes of ΔE and τ_0.

The observed behavior of $\tan\delta$ in a normal-pressure ceramic with frequency and temperature (cooling branch) is evidence of a strongly broadened relaxation time spectrum characteristic of the dipole system of clusters, which is accounted for by their increased concentration and size and, hence, by the increased cluster interaction.

The thermal hysteresis of ε' observed in the LNTN solid-solution system may be caused by the following processes.

As the temperature is brought below a certain level, the antipolar mode in the cluster system undergoes softening and condensation. This process is initiated by the presence of cooperative nonpolar distortions associated with oxygen octahedron tilting in the crystal lattice of the system. In the course of this process, the antipolar mode interacts with the system of nonpolar cooperative distortions. This may bring about a change not only in the magnitude of the nonpolar cooperative distortions but also in their type. The outcome of this change is the formation of a distortion system with which the cluster crystal lattice reaches the state of a global minimum of the atomic interaction potential. If the antipolar mode condensed without this change in the magnitude and type of nonpolar distortions, the cluster crystal lattice would transfer to a local minimum that is shallower than the global minimum. Hence, the condensation and decondensation of the antipolar mode occur in different energy states of the cluster crystal lattice and this is what accounts for the thermal hysteresis of ε'.

It should be noted that the interaction of the antipolar mode with nonpolar cooperative distortions is dependent on the solid-solution composition. For $y = 0.7$, the proportion of clusters is small and thermal hysteresis of ε' is absent.

The kinetics of the phase transition to the state of a global minimum follows a complex pattern governed by nonpolar-mode condensation and variations in the magnitude and type of nonpolar cooperative distortions in the clusters, as well as by the interaction of these distortions with the matrix. Equation (1) for $\varepsilon'(t)$, which follows from a consideration of experimental data, enables one to estimate the main features of the kinetics of this phase transition. Since the volume of clusters is only a small fraction of that of the system, we can assume, as an approximation, that the relative decrease in permittivity with time, $|\varepsilon'_c(0) - \varepsilon'_c(t)|/|\varepsilon'_c(0) - \varepsilon'_h|$, is related to the relative fraction v_t of the original phase transformed into the new phase. In this case, it follows from Eq. (1) that

$$V_t = 1 - \exp(-t/\tau_f). \quad (4)$$

According to the theory of crystallization kinetics [8], the fact that the power of *t* in Eq. (4) is equal to unity means that nuclei of the new phase do not grow and are zero-dimensional (clusters). This result may be considered more evidence supporting the existence of clusters in the system under study. The values of τ_f and the pattern of its variation with temperature imply that the work required for a new phase nucleus to form is large and decreases as the temperature decreases. The value of τ_f for the normal-pressure ceramic is far larger than that for the high-pressure ceramic. This means that clusters in the former ceramic are larger than those in the latter.

Since the transition to the new phase occurs fairly slowly, quenching in liquid nitrogen fixes the system in a paraelectric state above the thermal hysteresis of ε'. At low temperatures, this state is metastable, and heating to a certain temperature drives the system to the stable state of a global minimum.

ACKNOWLEDGMENTS

This study was supported by the Russian Foundation for Basic Research (project no. 03-03-32964) and the Belarus Foundation for Basic Research (project no. F02R-070).

REFERENCES

1. M. Palatnikov, O. Voloshina, J. Serebryakov, and V. Kalinnikov, Ferroelectrics **131**, 227 (1992).
2. L. A. Reznichenko and L. A. Shilkina, Izv. Akad. Nauk SSSR, Ser. Fiz. **39**, 1118 (1975).
3. L. A. Reznichenko, L. A. Shilkina, O. A. Razumovskaya, S. I. Dudkina, E. S. Gagarina, and A. V. Borodin, Neorg. Mater. **39**, 187 (2003).
4. K. A. Müller and H. Rukard, Phys. Rev. B **19** (7), 3593 (1979).
5. A. M. Glazer, Acta Crystallogr. B **29**, 3384 (1972).
6. P. M. Woodward, Acta Crystallogr. B **53**, 32 (1997).
7. A. Villusuzanne, C. Elissalde, M. Pouchard, and J. Kavez, Eur. Phys. J. B **6**, 307 (1998).
8. N. N. Sirota, in *Crystallization and Phase Transitions* (Akad. Nauk BSSR, Minsk, 1962), p. 11 [in Russian].

Translated by G. Skrebtsov

Physics of the Solid State, Vol. 47, No. 4, 2005, pp. 710–714. Translated from Fizika Tverdogo Tela, Vol. 47, No. 4, 2005, pp. 686–690.
Original Russian Text Copyright © 2005 by M. Kerimov, Kurbanov, Agaev, Musaeva, É. Kerimov.

Pyroelectric Effect in Composites Produced through Electric-Discharge Plasma–Assisted Crystallization

M. K. Kerimov, M. A. Kurbanov, F. G. Agaev, S. N. Musaeva, and É. A. Kerimov
Institute of Physics, National Academy of Sciences of Azerbaijan, pr. Guseĭna Djavida 33, Baku, 370143 Azerbaijan
e-mail: mKurbanov@physics.ab.az

Received May 11, 2004; in final form, July 12, 2004

Abstract—The effect of the electric discharge–enhanced thermal crystallization of the polymer phase on the structure and pyroelectric properties of a polymer–pyroelectric composite is considered. It is shown that the changes in the polymer-phase structure during the electric discharge–enhanced thermal crystallization cause the number of charge carriers localized at the interface due to electrothermal polarization and the pyroelectric coefficient of the polymer–ceramics composite to increase noticeably. *© 2005 Pleiades Publishing, Inc.*

1. INTRODUCTION

The mechanism of the pyroelectric effect in polymer–pyroelectric-ceramic composites was proposed by us in [1, 2]. This mechanism is associated with the presence of localized states in the quasigap of the polymer phase, stabilization of charges in these states during electrothermal polarization, and the orientation of pyroelectric-phase domains in the field of these charges with the formation of a charge–oriented-domain quasineutral system. It has been established, as a result of comprehensive studies of the polarization and relaxation phenomena, that the magnitude of the pyroelectric response in polymer–pyroelectric-ceramic composites is determined by the changed effective dipole moment of the quasi-neutral system formed during electrothermal polarization and consisting of oriented domains in pyroelectric particles and the charges stabilized in the polymer matrix on the interphase boundary [1–3]. Therefore, the ability of the polymer phase to stabilize charge carriers injected into the composite during electrothermal polarization is very important for generating pyroelectricity in the composite. Indeed, if charge carriers are localized on the traps in the polymer, the strong local field produced by them acts on the pyroelectric particles and causes domain orientation. Clearly, electric charges will be accumulated in composites if both pyroelectric and polymer phases have a great number of localized energy levels that act as charge traps [4–6]. It should be noted, however, that the processes related to the localization of injected charge carriers in composites are mainly determined by heterogeneity of the physical and chemical structures of the polymer phase, even though electronic, ionic, and polarization processes in one phase (polymer) have a significant effect on the analogous processes in the other phase (pyroelectric ceramics) [3]. Indeed, when an injected carrier is captured in the polymer during electrothermal polarization, its potential energy decreases and the carrier is localized and locked in one of the lowest energy states at the interphase boundary. The size of the carrier localization region is determined by the dimensions of the region in which the potential energy is changed.

The objective of the present work was to examine the effect of polymer phase heterogeneity, which is controlled by the electric discharge–enhanced plasma-assisted crystallization of the composite under variable-temperature conditions, on the pyroelectric properties of the composites.

2. EXPERIMENTAL

We propose a new technological method for varying the structural heterogeneity of polymers and their composites. The method is based on the air-discharge plasma-assisted crystallization (electric discharge–enhanced thermal crystallization), which begins at the melting point. We also studied the effect of the electric discharge–enhanced thermal crystallization on the pyroelectric properties of polymer composites.

The electric discharge–enhanced thermal crystallization was carried out as follows. After briefly compressing the composite at the melting point, the upper die was removed from the surface of the specimen and a special discharge cell was attached to the die. The discharge cell enabled one to activate electric discharges of different intensity in air. An electric discharge was generated in a 4-mm-thick air gap between the teflon plate of the cell and a composite specimen; therefore, a partial discharge was induced [7, 8]. A 15-kV sinusoidal electric voltage (50 Hz) was applied to the cell. Using the partial discharge for the electric discharge–enhanced thermal crystallization made it possible to treat the composite surface uniformly without causing noticeable mechanical damage.

1063-7834/05/4704-0710$26.00 © 2005 Pleiades Publishing, Inc.

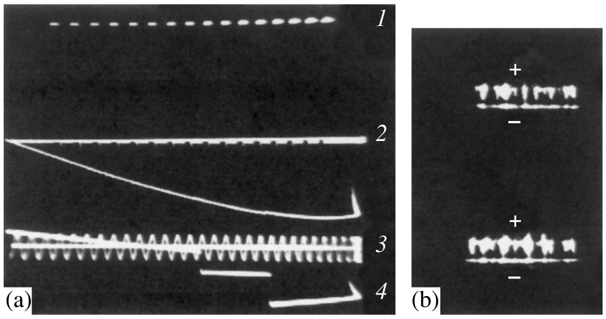

Fig. 1. Simultaneously recorded (a) electrical and (b) optical patterns of the discharge evolution in the air gap between dielectrics. In the oscillogram: (*1*) gate pulses of the electron-optic converter, (*2*) voltage change in the test cell, (*3*) calibrating voltage (T = 200 μs), and (*4*) voltage pulses corresponding to separate series of microdischarges.

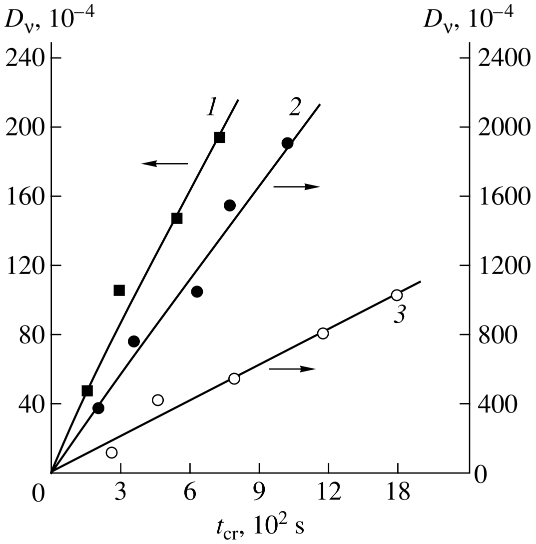

Fig. 2. Variations in the optical density of the bands that arise in the infrared spectrum of the polymer phase of the HDPE + 50 vol % PKR-57 composite during electric discharge–enhanced thermal crystallization. The cooling rate is 2 K/min, U_p = 11.8 kV, and $\Delta W = 1.4 \times 10^{-6}$ J; (*1*) 3380 cm^{-1}, (*2*) ν = 1735 cm^{-1} (C=O), and (*3*) ν = 1280 cm^{-1}.

Beginning from the melting point of the polymer phase of the composite, the temperature of the electric charge–enhanced plasma-assisted crystallization was changed stepwise (by 10 K over 0.5 h) at the first stage of cooling and then at a rate of 0.25–2 K/min down to the polarization temperature (~373 K) or room temperature. The changes in the structure were studied using the infrared spectra of the polymer phase of a composite. The following polymers were used as a polymer phase: high-density polyethylene (HDPE), polypropylene (PP), and polyvinylidene fluoride (PVDF). As the pyroelectric phase, we used the following pyroelectric ceramics with rhombohedral or tetragonal structure and different Curie temperatures T_C and pyroelectric coefficients γ: PKR-7M (T_C = 448 K, $\gamma = 5.6 \times 10^{-4}$ C/m^2 K), PKR-3M (T_C = 533 K, $\gamma = 5 \times 10^{-4}$ C/m^2 K), and PKR-57 (T_C = 463 K, $\gamma = 6 \times 10^{-4}$ C/m^2 K).

3. EXPERIMENTAL RESULTS AND DISCUSSION

Figure 1 shows the simultaneously recorded spatial (electron-optic converted image) and time (oscillogram) diagrams of the electric-discharge evolution in the air gap between the teflon plate and a composite. As is seen from Fig. 1, the electric discharge in the air gap between the composite and the dielectric is accompanied by separate series of discrete microdischarges. Each voltage pulse on the oscillogram (oscillogram *4* in Fig. 1) corresponds to one series of microdischarges. Each series, in turn, consists of a number of microdischarges generated in different regions of the sample surface. This character of the evolution of partial discharges (microdischarges) enables one to treat the composite surface uniformly and thus carry out effective crystallization of a composite under conditions of a discharge plasma in air with electronegative components.

Figure 2 shows the changes in the optical density of the bands corresponding to C–O–C, C=O, and OH that appeared in the infrared spectrum of the polymer matrix of the HDPE + PKR-57 composite during its crystallization under the simultaneous action of temperature, electric discharge, and discharge radiation. The results obtained by us show that the structure of the polymer matrix undergoes substantial changes in the course of electric-discharge crystallization. Indeed, the appearance of C–O–C, C=O, and OH groups in the infrared spectrum indicates changes in the chemical structure of the macromolecules, an enhancement of intermolecular interactions due to the polarity of these groups, and the formation of C–O–C bridges between macromolecules. Clearly, these chemical changes are accompanied by changes in the crystallization conditions and, therefore, in the physical structure of the polymer phase of the composite.

Figure 3 shows the temperature dependence of the pyroelectric current for several successive heating and cooling cycles of the PP + 50 vol % PKR-57 composite. Curve *1* corresponds to the first heating–cooling cycle and represents the nonreproducible part of the pyroelectric current. Curves *2*–*4* correspond to the reproducible part of the pyroelectric current. The heating (cooling) rate of the given pyroelectric element is 6 K/min. The pyroelectric current reverses direction under switching from heating to cooling, but its value remains the same as on heating; in other words, the heating–cooling cycle is characterized by a symmetric temperature-dependence plot of the reproducible part of the pyroelectric current.

Figure 4 shows the dependence of the pyroelectric coefficient of the PVDF + PKR-57 composite on the volume fraction Φ of the pyroelectric-ceramic phase. It can be seen that, under the same crystallization condi-

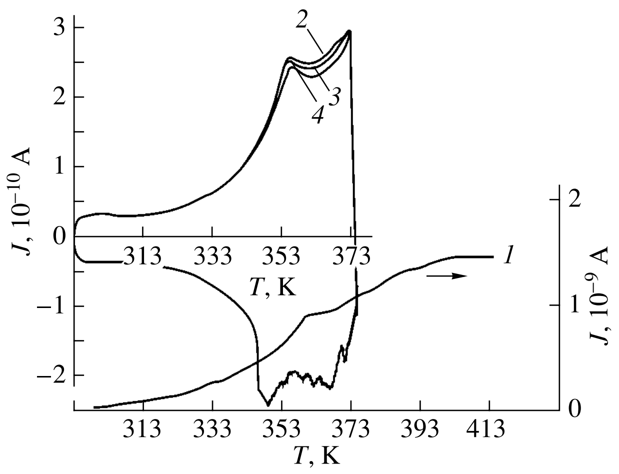

Fig. 3. Dependence of the pyroelectric current on the measuring temperature for the PP + 50 vol % PKR-57 composite. E_p = 8 MV/m, T_p = 373 K, and t_p = 1 h; (*1*) the nonreproducible part of pyroelectric current and (*2*–*4*) the reproducible pyroelectric current.

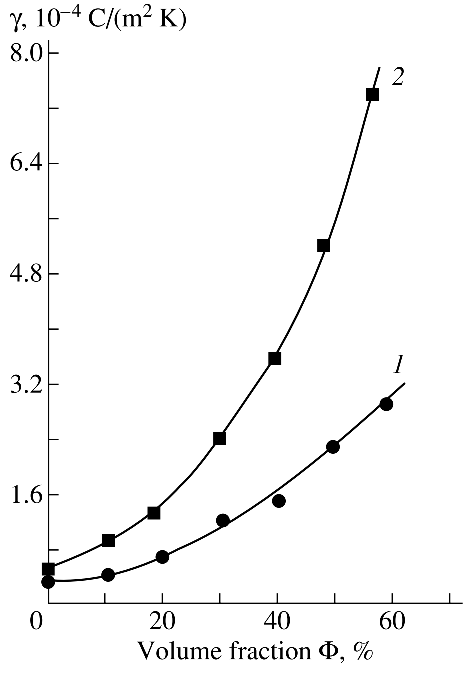

Fig. 4. Dependence of the pyroelectric coefficient γ on the volume fraction of the pyroelectric phase Φ in the PVDF + 50 vol % PKR-57 composite. T_p = 373 K, E_p = 4 MV/m, t_p = 1 h, and T = 358 K; (*1*) after thermal crystallization and (*2*) after electric discharge–enhanced thermal crystallization.

tions, γ increases faster than linearly with Φ. However, the pyroelectric coefficient of electrothermally crystallized composites is much higher than γ of thermally crystallized pyroelectric elements, all other polarization conditions (E_p, T_p) and the temperature of measurements T being equal.

We also studied the pyroelectric characteristics of a PVDF-based composite filled with particles of a PKR-3M pyroelectric ceramic, which has rhombohedral structure and a relatively high Curie temperature. The pyroelectric ceramics PKR-3M, as well as PKR-57, is characterized by a high pyroelectric coefficient, which, in combination with the low dielectric constant, ensures the high quality factor of this pyroelectric detector, $M_r = \gamma/\varepsilon = 1.4 \times 10^{-6}$ C/m^2K [9]. The fact that its pyroelectric coefficient is high at room temperature (Fig. 5) makes this composite promising for pyroelectric elements. It can be seen in Fig. 5 that the electric discharge–enhanced thermal crystallization of PVDF + PKR-3M composites results in a significant increase in their pyroelectric coefficients throughout the entire range of measurement temperatures T, including room temperature. Furthermore, the electric discharge–enhanced thermal crystallization significantly shifts the temperature of the onset of an abrupt increase in the value of the pyroelectric coefficient and, therefore, of the pyroelectric current. This experimental result shows that the electric charge–enhanced thermal crystallization increases the interphase interactions, which restrict the mobility of macromolecules of the polymer phase, and causes relaxation of charges on the polymer–pyroelectric-ceramic interface. The measured pyroelectric properties of other composites that were produced using electric discharge–enhanced plasma-assisted crystallization are shown in the Table.

It is of great interest to consider the kinetics of charge (electron) accumulation at the various stages of crystallization under discharge conditions. Figure 6a shows the space charge generated in an HDPE + PKR-57 composite as a function of the duration of electric discharge–enhanced thermal crystallization. The charge value was found from the depolarization current spectra immediately after electric discharge–enhanced thermal crystallization. The low values of the charge arising at the initial stage of crystallization can be due to electron traps being destroyed under the action of temperature, discharge, and voltage pulses generated during each series of microdischarges and also due to electrons being captured by free radicals of the polymer phase [10, 11]. It should be noted that, in ac electric fields, a fraction of the injected charges reappears at the electrode when the polarity is changed. The charges localized in deeper traps can enhance the electric-field intensity in the polymer composite at each air-gap breakdown during the electric discharge–enhanced thermal crystallization. The electron bombardment and the strong local field also initiate the formation of radicals [8, 10].

The results obtained allow us to suggest the following mechanism for changing the pyroelectric properties of composites during electric discharge–enhanced thermal crystallization. We believe that, in the course of electrical loading of the composite–gaseous medium–composite system, partial discharges occur and condi-

Pyroelectric coefficients of different composites after thermal crystallization and after electric discharge–enhanced thermal crystallization

Composites	Φ, % vol.	T, K	Polarization conditions		γ, 10^{-4} C/m^{2}K	
			E_p, MV/m	T_p, K	after thermal crystallization	after electric discharge–enhanced thermal crystallization
PVDF + PKR-7M	50	353	6	373	1.1	4.8
HDPE + PKR-7M	50	353	6	393	0.55	2.7
HDPE + PKR-57	50	353	6	373	0.82	4.2

tions are created for rather complex physicochemical processes in the bulk of the polymer phase caused by electron–ion bombardment, radiation, local heating of the contact between the microdischarge channel and the polymer (Fig. 1b), and active gas-discharge products (O_3, O, OH, NO). Together, these components of a partial discharge predetermine the specific features of the formation, transformation, and accumulation of free radicals, which account for all structural and energy changes in the polymer phase of the composite. It should be noted that the structural rearrangements that accompany the transition of the polymer from the fluid state to a highly elastic and finally to a glassy state in the course of the crystallization result in an abrupt change in the amplitude of the rotational segmental motion. Furthermore, under the action of temperature and an electric discharge–induced plasma, these rearrangements of the structure and the changes in the amplitude of the rotational segmental motion will be significantly different due to electronic, ionic, destructive, and oxidizing processes. For this reason, the conditions of injection, generation, and transfer of charge carriers and their interactions with the macromolecules are changed in the course of electric discharge–enhanced crystallization. Under the action of electron–ion bombardment and discharge radiation, free radicals will form during crystallization, especially in the temperature ranges corresponding to the fluid and highly elastic states.

The current understanding of the mechanism of free-radical formation in polymer dielectrics exposed to an intense electric field and electric discharge remains incomplete. The most probable mechanism consistent with the partial discharge conditions is the mechanism based on discharge radiation ionization of macromolecules followed by decomposition of the molecular cation (M^+) into a free radical ($R_1^{\bullet}$) and a cation fragment ($R_2^{\bullet}$) [10]:

$$M \longrightarrow M^+ + e; \quad M^+ \longrightarrow R_1^{\bullet} + \overset{+}{R_2}.$$

In ionized macromolecules, the chemical bonds are excited. Therefore, they break relatively easily, and oxidizing processes begin [10], resulting in the appearance of new local energy levels in the quasigap of the polymer and, therefore, in the formation of additional carrier traps, which is experimentally confirmed by the results shown in Fig. 6. The effective accumulation of carriers at the polymer–pyroelectric-ceramic interfaces and the strong orientational domain polarization of the pyroelectric phase (curves *3*, *4* in Fig. 6b) significantly increase the pyroelectric coefficient (curves *1*, *2* in Fig. 6b) of the composites produced through electric discharge–enhanced plasma-assisted crystallization.

The results obtained by us show that the method of electric discharge–enhanced thermal crystallization should be promising for the development of highly efficient active composites. However, these interesting results currently cannot be exhaustively explained, because these studies are at the initial stage. It may be said that the pyroelectric properties of polymer–pyroelectric-ceramic composites produced through electric discharge–enhanced plasma-assisted crystallization are significantly improved and that the concentration of charge carriers accumulated in them during electrothermal polarization increases.

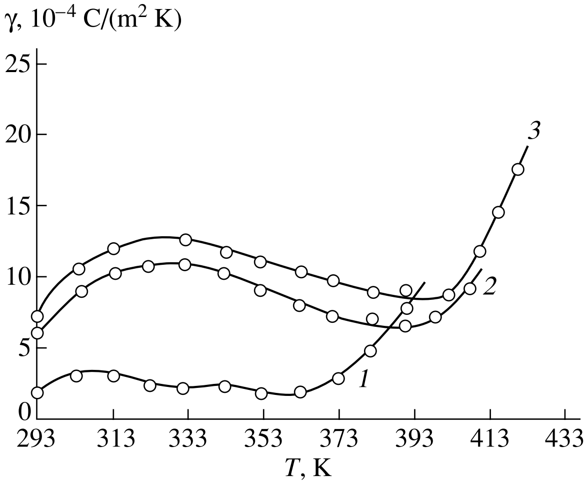

Fig. 5. Dependence of the pyroelectric coefficient γ on the measuring temperature T for the PVDF + 50 vol % PKR-3M composite. T_p = 373 K and t_p = 1 h; (*1*) after thermal crystallization (E_p = 1.5 MV/m) and (*2, 3*) after electric discharge–enhanced thermal crystallization at E_p = 1.5 and 3 MV/m, respectively.

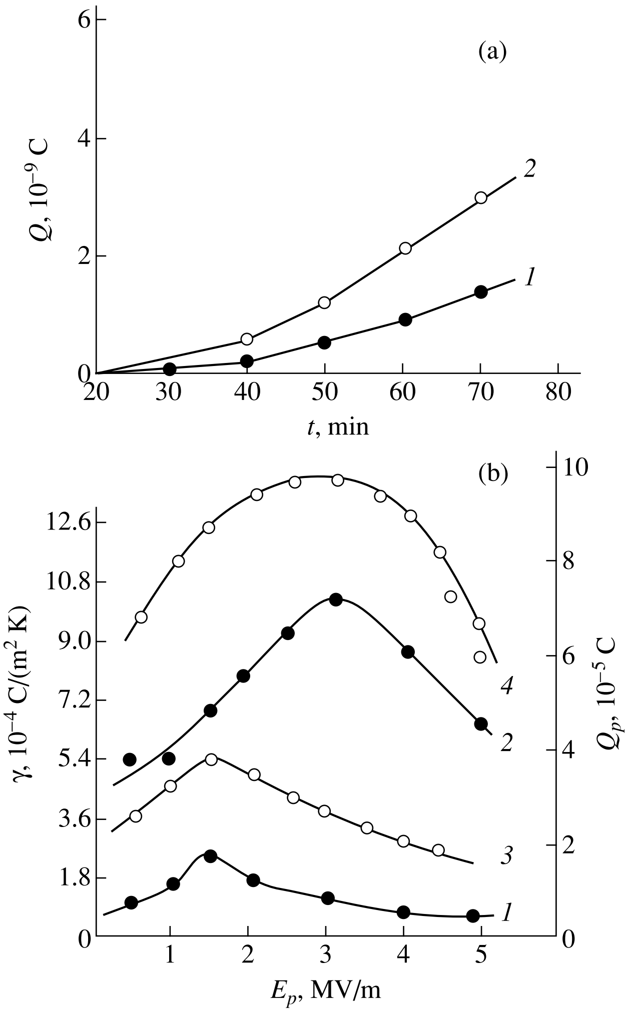

Fig. 6. (a) Dependence of the stabilized charge Q on the cooling duration in the course of electric discharge–enhanced thermal crystallization of the HDPE + 40 vol % PKR-57 composite. The cooling rate is 1.5 K/min; the treatment voltage U is (*1*) 16 and (*2*) 18 kV. (b) Dependence of (*1*, *2*) the pyroelectric coefficient γ and (*3*, *4*) the charge Q_p accumulated during polarization on the electric-field intensity E_p of the PVDF + PKR-3M composite. T_p = 373 K, t_p = 1 h, and T = 373 K; (*1*, *3*) after thermal crystallization and (*2*, *4*) after electric discharge–enhanced thermal crystallization.

The results obtained enable us to make the important conclusion that, in order to design highly efficient pyroelectric composites based on polymers and pyroelectric ceramics, it is necessary to increase the density of localized states in the quasigap of the polymer phase and at the interphase boundary, which can be achieved using electric discharge–enhanced thermal crystallization of the polymer phase of composites.

REFERENCES

1. M. G. Shakhtakhtinskiĭ, B. A. Guseĭnov, M. A. Kurbanov, Yu. N. Gazaryan, and A. O. Guliev, Fiz. Tverd. Tela (Leningrad) **25** (12), 3722 (1983) [Sov. Phys. Solid State **25**, 2145 (1983)].
2. M. G. Shakhtakhtinskiĭ, B. A. Guseĭnov, M. A. Kurbanov, Yu. N. Gazaryan, and A. O. Guliev, Dokl. Akad. Nauk AzSSR **40** (10), 34 (1984).
3. A. I. Mamedov, M. A. Kurbanov, S. N. Musaeva, and A. Sh. Gasanov, Fizika **4** (3), 50 (2001).
4. *Electrets*, Ed. by G. M. Sessler (Springer, Berlin, 1980; Mir, Moscow, 1983).
5. V. A. Marikhin and L. P. Myasnikova, *Permolecular Structure of Polymers* (Khimiya, Leningrad, 1977) [in Russian].
6. M. E. Lines and A. M. Glass, *Principles and Applications of Ferroelectrics and Related Materials* (Oxford Univ. Press, Oxford, 1977; Mir, Moscow, 1981).
7. M. K. Kerimov, M. A. Kurbanov, A. O. Orudzhev, G. G. Aliev, and I. N. Orudzhev, Izv. Nats. Akad. Nauk Azerb., Ser. Fiz.–Mat. Tekh. Nauk **5**, 46 (2003).
8. M. A. Bagirov, N. A. Nuraliev, and M. A. Kurbanov, Zh. Tekh. Fiz. **42**, 629 (1972) [Sov. Phys. Tech. Phys. **17**, 495 (1972)].
9. E. G. Fesenko, A. Ya. Dantsiger, and O. N. Razumovskaya, *New Piezoelectric Materials* (Rostov. Gos. Univ., Rostov-on-Don, 1983) [in Russian].
10. Kh. B. Gezalov and M. K. Kerimov, Zh. Tekh. Fiz. **52** (7), 1386 (1982) [Sov. Phys. Tech. Phys. **27**, 842 (1982)].
11. A. V. Vannikov and A. D. Grishina, *Photochemistry of Polymeric Donor–Acceptor Complexes* (Nauka, Moscow, 1984) [in Russian].

Translated by E. Borisenko

Physics of the Solid State, Vol. 47, No. 4, 2005, pp. 715–719. Translated from Fizika Tverdogo Tela, Vol. 47, No. 4, 2005, pp. 691–695.
Original Russian Text Copyright © 2005 by Bordonskiĭ.

Electromagnetic Properties of Ice near the Water–Ice Phase Transition Temperature

G. S. Bordonskiĭ

Chita Institute of Natural Resources, Siberian Division, Russian Academy of Sciences, ul. Butina 26, Chita, 672090 Russia
e-mail: bord@mail.chita.ru, Igc255@mail.ru

Received May 17, 2004

Abstract—Freshwater ice in a cavity was studied under heating to 0°C followed by cooling at a frequency of 6.3 GHz. Splitting of a resonant transmission line at 60–70 MHz was detected. This effect may be associated with the existence of two vibrational modes in ice, with the coupling between them increasing near 0°C. In such a medium, two waves with identical polarizations and similar wavenumbers can exist. This assumption was confirmed experimentally by measuring the 13-GHz radiation transmission through a natural freshwater ice cover. These measurements detected signal oscillations caused by the interference of two waves, with alternation of maxima and minima with a period of 4.6 m, which corresponds to a beat frequency of ~37 MHz. © *2005 Pleiades Publishing, Inc.*

1. INTRODUCTION

As was shown in [1], resonant transmission curves of a microwave cavity filled with H_2O and D_2O ice exhibit differences in their shape. The curves were extended to high frequencies for H_2O ice and to low frequencies for D_2O ice. The effect was most pronounced for temperatures near the water–ice phase transition. It was assumed that this effect is associated with the difference between the quantum statistics for protons and deuterons.

This paper aims to study the electromagnetic properties of freshwater H_2O ice near the phase transition temperature. To do this, we continued measurements of the microwave transmission near a frequency of 6 GHz using a cavity filled with ice, as well as studied microwave propagation at a frequency of 13 GHz through an ice bulk at distances of 40–100 m.

2. EXPERIMENTAL

The setup for measuring the ice parameters in a rectangular cavity is similar to that described in [1] and is based on a conventional meter of frequency characteristics (e.g., R2 series). A cavity completely filled with ice was placed into a discontinuity of a waveguide transmission line. An H_{101}-type half-wave rectangular duralumin cavity was used. The cavity was connected with a waveguide channel using diaphragms with slots in the magnetic-field plane. The cavity cross section and length were 8×17 and 20 mm, respectively. The cavity was completely filled with ice produced from distilled water. Water was frozen in the cavity at a temperature of –15°C, after which the sample was exposed to this same temperature for one day. The lowest resonant frequency was in the frequency range 6.3–6.4 GHz, depending on temperature, the specific features of sample preparation, and the diaphragms used. The signal frequency in the setup was measured using an external frequency meter with a measurement accuracy of ±1 MHz. The high-frequency channel was placed in a cold room at a temperature of –25°C. The temperature of the cavity containing a sample was maintained by special electric heaters and was measured with an accuracy of ±0.1°C using a thermistor inserted into the cavity body.

The electromagnetic properties of ice control the specific features of the electromagnetic wave propagation in it. Therefore, it is preferable to study the electromagnetic characteristics using methods for out-of-doors measurements on large samples. In this case, finer effects, e.g., gyrotropy of ice, can be detected, in contrast to laboratory measurements, where small samples are studied. For the sake of comparison, characteristics of microwaves transmitted through an ice bulk at distances up to 100 m were also measured. To this end, experiments with a freshwater ice cover were carried out. A schematic representation of these experiments is given in Fig. 1.

A transmitter based on a Gunn diode (*1*) and a superheterodyne radiometric receiver (*2*) were positioned at a depth of ~0.5 m in the ice cover (*3*). The distance between them was varied by moving the transmitter to within 100 to 40 m of them. To this end, ice blocks were cut out and removed. Emitted microwaves were vertically polarized, and both vertically and horizontally polarized waves were received. Experiments were performed on a lake with an ice mineralization of 5 mg/kg, which corresponds to the salt concentration of singly distilled water. Measurements were carried out at various ice temperatures under diurnal temperature variations when the temperature approached 0°C. The

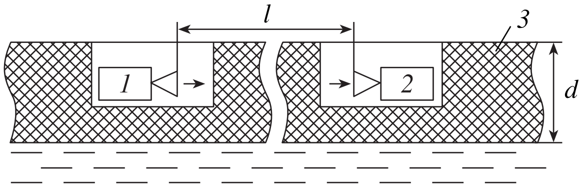

Fig. 1. Schematic diagram of experiments with radio-wave transmission of an ice cover for determining its electromagnetic characteristics: (*1*) transmitter, (*2*) receiver, and (*3*) ice cover; *l* is the distance between the transmitter and receiver microwave antennas and *d* is the ice thickness.

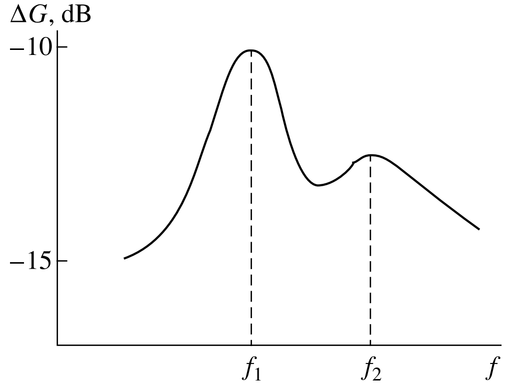

Fig. 2. Transmission line of the cavity containing ice after heating from –25°C to 0°C over approximately 4 h followed by 20-min cooling to –11.5°C; f_1 and f_2 are transmission maxima at frequencies of 6323 and 6387 MHz, respectively, and Δ*G* is the signal level measured from the initial resonance amplitude.

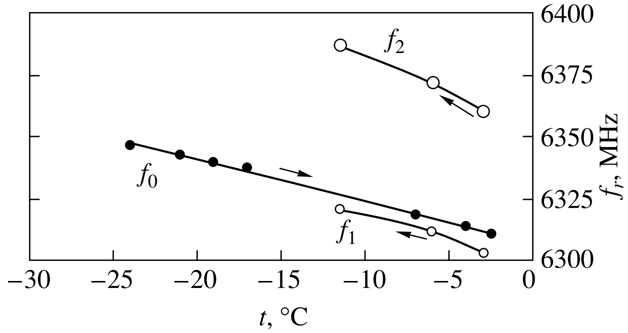

Fig. 3. Run of cavity resonance frequencies f_r upon heating (f_0 corresponds to the single-humped transmission curve) to a temperature close to 0°C, at which the signal disappeared, followed by 20-min cooling to –11.5°C (f_1 and f_2 correspond to transmission maxima of the two-humped curve). The direction of the change in temperature in time is indicated by arrows.

microwave frequency was 13 GHz. The half-widths of directional patterns of the horn antennas used were 0.1 rad. The thickness of the ice cover during measurements was 1.3–1.4 m.

3. EXPERIMENTAL RESULTS

In laboratory measurements, the cavity resonance frequency was determined and the changes in the amplitude, resonant curve width, and its shape were measured. The sample under study was slowly heated from –25°C at a rate of ~6 K/h. Initially, a single-humped resonant curve of signal transmission was observed. The curve was slightly asymmetric; it was extended to high frequencies. The FWHM of the resonant curve was 18 MHz and increased as the medium was heated with a simultaneous decrease in the resonance amplitude. Since the temperature measured by the sensor in the cavity body and the ice temperature near the phase transition point can slightly differ, the measurements were carried out as follows. Preliminary measurements upon slow heating showed that the cavity amplitude decreased by 10 dB as the sensor temperature reached –0.5°C. To reach a temperature of –0.1 to 0°C, the cavity was heated until total disappearance of the microwave signal, which can be detected using the setup, i.e., to –30 dB. Immediately after the signal disappeared, heating was stopped to avoid sample thawing. The measurement was continued when the signal became much higher than the noise level in the setup.

In this case, an interesting feature was detected: on reaching 0°C and subsequent cooling, two humps arose in the measured resonant curve (Fig. 2). Their distinguishing feature was that the heights of the two peaks differed by 3 dB. A less distinct peak was observed in the high-frequency region. The frequency shift of their maxima from the initial value was also asymmetric. The low- and high-frequency peaks were shifted by ~7 and 50 MHz, respectively. However, the two-humped feature did not disappear upon ice cooling but was retained to –11°C, as was the high absorption in the medium. The amplitude of the maximum resonant curve was 10 dB lower than that of the initial single-humped resonant curve. The detected hysteresis in the transmission curve shape is demonstrated in Fig. 3, which shows the dependences of the resonant frequencies upon heating to 0°C (one resonant frequency) and cooling from 0°C (two resonant frequencies). The experimentally observed frequency difference of the two peaks was 60–70 MHz.

Measurements were then terminated, and the cavity containing ice was placed in a cold room, where it was exposed to a temperature of –15°C for three weeks. After that, it turned out that the initial properties of the ice were restored and that a single-humped resonant characteristic was observed.

Experiments with extended objects, i.e., radio transmission of an ice cover, were carried out in March 2004 on Lake Arakhleĭ on the Yablonovyĭ Ridge (Transbaikalia). At this time, the ice temperature approached 0°C. The ice cover state was monitored using ten temperature and electric sensors, which determined the moisture and the temperature over the cover thickness. The first Stokes parameter S_1 of polarized microwaves was determined experimentally. This parameter characterizes the total radiation power passed through the distance between the receiving and transmitting antennas: $S_1 = P_H + P_V$, where P_V and P_H are the powers of signals with horizontal and vertical polarizations, respectively.

Figure 4 shows the measured dependence of the parameter S_1 on the transmitter–receiver distance. The ice temperature at the midplane of the ice cover was –1°C. The distance was varied by cutting out and removing ice in steps of 1 m. The duration of the experiment was 8 h.

As follows from Fig. 4, radiation damping in ice (at a rate of ~1 dB/m) and alternation of maxima and minima with a period of 4.6 m over the entire distance under study were observed. Damping with distance is caused by an increase in the beam path in the medium and by beam energy scattering over a larger area. However, the alternation of radiation minima and maxima observed for the two linear polarizations indicates that the field exhibits interference.

The interference can be caused by a partial reflection of microwave power from interfaces. The reflected beams may be given as a set of imaginary sources arranged in the emitter plane. An analysis of the beam path from imaginary sources shows that, for the given arrangement of the devices, the expected distance between interference minima exceeds that observed at a distance of 40–50 m by approximately three times. Moreover, this length increases monotonically with the emitter–receiver distance, which results in the interference disappearing. These considerations relate to a single reflection of beams, i.e., to the case of two imaginary sources. For a larger number of sources, the interference effect weakens and disappears at $l \gg d$, since the sources are antiphase; i.e., the reflectances from ice–air and ice–water interfaces are opposite in sign. For this reason, the interference effects associated with wave reflection from the interfaces are insignificant in this experiment.

The possible propagation of microwaves over lateral waves along the ice–air interface was also studied experimentally. When an emitter was placed beyond the ice, the signal at its surface disappeared almost completely. The absence of lateral waves is explained, first, by their significant damping with distance and, second, by the use of directed antennas when the major energy fraction propagates within the total internal reflection angle.

4. DISCUSSION

The anomalies in the transmission spectrum of the cavity containing ice near the ice–water phase transition point can be explained by the small amount of liquid water inclusions in the medium. This should result in a certain increase in the real (ε') and imaginary (ε'') parts of the relative permittivity, since these values for liquid water are $\varepsilon_1' = 63$ and $\varepsilon_1'' = 37$ [2] (as calculated from the Debye formula) at a frequency of 6 GHz at 0°C. These values significantly exceed those for freshwater ice, $-\varepsilon_2' = 3.19$ and $\varepsilon_2'' = 4.1 \times 10^{-3}$ [3].

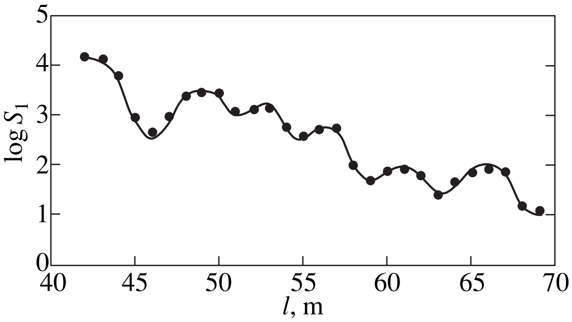

Fig. 4. Dependence of the logarithmic first Stokes parameter of 13-GHz microwaves on the distance between the receiver and transmitter in ice. The Stokes parameter is measured in relative units.

The effective permittivity ε_m of a mixture can be determined using formulas for heterogeneous mixtures, e.g., the Brown formula (see [4])

$$\varepsilon_m = w_1\varepsilon_1 + w_2\varepsilon_2 = \varepsilon_m' + i\varepsilon_m'', \tag{1}$$

where ε_1, ε_2, w_1, and w_2 are the permittivities and volume fractions of the components.

An increase in ε' should lower the resonant frequency of the cavity when its length is fixed, since the radiation wavelength λ_1 in the rectangular waveguide containing a medium decreases:

$$\lambda_1 = \frac{\lambda_0}{\sqrt{\varepsilon_m' - \left(\frac{\lambda_0}{2a}\right)^2}}, \tag{2}$$

where λ_0 is the wavelength in free space and a is the width of the wide wall of the waveguide. Assuming that the lower frequency resonant peak corresponds to a new resonant frequency decreased due to liquid inclusions, the corresponding small increment Δε', proceeding from formula (2), can be determined using the relation

$$\frac{\Delta f}{f} \approx \frac{1}{2}\frac{\Delta\varepsilon'}{\varepsilon_m' - \left(\frac{\lambda_0}{2a}\right)^2}, \tag{3}$$

where $\Delta f = f_0 - f_1$ and $\Delta\varepsilon' = \varepsilon_m' - \varepsilon_2'$. For the data given, we obtain $\Delta\varepsilon' = 1.7 \times 10^{-3}$. Using formula (1) to calculate w_1, we obtain $w_1 \approx \Delta\varepsilon'/\varepsilon_1' \approx 2 \times 10^{-5}$.

If we assume that the increment $\Delta\varepsilon'' \sim \varepsilon_1'' w_1$, then we obtain $\Delta\varepsilon'' \sim 6 \times 10^{-4}$. The resonant curve width Δf_r can be determined from the relation

$$\frac{\Delta f_r}{f} = \frac{\varepsilon_m''}{\varepsilon_m'}.$$

Considering that the increment $\Delta\varepsilon''$ dictates the resonance curve broadening, the data obtained for $\Delta\varepsilon''$ and w_1 yield $\Delta f_r \sim 1$ MHz. Near 0°C, Δf_r increases from 18 MHz (at –24°C) to ~30 MHz. Thus, the calculated frequency shift and resonant curve broadening do not agree with the case where there is liquid in the medium. Furthermore, the concept of effective permittivity cannot explain the splitting of the cavity transmission line. Hence, the observed effects are not associated with liquid water in the cavity.

As is known, the two-humped feature of the resonant curves is observed in a system of two identical coupled oscillators [5]. Therefore, it can be assumed that the observed splitting of the lowest resonant mode of the half-wave cavity (Fig. 1) is explained by the existence of two vibrational modes of water molecules in the medium. These states are most likely related to proton states, since the proton (according to data from structural studies) can occupy two positions along the hydrogen bond line, as well as vibrate along this line and transversely to it [6]. However, these states in water and ice seem to differ significantly. Therefore, it is conceivable that molecules of the medium near the phase transition point can be in two states, one corresponding to a low-temperature water phase, i.e., purely crystalline ice, and the other to a somewhat disordered state with a glass structure. This vitreous water state is formed during rapid cooling [6]. Some authors believe that the solid–liquid transition passes through a premelting phase [7]. In the case of ice, the premelting phase could arise when a medium absorbs a certain energy at 0°C, which is still insufficient to form liquid water. Upon further cooling, this state can be retained for some time, which results in a small temperature hysteresis of the electromagnetic properties of the medium.

Purely phenomenologically, the result shown in Fig. 1 can be interpreted as the water having two refractive indices near 0°C. A question arises as to whether this behavior is associated with the properties of the medium or is somehow caused by its location in the waveguide cavity. For example, an inhomogeneous medium in a waveguide can have negative dispersion [8].

As a rule, polycrystalline ice in electromagnetic studies is assumed to be a homogeneous medium. Nevertheless, it consists of isolated single crystals with macroscopic sizes characteristic in every case. Ice thawing begins over boundaries of ice crystals. As a result, a 3D network of conducting water films is formed in space; although strongly distorted it is close to periodic. If such a medium has two refractive indices, extraordinary birefringence arises, which relates to waves with orthogonal polarizations. Two values of the refractive index correspond to waves with a single polarization. This means that interference of two waves, causing maxima and minima of field amplitudes, can be observed in a medium when monochromatic radiation propagates at a temperature close to 0°C in ice having a certain thermal history.

The formation of a “new wave” was predicted for media with spatial dispersion when the interaction of waves with inhomogeneities, whose sizes are comparable to the wavelength near absorption lines, is substantial [9]. In particular, near quadrupole lines at weak absorption, the difference between the refractive indices of the new and ordinary waves will give rise to rather slow oscillations in the intensity with sample thickness [9].

A direct experiment with measurement of the first Stokes parameter of radiation passed through ice detected radiation power oscillations with distance. As follows from Fig. 4, alternation of maxima and minima of the signal power with a period of 4.6 m was observed against a background of a gradual increase in damping. The distortion of the curve in Fig. 4 can be explained by the features of the experiment, i.e., by the duration of the experiment (8 h), during which time the parameters varied due to the temperature variation of the medium.

The results obtained can be used to determine the difference Δk between wavenumbers and the corresponding beat frequency. For two waves with similar wavenumbers and identical polarizations, we can write the sum of their fields (disregarding damping and assuming the amplitudes and phases of individual waves to be equal) as

$$A_1 + A_2 = A_0 \exp\{i(\omega t - kx)\}[1 + \exp i\Delta kx]. \quad (4)$$

Considering the real part of sum (4), we can determine Δk by alternating the interference minima. They are reached at $\Delta kx = n\pi$ ($n = 1, 3, 5, \ldots$). From this we obtain $\Delta k = 2\pi/\Delta x$, where Δx is the distance between two measured interference minima of radiation. For the beat frequency f^*, taking into account the change in the wavelength in the medium, we can write

$$f^* = \frac{c}{\Delta x \sqrt{\varepsilon_2'}},$$

where c is the electromagnetic wave velocity in vacuum. From the values measured for Δx, the beat frequency is ~37 MHz. This value is close to the frequency difference in the cavity transmission spectrum found in laboratory measurements (Fig. 1).

We note that the previously observed distortion of the resonant line slopes in the cavity transmission spectrum [1] can also be related to the existence of two vibrational modes with close frequencies and different amplitudes. Due to a small frequency shift, these states were not resolved at a low Q factor of the cavity used.

However, as 0°C is approached, these modes for ice become observable due to strengthening of the coupling between orthogonal vibrational modes and an increase in the frequency difference.

Anomalies in the electromagnetic characteristics of ice were also previously observed by other authors. For example, during radar determination of glacier thickness in Antarctica, signal disappearance was observed in some regions when constructing thickness profiles [10]. This effect can be explained by the interference of two waves with the same polarization.

5. CONCLUSIONS

Anomalies in the electromagnetic properties of freshwater ice can be explained by the existence of two vibrational modes in the medium, whose coupling increases near 0°C. These anomalies manifest themselves in the formation of two waves with the same polarization and similar wavenumbers in measurements in waveguide systems and extended objects.

The formation of additional waves with similar wavenumbers can be explained by the influence of spatial dispersion on microwaves. The nature of spatial dispersion in ice can be related to the polycrystalline structure of ice, in which crystals are separated by water films. This problem calls for separate study.

ACKNOWLEDGMENTS

This study was supported by the Russian Foundation for Basic Research, project no. 03-02-16042.

REFERENCES

1. G. S. Bordonskiĭ and T. G. Filippova, Fiz. Tverd. Tela (St. Petersburg) **43** (9), 1575 (2001) [Phys. Solid State **43**, 1639 (2001)].
2. Ya. Yu. Akhadov, *Dielectric Properties of Pure Liquids* (Izd. Standartov, Moscow, 1972) [in Russian].
3. S. G. Warren, Appl. Opt., No. 23, 1206 (1984).
4. W. Brown, Jr., *Dielectrics*, in *Handbuch der Physik* (Springer, Berlin, 1956; Inostrannaya Literatura, Moscow, 1961), Vol. 17, Part 1.
5. K. Magnus, *Schwingungen Eine Einführung in die Theoretishe Behandlung von Schwingungsproblemen* (Teubner, Stuttgart, 1976; Mir, Moscow, 1982).
6. V. Petrenko and R. W. Whitworth, *Physics of Ice* (Oxford Univ. Press, Oxford, 2002).
7. G. D. Seleznev and L. A. Bityutskaya, Kondens. Sredy Mezhfaz. Granitsy **2** (2), 160 (2002).
8. R. A. Silin, *Periodical Waveguides* (Fazis, Moscow, 2001) [in Russian].
9. V. M. Agranovich and V. L. Ginzburg, *Crystal Optics with Spatial Dispersion, and Excitons*, 2nd ed. (Nauka, Moscow, 1979; Springer, New York, 1984).
10. V. V. Bogorodsky, C. R. Bentley, and P. E. Gudmandsen, *Radioglaciology* (Gidrometeoizdat, Leningrad, 1983; Reidel, Dordrecht, 1985).

Translated by A. Kazantsev

Physics of the Solid State, Vol. 47, No. 4, 2005, pp. 720–728. Translated from Fizika Tverdogo Tela, Vol. 47, No. 4, 2005, pp. 696–704.
Original Russian Text Copyright © 2005 by Flerov, Kartashev, Grankina.

LATTICE DYNAMICS AND PHASE TRANSITIONS

Heat Capacity and Phase Transitions in NH_4LiSO_4, $Cs_x(NH_4)_{1-x}LiSO_4$, and $RbLiSO_4$

I. N. Flerov, A. V. Kartashev, and V. A. Grankina
Kirensky Institute of Physics, Siberian Division, Russian Academy of Sciences, Akademgorodok, Krasnoyarsk, 660036 Russia
e-mail: flerov@ksc.krasn.ru

Received June 25, 2004

Abstract—The heat capacity of NH_4LiSO_4, $RbLiSO_4$, and $Cs_x(NH_4)_{1-x}LiSO_4$ crystals and its behavior over a broad temperature range including the phase transition regions were studied. The entropy changes corresponding to structural transformations in these crystals were found not to be characteristic of straightforward ordering of structural blocks. The results obtained are discussed in terms of phenomenological theory and model concepts. *© 2005 Pleiades Publishing, Inc.*

1. INTRODUCTION

The numerous compounds with the general chemical formula $AA'CX_4$ (A, A', and C are cations, and X is an anion) form a representative family of crystals possessing a β-K_2SO_4-type structure (space group $G_1 = D_{2h}^{16}$–$Pmcn$, $z = 4$) over a certain temperature interval. The praphase of this structure is the hexagonal α-K_2SO_4 structure (space group $G_0 = D_{6h}^{4}$–$P6_3/mmc$, $z = 2$), which can exist only if the tetrahedral ionic groups CX_4 are disordered in orientation [1]. However, the hexagonal phase has not been observed experimentally in all crystals with the β-K_2SO_4 structure. The $\alpha \longrightarrow \beta$ phase transition has been reliably established to occur in several oxygen-containing compounds with identical A and A' cations, for instance, in K_2SO_4, K_2SeO_4, and K_2CrO_4 [1]. However, in many crystals with $A \neq A'$, either phase transitions to the hexagonal phase with space group $P6_3/mmc$ have not been observed up to the melting point or the space group of the hexagonal phase has not been established unambiguously. Considered, however, from the standpoint of model concepts, the praphase G_0 may also exist in crystals of this type [2].

As the temperature is lowered, the stable crystal modification β-K_2SO_4 frequently transforms into a ferroelectric, ferroelastic, or incommensurate phase in single or successive reversible phase transitions. The diversity of distorted phases depends, to a considerable extent, on chemical pressure, which can be varied through proper isovalent substitutions of cations and anions in the β-K_2SO_4 structure. This is convincingly illustrated by the crystal series ALiSO$_4$, whose symmetry within a certain temperature interval is orthorhombic with space group $Pmcn$ [1]. In these compounds, the SO_4 tetrahedral groups are linked together by the LiO_4 tetrahedra to form a network. Depending on the size of the A cation, phase transitions to the ferroelastic phase with space group $G_2 = (C_{2h}^5)$–$P112_1/n$ and $z = 4$ occur under cooling either directly ($CsLiSO_4$–CLS) or via a series of intermediate structural forms including the incommensurate phase I: $Pmcn \longrightarrow I \longrightarrow P2_1/c11 \longrightarrow P11n \longrightarrow P112_1/n$ ($RbLiSO_4$–RLS). In NH_4LiSO_4 (NLS), the ferroelastic monoclinic phase $P112_1/n$ is not observed down to liquid-helium temperatures and the phase transition from $Pmcn$ is accompanied by the onset of a ferroelectric state (space group $P2_1cn$, $z = 4$) in the region of ~160 K. This transition is followed by a transition to the ferroelastic phase $P2_1/c11$ ($z = 8$). Recent studies of the $Cs_x(NH_4)_{1-x}LiSO_4$ (CNLS) have revealed that the $P112_1/n \longrightarrow P2_1cn$ phase transition occurs only in compounds corresponding to the narrow concentration region $x = 0.3$–0.5 [3].

The $TlLiSO_4$ crystal (TLS) has also been reported fairly recently to have an orthorhombic phase ($Pmcn$) at room temperature, which transfers, in a series of structural transformations under cooling, to a monoclinic phase with a still unknown space group [4–6]. When heated above 531 K, TLS transfers to a hexagonal phase; however, its space group, $P6_3$ ($z = 24$), does not fit with the α-K_2SO_4 structure.

As for the $KLiSO_4$ compound (KLS), it has been found to exist in a hexagonal and an orthorhombic phase, but their space groups have not yet been established unambiguously [1].

Some experimental data obtained, in particular, in structural studies suggest that the $G_0(P6_3/mmc) \longrightarrow G_1(Pmcn) \longrightarrow G_2$ phase transitions in $AA'CX_4$ and A_2CX_4 compounds are driven by ordering of the CX_4 tetrahedral ionic groups [1, 2, 7]. The fact that ordering of the NH_4 tetrahedra does not contribute noticeably to the mechanism of phase transitions in ammonium-containing crystals is supported convincingly by studies of ND_4LiSO_4 [8]. Data obtained in structural studies of

1063-7834/05/4704-0720$26.00 © 2005 Pleiades Publishing, Inc.

ALiSO$_4$ crystals, however, are not always convincing enough to warrant unambiguous conclusions regarding the mechanism of the transitions involved. It would seem at first glance that arguments for the ordering of tetrahedra carry more weight and that the order–disorder model is preferable [9–11]. However, a comparative analysis of the structure of a number of crystals [12] has shown that the extent of ionic disorder depends on the relative cation size.

It is known that, as a fundamental thermodynamic property, the entropy of a phase transition ΔS makes it possible to describe the mechanism of structural distortions and that its magnitude depends not to a small degree on the anharmonicity of critical-ion vibrations [13]. In the limiting cases, i.e., for a weakly anharmonic (displacive phase transformations) and a strongly anharmonic potential (order–disorder transitions), the values of ΔS differ greatly; they are $\sim 0.1R$ and $\geq 0.7R$ ($R\ln 2$), respectively.

Although many of the physical properties of ALiSO$_4$ crystals have been studied in considerable detail [1], the thermophysical aspects of phase transitions have not been probed adequately, in particular, using calorimetry. Reliable data on the entropy change associated with a second-order transition from the orthorhombic phase *Pmcn* have been obtained for CLS only [14]. It has been found that $\Delta S \approx 0.2R$ is much closer to the value characteristic of displacive transitions. Calculations made with the model of stage-by-stage ordering of tetrahedra as a result of $P6_3/mmc \longrightarrow Pmcn \longrightarrow P112_1/n$ structural distortions [2] revealed that correlations in vibrations of critical ions can cause a substantial decrease in transition entropy. In this case, ΔS for CLS is $\sim 0.3R$ for each of the two phase transitions.

The present communication reports on heat capacity measurements for the NLS, RLS, and CNLS crystals performed within a broad temperature interval including the regions of structural transformations. The measurements were carried out with the aim of broadening our understanding of possible values of the entropy and mechanisms of phase transitions in ALiSO$_4$ crystals.

2. EXPERIMENTAL TECHNIQUES

CNLS (x = 0.95), NLS, and RLS crystals were grown from aqueous solutions by slow evaporation at 310 K. The identification and characterization of the samples were performed in three steps. Room-temperature x-ray diffraction studies allowed us to verify the absence of starting components as impurities and of foreign phases. The optical homogeneity of the samples was established using a polarization microscope. In the last stage of characterization, a DSM-2M differential scanning microcalorimeter was employed to perform calorimetric studies in the temperature range 120–520 K. Samples were in both crystal and powder form. The phase transition temperatures of the samples under study were found to coincide satisfactorily with available data obtained earlier by other techniques [1]. The same calorimetric method was used in more thorough thermophysical measurements carried out in the region of high-temperature phase transitions in NLS and RLS. The rate of temperature variation in both heating and cooling runs was 8 K/min in all experiments, and the sample mass varied in the range 0.10–0.15 g. A more detailed description of experimental factors regarding the determination of the phase transition enthalpy and entropy can be found in [15].

Although the high-temperature phase transition in NLS was studied by us earlier using differential scanning calorimetry (DSC) [15, 16], we repeated these experiments in this work on a large number of powder and single-crystal samples prepared under different crystallization conditions. These statistical data permitted us, first, to unambiguously determine the number of phase transitions in NLS and, second, to obtain more reliable information concerning the behavior of the heat capacity.

Below 373 K, the behavior of the heat capacity of NLS and CNLS crystals was investigated with adiabatic calorimetry. The samples were plane plates with masses of 1.288 g (NLS) and 1.585 g (CNLS). The measurements were conducted in a fixture similar to that employed in [17] for heat capacity measurements on uniaxial ferroelectrics. The heat capacity of the fixture was determined in a separate experiment. The heat capacity of samples was measured in discrete (ΔT = 1.0–2.5 K) and continuous (dT/dt = 0.16–0.50 K min^{-1}) heating modes. In the immediate proximity of the low-temperature transition in NLS, quasi-static thermograms were obtained with a heating rate of 3×10^{-2} K min^{-1}.

3. EXPERIMENTAL RESULTS

3.1. NLS

Figure 1 presents experimental data on the specific heat $C_p(T)$ of an NLS crystal obtained within a broad temperature range with an adiabatic (110–373 K) and a differential scanning (350–520 K) calorimeter in continuous and discrete heating modes. DSC does not provide sufficient accuracy in determining the absolute values of heat capacity. Therefore, the data obtained using this method were referred to adiabatic calorimeter measurements in the range 355–373 K.

Two heat capacity anomalies associated with a sequence of phase transitions between the paraelectric (*Pmcn*), ferroelectric ($P2_1cn$), and ferroelastic ($P2_1/c11$) phases were detected.

The thermodynamic parameters of the high-temperature phase transition studied on a large series of samples proved reproducible to within acceptable limits. The location of the heat capacity maximum T_1 = 460.5 K varied from one sample to another within 1.5 K. To determine the magnitude of the excess specific heat ΔC_p and the temperature interval of its existence in the $P2_1cn$

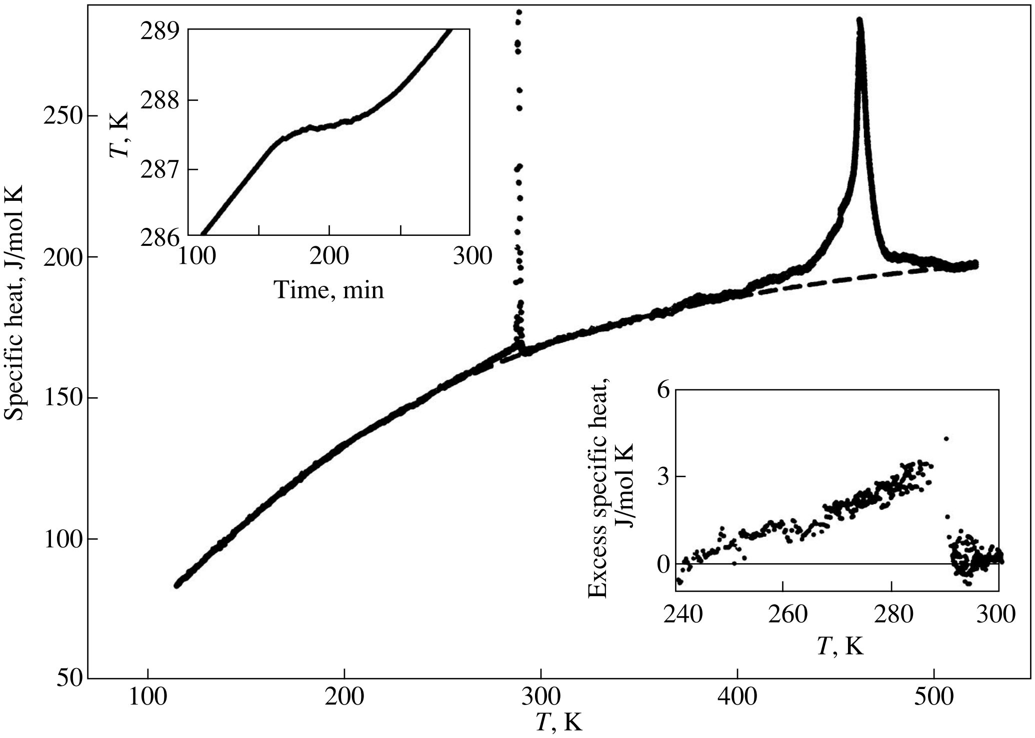

Fig. 1. Specific heat of NLS over a broad temperature interval. The dashed line is the lattice specific heat. The top inset shows a thermogram obtained in the heating mode near T_2. The lower inset shows the excess specific heat in the vicinity of T_2.

and $P2_1/c11$ phases, the regular component, i.e., lattice specific heat (shown in Fig. 1 by a dashed line) was found. We used the combined Debye–Einstein function $C_{\text{latt}}(T) = A_1D(\Theta_D/T) + A_2E(\Theta_E/T)$ to fit the experimental data obtained far from the phase transition points (114–203 and 308–373 K). The average deviation of the experimental points from the smoothed curve was approximately ±0.5%. This procedure revealed that an excess specific heat is present within a broad temperature interval both above and below T_1 (Fig. 1). These findings correlate with earlier data on the behavior of thermal expansion and birefringence [3, 18]. In this case, the increased change in the enthalpy due to the $Pmcn \longrightarrow P2_1cn$ transition obtained in the present measurements, $\Delta H_1 = 1300 \pm 150$ J mol^{-1}, as compared to the value of 1170 ± 200 J mol^{-1} derived from heat capacity measurements performed on NLS within a narrower temperature interval [15], appears natural. It should also be pointed out that none of the NLS samples studied by us revealed a splitting of the heat capacity anomaly at T_1 into two peaks, which was observed in [19] and assigned to the existence of a sequence of phase transitions within a range 2–3-K wide.

The position of the heat capacity peak maximum $T_2 = 287.7$ K, accepted in the first stage as the temperature of the second transition, agrees satisfactorily with the values reported, for instance, in [1]. No other heat capacity peaks were found between T_1 and T_2 and below T_2 within the scatter of experimental points. Thus, our high-precision measurements performed using the very sensitive calorimetric method also argue convincingly against the existence of additional anomalies in the NLS heat capacity allegedly associated with phase transitions occurring in the temperature range 330–350 K [20], near 250 K [21], and at 225 K [22].

Studies of NLS using quasi-static thermography in the immediate vicinity of the phase transformation at T_2 are illustrated in the upper inset to Fig. 1. The pattern of the thermogram suggests heat absorption at the transition. The phase transition temperature ($T_2 = 287.6 \pm 0.1$ K) was refined, and the enthalpy jump (latent heat) was determined, $\delta H_2 = 310 \pm 15$ J mol^{-1}.

Isolation of the lattice component revealed that the excess specific heat of NLS below T_2, which is not connected in any way with the absorption of latent heat, though small ($\Delta C_p \approx 0.025C_{\text{latt}}$ near T_2), does nevertheless exist within a fairly broad temperature interval (40-K wide) near T_2 (see lower inset to Fig. 1). With inclusion of $\Delta C_p(T)$, the total enthalpy change associated with the $P2_1/c11 \longrightarrow P2_1cn$ phase transition and defined as $\Delta H_2 = \int \Delta C_p dT + \delta H_2$ was found to be 385 ± 35 J mol^{-1}.

Repeated measurements of $C_p(T)$ in the vicinity of the low-temperature phase transition performed in the continuous heating mode at different rates (dT/dt =

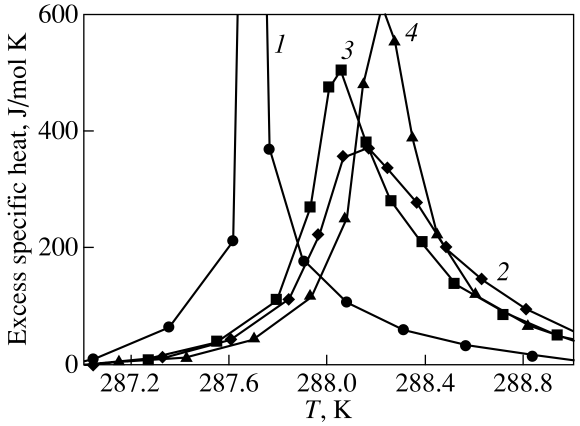

Fig. 2. Excess specific heat of NLS near T_2 measured in successive heating cycles. Numerals *1*–*4* label successive experiments.

0.28–0.47 K min^{-1}) revealed the influence of thermal cycling on the magnitude and position of the excess heat capacity peak maximum at T_2 (Fig. 2). The largest value of $(\Delta C_p)_{\max}$ was measured in the first experiment, which is characteristic of clearly pronounced first-order phase transitions. Subsequent deviations of the magnitude of $(\Delta C_p)_{\max}$ observed to occur from one experiment to another may be assigned, in particular, to degradation of the thermal contact between parts of the crystal, which may form as a result of sample cracking caused by a noticeable jump in volume. However, the changes in transition enthalpy from one experiment to another turned out considerably smaller than the determination error. Under these conditions, the temperature of the maximum $(\Delta C_p)_{\max}$ varied within 0.6 K. In view of a certain lack of reproducibility of the experimental data as a function of the sample heating rate, we should accept for the transition temperature the value obtained in the conditions closest to equilibrium, more specifically, that obtained in the quasi-static thermographic measurements.

3.2. CNLS

The behavior of the specific heat of CNLS with temperature was studied using adiabatic calorimetry and is displayed graphically in Fig. 3a. Also shown for comparison are earlier data on CLS obtained and reported in [14] (with the participation of one of the present authors). As expected, partial substitution of ammonium for cesium does affect the thermodynamic parameters, both far from and near the phase transition. The temperature of the heat capacity maximum, considered as the temperature of the $Pmcn \longrightarrow P112_1/n$ phase transition, rose in the solid solution by 5 K to become $T_0 = 207.2 \pm 0.7$ K. The regular specific heat determined using same approximating function as used earlier for NLS is shown in Fig. 3a by dashed lines. This

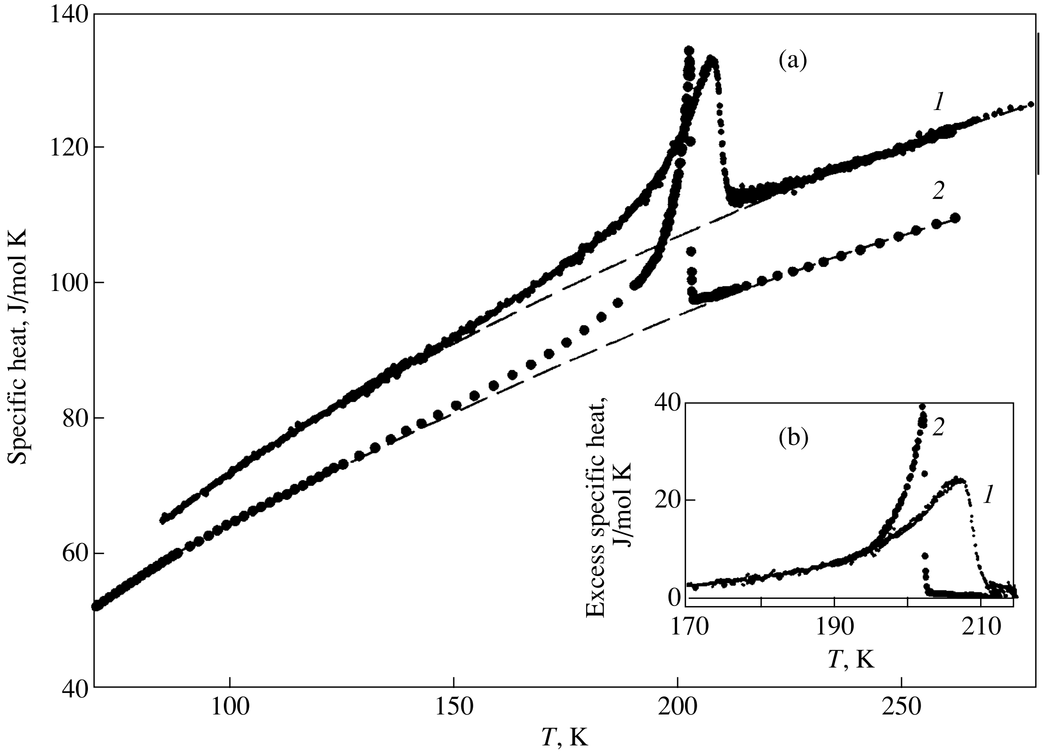

Fig. 3. Temperature dependence of (a) the specific heat and (b) excess specific heat of (*1*) CNLS and (*2*) CLS [14]. The dashed line is the lattice specific heat.

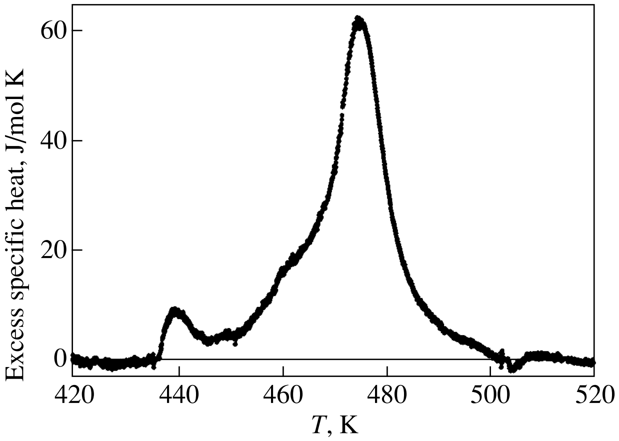

Fig. 4. Temperature dependence of the excess specific heat for RLS.

quantity turned out to be higher for the solid solution throughout the temperature interval studied. As for the excess specific heat, its behavior for CNLS changed markedly (Fig. 3b). The narrow $\Delta C_p(T)$ peak observed in CLS flattens out and becomes substantially smaller in magnitude at T_0. Note also that the regular specific heat was described in [14] by a polynomial. Both in CLS and CNLS, the $Pmcn \longrightarrow P112_1/n$ phase transition is a second-order transformation; therefore, the change in enthalpy was determined by integrating the $\Delta C_p(T)$ function. No noticeable effect was observed of the way in which $C_{\mathrm{latt}}(T)$ was represented on the enthalpy of the $Pmcn \longrightarrow P112_1/n$ phase transition in CLS ($\Delta H_{\mathrm{CLS}} = 335 \pm 25$ J mol^{-1}); indeed, the difference is within the accuracy of determining ΔH. In the case of CNLS, the enthalpy of the transition increased, as compared to CLS, to reach $\Delta H_{\mathrm{CNLS}} = 460 \pm 50$ J mol^{-1}.

3.3. RLS

Since the phase transitions in RLS occur at temperatures above 370 K, the heat capacity of this crystal was studied using the DSC method only. Figure 4 plots the temperature dependence of the anomalous specific heat. Three heat capacity peaks can be clearly discerned, with the maxima lying at $T_1 = 475$ K, $T_3 = 460$ K, and $T_4 = 439$ K. As for the anomaly at T_2, it merges with the heat capacity peak at T_1. This is, however, not of any importance here, because we are interested primarily in changes in the thermodynamic parameters associated with the symmetry change $Pmcn \longrightarrow P112_1/n$. This distortion of the structure is a result of four successive phase transitions occurring in RLS and of the direct transformation to CLS. Therefore, our analysis of the $\Delta C_p(T)$ dependence for RLS was not aimed at answering questions regarding with the separation of the contributions from each of the successive $Pmcn \longrightarrow I \longrightarrow P2_1c11 \longrightarrow P11n$ transitions to the enthalpy change $\Delta H_{1-3} = \Sigma(\Delta H_1 + \Delta H_2 + \Delta H_3) = 1030 \pm 150$ J mol^{-1}. As for the $P11n \longrightarrow P112_1/n$ transformation, the corresponding enthalpy change was small, $\Delta H_4 \approx 70$ J mol^{-1}. Thus, the total enthalpy change connected with the structural transition from $Pmcn$ to $P112_1/n$ in RLS is 1100 J mol^{-1}.

4. DISCUSSION OF THE RESULTS

The experimental results obtained in this work make it possible to determine and analyze the thermodynamic characteristics associated with the phase transitions in $A\mathrm{LiSO}_4$ crystals, in particular, the magnitude and behavior of the anomalous specific heat ΔC_p and entropy ΔS, as well as to establish the applicability of some thermodynamic relations connecting the thermophysical properties and other properties. The total entropy changes in the case of first-order phase transitions are defined by the sum of two contributions, $\Delta S = \delta S + \int(\Delta C_p/T)dT$. The first term is due to the abrupt change in the transition parameter at the transformation point and is calculated from the latent heat, $\delta S = \delta H/T_i$. For second-order transformations, the quantity ΔS is naturally identified with the second term only.

The thermodynamic description of the phase transition sequence in the NLS crystal is outlined in [23]. The free energy F was presented as a function of the transition parameters ξ and η corresponding to librations of the tetrahedral groups and macroscopic polarization P_s:

$$\begin{aligned}\Delta F &= \alpha\xi^2 + \beta\xi^4 + \gamma\xi^6 + \varepsilon\xi P_s + aP_s^2\\ &\quad + A(\eta_1^2 + \eta_2^2) + B_1(\eta_1^2 + \eta_2^2)^2 + B_2\eta_1^2\eta_2^2\\ &\quad + C(\eta_1^2 + \eta_2^2)^3 + \mu\xi^2(\eta_1^2 + \eta_2^2) + \dots\end{aligned} \tag{1}$$

Because both transitions in NLS are first-order transformations, the following relations were suggested in [23]: $\alpha = \alpha_T(T - T_1)$, $A = A_T(T - T_2)$, $T_1 > T_2$, $\beta < 0$, and $B_1 < 0$. The condition of the minimum $\partial\Delta F/\partial P = 0$ implied that $\xi = -(a/\varepsilon)P_s$, in which case the free energy can be written as a function of two variables, $\Delta F(P, \eta)$:

$$\begin{aligned}\Delta F &= \alpha(a/\varepsilon)^2P_s^2 + \beta(a/\varepsilon)^4P_s^4 + \gamma(a/\varepsilon)^6P_s^6\\ &\quad + A(\eta_1^2 + \eta_2^2) + B_1(\eta_1^2 + \eta_2^2)^2 + B_2\eta_1^2\eta_2^2\\ &\quad + C(\eta_1^2 + \eta_2^2)^3 + \mu(a/\varepsilon)^2P_y^2(\eta_1^2 + \eta_2^2) + \dots\end{aligned} \tag{2}$$

Because only the coefficients α and A are temperature-dependent, the total entropy change associated with the phase transition sequence $Pmcn \longrightarrow P2_1cn \longrightarrow P2_1/c12$ will be

$$\partial\Delta F/\partial T = -\Delta S = \alpha_T(a/\varepsilon)^2P_s^2 + A_T(\eta_1^2 + \eta_2^2). \tag{3}$$

In accordance with [23], the conditions of stability of the NLS phases can be written as

$$\begin{gathered}Pmcn\colon\quad P_s = \xi = \eta_i = 0;\quad \alpha > 0, a > 0, A > 0,\\ P2_1cn\colon\quad P_s \neq 0;\quad \xi \neq 0;\quad \eta_1 = \eta_2 = 0,\\ P2_1/c11\colon\quad P_s = 0;\quad \xi = 0;\quad \eta_1^2 = \eta_2^2 = \eta^2.\end{gathered}\tag{4}$$

Hence, the entropy change at the $Pmcn \longrightarrow P2_1cn$ phase transition can be identified with the first term on the right-hand side of Eq. (3). The corresponding relation connecting the jump in entropy δS_1 with the jump in polarization δP at the transformation point T_1 can be cast as

$$\delta S_1 = \alpha_T(a/\varepsilon)^2\delta P_s^2.\tag{5}$$

A specific feature of the DSC technique employed by us in high-temperature studies, in particular, on NLS, consists in that it does not permit separation of the contributions to enthalpy (and entropy) associated with the jump in the order parameter at a first-order phase transition point and the gradual approach of the order parameter to the saturation level. In other words, DSC data cannot always provide a reliable conclusion concerning the nature of a transition. The studies reported in [16, 24] did not reveal any clearly pronounced jumps in the birefringence Δn or polarization P_s at T_1. However, a study [18] carried out with the participation of one of the present authors showed that the pattern of the strain behavior and of the quasi-static thermogram argue persuasively for the presence of jumps in volume and enthalpy at the $Pmcn \longrightarrow P2_1cn$ transition point. It seems appropriate to quote a conclusion made in [25] on the determination of the order of a transition in controversial cases, which we believe to be correct: "*…the observation of latent heat (a jump in a transition parameter) in at least one of a set of samples indicates the transformation in a given substance to be a first-order transition*." Thus, according to experimental evidence [18], the transition occurring in NLS at T_1 can be unambiguously assigned to first-order transformations. At the same time, it is known that the polarization [24], birefringence [16], and thermal expansion coefficients [18] of NLS undergo a change within a broad temperature interval between T_1 and T_2. These facts imply that the parameter of the transition increases gradually with decreasing temperature. Because the entropy change, according to Eq. (3), scales as the square of the transition parameter, there should also be excess specific heat in a broad temperature interval below T_1. Experimental data convincingly demonstrate that the $Pmcn \longrightarrow P2_1cn$ phase transition is fairly close to the tricritical point. This conclusion follows from the relative magnitude of the jump in enthalpy and its total change, $\delta H_1/\Delta H_1 = 0.2$, which turned out to be substantially smaller than 1. It seems appropriate at this point to recall the studies of the anomalous part of birefringence in NLS below T_1 [16], which led to a similar conclusion concerning the position of the transition with respect to the tricritical point.

In view of the above, the calorimetric data presented in [19], where the excess specific heat was found to exist in NLS only within a narrow temperature region $\Delta T \approx 5$ K near T_1, cannot be considered reliable. In this case, most likely, the part of the anomalous heat capacity associated only with the absorption of latent heat was detected. Indeed, integrating the $\Delta C_p(T)$ function yielded $\Delta H_1 = 2.9$ J g^{-1} [19], which is close to the enthalpy jump $\delta H_1 = 2.2 \pm 0.9$ J g^{-1} determined and reported by us in [18].

Taking the value of δH_1 and the Curie–Weiss constant $C = 5.6$ K [24], we can use Eq. (5) to estimate the polarization jump at T_1 assuming the relation $\alpha_1(a/\varepsilon)^2 = (2\pi/C)T_1$ [26] to be valid. The calculated value $\delta P_s \approx 0.1$ μC cm^{-2} correlates satisfactorily with the figure 0.05–0.10 μC cm^{-2} corresponding to the fastest variation of polarization near T_1 [24]. The reliability of the experimental values is also corroborated by the results of fitting the changes in the enthalpy δH_1 and the relative volume $\delta V_1/V = 4 \times 10^{-4}$ [18], as well as of the parameter characterizing the response of the crystal to pressure, $dT_1/dp = 0.6$ K GPa^{-1} [1], to the Clapeyron–Clausius relation $dT_1/dp = T_1\delta V_1/(V\delta H_1)$. The calculated enthalpy jump $\delta H_1 = 1.5$ J g^{-1} agrees with the experimental value to within attainable accuracy [18].

The above data also make it possible to determine the electric field–induced temperature shift of the $Pmcn \longrightarrow P2_1cn$ phase transition with the use of the "electrical" Clapeyron–Clausius relation $dT_1/dE = -(\delta P_y/\delta H_1)T_1$ [26]. Unfortunately, we are not aware of any experimental study of the $T_1(E)$ dependence. A comparison of the calculated data (for T_1) with experimental data (for T_2) suggests, however, that the high-temperature phase transition (for which we have $dT_1/dE = 1 \times 10^{-7}$ K m V^{-1}) is more stable against an electric field than the $P2_1cn \longrightarrow P2_1/c12$ transformation ($dT_2/dE = 20 \times 10^{-7}$ K m V^{-1} [27]).

X-ray diffraction measurements performed on NLS show the SO_4 tetrahedra in the ferroelastic phase of NLS to be completely ordered. Thus, the $P2_1cn \longrightarrow P2_1/c11$ structural transformation is actually a transition between ordered phases, so the corresponding change in the entropy should be substantially smaller than $R\ln2$. However, since both space groups are subgroups of the $Pmcn$ phase, they are not connected with each other through a group–subgroup relation; therefore, this structural transformation occurs between two irreducible representations and should be a clearly pronounced first-order transition [1]. The experimental data obtained by us agree with the structure transformation model. The total entropy change $\Delta S_2 = 1.33 \pm 0.04$ J mol^{-1} K^{-1} (0.16 R) did turn out to be small and characteristic of displacive transformations. As for the relation connecting the

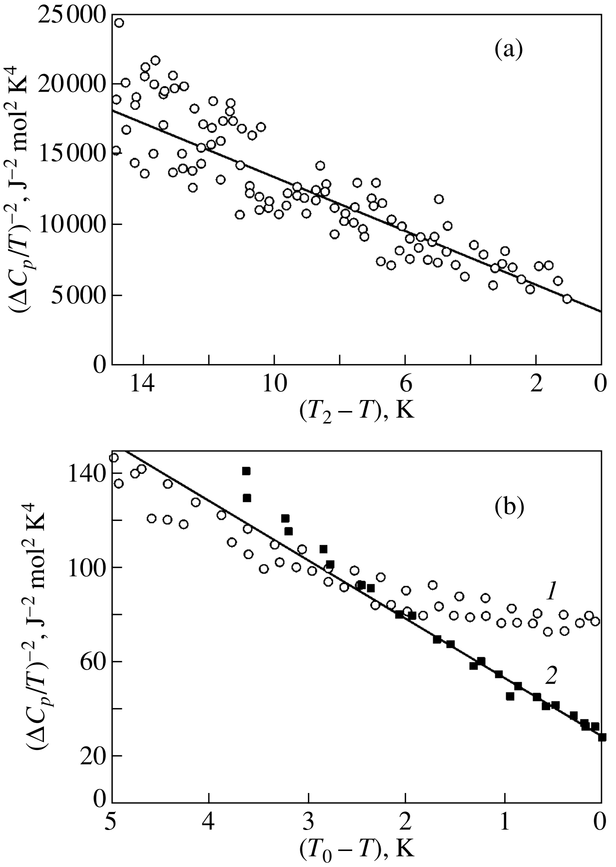

Fig. 5. Temperature dependence of the square of the inverse excess specific heat of (a) NLS and (b) (*1*) CNLS and (*2*) CLS.

enthalpy change at the transition point with its total change, $\delta H_2/\Delta H_2 = 0.81$, it argues for the $P2_1cn \longrightarrow P2_1/c11$ transition (unlike the transition at T_1) being fairly far from the tricritical point.

In accordance with [28], the excess specific heat below T_2 should satisfy, as follows from Eq. (1), the relation

$$\left(\frac{\Delta C_p}{T}\right)^{-2} = \left(\frac{2\sqrt{B^2 - 3A'C}}{A_T^2}\right)^2 + \frac{12C}{A_T^3}(T_2 - T). \qquad (6)$$

Here, in accordance with Eq. (4), $B = (4B_1 + B_2)$ and $A' = A_T(T_2 - T_c)$. As seen from Fig. 5a, the excess specific heat squared is indeed a linear function of temperature over a fairly broad interval (15-K wide) near T_2. This fact allowed us to derive expressions relating the coefficients of the potential in Eq. (1) $A_T^2/B = 1.7 \times 10^{-2}$ J mol^{-1} K^{-2} and $A_T^3/C = 1.2 \times 10^{-2}$ J^2 mol^{-2} K^{-3} and the quantity $T_2 - T_c = B^2/4A_TC = 10$ K. The degree of proximity of the first-order ($B < 0$) transition to the tricritical point was established using the expression [28] $N = (B^2/(3A_TCT_C))^{1/2} = -0.22$.

In accordance with Eqs. (3) and (4), the entropy change δS_2 is connected with the abrupt appearance of a new transition parameter, $\eta_1^2 + \eta_2^2$, at T_2. The corresponding jump in volume, $\delta V_2/V = -4.6 \times 10^{-4}$, is calculated from the Clapeyron–Clausius equation using the data on the effect of hydrostatic pressure, $dT_2/dp = -26$ K/GPa [1]. Thus, at the phase transitions $Pmcn \longrightarrow P2_1cn$ ($\delta V_1/V = -4.0 \times 10^{-4}$) and $P2_1cn \longrightarrow P2_1/c11$, the unit cell volume of NLS undergoes changes in volume which are similar in magnitude and opposite in sign.

Studies of the elasticity and optical properties showed the $Pmcn \longrightarrow P112_1/n$ transition in CLS to be satisfactorily described in terms of the Landau phenomenological theory [29]. We carried out a similar analysis for the temperature dependence of the heat capacity of this crystal. The behavior of the square of the inverse excess specific heat of CLS near T_0 turned out to be in agreement with Eq. (6) (Fig. 5b). As seen from Fig. 5b, this relation is not met for CNLS. The reason for these discrepancies is most probably associated with the fact that, although CNLS was characterized as a crystalline compound, the ammonium ion could play the part of an impurity that makes the phase transition diffuse and distorts the real behavior of the excess specific heat.

As for the entropies of the phase transitions in CLS ($\Delta S_{\text{CLS}} = 1.66 \pm 0.13$ J mol^{-1} K^{-1}) and CNLS ($\Delta S_{\text{CNLS}} = 2.24 \pm 0.23$ J mol^{-1} K^{-1}), the difference between them is seen to be larger than the experimental error of their determination. One of the reasons for the increase in ΔS may be associated with the fact that the transition in the solid solution approaches the tricritical point lying on the $T(x)$ line [3], which governs the stability of the $Pmcn$ phase.

As already pointed out, the assignment of heat effects in RLS to particular phase transitions is complicated by their being close in temperature. However, the structure of RLS contains, within certain temperature intervals, ferroelastic phases $P2_1/c11$ and $P112_1/n$, which also occur in NLS and CLS, respectively. While the entropy changes due to the same $P2_1/c11$ monoclinic distortion are relatively small, the total value for NLS ($\Delta S_1 + \Delta S_2 = 4.24 \pm 0.42$ J mol^{-1} K^{-1}) is substantially larger than that for RLS ($\Delta S_1 + \Delta S_2 + \Delta S_3 = 2.08 \pm 0.20$ J mol^{-1} K^{-1}). Also, the difference between the entropies greatly exceeds the error of their determination. However, the entropy changes due to the formation of the $P112_1/n$ monoclinic phase in CLS (1.66 ± 0.16 J mol^{-1} K^{-1}) and RLS $\Delta S_1 + \Delta S_2 + \Delta S_3 + \Delta S_4 = 2.25 \pm 0.22$ J mol^{-1} K^{-1}) are closer in magnitude.

The mechanisms of the phase transitions occurring in crystals with an α-K_2SO_4 or β-K_2SO_4 structure have been considered in several experimental and theoretical studies [1, 2, 7]. In many cases, the researchers were inclined to believe that the SO_4 tetrahedra, which are disordered over four positions in the α-K_2SO_4 phase and over two positions in the β-K_2SO_4 phase, become ordered after phase transitions and occupy only one position in different distorted phases of symmetry lower than *Pmcn*; in other words, transitions from the α and β phases should be of the order–disorder type. Straightforward model concepts suggest that the sequence of these transitions should be accompanied by changes in the entropy of $R(\ln2 + \ln2)$.

However, available experimental data do not always agree with the expected large value of ΔS. As established reliably by repeated measurements [1], only for K_2SO_4 undergoing a single transition $G_0 \longrightarrow G_1$ (*Pmcn*) is ΔS indeed equal to $R\ln4$. The situation is different for K_2SeO_4, where the same phase transition involves one-half the above entropy change, $\Delta S = R\ln2$ [2], and is apparently accompanied by partial ordering of the tetrahedra. As the temperature decreases further, however, this crystal undergoes three successive phase transitions [1], for which the changes in entropy are very small (<0.1 R) and argue rather for the mechanism of slight atomic displacement than for ordering in the case where the symmetry is lower than *Pmcn*. This suggestion is also substantiated by the observation of a soft mode in the β phase of this crystal [1].

As already mentioned, the α phase does not form in $ALiSO_4$ up to the melting or decomposition temperature. The entropy changes due to the phase transitions from the *Pmcn* orthorhombic phase in the crystals studied in [4, 14] and the present work are summed up in the table. The main point to mention is that, except for TLS, all the entropy changes ΔS determined by various methods are substantially smaller than the expected value $R\ln2 \approx 0.7R$, if we assume that the SO_4 tetrahedra occupy two equivalent positions in the *Pmcn* phase.

It would be instructive to point out that the kind of phase transition that occurs and its proximity to the tricritical point for different $ALiSO_4$ compounds turned out to be different. The *Pmcn* structure suffers distortions as a result of a second-order transformation in CLS and CNLS and of a first-order transition in the other crystals. Note also that, according to [4], the total entropy change of $R\ln2$ occurs in TLS in a narrow region near T_0; therefore, the distance of the transition from the tricritical point is quite large (at least as compared to NLS).

It is known [13] that second-order transitions may give rise to strong correlations, which appear in the initial phase long before the transition temperature is reached. The analysis of CLS in [9] was based on the structural model of disordered tetrahedra, because inclusion of the anisotropy of thermal vibrations resulted in an improvement of the magnitude of the *R* factor. Monte Carlo studies of the order–disorder model (four-state model [1]) were applied in [2] to $P6_3/mmc \longrightarrow Pmcn \longrightarrow P112_1/n$ successive phase transitions in CLS under the assumption that the crystal has a hexagonal phase, which has not been observed experimentally. It was established that the presence of strong short-range tetrahedron correlations (caused by competitive interactions among the tetrahedra) in the disordered hexagonal and the partially ordered orthorhombic phases results in a decrease in the transition entropy by a factor of more than 2 with respect to $R\ln2$. This conclusion is in satisfactory agreement with the experimental value of the entropy change for CLS (see table).

Thermodynamic parameters of the phase transition (PT) from the *Pmcn* phase in $ALiSO_4$ crystals

Crystal	T_1, K	$\Delta S_1/R$	PT order	Reference
NLS	461	0.35	I	This work
RLS	475	0.25	I	"
CNLS	207	0.27	II	"
CLS	202	0.20	II	[14]
TLS	288	0.69	I	[4]

The above reasoning no longer seems convincing when one invokes data obtained by other researchers who analyzed competing models of the structure of $ALiSO_4$ crystals. It was found in [11], for instance, that for RLS the model that considers anharmonic vibrations of the tetrahedra is the most appropriate. Preference was given, however, to the model assuming their disorder over two positions, in accordance with the observation of two maxima in the electron density distribution for oxygen atoms. However, the data reported in [12], where, as we believe, the structure was most carefully analyzed, seems more substantiative. Evidence for the vibrations of SO_4 tetrahedra in the *Pmcn* phase of NLS, RLS, and RCLS being characterized by different degrees of anharmonicity was presented. Electron density maps for NLS indicate that the oxygen atom does indeed have two equilibrium positions coupled by tilting of the SO_4 group. After the transition to the G_2 phase, the oxygen atom orders in one of these positions. The rubidium analog reveals the same situation, although less clearly pronounced. However, small additions of cesium (~9 mol %) radically change the electron density distribution around the oxygen atom in the RCLS structure [12] and the double-peak pattern corresponding to two oxygen positions disappears. The structural data obtained were used to calculate the parameters of the two-minimum potential confining the vibrations of a regular rigid tetrahedron. It turned out that the height of the potential barrier $1.2k_BT_1$ permits assignment of the transition from the *Pmcn* phase to “pure” order–disorder transformations only in NLS. In the ferroelectric phase, the potential becomes asymmetric, with the stable tetrahedron configuration corresponding to one of the disordered phase configurations. The barrier height in RLS is only $0.75k_BT_1$, which indicates a considerable decrease in tetrahedron vibration anharmonicity as a result of the tetrahedral cation being replaced by a spherical one. The most remarkable observation is that, as the Rb ion is partially replaced by the larger Cs in the RCLS compound ($Rb_{0.9}Cs_{0.1}LiSO_4$), the potential barrier decreases in height by nearly four times ($<0.2k_BT_1$). This convincingly shows that the vibrations of critical ions in each of the crystals are anharmonic to different degrees, which should naturally manifest itself in the entropy of a phase transition. As seen from the table, the variation in ΔS from one sample to another correlates with this hypothesis; indeed, the transition entropy decreases with increasing cation size. Thus, the increase in the cation ionic radius in the $ALiSO_4$ series [(NH_4^+ (1.43 Å) $\longrightarrow$ Rb^+ (1.48 Å) $\longrightarrow$ Cs^+ (1.65 Å))] is apparently capable of suppressing disordering of the SO_4 tetrahedra.

ACKNOWLEDGMENTS

This study was supported by the Russian Ministry of Industry, Science, and Technologies (project no. NSh-939.2003.2) and a program under the Presidium of the RAS (project no. 9.1).

REFERENCES

1. K. S. Aleksandrov and B. V. Beznosikov, *Structural Phase Transitions in Crystals (Potassium Sulfate Family)* (Nauka, Novosibirsk, 1993) [in Russian].
2. N. G. Zamkova and V. I. Zinenko, J. Phys.: Condens. Matter **6** (43), 9043 (1994).
3. S. V. Mel'nikova and V. A. Grankina, Fiz. Tverd. Tela (St. Petersburg) **46** (3), 500 (2004) [Phys. Solid State **46**, 515 (2004)].
4. H. Mashiyama, J. Wu, F. Shimizu, and M. Takashige, J. Phys. Soc. Jpn. **67** (1), 359 (1998).
5. A. Elfakir, J.-P. Souron, G. Wallez, M. Quarton, and M. Touboul, Solid State Ionics **110**, 145 (1998).
6. H. Kasano, Sh. Tsuchiyama, Y. Kawamura, and H. Mashiyama, Ferroelectrics **217**, 121 (1998).
7. V. I. Zinenko and N. G. Zamkova, Phys. Rev. B **57** (1), 211 (1998).
8. G. M. Loiacono, M. Delfino, W. A. Smith, M. I. Bell, A. Shaulov, and Y. H. Tsuo, Ferroelectrics **23**, 89 (1980).
9. A. I. Kruglik, M. A. Simonov, E. P. Zhelezin, and N. V. Belov, Dokl. Akad. Nauk SSSR **247** (6), 1384 (1979) [Sov. Phys. Dokl. **24**, 596 (1979)].
10. K. Itoh, H. Ishikura, and E. Nakamura, Acta Crystallogr. B **37**, 664 (1981).
11. W. Steurer, H. Wittmann, H. Jagodzinski, and A. Pietraszko, Acta Crystallogr. B **42**, 11 (1986).
12. K. Hasebe and T. Asahi, Phys. Rev. B **41** (10), 6794 (1990).
13. V. G. Vaks, *Introduction to the Microscopic Theory of Ferroelectrics* (Nauka, Moscow, 1973) [in Russian].
14. A. I. Kruglik, K. S. Aleksandrov, O. V. Rozanov, I. M. Iskornev, L. I. Zherebtsova, and I. N. Flerov, Fiz. Tverd. Tela (Leningrad) **22** (12), 3673 (1980) [Sov. Phys. Solid State **22**, 2150 (1980)].
15. S. V. Mel'nikova, A. V. Kartashev, V. A. Grankina, and I. N. Flerov, Fiz. Tverd. Tela (St. Petersburg) **45** (8), 1497 (2003) [Phys. Solid State **45**, 1572 (2003)].
16. S. V. Mel'nikova, V. A. Grankina, and A. V. Kartashev, Fiz. Tverd. Tela (St. Petersburg) **44** (2), 365 (2002) [Phys. Solid State **44**, 379 (2002)].
17. I. N. Flerov and I. M. Iskornev, Metrologia, No. 1, 21 (1979).
18. I. M. Iskornev and I. N. Flerov, Fiz. Tverd. Tela (Leningrad) **19** (4), 1040 (1977) [Sov. Phys. Solid State **19**, 605 (1977)].
19. M. Gaafar, M. E. Kassem, and S. H. Kandil, Solid State Commun. **115**, 509 (2000).
20. X. Solans, J. Mata, M. T. Calvet, and M. Font-Bardia, J. Phys.: Condens. Matter **11**, 8995 (1999).
21. M. L. Martinez Sarrion, L. Mestres, A. A. Bakkali, and E. H. Bocanegra, Mater. Res. Bull. **33** (2), 269 (1998).
22. J. E. Diosa, G. M. Aparicio, R. A. Vargas, and J. F. Jurado, Phys. Status Solidi B **220**, 651 (2000).
23. V. I. Torgashev, V. Dvorak, and F. Smutny, Phys. Status Solidi B **126**, 459 (1984).
24. T. Mitsui, T. Oka, Y. Shiroishi, M. Takashige, K. Ito, and Sh. Sawada, J. Phys. Soc. Jpn. **39** (3), 845 (1975).
25. S. R. Garber and L. A. Smolenko, Zh. Éksp. Teor. Fiz. **55** (6), 2031 (1968) [Sov. Phys. JETP **28**, 1072 (1969)].
26. A. Smolenskiĭ, V. A. Bokov, V. A. Isupov, N. N. Kraĭnik, R. E. Pasynkov, and M. S. Shur, *Ferroelectrics and Antiferroelectrics* (Nauka, Leningrad, 1971) [in Russian].
27. N. R. Ivanov and L. F. Kirpichnikova, Izv. Akad. Nauk SSSR, Ser. Fiz. **51** (12), 2216 (1987).
28. K. S. Aleksandrov and I. N. Flerov, Fiz. Tverd. Tela (Leningrad) **21** (2), 327 (1979) [Sov. Phys. Solid State **21**, 195 (1979)].
29. A. T. Anistratov, A. V. Zamkov, L. A. Kot, I. N. Stolovitskaya, and L. A. Shabanova, Fiz. Tverd. Tela (Leningrad) **24** (9), 2763 (1982) [Sov. Phys. Solid State **24**, 1565 (1982)].

Translated by G. Skrebtsov

Physics of the Solid State, Vol. 47, No. 4, 2005, pp. 729–732. Translated from Fizika Tverdogo Tela, Vol. 47, No. 4, 2005, pp. 705–707.
Original Russian Text Copyright © 2005 by Sannikov, Kessenikh.

A New Commensurate Phase on the Theoretical Phase Diagram of the $[N(CH_3)_4]_2CuCl_4$ Crystal

D. G. Sannikov and G. A. Kessenikh
Shubnikov Institute of Crystallography, Russian Academy of Sciences, Leninskiĭ pr. 59, Moscow, 119333 Russia
e-mail: sannikov@ns.crys.ras.ru

Received July 26, 2004

Abstract—A theoretical phase diagram of the $[N(CH_3)_4]_2CuCl_4$ crystal with a new commensurate phase characterized by a dimensionless wavenumber $q = 2/5$ is constructed on a plane specified by two coefficients of the thermodynamic potential. This diagram is used as the basis for the construction of a theoretical pressure–temperature (P–T) phase diagram. The theoretical P–T phase diagram thus obtained is compared with the experimental P–T phase diagram. *© 2005 Pleiades Publishing, Inc.*

1. THERMODYNAMIC POTENTIALS

The experimental pressure–temperature (P–T) phase diagram for an $[N(CH_3)_4]_2CuCl_4$ (*TMA*–CuCl) crystal (*TMA* is tetramethylammonium) was measured using x-ray scattering at temperatures T = 22–160°C and pressures P = 0.25–0.95 GPa and presented in the work by Asahi and Izutsu [1]. This diagram differs from the phase diagrams obtained earlier [2–4] in that it contains the commensurate phase $C_{2/5}$ with a dimensionless wavenumber $q_{2/5} = 2/5$. The purpose of this study is to construct a theoretical P–T phase diagram with the commensurate phase $C_{2/5}$ on the basis of the phenomenological approach developed in [5, 6] (see also [7, 8]). We will not describe again the theoretical approach and will begin with writing the thermodynamic potentials for the initial phase C (*Pmcn* symmetry), the incommensurate phase *IC*, and the commensurate phase $C_{m/l}$, where m/l specifies the value of the corresponding wavenumber $q = q_{m/l} = m/l$ ($C_{0/1}$ is the phase with wavenumber $q = 0$):

$$\Phi_{IC} = \alpha(b)\rho^2 + \beta\rho^4 + \gamma\rho^6,$$
$$\Phi_{m/l} = \alpha(q_{m/l})\rho^2 + \beta\rho^4 + \gamma\rho^6 - \alpha'_l\rho^{2l}\cos 2l\varphi, \quad (1)$$
$$\Phi_{0/l} = \alpha\zeta^2 + (2/3)\beta\zeta^4 + (2/5)\gamma\zeta^6.$$

The thermodynamic potential of the initial phase is equal to zero ($\Phi_C = 0$). Despite the fact that, in relationships (1), we have the coefficient $\beta > 0$, it is necessary to take into account the invariant with the coefficient γ ($\gamma > |\alpha'_3|$), because, away from the C–IC phase transition, the expression for the thermodynamic potential $\Phi_{1/3}$ at the coefficient $\gamma = 0$ becomes inapplicable. It is evident that the invariant with the coefficient γ must be taken into account in all the potentials.

The dependence of the coefficient of elasticity $\alpha(q)$ for the soft optical branch of the normal oscillation spectrum of the crystal on the dimensionless wavenumber ($k_z = qc^*$) can be described by the expression

$$\alpha(q) = \alpha - \delta q^2 - \kappa q^4 + \tau q^6, \quad \kappa > 0, \quad \tau > 0. \quad (2)$$

This expression can be rewritten in the form

$$\alpha(q) = a + \Delta(q),$$
$$\Delta(q) = \tau(b^2 - q^2)^2[q^2 + 2(b^2 - q_L^2)],$$
$$\alpha(b) = a, \quad \alpha(q_{m/l}) = a + \Delta_{m/l}, \quad (3)$$
$$\Delta_{m/l} = \Delta(q_{m/l}), \quad \alpha = a + \Delta_0,$$
$$\Delta_0 = \Delta(0), \quad \delta = \tau b^2(3b^2 - 4q_L^2), \quad q_L^2 = \kappa/2\tau,$$

where a and b are the coordinates of the minimum in the soft branch [described by expression (2)] at an arbitrary point of the Brillouin zone.

By varying the parameter φ in relationship (1) for the thermodynamic potential $\Phi_{m/l}$, we obtain two solutions: (i) $\sin l\varphi = 0$, which is stable for $\alpha'_l > 0$, and (ii) $\cos l\varphi = 0$, which is stable for $\alpha'_l < 0$. For both solutions, the thermodynamic potential $\Phi_{m/l}$ takes the form

$$\Phi_{m/l} = \alpha(q_{m/l})\rho^2 + \beta\rho^4 + \gamma\rho^6 - |\alpha'_l|\rho^{2l}. \quad (4)$$

It is convenient to change over to the dimensionless variables ϕ and R and the parameters A, D_0, D_l, B, Q_l, Q_L, D, A_γ, A_3, and A_l (where Q is a number):

$$\Phi = \phi\Phi_0, \quad \rho = RR_0, \quad \zeta = RR_0, \quad \Phi_0 = (\tau Q^6)^2/\beta,$$
$$R_0^2 = \tau Q^6/\beta, \quad a = -A\tau Q^6, \quad \Delta_0 = D_0\tau Q^6,$$
$$\Delta_{m/l} = D_l\tau Q^6, \quad b = BQ, \quad q_{m/l} = Q_lQ, \quad (5)$$
$$q_L = Q_LQ, \quad \delta = D\tau Q^4, \quad \gamma = (2\beta A_\gamma)^2/\tau Q^6,$$

$$|\alpha_3'| = (2\beta A_3)^2/\tau Q^6, \quad |\alpha_l'| = (2\beta A_l)^{l-1}/(\tau Q^6)^{l-2}.$$

As a result, the thermodynamic potentials Φ_{IC} and $\Phi_{0/1}$ defined by relationships (1) and the potential $\Phi_{m/l}$ described by expression (4) take the following form:

$$\begin{aligned} \phi_{IC} &= -AR^2 + R^4 + 4A_\gamma^2 R^6, \\ \phi_{m/l} &= -(A-D_l)R^2 + R^4 + 4A_\gamma^2 R^6 - (2A_l)^{l-1}R^{2l}, \\ \phi_{0/1} &= -(A-D_0)R^2 + (2/3)R^4 + (8/5)A_\gamma^2 R^6. \end{aligned} \tag{6}$$

By varying the dimensionless parameter R in expressions (6) for the thermodynamic potentials, we obtain

$$\begin{aligned} \phi_{IC} &= -(1/6^3A_\gamma^4)\{[1+12A_\gamma^2 A]^{3/2} - [1+18A_\gamma^2 A]\}, \\ \phi_{0/1} &= -(1/0.54\times 6^3 A_\gamma^4) \\ &\quad\times\{[1+0.9\times 12A_\gamma^2(A-D_0)]^{3/2} \\ &\quad- [1+0.9\times 18A_\gamma^2(A-D_0)]\}, \\ \phi_{1/3} &= -[1/6^3(A_\gamma^2 - A_3^2)^2] \\ &\quad\times\{[1+12(A_\gamma^2-A_3^2)(A-D_3)]^{3/2} \\ &\quad- [1+18(A_\gamma^2-A_3^2)(A-D_3)]\}, \\ \phi_{m/l} &= -(1/6^3A_\gamma^4)\{[1+12A_\gamma^2(A-D_l)]^{3/2} \\ &\quad- [1+18A_\gamma^2(A-D_l)]\} - (1/2A_l)\{(A_l/6A_\gamma^2) \\ &\quad\times([1+12A_\gamma^2(A-D_l)]^{1/2}-1)\}^l, \\ &\quad l > 3. \end{aligned} \tag{7}$$

In the above expression for the thermodynamic potential $\phi_{m/l}$, the second term is assumed to be small as compared to the first term (the condition of weak anisotropy is satisfied). The expansion into a series is carried out with respect to this small term.

2. BOUNDARIES BETWEEN THE PHASES

By equating the thermodynamic potentials described by relationships (7) to each other, we obtain the expressions for the boundaries between the phases. Let us write the expressions for the *C*–*IC* and *C*–$C_{0/1}$ phase boundaries, which have the simple form

$$A = 0, \quad A = D_0. \tag{8}$$

The expressions for the *IC*–$C_{m/l}$ and $C_{m/l}$–$C_{m'/l'}$ ($l > 3$) phase boundaries derived from relationships (7) under the condition $D_l \ll A$ (and $D_{l'} \ll A$), which holds good, have the following form:

$$\begin{aligned} D_l &= \{(A_l/6A_\gamma^2)([1+12A_\gamma^2 A]^{1/2}-1)\}^{l-1}, \\ D_l &- \{(A_l/6A_\gamma^2)([1+12A_\gamma^2 A]^{1/2}-1)\}^{l-1} \\ &= D_{l'} - \{(A_{l'}/6A_\gamma^2)([1+12A_\gamma^2 A]^{1/2}-1)\}^{l'-1}. \end{aligned} \tag{9}$$

It would make no sense to present here the expressions for the other phase boundaries, because this would lead to multiple rewriting of the thermodynamic potentials (7) equated to each other (only the common factors 6^3 would cancel out everywhere). It should be noted that three phase boundaries, namely, *C*–*IC*, *C*–$C_{0/1}$ [see relationships (8)], and *IC*–$C_{0/1}$, meet at a common point (the *LT* point [5]). As should be expected, three other phase boundaries, namely, *IC*–$C_{1/3}$, *IC*–$C_{0/1}$, and $C_{1/3}$–$C_{0/1}$, also meet at a common point.

3. THERMODYNAMIC POTENTIALS AND THE PHASE BOUNDARIES FOR SMALL PARAMETERS *A*

In the case where the parameters A in formulas (5) are small enough to satisfy the condition $A_\gamma^2 A \ll 1$, expressions (7) for the thermodynamic potentials can be simplified as follows:

$$\begin{aligned} \phi_{IC} &= -(1/4)A^2[1-2A_\gamma^2 A], \\ \phi_{0/1} &= -(3/8)(A-D_0)^2[1-(9/5)A_\gamma^2(A-D_0)], \\ \phi_{1/3} &= -(1/4)(A-D_3)^2[1-2(A_\gamma^2-A_3^2)(A-D_3)], \\ \phi_{m/l} &= -(1/4)(A-D_l)^2[1-2A_\gamma^2(A-D_l)] \\ &\quad- (1/2)A_l^{l-1}(A-D_l)^l[1-3lA_\gamma^2(A-D_l)], \end{aligned} \tag{10}$$

where the second terms in the square brackets are small as compared to unity.

By equating the thermodynamic potentials determined by relationships (10) to each other, we obtain the following expressions for the boundaries between the corresponding phases:

$$\begin{aligned} &IC\text{–}1/3{:}\quad A_3^2A^2 + 2(A_\gamma^2 - A_3^2)D_3A \\ &\qquad - D_3 - (A_\gamma^2-A_3^2)D_3^2 = 0, \\ &IC\text{–}0/1{:}\quad A = c_0D_0 - (c_0-1)A_\gamma^2A^2 \\ &\qquad + (9/10)c_0A_\gamma^2(A-D_0)^2, \\ &\qquad c_0 \equiv 3+\sqrt{6}, \\ &1/3\text{–}0/1{:}\quad A = c_0D_0 - (c_0-1)D_3 \\ &\qquad + (9/10)c_0A_\gamma^2(A-D_0)^2 - (c_0-1)(A_\gamma^2-A_3^2)(A-D_3)^2. \end{aligned} \tag{11}$$

One can try to simplify these expressions further by using the initial condition $A_\gamma^2 A \ll 1$. However, in this case, it is necessary to ensure that the three phase boundaries described by expressions (11) would meet at a common point, as before. We will not carry out these simplifications here, the more so as all the equations (11) are quadratic in the parameter A and, consequently, can be readily solved.

The phase boundaries IC–$C_{m/l}$ described by relationships (9) can be given in the form

$$A = (1/A_l)D_l^{1/(l-1)}[1 + 3A_\gamma^2(1/A_l)D_l^{1/(l-1)}]. \quad (12)$$

4. PHASE DIAGRAMS

According to relationships (3), the quantities D_0 and D_l involved in expressions (5) can be given in terms of the parameter B^2 as follows:

$$\begin{aligned} D_0 &= 2B^4(B^2 - Q_L^2), \\ D_l &= (B^2 - Q_L^2)[Q_1^2 + 2(B^2 - Q_L^2)]. \end{aligned} \quad (13)$$

By specifying the values of B^2, we determine the quantities D_0 and D_l from expressions (13) and the parameter A from relationships (7)–(9) or from formulas (11) and (12). This allows us to construct the phase boundaries on the D_0–A plane.

For the parameter $B^2 = (2/3)Q_L^2$, the minimum in the soft branch at an arbitrary point of the Brillouin zone disappears. Simultaneously, the quantities a and b (A and B) lose their meaning. Therefore, the phase diagram on the D_0–A plane has meaning only when the condition $D_0 \geq -(2Q_L^2/3)^3$ is satisfied [see relationship (13)].

Figure 1 shows the experimental P–T phase diagram obtained during cooling in [1]. The theoretical phase diagram on the D_0–A plane, which was constructed according to relationships (7), (11), and (12), is presented in Fig. 2. This diagram was constructed using the following parameters:

$$\begin{gathered} A_\gamma = A_3 = 0.6, \quad A_8 = 1.5, \quad A_5 = 0.8, \\ Q_L^2 = 0.2, \quad Q = 0.5. \end{gathered} \quad (14)$$

In Fig. 2, the phase boundaries constructed according to formulas (11) and (12) are indicated by thin lines and the phase boundaries constructed from expressions (7)–(9) are depicted by solid lines. Some boundaries (IC–0/1, IC–3/8, IC–2/5) on the scale of Fig. 2 are indistinguishable. Other boundaries (IC–1/3 and, especially, 1/3–0/1) differ significantly, and this difference increases with an increase in the parameter A. It should be noted that the $C_{2/5}$–$C_{1/3}$ phase boundary substantially deviates from the IC–$C_{1/3}$ phase boundary (in contrast to the $C_{3/8}$–$C_{1/3}$ and IC–$C_{1/3}$ phase boundaries). In order to emphasize this deviation, the IC–$C_{1/3}$ phase boundary is depicted by a dotted line.

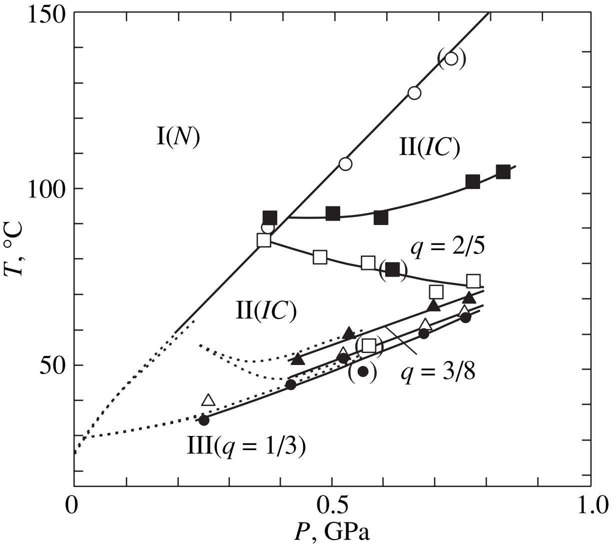

Fig. 1 Experimental P–T phase diagram obtained during cooling in [1]. Dotted lines indicate the phase diagrams given in [2–4].

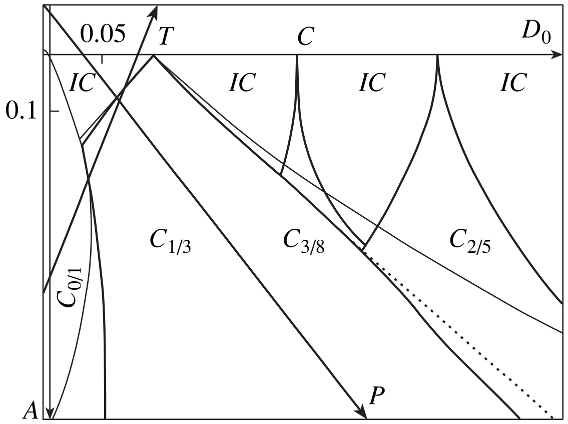

Fig. 2. Theoretical phase diagram on the D_0–A plane. The axes P and T are also shown.

The P–T phase diagram was constructed from the D_0–A phase diagram under the assumption that the coefficients D_0 and A are linearly dependent on the temperature T and pressure P. In this case, the axes P and T in Fig. 2 are straight lines. Their position and orientation are shown in Fig. 2.

Figure 3 presents the theoretical P–T phase diagram. The phase diagrams shown in Figs. 1 and 3 are similar to each other in the region near the C–IC phase transition. However, in the region close to the IC–$C_{1/3}$ phase transition in Fig. 1 (as in the phase diagrams presented in [2–4]), there exists a noticeable nonlinearity. This nonlinearity is absent in Fig. 3. Possibly, this is associated with the fact that the single-harmonic approxima-

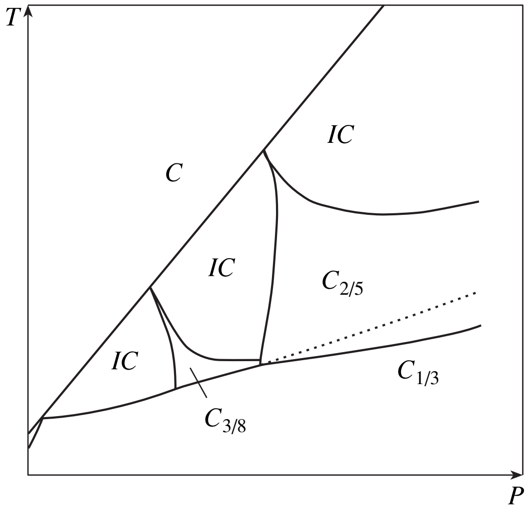

Fig. 3. Theoretical phase diagram obtained from the phase diagram on the D_0–A plane (Fig. 2).

tion was used for the *IC* phase. The approximations and assumptions used to construct the theoretical phase diagrams are presented in [5].

ACKNOWLEDGMENTS

This work was supported by the Russian Foundation for Basic Research, project no. 03-02-16104.

REFERENCES

1. T. Asahi and K. Izutsu, J. Phys. Soc. Jpn. **72** (2), 330 (2003).
2. S. Shimomura, H. Terauchi, N. Hamaya, and Y. Fujii, Phys. Rev. B **54** (10), 6915 (1996).
3. K. Gesi, J. Phys. Soc. Jpn. **65** (6), 1963 (1996).
4. K. Gesi, Kristallografiya **44** (1), 89 (1999) [Crystallogr. Rep. **44**, 84 (1999)].
5. D. G. Sannikov, Fiz. Tverd. Tela (St. Petersburg) **42** (12), 2213 (2000) [Phys. Solid State **42**, 2282 (2000)].
6. H. Mashiyama, G. A. Kessenikh, and D. G. Sannikov, Ferroelectrics **283**, 109 (2003).
7. D. G. Sannikov, G. A. Kessenikh, and H. Mashiyama, J. Phys. Soc. Jpn. **69** (1), 130 (2000); J. Phys. Soc. Jpn. **71** (6), 1435 (2002).
8. D. G. Sannikov and H. Mashiyama, J. Phys. Soc. Jpn. **71** (7), 1698 (2002); J. Phys. Soc. Jpn. **72** (6), 1423 (2003).

Translated by O. Moskalev

Physics of the Solid State, Vol. 47, No. 4, 2005, pp. 733–737. Translated from Fizika Tverdogo Tela, Vol. 47, No. 4, 2005, pp. 708–712.
Original Russian Text Copyright © 2005 by Gorbunov, Zatsepin, Pustovarov, Cholakh, Yakovlev.

Electronic Excitations and Defects in Nanostructural Al_2O_3

S. V. Gorbunov*, A. F. Zatsepin*, V. A. Pustovarov*, S. O. Cholakh*, and V. Yu. Yakovlev**

**Ural State Technical University, ul. Mira 19, Yekaterinburg, 620002 Russia*
e-mail: zats@dpt.ustu.ru
***Tomsk Polytechnic University, pr. Lenina 30, Tomsk, 634034 Russia*

Received June 15, 2004

Abstract—A time-resolved cathodo- and photoluminescence study of nanostructural modifications of Al_2O_3 (powders and ceramics) excited by heavy-current electron beams, as well as by pulsed synchrotron radiation, is reported. It was found that Al_2O_3 nanopowders probed before and after Fe^+ ion irradiation have the same phase composition (the γ-phase/δ-phase ratio is equal to 1), an average grain size equal to ~17 nm, and practically the same set of broad cathodoluminescence (CL) bands peaking at 2.4, 3.2, and 3.8 eV. It was established that Al_2O_3 nanopowders exhibit fast photoluminescence (PL) (a band at 3.2 eV), whose decay kinetics is described by two exponential stages ($\tau_1 = 0.5$ ns, $\tau_2 = 5.5$ ns). Three bands, at 5.24, 6.13, and 7.44 eV, were isolated in the excitation spectrum of the fast PL. Two alternate models of PL centers were considered, according to which the 3.2-eV luminescence either originates from radiative relaxation of the P^- centers (anion–cation vacancy pairs) or is due to the formation of surface analogs of the F^+ center (F_S^+-type centers). In addition to the fast luminescence, nano-Al_2O_3 was found to produce slow luminescence in the form of a broad band peaking at 3.5 eV. The excitation spectrum of the 3.5-eV luminescence obtained at $T = 13$ K exhibits two doublet bands with maxima at 7.8 and 8.3 eV. An analysis of the luminescent properties of nanostructural and single-crystal Al_2O_3 suggests that the slow luminescence of nanopowders at 3.5 eV is due to radiative annihilation of excitons localized near structural defects. © *2005 Pleiades Publishing, Inc.*

1. INTRODUCTION

We are witnessing intense progress in the physics of nanosized systems, which was initiated by the discovery of novel physical effects and unusual properties of materials residing in a nanostructural state. One of the areas that offer promise for controlling the properties of nanomaterials and deal with developing the basis of nanotechnology is the investigation of optical phenomena in nanostructures.

Optical properties of crystalline dielectrics are known to be determined to a considerable extent by defects produced by radiation, as well as by chemical treatment performed in reducing or oxidizing conditions at elevated temperatures. Leucosapphire (α-Al_2O_3) crystals are among the best studied in this respect. Data on the luminescence and EPR spectra have provided a basis for reliable identification of the nature of some intrinsic defects. However, the question of the influence of size effects and the specific features of the processes that occur on the surface and in the bulk of the material as the aluminum oxide crosses over from the crystalline to a nanostructural state remains open.

This communication reports on a study of the optical properties and defects of nanostructural Al_2O_3 using luminescence spectroscopy with nanosecond-range time resolution.

2. SAMPLES AND EXPERIMENTAL TECHNIQUES

The nanostructural Al_2O_3 powder samples for study were prepared by electrically exploding a metallic aluminum wire in air, with subsequent sedimentation of the resulting oxide powder in water [1]. A comparative study of the luminescence spectra was carried out on the starting nanopowders and on nano-Al_2O_3 powder samples irradiated by iron ions from a MEVVA pulsed ion source ($t_{\text{pulse}} = 0.4$ ms, $f = 25$ Hz, $E = 30$ keV, $j = 3$ mA/cm^2), as well as on Al_2O_3 ceramic samples prepared by magnetic pulse compaction [2].

X-ray diffraction patterns of the samples were obtained with CuK_α radiation on a DRON-4 diffractometer equipped with a graphite monochromator. Interpretation of the x-ray diffractograms and an analysis of the phase composition were performed with the PowderCell program using the ASTM database. The average grain size was estimated from the integrated width of the (118) reflection of the δ-Al_2O_3 phase using the Scherer method. Cathodoluminescence (CL) measurements in the range 2.0–4.5 eV were carried out at 295 K on a pulsed luminescence spectroscopy setup with a nanosecond-range time resolution. The excitation was provided by a GIN-600 pulsed electron accelerator with the following beam parameters: $E_e = 0.25$ MeV, $t_{\text{pulse}} = 10^{-8}$ s, and $W = 20$–250 mJ/cm^2. The spectrometer setup

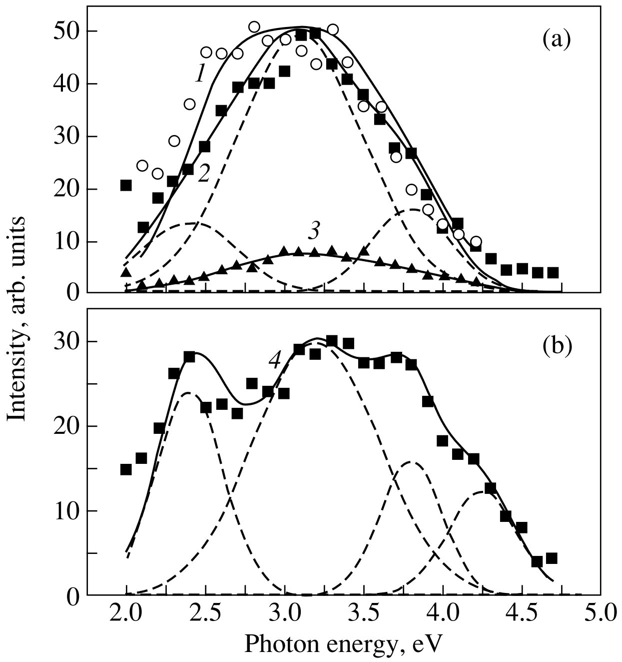

Fig. 1. Cathodoluminescence spectra of Al_2O_3 measured (*1*, *2*, *4*) at 295 K at the end of the electron beam pulse and (*3*) with a 100-ns delay. (a) (*2*, *3*) Starting and (*1*) Fe^+-irradiated nanopowders and (b) (*4*) nanoceramics.

included an MDR-3 grating monochromator, an FÉU-97 PM tube, and an S8-12 broad-band storage oscillograph.

Photoluminescence (PL) and PL excitation spectra were measured at 295 and 13 K on a pulsed synchrotron radiation (SR) beam at the SUPERLUMI station (HASYLAB laboratory, DESY, Hamburg) [3]. Excitation in the range 5–21 eV was effected with a 2-m Al-grating vacuum monochromator. The PL excitation spectra were normalized against an equal number of photons incident on a sample. PL spectra in the region 2–6 eV were analyzed with a 0.3-m ARC Spectra Pro-308i monochromator and an R 6358P PM tube. The PL and PL excitation spectra were obtained in the time-integrated luminescence mode, as well as in gated time windows (Δt wide) delayed by δ_t from the beginning of an exciting SR pulse. Based on the decay kinetics, the parameters δ_t and Δt were set at 1.9 and 14 ns for the fast PL component and at 47 and 115 ns for the slow PL component, respectively. The PL decay kinetics parameters were determined by deconvolution.

3. RESULTS AND DISCUSSION

An x-ray diffraction analysis of the starting nonirradiated nanosized Al_2O_3 powder showed the sample to consist of a mixture of aluminum oxide and hydroxide. The hydroxide was a mixture of the bayerite and gibbsite phases and made up about 30% of the total sample composition. The oxide component was, in turn, a mixture of the γ- and δ-Al_2O_3 modifications. The x-ray diffraction spots of the γ phase (defected spinel) almost completely overlap the reflections of the tetrahedral δ phase and can be unfolded by computer modeling. The analysis showed these phases to be in a 1 : 1 ratio.

The x-ray diffractograms of the samples bombarded by iron ions ($\Phi = 10^{17}$ cm^{-2}) differ from those of the starting nanostructural Al_2O_3 by the absence of the aluminum hydroxide lines. The ratio between the amounts of γ and δ phases remains unchanged. Note also that the diffractograms contain no traces of the high-temperature θ and α phases of Al_2O_3. The average grain size in both the starting and Fe^+-irradiated samples was found to be the same, 17 nm.

Excitation of nanostructural Al_2O_3 powders at 295 K by a pulsed accelerated electron beam generates CL over a broad spectral region (Fig. 1a). An analysis of the CL spectral response of starting samples revealed that the experimental curves could be well fitted by a set of Gaussian-shaped bands with maxima at 2.4, 3.2, and 3.8 eV. The samples bombarded by Fe^+ ions produce a set of the same bands as do the nonirradiated ones. This implies that the presence of aluminum hydroxide does not have a noticeable effect on the luminescence of nanostructural Al_2O_3. However, the samples irradiated by ions exhibit a weak increase in the intensity of the 2.4-eV band and a decrease in intensity in the region of the 3.2- and 3.8-eV bands.

The CL spectra of Al_2O_3 nanoceramics (Fig. 1b) differ from the CL spectra of nanopowders by a noticeable narrowing and simultaneous growth in intensity of the bands at 2.4, 3.2, and 3.8 eV. In contrast to nanopowders, an additional luminescence band peaking at 4.3 eV appears in the CL spectrum of nanoceramics. The pulsed magnetic-field compaction used to prepare Al_2O_3 nanoceramics differs from the standard ceramic technology by the lower processing temperature (<600°C). Additional heat treatment at $T = 1100$°C accounts for the formation of other high-temperature Al_2O_3 modifications in addition to the γ and δ phases. The observed differences in the optical properties of the nanoceramic, as contrasted with the unchanging main band set in the CL spectrum, can be assigned to an increase in the average grain size up to 100–150 nm.

Considering now the nature of the CL band at 2.4 eV, we can point out that a spectrally similar band was observed in neutron-irradiated α-Al_2O_3 crystals [4]. The model proposed in [4] assigns the formation of the 2.4-eV band to pairs of anion vacancies with electrons trapped in them (*F*-type aggregate centers). The origin of the structural defects in the starting Al_2O_3 nanopowders may be associated with the conditions of their formation being thermodynamically nonequilib-

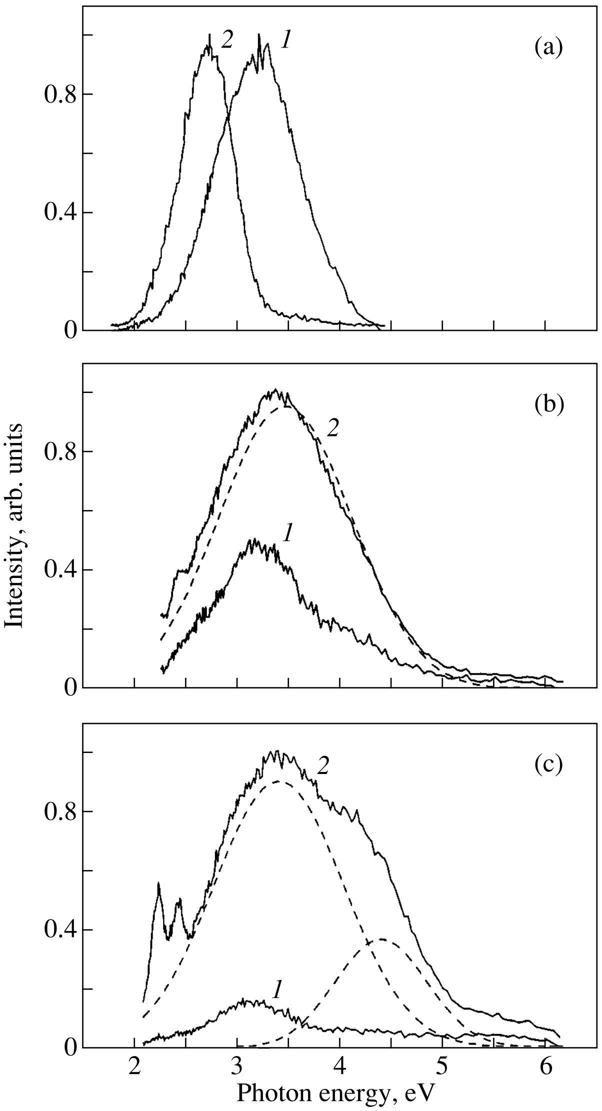

Fig. 2. Time-resolved photoluminescence spectra of Al_2O_3 nanopowders measured at $T = 13$ K under excitation by photons of energy (a) 5.9, (b) 7.75, and (c) 11.3 eV. (*1*) Fast time window and (*2*) slow time window.

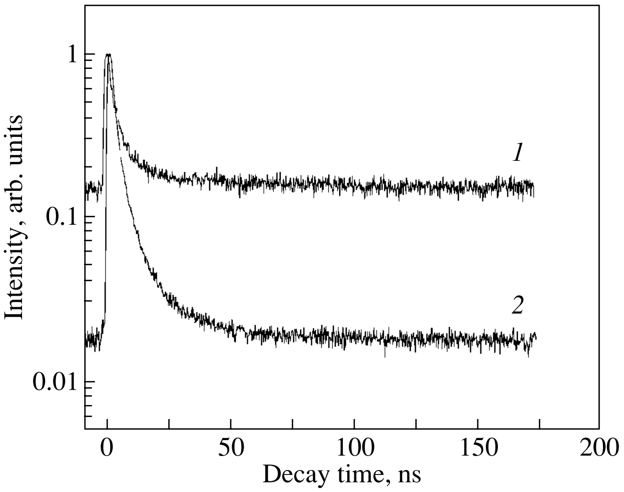

Fig. 3. 3.1-eV photoluminescence decay kinetics of an Al_2O_3 nanopowder measured at an excitation energy of (*1*) 11.3 and (*2*) 6 eV. $T = 13$ K.

rium. The slight increase in the CL intensity at 2.4 eV observed under ion beam treatment of the starting samples demonstrates an additional radiation-induced production of centers of the above type.

CL spectra of the starting and ion-irradiated nanostructural Al_2O_3 powders are dominated by the 3.2-eV band with a FWHM of ≈ 1.0 eV (Fig. 1). Preliminary measurements of the CL kinetics showed the 3.2-eV luminescence to undergo fast decay. To determine the nature of this band, time-resolved PL spectra obtained at different exciting photon energies were studied (Fig. 2). As seen from Fig. 2, the band at 3.2 eV is observed only in the "fast" PL time window. The decay kinetics of the 3.2-eV PL in a nanostructural Al_2O_3 powder observed at $T = 13$ K under excitation by photons with an energy of 5.2 to 6.2 eV can be fitted by two exponential functions with time constants $\tau_1 = 0.5$ ns and $\tau_2 \approx 5.5$ ns (Fig. 3). The excitation spectrum of the fast PL component (Fig. 4) exhibits three strong bands peaking at 5.24, 6.13, and 7.44 eV in the transmission window of crystalline α-Al_2O_3. The efficiency of excitation for $E > 8.5$ eV near the long-wavelength fundamental absorption edge and of creation of separated electron–hole pairs is low.

The data on the three-band structure of the 3.2-eV PL excitation spectrum are in good agreement with the spectral response of the 3.0-eV luminescence in α-Al_2O_3 single crystals subjected to high-temperature treatment and quenching in air [5]. The nature of this luminescence was assigned in [5] to the formation of P^- centers (anion–cation vacancy pairs).

The model of these centers assumes optical transitions to proceed through charge transfer from the oxygen ion to the anion vacancy. This assumption was not in conflict with the decay time of the 3.0-eV luminescence, which was found to be $\tau = 50$ μs at $T = 300$ K. The considerable decrease in the lifetime of P^- center excited states observed to occur in nanostructural Al_2O_3 is a manifestation of the size effect. The slight short-wavelength shift (~0.2 eV) of the luminescence band and the fast radiative decay of P^- centers in nanostructural Al_2O_3 may be governed by the states of these centers changing in interaction with localized surface states.

An alternate model of centers exhibiting fast luminescence at 3.2 eV in Al_2O_3 nanopowders is also worth mentioning. In view of the substantial contribution that

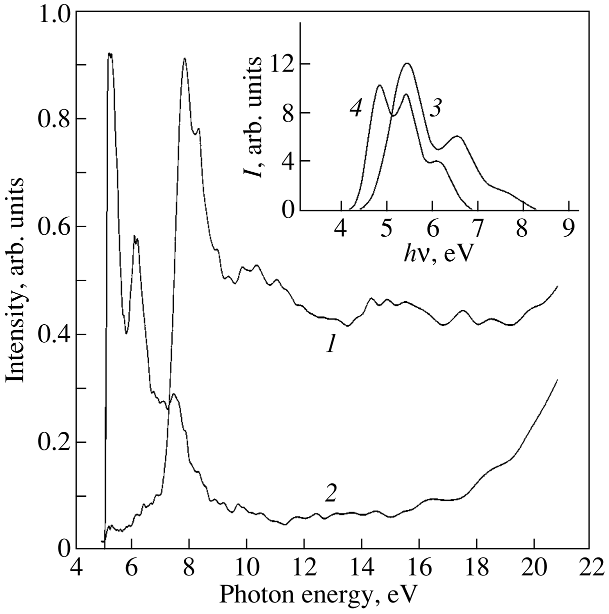

Fig. 4. Photoluminescence excitation spectra of Al_2O_3 nanopowders measured at $T = 13$ K. (*1*) Slow component at 3.5 eV and (*2*) fast component at 3.2 eV. The inset shows the spectra of (*3*) P^--center absorption and (*4*) F^+-center luminescence excitation in α-Al_2O_3 single crystals [5, 7].

size effects make to the properties of nanoparticles, the possible formation of vacancy-type surface luminescence-active defects in nanosized materials should not be disregarded. A comparison of the spectral responses of bulk and surface oxygen-deficient centers in SiO_2 [6] revealed a short-wavelength shift of the excitation band maxima of surface defects. A comparative analysis of the spectral response and kinetics of F^+-center luminescence excitation in α-Al_2O_3 crystals [7] and of excitation spectra of the 3.2-eV fast luminescence in nanostructural Al_2O_3 likewise reveals a short-wavelength shift of the three-band structure. This fact suggests the possibility that surface analogs of the F^+ center (the so-called F_S^+ centers) can form in nano-Al_2O_3. Naturally, this hypothesis requires that further studies be made, for instance, with the use of a surface-sensitive method of photostimulated electron emission [8].

In addition to the fast component, a slow component with $\tau > 200$ ns is observed in the PL decay kinetics of nano-Al_2O_3 (Fig. 3). This component manifests itself in the PL spectrum (Fig. 2) as a broad band peaking at 3.5 eV with an FWHM ≈ 1.5 eV. Measurements of pulsed CL showed that the decay kinetics of the luminescence in the 3.5-eV region can be given in the time range from 0.1 to 10 μs by a sum of two exponential functions with time constants of 0.5 and 4.5 μs. As follows from Fig. 4, the 3.5-eV PL excitation spectrum at $T = 13$ K contains two intense doublet-structured bands with maxima at 7.8 and 8.3 eV. The weak efficiency of the 3.5-eV PL excitation in the transmission region of Al_2O_3 crystals for $E < 7.0$ eV can also be mentioned. Note the considerable difference in excitation efficiency between the slow luminescence at 3.5 eV and fast luminescence at 3.2 eV in the region of $E > 9.5$ eV, which is characteristic of the formation of free electron–hole pairs. The excitation spectrum of the 3.5-eV luminescence has a pattern typical of the creation of electronic excitations localized near impurity or native defects. A study of anion-defected α-Al_2O_3 crystals reported in [9] showed that the excitation spectra of *F*-center luminescence ($E = 3.0$ eV) contains, in addition to the band at 6.0 eV associated with intracenter transitions, an excitation band at 8.8 eV, which lies at the long-wavelength fundamental absorption edge. At low temperatures, this band transforms into a doublet with maxima at 8.52 and 9.02 eV. The data from [9] allow one to assign this band to excitons bound to *F*-type centers.

An analysis of the above results suggests that the slow 3.5-eV luminescence of Al_2O_3 nanopowders originates from radiative annihilation of excitons localized near structural defects. The splitting (0.5 eV) in the doublet excitation lines of bound excitons in crystalline and nano-Al_2O_3 is the same. In the latter case, however, the doublet excitation structure of bound excitons is shifted to longer wavelengths. This shift may be caused by the fact that, in the γ and δ phases of Al_2O_3 nanoparticles, the electronic energy structure changes noticeably in comparison with that in the crystalline α-Al_2O_3 modification. Similar relations were observed earlier in x-ray emission spectra of nanostructural Al_2O_3 [10]. Furthermore, LDA band structure calculations carried out in [10] revealed a shift of the partial valence-band density of states in nano-Al_2O_3 as compared to that of α-Al_2O_3.

ACKNOWLEDGMENTS

The authors are indebted to Yu.A. Kotov and V.V. Ivanov for providing the samples and N.V. Gavrilov, V.S. Kortov, A.I. Kukharenko, and A.I. Medvedev for helpful discussions and assistance in the work.

This study was supported by the Russian Foundation for Basic Research (project no. 02-02-16322), CRDF REC-005 (project no. EK-005-X1), and INTAS (project no. 01-0458).

REFERENCES

1. I. V. Beketov, Yu. A. Kotov, A. M. Murzakaev, O. V. Samatov, V. P. Volkov, R. Böhme, and G. Schumacher, Mater. Sci. Forum **225–227**, 913 (1995).

2. C.-K. Rhee, W. W. Kim, G. H. Lee, V. V. Ivanov, S. V. Zajats, and A. I. Medvedev, J. Metastable Nanocryst. Mater. **15–16**, 401 (2003).
3. G. Zimmerer, Nucl. Instrum. Methods Phys. Res. A **308**, 178 (1991).
4. M. J. Springis and J. A. Valbis, Phys. Status Solidi B **123**, 335 (1984).
5. A. V. Puyats, M. J. Springis, and J. A. Valbis, Phys. Status Solidi A **62**, 85 (1980).
6. A. A. Chudinov, A. F. Zatsepin, D. Yu. Biryukov, and V. S. Kortov, Vestn. UGTU–UPI, No. 5, 50 (2004).
7. B. D. Evans and M. Stapelbroek, Phys. Rev. B **18**, 7089 (1978).
8. A. F. Zatsepin, V. S. Kortov, and D. Yu. Biryukov, Radiat. Eff. Defects Solids **157**, 595 (2002).
9. A. I. Surdo, V. S. Kortov, and V. A. Pustovarov, in *Proceedings of 12th International Conference on Radiation Physics and Chemistry of Inorganic Materials* (Tomsk, Russia, 2003), p. 456.
10. D. A. Zatsepin, V. M. Cherkashenko, É. Z. Kurmaev, S. N. Shamin, V. V. Fedorenko, N. A. Skorikov, S. V. Plastinin, N. V. Gavrilov, A. I. Medvedev, and S. O. Cholakh, Fiz. Tverd. Tela (St. Petersburg) **46** (11), 2064 (2004) [Phys. Solid State **46**, 2134 (2004)].

Translated by G. Skrebtsov

Physics of the Solid State, Vol. 47, No. 4, 2005, pp. 738–741. Translated from Fizika Tverdogo Tela, Vol. 47, No. 4, 2005, pp. 713–715.
Original Russian Text Copyright © 2005 by Granovsky, Kozlov, Bagmut, Nedukh, Tarapov, Clerc.

Microwave-Frequency Spin-Dependent Tunneling in Nanocomposites

A. B. Granovsky*, A. A. Kozlov*, T. V. Bagmut,**
S. V. Nedukh, S. I. Tarapov**, and J. P. Clerc*****
**Moscow State University, Vorob'evy gory, Moscow, 119992 Russia*
e-mail: granov@magn.ru
***Institute of Radiophysics and Electronics, National Academy of Sciences of Ukraine, Kharkov, 61085 Ukraine*
****École Polytechnique, Université de Marseille, ME, Technopole de Château-Gombert, Marseille, 13453 France*

Received July 20, 2004

Abstract—The transmission coefficient of films of $Co_{51.5}Al_{19.5}O_{29}$, $Co_{50.2}Ti_{9.1}O_{40.7}$, $Co_{52.3}Si_{12.2}O_{35.5}$, and $(Co_{0.4}Fe_{0.6})_{48}(MgF)_{52}$ ferromagnetic metal–insulator magnetic nanocomposites exhibiting tunneling magnetoresistance and the magnetorefractive effect for electromagnetic waves was studied in the frequency range 30–50 GHz. The transmission coefficient of the first two compositions varies strongly under an applied magnetic field, and its variation exhibits a linear correlation with the field dependence of magnetoresistance. For the other two compositions, the transmission coefficient does not depend on magnetic field. The data obtained are interpreted in terms of the concept of microwave spin-dependent tunneling. *© 2005 Pleiades Publishing, Inc.*

The high-frequency properties of metallic multilayers with giant magnetoresistance have been studied over a fairly broad frequency range (see [1–6] and references therein). Magnetization of multilayers gives rise not only to a substantial reduction in resistivity but also to a change in the permittivity. As a consequence, the impedance and optical properties of multilayers become dependent on magnetic field. In the optical range, this phenomenon was termed the magnetorefractive effect [6], and in the radio-frequency and microwave ranges, high-frequency magnetoresistance or magnetoimpedance [1–5]. Similar effects are also expected to occur in systems with a considerable magnetoresistance of any type, including systems with tunneling magnetoresistance (TMR). Ferromagnetic metal–insulator nanocomposites with a metal content near the value corresponding to the percolation threshold, as well as magnetic trilayer and multilayer systems with tunneling barriers, belong to TMR systems. Investigation of the microwave properties of these systems will make it possible to determine the mechanisms of spin-dependent tunneling, establish the frequency dispersion of conductivity, check the recent concept of magnetocapacitance [7], determine the possible operational range of spintronic devices based on TMR systems (for example, spin filters, magnetic storage devices, magnetic sensors), and suggest new possible areas of their application [6]. Recent studies of the magnetorefractive effect (MRE) in reflection performed in nanocomposites in the near IR region [6, 8, 9] have confirmed the existence of spin-dependent tunneling up to optical frequencies. The present paper reports on an experimental study of the transmission of millimeter-range electromagnetic waves (30–50 GHz) through films of ferromagnetic metal–insulator magnetic nanocomposites possessing TMR.

As subjects for the study, we chose films of nanocomposites of various compositions with metal contents in the immediate vicinity of the percolation threshold. The techniques employed in the preparation and structural characterization of the samples are described in [8, 9]. The composition, film thickness d, residual electrical resistivity ρ ($H = 0$), TMR parameter $\Delta\rho/\rho = \dfrac{\rho(H=0)-\rho(H)}{\rho(H=0)}$, and MRE parameter in reflection $\zeta = \Delta R/R = \dfrac{R(H=0)-R(H)}{R(H=0)}$ measured in a field $H = \pm1.5$ kOe, as well as the relative changes in the transmission coefficient $\dfrac{\Delta D}{D} = \dfrac{D(H=0)-D(H)}{D(H=0)}$ in the same field $H = \pm1.5$ kOe at 44 GHz, are listed in the table. Because the reflectance R at optical frequencies and the MRE depend strongly on the light frequency ν, the table specifies, for each composition, the maximum values of the MRE at the corresponding frequency, which were taken from [8–10]. Also presented are the values of TMR in a field of ±10 kOe; for simplicity, we neglect a certain difference between the values of the corresponding parameters in a zero external magnetic field and in the state with zero magnetization (which occurs in a field equal to the coercive force). All measurements were conducted at room temperature with an in-plane field.

The microwave transmission coefficient D of nanocomposites in the range 30–50 GHz and its relative

Parameters of the films under study

No.	Sample composition, vol %	d, μm	$\Delta\rho/\rho$, %		$\Delta D/D$, %	ρ, μΩ cm	$\zeta = \Delta R/R$, % (ν, cm^{-1})
			$H = \pm10$ kOe	$H = \pm1.5$ kOe			
1	$Co_{51.5}Al_{19.5}O_{29}$	1.91	9.2	5.08	2.28	2.9×10^5	–0.9 (1100)
2	$Co_{50.2}Ti_{9.1}O_{40.7}$	2.02	5.8	2.42	1.6	6.1×10^6	–0.7 (1030)
3	$Co_{52.3}Si_{12.2}O_{35.5}$	1.67	4.1	2.99	Not detected	4.5×10^8	+0.7 (1300)
4	$(Co_{0.4}Fe_{0.6})_{48}(MgF)_{52}$	1	13	1.32	″	$\sim10^9$	–1.3 (1000)

change under magnetization, $\Delta D/D$, which can be called the magnetoimpedance parameter in transmission, were measured using the open-resonator technique described in detail in [5]. It should be stressed that, in contrast to the optical reflectance or transmittance, the transmission coefficient relates to the ratio of the wave amplitudes rather than the ratio of the intensities. We also studied ferromagnetic resonance (FMR) in our samples in fields of up to 20 kOe. We note that, in the frequency range 30–50 GHz, the FMR is observed to exist only above 8 kOe, i.e., in fields considerably stronger than those in the case of $\Delta D/D$ measurements.

The measured values of $\Delta D/D$ suggest several conclusions. First, the $Co_{51.5}Al_{19.5}O_{29}$ and $Co_{50.2}Ti_{9.1}O_{40.7}$ nanocomposites exhibit considerable changes in the transmission coefficient under magnetization, with the magnetoimpedance parameter $\Delta D/D$ being of the order of the TMR. A comparison of the field dependences of $\Delta D/D$ and TMR (see Fig. 1) argues convincingly for the observed effect being (as should be expected) a frequency analog of the TMR. Because no FMR is observed in our samples in the frequency range 30–50 GHz in fields of up to 1.5 kOe, one can also conclude that this effect is not related to the dependence of magnetic per-

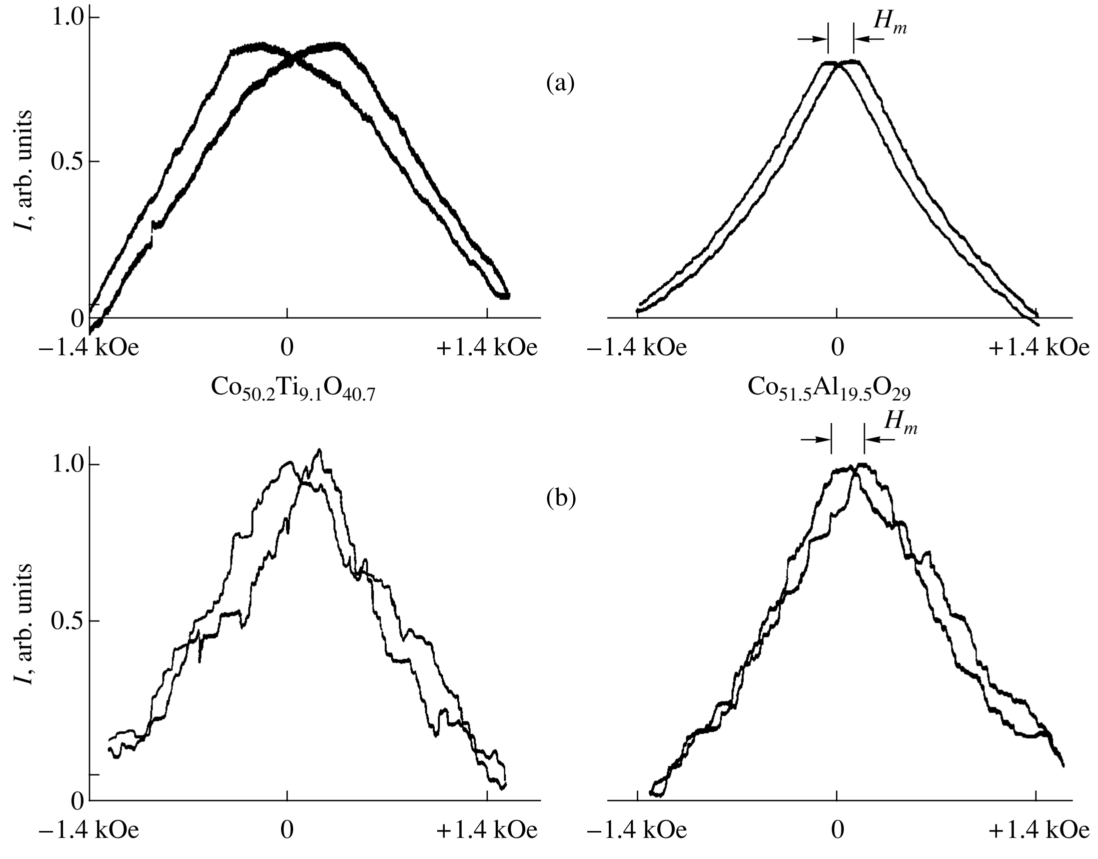

Fig. 1. (a) Magnetoimpedance at 44 GHz and (b) magnetoresistance of the $Co_{50.2}Ti_{9.1}O_{40.7}$ and $Co_{51.5}Al_{19.5}O_{29}$ nanocomposites. $2H_m$ is the distance between the maxima in magnetoimpedance and magnetoresistance.

meability on magnetic field. Second, the magnetoimpedance $\Delta D/D$ for these two compositions is only weakly frequency-dependent (unlike the MRE). This feature correlates with the magnetoimpedance measurements carried out on metallic multilayers [4] and corroborates the interference nature of the strong dependence of the MRE on the frequency of light [8]. Third, the magnetoimpedance parameter for these samples turns out to be larger than the MRE. Finally, no magnetoimpedance was detected in samples with the compositions $Co_{52.3}Si_{12.2}O_{35.5}$ and $(Co_{0.4}Fe_{0.6})_{48}(MgF)_{52}$, which exhibit appreciable MRE and TMR; this result, at first glance, is at odds with the concept of the magnetoimpedance being a frequency analog of the TMR.

Let us show that these features of magnetoimpedance do find explanation within a simple model. In calculating the impedance, we have to take into account that, near the percolation threshold ($x \approx x_c$), the electrical resistivity of nanocomposites exceeds the resistivity of conventional metals by 7 to 10 orders of magnitude and increases strongly (by a few orders of magnitude) when crossing over from metallic conduction ($x \geq x_c$) to tunneling and hopping transport ($x \leq x_c$).

As in [4], we neglect the difference between the wave impedance of the insulating substrate and that of free space $Z = (\mu_0/\varepsilon_0)^{1/2}$. Under these conditions, the transmission coefficient of the air–film–air trilayer system can be written as

$$D = \frac{2Z_2Z}{2Z_2Z\cosh k_2d + (Z_2^2 + Z^2)\sinh k_2d}, \tag{1}$$

where $Z_2 = (\tilde{\mu}/\tilde{\varepsilon})^{1/2}$ is the impedance of the nanocomposite and $k_2 = i\omega(\tilde{\varepsilon}_2\tilde{\mu}_2)^{1/2}$ is the wavenumber. For microwave frequencies and far from the FMR region, we can assume the magnetic permeability of the nanocomposite to be $\tilde{\mu}_2 = \mu_0$ and, in the expression for the complex permittivity

$$\tilde{\varepsilon}_2 = \varepsilon_2 - i\frac{\sigma(\omega)}{\omega} \tag{2}$$

the second term is of the order of or less than the first for the high-resistivity systems under study here (see table). Considering the limiting case where $\sigma(\omega)/\omega\varepsilon_2$ is a small parameter, we obtain from Eq. (1)

$$\begin{aligned} D &= \exp\left[-i\frac{\omega}{c}d - \frac{\omega}{c}d\frac{\sigma(\omega)}{2\omega\varepsilon_2}\right] \\ &\approx \exp\left[-i\frac{\omega}{c}d\right]\left(1 - \frac{\omega}{c}d\frac{\sigma(\omega)}{2\omega\varepsilon_2}\right), \end{aligned} \tag{3}$$

$$\frac{\Delta D}{D} = \frac{D(H) - D(H=0)}{D(H=0)} = \frac{1}{2}\frac{d}{c}\frac{1}{\varepsilon_2\rho}\frac{\Delta\rho}{\rho}, \tag{4}$$

where we neglected the possible dependence of the conductivity on frequency and set $\sigma(\omega, H) = 1/\rho(H)$. It should be pointed out that the above approximations are too rough to be used in a quantitative description, because the parameter $\sigma(\omega)/\omega\varepsilon_2$ is not small for the first two compositions in the table. We also cannot disregard the frequency dependence of the conductivity (see discussion of the possible frequency dependence of the conductivity of magnetic composites in [6]). Nevertheless, Eq. (4) offers an interpretation for the observed relations. As follows from Eq. (4), the magnetoimpedance parameter $\Delta D/D$ and the TMR are linearly correlated. Furthermore, the magnetoimpedance is inversely proportional to the sample resistivity ρ. For the last two samples in the table, which are located on the insulating side of the percolation transition, the resistivity exceeds that of the first two samples by about four orders of magnitude. Therefore, the parameter $\Delta D/D$ for the former samples is negligible, despite the fact that the values of MRE and TMR for them are higher. Equation (4) also shows that the parameter $\Delta D/D$ is of the same sign as the TMR and is not larger than the TMR. All these conclusions fit the results displayed in the figure and in the table. The frequency dependence of the conductivity and of the magnetoimpedance parameter of magnetic nanocomposites over a broader frequency range, as well as the problem of quantitative description of the experiment, will be treated in a future publication.

We can conclude that the giant magnetoimpedance of nanocomposites at 30–50 GHz is a consequence of microwave spin-dependent tunneling and is observed only in compositions on the metallic side of the percolation transition.

ACKNOWLEDGMENTS

The authors are grateful to S. Ohnuma for providing the samples and performing their structural characterization.

This study was supported by the Russian Foundation for Basic Research (project no. 03-02-16127), the program "Universities of Russia," and, in part, URC (project no. 1916).

REFERENCES

1. J. J. Krebs, P. Lubitz, A. Chaiken, and G. A. Prinz, J. Appl. Phys. **69** (8), 4795 (1991).
2. A. B. Drovosekov, N. M. Kreĭnes, D. I. Kholin, V. F. Meshcheryakov, M. A. Milyaev, L. N. Romashev, and V. V. Ustinov, Pis'ma Zh. Éksp. Teor. Fiz. **67**, 690 (1998) [JETP Lett. **67**, 727 (1998)].
3. A. B. Rinkevich, L. N. Romashev, and V. V. Ustinov, Zh. Éksp. Teor. Fiz. **117** (5), 960 (2000) [JETP **90**, 834 (2000)].
4. V. V. Ustinov, A. B. Rinkevich, L. N. Romashev, A. M. Burkhanov, and E. A. Kuznetsov, Fiz. Met. Metalloved. **96** (3), 52 (2003) [Phys. Met. Metallogr. **96**, 291

(2003)]; Fiz. Tverd. Tela (St. Petersburg) **37** (2), 561 (1995) [Phys. Solid State **37**, 306 (1995)].

5. D. P. Belozorov, V. N. Derkach, S. N. Nedukh, A. G. Ravlik, S. T. Roschenko, I. G. Shipkova, S. I. Tarapov, F. Yidiz, and B. Aktas, J. Magn. Magn. Mater. **263** (3), 315 (2003).
6. A. Granovsky and M. Inoue, J. Magn. Magn. Mater. **272–276** (Suppl. 1), E1601 (2004).
7. S. T. Chui and Liangbin Hu, Appl. Phys. Lett. **80** (2), 273 (2002).
8. A. B. Granovsky, I. V. Bykov, E. A. Gan'shina, V. S. Gushchin, M. Inoue, Yu. E. Kalinin, A. A. Kozlov, and A. N. Yurasov, Zh. Éksp. Teor. Fiz. **123** (6), 1256 (2003) [JETP **96**, 1104 (2003)].
9. A. Granovsky, V. Gushchin, I. Bykov, A. Kozlov, N. Kobayashi, S. Ohnuma, T. Masumoto, and M. Inoue, Fiz. Tverd. Tela (St. Petersburg) **45** (5), 868 (2003) [Phys. Solid State **45**, 911 (2003)].
10. I. V. Bykov, E. A. Gan'shina, A. B. Granovsky, V. S. Gushchin, A. A. Kozlov, T. Masumoto, and S. Ohnuma, Fiz. Tverd. Tela (St. Petersburg) **47** (2), 268 (2005) [Phys. Solid State **47**, 281 (2005)].

Translated by G. Skrebtsov

Physics of the Solid State, Vol. 47, No. 4, 2005, pp. 742–753. Translated from Fizika Tverdogo Tela, Vol. 47, No. 4, 2005, pp. 716–727.

Vibrational Spectra of AlN/GaN Superlattices: Theory and Experiment

M. B. Smirnov*, S. V. Karpov*, V. Yu. Davydov, A. N. Smirnov**, E. E. Zavarin**, and V. V. Lundin****

**Fock Institute of Physics, St. Petersburg State University, Ul'yanovskaya ul. 1, St. Petersburg, 198504 Russia*

***Ioffe Physicotechnical Institute, Russian Academy of Sciences, Politekhnicheskaya ul. 26, St. Petersburg, 194021 Russia*

e-mail: valery.davydov@mail.ioffe.ru

Received July 27, 2004

Abstract—Computer simulation of the dynamics of layered AlN/GaN superlattices is performed to elucidate the microscopic nature of the vibrational states corresponding to the strongest bands in the Raman spectra. Experimental Raman spectra are shown to consist of two groups of lines, one of which exhibits a two-mode behavior and the other shows a one-mode behavior as the relative layer thicknesses are varied. The results of computer simulation and calculations within the dielectric-continuum approximation suggest that the behavior of the observed vibrational modes is dictated by the degree of their localization and that the interlayer coupling is due to long-range dipole–dipole interactions. It is shown that the delocalized modes, which exhibit one-mode behavior, can be used as a sensitive probe of the structure and composition of superlattices. © *2005 Pleiades Publishing, Inc.*

1. INTRODUCTION

For the past ten years, there has been a growing interest in the application of semiconductors based on nitrides of Group-III elements (Al, Ga, In) to develop various optoelectronic devices operating over a wide spectral range from the infrared to ultraviolet region. Multilayered periodic structures are of great importance in these devices [1]. In order to optimize the technology for fabricating perfect superlattices (SLs), methods need to be found to control the structure and quality of grown samples. Experimental data [2, 3] strongly suggest that Raman scattering spectroscopy is appropriate for nondestructive examination with a high space resolving power.

Experiments performed on nitride SLs have revealed that the Raman spectral lines differ in terms of their sensitivity to details of the SL structure [4–6]. Indeed, the Raman spectra of SLs contain not only bands that are close in position to those characterizing the bulk materials (and their intensity is proportional to the concentration of the corresponding bulk SL component) but also bands that are absent in the Raman spectra of the bulk SL components. The latter bands cannot be interpreted as being due to frequency shifts caused by strains, which always arise in the materials making up an SL. The frequencies of these new Raman lines depend crucially on the composition and structure of the SL and, therefore, can be considered to be indicators of the SL structure.

The microscopic nature of the vibration states associated with these Raman lines is not clearly understood. Theoretical studies of vibrational states of SLs are concerned primarily with the frequencies and shapes of phonon modes and, as a rule, do not consider their ability to contribute to optical spectra and, in particular, the intensity of the corresponding Raman lines, which makes applying their results in the analysis of actual Raman spectra difficult. The few papers available in the literature that deal with theoretical analysis of the Raman line intensities are either restricted to SLs with a very small period [7] or employ the oversimplified and unrealistic linear-chain model [8]. Therefore, it is of importance to perform computer simulations of the Raman spectra of SLs with a period comparable to the periods of actual SLs. There is good reason to believe that simulation will give reliable results if it is based on model interatomic interactions that adequately describe the dynamic properties of the bulk pure compounds, AlN and GaN, making up an SL [9]. In this paper, we present the results of such simulations and interpret them in terms of the macroscopic dielectric continuum model. The results are compared with experimental data.

2. MODEL AND COMPUTATIONAL PROCEDURE

In this study, we do not consider the influence exerted on the vibrational spectrum of SLs by strains due to a mismatch between the SL layers. We assume that the lattice parameters of AlN and GaN are equal and use average values of the parameters of the wurtzite structure $a = 3.15$ Å, $c = 5$ Å, and $z = 0.88$. The SL is assumed to be an infinite crystal. The periodically repeated motif of the SL consists of m elementary layers of GaN (medium 1) and n elementary layers of AlN (medium 2). The interfaces between the SL layers are perpendicular to the hexagonal axis of the bulk wurtzite structure (the z axis). The thickness of an elementary layer along the z axis covers one unit cell of the wurtzite structure; i.e., an elementary layer consists of two atomic layers of a metal and two nitrogen atomic layers. The spatial period of the SL is taken to be $n + m = 20$, and the relative thickness of AlN and GaN layers (i.e., the ratio n/m) is varied. Therefore, the SL unit cell consists of 80 atoms.

The potential function is based on the model potentials of the perfect AlN and GaN crystals [9] and includes the Coulomb interaction between rigid (nonpolarizable) ions. The cationic charges are $Z(\mathrm{Al}) = 1.27e$ and $Z(\mathrm{Ga}) = 1.14e$. The charge of each nitrogen ion is dictated by the electrical-neutrality condition, depending on its environment, and is calculated from the formula

$$Z(N) = -\frac{1}{4}[N(\mathrm{Al})Z(\mathrm{Al}) + N(\mathrm{Ga})Z(\mathrm{Ga})],$$

where $N(\mathrm{Al})$ and $N(\mathrm{Ga})$ are the numbers of the nearest neighbor cations of the indicated species, which satisfy the condition $N(\mathrm{Al}) + N(\mathrm{Ga}) = 4$. The short-range repulsion is described in terms of the Born–Kármán model with parameters $A = \frac{\partial^2 E}{\partial R^2}$ and $B = \frac{1}{R}\frac{\partial E}{\partial R}$ (where E is the energy and R is the bond length), whose values are taken to be (in newtons per meter) [9]

$$A(\mathrm{Al–N}) = 265, \quad B(\mathrm{Al–N}) = -22,$$
$$A(\mathrm{Ga–N}) = 230, \quad B(\mathrm{Ga–N}) = -17,$$
$$A(\mathrm{Al–Al}) = A(\mathrm{Ga–Ga}) = 20, \quad A(\mathrm{N–N}) = 10.$$

The Raman line intensity is calculated in the polarizable-bond model [10]. In this model, the polarizability of a polyatomic system is assumed to be the sum of the contributions from individual valence bonds and the polarizability of each bond is described by a tensor with two independent components α_1 (along the bond) and α_2 (across the bond), whose values are assumed to be dependent on the bond length. The Raman line intensity is described in terms of three parameters:

$$\gamma_1 = \frac{d\alpha_1}{dR}, \quad \gamma_2 = \frac{d\alpha_2}{dR}, \quad \gamma_3 = \alpha_1 - \alpha_2.$$

The parameter γ_3 determines the anisotropy of the static bond polarizability. Its value influences primarily the intensities of bands in the low-frequency part of the Raman spectrum, where the bands are associated with atomic motions due to bond stretching rather than bond bending. The parameters γ_1 and γ_2 are the derivatives of the polarizability with respect to bond length and determine the intensities of the Raman bands corresponding to high-frequency modes, whose eigenvectors involve variations in the bond lengths. The numerical values of the parameters γ are adjusted to obtain the best fit to the relative intensities of the Raman lines for bulk AlN and GaN crystals. The Ga-ion polarizability is noticeably higher than that of Al ions, which is reflected in the value of ε_∞ (its value for GaN related to that for AlN is nearly one-third larger than unity). For this reason, we used different values for the polarizability parameters of the Al–N and Ga–N bonds, more specifically, $\gamma(\mathrm{Ga–N})/\gamma(\mathrm{Al–N}) = 1.5$.

Since the objective of this paper is to interpret the Raman spectra, we considered only vibrational states at the center of the Brillouin zone. The Coulomb contribution to the dynamical matrix is calculated using the Ewald method. Calculations are carried out in the long-wavelength approximation $q \longrightarrow 0$. The spectrum of transverse (TO) vibrations is calculated first by diagonalizing the dynamical matrix without the singular term due to the macroscopic field. The spectrum of longitudinal (LO) vibrations is calculated by diagonalizing the "longitudinal" dynamical matrix, which is obtained from the "transverse" matrix by adding the term associated with the long-range dipole–dipole interaction:

$$D_{ij}^{\mathrm{LO}} = \delta_{ij}\omega_i^2(\mathrm{TO}) + \frac{4\pi}{V_c}\frac{(\boldsymbol{\xi}_i q)(\boldsymbol{\xi}_j q)}{q^2},$$

where ω_i is the frequency, V_c is the unit cell volume, $\mathbf{q}$ is the wave vector, and $\boldsymbol{\xi}_i$ and $\boldsymbol{\xi}_j$ are the derivatives of the dipole moment vector with respect to the amplitudes of the corresponding LO modes. The representations (A, E) according to which the vibration modes transform under symmetry operations are determined by the form of the vibrations. The modes in which the atoms move along the z axis (perpendicular to the interfaces between the SL layers) transform according to the A representation, whereas the doubly degenerate modes in which the atoms move in the xy plane transform according to the E representation. By substituting the wave vector directed either along the z axis or perpendicular to this axis into the longitudinal dynamical matrix, we calculated the spectra of A(LO) and E(LO) vibrations. In this way, we found all four independent modes at the center of the Brillouin zone: A(TO), A(LO), E(TO), and E(LO).

As shown in [11], the point symmetry of $(\mathrm{GaN})_m(\mathrm{AlN})_n$ superlattices depends on the number of monolayers in the SL unit cell ($m + n$) and corresponds to the C_{3v}^1 space group if $m + n$ is an even number and to C_{6v}^4 if $m + n$ is an odd number. In this paper, we discuss the calculations performed for the former case, and the experimental data obtained are also consistent with the C_{3v} symmetry. This lowered symmetry can be associated with the fact that, due to the difference in polarizability between the materials making up the SL

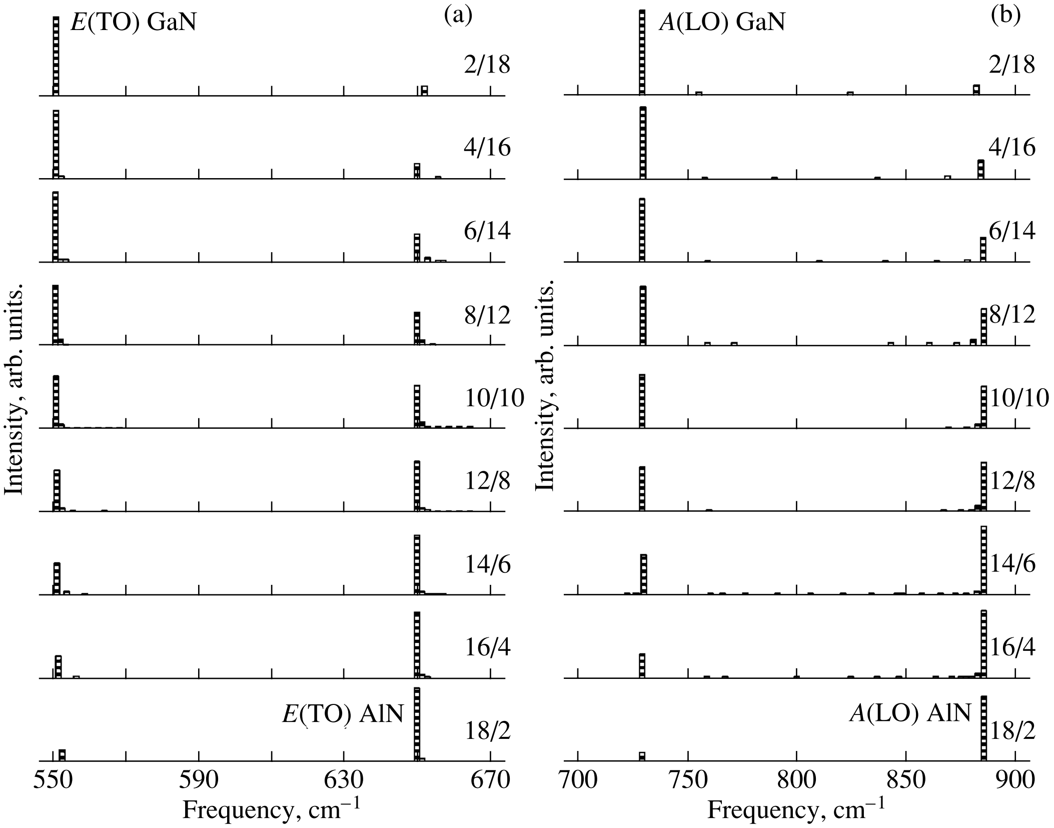

Fig. 1. Calculated (a) *E*(TO) and (b) *A*(LO) Raman spectra of $(AlN)_n/(GaN)_m$ superlattices at various values of the ratio n/m (given on the right of the spectra).

and to strains, the wurtzite structure allows the appearance of a spontaneous electric field directed along the z axis, which lowers the symmetry of the SL to C_{3v}. The same symmetry is possessed by solid solution–based $(GaN)_m(Ga_xAl_{1-x}N)_n$ superlattices, whose spectra are also discussed in this paper.

As the symmetry is lowered from C_{6v} to C_{3v}, the irreducible representations are mixed: $A_1 \oplus B_1 \Rightarrow A$ and $E_1 \oplus E_2 \Rightarrow E$. We note that, strictly speaking, the separation of the degenerate E modes into E_1 and E_2 modes in SLs is incorrect. However, we can use this separation when analyzing the Raman scattering intensity tensor of SLs. For example, the doubly degenerate modes for which the xz of yz components of the Raman tensor are maximum are conventionally assigned to the E_1 representation and the modes for which the xy component of the Raman tensor is maximum are assigned to the E_2 representation. Furthermore, the modes that are assigned to the E_1 and E_2 representations differ in terms of the derivative of the dipole moment. However, we did not use the a priori assignment of modes to representations in our calculations; the relative contributions from different modes to Raman spectra with a certain symmetry are determined by the Raman tensor.

3. THE RESULTS OF COMPUTER SIMULATION

3.1. Vibration Frequencies

Our calculations revealed that the bands in the Raman spectrum of the SL can be separated into two groups according to their behavior. In one group, the bands exhibit a two-mode behavior. Their frequencies are close to the frequencies of the analogous modes in bulk crystals and depend on the SL structure only weakly; the intensities of these modes vary in proportion to the relative thickness of the corresponding SL basic layer, i.e., the percentage of GaN or AlN. Such behavior is exhibited by the polar *E*(TO) and *A*(LO) modes, as well as the nonpolar *E* modes originating from the E_2 modes in the bulk SL constituents. Figure 1a shows the calculated Raman spectra for the *E*(TO) mode at various thicknesses of the AlN (n) and GaN (m) layers. It can be seen that, at any ratio between the basic-layer thicknesses, even for very thin layers (down to two monolayers), the Raman spectrum of the *E*(TO) mode has two bands whose frequencies are close to the frequencies of the *E*(TO) vibration modes in bulk AlN and GaN. An analogous behavior is exhibited by the lines of the *A*(LO) mode (Fig. 1b). The group of bands that have a two-mode character also includes the non-

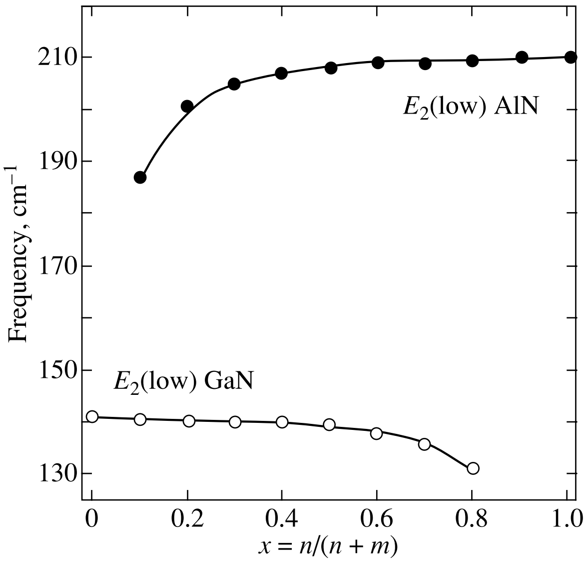

Fig. 2. Calculated frequencies of low-frequency E_2(low) vibrations of $(AlN)_n/(GaN)_m$ superlattices as a function of the relative AlN layer thickness $x = n/(n + m)$.

polar E modes originating from the E_2 modes of the corresponding bulk crystals. Figure 2 shows the dependence of the frequencies of two low-frequency bands of E_2 modes on the relative layer thickness. It can be seen that these bands are close in position to the respective bands in the Raman spectra of the bulk SL constituents even for very thin layers, with a relative thickness as small as 30% of the SL period.

A qualitatively different behavior is exhibited by the E(LO) and A(TO) modes (Fig. 3). For each of these modes, the Raman spectra have a dominant band whose intensity varies only weakly with the SL layer thickness and whose frequency varies monotonically between the frequencies of the corresponding modes in the bulk SL constituents. The deviation of the frequencies of these dominant bands from the frequency ω(GaN) or ω(AlN) is approximately proportional to the percentage of the corresponding SL constituent. An analogous one-mode behavior is exhibited by certain modes in the Raman spectra of solid solutions.

Our calculations predict that, in addition to the dominant band in the range between the frequencies of the E(LO) mode of GaN and the E(LO) mode of AlN, the Raman spectrum of the E(LO) modes also has a group of weaker bands in the range between the frequencies of the E(TO) mode of GaN and the E(TO) mode of AlN (Fig. 3a). The calculated Raman spectrum of the A(TO) modes has an analogous pattern (Fig. 3b); namely, there is a group of weak bands whose frequencies lie between the frequencies of the A_1(LO) mode of GaN and the A_1(LO) mode of AlN.

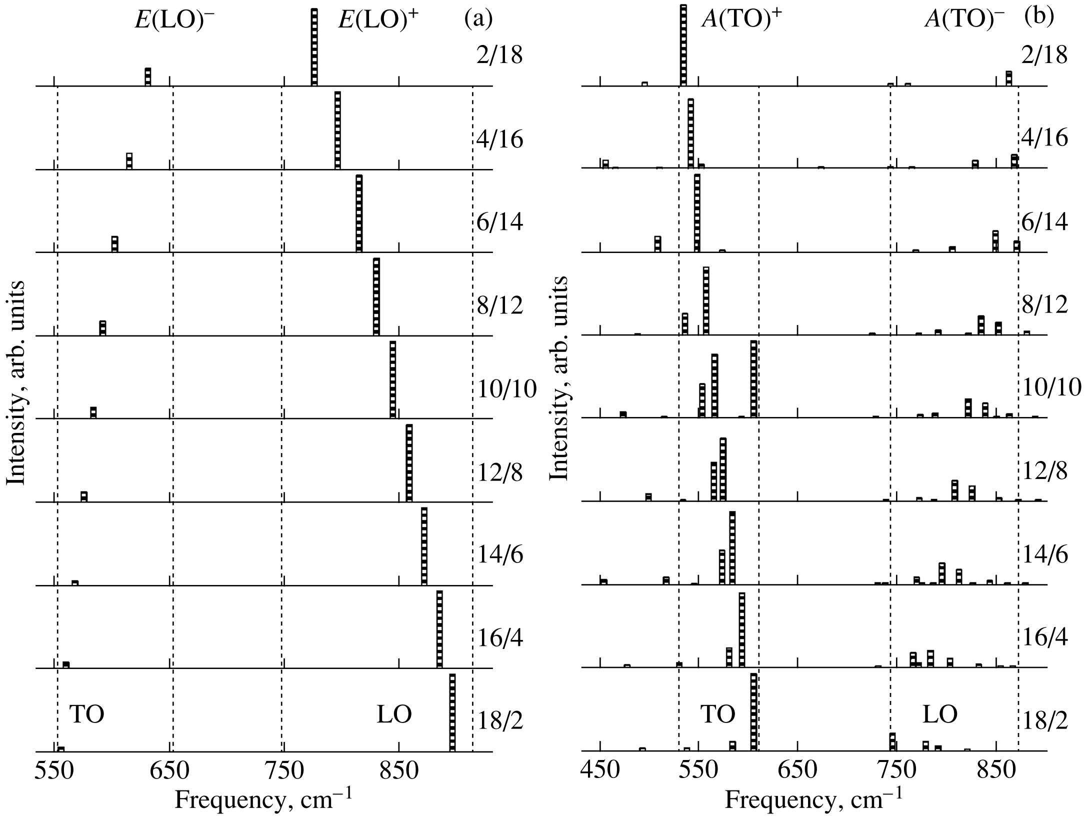

Fig. 3. Calculated (a) E(LO) and (b) A(TO) Raman spectra of $(AlN)_n/(GaN)_m$ superlattices at various values of the ratio n/m (given on the right of the spectra).

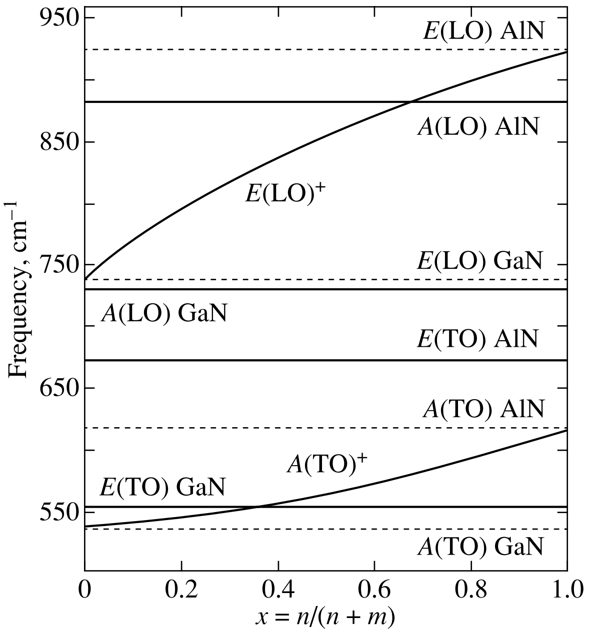

Fig. 4. Calculated frequencies of polar vibrations of $(\mathrm{AlN})_n/(\mathrm{GaN})_m$ superlattices as a function of the relative AlN layer thickness $x = n/(n + m)$. The frequencies of only the dominant components $E(\mathrm{LO})^+$ and $A(\mathrm{TO})^+$ are shown for the E(LO) and A(TO) modes propagating in the SL layers.

We denote the dominant modes in these representations by $E(\mathrm{LO})^+$ and $A(\mathrm{TO})^+$ and the weak modes by $E(\mathrm{LO})^-$ and $A(\mathrm{TO})^-$. This notation reflects the inphase and antiphase displacements of atoms in adjacent layers, as will be seen from the analysis of the eigenvectors. It should be noted that the frequency deviation of this group of bands in the frequency range of transverse vibrations varies in inverse proportion to the percentage of the corresponding SL constituent. For example, for thick AlN layers, the frequency of the $E(\mathrm{LO})^-$ band is close to that of the E(TO) mode of GaN.

The dependence of the calculated frequencies of the polar optical modes on the relative basic-layer thickness for GaN/AlN SLs is shown in Fig. 4.

3.2. The Shape of Vibrations

The fundamental advantage of computer simulations of Raman spectra is that this method makes it possible not only to predict and explain the observed spectral curves but also to obtain a microscopic pattern of the atomic displacements for individual vibration modes. An analysis of the calculated eigenvectors revealed that, in the Raman spectrum of an SL, the lines exhibiting two-mode behavior correspond to modes localized within one of the SL basic layers. Figure 5 shows the atomic displacements in the A(LO) and E(LO) vibration modes for various values of the ratio between the SL layer thicknesses. The patterns arranged one above another in Figs. 5a and 5b correspond to different SLs. The top patterns correspond to SLs with thin AlN layers (n/m = 18/2). The patterns in the middle part of Figs. 5a and 5b correspond to SLs with layers of equal thickness (n/m = 10/10), and the bottom patterns show the atomic displacements in SLs with thin GaN layers (n/m = 2/18). The left-hand and right-hand parts of Fig. 5a show the eigenvectors of modes that are close in frequency to the A(LO) mode in GaN (see Fig. 1b) and to the A(LO) mode in AlN (Fig. 1b), respectively. These patterns of atomic displacements clearly indicate that one of the modes is localized within the GaN layer and the other is localized within the AlN layer for any ratio between the SL layer thicknesses. This character of atomic displacements also explains the fact that the intensities of these vibration modes vary in proportion to the relative thickness of the corresponding SL basic layer. Calculations show that the E(TO) modes exhibit similar behavior.

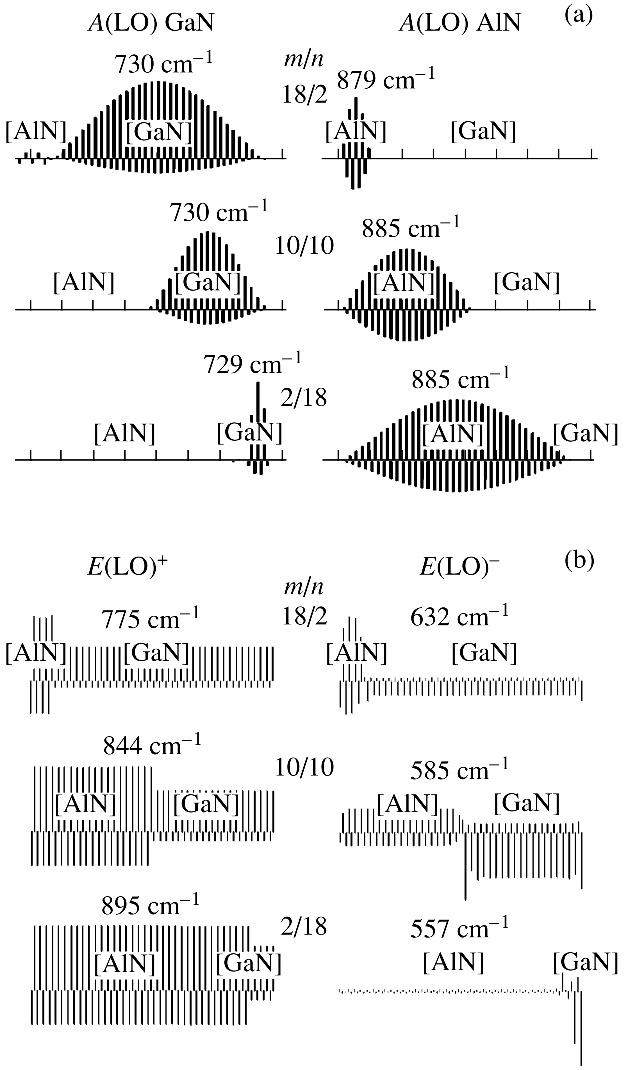

Fig. 5. Calculated amplitudes of atomic displacements in (a) the A(LO) and (b) E(LO) modes in $(\mathrm{AlN})_n/(\mathrm{GaN})_m$ superlattices for n/m = 2/18, 10/10, and 18/2.

The pattern of atomic displacements in the *E*(LO) and *A*(TO) vibration modes is qualitatively different. The calculated eigenvectors of the $E(\mathrm{LO})^+$ and $E(\mathrm{LO})^-$ modes (Fig. 5b) clearly indicate that these modes are delocalized over the entire SL at any value of the ratio between the SL layer thicknesses. The eigenvectors of the $E(\mathrm{LO})^+$ and $E(\mathrm{LO})^-$ modes are equal to the sum and difference, respectively, of the eigenvectors of the individual layers. This specific form of the latter mode explains the low intensity of the $E(\mathrm{LO})^-$ mode in the infrared and Raman spectra; due to the antiphase atomic displacements, the contributions from adjacent layers to both the derivative of the dipole moment and the derivative of the polarizability are opposite in sign.

By analyzing the shape of the $E(\mathrm{LO})^+$ and $E(\mathrm{LO})^-$ vibration modes shown in Fig. 5b, we can draw the following conclusions concerning the behavior of their frequencies. It is easily understood that the frequency of the $E(\mathrm{LO})^+$ mode lies between the frequencies of the corresponding modes of the bulk SL constituents. Indeed, in this mode, the atomic displacements in each layer (shown in the left-hand part of Fig. 5b) are similar in character to those in the bulk SL constituents and the parameters of the potential that determine the vibration frequency (the short-range force constant, the effective charge) vary continuously between their values in the bulk SL constituents as the SL structure varies from AlN (at $n = 0$) to GaN (at $m = 0$).

It is more difficult to explain the mode frequency varying in inverse proportion to the relative SL layer thickness observed for the $E(\mathrm{LO})^-$ mode. The shape of this vibration mode is shown in the right-hand part of Fig. 5b. It can be seen that the atomic displacements in adjacent SL layers are antiphase and that only the displacements of nitrogen atoms are large due to their relatively small mass. Note that the amplitudes of the atomic displacements in different basic layers vary in inverse proportion to the layer thickness, because the position of the center of gravity must remain unchanged. This relation between the vibration amplitudes in different layers is the reason why the frequency of this mode is determined primarily by the vibrations of the atoms in the thin layer. However, this simple consideration provides no explanation for the fact that the frequency of this LO mode lies in the frequency range of TO vibrations.

3.3. Angular Dispersion

From the results of calculations presented above, it follows that the *A*(TO) and *E*(LO) vibration modes exhibit one-mode behavior and are delocalized over the entire SL and that the *A*(LO) and *E*(TO) modes exhibit two-mode behavior and are localized within one of the basic layers. The *A*(LO) and *E*(TO) modes correspond to wave vectors $\mathbf{q} \parallel z$, and the *A*(TO) and *E*(LO) modes are observed at $\mathbf{q} \perp z$. Therefore, as the angle $\theta = \arccos(q_z/|\mathbf{q}|)$ varies from 0 to π/2, the former group of modes transforms into the latter group and vice versa. At θ = 0, the entire spectrum is a superposition of the spectra shown in Figs. 1a and 1b. As the angle θ increases to π/2, these spectra transform into those shown in Figs. 3a and 3b. The θ dependence of the frequencies of all polar modes in the calculated Raman spectrum of an SL with equally thin layers is shown by dots in Fig. 6.

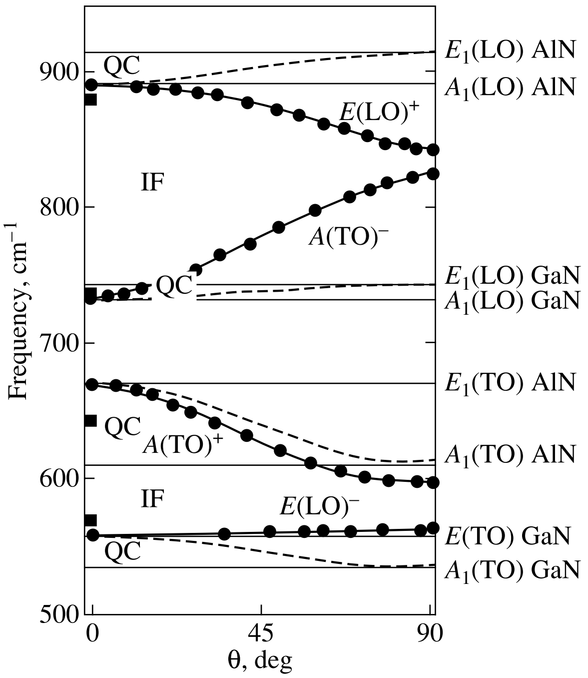

Fig. 6. Angular dispersion of polar E_1 and A_1 phonons in bulk GaN and AlN crystals (dashed lines) and angular dispersion of phonons in an SL with equally thin layers ($m/n = 1$) predicted by computer simulation (dots) and the dielectric-continuum model (solid lines). Squares are experimental values determined from Raman spectra. The frequency regions of quasi-confinement (QC) and interface (IF) modes in SLs [12] are also indicated.

In the course of this transformation of modes, according to our calculations, vibrations change in character from vibrations localized within one basic layer to vibrations delocalized over the entire SL. Therefore, in the range $0 < \theta < \pi/2$, the Raman-active phonon modes have an intermediate character of localization. The change in the shape of vibrations is accompanied by a change in the intensity of the Raman bands. Indeed, at θ = 0, the ratio between the Raman line intensities calculated for an SL with equally thin layers ($m = n$) is approximately 1 : 2 and corresponds to the ratio of the polarizabilities of the Al–N and Ga–N bonds (Fig. 1), whereas at θ = π/2 the intensities differ more significantly (Fig. 3). As the direction of the wave vector varies from θ = 0 to π/2, the $A(\mathrm{TO})^-$ and $E(\mathrm{LO})^-$ bands disappear.

Computer simulations make it possible to study the behavior of the Raman spectrum of SLs with various layer thicknesses, but they do not reveal the reason why the *E*(TO) and *A*(LO) modes are localized within one basic layer and why the *E*(LO) and *A*(TO) modes are delocalized. It is surprising that, due to the behavior of the *A*(TO)$^-$ and *E*(LO)$^-$ modes, in the Raman spectrum of an SL, there appear bands with frequencies corresponding to the LO-mode bands of the bulk SL constituents in the TO-mode frequency range and vice versa. In the model used by us, the coupling between vibrations in adjacent layers is due to Coulomb forces. Therefore, there is reason to believe that the specific features of the dipole vibration spectrum are associated with dipole–dipole interactions. Macroscopic consideration of the propagation of polarization waves in a layered elastic medium may give some insight into this situation. The next section is devoted to this issue.

4. DIELECTRIC-CONTINUUM MODEL

Within the dielectric continuum approximation, the microscopic details of the crystal structure are ignored and an SL is considered a uniform elastic medium with a certain permittivity. The complete solution to this problem for GaN/AlN-type structures, in which the dispersion dependences of the permittivities of both materials overlap, is given in [12]. One of the first applications of this model to describe polar vibrations in SLs was made in [13] using the formulas derived earlier in [14] for radio waves propagating in a thin-layer medium. Polar vibrations of a dielectric elastic continuum were considered in an infinite system consisting of plane-parallel layers with thicknesses d_1 and d_2 and dielectric constants ε_1 and ε_2, which are arranged periodically along the direction (*z* axis) perpendicular to the interfaces between the layers. By solving the equation of elastic vibrations in combination with Maxwell's equations and taking a volume average, the following expressions were derived in [14] for the effective dielectric constant:

$$\varepsilon_{x,y} = d^{-1}(d_1\varepsilon_1 + d_2\varepsilon_2), \tag{1}$$

$$\varepsilon_z = d\varepsilon_1\varepsilon_2(d_1\varepsilon_2 + d_2\varepsilon_1)^{-1}, \tag{2}$$

where $d = d_1 + d_2$.

The rigorous derivation of Eqs. (1) and (2) carried out in [14] involves complicated mathematical manipulation. However, in the limiting case of long wavelengths, the result can be interpreted in the following way. Let us consider the states with a uniform polarization in each layer. It is these states that correspond to atomic displacements along the eigenvectors of zone-center phonons whose lines in optical-vibration spectra are the strongest. The electric field in the basic layers is described by vectors $\mathbf{E}_1$ and $\mathbf{E}_2$ and electric inductions $\mathbf{D}_1 = \varepsilon_1\mathbf{E}_1$ and $\mathbf{D}_2 = \varepsilon_2\mathbf{E}_2$.

In the case where the electric field is parallel to the interface between the layers (the *xy* plane), the equation curl$\mathbf{E}$ = 0 leads to the condition of the tangential component of the electric field being continuous at the interfaces:

$$E_{1,x} = E_{2,x} = \bar{E}.$$

Therefore, the average electric induction is given by

$$\bar{D} = \frac{d_1}{d}D_1 + \frac{d_2}{d}D_2 = \frac{\bar{E}}{d}(d_1\varepsilon_1 + d_2\varepsilon_2) = \varepsilon_x\bar{E},$$

from which we immediately obtain Eq. (1).

In the case where the electric field is parallel to the *z* axis, the equation div$\mathbf{D}$ = 0 leads to the condition that the electric induction be continuous at the interfaces:

$$D_{1,z} = D_{2,z} = \bar{D}.$$

Therefore, the average electric field is

$$\bar{E} = \frac{d_1}{d}E_1 + \frac{d_2}{d}E_2 = \frac{\bar{D}}{d}\left(\frac{d_1}{\varepsilon_1} + \frac{d_2}{\varepsilon_2}\right) = \frac{\bar{D}}{\varepsilon_z},$$

from which we immediately obtain Eq. (2).

Equations (1) and (2) correspond to the case of long-wavelength vibrations with a polarization perpendicular to the *z* axis and parallel to this axis, respectively, i.e., to *E*-type and *A*-type vibrations, respectively. The roots of the equation $\varepsilon(\omega) = 0$ correspond to LO modes, and the frequencies at which $\varepsilon(\omega)$ becomes infinitely large correspond to TO modes.

From Eq. (2) for the dielectric constant $\varepsilon_z(\omega)$ of the SL, it follows that the zeros of $\varepsilon_z(\omega)$ are zeros of the dielectric constant of either of the two basic layers; i.e., $\varepsilon_z(\omega) = 0$ if $\varepsilon_1(\omega) = 0$ or $\varepsilon_2(\omega) = 0$. Therefore, the frequencies of *A*(LO) vibrations of the SL coincide with the frequencies of *A*(LO) vibrations of the bulk SL constituent materials. The same is also true for *E*(TO) vibrations. From Eq. (1) for the dielectric constant $\varepsilon_{x,y}(\omega)$ of the SL, it follows that the poles of $\varepsilon_{x,y}(\omega)$ coincide with the poles of the dielectric constant of either of the two basic layers; i.e., $\varepsilon_{x,y}(\omega) = \infty$ if $\varepsilon_1(\omega) = \infty$ or $\varepsilon_2(\omega) = \infty$. Therefore, the frequencies of *E*(TO) vibrations of the SL coincide with the frequencies of *E*(TO) vibrations of the bulk SL constituents.

Thus, Eqs. (1) and (2), which describe polarization waves propagating in a layered medium, confirm our conclusion that SLs support long-wavelength polar optical vibrations at frequencies coinciding with those of the *A*(LO) and *E*(TO) vibration modes in the pure SL constituents.

The solutions to equations $\varepsilon_{x,y}(\omega) = 0$ and $\varepsilon_z(\omega) = \infty$ differ in character. They correspond to the *A*(TO) and *E*(LO) modes propagating along the SL layers. For the *E*(LO) vibration modes, it follows from Eq. (1) that

$$\varepsilon_{x,y}(\omega) = 0 \Rightarrow \frac{\varepsilon_1(\omega)}{\varepsilon_2(\omega)} = -\frac{d_2}{d_1}, \tag{3}$$

and for the *A*(TO) modes Eq. (2) immediately gives

$$\varepsilon_z(\omega) = \infty \Rightarrow \frac{\varepsilon_1(\omega)}{\varepsilon_2(\omega)} = -\frac{d_1}{d_2}. \qquad (4)$$

The $\varepsilon(\omega)$ dependence for each SL constituent material is given by

$$\varepsilon(\omega) = \varepsilon_\infty \frac{\omega^2 - \omega_{LO}^2}{\omega^2 - \omega_{TO}^2}, \qquad (5)$$

where the components $\varepsilon_{x,y}(\omega)$ are determined by the E modes and the component $\varepsilon_z(\omega)$ is determined by the A modes. Using these relations and solving Eqs. (3) and (4) for ω, we can express the frequencies of the A(TO) and E(LO) modes in the SL in terms of the parameters of the vibration spectra of the bulk SL constituents and the layer thicknesses. However, instead of deriving cumbersome expressions, we consider the dependence of the solutions on the ratio d_1/d_2 in a qualitative manner. It will be recalled that, for crystals of GaN (medium 1) and AlN (medium 2), the frequencies of the A and E vibration modes satisfy the inequalities

$$\text{TO1} < \text{TO2} < \text{LO1} < \text{LO2}.$$

Using Eq. (5), we calculate the ratio between the dielectric constants of the bulk SL constituents as a function of frequency, $f(\omega) = \varepsilon_1(\omega)/\varepsilon_2(\omega)$. This function is plotted in Fig. 7. It can be seen that $f(\omega)$ is negative in the ranges TO1 < ω < TO2 and LO1 < ω < LO2. Over each of these ranges, $f(\omega)$ varies monotonically from 0 to $-\infty$; therefore, each of Eqs. (3) and (4) has a unique solution in these ranges at any value of d_1/d_2. In each pair of these solutions, there is a normal member, $A(\text{TO})^+$ or E(LO)+, whose frequency lies in the range between the corresponding frequencies in the bulk SL constituents

$$A(\text{TO1}) < A(\text{TO})^+ < A(\text{TO2}),$$

$$E(\text{LO1}) < E(\text{LO})^+ < E(\text{LO2}),$$

and an anomalous member, $A(\text{TO})^-$ or $E(\text{LO})^-$, whose frequency satisfies the inequalities

$$A(\text{LO1}) < A(\text{TO})^- < A(\text{LO2}),$$

$$E(\text{TO1}) < E(\text{LO})^- < E(\text{TO2}).$$

From the curve plotted in Fig. 7, we can qualitatively determine the dependence of the frequencies of the normal and anomalous modes on the ratio between the SL layer thicknesses. Let us consider, e.g., the E(LO) modes whose frequencies are defined by Eq. (3). The normal root of this equation lying within the (LO1, LO2) range tends to LO1 and LO2 as $d_2 \longrightarrow 0$ $d_1 \longrightarrow 0$, respectively; i.e., the frequency of this mode varies in proportion to the percentage of the corresponding SL constituent. The anomalous root of this equation lying within the (TO1, TO2) range approaches TO1 and TO2 as $d_1 \longrightarrow 0$ and $d_2 \longrightarrow 0$, respectively; i.e., the frequency of this mode varies in inverse proportion to the percentage of the corresponding SL constituent. Analogous conclusions can be drawn concerning the $A(\text{LO})^+$ and $A(\text{LO})^-$ modes.

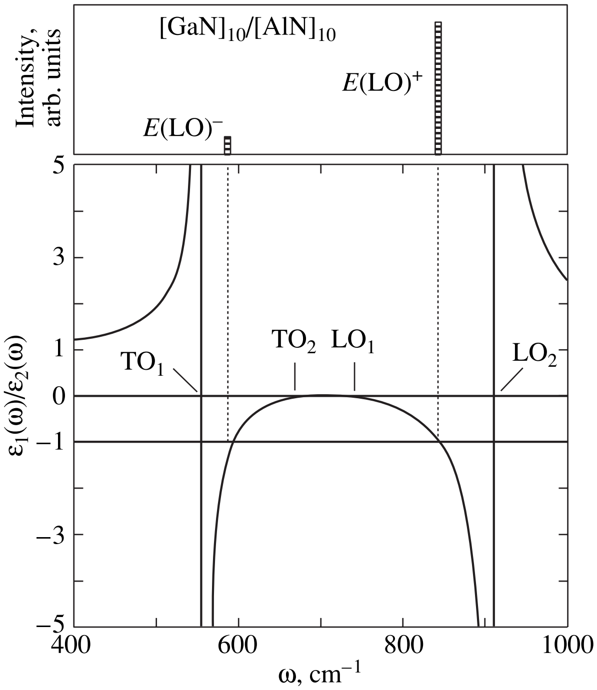

Fig. 7. Ratio $\varepsilon(\text{GaN})/\varepsilon(\text{AlN})$ calculated as a function of frequency. The frequency regions of the $E(\text{LO})^+$ and $E(\text{LO})^-$ modes are indicated. The calculated vibration spectrum of an SL with equally thin layers (n/m = 10/10) is shown in the top panel (see also Fig. 3a); the calculated frequencies correspond to $\varepsilon(\text{GaN})/\varepsilon(\text{AlN}) = -1$.

Using Eqs. (1), (2), and (5), we can find the zeros and poles of the function $\varepsilon(\omega)$ for an arbitrary direction of the wave vector and thus investigate the angular dispersion of the normal vibration modes of the SL. The results of these calculations for an SL with equally thin layers ($m/n = 1$) are shown in Fig. 6 (solid lines) and are seen to agree well with the results of computer simulation (shown by dots in Fig. 6).

On the whole, the dielectric continuum model confirms the conclusions drawn from computer simulations. Furthermore, there is close agreement between the numerical values obtained using these two methods even for SLs with very thin layers. However, computer simulation enables one to study the Raman band intensities and explain the observed phenomena on a microscopic level.

5. EXPERIMENTAL RESULTS

The Raman spectra of SLs fabricated from hexagonal gallium and aluminum nitrides (GaN, AlN) have not been adequately studied experimentally [4, 15–17]. The reason for this is above all the technological problems associated with producing these heterostructures.

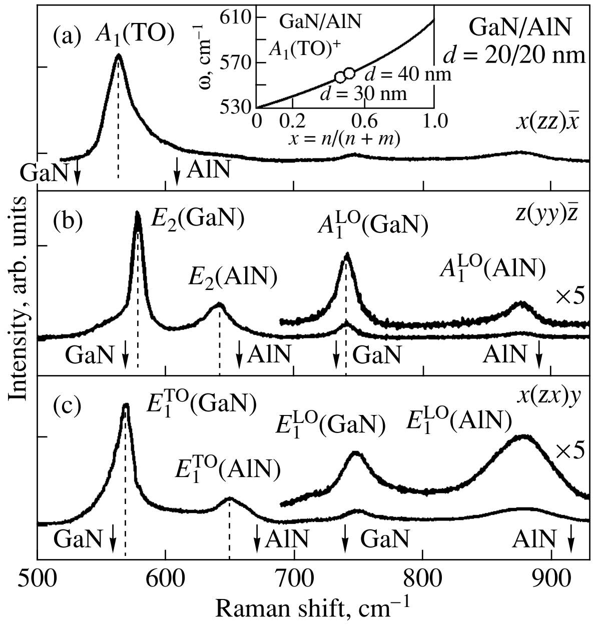

Fig. 8. Polarized Raman spectra of a GaN/AlN SL with a period of $d = 20 + 20$ nm. (a) Delocalized A_1(TO) mode, and (b, c) A_1(LO) and E_1(TO) modes localized within certain layers. The inset compares the theoretical dependence of the $A_1(\mathrm{TO})^+$ mode frequency in an $(\mathrm{AlN})_n/(\mathrm{GaN})_m$ SL on the relative layer thickness $x = n/(n + m)$ and experimental data obtained for SLs with equally thin layers and d = 30 and 40 nm.

We studied the Raman spectra of GaN/AlN superlattices grown on Al_2O_3 (0001) substrates using vapor-phase epitaxy from organometallic compounds (with periods d = 30, 40, 100 nm) and of GaN/$Al_xGa_{1-x}N$ superlattices with x = 0.28 and periods d from 320 to 5 nm [18].

Figure 8 shows the Raman spectra of a GaN/AlN SL with a period $d = 20 + 20$ nm in the region of high-frequency optical vibrations. These spectra confirm the prediction from model calculations that the Raman spectrum of SLs has a group of lines at frequencies close to the phonon frequencies in unstrained bulk GaN and AlN crystals. This group includes the lines that correspond to E_2 phonons and polar A(LO) and E(TO) vibration modes propagating perpendicular to the SL layers. This result agrees with the model calculations according to which the SL supports vibrations localized within one basic layer. The observed shifts of lines from their positions in unstrained bulk crystals are certainly due to elastic stresses that arose during the SL growth. This interpretation has already been given in the literature [4]. However, only the fact that these vibrations are localized (as was revealed by our calculations) can be considered a theoretical substantiation of this interpretation and this makes it possible to reliably estimate the sign and magnitude of the strains in the SL layers from the observed frequency shifts. For example, it can be seen from Fig. 8 that the shifts in the position of the lines corresponding to the localized E_1(TO) vibration modes in the AlN and GaN layers differ in sign, which indicates that the strains in these layers are also opposite in sign. Using the data on phonon deformation potentials in GaN [19] and AlN [20], we determined the magnitude of stresses in the SL layers. These stresses are found to be –3.7 and 5.6 GPa in GaN and AlN, respectively, for GaN/AlN SLs with a period of 20/20 nm and –4.5 and 8.7 GPa in GaN and AlN, respectively, for SLs with a period of 15/15 nm.

The experimental data also indicate that the Raman spectrum of an SL is not a superposition of the Raman spectra of the bulk SL constituents; indeed, there is also a group of lines at frequencies that differ significantly from the frequencies of the Raman bands observed in bulk GaN and AlN crystals. The experiment shows that these lines correspond to A_1(TO) phonons and, under certain conditions, E_1(LO) phonons. Note that these phonons propagate along the SL layers and, according to calculations, are delocalized vibrations involving all SL layers. Indeed, the Raman spectrum corresponding to A(TO) phonons (Fig. 8a) contains a 570-cm^{-1} line, which lies between the A_1(TO) line of GaN and the A_1(TO) line of AlN. It is natural to assign this strong line to the normal $A(\mathrm{TO})^+$ mode, whose frequency is 565 cm^{-1} according to computer simulation and 570 cm^{-1} in the dielectric-continuum model. Experimental values of the $A(\mathrm{TO})^+$ mode frequency measured in different SLs are given in the inset to Fig. 8a and are compared with the theoretical dependence of this frequency $A(\mathrm{TO})^+$ on the relative SL layer thickness. The line corresponding to the $A(\mathrm{TO})^-$ mode is not observed in the spectrum in Fig. 8a. The frequency of this mode is predicted to be 845 cm^{-1} according to computer simulation and 840 cm^{-1} in the dielectric-continuum model. It is likely that this mode is not visible because its intensity is very low (in complete agreement with theory).

Theory predicts that a similar situation will be observed in the Raman spectrum corresponding to longitudinal E_1 vibrations. Experimentally, however, a Raman spectrum of E_1(LO) modes recorded for a GaN/AlN SL with $d = 20 + 20$ nm exhibits two strong lines (rather than one) at frequencies close to the E_1(LO) mode frequencies in bulk GaN and AlN (Fig. 8c). This discordance between theory and experiment may be explained by the fact that the calculations are carried out for an SL with a period equal to 20 lattice parameters, i.e., approximately 10 nm, whereas the experimental spectra are recorded for SLs with periods of 30, 40, and 100 nm. The delocalization effects are not likely to arise in this case, because the interaction between widely spaced layers via the longitudinal electric field is weak due to the large difference between the natural frequencies of longitudinal LO vibrations in bulk GaN and AlN crystals. For this reason, we also studied GaN/$Al_xGa_{1-x}N$ superlattices with x = 0.28

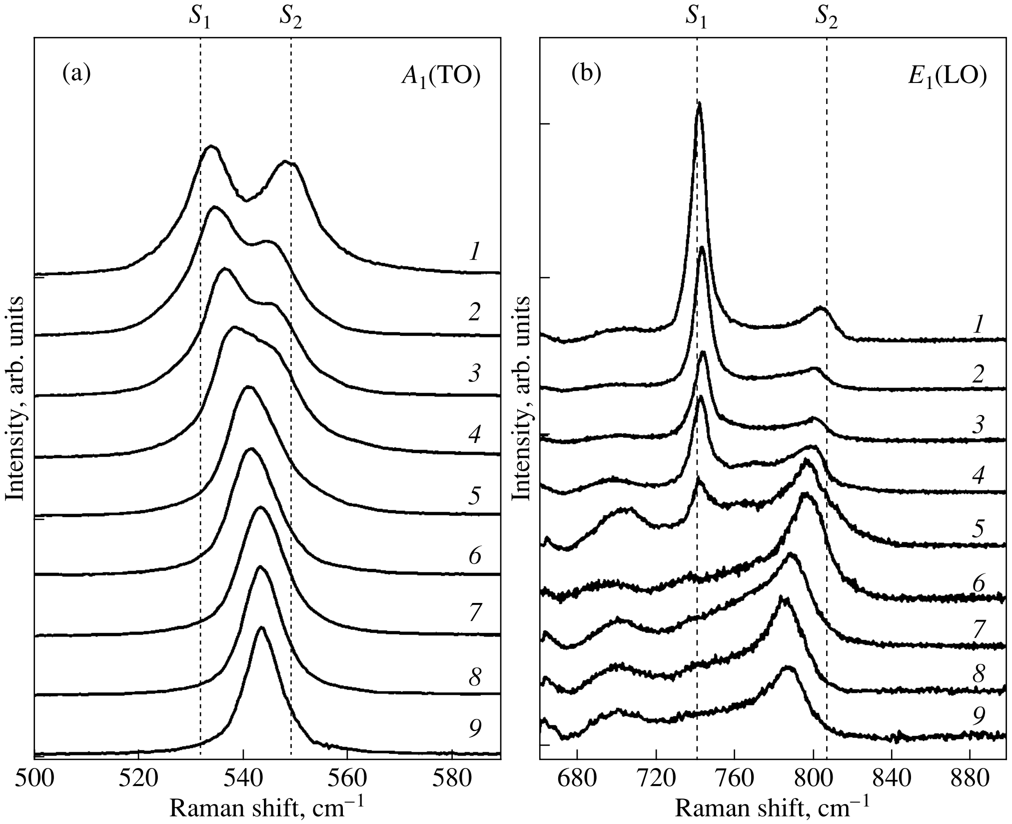

Fig. 9. Raman spectra for (a) the A_1(TO) and (b) E_1(LO) phonon modes propagating along the layers of GaN/$Al_{0.28}Ga_{0.72}N$ SLs with various periods *d*. The SL layer thicknesses d_{GaN}/d_{AlGaN} are (*1*) 1500/1500, (*2*) 320/320, (*3*) 160/160, (*4*) 80/80, (*5*) 40/40, (*6*) 20/20, (*7*) 10/10, (*8*) 5/5, and (*9*) 2.5/2.5 nm. The mode frequencies in bulk crystals are indicated by vertical dashed lines: S_1 for GaN and S_2 for $Al_{0.28}Ga_{0.72}N$.

and periods ranging from 320 to 5 nm, in which the difference in bulk phonon frequencies between GaN and an $Al_xGa_{1-x}N$ solid solution is less than that between GaN and pure AlN (70 instead of 172 cm^{-1}). The experimental data obtained are shown in Fig. 9. It can be seen that, as the period of GaN/$Al_xGa_{1-x}N$ superlattices decreases, the longitudinal E_1 phonon mode becomes progressively more delocalized. Indeed, for the GaN/$Al_xGa_{1-x}N$ SL with $x = 0.28$ and $d = 160$ nm, the Raman spectrum is similar to that of the GaN/AlN SL with $d = 40$ nm. However, the Raman spectra of GaN/$Al_xGa_{1-x}N$ SLs with a period less than 40 nm (curve *6* in Fig. 9b) agree well with the microscopically calculated spectrum. The spectra have only one line, which corresponds to the delocalized normal E(LO)$^+$ mode and is positioned in the frequency range between the lines of the longitudinal E_1(LO) modes of different basic layers. The anomalous E(LO)$^-$ mode is not observed, which is likely due to the peculiar shape of this mode (predicted from theory) having antiphase atomic displacements in different basic layers. The Raman spectrum corresponding to A_1(TO) vibrations exhibits a similar behavior (Fig. 9a).

6. DISCUSSION OF THE RESULTS

In our model of the potential functions of AlN and GaN crystals, the short- and long-range interactions are separated. The short-range forces are restricted to the valence tetrahedra and are characterized by the force constants for the nearest and next-to-nearest neighbor atoms. The long-range forces are described within the rigid-ion approximation. Despite its simplicity, this model reproduces the spectrum of all phonon states and agrees well with the results of nonempirical quantum-mechanical calculations [21, 22].

Our study shows that application of this microscopic model in simulating the dynamics of the AlN/GaN superlattice (and, in particular, the Raman spectrum) makes it possible to describe and interpret the main experimentally observed features. The specific feature of the vibration spectra of the SLs under study that is of most interest for both theory and practical application is the presence of strong lines in the Raman spectrum at frequencies lying between the frequencies of the corresponding modes in bulk AlN and GaN.

The good agreement between numerical solutions of the problem on atomic-lattice vibrations and solutions to the macroscopic equations that describe vibrations of an elastic continuum suggests that the long-range dipole–dipole interactions are of primary importance. Interestingly, the macroscopic description is valid even for SLs with very thin layers (down to four atomic monolayers). The solutions considered in this paper correspond to vibrations of almost uniformly polarized layers. Of course, the entire phonon spectrum of an SL contains many other vibration modes that originate from phonons at different points of the Brillouin zone in the bulk SL constituents and are similar in character to standing waves in separate layers. However, it is the abovementioned quasi-uniform vibrations originating from zone-center phonons in the bulk SL constituents that correspond to the strongest lines in the experimental optical-vibration and Raman spectra of SLs.

In the Raman spectra of SLs, there are two groups of modes that exhibit different dependences on the relative SL layer thicknesses. One group includes the A_1(LO) and E_1(TO) modes, whose frequencies coincide with those in the bulk SL constituents, and the other group includes the A_1(TO) and E_1(LO) modes, whose frequencies differ significantly from the frequencies of the respective modes in the bulk SL constituents. The results of computer simulations make it possible to explain the different behavior of these modes in terms of the degree of their localization.

In terms of the dielectric-continuum model, the modes of these two groups are referred to as confinement and interface modes, respectively [23]. These names originate from the solution of the problem of propagation of elastic waves in two semi-infinite media with a plane interface between them.

Among the possible solutions to this problem, there are modes whose wave vector is directed along the z axis (perpendicular to the interface) and has real values in both media. Certain combinations of these modes describe standing waves that are confined to one of the media (confinement modes). Of the SL vibration modes considered by us, the A(LO) and E(TO) modes with a wave vector directed along the z axis are confinement modes. It can be seen in Fig. 5a that these modes decay rapidly in the adjacent layer and that their penetration depth is two to three elementary layers. The localization (confinement) of vibrations within separate layers is due to two factors: sufficiently short–range forces and screening of the long-range dipole–dipole forces by the interface charges induced by atomic displacements.

The interface modes correspond to solutions for which the x and y components of the wave vector are real and the z component has complex values in both media. These solutions describe waves that propagate along the interface, with the atomic-displacement amplitude decaying exponentially with distance from the interface. Therefore, an interface mode is localized near the interface. Note that, in periodic layer structures, the term “interface mode” is applicable only to waves for which the decay length is much less than the spatial period of the structure. Otherwise, the amplitude of atomic displacements decreases only slightly through the thickness of a layer and the notion of interface modes as vibrations localized near the SL interfaces loses its meaning. In this case, the solutions in which the vibration amplitude decreases only slightly with distance from an interface into both layers correspond not to vibrations localized near the interface but rather to vibrations that involve all atoms of all SL layers, i.e., to completely delocalized vibrations. Among the SL vibration modes considered by us, the A(TO) and E(LO) modes with a wave vector directed along the x or y axis are delocalized. The interaction between SL layers occurs mainly via the long-range dipole–dipole forces, as indicated by the high accuracy of the results obtained using the macroscopic approximation. Due to this dipole–dipole interaction, the $A(\mathrm{TO})^+$ and $A(\mathrm{TO})^-$ modes (with inphase and antiphase atomic displacements in adjacent layers, respectively) differ greatly in frequency and the frequency of the latter mode falls within the range of the LO-mode frequencies.

The frequencies of the delocalized modes (or interface modes, according to established terminology) in GaN/AlN SLs lie within the band gaps of the vibration spectra of the bulk SL constituents, as can be seen in Fig. 6, which shows the angular dependence of the frequencies of these modes in an SL with equally thin layers and the angular dispersion of the polar vibration modes of bulk AlN and GaN crystals. The frequency bands of the TO and LO modes of pure AlN and GaN crystals are labeled QC. At $\mathbf{q} \parallel z$ ($\theta = 0$, the left-hand extreme of Fig. 6), all polar modes of the SL are confinement modes, i.e., are localized within separate layers. At $\mathbf{q} \perp z$ ($\theta = \pi/2$, the right-hand extreme of Fig. 6), these modes transform into interface modes delocalized over the entire SL. Therefore, over the range $0 < \theta < \pi/2$, the localization of the polar optical phonon modes is intermediate in character. Such modes are referred to as quasi-confinement modes [12]. In the case of two semi-infinite dielectric media, these modes correspond to standing waves with a real-valued wave vector in one medium and a complex-valued wave vector in the other. Therefore, these waves are localized in the former medium and penetrate into the latter, decaying exponentially with distance from the interface.

7. CONCLUSIONS

It has been shown that, as the relative layer thickness of GaN/AlN and GaN/$\mathrm{Al}_x\mathrm{Ga}_{1-x}\mathrm{N}$ superlattices varies, the Raman lines exhibit a one-mode or two-mode behavior. The one-mode behavior is exhibited by the A(TO) and E(LO) modes; their intensity varies only slightly, and their frequency varies monotonically between the frequencies of the corresponding modes in the bulk SL constituent materials. The two-mode behavior is exhibited by the A(LO) and E(TO) modes and the nonpolar E modes originating from the E_2 modes of the bulk SL constituents; their frequency almost coincides with the frequency of the analogous mode in the corresponding bulk SL constituent, and their intensity varies in proportion to the percentage of the corresponding SL constituent.

Computer simulations of the lattice dynamics have made it possible to explain this behavior of the optical SL vibration modes in terms of the degree of their localization. The Raman lines that exhibit two-mode behavior originate from vibrations localized in certain SL layers, whereas the Raman lines that exhibit one-mode behavior are associated with vibrations delocalized over the entire SL. The vibration frequencies calculated using the dielectric-continuum model (elastic polarizable medium) agree well with the results of computer simulations. This fact indicates conclusively that the specific features of the optical vibration modes of SLs are due to the long-range dipole–dipole interactions. These interactions couple vibrations of separate SL layers in the delocalized A(TO) and E(LO) modes. Due to screening of the internal electric field by surface charges at the interfaces, the A(LO) and E(TO) modes are localized in certain layers, i.e., behave as confinement modes.

The frequencies of delocalized SL vibrations depend crucially on the relative thickness of the SL layers. The delocalized mode in which the atoms of adjacent layers move in phase produces a very strong Raman line. Due to these properties, Raman spectroscopy is considered an efficient and fairly accurate method for quantitatively characterizing the structure and composition of SLs.

ACKNOWLEDGMENTS

This study was supported by the Russian Foundation for Basic Research (project no. 03-02-17562) and the programs of the Presidium of the RAS “Low-Dimensional Structures” and “New Structures and Materials.”

REFERENCES

1. *Gallium Nitrides I*, Ed. by J. I. Pankove and T. Moustakas (Academic, San Diego, 1998), Semicond. Semimet., Vol. 50.
2. B. Jusserand, D. Paquet, F. Mollot, F. Alexandre, and G. Le Roux, Phys. Rev. B **35** (6), 2808 (1987).
3. H. Brugger, G. Abstreiter, H. Jorke, H. J. Herzog, and E. Kasper, Phys. Rev. B **33** (8), 5928 (1986).
4. J. Gleize, F. Demangeot, J. Frandon, M. A. Renucci, F. Widmann, and B. Daudin, Appl. Phys. Lett. **74** (5), 703 (1999).
5. V. Yu. Davydov, A. A. Klochikhin, I. E. Kozin, V. V. Emtsev, I. N. Goncharuk, A. N. Smirnov, R. N. Kyutt, M. P. Scheglov, A. V. Sakharov, W. V. Lundin, E. E. Zavarin, and A. S. Usikov, Phys. Status Solidi A **188** (2), 863 (2001).
6. V. Yu. Davydov, A. N. Smirnov, I. N. Goncharuk, R. N. Kyutt, M. P. Scheglov, M. V. Baidakova, W. V. Lundin, E. E. Zavarin, M. B. Smirnov, S. V. Karpov, and H. Harima, Phys. Status Solidi B **234** (3), 975 (2002).
7. G. Wei, J. Zi, K. Zhang, and X. Xie, J. Appl. Phys. **82** (2), 622 (1997).
8. E. Bezerra, V. N. Freire, A. M. R. Teixeira, M. A. Araújo Silva, P. T. C. Freire, J. Mendes Filho, and V. Lemos, Phys. Rev. B **61** (19), 13060 (2000).
9. V. Yu. Davydov, Yu. E. Kitaev, I. N. Goncharuk, A. N. Smirnov, J. Graul, O. Semchinova, D. Uffmann, M. B. Smirnov, A. P. Mirgorodsky, and R. A. Evarestov, Phys. Rev. B **58**, 12899 (1998).
10. M. V. Vol’kenshteĭn, L. A. Gribov, M. A. El’yashevich, and B. I. Stepanov, *Molecule Vibrations* (Nauka, Moscow, 1972) [in Russian].
11. Yu. E. Kitaev, M. F. Limonov, P. Tronc, and G. N. Yushin, Phys. Rev. B **57** (22), 14209 (1998).
12. J. Gleize, M. A. Renucci, J. Frandon, and F. Demangeot, Phys. Rev. B **60** (23), 15985 (1999).
13. C. Colvard, T. A. Gant, and M. V. Klein, Phys. Rev. B **31** (4), 2080 (1985).
14. S. M. Rytov, Zh. Éksp. Teor. Fiz. **29**, 605 (1955) [Sov. Phys. JETP **2**, 466 (1955)].
15. J. Gleize, J. Frandon, F. Demangeot, M. A. Renucci, M. Kuball, J. M. Hayes, F. Widmann, and B. Daudin, Mater. Sci. Eng. B **82**, 27 (2001).
16. J. Gleize, J. Frandon, and M. A. Renucci, Phys. Status Solidi A **195** (3), 605 (2003).
17. M. Dutta, D. Alexson, L. Bergman, R. J. Nemanich, R. Dupuis, K. W. Kim, S. Komirenko, and M. Stroscio, Physica E (Amsterdam) **11**, 277 (2001).
18. W. V. Lundin, A. V. Sakharov, A. F. Tsatsulnikov, E. E. Zavarin, A. I. Besulkin, M. F. Kokorev, R. N. Kyutt, V. Yu. Davydov, V. V. Tretyakov, D. V. Pakhnin, and A. S. Usikov, Phys. Status Solidi A **188** (2), 885 (2001).
19. V. Yu. Davydov, N. S. Averkiev, I. N. Goncharuk, D. K. Nelson, I. P. Nikitina, A. S. Polkovnikov, A. N. Smirnov, M. A. Jacobson, and O. K. Semchinova, J. Appl. Phys. **82** (10), 5097 (1997).
20. A. Sarua, M. Kubal, and J. E. Van Nostrand, Appl. Phys. Lett. **81** (8), 1426 (2002).
21. K. Karch and F. Bechstedt, Phys. Rev. B **56** (12), 7404 (1997).
22. K. Karch, J.-M. Wagner, and F. Bechstedt, Phys. Rev. B **57** (12), 7043 (1998).
23. P. Y. Yu and M. Cardona, *Fundamentals of Semiconductors* (Springer, Berlin, 1998; Fizmatlit, Moscow, 2002).

Translated by Yu. Epifanov

Physics of the Solid State, Vol. 47, No. 4, 2005, pp. 754–757. Translated from Fizika Tverdogo Tela, Vol. 47, No. 4, 2005, pp. 728–730.
Original Russian Text Copyright © 2005 by Kurmaev, Zatsepin, Cholakh, Schmidt, Harada, Tokushima, Osawa, Shin, Takeuchi.

LOW-DIMENSIONAL SYSTEMS AND SURFACE PHYSICS

Iron Nanoparticles in Amorphous SiO_2: X-ray Emission and Absorption Spectra

É. Z. Kurmaev*, D. A. Zatsepin*, S. O. Cholakh, B. Schmidt***, Y. Harada****,**
T. Tokushima**, H. Osawa*****, S. Shin*****, and T. Takeuchi********
** Institute of Metal Physics, Ural Division, Russian Academy of Sciences,*
ul. S. Kovalevskoĭ 18, Yekaterinburg, 620219 Russia
e-mail: kurmaev@ifmlrs.uran.ru
*** Ural State Technical University, ul. Mira 19, Yekaterinburg, 620002 Russia*
**** Research Center Rossendorf, Institute of Ion Beam Physics and Materials Research, Dresden, D-01314 Germany*
***** Harima Institute, Hyogo, 679-5138 Japan*
****** Institute for Solid State Physics, University of Tokyo, Chiba, 277-8581 Japan*
******* Tokyo University of Science, Chiba, 162-8601 Japan*

Received August 6, 2004

Abstract—The local structure of the chemical bond of iron ions implanted into SiO_2 glasses (implantation energy, 100 keV; fluence, 1×10^{16} cm^{-2}) is investigated using x-ray emission and absorption spectroscopy. The Fe *L* x-ray emission and absorption spectra are analyzed by comparing them with the corresponding spectra of reference samples. It is established that iron nanoparticles implanted into the SiO_2 vitreous matrix are in an oxidized state. The assumption is made that the most probable mechanism of transformation of iron nanoparticles into an oxidized state during implantation involves the breaking of Si–O–Si bonds with the formation of Si–Si and Fe–O bonds. *© 2005 Pleiades Publishing, Inc.*

1. INTRODUCTION

Nanoclusters of 3*d* transition metals (iron, nickel, cobalt) dispersed into dielectric matrices are characterized by large values of the magnetic moment, coercive force, and shift in the hysteresis loop and exhibit a great variety of interesting magneto-optical properties [1]. This makes it possible to use these materials as optical switches, shutters or waveguides [2], enhanced magnetic refrigerants, and high-density magnetic recording media [3, 4]. Amorphous silicon dioxide SiO_2, which is the most important dielectric material in modern electronics, has been widely used as a matrix for dispersion of metal nanoparticles. At present, ion implantation is a powerful tool for introducing metal nanoparticles into dielectric matrices owing to the simplicity and accuracy of the control of the nanocomposite microstructure, the quantitative analysis of implanted ions and their distribution over the depth of the matrix and particle size, the distribution of implanted ions in a nanocluster, etc. Moreover, ion implantation is entirely compatible with modern technology for producing silicon semiconductors and can be accomplished with an almost arbitrary metallic dopant. In this work, the local configurations of the chemical bonds of iron ions implanted into SiO_2 glasses were investigated using soft x-ray emission and absorption spectroscopy.

2. SAMPLE PREPARATION AND EXPERIMENTAL TECHNIQUE

Silicon dioxide SiO_2 was irradiated by iron ions at a dose of 16^{16} ions/cm^2 with the use of $^{56}Fe^+$ (which is close to the natural mixture of isotopes, sample *a*) and $^{57}Fe^+$ (isotope 57, sample *b*). Prior to ion implantation, glass samples 10 mm in diameter and 0.8 mm in thickness were subjected to wet chemical cleaning in a solution of $H_2O_2 : H_2SO_4 = 1 : 1$ at a temperature of 120°C, after which the samples were washed with deionized water and dried. The implantation of ^{57}Fe ions was accomplished on a DANFYSIK high-current implanter operating at a voltage of 200 kV at the Research Center Rossendorf, Institute of Ion Beam Physics and Materials Research, Germany. The samples were mounted on a target holder and affixed to it with an adhesive carbon tape. The implantation was performed with separated (according to mass) charged ^{57}Fe ions along the normal to the surface of the sample at room temperature. The residual pressure in the ion implantation chamber reached 10^{-6} Torr. The samples were irradiated at fluences ranging from 1×10^{14} to 1×10^{16} cm^{-2} and at a current density of 0.1–0.2 μA/cm^{-2}. In each event of implantation, the energy E of iron ions was equal to 100 keV, which corresponded to their path in silicon dioxide $R_p = 83$ nm (the maximum in the Gaussian distribution) for doses up to 1×10^{16} cm^{-2}. For the greatest dose of ion implantation, which is equal to 1×10^{17} cm^{-2}, the maximum in the ^{57}Fe distribution is located at a lesser depth (68 nm) due to an increase in the degree of sputtering (at approximately 15 nm for SiO_2). The maximum atomic fraction of ^{57}Fe in SiO_2 amounted to 20% for a dose of 1×10^{16} cm^{-2}. The relative content of ^{57}Fe isotope in the implanted glass samples was approximately equal to 90% (the remaining 10% were accounted for by other iron isotopes). The implantation of $^{56}Fe^+$ ions was accomplished on a high-voltage implanter operating at a voltage of 500 kV at the Research Center Rossendorf, Institute of Ion Beam Physics and Materials Research, Germany. In this case, the conditions used for preparing the samples and for their implantation were similar to those described above. Since the ionic current provided by the second implanter was weaker, the mass separation used was smaller. As a result, the isotope composition of the implanted samples involved isotopes 55, 56, and 57 with the maximum concentration of ^{56}Fe.

The x-ray emission and absorption spectra were measured on a BL27SU Spring-8 beam line (Japan) with a soft x-ray fluorescence spectrometer. The well-focused ion beam (less than 10 μm in the transverse direction) made it possible to use a slitless spectrometer, which improved the throughput of the instrument and the detection efficiency. The slitless spectrometer with a spherical varied-line-spacing (VLS) grating and a back-illuminated (BI) charged-coupled device (CCD) detector [5] provided an energy resolution $E/\Delta E = 1000$.

3. RESULTS AND DISCUSSION

Our analysis of the Fe 2*p* x-ray absorption spectra is based on the data obtained by van der Laan and Kirkman [6] and de Groot [7], who carried out systematic investigations and interpreted the calculated 2*p* absorption spectra of 3*d* transition metal compounds. The 2*p* x-ray absorption spectra are allowed by the dipolar selection rules and correspond to electronic transitions from the 2*p* core level to the 3*d* vacant states, i.e., to the transition from the ground state with electronic configuration $2p^63d^n$ to the excited state with electronic configuration $2p^53d^{n+1}$. Since the Coulomb interaction between a hole at the 2*p* core level and 3*d* electrons is significant, the 2*p* x-ray absorption spectra are determined by the local electronic structure and provide information on the oxidation state and the symmetry of 3*d* transition metal ions in a particular compound. The $2p_{3/2}$ and $2p_{1/2}$ spectral components are well resolved by virtue of the core-hole spin–orbit interaction and have a multiplet structure because the broadening due to the core-hole lifetime is very small. As was shown in [6, 7], there is a clearly pronounced difference between the calculated 2*p* spectra for the ground states of different iron ions (Fe^{2+} and Fe^{3+}), which can be used to identify the chemical state of iron ions implanted into SiO_2 glasses. Figure 1 presents the experimental Fe 2*p* x-ray absorption spectra of iron-implanted SiO_2. The intensity of these spectra is normalized to the low-energy peak *A*, which is located at an energy of ~707.8 eV. We could measure the Fe 2*p* x-ray absorption spectra only for the samples irradiated at a maximum dose ($D = 1 \times 10^{16}$ cm^{-2}). The 2*p* x-ray absorption spectra consist of low-energy $2p_{3/2}$ (L_3) and high-energy $2p_{1/2}$ (L_2) components separated by approximately 13 eV. The relative intensity of the peak *B* located at an energy of ~709.3 eV in the x-ray absorption spectra for all samples of iron-implanted SiO_2 is very close to that of divalent iron (the spectrum is characterized by a higher intensity of the peak *A*); however, it differs substantially from the relative intensity of the peak *B* attributed to trivalent iron. It should be noted that the 2*p* x-ray absorption spectra cannot be described in terms of the one-particle density of states, because the electronic correlations in atoms with a partially filled 3*d* shell are very significant [6]. As a rule, the solid-state effects are introduced into atomic-like calculations of the 2*p* absorption spectra through the inclusion of a crystal field that accounts for the local symmetry of the metal atom and the matrix elements of different hybridizations of the 3*d* orbitals

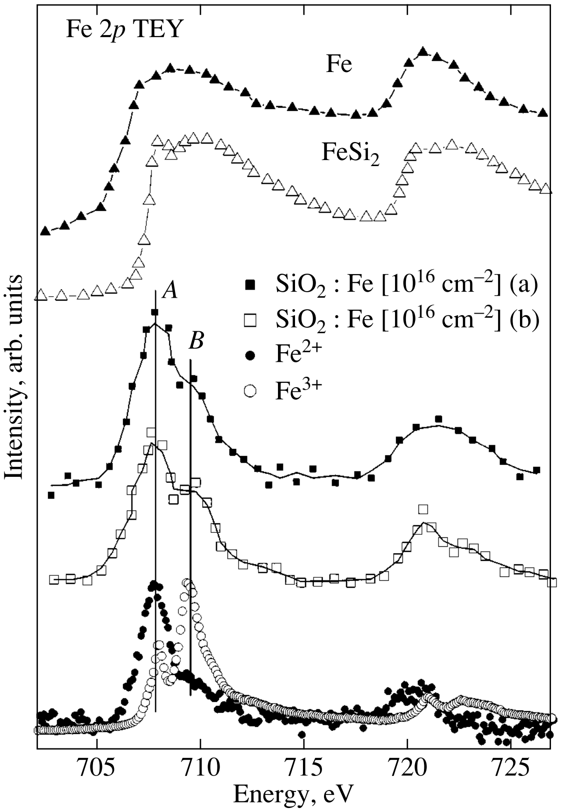

Fig. 1. Fe 2*p* x-ray absorption (TFY) spectra of iron-implanted SiO_2 glasses. The spectra of the reference samples are shown for comparison.

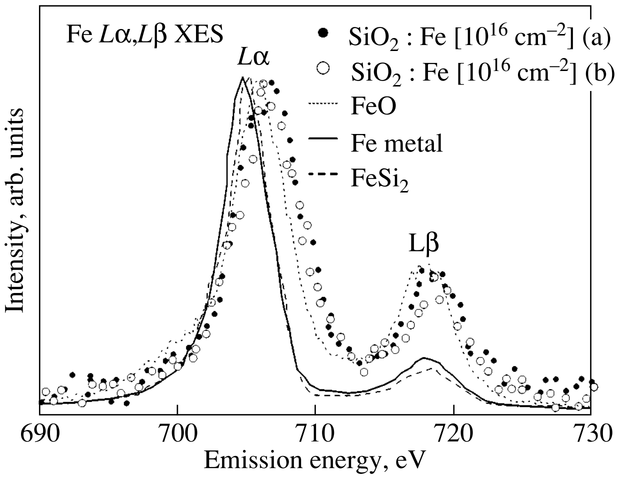

Fig. 2. Comparison of Fe *L*α and Fe *L*β x-ray emission (Fe *L*α, *L*β XES) spectra of iron-implanted SiO_2 glasses with the spectra of the pure iron metal and FeO oxide.

with the surrounding ligands [6]. It is found that, within the single-configuration approach, the experimental *L* x-ray absorption spectra of 3*d* metals in different compounds can be reproduced fairly well. According to the experimental x-ray absorption spectra of trivalent and divalent iron atoms (Fig. 1), the double-peak structure of the Fe 2*p* absorption spectra is assigned to the final state with electronic configuration d^5 (Fe^{3+}) and the single-peak structure of these spectra is attributed to the final state with electronic configuration d^6 (Fe^{2+}), which roughly reflects the multiplet structure. Therefore, the above results allow the conclusion that dispersed iron nanoparticles interact with SiO_2 and can oxidize to the Fe^{2+} state. It was also established that the chemical state of iron atoms in iron-implanted silicon dioxide is not sensitive to the substitution for an iron isotope.

The Fe *L*α and Fe *L*β nonresonant x-ray emission spectra of SiO_2 : Fe (Fig. 2) can be analyzed in a similar manner. As in the case with the Fe 2*p* x-ray absorption spectra, we could measure only the samples irradiated at the dose $D = 1 \times 10^{16}$ cm^{-2}. The Fe *L*α and Fe *L*β x-ray emission spectra are associated with the electronic transitions Fe $3d4s \longrightarrow 2p_{3/2,\ 1/2}$ and provide probing the Fe 3*d*4*s* occupied states. It can be seen from Fig. 2 that the intensity ratio *L*β/*L*α is very small for the pure metal and differs from the value of 0.5 expected for the statistical mean occupancy of the inner levels with $j = 3/2$ and 1/2 due to the Coster–Kronig nonradiative transition $L_2L_3M_{4,\ 5}$ [8]. It is known that the intensity ratio *L*β/*L*α increases upon changing over from pure 3*d* metals to their oxides, because the probability of the Coster–Kronig nonradiative transition $L_2L_3M_{4,\ 5}$ occurring in 3*d* metal oxides is considerably lower than that in pure metals [9]. The intensity ratio *L*β/*L*α in the spectra of the SiO_2 : Fe samples under investigation is larger than that in the spectra of metallic iron and $FeSi_2$ and is almost identical to that in the spectrum of FeO. From the aforesaid, we can make the inference that, after the implantation, iron atoms in SiO_2 : Fe are in a valence state of 2+. This inference is in complete agreement with the results of measuring the Fe 2*p* x-ray absorption spectra (Fig. 1).

The results obtained can be interpreted as follows. It is known that nanocrystalline metal particles are thermodynamically metastable and chemically active. Iron nanoparticles are pyrophoric and can be readily oxidized [10]. According to our investigations, iron ions transform into an oxidized state with the subsequent formation of clusters during implantation of the SiO_2 glass. It is assumed that the ion implantation brings about the breaking of Si–O–Si bonds, the formation of Si–Si bonds, and the subsequent capture of oxygen atoms by iron atoms with the formation of FeO oxide in the form of small-sized clusters. A similar behavior is observed in the case of SiO_2 implanted by cobalt atoms [11].

4. CONCLUSION

The local structure of the chemical bond in amorphous silicon dioxide after iron ion implantation was studied using x-ray emission and absorption spectroscopy. It was revealed that the ion implantation is accompanied by the formation of iron nanoparticles in an oxidized state due to the breaking of Si–O–Si bonds and the formation of Si–Si and Fe–O bonds. In this case, the iron atoms have a valence of 2+. It was demonstrated that the valence state of iron atoms in implanted amorphous silicon dioxide is not sensitive to substitution for an iron isotope.

ACKNOWLEDGMENTS

This work was supported by the Russian Foundation for Basic Research (project nos. 05-02-16448, 05-02-16438) and by the Council on Grants from the President of the Russian Federation within the program for the support of leading scientific schools (project no. NSh-1026.2003.2).

REFERENCES

1. F. Conella and P. Mazzoldi, in *Handbook of Nanostructured Materials and Nanotechnology*, Ed. by H. S. Nalwa (Academic, San Diego, 2000), p. 81.
2. H. Gleiter, Prog. Mater. Sci. **33**, 223 (1989).
3. R. D. Shull, R. D. McMichael, L. J. Swartzendruber, and L. H. Bennett, in *Magnetic Properties of Fine Particles*, Ed. by J. L. Dormann and D. Fiorani (North-Holland, Amsterdam, 1992), p. 161.

4. J. Loffler, H. van Swygenhoven, W. Wagner, J. Meier, B. Doudin, and J.-Ph. Ansermet, Nanostruct. Mater. **9**, 523 (1997).
5. T. Tokushima, PhD Thesis (Hiroshima Univ., 2003).
6. G. van der Laan and I. W. Kirkman, J. Phys.: Condens. Matter **53**, 1185 (1992).
7. F. de Groot, Chem. Rev. **101**, 1779 (2001).
8. H. V. Skinner, T. G. Bullen, and J. Jonston, Philos. Mag. **45**, 1070 (1954).
9. V. R. Galakhov, E. Z. Kurmaev, and V. M. Cherkashenko, Izv. Akad. Nauk SSSR, Ser. Fiz. **49**, 1513 (1987).
10. S. Gangopadhaya, G. C. Hadjipanayis, S. I. Shah, C. M. Sorensen, K. J. Klabunde, V. Papaefthymiou, and A. Kostikas, J. Appl. Phys. **70**, 5888 (1991).
11. O. Cintora-Gonzales, D. Muller, C. Estournes, M. Richard-Plouet, R. Poinsot, J. J. Grob, and J. Guille, Nucl. Instrum. Methods Phys. Res. B **178**, 144 (2001).

Translated by O. Moskalev

Physics of the Solid State, Vol. 47, No. 4, 2005, pp. 758–764. Translated from Fizika Tverdogo Tela, Vol. 47, No. 4, 2005, pp. 731–737.
Original Russian Text Copyright © 2005 by Eremeev, Rusina, Sklyadneva, Borisova, Chulkov.

LOW-DIMENSIONAL SYSTEMS AND SURFACE PHYSICS

Diffusional and Vibrational Properties of Cu(001)–$c(2 \times 2)$–Pd Surface Alloys

S. V. Eremeev[1], G. G. Rusina[1], I. Yu. Sklyadneva[1, 2], S. D. Borisova[1], and E. V. Chulkov[2, 3]

[1] Institute of Strength Physics and Materials Science, Siberian Division, Russian Academy of Sciences,
Akademicheskiĭ pr. 2/1, Tomsk, 634021 Russia
e-mail: waaerers@mail.ru

[2] Donostia International Physics Center (DIPC), San Sebastián/Donostia, 20018 Spain

[3] Departamento de Física de Materiales, Facultad de Ciencias Químicas,
Universidad del País Vasco/Euskal Herriko Unibertsitatea, Apdo. 1072, San Sebastián/Donostia, 20018 Spain

Received May 20, 2004

Abstract—Interatomic interaction potentials constructed in the framework of the embedded-atom method are used to study the structural, diffusional, and vibrational properties of ordered Cu(001)–$c(2 \times 2)$–Pd surface and subsurface alloys. The equilibrium structures obtained for these alloys are in good agreement with experimental data and the results of other calculations. The calculated diffusional characteristics are consistent with the experimental kinetics and evolution of the surface alloys and attest to the stability of the subsurface alloy. The activation energy for planar diffusion of palladium in the initial stage of the alloy formation agrees with the value measured using scanning tunneling microscopy. The calculated surface phonon frequencies agree well with the experimental values obtained using electron-energy-loss spectroscopy. The results show that the Cu–Pd bond is strong and that the bond between surface copper atoms weakens. *© 2005 Pleiades Publishing, Inc.*

1. INTRODUCTION

The formation of surface alloys at the initial stages of epitaxial growth has been attracting considerable interest [1]. One of the most extensively studied systems is Pd/Cu(001), since this system is characterized by high surface catalytic activity [2–15]. Experimental studies of the Pd/Cu(001) structure by low-energy electron diffraction (LEED) have shown that palladium atoms deposited at room temperature are incorporated in the surface layer of copper and that an ordered Cu(001)–$c(2 \times 2)$–Pd surface alloy forms at a covering of 0.5 monolayer (ML) [3, 5]. The formation of a surface alloy in this system was also experimentally confirmed by photoemission [3], LEED [6], and Rutherford back scattering data [4]. The fact that the surface alloy is preferred over the ordered $c(2 \times 2)$ coating was also confirmed by a number of computations using *ab initio* [7] and semiempirical [6, 8] methods. To reveal the formation kinetics of the surface alloy, the authors of [16] applied scanning tunneling microscopy (STM) to study the diffusion mechanisms of the surface-alloy formation. They analyzed two mechanisms: (1) the formation of a copper adatom and the migration of incorporated Pd in the newly formed copper vacancy (as in the case of a Cu/Co monolayer on Ru(001) [17]) and (2) lateral diffusion of Pd atoms via surface vacancies (as in the case of Mn and In on Cu(001) [18, 19]). It was found that the second mechanism is realized in this system, which was also supported by Monte Carlo calculations [16]. Moreover, it has also been found that palladium diffuses into the subsurface layer and tends to form a $c(2 \times 2)$ ordered alloy [5, 13, 20]. For example, LEED was used in [20] to determine the migration energy of palladium into the second layer. To study the stability of the Cu(001)–$c(2 \times 2)$–Pd surface alloy, the authors of [21] used electron-energy-loss spectroscopy (EELS) to measure surface vibrational modes in the $\overline{\Gamma X}$ direction. At room temperature, the only surface state was found to exist at the $\bar{X}$ point and was identified as a mixed state of copper and palladium. However, upon annealing, a high-frequency peak appeared and became dominant. This state was interpreted as the vertical-vibration mode in surface copper islands. Apart from the experimental determination of vibrational frequencies, a phonon spectrum in the $\overline{\Gamma X}$ direction was calculated in that work using the effective-medium theory. Sklyadneva *et al.* [22], using the embedded-atom method (EAM) and a potential for the alloy proposed in [23], performed calculations along all the symmetric directions of the two-dimensional Brillouin zone. The calculations showed that, in addition to the mixed state, states localized at adatoms and the surface atoms of the substrate are present at the $\bar{X}$ point.

It should be noted that the surface diffusion and stability of this system have been studied for specific cases, though complete understanding and description of these problems would require complementary studies. In this work, we calculated the atomic structures of

1063-7834/05/4704-0758$26.00 © 2005 Pleiades Publishing, Inc.

surface and subsurface alloys and the diffusional characteristics of the system at all stages of alloy formation, namely, from the initial deposition of palladium to the formation of a subsurface structure. To support the adequacy of the potentials used for diffusion calculations, we calculated the vibrational properties of surface and subsurface Cu(001)–$c(2 \times 2)$–Pd alloys with allowance for the symmetry of the crystal.

2. CALCULATION PROCEDURE

For calculation, we use the embedded-atom method proposed in [23] with a potential energy in the form

$$E = 1/2\sum_{ij}\varphi(r_{ij}) + \sum_i F_i\left[\sum_{j \neq i}\rho_j^a(r_{ij})\right]. \qquad (1)$$

In Eq. (1), the first term is the pair interaction potential, where r_{ij} is the distance between atoms i and j, and the second term describes many-particle effects. The embedding function F_i is specified at a site r_i and is controlled by the electron density, which is equal to the sum of the electron densities of all other atoms located at sites r_j; the values of ρ_j^a are obtained by solving the problem for a free atom in the local density–functional approximation. The potential applied in this work includes interatomic interactions up to the fifth coordination shell. The parameters of the method were fitted to experimental data on the equilibrium volume, vacancy-formation energy, bulk modulus of elasticity, and elastic constants for pure palladium and copper. The pair potential has the form of a screened Coulomb potential. To describe the interatomic interaction of different elements, this potential is chosen in the form [24]

$$\varphi_{AB}(r) = \frac{1}{2}\left[\frac{\rho_B(r)}{\rho_A(r)}\varphi_A(r) + \frac{\rho_A(r)}{\rho_B(r)}\varphi_B(r)\right], \qquad (2)$$

where φ_A and φ_B are the pair potentials of copper and palladium, respectively. These potentials describe well both the diffusional and vibrational properties of the surface.

The equilibrium surface geometry is found by molecular-dynamics simulation. The vacancy-formation energy E_f is defined as

$$E_f = E_{N-1} - E_N - E_1, \qquad (3)$$

where E_N, E_{N-1}, and E_1 are the energy of the vacancy-free system, the energy of the system with a vacancy, and the energy per atom in the bulk, respectively. The migration energy E_m is defined as

$$E_m = E_{sp} - E_0, \qquad (4)$$

where E_{sp} and E_0 are the energies of the system with a migrating atom at the saddle point and at the initial point of a migration path, respectively. The diffusion activation energy Q is calculated as the sum of the formation and migration energies. The vibrational spectra along the symmetric directions of the two-dimensional Brillouin zone are calculated for a relaxed 31-layer Cu(001)–$c(2 \times 2)$–Pd film, with palladium atoms being present in both the surface and subsurface layers.

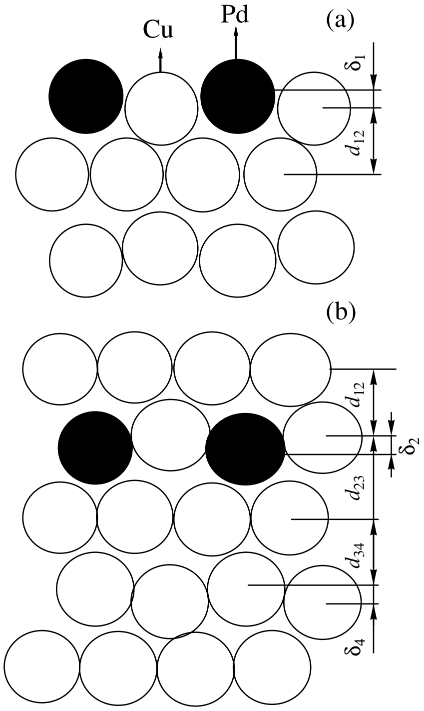

Fig. 1. Atomic structure of (a) a surface and (b) a subsurface Cu(001)–$c(2 \times 2)$–Pd alloy.

3. ATOMIC STRUCTURE

To obtain an equilibrium structure, we performed molecular-dynamics simulation of surface relaxation. It is found that, due to relaxation of the Cu(001) surface, the change in the interplanar spacings between the first and second layers Δd_{12} is –0.027 Å (the minus sign means a decrease in the interplanar spacings as compared to the ideal structure) and the change in the spacing between the second and third layers is $\Delta d_{23} = -0.005$ Å. In deeper layers, the interplanar spacings correspond to the bulk value, which agrees well with the well-known experimental data [6]. The equilibrium structure of the Cu(001)–$c(2 \times 2)$–Pd surface alloy is shown in Fig. 1a. As a result of relaxation, surface copper atoms are shifted to the bulk, as in the case of the pure surface, whereas palladium atoms undergo outward relaxation. The change in the interplanar spacings between the copper atoms of the first and second atomic layers Δd_{12} is –0.05 Å. Moreover, a splitting $\delta_1 = 0.09$ Å appears between Cu and Pd atoms in the first layer. The calculations agree with the experimentally determined structure of the surface alloy. For example, the displace-

Energy of copper-vacancy formation E_f, migration energy of palladium atoms E_m, and diffusion activation energy Q for single palladium on Cu(001), as well as for surface (Pd : 1) and subsurface (Pd : 2) Cu(001)–$c(2 \times 2)$–Pd alloys. Superscripts indicate the numbers of atomic layers, and I and II designate different mechanisms for the formation of surface vacancies (see text)

Single Pd/Cu(001)

E_f^1	E_m^{11}	Q^{11}	E_f^2	E_m^{12}	Q^{12}
0.61 0.474*	0.50 0.466*	1.11 0.94* 0.88* (expt.)	1.42	0.085	1.50

Cu(001)–$c(2 \times 2)$–Pd : 1

E_f^1	E_m^{11}	Q^{11}	E_f^2	E_m^{12}	Q^{12}
0.69	0.64	1.33	1.50	0.36	1.86 1.13** (expt.)

Cu(001)–$c(2 \times 2)$–Pd : 2

E_f^1	E_m^{21}	Q^{21}	E_f^1(I)	E_f^{21}(II)	$Q^{21}_{\text{I, II}}$
0.66	1.39	2.05	2.67	1.22	(I) 4.06 (II) 2.61
E_f^2	E_m^{22}	Q^{22}	E_f^3	E_m^{23}	Q^{23}
1.46	1.01	2.47	1.38	1.07	2.45

* Data from [16].

** Data from [20].

ments of palladium atoms with respect to the copper substrate were determined by LEED to be 0.02–0.03 Å, with the interplanar spacing Cu_{12} being close to its bulk value [3]. However, the splittings δ_1 between Pd and Cu atoms in the first layer were experimentally determined in [6] using medium-energy electron diffraction and found to be 0.04–0.08 Å. The relaxation $\Delta d_{12} = -0.05$ Å and the splitting $\delta_1 = 0.12$ Å determined with the EAM in [6] virtually coincide with our values (we note that the value of δ_1 found in this work is closer to the experimental results).

A more complex geometry is observed for the structure of the subsurface alloy (Fig. 1b). The changes in the relaxed interplanar spacings are calculated to be $\Delta d_{12} = 0.022$ Å, $\Delta d_{23} = 0.035$ Å, and $\Delta d_{34} = -0.022$ Å. The splittings in the second and fourth layers are calculated to be $\delta_2 = 0.02$ Å and $\delta_4 = 0.001$ Å. These results are in satisfactory agreement with the LEED data from [20].

4. DIFFUSION ACTIVATION ENERGY

As a model for the initial stage of the formation of a two-dimensional ordered Cu(001)–$c(2 \times 2)$–Pd surface alloy, we considered the diffusion of a single palladium adatom on the Cu(001) surface. First, we calculated the migration energy of the adatom on the Cu(001) surface; it was found to be 0.62 eV, which is comparable to the migration energy of Pd on the Pd(001) surface (0.63 eV) [25]. In this work, we considered the vacancy-mediated diffusion, since this mechanism is preferable in the system under study [16]. The calculated formation energy of a surface vacancy on Cu(001) (0.58 eV) agrees well with the experimental value (0.59 eV) [26]. The calculation shows that the migration of adsorbed Pd to the surface copper vacancy occurs without activation ($E_m < 0$), which is observed experimentally [16].

Next, we considered the migration of an incorporated Pd atom into the nearest copper surface vacancy. As is seen from the table, the migration energy E_m^{11} calculated by us is consistent with the *ab initio* value calculated using the VASP code [16]. In our case, the formation energy of a copper vacancy in the site nearest to the palladium atom is slightly higher than the corresponding value for the pure surface, whereas the vacancy-formation energy obtained in [16] is 0.474 eV. As a result, the agreement between the activation energy $Q^{11} = E_f^1 + E_m^{11}$ calculated in this work and the experimental value is worse than that for the *ab initio* calculation. We also analyzed the diffusion of the surface palladium into the second atomic layer. To this end, we calculated the formation energy of a copper vacancy in the second layer at the site nearest to the surface palladium atom. The calculated energy is higher than the vacancy-formation energy in the second atomic layer in Cu(001) (1.38 eV) [27], which is due to the different atomic environments, i.e., to the effect of palladium. Although the migration barrier to the diffusion of palladium to the vacancy site in the second layer is very low, the activation energy for this process Q^{12} is significantly higher than the diffusion activation energy in the first layer. This fact indicates the predominance of surface diffusion at the initial stage of the alloy formation.

To study diffusion in the ordered surface alloy, we considered both the diffusion of Pd within the surface layer (i.e., disordering of the surface alloy) and the diffusion of Pd atoms to the second layer. The data listed in the table show that the activation energy Q^{11} exceeds the corresponding value for single a palladium atom. This fact indicates that the diffusion activation energy increases with coverage. The formation of a copper vacancy in the second layer and the migration of palladium into this vacant site also require higher energies than in the case of a single palladium layer. Accordingly, the activation energy for diffusion to the subsurface layer Q^{12} exceeds the activation energy for diffu-

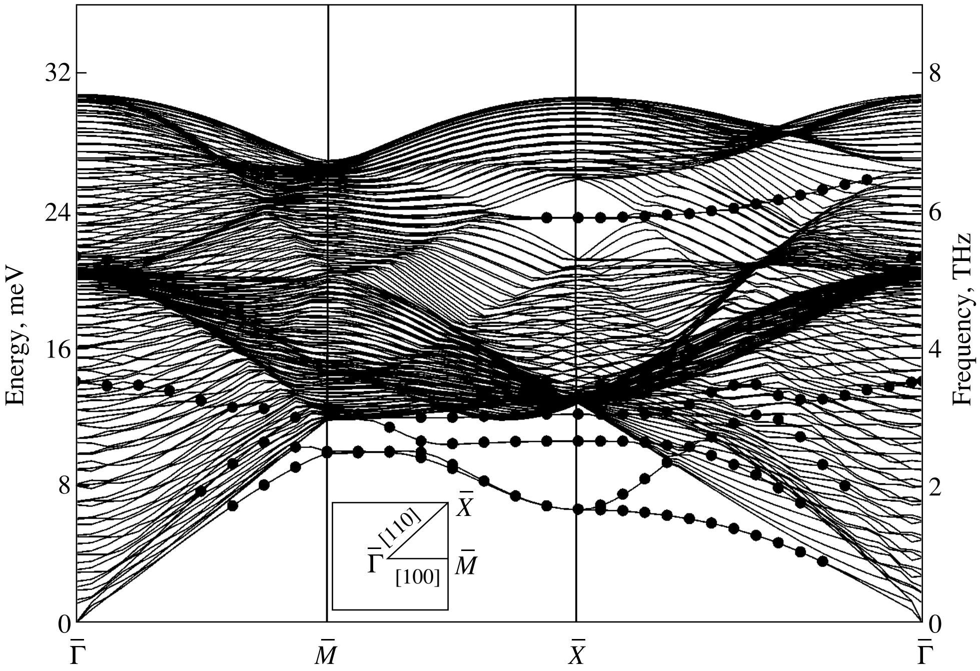

Fig. 2. Phonon spectrum of a Cu(001)–$c(2 \times 2)$–Pd surface alloy. Points show surface states.

sion to the second layer in the case where a single palladium atom is present in the surface layer. This energy ratio should explain the penetration of Pd into the subsurface layer prior to the formation of a continuous ordered structure on the surface, which is corroborated experimentally [5, 13, 21]. The activation barrier to the migration of Pd from the first to the second layer was estimated in [20] to be 1.13 eV, which exceeds the activation energy for planar surface diffusion measured in [16]. The activation energy calculated in our work adequately describes the tendency toward the formation of a subsurface alloy.

When considering possible diffusion paths for the migration of the palladium of the subsurface alloy, we calculated both the activation energy for diffusion in the alloy layer and the diffusion barriers to the migration of palladium to the first and second layers. The vacancy-formation energy in the third layer E_f^3 exceeds the energy of formation of a vacancy on the third layer of the pure Cu(001) surface (1.33 eV) [27]. The migration energy E_m^{23} is also high, which gives a high activation barrier Q^{23} to the diffusion of Pd into the third layer. As is seen from the table, the activation energy for diffusion in the alloy layer Q^{22} is also fairly high, which indicates that disordering of the $c(2 \times 2)$ subsurface structure is unfavorable. To determine the activation energy for palladium diffusion to the surface layer, we also analyzed two possibilities for the formation of a copper vacancy in the surface layer (labeled I and II in the table), namely, through the migration of Cu atoms into a vacancy in the second layer or the formation of a surface adatom. In the first case, the vacancy-formation energy is the sum of the energy of formation of a copper vacancy on the second layer E_f^2 and the energy of migration of a Cu atom from the first layer into this vacant site. In the second case, the vacancy-formation energy is, in essence, the formation energy of an adatom–vacancy pair. For the second case, we also considered two variants of the "hollow" position of the adatom formed (over a Pd atom and over a Cu atom). The energy of migration of surface copper into the vacant site in the second layer E_m^{12} is calculated to be 1.21 eV, which gives a formation energy of 2.67 eV for the first case. Our calculation shows that the formation energy of an adatom–vacancy pair varies with the adatom position only in the third decimal place: 1.225 eV for the position over Pd and 1.224 eV for the position over Cu (one value to the second decimal place is given in the table). The energy of migration of palladium from the alloy into the surface alloy is 1.39 eV. As a result, the activation energy for Pd diffusion from the subsurface layer to the surface for the second (Q_{II}^{21}) and, especially, for the first (Q_{I}^{21}) variant of the formation of a surface vacancy is very high, which indicates that the subsurface alloy is stable.

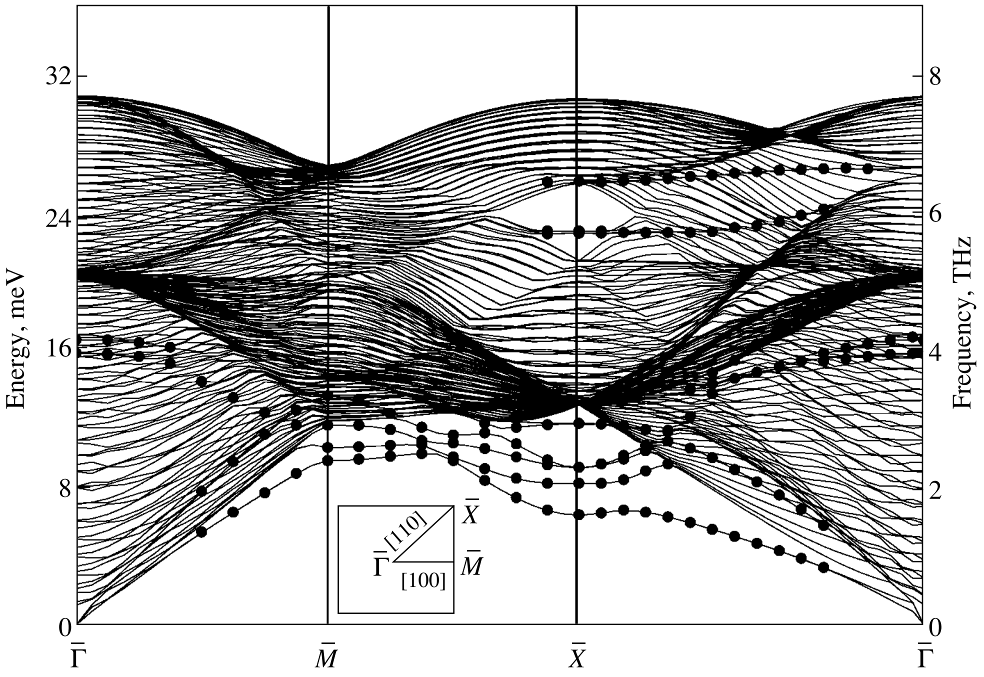

Fig. 3. Phonon spectrum of a Cu(001)–*c*(2 × 2)–Pd subsurface alloy.

5. VIBRATIONAL PROPERTIES OF THE Cu(001)–*C*(2 × 2)–Pd SURFACE AND SUBSURFACE ALLOYS

Figure 2 shows the calculated dispersion curves for the Cu(001)–*c*(2 × 2)–Pd surface alloy. According to experimental studies [21, 28–30], one surface mode (11.79 meV) was detected at the $\bar{X}$ point; its energy lies in the energy range corresponding to the energies of the Rayleigh modes of pure copper and palladium surfaces (13.4 and 11.17 meV, respectively). As is seen from Fig. 2, our calculation reveals three surface states at the $\bar{X}$ point below the bottom of the projections of the bulk states. The lower mode with an energy of 6.82 meV involves a simultaneous displacement of Pd and Cu atoms in the surface plane. An analysis of this state indicates that predominant localization (67%) occurs at Pd atoms and that this state corresponds to the analogous state of a pure Pd(001) surface with an energy of 5.9 meV, which was determined experimentally [30]. Apart from this mode, two surface states are observed at the $\bar{X}$ point. The second and third states (with energies of 10.96 and 12.53 meV) are typical Rayleigh modes of Pd and Cu, and their energies agree well with the experimental values [28, 29]. The state with an energy of 13.44 meV and transverse atomic displacements is located at the boundary of the projection of the bulk states and is completely localized in the second substrate layer. The band gap contains a surface state with *xy* polarization, which is localized at both Cu and Pd atoms. It should be noted that, in contrast to the experimental result and our calculations, the authors of [22] found two surface modes at the $\bar{X}$ point, which were characterized by simultaneous displacements of copper and palladium atoms. At the $\bar{M}$ point, there are two states, which are completely localized at Pd atoms and have energies of 10.34 and 12.9 meV, respectively. These states correspond to the Rayleigh mode and the *y*-polarized mode of the pure palladium surface. We detected no states localized at Cu substrate atoms at this point. At the center of the Brillouin zone (the $\bar{\Gamma}$ point) of the Cu(001)–*c*(2 × 2)–Pd surface, there are *z*-polarized states. These states appear due to the formation of a new two-dimensional Brillouin zone with a periodicity of *c*(2 × 2) and are reflected from the $\bar{M}$ point, which belongs to the Brillouin zone of the pure surface. An analysis of the force constants shows that, in the case of the Cu(001)–*c*(2 × 2)–Pd surface, the Pd_1–Cu_1 and Pd_1–Cu_2 interactions increase by 60 and 40%, respectively, as compared to those in the bulk. However, the Cu_1–Cu_2 and Pd_1–Pd_1 interactions weaken by 8 and 25%, respectively, as compared to those on the pure surface (numerals 1 and 2 number the atomic layers beginning from the surface layer). This behavior results in the dominating role of vertically polarized vibrations, which is clearly revealed in the phonon spectrum analysis. Moreover, this change in the force constants (in the presence of Pd atoms on the Cu(001) surface) and the significant difference in the atomic masses can explain the absence of surface states localized at copper atoms at the $\overline{M}$ point and the weak manifestation of the Rayleigh mode of copper at the $\overline{X}$ point. For this change in the force constants, the penetration of palladium atoms into the substrate becomes energetically favorable. Figure 3 shows the calculated dispersion curves for the Cu(001)–$c(2 \times 2)$–Pd subsurface alloy. Unlike the case of a surface alloy, a set of surface modes is found here at the $\overline{X}$ point below the bottom of the projections of the bulk states. These modes are predominantly localized at the surface copper atoms Cu_1, which are displaced in the surface plane in mutually perpendicular directions. The next two states are localized at the palladium atoms located in the second atomic layer. The mode with an energy of 9.43 meV and horizontal transverse shifts of palladium atoms corresponds completely to the mode localized in the second (from the surface) Pd(001) atomic layer, and its energy agrees well with the experimental value (9.47 meV) [28]. At the very bottom of the projections of the bulk states, a mode is found at an energy of 12.1 meV, which can be related to the experimentally determined Rayleigh mode (11.17 meV) of the Pd(001) surface [29]. Unlike the surface alloy, the band gap in this case contains two states, which are predominantly localized at substrate atoms with longitudinal polarization and a small addition of displacements of surface-layer Cu_1 atoms in the z direction. The force constants calculated for this case show that the Cu_1– Cu_1 interaction weakens by 8% as compared to that for the pure Cu(001) surface and that the interlayer Cu_1– Cu_2 interaction increases by 20% as compared to that in the bulk. The Pd_2–Cu_2 interaction inside the layer is similar to that in the surface alloy and increases by 60%. The interlayer interactions between Pd_2 and substrate atoms Cu_1 and Cu_3 increase by 30–50% as compared to their bulk values.

6. CONCLUSIONS

We have studied the structures, diffusion activation energies, and phonon spectra of ordered Cu(001)–$c(2 \times 2)$–Pd surface and subsurface alloys. On the whole, the equilibrium atomic structures of the alloys calculated using the molecular-dynamics method adequately describe the experimentally observed structures.

The analysis of the calculated diffusional characteristics is consistent with the experimentally established evolution of the surface alloy: in the initial stage of deposition, palladium penetrates into copper vacancies on the surface without an activation barrier; under these conditions, palladium diffusion along the surface is predominant, which results in the formation of a surface alloy. Before the completion of the $c(2 \times 2)$ top layer alloy, Pd atoms begin to diffuse into the second layer. As a result, all palladium penetrates into the underlayer. Thus, there appears a two-dimensional subsurface alloy covered by a monolayer of copper. In the course of the formation of the Cu(001)–$c(2 \times 2)$–Pd alloy in the second layer and after the formation of this layer, there are significant activation barriers to palladium diffusion from the second layer to the first and third layers.

The analysis of the phonon spectra and of the changes in the force constants for the surface and subsurface alloys shows that a very strong Cu_1–Pd_1 interatomic interaction appears when palladium is adsorbed on the copper surface. Simultaneously, the interactions of the pure components of the alloy become weaker. The surface phonon modes of Cu(001)–$c(2 \times 2)$–Pd are strongly hybridized with the dominating component of palladium atoms or are completely determined by palladium atoms. In the subsurface alloy, the maximum density of surface modes corresponds to longitudinal vibrations of the atoms of the substrate surface layer under strong intralayer Cu_2–Pd_2 interaction.

ACKNOWLEDGMENTS

This work was supported by the Ministry of Industry, Science, and Technology of the Russian Federation (project no. 40-012.1.1.1153) and the NATO Science Program (project no. PST.CLG.980395).

REFERENCES

1. U. Bardi, Rep. Prog. Phys. **57** (10), 939 (1994).
2. G. W. Graham, Surf. Sci. **171** (1), L432 (1986).
3. S. C. Wu, S. H. Lu, Z. Q. Wang, C. K. C. Lok, J. Quinn, Y. S. Li, D. Tian, F. Jona, and P. M. Marcus, Phys. Rev. B **38** (8), 5363 (1988).
4. T. D. Pope, G. W. Anderson, K. Griffiths, P. R. Norton, and G. W. Graham, Phys. Rev. B **44** (20), 11518 (1991).
5. A. R. Koymen, K. H. Lee, G. Yang, K. O. Jensen, and A. H. Weiss, Phys. Rev. B **48** (3), 2020 (1993).
6. T. D. Pope, M. Vos, H. T. Tang, K. Griffiths, I. V. Mitchell, P. R. Norton, W. Liu, Y. S. Li, K. A. R. Mitchell, Z. J. Tian, and J. E. Black, Surf. Sci. **337** (1–2), 79 (1995).
7. J. Kudrnovsky, S. K. Bose, and V. Drchal, Phys. Rev. Lett. **69** (2), 308 (1992).
8. J. E. Black, Phys. Rev. B **46** (7), 4292 (1992).
9. M. S. Chen, D. Terasaki, S. Mizuno, H. Tochihara, I. Ohsaki, and T. Oguchi, Surf. Sci. **470** (1–2), 53 (2000).
10. J. E. Garcés, H. O. Mosca, and G. H. Bozzolo, Surf. Sci. **459** (3), 365 (2000).
11. M. Valden, J. Aaltonen, M. Pesa, M. Gleeson, and C. J. Barnes, Chem. Phys. Lett. **228** (6), 519 (1994).
12. G. W. Graham, P. J. Schmitz, and P. A. Thill, Phys. Rev. B **41** (6), 3353 (1990).
13. P. W. Murray, I. Stensgaard, E. Laegsgaard, and F. Besenbacher, Phys. Rev. B **52** (20), R14404 (1995).
14. M. A. Newton, S. M. Francis, Y. Li, D. Law, and M. Bowker, Surf. Sci. **259** (1–2), 45 (1991).
15. R. W. Vook and B. Oral, Appl. Surf. Sci. **60/61**, 681 (1992).

16. M. L. Grant, B. S. Swatrzentruber, N. C. Bartelt, and J. B. Hannon, Phys. Rev. Lett. **86** (20), 4588 (2001).
17. A. K. Schmid, J. C. Hamilton, N. C. Bartelt, and R. Q. Hwang, Phys. Rev. Lett. **77** (14), 2977 (1996).
18. T. Flores, S. Junghans, and M. Wuttig, Surf. Sci. **371** (1), 14 (1997).
19. R. van Gastel, E. Somfai, S. B. van Albada, W. van Saarloos, and J. W. M. Frenken, Phys. Rev. Lett. **86** (8), 1562 (2001).
20. C. J. Barnes, E. Alshamaileh, T. Pitkänen, P. Kaukasoina, and M. Lindroos, Surf. Sci. **492** (1–2), 55 (2001).
21. J. B. Hannon, H. Ibach, and P. Stoltze, Surf. Sci. **355** (1–3), 63 (1996).
22. I. Yu. Sklyadneva, G. G. Rusina, and E. V. Chulkov, Phys. Rev. B **68** (4), 045413 (2003).
23. S. M. Foiles, M. I. Baskes, and M. S. Daw, Phys. Rev. B **33** (12), 7983 (1986).
24. R. A. Johnson, Phys. Rev. B **39** (17), 12554 (1989).
25. S. V. Eremeev, A. G. Lipnitskii, A. I. Potekaev, and E. V. Chulkov, Phys. Low-Dimens. Semicond. Struct., No. 3/4, 127 (1997).
26. M. Karimi, T. Tomkowski, G. Vidali, and O. Biham, Phys. Rev. B **52** (7), 5364 (1995).
27. S. V. Eremeev, A. G. Lipnitskiĭ, A. I. Potekaev, and E. V. Chulkov, Fiz. Tverd. Tela (St. Petersburg) **39** (8), 1386 (1997) [Phys. Solid State **39**, 1230 (1997)].
28. Y. Chen, S. Y. Tong, K. P. Bohnen, T. Rodach, and K. M. Ho, Phys. Rev. Lett. **70** (5), 603 (1993).
29. G. Benedek, J. Ellis, N. S. Luo, A. Reichmuth, P. Ruggerone, and J. P. Toennies, Phys. Rev. B **48** (7), 4917 (1993).
30. L. Chen and L. L. Kesmodel, Surf. Sci. **320** (1–2), 105 (1994).

Translated by K. Shakhlevich

Physics of the Solid State, Vol. 47, No. 4, 2005, pp. 765–768. Translated from Fizika Tverdogo Tela, Vol. 47, No. 4, 2005, pp. 738–741.
Original Russian Text Copyright © 2005 by Belyaev, Drokin, Shabanonov.

POLYMERS AND LIQUID CRYSTALS

Temperature Dependence of the Dielectric Characteristics of a 5CB Liquid Crystal within the Relaxation Region

B. A. Belyaev, N. A. Drokin, and V. F. Shabanov

Kirensky Institute of Physics, Siberian Division, Russian Academy of Sciences, Akademgorodok, Krasnoyarsk, 660036 Russia
e-mail: belyaev@iph.krasn.ru

Received July 19, 2004

Abstract—The temperature dependence of the real part of the permittivity of a 4-*n*-pentyl-4-cyanobiphenyl liquid crystal was studied within a broad frequency range of 30–5000 MHz and in the temperature interval 20–60°C in the vicinity of the nematic–isotropic-liquid phase transition. It was established that the dispersion of the longitudinal component of the permittivity can be fitted well by a sum of two Debye terms with strongly differing relaxation times. The temperature and frequency dependence of the shorter relaxation time was determined for which the best fit between calculations and experiment was achieved. *© 2005 Pleiades Publishing, Inc.*

As is well known, the frequency dispersion and anisotropy of the permittivity of nematic liquid crystals (LCs) is described by the Debye equations, from which one extracts, in particular, the relaxation times associated with molecular rotation about the short and long axes. This description, however, agrees well with experiment only up to the frequencies at which the orientational region of dispersion ends. At higher frequencies, the dielectric spectra of LCs quite frequently exhibit an additional extended interval of dispersion that is connected with various intramolecular motions of alkyl fragments and seen against the background of librations of molecules about the equilibrium position. Particularly strong dispersion at frequencies above the orientational spectral region has been observed for the perpendicular component of permittivity, $\varepsilon'_\perp(\omega)$, in LCs of the *n*-CB series [1–5]. It was shown in [1–5] that the high-frequency part of the permittivity spectrum can be fitted fairly well with a Debye equation in which a continuous distribution of relaxation times within a certain interval is assumed.

The observed frequency dependence of the parallel component of permittivity, $\varepsilon'_\parallel(\omega)$, in the same LC series implies the existence of two separated dispersion regions each of which can be approximated by a Debye equation with its own relaxation time. The resulting dielectric spectrum of the LC can be fitted well by a sum of two Debye terms with different relaxation times and different relative weighted contributions. The two observed regions of dispersion are usually assigned to rotation of molecules about the short axis and about the long axis (low- and high-frequency relaxation, respectively). Both in the nematic and in the isotropic phase, the behavior of the low-frequency relaxation time τ_1 with temperature has been studied sufficiently well and is described by an exponential relation,

$$\tau_1 = \tau_0 \exp(-\Delta H/RT), \tag{1}$$

where τ_0 is the time corresponding to the inverse of the libration frequency, ΔH is the activation enthalpy, R is the gas constant, and T is the absolute temperature. For the nematic phase of the 5CB LC, we have ΔH = 66.3–66.7 kJ/mol, and for the isotropic phase, ΔH = 33.2 kJ/mol [5, 6].

As for the temperature dependence of the high-frequency relaxation time $\tau_2(t)$, determining its character from dielectric spectra in the nematic and isotropic phases is problematic. The problems can be traced in large measure to the difficulties entailed in obtaining dielectric spectra in the microwave frequency range at an accuracy high enough to permit their subsequent approximation. The only thing known presently is that the $\tau_2(t)$ relation is substantially weaker than $\tau_1(t)$.

The present study deals with the behavior of the 5CB LC in the parallel-ordered nematic phase, as well as in the isotropic state, within a broad range of frequencies and temperatures. The resonance technique employed in our study to measure $\varepsilon'(\omega)$ made it possible to accurately determine the temperature and frequency dependences of the permittivity, which were subsequently used to derive the behavior of the relaxation time τ_2 with temperature. To do this, the temperature dependences of $\varepsilon'(\omega)$ were measured in the range 20–60°C at several fixed frequencies in the range 30–5000 MHz. This was followed by numerical approximation of each of these dependences, which permitted us not only to determine the contribution of high-frequency dispersion to the general dielectric spectrum of the LC but also to establish the temperature and frequency dependences of the τ_2 relaxation time.

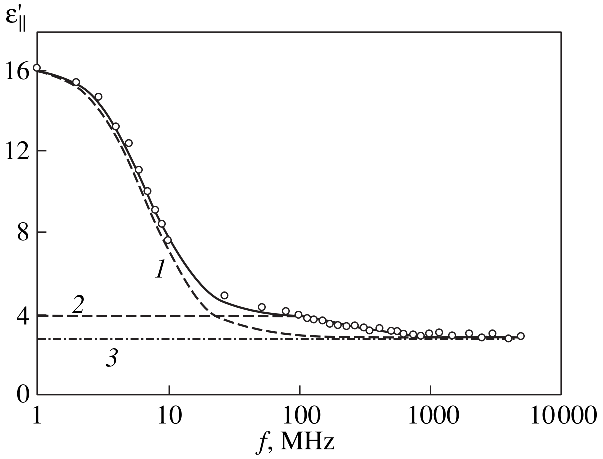

Fig. 1. Dispersion of the parallel permittivity of the 5CB LC at 30°C and its fitting (solid line) with a sum of two Debye terms differing in relaxation time. (*1*, *2*) Debye approximations with one, long or short, relaxation time, respectively, and (*3*) the n^2 level.

High-sensitivity resonance-type microstrip sensors, tuned to fixed frequencies in the above range, were fabricated. The LC was sandwiched between two metallic electrodes of a sensor in a ~100-μm-wide gap. Some design features of the sensors and the measurement technique employed are described in [7]. The absolute accuracy in determining $\varepsilon'(t, \omega)$ was not worse than ±0.02 throughout the frequency and temperature ranges covered. The sensors with LC samples were mounted in a thermostat, with the temperature varied within the range 20–60°C; in each measurement, the temperature was fixed to an accuracy of better than ±0.3°C. The director was oriented with respect to the direction of microwave electric field polarization by means of a dc magnetic field of 3 kOe.

The temperature dependences of the real part of permittivity $\varepsilon'(t)$, measured at fixed frequencies, was numerically fitted, as in [4, 5], using the relation (1)

$$\varepsilon'(t, \omega) - n^2(t) = \frac{\varepsilon'_0(t) - n^2(t)}{1 + \omega^2\tau_1^2(t)} g_1(t) + \frac{\varepsilon'_0(t) - n^2(t)}{1 + \omega^2\tau_2^2(t)} g_2(t), \tag{2}$$

where $\omega = 2\pi f$; $n(t)$ is the optical refractive index; $\varepsilon'_0(t)$ is the static permittivity; $\tau_1(t)$ and $\tau_2(t)$ are the low- and high-frequency Debye relaxation times, respectively; and $g_1(t)$ and $g_2(t)$ are the respective weighting factors satisfying the condition $g_1 + g_2 = 1$. The temperature dependences of $n(t)$, $\varepsilon'_0(t)$, and $\tau_1(t)$ for the 5CB LC are well known; they were taken from [8, 9]. The $\varepsilon'(t)$ dependence was calculated in the following way. When fitting $\varepsilon'(t)$ in the low-frequency domain (~30–40 MHz), where $(\omega\tau_2)^2 \ll 1$, Eq. (1) was used to find the weighting coefficient $g_2(t)$, which governs the static contribution of the high-frequency permittivity to the resulting spectrum. After this, the values of $\tau_2(t)$ were adjusted numerically in the high-frequency dispersion region to obtain the best fit of the calculation to experiment at all frequencies. The value of the optical permittivity $\varepsilon_\infty = n^2$ was determined at the beginning of the experiment at the highest possible sensor frequency (5 GHz) for the nematic ($n = 1.69$) and isotropic ($n = 1.59$) phases.

To illustrate the validity of this approach in our calculations, we first consider the frequency behavior of the real part of permittivity $\varepsilon'(f)$ of the 5CB LC measured at a fixed sample temperature $t = 30$°C (points in Fig. 1). The solid line is a fit of the dispersion using Eq. (2). Dashed line *1* in Fig. 1 is a numerical fit of the dielectric spectrum for $g_1 = 1$ and $g_2 = 0$. This line is seen to fit well to experiment only in the low-frequency region of dispersion. Dashed line *2* corresponds to fitting with $g_1 = 0$ and $g_2 = 0.08$; this graph, by contrast, agrees fairly well with the experimental data only in the high-frequency region of dispersion. Finally, curve *3* corresponds to $n^2 = 1.69$. The following parameters were used to fit the spectrum of the LC under study at $t = 30$°C: $\varepsilon'_0 = 16.4$, $n = 1.69$, $\tau_1 = 24$ ns, $\tau_2 = 0.7$ ns, $g_1 = 0.92$, and $g_2 = 0.08$. We readily see that the proposed fit reflects the existence of two relaxation processes in the crystal and is fairly close to the experimental data throughout the frequency range covered.

It is important to note that the frequency range was extended to 5000 MHz in measurements of the temperature dependence of the LC dielectric characteristics because of the substantial increase in the relaxation rate that was observed to occur in $\varepsilon'(f)$ spectra with an increase in temperature. The well-known decrease in the permittivity of LCs with an increase in frequency, which gives rise to an increased relative error of ε' measurement, precludes reaching the desired accuracy in fitting the dielectric spectra, which are usually taken at fixed temperatures. As a result, this approach makes it difficult to determine $\tau_2(t)$, and this is why we resorted instead to measuring the temperature dependences of the permittivity of LC samples at fixed frequencies.

Figure 2 displays, by way of illustration, three measured $\varepsilon'(t)$ dependences and their numerical fits for frequencies of 40, 260, and 5000 MHz. The solid lines plot a temperature dependence obtained using Eq. (2), and dashed lines *1* and *2* indicate the contributions to the observed dependence from the first and second terms in Eq. (2), respectively.

First, we consider the $\varepsilon'(t)$ dependence at different frequencies. For 40 MHz, the temperature dependence of ε' is governed primarily by the first term in Eq. (2) and reflects, accordingly, the temperature dependence of $\tau_1(t)$. The second, high-frequency region of ε' dispersion is distant enough (Fig. 1) to permit us to disregard the term $(\omega\tau_2)^2 \ll 1$ in Eq. (2). As a result, using the numerical technique, it is easy to obtain the $g_2(t)$ relation, which, when substituted into Eq. (2), provides the

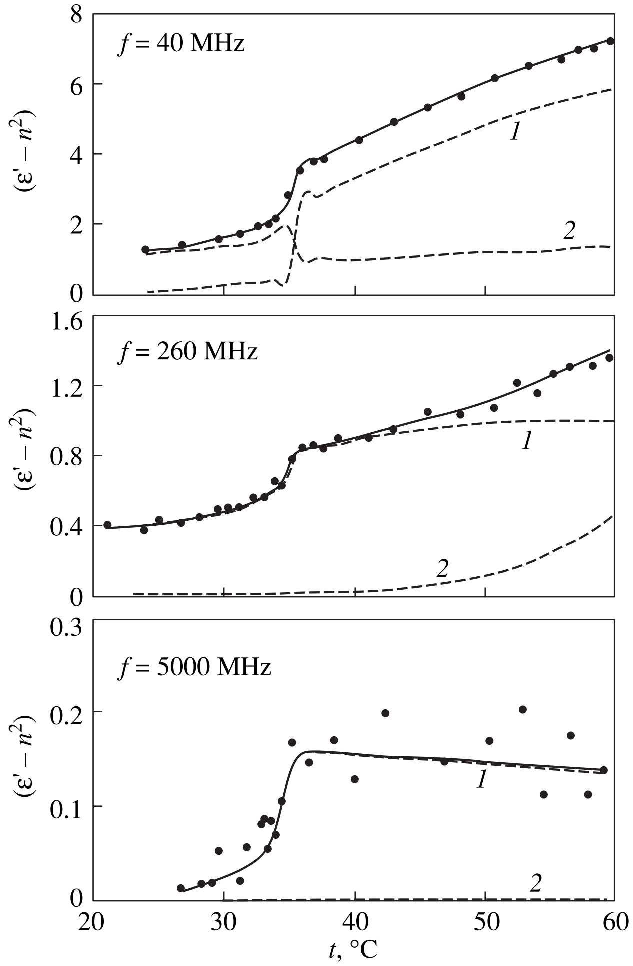

Fig. 2. Temperature dependences of the difference between the permittivity and the square of the refractive index measured at three frequencies. The solid line is a fit to a sum of two Debye terms differing in relaxation time. (*1*, *2*) Debye approximation with one, long or short, relaxation time, respectively.

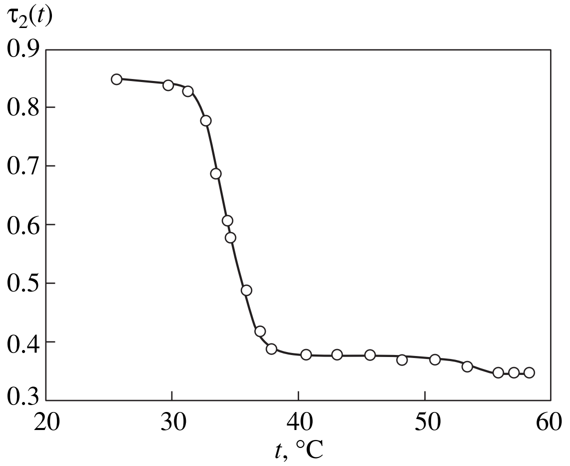

Fig. 3. Temperature dependence of the second (high-frequency) relaxation time measured at a frequency f = 260 MHz.

best fit to the experimental data. As the region of high-frequency dispersion is approached with increasing frequency (for instance, for the $\varepsilon'(t)$ relation measured at a frequency of 260 MHz), we see that the temperature dependence of $\varepsilon'(t)$ is governed primarily by the second term in Eq. (2), while the contribution from the first term becomes noticeable only at temperatures $t > 40$°C. Using the $g_2(t)$ relation thus obtained, we numerically adjust the temperature dependence of the relaxation time $\tau_2(t)$, which is plotted specifically for this case in Fig. 3. Interestingly, in both the nematic and the isotropic phase, the relaxation time is practically temperature-independent. This implies that high-frequency relaxation does not involve the overcoming of potential barriers by a molecule but rather is caused by the rotation of molecules or their fragments through small angles near the equilibrium position. However, the effect of liquid-crystal ordering of molecules on the relaxation time $\tau_2(t)$ is seen to be fairly large in the region of the transition from the nematic to an isotropic state.

When fitting the $\varepsilon'(T)$ relations with Eq. (2) at higher frequencies, it was established that the relaxation time τ_2 not only depends on temperature but is also a function of frequency, $\tau_2(t, \omega)$. For instance, at 5000 MHz, where the $\varepsilon'(t)$ dependence is determined fully by the second term in Eq. (2) (Fig. 2), the relaxation time is found to be shorter by nearly an order of magnitude than that for frequencies below 1000 MHz. Figure 4 presents the above result in a more instructive form by displaying the high-frequency relaxation time over broad ranges of temperatures and frequencies for the LC under study.

The fact that τ_2 depends on frequency indicates that high-frequency relaxation of the 5CB LC should be described by a dispersion relation with a spectrum of relaxation times lying within a certain interval. In this case, in fitting the high-frequency dispersion and the temperature dependence of $\varepsilon'(t)$ numerically, one can represent the last term in Eq. (2) in the form of the following simple empirical relation, which was proposed by Gavril'yak and Negami and is essentially a generalization of the Debye equation:

$$\varepsilon(t, \omega) = \frac{(\varepsilon'_0(t) - n^2(t))g_2(t)}{[1 + (i\omega\tau)^{1-\alpha}]^{\beta}}. \qquad (3)$$

In this expression, the coefficients α and β are numerical parameters characterizing a continuous relaxation-time distribution and τ is a time constant, which can be identified with an effective relaxation time. For $\alpha = 0$ and $\beta = 1$, the right-hand part of Eq. (3) is equivalent to the Debye equation with one relaxation time. For $\beta = 1$ and $\alpha \neq 0$, the right-hand part of Eq. (3) corresponds to the Cole–Cole model with a symmetric relaxation time

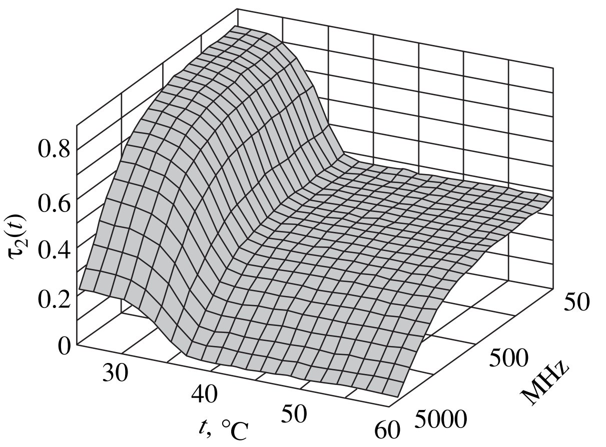

Fig. 4. Dependence of the second relaxation time on frequency and temperature.

distribution, and for $\alpha = 0$ and $\beta \neq 1$, to the Cole–Davidson model with an asymmetric distribution of relaxation times. In the latter case, by isolating the real part of Eq. (3), one can write the following equality describing the Cole–Davidson model:

$$\frac{\varepsilon'(t, \omega)}{[\varepsilon'_0(t) - n^2(t)]g_2(t)} = (\cos\theta)^{\beta}\cos\beta\theta, \qquad (4)$$

where $\tan\theta = \omega\tau$. We used this expression to fit the experimental data numerically and determined the parameter β (characterizing the extent to which the dielectric spectrum deviates from the Debye law) and the experimental temperature dependence of $\tau_2(t)$. The parameter β turned out to be ~0.5–0.7 for the nematic and isotropic LC phases. As already mentioned, the fact that β is not equal to unity is due to the asymmetric relaxation time distribution, which, in turn, should possibly be attributed to the contribution from various intramolecular motions, for example, vibrations of mobile alkyl groups of molecules, to the high-frequency permittivity of the LC under study. These motions are known to become particularly strongly manifest in the transverse component of the permittivity.

ACKNOWLEDGMENTS

This study was supported by the Russian Foundation for Basic Research, project no. 03-03-32470.

REFERENCES

1. P. G. Gummins, D. A. Dummur, and D. A. Laidler, Mol. Cryst. Liq. Cryst. **30**, 109 (1975).
2. B. R. Ratna and R. Shashidar, Mol. Cryst. Liq. Cryst. **42**, 185 (1977).
3. J. M. Wacrenier, C. Druon, and D. Lippens, Mol. Phys. **43** (1), 97 (1981).
4. B. A. Belyaev, N. A. Drokin, V. F. Shabanov, and V. N. Shepov, Fiz. Tverd. Tela (St. Petersburg) **45** (3), 567 (2003) [Phys. Solid State **45**, 598 (2003)].
5. B. A. Belyaev, N. A. Drokin, V. F. Shabanov, and V. A. Baranova, Fiz. Tverd. Tela (St. Petersburg) **46** (3), 554 (2004) [Phys. Solid State **46**, 574 (2004)].
6. B. Urban, B. Gestblom, and A. Wurflinger, Mol. Cryst. Liq. Cryst. **331**, 113 (1999).
7. B. A. Belyaev, N. A. Drokin, and V. N. Shepov, Zh. Tekh. Fiz. **65** (2), 189 (1995) [Tech. Phys. **40**, 216 (1995)].
8. D. A. Dunmur, M. R. Manterfield, W. H. Miller, and J. K. Dunleavy, Mol. Cryst. Liq. Cryst. **45**, 127 (1978).
9. E. M. Aver'yanov, V. A. Zhuĭkov, V. F. Shabanov, and P. V. Adomenas, Kristallografiya **27** (2), 333 (1982) [Sov. Phys. Crystallogr. **27**, 210 (1982)].

Translated by G. Skrebtsov

Physics of the Solid State, Vol. 47, No. 4, 2005, pp. 769–771. Translated from Fizika Tverdogo Tela, Vol. 47, No. 4, 2005, pp. 742–744.
Original Russian Text Copyright © 2005 by Bogomolov, Kurdyukov, Parfen'eva, Smirnov, Misiorek, Jezowski.

FULLERENES AND ATOMIC CLUSTERS

Low-Temperature Thermal Conductivity of an Opal + Epoxy-Resin Nanocomposite

V. N. Bogomolov*, D. A. Kurdyukov*, L. S. Parfen'eva*,
I. A. Smirnov*, H. Misiorek, and A. Jezowski****

**Ioffe Physicotechnical Institute, Russian Academy of Sciences, Politekhnicheskaya ul. 26, St. Petersburg, 194021 Russia*
e-mail: igor.smirnov@pop.ioffe.rssi.ru
***Institute of Low-Temperature and Structural Research, Polish Academy of Sciences, Wrocław, 50-950 Poland*

Received June 30, 2004

Abstract—The thermal conductivity of an opal + epoxy-resin nanocomposite under 100% filling of first-order opal voids by epoxy resin was measured in the range 5–100 K. For $T < T_0$ (T_0 is the temperature at which the thermal conductivity of epoxy resin becomes equal to that of amorphous SiO_2 opal spheres, with inclusion of their porosity associated with second- and third-order voids), the thermal conductivity of the opal + epoxy-resin nanocomposite undergoes a sharp decrease, which is qualitatively accounted for by the appearance of Kapitsa heat resistance at the contacts between the amorphous opal spheres and epoxy resin. © *2005 Pleiades Publishing, Inc.*

This communication reports on the concluding stage in our studies of the thermal conductivity of opal + epoxy-resin nanocomposites [1, 2].

Let us recall the main features of the unusual crystal structure of opal [3, 4], which knowledge will be needed to analyze the results obtained.

The crystal structure of opal is made up of close-packed spheres of amorphous SiO_2. The opals used in our experiment had spheres ~2000–2500 Å in diameter (first-order spheres). Each of these spheres is an array of close-packed spheres of a smaller size, ~300–400 Å (second-order spheres), which, in turn, are formed of close-packed spherical particles ~100 Å in size (third-order spheres).

An array of close-packed spheres has octahedral and tetrahedral voids interconnected by horn-shaped channels. Depending on the actual order number of the amorphous SiO_2 spheres, these voids can likewise be subdivided into voids of first, second, and third order. The total theoretical porosity of opal is 59%.

Actually, the porosity of the opal single crystals grown by us added up to ~46% (because of partial sintering of the second- and third-order spheres) [5]. The relative volume of the first-order voids was ~26%. The amorphous SiO_2 spheres and first-order voids of the opal form face-centered cubic lattices, whose parameters for the opal used by us were ~3000–4000 Å. The first-order voids of the opal can be filled by metals, semiconductors, or insulators using various methods (chemical methods, pressure injection from a melt, or impregnation of a sample with a filler material) to form (in the case of 100% filling of first-order voids) regular three-dimensional nanocomposites, which can be considered a system made up of two nested regular lattices (an opal and a filler lattice) with giant parameters and giant "atomic" masses.

It was shown in [6] that, within the temperature interval 5–300 K, the thermal conductivity κ of single crystals of synthetic opals is governed primarily by the quality of contacts between the amorphous SiO_2 spheres (i.e., by contact heat resistance between these spheres). The more perfect the crystal structure of the opal (up to the limit where the contacts between all spheres are strictly identical and approach point contacts), the lower its thermal conductivity.

Assuming the structure described above of an opal-based nanocomposite, the heat flux through it will propagate over two parallel channels, one of which is the spheres of amorphous SiO_2 making up the opal and the other is "chains" of the filler material: filled tetrahedral (octahedral) void–filled horn-shaped channel–filled tetrahedral (octahedral) void–filled horn-shaped channel, and so on.

The following three variants are conceivable: (1) $\kappa(\text{filler}) \gg \kappa(\text{opal matrix})$, (2) $\kappa(\text{filler}) \ll \kappa(\text{opal matrix})$, and (3) $\kappa(\text{filler}) \approx \kappa(\text{opal matrix})$.

The first variant is typical of opal + HgSe [6] and opal + NaCl [7] nanocomposites, in which the heat flux propagates predominantly over chains of the filler material. At low temperatures (5–20 K), the heat conductivities of HgSe and NaCl contained in first-order opal voids are determined by boundary scattering of phonons in the bottlenecks of horn-shaped channels (~100 Å in diameter) interconnecting the filled octahedral (tetrahedral) opal voids. In this particular case, the phonon mean free path l is much larger than the bottleneck size.

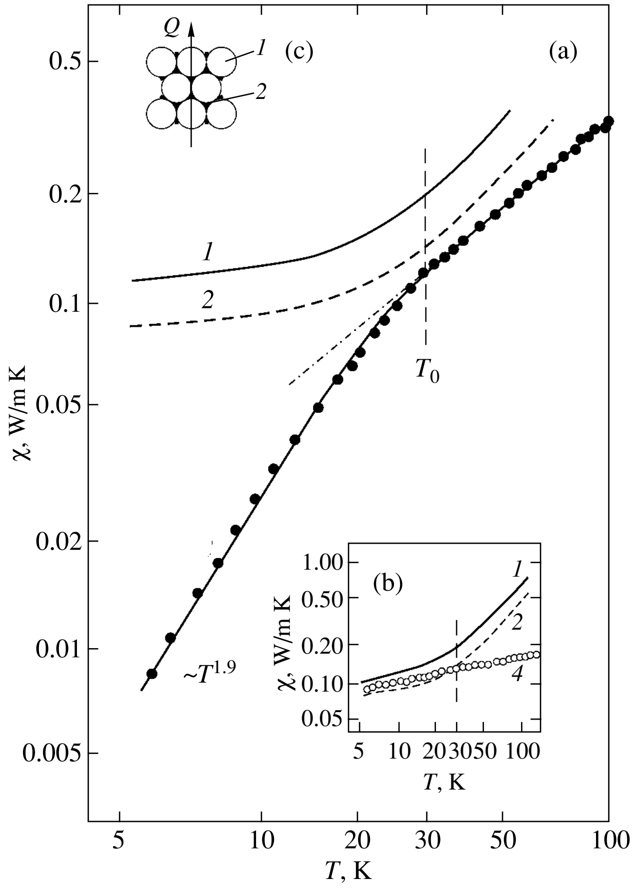

Fig. 1. (a) Thermal conductivities of (*1*) fused quartz [9], (*2*) amorphous SiO_2 spheres calculated with allowance for their porosity due to second- and third-order voids, and (*3*) an opal + 100% epoxy-resin nanocomposite. (b) Thermal conductivities of (*4*) epoxy resin [2], (*1*) fused quartz, and (*2*) amorphous opal SiO_2 spheres (κ_0). (c) Structure of an opal + epoxy-resin nanocomposite (schematic): (*1*) amorphous opal SiO_2 spheres with thermal conductivity κ_0 and (*2*) epoxy resin; *Q* indicates the direction of heat flux in the nanocomposite.

At high temperatures (up to 300 K), *l* becomes smaller than the dimensions of the horn-shaped channels. The thermal conductivity of a filler material in this case is lower than that of the corresponding bulk crystalline material because of the presence of specific defects (vacancy clusters and breaks in the filler lattice, surface defects, defects originating from strains in the filler matrix, etc.), which are absent in the bulk materials.

The second variant applies to opal + epoxy-resin nanocomposites for $T > 100$ K [2]. In this case, the heat flux generated to measure the thermal conductivity of a nanocomposite propagates primarily over the matrix (amorphous SiO_2 spheres), so the thermal conductivity of the nanocomposite is close to that of the opal matrix.

The third variant is assumed to take place in an opal + epoxy-resin nanocomposite for $T < 100$ K. This is the subject of the present work.

An opal + epoxy-resin nanocomposite based on single-crystal opal was prepared using the technique described in [1, 2]. This nanocomposite had 100% filling of first-order voids by epoxy resin (opal + 100% epoxy resin).

The thermal conductivity of the nanocomposite was studied in the temperature interval 5–300 K on a setup similar to that employed in [8]. The thermal conductivity measured in our experiment is that of the crystal lattice.

The data reported in [2] suggest that the thermal conductivity of epoxy resin should be close to that of fused quartz at temperatures below 100 K.

Epoxy resin injected into first-order voids of the opal is in contact with the amorphous SiO_2 spheres, which have a porosity of 20% in our case due to opal second- and third-order voids.

Figure 1a displays the thermal conductivity of amorphous quartz [9] and of amorphous opal SiO_2 spheres (κ_0) corrected for the above porosity. The calculation was conducted using the relation of Litovskiĭ [10]:

$$\kappa_0 = \kappa_{SiO_2}(1-p)\sqrt{1-p}, \tag{1}$$

where *p* is the porosity, taken to be 0.2.

Figure 1a also shows experimental results obtained for the thermal conductivity of the opal + 100% epoxy-resin nanocomposite (κ_{comp}), and Fig. 1b shows our data for the thermal conductivity of the epoxy resin (κ_{epox}) taken from [2] and, for comparison, the results on the thermal conductivity of fused quartz and amorphous opal SiO_2 spheres.

As seen from Fig. 1b, the thermal conductivity of epoxy resin at $T < 30$ K approaches that of amorphous opal SiO_2 spheres (κ_0).

In these conditions, one would expect κ_{comp} to increase with decreasing temperature for $T < 30$ K and finally become equal to the thermal conductivity of the amorphous opal SiO_2 spheres.

However, experiment revealed a different pattern. At $T \approx T_0$, the thermal conductivity of the nanocomposite exhibits not an increase but rather a fairly sharp decrease in the thermal conductivity of the nanocomposite (Fig. 1a).[1]

The question arises as to what mechanism of phonon scattering in the composite is responsible for this behavior of $\kappa_{comp}(T)$.

If $\kappa_0 \approx \kappa_{epox}$, the heat flux *Q* will be distributed uniformly over the nanocomposite sample (Fig. 1c) and cross the boundaries between the epoxy resin and amorphous opal SiO_2 spheres. At low temperatures, the behavior of the thermal conductivity of the composite

---

[1] The temperature dependence of the thermal conductivity of the opal single crystal used as a matrix for the opal + epoxy-resin nanocomposite has no breaks (including in the temperature region near 30 K).

may be significantly influenced by the Kapitsa heat resistance r_K [11–13], which arises at the interface between two media in a nanocomposite due to acoustic mismatch.

According to theory [11–13], $r_K \sim T^{-3}$ and is proportional to the ratio of the acoustic impedances of these media, $\bar{v}\rho$ ($\bar{v}$ is the average velocity of sound, ρ is the density of the material).

The larger the ratio of the matrix to filler impedances, the larger the value of r_K.

The ratio of the impedance of amorphous quartz to that of epoxy resin is 4.28 [14–16]. This is a fairly large value. The ratio of the impedance of amorphous quartz to that of NaCl, for instance, is only 1.449 [15–17].

Rather than scaling as T^{-3}, our experimental temperature dependence of r_K is substantially weaker, $r \sim T^{-1.9}$. The same relation for $r(T)$ was obtained in [13] by analyzing the data on the epoxy resin + copper composite in terms of the model of Kapitsa heat resistance.

Thus, in our case, the experimental results obtained for the opal + epoxy-resin nanocomposite also agree only qualitatively with the model of Kapitsa heat resistance.

ACKNOWLEDGMENTS

This study was carried out as part of a bilateral agreement between the Russian and Polish Academies of Sciences and was supported by the Russian Foundation for Basic Research (project no. 02-02-17657) and the Polish State Committee on Research (KBN; project no. 3 T08A 054 26).

REFERENCES

1. V. N. Bogomolov, L. S. Parfen'eva, L. M. Sorokin, I. A. Smirnov, H. Misiorek, A. Jezowski, and J. Hutchison, Fiz. Tverd. Tela (St. Petersburg) **44** (6), 1017 (2002) [Phys. Solid State **44**, 1061 (2002)].
2. V. N. Bogomolov, N. F. Kartenko, D. A. Kurdyukov, L. S. Parfen'eva, I. A. Smirnov, N. V. Sharenkova, H. Misiorek, and A. Jezowski, Fiz. Tverd. Tela (St. Petersburg) **45** (5), 911 (2003) [Phys. Solid State **45**, 957 (2003)].
3. V. G. Balakirev, V. N. Petranovskiĭ, S. G. Romanov, and L. A. Samoĭlovich, Kristallografiya **38** (3), 111 (1993) [Crystallogr. Rep. **38**, 348 (1993)].
4. V. N. Bogomolov and T. M. Pavlova, Fiz. Tekh. Poluprovodn. (St. Petersburg) **29** (5/6), 826 (1995) [Semiconductors **29**, 428 (1995)].
5. V. V. Ratnikov, Fiz. Tverd. Tela (St. Petersburg) **39** (5), 956 (1997) [Phys. Solid State **39**, 856 (1997)].
6. V. N. Bogomolov, N. F. Kartenko, D. A. Kurdyukov, L. S. Parfen'eva, V. V. Popov, L. M. Sorokin, I. A. Smirnov, H. Misiorek, A. Jezowski, and J. Hutchison, Fiz. Tverd. Tela (St. Petersburg) **45** (3), 535 (2003) [Phys. Solid State **45**, 566 (2003)].
7. V. N. Bogomolov, N. F. Kartenko, D. A. Kurdyukov, L. S. Parfen'eva, I. A. Smirnov, N. V. Sharenkova, H. Misiorek, J. Mucha, and A. Jezowski, Fiz. Tverd. Tela (St. Petersburg) **46** (10), 1893 (2004) [Phys. Solid State **46**, 1961 (2004)].
8. A. Jezowski, J. Mucha, and G. Pompe, J. Phys. D: Appl. Phys. **20**, 1500 (1987).
9. *Thermal Conductivity of Solids: Handbook*, Ed. by A. S. Okhotin (Énergoatomizdat, Moscow, 1984) [in Russian].
10. E. Ya. Litovskiĭ, Izv. Akad. Nauk SSSR, Neorg. Mater. **16** (3), 559 (1980).
11. W. A. Little, Can. J. Phys. **37**, 334 (1959).
12. J. A. Katerberg, C. L. Reynolds, and A. C. Anderson, Phys. Rev. B **16** (2), 673 (1977).
13. C. Schmidt, Cryogenics **15**, 17 (1975).
14. K. W. Garret and H. M. Rosenberg, J. Phys. D: Appl. Phys. **7**, 1247 (1974).
15. H. J. McSkimin, J. Appl. Phys. **24** (8), 988 (1953).
16. J. J. Freeman and A. C. Anderson, Phys. Rev. B **34** (8), 5684 (1986).
17. *Acoustic Crystals*, Ed. by M. P. Shaskol'skaya (Nauka, Moscow, 1982) [in Russian].

Translated by G. Skrebtsov

Physics of the Solid State, Vol. 47, No. 4, 2005, pp. 772–777. Translated from Fizika Tverdogo Tela, Vol. 47, No. 4, 2005, pp. 745–750.

Investigation of the Initial Stages of Defect Formation in Carbon Nanotubes under Irradiation with Argon Ions

M. M. Brzhezinskaya*, E. M. Baĭtinger*, V. V. Shnitov, and A. B. Smirnov****

** Chelyabinsk State Pedagogical University, pr. Lenina 69, Chelyabinsk, 454080 Russia*
e-mail: brzhezinskaya@fromru.com
*** Ioffe Physicotechnical Institute, Russian Academy of Sciences, Politekhnicheskaya ul. 26, St. Petersburg, 194021 Russia*

Received June 3, 2004

Abstract—The formation of defects in carbon nanotubes under irradiation with argon ions is investigated. The π plasmons generated in single-walled and multiwalled carbon nanotubes are examined using electron energy-loss spectroscopy. In the course of experiments, the supramolecular structure of nanotubes is stepwise modified by an argon ion beam (the maximum irradiation dose is 360 μC/cm^2). The content of argon ions implanted into a nanotube structure is controlled using Auger electron spectroscopy. The effect of ion irradiation on the π-plasmon energy E_π and on the half-width at half-maximum δE of the π-plasmon spectrum is determined experimentally. An expression relating the above quantities and the concentration of implanted argon is derived. It is shown that the formation of defects under ion irradiation is a discontinuous process occurring in a stepwise manner. A qualitative phenomenological interpretation is proposed for the experimentally revealed decrease in the π-plasmon energy E_π and for its attendant broadening of the π-plasmon spectrum. The assumption is made that the microscopic mechanism of the observed phenomena is associated with the narrowing of the energy π subbands in the electric field of charged defects generated by ions. © *2005 Pleiades Publishing, Inc.*

1. INTRODUCTION

Carbon nanotubes synthesized in the early 1990s are promising materials for use in nanoelectronics [1]. Nanotubes and their fragments have a symmetric cylindrical structure that, in principle, makes it possible to fabricate functional nonlinear nanoelectronic elements, such as diodes and transistors [2]. However, the technological nanoscale manipulations required for the formation of a specially modified supramolecular structure in nanotubes [3] are fairly complicated and necessitate the use of expensive equipment [4]. Ion bombardment is a relatively simple method that provides a means not only for successfully modifying the geometric structure of nanotubes but also for purposefully changing their physical properties [5].

Ion bombardment has a twofold effect on the structure of carbon nanotubes; namely, it brings about the formation of point and extended defects and the intercalation of ions into the intratubular and intertubular spaces.

Technologically, noble-gas ions with mean energies ranging from 0.5 to 10.0 keV are found to be most suitable for the above purposes. The use of these ions makes it possible not only to exert a destructive effect on the walls of carbon nanotubes (i.e., to produce point defects and to deform nanotubes) but also, under specific conditions, to weld the adjacent nanotubes due to the formation of strong covalent bonds between the knocked-on carbon atoms and the nanotube walls [6].

In the present work, we proposed using π plasmons (collective longitudinal oscillations of π electrons of carbon atoms) as an efficient tool for analyzing the specific features of the nanoscopic processes occurring under ion irradiation of carbon nanotubes.

Even the first investigations of the plasma oscillations in nanotubes revealed that the location and the half-width at half-maximum of the plasmon peak in the spectra of the nanotubes depend on their diameter and the number of walls [7].

The lifetime of a quasi-one-dimensional plasmon in a finite cylindrical carbon system is determined by the length, the diameter, and the degree of perfection of this system. It is these characteristics that must be known exactly when performing ion irradiation of carbon nanotubes. In carbon nanotubes, π plasmons generated by interband transitions of π electrons have an energy ranging from 5.0 to 6.5 eV [7–12]. This range of π-plasmon energies is relatively wide, because, apart from the experimental conditions (excitation energy, experimental geometry), the properties of the carbon nanotubes themselves affect the plasmon spectrum.

In this work, the changes in the π-plasmon energy and in the half-width at half-maximum of the plasmon spectrum were used to analyze the initial stages of the destruction of single-walled and multiwalled nanotubes in the course of their stepwise irradiation with argon ions at an energy of 1 keV. The experiments were performed using reflection electron energy-loss spectroscopy (the mean energy was 1 keV).

Section 2 of this paper describes the preparation of samples and the experimental technique. Section 3 presents the main experimental results. In Section 4, these results are discussed.

2. SAMPLE PREPARATION AND EXPERIMENTAL TECHNIQUE

The electron energy-loss spectra were measured with samples of single-walled and multiwalled carbon nanotubes applied to a ceramic substrate. A condensate was rubbed into the substrate until a 50-μm-thick film uniform in consistency and color was obtained. In order to prevent charging of the sample, the condensate was uniformly applied over the entire surface of the substrate. This ensured proper contact between the condensate and the metal parts of the sample holder. The absence of charging was confirmed by the fact that the position of the Auger line (which changed in the course of the experiments) was independent of the electric current of primary electrons or the time required to measure the electron energy-loss spectrum.

Multiwalled nanotubes were produced through carbon arc plasma deposition [13]. The mean diameter of these nanotubes was approximately equal to 10 nm, and their length was of the order of 10 μm. Single-walled nanotubes were prepared by electric-arc synthesis [14, 15]. Their diameter varied from 1.2 to 1.6 nm, and the length fell in the range 1–10 μm.

The surface composition of the studied samples was determined using Auger electron spectroscopy immediately prior to the experiment. The surface of the initial samples contained 98.0 at. % C and from 1.0 to 1.7 at. % O. The multiwalled nanotubes also contained nitrogen and sulfur in small amounts (0.7 at. %).

Irradiation of the samples with Ar^+ ions (energy, 1 keV; current density $j = 0.75$ μC/cm^2 s) and measurements of the electron energy-loss spectra (beam energy, 1 keV; half-width at half-maximum, 0.5 eV) were performed in an ultrahigh-vacuum chamber (10^{-9} Torr) after heating and holding of the samples at a specified temperature for ≈70 h.

The electron energy-loss spectra were recorded at the Ioffe Physicotechnical Institute (Russian Academy of Sciences, St. Petersburg, Russia). The experiments were carried out using reflection electron energy-loss spectroscopy on a multichannel electron spectrometer equipped with a conical energy analyzer (the experimental details were described, for example, in [16]) for multiwalled nanotubes and on a Perkin-Elmer PHI-5500 electron spectrometer for single-walled nanotubes. The reflection electron energy-loss spectra were measured in specular geometry: the angle of incidence of the electron beam on the surface was 45°–50°, and the aperture of the energy analyzer was approximately equal to 12°. When the transmission energy of the analyzer was 10–30 eV, the absolute energy resolution for inelastically scattered electrons was equal to 0.1–0.2 eV.

The differential Auger electron spectra were measured at a constant absolute energy resolution of 0.6 eV after each stage of irradiation in order to determine the concentration of argon deposited on the surface. In the measurements of the Auger electron spectra, the energy of primary electrons was equal to 2.5 keV. The argon concentration was estimated from the standard relationship

$$C_{\mathrm{Ar}} = \frac{I_{\mathrm{Ar}}}{S_{\mathrm{Ar}}} \Big/ \left(\frac{I_{\mathrm{C}}}{S_{\mathrm{C}}} + \frac{I_{\mathrm{Ar}}}{S_{\mathrm{Ar}}} \right), \qquad (1)$$

where I_{C} and I_{Ar} are the linear intensities of the C and Ar Auger lines, respectively, and S_{C} and S_{Ar} are the relative Auger excitation cross sections of the C and Ar *KLL* lines, respectively.

Irradiation of the samples with argon ions was performed in a stepwise manner at short time intervals t. The total irradiation dose was determined from the expression $Q = jt$.

The determination of the position E_π and the half-width at half-maximum δE of the plasmon peak is illustrated in the inset to Fig. 1. Initially, the background of inelastically scattered electrons (the dashed line in the inset to Fig. 1) was subtracted, and then the quantities E_π and δE were determined.

3. EXPERIMENTAL RESULTS

This section reports on the experimental data on the influence of argon ion irradiation on the properties of π plasmons in single-walled and multiwalled carbon nanotubes according to electron energy-loss spectroscopy.

The experimental electron energy-loss spectra in the energy loss range 0–12 eV are shown in Fig. 1. It can be seen from this figure that an increase in the irradiation dose Q leads to a shift in the position E_π of the plasmon peak toward the low-energy range by 0.9 eV for single-walled nanotubes and by 1.2 eV for multiwalled nanotubes. This shift is accompanied by a broadening of the π-plasmon spectrum.

The dependence of the π-plasmon energy E_π on the ion irradiation dose Q for single-walled nanotubes is depicted in Fig. 2.

Figure 2 illustrates the character of the decrease in the π-plasmon energy with an increase in the irradiation dose Q: the π-plasmon energy E_π decreases most drastically in the initial stage of irradiation when the dose Q is not very high (i.e., when it is less than 100 μC/cm^2). In the inset to Fig. 2, the same experimental data are presented on a log–log scale. The magnitude of the slope of the experimental straight line on the log–log scale is determined to be $\eta = 0.95$. Therefore, by setting the slope close to –1, we can make the inference that the dependence of the π-plasmon energy on the irradiation dose Q can be empirically represented by the simple hyperbolic function

$$E_\pi(Q) = \mathrm{const}/Q. \qquad (2)$$

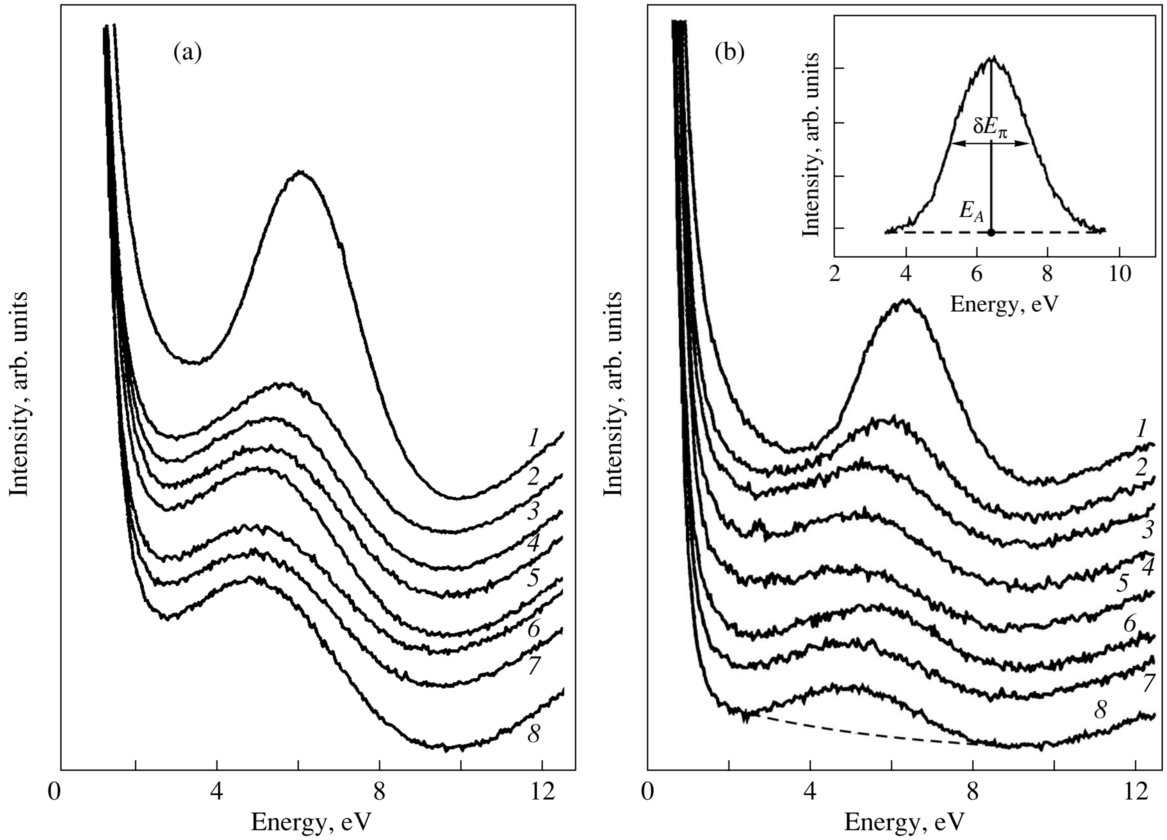

Fig. 1. Experimental electron energy-loss spectra of (a) single-walled and (b) multiwalled carbon nanotubes: (*1*) the initial spectrum and the spectra of the samples exposed to argon ion irradiation at doses Q = (*2*) 9, (*3*) 27, (*4*) 36, (*5*) 72, (*6*) 144, (*7*) 216, and (*8*) 360 μC/cm^2. The inset illustrates the determination of the π-plasmon energy E_π and the half-width at half-maximum δE of the π-plasmon peak.

As was noted above, the decrease in the π-plasmon energy is accompanied by the broadening of the plasmon spectrum. The half-width at half-maximum of the plasmon spectrum increases only slightly (from 2.7 to 3.4 eV). This increase amounts approximately to 25% of the initial half-width at half-maximum. However, this change in the half-width at half-maximum exceeds the experimental error. The broadening of the plasmon peak is nonlinear with respect to the irradiation dose; namely, the π-plasmon peak is considerably more broadened in the initial stage of ion irradiation at low doses Q.

The experimental results obtained for multiwalled nanotubes are presented in Fig. 3 (see also our previous paper [16]). The experiments performed for multiwalled nanotubes revealed that, with an increase in the irradiation dose, the π-plasmon energy E_π also decreases in the initial stage of ion irradiation. The empirical dependence of the plasmon energy on the ion irradiation dose for multiwalled nanotubes appears to be more complex. The difference in the character of the decrease in the plasmon energy E_π with an increase in the irradiation dose Q is most likely associated with the difference in the absorption of argon ions by inner carbon walls in the multiwalled nanotubes. It can be seen from Fig. 3b that, as in the case of the single-walled nanotubes, the decrease in the plasmon energy E_π is accompanied by the broadening of the plasmon peak. It is worth noting that this broadening is also most pronounced in the initial stage of ion irradiation.

The chemical composition of the surface of the multiwalled and single-walled carbon nanotubes under investigation was determined by Auger electron spectroscopy in the course of ion irradiation. It is revealed that an increase in the ion irradiation dose Q leads to an increase in the concentration of argon deposited on the surface of the carbon nanotube samples. As can be seen from the experimental data presented in Fig. 4, the concentration of argon deposited on the nanotube surface correlates with the irradiation dose. At a relatively low dose (i.e., when it is less than 100 μC/cm^2), argon is adsorbed at a rather high rate. As the irradiation dose increases, the process is retarded and the argon concentration tends to saturation. In Fig. 4, the range of relatively low doses at which argon is adsorbed at a high rate is conventionally separated from the range of high doses by a vertical dashed line.

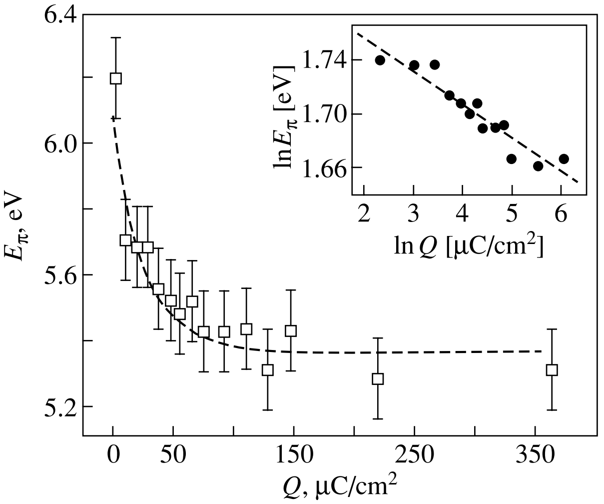

Fig. 2. Dependence of the π-plasmon energy E_π on the dose of irradiation with argon ions for single-walled carbon nanotubes. The inset shows the same dependence on a log–log scale.

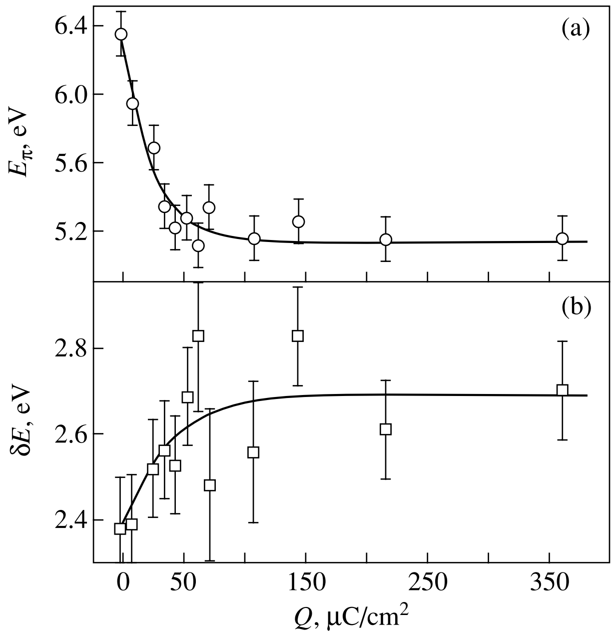

Fig. 3. Dependences of (a) the π-plasmon energy E_π and (b) the half-width at half-maximum δE of the π-plasmon peak on the dose of irradiation with argon ions for multiwalled carbon nanotubes.

4. DISCUSSION

4.1. Irradiation of the samples with argon ions at mean energies favors the generation of vacancy defects (which, in turn, bring about the transformation of two hexagons into pentagon–heptagon pairs [17] in walls of carbon nanotubes) and the formation of clusters composed of knocked-on carbon atoms inside the nanotubes and in the intertubular space [6]. Of course, this is accompanied by the intercalation of argon atoms into the intratubular and intertubular spaces. Consequently, there occur inelastic nanotube deformations that manifest themselves in bending of the nanotubes, a change in their diameter, etc. These deformations are schematically shown in Fig. 5. Probably, argon atoms are attached to defect sites. In this case, their concentration at the surface approximately corresponds to the concentration of defects generated under ion irradiation. If the interatomic distances in nanotube walls differ only slightly from those in a graphene sheet (0.142 nm), the concentration of carbon atoms at the surface of carbon nanotubes is equal to 4×10^{15} cm^{-2}. When the argon concentration amounts to 4–5% of the carbon concentration (see the data presented in Fig. 4), it is easy to verify that the surface concentration of argon atoms is approximately equal to 2×10^{14} cm^{-2}. The mean interdefect distance estimated from this maximum concentration of argon atoms in the case of a uniform distribution of defects is approximately equal to 10–15 interatomic distances, i.e., 1.5–2.0 nm. In Fig. 5, this distance is designated as l. Note that the distance l is considerably shorter than the de Broglie wavelength of π plasmons $L_0 \approx 200$ nm.

As follows from the experimental data, the modification of both multiwalled and single-walled nanotubes by an argon ion beam is retarded at an argon concentration of 10^{14} cm^{-2}. The irradiation dose corresponding to saturation is marked by the vertical dashed line in Fig. 4

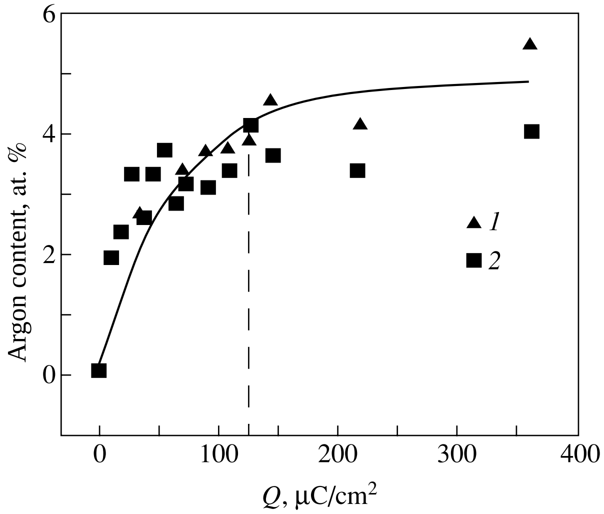

Fig. 4. Dependences of the argon content at the nanotube surface on the dose of irradiation with argon ions for (*1*) multiwalled and (*2*) single-walled carbon nanotubes.

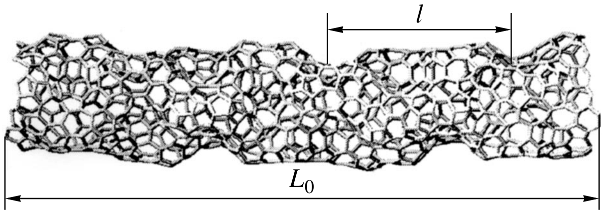

Fig. 5. Schematic drawing of a deformed single-walled carbon nanotube.

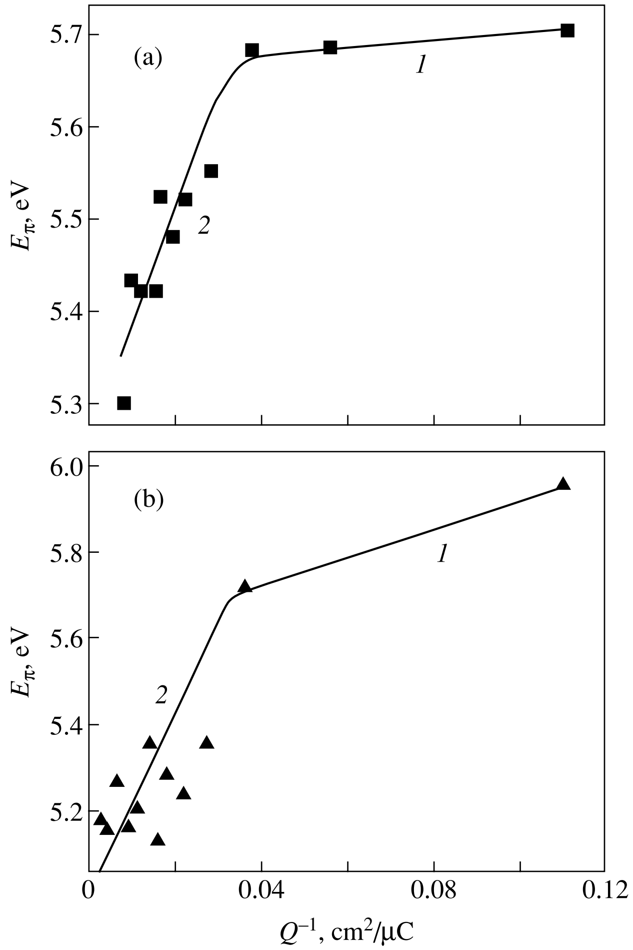

Fig. 6. Dependences of the π-plasmon energy on the reciprocal of the irradiation dose Q^{-1} for (a) single-walled and (b) multiwalled carbon nanotubes.

and is approximately equal to 100–150 μC/cm^2. Let us assume that the argon ions are singly charged. Hence, the total number of singly charged argon ions that pass through the surface of the compact sample at the aforementioned dose is equal to (5–7) × 10^{14} ions/cm^2. Comparison of this number of ions with the number of formed defects shows that, on the average, only one out of every 20–25 argon ions efficiently interacts with the surface.

4.2. The approximation of the experimental dependence of the π-plasmon energy E_π on the irradiation dose Q by hyperbolic function (2) suggests that the plasmon energy E_π should depend linearly on the reciprocal of the irradiation dose Q^{-1}. The experimental data (closed symbols) in the Q^{-1}–E_π coordinates are presented in Fig. 6. It turns out that the linear dependence of the plasmon energy E_π on the reciprocal of the irradiation dose exhibits a kink at $Q^{-1} \approx$ 0.035–0.04 cm^2/μC. This corresponds to the irradiation dose Q = 25–30 μC/cm^2. The solid lines in Fig. 6 are described by the following empirical relationships: for single-walled nanotubes,

$$E_\pi\ (\mathrm{eV}) = 5.66\ \mathrm{eV} + \alpha_1/Q, \quad Q < 30\ \mu\mathrm{C/cm}^2, \quad (3a)$$

$$E_\pi\ (\mathrm{eV}) = 5.25\ \mathrm{eV} + \alpha_2/Q, \quad Q > 30\ \mu\mathrm{C/cm}^2; \quad (3b)$$

for multiwalled nanotubes,

$$E_\pi\ (\mathrm{eV}) = 5.6\ \mathrm{eV} + \beta_1/Q, \quad Q < 30\ \mu\mathrm{C/cm}^2, \quad (4a)$$

$$E_\pi\ (\mathrm{eV}) = 5\ \mathrm{eV} + \beta_2/Q, \quad Q > 30\ \mu\mathrm{C/cm}^2. \quad (4b)$$

The ratios between the slopes of two linear portions are estimated as follows: $\alpha_2/\alpha_1 \approx 30$ [relationships (3a), (3b)] for single-walled nanotubes and $\beta_2/\beta_1 \approx 6$ [relationships (4a), (4b)] for multiwalled nanotubes. This implies that, in the initial stage of ion irradiation, the defect formation is hindered and occurs at a low rate. Only when the concentration of defects reaches a critical value is this process accelerated by more than one order of magnitude for single-walled nanotubes and by a factor of approximately six for multiwalled nanotubes.

The specific features of this phenomenon call for further comprehensive experimental investigation at different energies of bombarding ions. However, the slow formation of defects in initial portions *1* of the dependences $E_\pi(Q^{-1})$ (Fig. 6) can be qualitatively explained by the recombination of knocked-on atoms and vacancies [18]. Fast channeling of a knocked-on carbon atom along the nanotube leads to a rather easy recombination with any of the already existing vacancies.

The slow accumulation of deformations and the appearance of contractions in deformed regions (see the schematic drawing of a deformed single-walled carbon nanotube in Fig. 5) are accompanied by the acceleration of the formation and growth of carbon clusters in the intratubular and intertubular spaces. This leads to the acceleration of the defect formation, which manifests itself in an increase in the slope of portions *2* in the dependences $E_\pi(Q^{-1})$ (Fig. 6). Possibly, the revealed features of the defect formation in the nanotubes are indirectly confirmed by the ratio $\beta_1/\alpha_1 \approx 8$ [see relationships (3a), (3b), (4a), (4b)]. This ratio indicates that, even in the initial stage, the defect formation in the multiwalled nanotubes occurs at a substantially higher rate due to the presence of inner carbon walls that prevent fast channeling of knocked-on carbon atoms.

4.3. From the microscopic standpoint, the decrease in the π-plasmon energy can be explained by assuming that this decrease is associated with the deformation (narrowing) of the energy π subbands. In our opinion, the deformation of the subbands is due to the accumulation of the aforementioned defects. All defects (vacancies, clusters of carbon or argon atoms) can exhibit donor–acceptor properties; i.e., the presence of defects in nanotubes encourages the accumulation of a positive or negative charge at the sites where these defects are located. As was estimated above, the distance between defects at sufficiently high irradiation doses is relatively short and is equal to 10–15 interatomic distances. The electric field of charged defects in the vicinity of their location brings about a shift of the energy levels of π electrons in the valence and conduction bands. This is a manifestation of the nonrigidity of the energy bands in carbon nanotubes. The revealed decrease in the π-plasmon energy by 0.8–1.2 eV can be explained by the fact that the band gaps in nanotubes irradiated with argon ions become narrower by approximately the same value. Therefore, the deformation of either of these two bands (the valence band or the conduction band) in the case of their “mirror reflection” can be equal to half the above values, i.e., 0.4–0.6 eV.

5. CONCLUSIONS

Thus, we investigated the destruction of carbon nanotubes under exposure to a beam of argon ions with an energy of 1 keV. The results obtained have demonstrated that the amorphization of a carbon system in the course of ion bombardment is characterized by a number of specific features. It is found that both single-walled and multiwalled carbon nanotubes undergo stepwise destruction. This process occurs at a low rate in the initial stage of ion irradiation (at irradiation doses of less than 30 $\mu C/cm^2$), is then somewhat accelerated, and tends to saturation at rather high doses (100–150 $\mu C/cm^2$). Of course, solving the problem under consideration calls for special investigation for other energies and properties of bombarding ions. However, the main result obtained in this work is obvious and can be formulated as follows: π plasmons can serve as a sufficiently subtle tool for studying processes occurring in carbon nanotubes irradiated with fast ions, especially in the early stages when other methods can provide a very small amount of information.

ACKNOWLEDGMENTS

We would like to thank A.S. Lobach (Institute of Problems of Chemical Physics, Russian Academy of Sciences) for supplying the samples of single-walled carbon nanotubes used in the measurements.

This work was supported by the Ministry of Education of the Russian Federation, project no. PD02-1.2-170.

REFERENCES

1. W. Hoenlein, Jpn. J. Appl. Phys., Part 1 **41**, 4370 (2002).
2. P. Avouris, J. Appenzeller, R. Martel, and S. J. Wind, Proc. IEEE **91** (11), 1772 (2003).
3. J. C. Charlier, M. Terrones, T. Bauhart, N. Grobert, H. Terrones, and P. M. Ajayan, IEEE Trans. Nanotechnol. **2** (4), 349 (2003).
4. T. Fukuda, F. Arai, and L. Dong, Proc. IEEE **91** (11), 1803 (2003).
5. A. V. Krasheninnikov, K. Nordlund, and J. Keinonen, Phys. Rev. B **65**, 165423 (2002).
6. Z. Klusek, S. Datta, P. Biszewski, and P. Kowalcsuk, Surf. Sci. **507**, 577 (2002).
7. P. M. Ajayan, S. Iijima, and T. Ichihashi, Phys. Rev. B **47** (11), 6859 (1993).
8. R. Kuzuo, M. Terauchi, M. Tanaka, and Y. Saito, Jpn. J. Appl. Phys., Part 2 **33** (9B), L1316 (1993).
9. B. W. Reed and M. Sarikaya, Phys. Rev. B **64** (19), 195404 (2001).
10. M. Kociak, L. Henrard, O. Stephan, K. Suenaga, and C. Collix, Phys. Rev. B **61** (20), 13936 (2000).
11. M. M. Brzhezinskaya, E. M. Baitinger, and V. V. Shnitov, in *Proceedings of the 2003 MRS Fall Meeting, Boston* (2004), Mater. Res. Soc. Symp. Proc., Vol. 792, p. 371.
12. P. Chen, X. Wu, X. Sun, J. Lin, W. Ji, and K. L. Tan, Phys. Rev. Lett. **82** (12), 2548 (1999).
13. S. Iijima, Nature **354**, 56 (1991).
14. E. D. Obraztsova, J.-M. Bonard, V. L. Kuznetsov, V. I. Zaikovskii, S. M. Pimenov, A. S. Pozarov, S. V. Terekhov, V. I. Konov, A. N. Obraztsov, and A. P. Volkov, Nanostruct. Mater. **12**, 567 (1999).
15. A. S. Lobach, N. G. Spitsyna, S. V. Terekhov, and E. D. Obraztsova, Fiz. Tverd. Tela (St. Petersburg) **44** (3), 457 (2002) [Phys. Solid State **44**, 475 (2002)].
16. M. Brzhezinskaya, E. Baitinger, and V. Shnitov, Physica B (Amsterdam) **348** (1–4), 95 (2004).
17. V. N. Popov, Mater. Sci. Eng. R **43** (3), 61 (2004).
18. Y. Lee, S. Kim, and D. Tomanek, Phys. Rev. Lett. **78**, 2393 (1997).

Translated by O. Borovik-Romanova

Physics of the Solid State, Vol. 47, No. 4, 2005, pp. 778–784. Translated from Fizika Tverdogo Tela, Vol. 47, No. 4, 2005, pp. 751–757.
Original Russian Text Copyright © 2005 by Davydov, Podlivaev, Openov.

FULLERENES AND ATOMIC CLUSTERS

Anomalous Thermal Stability of Metastable C_{20} Fullerene

I. V. Davydov, A. I. Podlivaev, and L. A. Openov
Moscow Engineering Physics Institute (State University), Kashirskoe sh. 31, Moscow, 115409 Russia
e-mail: opn@supercon.mephi.ru

Received May 17, 2004

Abstract—The results of computer simulation of the dynamics of fullerene C_{20} at different temperatures are presented. It is shown that, although it is metastable, this isomer is very stable with respect to the transition to a lower energy configuration and retains its chemical structure under heating to very high temperatures, $T \approx 3000$ K. Its decay activation energy is found to be $E_a \approx 7$ eV. Possible decay channels are studied, and the height of the minimum potential barrier to decay is determined to be $U = 5.0$ eV. The results obtained make it possible to understand the reasons for the anomalous stability of fullerene C_{20} under normal conditions. *© 2005 Pleiades Publishing, Inc.*

1. INTRODUCTION

After the discovery of fullerene C_{60} [1], the interest in carbon clusters has sharply increased, due both to their unusual physical and chemical properties and to their prospects for practical applications [2]. In spite of numerous experimental and theoretical studies, the mechanisms of carbon cluster formation and some of their properties are still not entirely clear.

The smallest of the experimentally observed "three-dimensional" carbon clusters is the C_{20} cluster [3], which is one of the fullerenes with a spherelike structure having carbon atoms located at their "surface" at the vertices of pentagons or hexagons. In fullerene C_{20}, there are only pentagons. A C_{20} cluster can exist both in the form of a fullerene (a cage) and in the form of a bowl, ring, chain, etc. (Fig. 1). The problem of relative stability of these isomers remains to be fully resolved. Experimental data are still incomplete and inconsistent, and theoretical calculations performed using various methods give appreciably different results [4–11]. Partly, this is due to the difficulty in finding the correlation contribution to the total energy of the cluster and also to the fact that the differences in the isomer energies are comparable to the errors of calculation in the methods used.

Nevertheless, most authors who use the most exact modern computing algorithms agree that, of all C_{20} isomers, the bowl has the minimum energy, whereas the cage is a metastable configuration [8, 11]. At the same time, there is no question that, experimentally [3], both C_{20} bowls and C_{20} cages have been synthesized [12, 13]. Thus, there is a problem as to why fullerene C_{20} retains an energetically unfavorable chemical structure under real experimental conditions and does not pass to the lower energy configuration.

In this study, the energy and structural characteristics of some C_{20} isomers are calculated using the tight-binding method with a "transferable" potential of interatomic interaction. The dynamics of fullerene C_{20} is studied in detail at different temperatures. It is shown that, though this three-dimensional isomer is metastable, its lifetime under normal conditions is very long because of a high potential barrier separating the metastable state from the lower energy atomic configuration.

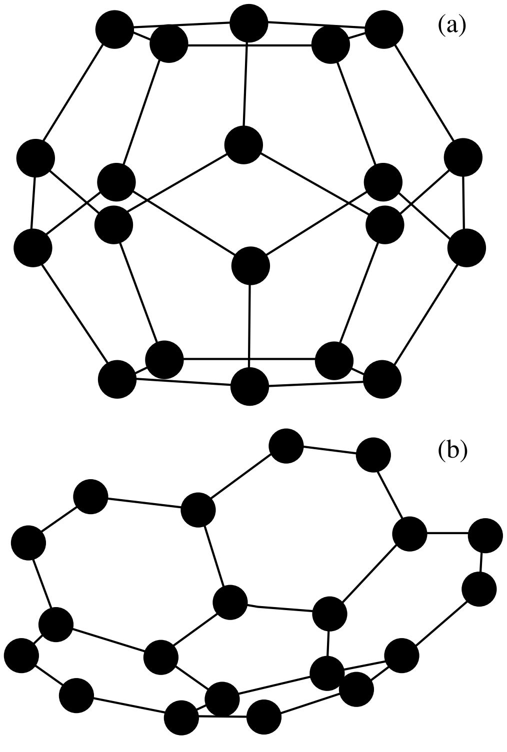

Fig. 1. Isomers of a C_{20} cluster. (a) Fullerene (cage) and (b) bowl.

1063-7834/05/4704-0778$26.00 © 2005 Pleiades Publishing, Inc.

2. METHODS OF CALCULATION

To calculate the energies of different configurations of the C_{20} fullerene, we used the tight-binding method with a transferable interatomic potential suggested for carbon compounds in [14]. This method differs favorably from the majority of empirical approaches and allows one to more correctly determine the contribution of the electronic subsystem to the total energy. Thus, four valence electrons of each carbon atom are taken into account and the interatomic potential is actually an N-particle potential, where N is the number of atoms in the system. Though the tight-binding method is not as exact as the *ab initio* methods, it adequately describes both small carbon clusters and macroscopic forms of carbon [7, 14] and, in addition, strongly simplifies calculations even for rather large clusters. In particular, in using the Monte Carlo method, this method makes it possible to collect statistics sufficient for estimating the decay activation energy and the lifetime of the metastable state. Earlier, this method was applied in computer simulation of a metastable C_8 cluster [15–18].

To find equilibrium and metastable configurations of a C_{20} cluster, we used the method of structural relaxation. First, an initial configuration of atoms was chosen, which then relaxed to a state corresponding to a global or local energy minimum under the action of intracluster interactions only. At each time step of the relaxation, the velocities of all atoms were decreased by 1–10%, which is equivalent physically to cooling of the system. The time step was $t_0 = 2.72 \times 10^{-16}$ s, which was approximately equal to one percent of the vibration period for a C_2 dimer.

To determine the decay activation energy of the metastable configuration, we used the method of molecular dynamics with a transferable tight-binding potential (tight-binding molecular dynamics, TBMD [7]) and a time step t_0. Calculations were performed at a fixed total energy, which corresponds to the case of a heat-insulating system. The temperature T of the cluster was determined from the formula [15]

$$\frac{3}{2}k_B T = \langle E_{\text{kin}} \rangle, \tag{1}$$

where k_B is the Boltzmann constant and $\langle E_{\text{kin}} \rangle$ is the ion kinetic energy per atom averaged over several vibration periods.

When calculating the forces $\mathbf{F}_i$ acting on the atoms (i is the atom number), we assumed the electron temperature T_{el} to be equal to T and used the formula

$$\mathbf{F}_i = -2\sum_n \langle \psi_n | \nabla_i \hat{H} | \psi_n \rangle f(\varepsilon_n) - \nabla_i U, \tag{2}$$

which is a generalization of the Hellmann–Feynman formula to finite temperatures [19, 20]. Here, U is the classical component of the total energy taking into account the repulsion of atoms at close distances; $\hat{H}$ is the electron Hamiltonian in the tight-binding approximation [14]; $|\psi_n\rangle$ and ε_n are the eigenstates and eigenenergies of $\hat{H}$, respectively (n = 1–80); and $f(\varepsilon_n)$ is the Fermi–Dirac distribution function. The chemical potential was determined at each step of molecular-dynamics simulation from the condition that the total number of valence electrons was constant, $N_{\text{el}} = 80$. To find the effect of the heating of the electron subsystem on the cluster dynamics, we also performed calculations at $T_{\text{el}} = 0$.

The height of the potential barrier preventing the transition of the system from the metastable configuration to a state with a lower energy was calculated by the same method that we used previously in [16]. In this method, calculation reduces to finding the saddle points of the potential energy of the system considered as a function of the coordinates of all atoms. These saddle points correspond to unstable equilibrium positions of atoms in the cluster and possess the property that infinitesimal deviations from the equilibrium positions result either in relaxation of the system to the initial state or in a transition to a new configuration. To find saddle points, the cluster is deformed continuously in the $3N$-dimensional space of atomic coordinates along the direction of the vibration mode with a minimum frequency so that the cluster energy monotonically increases with deformation, while at the same time having local minima in all others directions (orthogonal to the one chosen) [16].

3. RESULTS

We calculated the structural and energy characteristics of four C_{20} isomers: a cage, a bowl (Fig. 1), a ring, and a chain. For each isomer, the binding energy E_b was calculated from the formula

$$E_b = 20E(C_1) - E(C_{20}), \tag{3}$$

where $E(C_{20})$ is the energy of a C_{20} cluster and $E(C_1)$ is the energy of an isolated carbon atom. The configuration with a maximum energy E_b is stable (equilibrium), since its total energy is minimum. The configurations with smaller (but positive) values of E_b are metastable; they correspond to local minima of the total energy in the space of atomic coordinates.

We obtained the following values of the binding energy E_b per atom: 6.08, 6.14, 5.95, and 5.90 eV/atom for a cage, a bowl, a ring, and a chain, respectively (Table 1). Our results indicate that the C_{20} cage is metastable, which is in agreement with Monte Carlo calculations [8, 11]. The bond lengths between the nearest neighbors in the C_{20} fullerene are listed in Table 2; these results are in good agreement with the results obtained by other authors.

Table 1. Binding energies E_b (eV/atom) for some isomers of C_{20} clusters calculated using different methods: tight-binding method (TB), Hartree–Fock method (HF), density functional method in the local density approximation (LDA), density functional method with allowance for gradient corrections (GCA), and Tersoff–Brenner empirical method (Tersoff)

C_{20} isomer	Method of calculation					
	TB [6]	HF [8]	LDA [8]	GCA [9]	Tersoff [21]	present study
Cage	6.08	4.01	7.95	6.36	6.36	6.08
Bowl	–	4.15	7.87	–	6.19	6.14
Ring	6.01	4.23	7.77	6.45	6.11	5.95
Chain	6.05	–	–	6.35	–	5.90

Table 2. Bond lengths in the C_{20} fullerene calculated using different methods: Hartree–Fock method (HF), method of modified neglect of differential overlap (MNDO), and Tersoff–Brenner empirical method (Tersoff)

Method of calculation	Bond length, Å	
	minimum	maximum
HF [4]	1.42	1.47
MNDO [5]	1.41	1.52
Tersoff [21]	1.44	1.53
Present study	1.44	1.52

Heating can transform a metastable isomer to another configuration. The characteristic time of such transformation (the lifetime τ) depends on temperature and the height of the energy barrier separating these configurations. Following from general arguments [15], we can see that the cluster decay probability W per unit time is given by the statistics formula

$$W = W_0 \exp(-E_a/k_B T), \tag{4}$$

where the factor W_0 has dimensions of inverse time (s^{-1}) and E_a is the activation energy for cluster decay. This energy is close to the height of the minimum energy barrier separating the metastable state from the equilibrium state or from another metastable state but can differ from it due to the presence of several different decay paths. The cluster lifetime can be defined as [15]

$$\tau = 1/W = \tau_0 \exp(E_a/k_B T), \tag{5}$$

where $\tau_0 = 1/W_0$ is of the order of the characteristic cluster vibration period ($\sim 10^{-13}$ s). It is convenient to pass over from the cluster lifetime to the critical number of steps of molecular-dynamics simulation N_c corresponding to cluster decay:

$$N_c = N_0 \exp(E_a/k_B T), \tag{6}$$

where $N_0 = \tau_0/t_0$.

We performed molecular-dynamics simulation of the "life" of the C_{20} fullerene at different initial temperatures T of the ionic subsystem; in this way, we directly determined the quantity N_c as a function of T. Different values of T corresponded to different sets of initial velocities of the cluster atoms V_{i0}, which were chosen randomly each time (but subjected to the condition $\sum_i \mathbf{V}_{i0} = 0$).

The results obtained are shown in Fig. 2. Since the nature of the decay of a metastable state is probabilistic, the quantity N_c at a given temperature T is not determined uniquely. Nevertheless, it is seen from Fig. 2 that, in first approximation, the results of simulation are described by Eq. (6), according to which the dependence of $\ln(N_c)$ on $1/T$ is linear. The slope of this line is the activation energy for the cluster decay and is found to be $E_a = 8 \pm 1$ eV at the temperature of the electronic subsystem $T_{el} = T$ and $E_a = 7 \pm 1$ eV at $T_{el} = 0$.

Figure 3 shows the results of calculating the "potential landscape" for a C_{20} cluster in the vicinity of the metastable cage configuration (point *1* in Fig. 3). Saddle point *2* is the nearest to the cage state and corresponds to a configuration in which two C–C bonds begin to break and two adjoining octagons form (Fig. 4). The energy of this configuration is 4 eV higher than that of a cage. Analysis of the data of molecular-dynamics simulation shows that, though this configuration actually appears from time to time during thermal vibrations, the cluster does not decay. The reason for this behavior is that the energy of the metastable state at point *3*, which is the nearest to saddle point *2* (Fig. 3), is only 0.1 eV lower than the energy at the saddle point (visually, atomic configurations *2* and *3* are practically the same; each of them has two octagons). Therefore, after arriving at a new metastable state, the system does not stay there but, due to the thermal motion of atoms, returns (again via saddle point *2*) to the vicinity of the initial metastable state at point *1*.

Metastable saddle point *4*, next to metastable state *3* (Fig. 3), corresponds to a configuration in which two C–C bonds are broken and the breaking of the third bond begins, resulting in the formation of a cluster of three adjoining octagons on the "lateral surface" (Fig. 5). The energy of this configuration is 4.8 eV higher than that of a cage. Metastable state *5*, which is the nearest to saddle point *4*, also has three octagons (and three broken C–C bonds). Molecular-dynamics simulation shows that, after passing to metastable state *5*, the system can either return to the vicinity of metastable state *1* via saddle points *4* and *2* or pass to metastable state *7* via saddle point *6* (Fig. 3). In atomic configuration *6*, three C–C bonds are broken and the breaking of another bond begins; because of this, four octagons form on the lateral surface of the cluster (Fig. 6). In metastable configuration *7*, there are also four octagons. As a rule, the system does not return from this configuration to the original state *1* (we observed such a return only once). Thus, the difference

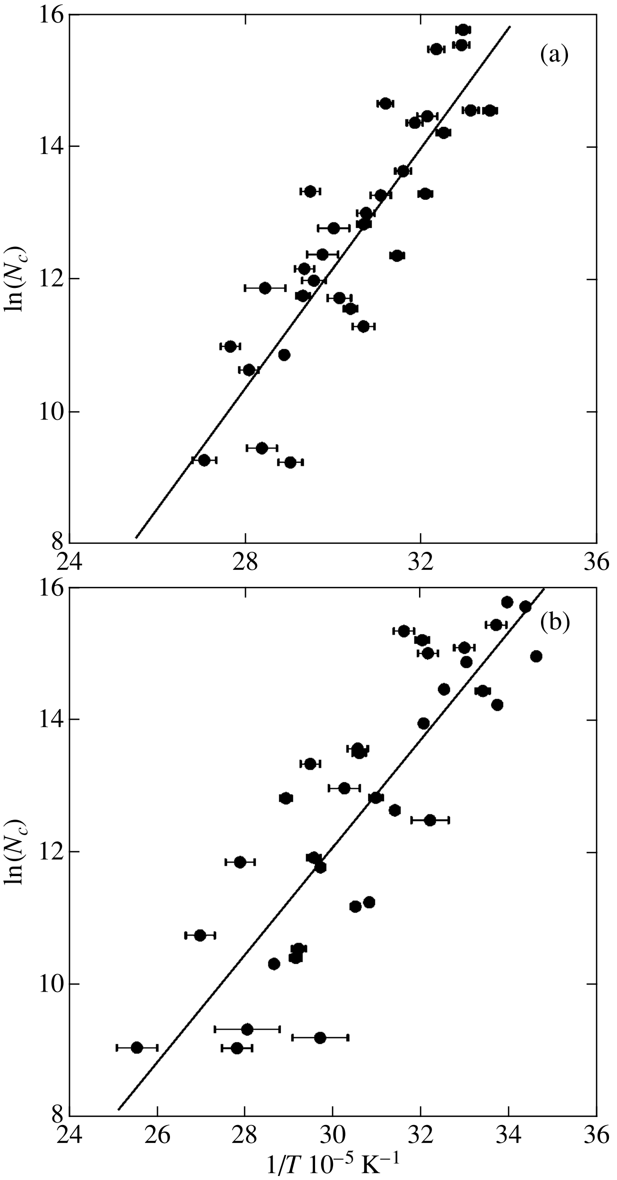

Fig. 2. Logarithm of the critical number of steps of molecular-dynamics simulation N_c for the onset of the decay of the C_{20} fullerene as a function of the temperature T of the ionic subsystem for electron temperature (a) $T_{el} = T$ and (b) $T_{el} = 0$. Circles are the results of calculation, and the solid line is a linear least squares fit.

between the energies of configurations *6* and *1* is the height $U = 5.0$ eV of the minimum potential barrier preventing the cage decay.

Having passed over this barrier and appeared in metastable state *7*, the system, in the overwhelming majority of cases, very rapidly passes via saddle point *8* to metastable state *9* (Fig. 3), where it resides for a time corresponding to 10^3–10^4 steps of molecular-dynamics simulation. Configuration *9* has the form of a star and is shown in Fig. 7. In this symmetric configuration, there are five octagons on the lateral surface of the cluster. The decay of the star leads to the formation of different quasi-two-dimensional or quasi-one-dimensional configurations (Fig. 8) and occurs through transitions via different saddle points (only one of them is shown in Fig. 3). No transition occurs to the equilibrium bowl configuration.

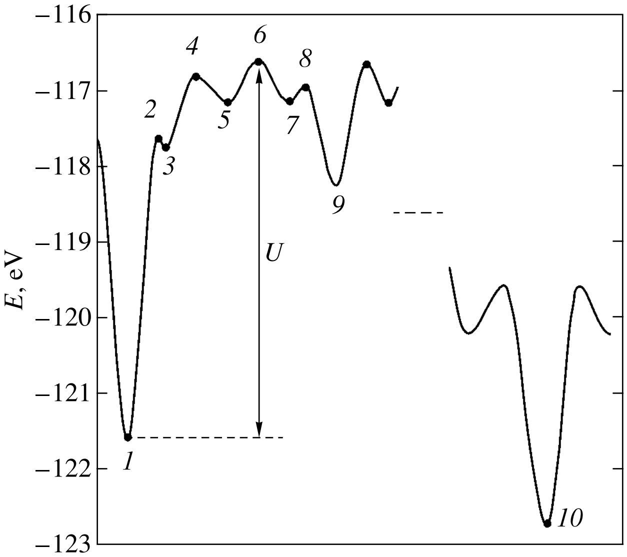

Fig. 3. Dependence of the total energy E of a C_{20} cluster on “the generalized coordinate” in the $3N$-dimensional space of atomic coordinates $\{\mathbf{R}_i\}$ in the vicinity of the metastable cage configuration (schematic). The energies are measured from the energy of an isolated carbon atom. The numerals correspond to the following configurations: (*1*) fullerene (cage), $E = -121.56$ eV (Fig. 1a); (*2*) saddle point, $E = -117.62$ eV (Fig. 4); (*3*) metastable state, $E = -117.73$ eV; (*4*) saddle point, $E = -116.79$ eV (Fig. 5); (*5*) metastable state, $E = -117.13$ eV; (*6*) saddle point determining the height of the minimum potential barrier ($U = 5.0$ eV) to the decay of the cage, $E = -116.61$ eV (Fig. 6); (*7*) metastable state, $E = -117.12$ eV; (*8*) saddle point, $E = -116.94$ eV; (*9*) metastable star state, $E = -118.23$ eV (Fig. 7); and (*10*) equilibrium bowl configuration, $E = -122.71$ eV (Fig. 1b).

4. DISCUSSION

It should be noted that the problem of the choice of the temperature of the electron subsystem T_{el} in simulating the dynamics of an electron–ion system is not at all trivial. It is shown in [19] that the use of Eq. (2) in integrating the classical equations of motion for ions corresponds to the conservation of the so-called Mermin free energy [22] $\Omega = E - T_{el}S$, where E is the total internal energy of the system and S is the electronic entropy. Generally, the quantity T_{el} does not necessarily coincide with the average ionic temperature T [19]. Calculations of the dynamics of different fullerenes at high temperatures performed in [20] showed, in particular, that the stability of the cluster at $T_{el} = T$ appears to be somewhat lower than at $T_{el} = 0$ but that there are no basic qualitative distinctions between these two cases.

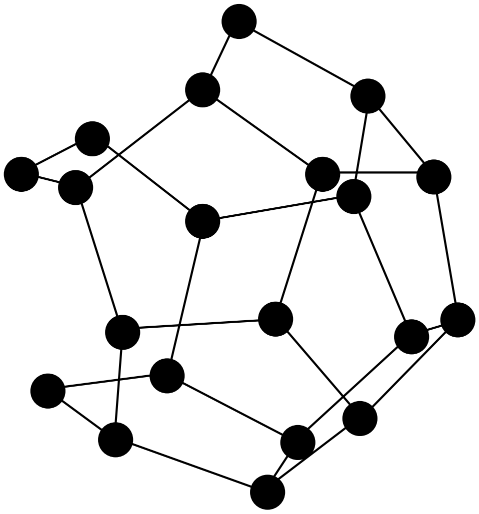

Fig. 4. Atomic configuration corresponding to saddle point *2* in Fig. 3.

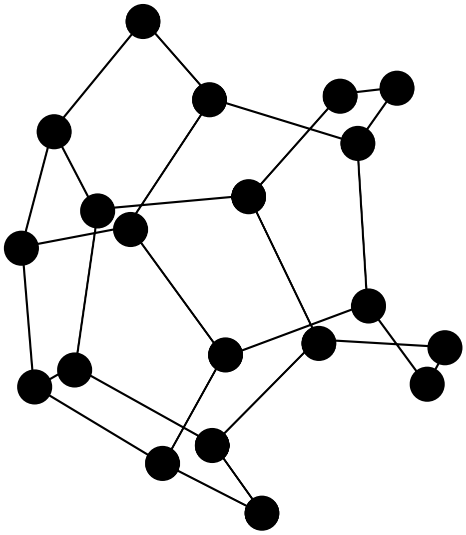

Fig. 5. Atomic configuration corresponding to saddle point *4* in Fig. 3.

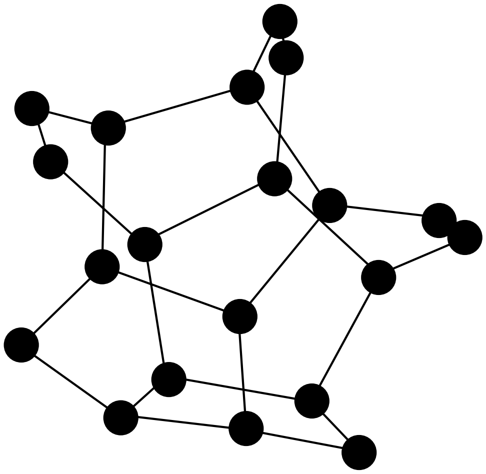

Fig. 6. Atomic configuration corresponding to saddle point *6* in Fig. 3. This configuration determines the height of the minimum potential barrier (U = 5.0 eV) to the decay of the cage.

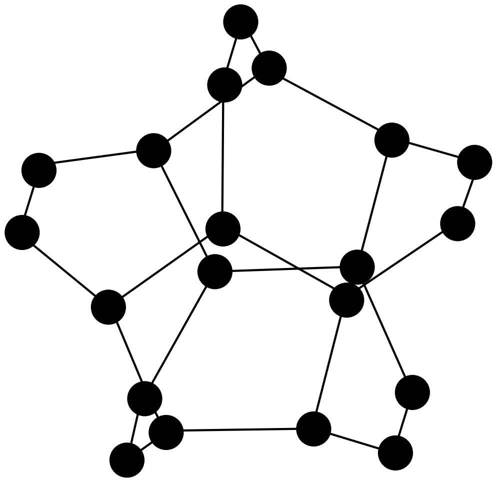

Fig. 7. Star atomic configuration corresponding to metastable state *9* in Fig. 3.

According to [20], the fragmentation temperature $T_{\rm fr}$ of fullerene C_{20}, defined as the temperature above which the metastable configuration decays, is $T_{\rm fr} \approx 3600$ and 4000 K at $T_{\rm el} = T$ and 0, respectively.

According to our data, the activation energy $E_{\rm a}$ for the decay of fullerene C_{20} is the same at $T_{\rm el} = T$ and $T_{\rm el} = 0$ to within the limits of error (see Section 3), although the average value of $E_{\rm a}$ at $T_{\rm el} = T$ is somewhat greater than that at $T_{\rm el} = 0$. Thus, the cluster dynamics weakly depends on the temperature of the electronic subsystem. Partly, this is due to a rather large gap (0.4 eV) between the energies of the lower empty and the upper filled molecular orbital (HOMO–LUMO gap). Here, we should emphasize that the "physical time" during which we controlled the dynamics of the C_{20} cluster for each set of initial velocities (i.e., at each initial temperature) exceeded 1.5 ns, which is two orders of magnitude greater than the corresponding time (about 10 ps) in [20, 23], where simulations of the thermal stability of fullerenes were performed. Due to this, we could find the temperature dependence of N_c (i.e., the cluster lifetime) over a fairly large temperature range and estimate the activation energy $E_{\rm a}$. Obviously, the lifetime of a metastable state is dependent on temperature. Therefore, it makes no sense to determine (as in [20]) "the temperature of cluster fragmentation" regardless of the time in which this fragmentation occurs.

Using the calculated energy $E_{\rm a}$, the lifetime of a C_{20} cage at room temperature, τ(300 K), is found from

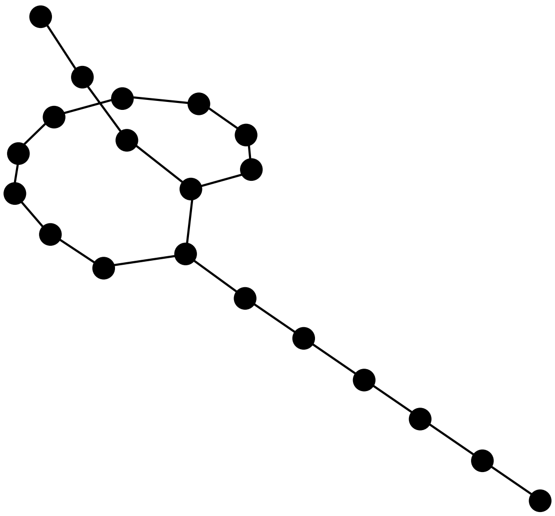

Fig. 8. One of the atomic configurations that can form after the decay of the star.

Eq. (5) to be very large (practically, infinite). This result allows us to understand the reason for the success of experiments [3] on the synthesis of metastable C_{20} fullerenes. We note that the height of the minimum potential barrier to the decay of a C_{20} cage ($U = 5.0$ eV) is somewhat lower than the decay activation energy $E_a = (6–9)$ eV determined directly from the molecular-dynamics simulation data. This is partly due to the fact that the cluster can decay in different ways by passing through potential barriers of different heights, including those that are higher than the lowest barrier.

In [24], calculations of the temperature dependence of the relative root-mean-square fluctuation of bond lengths δ led to the conclusion that the C_{20} cluster melts at a temperature $T_m \approx 1900$ K. According to our calculations, δ monotonically increases with temperature without exhibiting any features at $T < 3000$ K. Moreover, an abrupt cooling of the cluster at any instant prior to its decay results either in its transition to one of the intermediate metastable states (states *3*, *5* in Fig. 3) or in its return to the original metastable state (state *1*). Thus, the problem of melting of the C_{20} fullerene at a certain temperature T_m requires further study.

Let us now discuss in more detail the character of transition of the C_{20} fullerene to other states. Above all, we note that we never observed a transition to the equilibrium bowl configuration with a lower total energy (higher binding energy). As a rule, the decay of the C_{20} fullerene begins with a transition to the metastable star configuration via a sequence of several saddle points and intermediate short-lived metastable states (Fig. 3). For a star (Fig. 7), the binding energy $E_b = 5.91$ eV/atom is lower than that for a cage. A transition from the cage to the star is accompanied by a decrease in the cluster temperature by 500–800 K. Over the course of time, the star passes to different (as a rule, quasi-two-dimensional or quasi-one-dimensional) configurations with a lower binding energy and the cluster temperature decreases from 3000–4000 to 1000–1500 K. These configurations are very different in structure from both the cage and the bowl (one of such configurations is shown in Fig. 8). Thus, the ability of carbon structures to form numerous intermediate metastable (but fairly stable) states prevents the transition of the metastable cage to the stable bowl configuration.

5. CONCLUSIONS

The main result of this study is that the metastable C_{20} fullerene (cage) was demonstrated to have very high thermal stability with respect to transition to an equilibrium state with a lower total energy. The reason for this stability is the high potential barrier, which prevents the decay of the C_{20} cage and the corresponding high decay activation energy. For this reason, the lifetime of the C_{20} cage is very long even at room temperature. Therefore, once created at a certain stage of synthesis, a C_{20} cage retains its chemical structure.

Although all this applies to an isolated C_{20} cage, by analogy to a C_{60} cluster, we may hope that a C_{20} fullerene-based cluster material (fullerite) exists. In any case, the preliminary data are rather encouraging [21, 25, 26]. Final solution of this problem requires further experimental and theoretical studies, one stimulus for which is the conjecture that the C_{20} fullerite (if synthesized) could be a high-temperature superconductor [27].

ACKNOWLEDGMENTS

This study was supported by the CRDF, project "Scientific and Educational Center for Basic Research of Matter in Extremal States."

REFERENCES

1. H. W. Kroto, J. R. Heath, S. C. O'Brien, R. F. Curl, and R. E. Smalley, Nature **318** (6042), 162 (1985).
2. A. V. Eletskiĭ and B. M. Smirnov, Usp. Fiz. Nauk **165**, 977 (1995) [Phys. Usp. **38**, 935 (1995)].
3. H. Prinzbach, A. Weller, P. Landenberger, F. Wahl, J. Worth, L. T. Scott, M. Gelmont, D. Olevano, and B. von Issendorff, Nature **407** (6800), 60 (2000).
4. V. Parasuk and A. Almlöf, Chem. Phys. Lett. **184** (1–3), 187 (1991).
5. D. Bakowies and W. Thiel, J. Am. Chem. Soc. **113** (10), 3704 (1991).
6. D. Tománek and M. A. Schluter, Phys. Rev. Lett. **67** (17), 2331 (1991).
7. C. H. Xu, C. Z. Wang, C. T. Chan, and K. M. Ho, Phys. Rev. B **47** (15), 9878 (1993).
8. J. C. Grossman, L. Mitas, and K. Raghavachari, Phys. Rev. Lett. **75** (21), 3870 (1995).
9. R. O. Jones and G. Seifert, Phys. Rev. Lett. **79** (3), 443 (1997).

10. R. O. Jones, J. Chem. Phys. **110** (11), 5189 (1999).
11. S. Sokolova, A. Lüchow, and J. B. Anderson, Chem. Phys. Lett. **323** (3–4), 229 (2000).
12. M. Saito and Y. Miyamoto, Phys. Rev. Lett. **87** (3), 035503 (2001).
13. J. Lu, S. Re, Y. Choe, S. Nagase, Y. Zhou, R. Han, L. Peng, X. Zhang, and X. Zhao, Phys. Rev. B **67** (12), 125415 (2003).
14. C. H. Xu, C. Z. Wang, C. T. Chan, and K. M. Ho, J. Phys.: Condens. Matter **4** (28), 6047 (1992).
15. L. A. Openov and V. F. Elesin, Pis'ma Zh. Éksp. Teor. Fiz. **68** (9), 695 (1998) [JETP Lett. **68**, 726 (1998)].
16. V. F. Elesin, A. I. Podlivaev, and L. A. Openov, Phys. Low-Dimens. Semicond. Struct. **11/12**, 91 (2000).
17. L. A. Openov and V. F. Elesin, Mol. Mater. **13** (1–4), 391 (2000).
18. N. N. Degtyarenko, V. F. Elesin, N. E. L'vov, L. A. Openov, and A. I. Podlivaev, Fiz. Tverd. Tela (St. Petersburg) **45** (5), 954 (2003) [Phys. Solid State **45**, 1002 (2003)].
19. R. M. Wentzcovitch, J. L. Martins, and P. B. Allen, Phys. Rev. B **45** (19), 11372 (1992).
20. B. L. Zhang, C. Z. Wang, C. T. Chan, and K. M. Ho, Phys. Rev. B **48** (15), 11381 (1993).
21. A. J. Du, Z. Y. Pan, Y. K. Ho, Z. Huang, and Z. X. Zhang, Phys. Rev. B **66** (3), 035405 (2002).
22. N. D. Mermin, Phys. Rev. A **137** (5), 1441 (1965).
23. S. G. Kim and D. Tománek, Phys. Rev. Lett. **72** (15), 2418 (1994).
24. X. Z. Ke, Z. Y. Zhu, F. S. Zhang, F. Wang, and Z. X. Wang, Chem. Phys. Lett. **313** (1–2), 40 (1999).
25. V. Paillard, P. Mélinon, V. Dupuis, A. Perez, J. P. Perez, G. Guiraud, J. Fornazero, and G. Panczer, Phys. Rev. B **49** (16), 11433 (1994).
26. S. Okada, Y. Miyamoto, and M. Saito, Phys. Rev. B **64** (24), 245405 (2001).
27. I. Spagnolatti, M. Bernasconi, and G. Benedek, Europhys. Lett. **59** (4), 572 (2002).

Translated by I. Zvyagin

Physics of the Solid State, Vol. 47, No. 4, 2005, pp. 785–794. Translated from Fizika Tverdogo Tela, Vol. 47, No. 4, 2005, pp. 758–766.
Original Russian Text Copyright © 2005 by Magomedov.

On the Properties of Face-Centered Cubic Fullerites

M. N. Magomedov

Institute of Geothermal Problems, Dagestan Scientific Center, Russian Academy of Sciences,
pr. Kalinina 39a, Makhachkala, 367003 Russia
e-mail: mahmag@iwt.ru

Received May 27, 2004

Abstract—The molecular mass of the fullerene C_{nc} (where the subscript nc is the number of carbon atoms in a molecule of the fullerene C_{nc}) is found to be correlated with characteristics of face-centered cubic fullerites, such as the sublimation energy, the distance between the centers of the nearest neighbor molecules, the Grüneisen parameter, and the bulk modulus at zero pressure and zero temperature. The correlation dependences revealed are used to determine the parameters of the Mie–Lennard-Jones pair potential for the interfullerene interaction in face-centered cubic fullerites. The parameters of the pair potential obtained are evaluated by calculating the properties of fullerites. The results of these calculations demonstrate that the C_{nc} fullerite crystals at nc ≤ 15–20 are unstable. The parameters of the triple and critical points of the fullerites are estimated, and the evolution of the parameters of the pair potential and properties of the fullerites with a variation in the fullerene molecular mass is investigated. *© 2005 Pleiades Publishing, Inc.*

1. INTRODUCTION

Fullerite crystals are composed of spherical carbon molecules C_{nc}, namely, fullerenes with various molecular masses (nc = 24–96, where nc is the number of carbon atoms in a molecule of the fullerene C_{nc}). The most widespread and, hence, most extensively studied fullerene is the buckminsterfullerene C_{60}, which consists of 20 hexagons and 12 pentagons forming a truncated icosahedron [1–7]. However, even for the C_{60} fullerene, there is no agreement between researchers regarding the parameters of the pair potential for the interfullerene interaction. The point is that the experimental data used for estimating the parameters of the pair potential for the C_{60} face-centered cubic fullerite (molecular mass m_{60} = 720.66 amu) are extremely contradictory. For example, the Debye temperature varies from $\Theta_{\min}$ = 37 K to $\Theta_{\max}$ = 180 K [2, 3], the Grüneisen parameter ranges from $\gamma_{\min}$ = 1.40 to $\gamma_{\max}$ = 9.15 [4], the sublimation energy lies in the range L_{00} = 161–189 kJ/mol [5], and the isothermal bulk modulus B_0 under atmospheric pressure and at room temperature falls in the range between 10.3 [3] and 18.1 GPa [7]. The data available in the literature on the properties of higher and lower fullerenes are even more contradictory because of the difficulties encountered in performing the experiments. In this respect, the purpose of the present work was to reveal and analyze a correlation between the parameters of the potential for the pair interaction of C_{nc} fullerenes and their molecular mass in the range 20 ≤ nc ≤ 120. The results obtained were used to investigate the evolution of the properties of the face-centered cubic fullerites with a variation in the molecular mass of the C_{nc} fullerene.

2. DETERMINATION OF THE PARAMETERS OF THE INTERFULLERENE POTENTIAL

The intermolecular pair interaction of C_{nc} fullerenes can be described by the Mie–Lennard-Jones potential [8–11]

$$\varphi(r) = [D/(b-a)][a(r_0/r)^b - b(r_0/r)^a]. \qquad (1)$$

Here, D is the depth of the potential well, r_0 is the coordinate of the minimum of the potential well, b is the stiffness parameter of the potential, and a is the parameter characterizing the long-range interaction.

All four parameters of potential (1) can be self-consistently determined using different methods described in [8, 9]. Zubov *et al.* [11] demonstrated that fullerites are classical van der Waals crystals for which the de Buhr parameter Λ_B is very small. In particular, the de Buhr parameter for the C_{60} molecule is 20 times smaller than that for xenon: $\Lambda_B(C_{60}) \cong 0.003 \ll \Lambda_B(Xe) \cong 0.06$. Therefore, the energy of zero-point vibrations of the fullerite lattice can be ignored. Moreover, the nearest neighbor interaction approximation for fullerites holds with a high accuracy because of the large size of the fullerene molecule and the short-range van der Waals character of the chemical bonding. As a consequence, the parameters of the pair potential for fullerites can be determined from the relationships [9]

$$\begin{gathered} r_0 = c_{00}, \quad D = L_{00}/(N_A k_n/2), \\ b = 6\gamma_{00} - 2, \quad a = (3\pi r_0^3)B_{00}/(k_y k_n D b). \end{gathered} \qquad (2)$$

Here, c is the distance between the centers of the nearest neighbor molecules in the fullerite lattice; N_A is the Avogadro number; k_n and k_y are the coordination num-

Table 1. Physical parameters (taken from different works) used to construct relationships (3) for C_{nc} fullerites with a cubic lattice [1 cal = 4.1868 J, 1 kJ/mol = 120.27323 K, 1 cal/mol = 0.43393×10^{-4} eV = 6.9524×10^{-24} J, 1 amu = $(10^3 N_A)^{-1}$ = 1.6606×10^{-27} kg, $N_A = 6.0221 \times 10^{23}$ mol^{-1}]

C_{nc}	m_{nc}, amu	L_{00}, kJ/mol	r_0 or c_{00}, 10^{-10} m	γ_{00} [12]	B_{00}, GPa [12]
C_{24}^* (simple cubic)	288.26		5.545 [14]		
C_{36}^* (face-centered cubic)	432.40	121 [13]	8.4 [12, 13]		
C_{60} (face-centered cubic)	720.66	175 [5]	10.02 [15], 10.04 [12, 13]	8.4	16.2
C_{70} (face-centered cubic)	840.77		10.47 [16], 10.53 [17], 10.588 [17], 10.61 [1, 15]		
C_{76} (face-centered cubic)	912.84		10.943 [18], 10.946 [12, 13]	9.2	17.1
C_{84} (face-centered cubic)	1008.92		11.24 [15], 11.357 [12, 13]	9.6	17.5
C_{96}^* (face-centered cubic)	1153.06	238 [13]	11.9 [12, 13]		

* Fullerites not yet synthesized but whose preparation is predicted [13, 14].

ber and the packing coefficient of the crystal structure, respectively; and the subscript 00 indicates that the quantity is determined at zero pressure and zero temperature.

Table 1 presents the data available in the literature [5, 12–18] on the sublimation energy L_{00}, the distance between the centers of the nearest neighbor molecules r_0 (or c_{00}), the Grüneisen parameter γ_{00}, and the isothermal bulk modulus B_{00} for different fullerites with a cubic structure. Analysis of the above data demonstrated that all these parameters increase with an increase in the number nc of carbon atoms in a molecule of the fullerene C_{nc} (Fig. 1) and can be described by the relationships

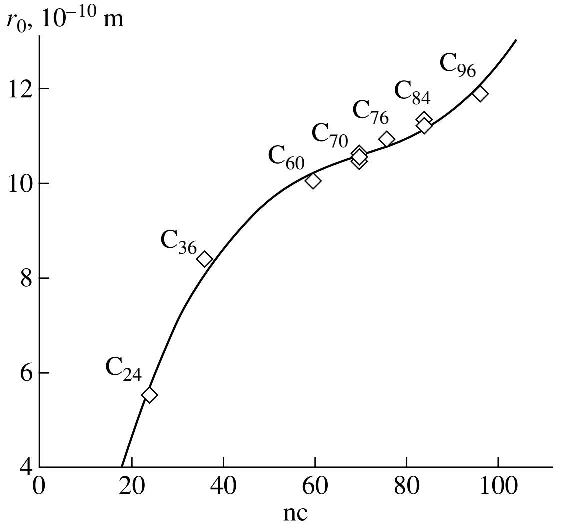

Fig. 1. Dependence of the distance r_0 between the centers of the nearest neighbor molecules C_{nc} in fullerites (T = 0 K, P = 0) on the number nc of carbon atoms in a molecule of the fullerene C_{nc}. The solid line represents the approximation of the data presented in Table 1 by the polynomial $r_0 = -3.23603 + 0.5174\text{nc} - 0.00682\text{nc}^2 + 3.21409 \times 10^{-5}\text{nc}^3$ (with the correlation coefficient $R_{corr} = 0.9902$).

$$L_{00}\ [\text{kJ/mol}] = 22 + 3.05\text{nc} - 0.00833\text{nc}^2,$$
$$R_{corr} = 1,$$
$$r_0\ [10^{-10}\ \text{m}] = -3.23603 + 0.5174\text{nc} - 0.00682\text{nc}^2 + 3.21409 \times 10^{-5}\text{nc}^3,$$
$$R_{corr} = 0.9902, \tag{3}$$
$$\gamma_{00} = 5.4 + 0.005\text{nc}, \quad R_{corr} = 1,$$
$$B_{00}\ [\text{GPa}] = 11.6375 + 0.09167\text{nc} - 2.60417 \times 10^{-4}\text{nc}^2,$$
$$R_{corr} = 1,$$

where R_{corr} is the correlation coefficient of the polynomial relationship. Figure 1 shows the most complex dependence r_0(nc). The other expressions exactly describe the data presented in Table 1.

By using expressions (3), we obtain the following polynomial relationships between the parameters of potential (1) and the number nc:

$$D/k_B\ [\text{K}] = 441 + 61.1388\text{nc} - 0.167\text{nc}^2,$$
$$b = 30.4 + 0.03\text{nc}, \tag{4}$$
$$a = 76.817(r_0\ [10^{-10}\ \text{m}])^3 B_{00}\ [\text{GPa}]/\{b(D/k_B)\ [\text{K}]\},$$

where k_B is the Boltzmann constant.

The parameters thus calculated are listed in Table 2.

Table 2. Physical parameters at $T = 0$ K and $P = 0$ and the parameters of the potential for C_{nc} fullerites with a cubic lattice according to calculations from relationships (3) and (4)

C_{nc}	L_{00}, kJ/mol (3)	γ_{00} (3)	B_{00}, GPa (3)	D/k_B, K (4)	r_0, Å (3)	b (4)	a (4)	B'_{00} (5)	Θ_{00}, K (6)
C_{24} (simple cubic)	90.4	6.6	13.7	1812.16	5.698	37.6	2.86	15.49	43.01
C_{36} (face-centered cubic)	**121**	7.2	14.6	2425.60	8.051	41.2	5.86	17.69	63.34
C_{60} (face-centered cubic)	**175**	**8.4**	**16.2**	3508.21	**10.198**	48.4	7.77	20.73	58.75
C_{70} (face-centered cubic)	195	8.9	16.8	3902.53	**10.588**	51.4	7.63	21.68	55.98
C_{76} (face-centered cubic)	206	9.2	**17.1**	4123.08	10.803	53.2	7.55	22.25	54.56
C_{84} (face-centered cubic)	219	9.6	**17.5**	4398.46	11.154	55.6	7.63	23.08	53.19
C_{96} (face-centered cubic)	**238**	10.2	18.1	4771.45	12.018	59.2	8.51	24.57	52.61

Note: The parameters that exactly coincide with those used for constructing polynomials (3) (see Table 1) are marked with bold type.

3. EVALUATION OF THE PARAMETERS OF THE PAIR POTENTIAL FOR FULLERITES

Before proceeding further, we note that the parameters of the pair potential obtained for the C_{60} fullerite are in good agreement with those used by Yakub [10], who calculated the thermodynamic properties of the C_{60} face-centered cubic fullerite on the basis of potential (1) with parameters $r_0 = 10.04 \times 10^{-10}$ m, $D/k_B = 3218.4$ K, $b = 43$, and $a = 9$. These parameters were determined by approximating the Girifalko potential [4] with the Mie–Lennard-Jones potential (1). The potential determined in [10] was subsequently used by Zubov *et al.* [11] and worked well in calculating the properties of the C_{60} face-centered cubic fullerite.

The potential depth determined for the C_{60} fullerite is well within the range of bonding energies, which was estimated experimentally or theoretically for two buckminsterfullerene molecules by various authors (see the review in [19]); that is,

$$2785\ \text{K} = 0.24\ \text{eV} \le D/k_B(C_{60}) \le 0.4\ \text{eV} = 4641.6\ \text{K}.$$

The following experimentally measurable quantities were calculated with the use of the parameters obtained for the pair potential (Table 2):

(1) The derivative of the bulk modulus at $T = 0$ K and $P = 0$ was calculated from the formula [8, 9]

$$B'_{00} = [dB_{T=0}(P)/dP]_{P=0} = 2 + (a+b)/3. \tag{5}$$

(2) The Debye temperature at $T = 0$ K and $P = 0$ (i.e., at $c = r_0$) was determined from the expression [20]

$$\Theta_{00} = A_w\xi_n\{-1 + [1 + (8D/k_B A_w \xi_n^2)]^{1/2}\}. \tag{6}$$

Here, we introduced the following designations:

$$A_w = K_R[5k_n ab(b+1)/144(b-a)](r_0/c)^{b+2},$$

$$K_R = \hbar^2/k_B r_0^2 m_{nc}, \quad \xi_n = 9/k_n,$$

where $\hbar$ is the Planck constant and $m_{nc} = m(C_1)nc = 12.011nc$ [amu] is the mass of the C_{nc} molecule.

(3) The longitudinal velocity of sound at $T = 0$ K and $P = 0$ was determined from the relationship [21]

$$\begin{aligned}\omega_{0l} &= [3B_{00}V_{00}(1-\mu)/N_A m_{nc}(1+\mu)]^{1/2} \\ &= [k_n abD(1-\mu)/6m_{nc}(1+\mu)]^{1/2},\end{aligned} \tag{7}$$

where μ is the Poisson ratio and $V_{00} = \pi N_A r_0^3/6k_y$ is the molar volume at $P = 0$ and $T = 0$ K.

(4) The thermal expansion coefficient at $T \gg \Theta$ and $P = 0$ was calculated from the formula [22]

$$\begin{aligned}\alpha_p(T \gg \Theta) &= (\gamma C_v/BV)_{T=\infty} \cong 3k_B N_A \gamma_0/B_{00}V_{00} \\ &= 54\gamma_0 k_B/k_n abD,\end{aligned} \tag{8}$$

under the assumption that the product BV only weakly changes with a variation in the temperature at $P = 0$ [23].

(5) The enthalpy of formation of a monovacancy was determined from the expression [24, 25]

$$E_v = (m_{nc}/k_n) f_y (3ck_B\Theta_{00}/8\hbar)^2. \tag{9}$$

It should be noted that the case in point is the energy required to transfer the fullerene molecule as a whole spherical object from the site of the face-centered cubic lattice to the surface. The function f_y accounts for the role played by the zero-point vibrations in the activation process and is related to the temperature by the expressions

$$f_y = (2/y)[1 - \exp(-y)]/[1 + \exp(-y)],$$

$$y = 3\Theta_{00}/4T.$$

It is easily seen that, at $T/\Theta_{00} > 1.5$ (the classical range in which the role of zero-point vibrations can be disregarded), the function f_y can be approximated as $f_y \cong 1$. However, at $T/\Theta_{00} < 0.3$ (when the contribution from the quantum effects becomes dominant), the function f_y is described by the linear relationship $f_y \cong 8T/3\Theta_{00}$.

Table 3. Physical parameters calculated using the potential with the parameters represented by polynomials (3) and (4) and in Table 2 for C_{nc} fullerites with a cubic lattice [$k_n = 12$, $k_y = 0.7405$, $\xi_n = 9/k_n = 0.75$, $\alpha_s = (\pi/6k_y)^{2/3} = 0.7937$ for the face-centered cubic lattice; $k_n = 6$, $k_y = \pi/6 = 0.5236$, $\xi_n = 1.5$, $\alpha_s = 1$ for the simple cubic lattice]

C_{nc}	ω_{0l}, m/s (7)*	ω_{0t}, m/s (7)**	$\alpha_p(T \gg \Theta)$, 10^{-6}, K^{-1} (8)	E_v, eV (9)***	E_d, eV (10)***	$\sigma(100)_0$, mJ/m^2 (11)	$\sigma(111)_0$, mJ/m^2 (11)****
C_{24} (simple cubic)	1738	929	304.1	0.72–0.72	1.01–1.01	38.52	
C_{36} (face-centered cubic)	3482	1860	55.2	2.33–2.34	5.19–5.22	65.08	53.36
C_{60} (face-centered cubic)	4050	2165	28.6	5.36–5.39	11.95–12.00	58.67	50.81
C_{70} (face-centered cubic)	4037	2158	26.1	6.13–6.15	13.65–13.70	60.55	52.44
C_{76} (face-centered cubic)	4031	2155	25.0	6.58–6.60	14.66–14.71	61.45	53.22
C_{84} (face-centered cubic)	4069	2175	23.0	7.37–7.39	16.41–16.49	61.50	53.26
C_{96} (face-centered cubic)	4321	2310	19.1	9.56–9.59	21.31–21.38	57.46	49.76

* The longitudinal velocity of sound ω_{0l} was calculated using the Poisson ratio taken from [6] ($\mu = 0.3$ for the C_{60} fullerite) at $T = 0$ K and $P = 0$ under the assumption that this parameter is identical for all fullerites (as is the case with noble-gas crystals [28, p. 368]).

** The calculation was performed according to the formula $\omega_t = \omega_l[(1 - 2\mu)/2(1 - \mu)]^{1/2}$ [29, p. 125]; i.e., $\omega_t = \omega_l/1.8708$ at $\mu = 0.3$.

*** The first value was calculated at $T = 200$ K, and the second value corresponds to the high-temperature limit $T \gg \Theta$ when $f_y = 1$ [see relationship (8)].

**** The specific surface energy $\sigma(111)$ was determined from the specific surface energy $\sigma(100)$ according to the formula $\sigma(111) = (3^{1/2}/2)\sigma(100)$ [30], which is valid for the face-centered cubic structure.

(6) The activation enthalpy of self-diffusion was calculated from the expression [24, 25]

$$E_d = (3/8k_y^{2/3}) m_{nc} f_y (3ck_B\Theta_{00}/4\pi\hbar)^2. \qquad (10)$$

Here, we are dealing with the migration of the fullerene molecule as an undeformable spherical object. In order to elucidate how the functions $E_v(T)$ and $E_d(T)$ depend on the temperature, they were calculated at $T = 200$ K and $T \gg \Theta_{00}$ (when $f_y = 1$).

(7) The specific surface energy of the (100) face at $T = 0$ K and $P = 0$ (i.e., at $c = r_0$) was calculated from the formula [26]

$$\sigma(100)_0 = (1/c^2\alpha_s)$$
$$\times\{(k_nD/12) - [3k_B\Theta_{00}^2/32(\Theta_{00} + A_w\xi_n)]\}, \qquad (11)$$
$$\alpha_s = (\pi/6k_y)^{2/3}.$$

The Debye temperature, which was determined with the use of the pair potential obtained in this work, coincides with recent experimental data: Θ_{00} (C_{60} face-centered cubic fullerite) = 55 K [3, 27]. The velocities of sound at $T = 0$ K and $P = 0$ (Table 3) agree well with the experimental data for the C_{60} face-centered cubic fullerite [6]: the longitudinal velocity of sound varies from $\omega_{0l} = 4130$ m/s (for the $\langle 111 \rangle$ direction) to $\omega_{0t} = 3550$ m/s (for the $\langle 100 \rangle$ direction) and 1920 m/s (for the $\langle 111 \rangle$ direction). The high-temperature value of the thermal expansion coefficient (Table 3) is in good agreement with the theoretical estimates made for the C_{60} face-centered cubic fullerite [10, 12]: $\alpha_p(T = 1000 \text{ K}) = (2\text{–}4) \times 10^{-5}\ \text{K}^{-1}$. It should be noted that, according to the data obtained in [12], as in the present work (Table 3), the thermal expansion coefficient $\alpha_p(T \gg \Theta)$ decreases with an increase in the number nc of carbon atoms in the C_{60} fullerene molecule from 60 to 84. The derivative of the bulk modulus with respect to pressure is in close agreement with the theoretical estimates of this parameter [31]: B'_{00} (C_{60} face-centered cubic fullerite) = 16.5–18.5. Thus, the comparison of the results of our calculations with the data available in the literature confirms the correctness of the method used for determining the parameters of potential (1).

4. DISCUSSION AND PREDICTIONS

The above analysis of the obtained dependences and the parameters listed in Tables 2 and 3 allows us to make the following inferences and predictions.

(1) The quantities L_{00}, γ_{00}, B_{00}, D, r_0, b, and B'_{00} increase monotonically with an increase in the number nc of carbon atoms in the C_{nc} fullerene molecule from 15 to 120, i.e., with an increase in the molecular mass of the fullerene from $m_{15} = 180.165$ amu to $m_{120} = 1441.320$ amu [see relationships (3), (4); Fig. 1].

(2) The long-range interaction parameter a in the range $40 \le nc \le 90$ varies only slightly: $a = 7\text{–}8$ (Fig. 2). This suggests the van der Waals character of the interaction [8, 28]. However, for numbers $nc \le 29$, we obtain $a \le 4$. This indicates a possible crossover to covalent bonding in the molecules [9]. The same conclusion was drawn in [14] for the C_{24} fullerite. As can be seen from Fig. 2, the condition $a \le 1$ is satisfied for numbers $nc \le 17$. This suggests that the system is unstable.

(3) The velocities of sound (ω_{0l}, ω_{0t}) at $T = 0$ K and $P = 0$ for $50 \le nc \le 90$ are nearly constant and fall in the

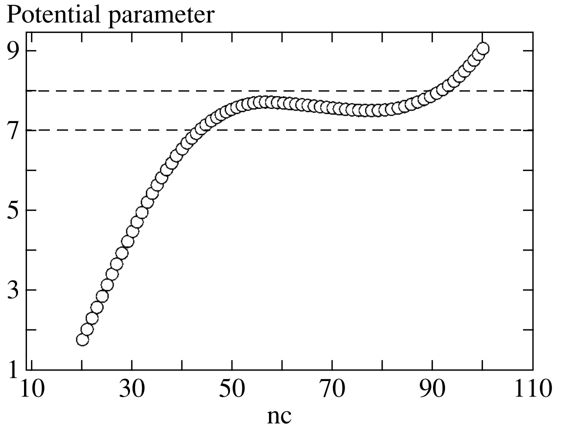

Fig. 2. Dependence of the long-range interaction parameter in the interfullerene potential (1) for the face-centered cubic fullerites on the number of carbon atoms in the C_{nc} fullerene. Calculations were performed using polynomials (3) and (4). The long-range interaction parameters for fullerene masses in the range $40 \le nc \le 90$ lie in the narrow range $7 \le a \le 8$.

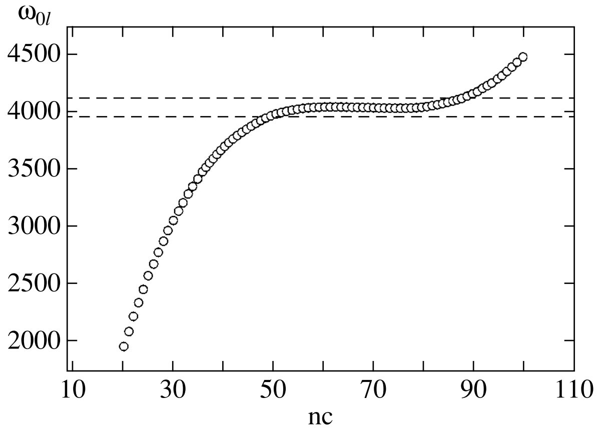

Fig. 3. Dependence of the longitudinal velocity of sound ω_{0l} ($T = 0$ K, $P = 0$) in the face-centered cubic fullerites on the number of carbon atoms in the C_{nc} fullerene. Calculations were performed according to formula (7) with the use of polynomials (3) and (4). The velocities of sound for fullerene masses in the range $50 \le nc \le 90$ lie in the narrow range $3980 \le \omega_{0l} \le 4120$ m/s.

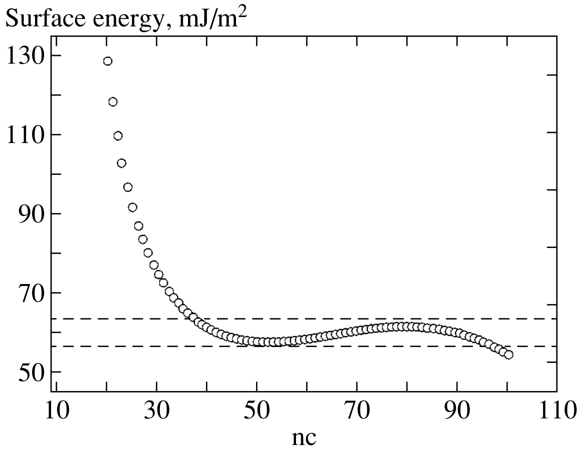

Fig. 4. Dependence of the specific surface energy ($T = 0$ K, $P = 0$) of the face-centered cubic fullerites on the number of carbon atoms in the C_{nc} fullerene. Calculations were performed according to formula (11) with the use of polynomials (3) and (4). The specific surface energies for fullerene masses in the range $37 \le nc \le 97$ lie in the range $56 \le \sigma(100)_0 \le 63$ mJ/m^2.

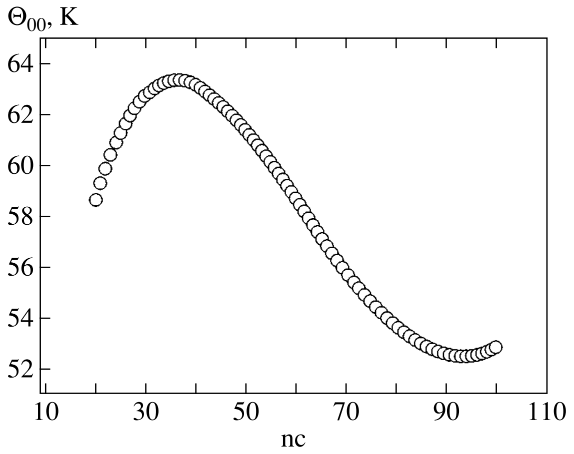

Fig. 5. Dependence of the Debye temperature Θ_{00} of the face-centered cubic fullerites on the number of carbon atoms in the C_{nc} fullerene. Calculations were performed according to formula (6) with the use of polynomials (3) and (4). The Debye temperature is maximum [$\Theta_{00}(C_{36}) = 63.34$ K] for nc = 36 and minimum [$\Theta_{00}(C_{93}) = 52.57$ K] for nc = 93.

ranges 3890 m/s $\le \omega_{0l} \le$ 4120 m/s (Fig. 3) and 2130 m/s $\le \omega_{0t} \le$ 2200 m/s. Consequently, in this range of numbers nc, an increase in the elastic modulus is compensated for by an increase in the density $\rho = m_{nc}/V_{00}$ [see expression (7)]. However, for numbers nc < 35, the velocity of sound drastically decreases with a decrease in the value of nc. This suggests an anomalous decrease in the elastic modulus.

(4) The specific surface energy of the C_{nc} face-centered cubic fullerites at $T = 0$ K and $P = 0$ for molecular masses in the range $37 \le nc \le 97$ varies in the narrow ranges $56 \le \sigma(100)_0 \le 63$ mJ/m^2 (Fig. 4) and $49 \le \sigma(111)_0 \le 55$ mJ/m^2. However, for numbers nc ≤ 30, the specific surface energy sharply increases with a decrease in the value of nc.

(5) The Debye temperature at $T = 0$ K and $P = 0$ for $20 \le nc \le 110$ varies in a wavelike manner (Fig. 5) from $\Theta_{00}(C_{36}) = 63.34$ K (maximum) to $\Theta_{00}(C_{93}) = 52.57$ K (minimum).

(6) The thermal expansion coefficient at $T \gg \Theta$ and $P = 0$ for $45 \le nc \le 95$ lies in the range $3.6 \times 10^{-5} \ge \alpha_p(T \gg \Theta) \ge 2.0 \times 10^{-5}$ K^{-1} (Fig. 6). However, for nc <

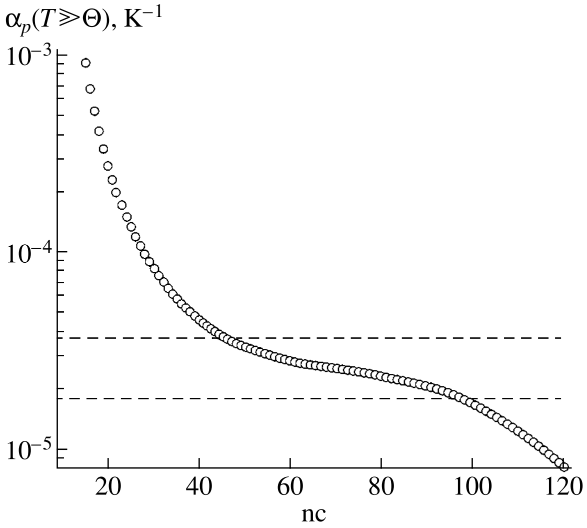

Fig. 6. Dependence of the thermal expansion coefficient α_p ($T \gg \Theta$, $P = 0$) of the face-centered cubic fullerites on the number of carbon atoms in the C_{nc} fullerene. Calculations were performed according to formula (8) with the use of polynomials (3) and (4). The thermal expansion coefficients for fullerene masses in the range $45 \le nc \le 95$ lie in the range $3.6 \times 10^{-5} \ge \alpha_p(T \gg \Theta) \ge 2.0 \times 10^{-5}$ K^{-1}.

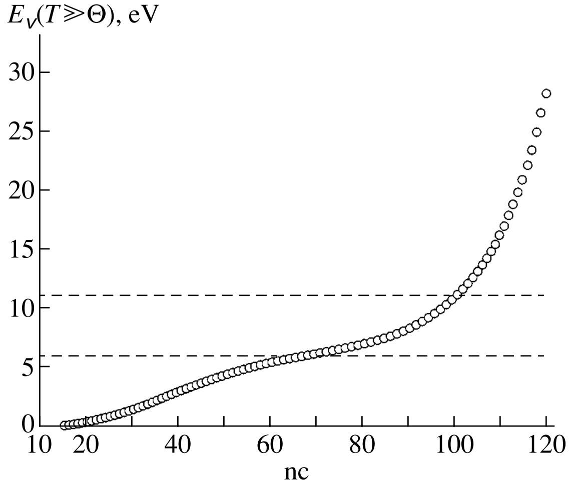

Fig. 7. Dependence of the energy of vacancy formation E_v ($T \gg \Theta$, $P = 0$) in the face-centered cubic fullerites on the number of carbon atoms in the C_{nc} fullerene. Calculations were performed according to formula (9) with the use of polynomials (3) and (4). The energy of vacancy formation increases almost linearly for nc ≤ 100 and increases sharply for nc > 110.

20, the thermal expansion coefficient $\alpha(T \gg \Theta)$ substantially increases with a decrease in the molecular mass. This indicates that the system is unstable.

(7) The energy of the formation of a monovacancy E_v, the self-diffusion energy E_d, and the migration energy $E_m = E_d - E_v$ for the C_{nc} fullerene in the face-centered cubic fullerite increase almost linearly with an increase in the number nc (up to nc ≤ 100). However, these energies drastically increase for numbers nc ≥ 110 (Fig. 7). The results of calculations demonstrate that the face-centered cubic fullerites have a highly stable lattice for nc > 40, because the energy of the formation of a monovacancy and the self-diffusion energy of the fullerene molecule (as a whole, undeformable spherical object) in the face-centered cubic fullerite appear to be higher (due to the larger mass and size of the molecule) than those of carbon atoms in a diamond. For nc ≤ 20, the anomalously small activation parameters indicate that the system is unstable.

(8) Since the depth of the potential well increases monotonically with an increase in the number nc, it should be expected that the melting temperature T_m and the temperatures of polymorphic transitions at atmospheric pressure for the face-centered cubic fullerites will increase monotonically with an increase in the molecular mass of the fullerene. The same inference can be made with due regard for the phenomenological relationships $T_m = \text{const}(g)(D/k_B)$ [19, 30], $\alpha_p(T \gg \Theta)T_m = \text{const}(a)$ [22], $E_v/k_B T_m = \text{const}(v)$ [32], and $E_d/k_B T_m = \text{const}(d)$ [33], where the numerical values of the constants are different in each relationship.

(9) The latent heats of first-order phase transitions at atmospheric pressure, as a rule, are proportional to the sublimation energies of the crystals [8, 30]. Therefore, we can expect that the molar enthalpy of polymorphic phase transitions and the latent heat of melting of the C_{nc} fullerites should increase with an increase in the number nc.

(10) The large value of the derivative of the bulk modulus B'_{00} for the fullerites indicates that, under a high pressure, there can arise an ultrahard state [34], in which the bulk modulus of the fullerite $B_{0P} = B_{00} + PB'_{00}$ becomes larger than the bulk modulus of the diamond (443 GPa [9, 34]). The pressure above which this state can be observed for the C_{60} face-centered cubic fullerite is easily estimated from the data presented in Table 2: $P = [B_{0P}(\text{C-diam}) - B_{00}(C_{60})]/B'_{00}(C_{60}) = (443 - 16.2)/20.73 = 21.34$ GPa. This pressure is in excellent agreement with the estimates made by Blank *et al.* [34]; namely, the linear extrapolation of the P–T phase lines obtained in [34] to the temperature $T = 0$ K gives $P \approx 21$–23 GPa. Moreover, as follows from the data presented in Table 3, an increase in the number nc should be accompanied by a decrease in the pressure corresponding to the ultrahard state. However, the experimental data reported in [35] demonstrate that, at high pressures and temperatures ($P \ge 8$–12 GPa, $T \ge 400$ K), hollow molecules C_{60} undergo irreversible destruction with the formation of ordered or disordered phases based either on atomic carbon or on covalently bonded structures composed of fragments of the

destroyed fullerites, such as $(C_{60})_2$ dimers or one-, two-, or three-dimensional polymers. Therefore, an increase in the number nc leads not only to a decrease in the pressure necessary for the transition to the ultrahard state but also to a decrease in the pressure at which hollow fullerene molecules C_{nc} undergo destruction.

(11) As a rule, the temperature, the molar volume, and the pressure at phase transition points (triple, critical, polymorphic phase transition points) are proportional to the parameters of the intermolecular interaction potential [8, 19, 30, 36]: $T_f \sim D/k_B$, $V_f \sim r_0^3$, and $P_f \sim D/r_0^3$. Consequently, it should be expected that the temperature T_f and the molar volume V_f will increase and the pressure P_f with decrease with an increase in the molecular mass of fullerenes. In this case, it is assumed that the solid, liquid, and gaseous phases of fullerenes are formed by undeformable spherical monomolecules; i.e., C_{nc} fullerene molecules at these temperatures and pressures are not destroyed and their interaction potential remains unchanged.

(12) The data presented in Figs. 1–3, 6, and 7 indicate that C_{nc} fullerite crystals are unstable for nc ≤ 15–20. This is consistent with the conclusions drawn by V. Pokropivny and A. Pokropivny [14] on the basis of the geometric simulation of fullerites. Furthermore, this is in agreement with the results obtained by Cai *et al.* [37], who used the complex Brenner potential in the calculation of the energy parameters of different structures that can be formed by nc carbon molecules. In [37], it was found that the most stable structures are linear carbon clusters for numbers nc ≤ 4, two-dimensional carbon monorings in the range 5 ≤ nc ≤ 17, and fullerene-like clusters for numbers nc ≥ 18. Note that high-symmetry stable fullerenes in the range 18 ≤ nc ≤ 71 are observed only for nc = 20, 24, 28, 36, 50, 60, and 70.

5. ESTIMATION OF THE PARAMETERS OF THE TRIPLE AND CRITICAL POINTS BY THE SCALING METHOD

The parameters of the potential obtained in this work can be used to estimate roughly the parameters of the triple and critical points of the liquid–vapor phase transition. This estimation can be performed by the scaling procedure [19, 30, 36], according to which the parameters of potential (1) are used as the "natural units" (or scaling parameters), namely, the natural unit of length r_0 and the natural unit of energy D. Then, the natural units of molar volume, mass density, temperature, pressure, and surface tension can be written in the form $V_{sc} = N_A r_0^3$, $\rho_{sc} = m/r_0^3$, $T_{sc} = D/k_B$, $P_{sc} = D/r_0^3$, and $\sigma_{sc} = D/r_0^3$, respectively. For compounds of a particular class, different properties are universally expressed through the natural units characterizing the material. For example, the parameters of the critical point for noble gases can be represented in natural units in the following form:

$$T_{cr} = (1.040 \pm 0.020)T_{sc}\ [19, 30], \qquad (12a)$$

$$P_{cr} = (0.130 \pm 0.006)P_{sc}\ [30],\quad (0.131 \pm 0.001)P_{sc}\ [19], \qquad (12b)$$

$$V_{cr} = (2.380 \pm 0.008)V_{sc}\ [30]. \qquad (12c)$$

As a result, we have $N_A k_B T_{cr}/(P_{cr}V_{cr}) = Z_{cr}^{-1} = 3.4 \pm 0.1$ or $Z_{cr} = 0.294 \pm 0.09$ [30]. The boiling temperature at atmospheric pressure is given by the relationship $T_B = (0.61 \pm 0.020)T_{sc}$ [19, 30]; that is, the temperatures T_B and T_{cr} are related by the expression $T_B = (0.5865 \pm 0.02)T_{cr}$.

The parameters of the triple point for noble gases in natural units can be written as follows [30]:

$$T_{tr} = (0.579 \pm 0.007)T_{sc}; \qquad (13a)$$

$$P_{tr} = (0.19 \pm 0.2) \times 10^{-3} P_{sc}; \qquad (13b)$$

$$V_{sol} = (0.76 \pm 0.01)V_{sc}, \qquad (13c)$$

[i.e., $N_A k_B T_{tr}/(P_{tr}V_{sol}) = 410 \pm 50$;

$$V_{liq} = (0.88 \pm 0.02)V_{sc}, \qquad (13d)$$

(i.e., $\Delta V_{tr}/V_{sol} = 0.158$);

$$\Delta H_m = (0.98 \pm 0.02)D, \qquad (13e)$$

where ΔH_m is the latent heat (enthalpy) of melting (i.e., $\Delta S_m/k_B = \Delta H_m/k_B T_{tr} = 1.68 \pm 0.03$);

$$(dP/dT)_m = (14.105 \pm 0.02)k_B/r_0^3, \qquad (13f)$$

where $(dP/dT)_m$ is the slope of the melting line;

$$\sigma_{liq} = (0.94 \pm 0.02)\sigma_{sc}, \qquad (13g)$$

where σ_{liq} is the surface tension of the liquid phase.

In [19], the properties of C_{60} fullerenes were evaluated by the scaling method under the assumption that fullerenes, like noble gases, belong to the class of systems formed by spherically symmetric close-packed particles with a short-range interaction. Without calculating the exponents of the potential, the depth and the coordinate of the minimum of the potential were determined to be $D/k_B = 257 \pm 13$ meV $= 2982.23 \pm 150.85$ K and $r_0 = 10.06 \times 10^{-10}$ m, respectively [19]. On the basis of these parameters and relationships (12), Bezmen'nitsyn *et al.* [19] estimated the parameters of the critical point for the C_{60} fullerene gas, the melting temperature at atmospheric pressure (Table 4) and the Debye temperature for the C_{60} face-centered cubic fullerite, as is the case with noble gases. Note that the expression $(D/r_0^2 m_{60})^{1/2}$ was used as the natural unit of frequency. As a result, the formula $\Theta \approx$

Table 4. Temperatures, pressures, molar volumes, and mass densities at the triple and critical points for C_{nc} fullerites with a face-centered cubic lattice according to calculations from relationships (12) and (13) with the parameters of the potential [represented by polynomials (3), (4) and in Table 2]

C_{nc}	Triple point [relationships (13)]									Critical point [relationships (12)]			
	T_{tr}, K	P_{tr}, atm	V_{tr} (sol), cm^3/mol	V_{tr} (liq), cm^3/mol	ρ_{tr} (sol). g/cm^3	ρ_{tr} (liq). g/cm^3	ΔH_m, kJ/mol	$(dP/dT)_m$, atm/K	σ_{liq}, mJ/m^2	T_{cr}, K	P_{cr}, atm	V_{cr}, cm^3/mol	ρ_{cr}, g/cm^3
C_{24}										1885	173.56	265.09	1.087
C_{36}	1404	1.203	238.9	276.6	1.810	1.563	19.56	3.68	48.56	2523	82.33	748.0	0.578
C_{60}	2031	0.856	485.5	562.1	1.484	1.282	28.29	1.81	43.78	3649	58.59	1520.3	0.474
	(1730)									(3100)	(53.6)	(1441.3)	(0.5)
C_{70}	2260	0.851	543.3	629.1	1.547	1.336	31.47	1.62	45.16	4059	58.23	1701.4	0.494
C_{76}	2387	0.847	577.0	668.2	1.582	1.366	33.25	1.52	45.85	4288	57.93	1807.1	0.505
C_{84}	2547	0.821	635.1	735.3	1.589	1.372	35.47	1.39	45.89	4574	56.15	1988.8	0.507
C_{96}	2763	0.712	794.3	919.7	1.452	1.254	38.48	1.11	42.88	4962	48.70	2487.5	0.464

Note: The volume and density at the triple point were calculated from relationships (13) for the solid (sol) and liquid (liq) phases. The latent heat (enthalpy) ΔH_m, the slope of the melting line $(dP/dT)_m$, and the surface tension of the liquid phase σ_{liq} at the triple point were determined from relationships (13). The estimates taken from [19] for the C_{60} fullerite are given in parentheses. Since the C_{24} fullerite has a simple cubic crystal lattice [14], the parameters of the triple point for this compound were not determined.

$27(\hbar/k_B)(D/r_0^2 m_{60})^{1/2}$ was derived for noble-gas crystals. The Debye temperature for the buckminsterfullerite was estimated as $\Theta(C_{60}) \approx 40$ K, which is close to the Debye temperature obtained in our work (Table 2).

The parameters of the triple point (for the face-centered cubic fullerites) and the critical point (for the monomolecular gas of spherical particles) of fullerenes were calculated by the scaling method with formulas (12) and (13). These parameters are given in Table 4. The results obtained can be summarized as follows.

(1) The dependences of the pressure and the mass density at the triple and critical points on the molecular mass (i.e., on nc) exhibit a nonlinear behavior (Figs. 8, 9).

(2) The dependence of the surface tension at the triple point on the molecular mass nc for the liquid phase is similar to that of the specific surface energy for the face-centered cubic fullerite crystal (Fig. 4).

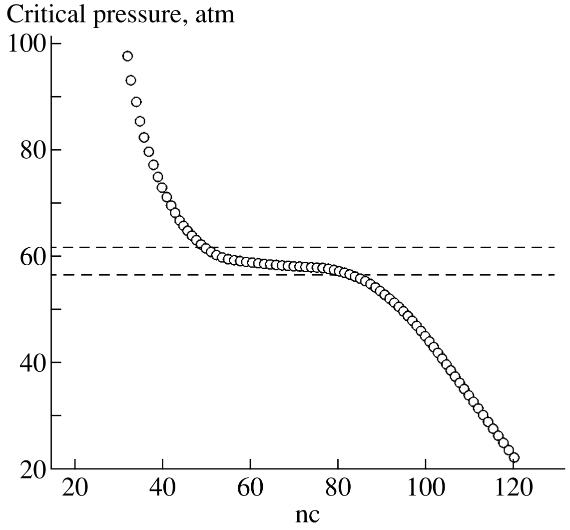

Fig. 8. Dependence of the pressure at the critical point on the number of carbon atoms in the C_{nc} fullerene. Calculations were performed according to formulas (12) with the use of polynomials (3) and (4). The critical pressure for fullerene masses in the range $50 \le nc \le 85$ lies in the range 55.77atm $\le P_{cr} \le 61.65$ atm.

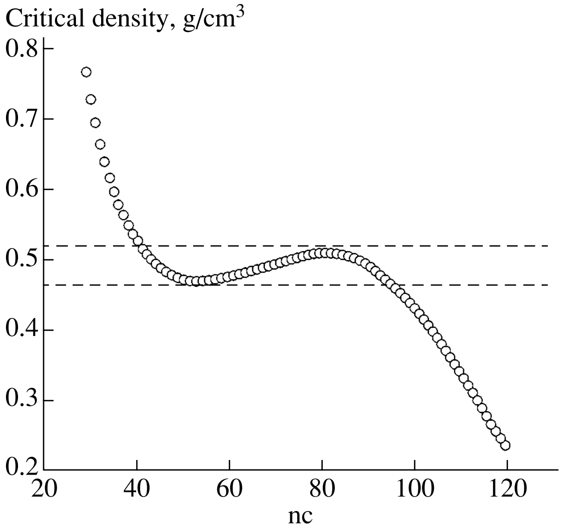

Fig. 9. Dependence of the critical density on the number of carbon atoms in the C_{nc} fullerene. Calculations were performed according to formulas (12) with the use of polynomials (3) and (4). The critical density for fullerene masses in the range $40 \le nc \le 96$ lies in the range 0.464 g/cm$^3 \le \rho_{cr} \le 0.526$ g/cm^3.

(3) The temperature and the molar volume at the triple and critical points and the latent heat of melting increase monotonically with an increase in the number nc.

(4) The pressures P_{tr} and P_{cr} and the slopes of all the lines corresponding to the phase transitions in the *P–T* diagram (i.e., the values of dP_f/dT_f) decrease with an increase in the number of carbon atoms in the fullerene molecule. As a consequence, an increase in the number nc leads to the evolution of the *P–T* diagram, as is schematically shown in Fig. 10.

(5) It is easy to see from Fig. 10 that isobaric heating of a mixture of microcrystals formed by higher and lower face-centered cubic fullerites should lead to the "burning out" (i.e., melting, sublimation) primarily of lower fullerites. Upon isobaric cooling of a gas (or liquid) mixture of higher and lower fullerene molecules, face-centered cubic fullerites of higher fullerenes will be formed initially.

Note that all the aforementioned numerical estimates hold true for monomolecular phases of spherical particles whose interaction is similar to the interaction of noble-gas atoms. However, when using the scaling relations, it should be remembered that an increase in the molecular mass of the fullerene results in an increase in the nonsphericity of molecules [1]. Therefore, within the scaling approach, it is necessary to take into account the "acentricity factor" of molecules (see [36, Chapter 2]). This factor is usually determined from the relationship

$$W_a = (0.291 - Z_{cr})/0.08, \quad (14)$$

where $Z_{cr} = P_{cr}V_{cr}(N_A k_B T_{cr})$. Even for noble gases, the acentricity factor is not necessarily equal to zero: W_a = 0 (Ne), –0.004 (Ar), –0.002 (Kr), and +0.002 (Xe) [36]. Relationships (12) and (13) become more complicated with allowance made for the acentricity factor. For example, the critical temperature is defined by the expression

$$T_{cr} = 1.263(D/k_B)/(1 + 0.214W_a). \quad (15)$$

Unfortunately, reliable data on the quantity Z_{cr} for fullerenes are not available in the literature. In this respect, the use of expression (15) requires the development of a technique for calculating the acentricity factor W_a from the parameters of fullerene ellipsoids. Since the acentricity factors W_a for fullerenes were not known, the parameters of the critical and triple points were estimated from relationships (12) and (13).

It should also be noted that the interfullerene interaction (which is intimately related to the interaction of carbon atoms) differs from the interaction between atoms of the noble-gas group. This can be judged from the fact that the rigidity parameter of potential (1) for the fullerenes increases with an increase in the molecular mass (Table 2): $b = 36.4(C_{20}) - 66.4(C_{120})$. This behavior is characteristic of elements belonging to the carbon group [9]. However, the rigidity parameter for noble gases decreases with an increase in the atomic mass: b = 20(Ne)–15(Xe) [38]. This is typical of elements with a filled electron shell (the thicker the electron shell of neutral atoms, the softer the shell). Therefore, it should be expected that the numerical coefficients in relationships (12) and (13) for the fullerenes will be different, as is the case with the scaling relations for molecular systems [30] or metals [39]. In this respect, the obtained estimates should be treated as a first approximation for investigating the evolution of the phase diagram for fullerenes with a variation in the molecular mass.

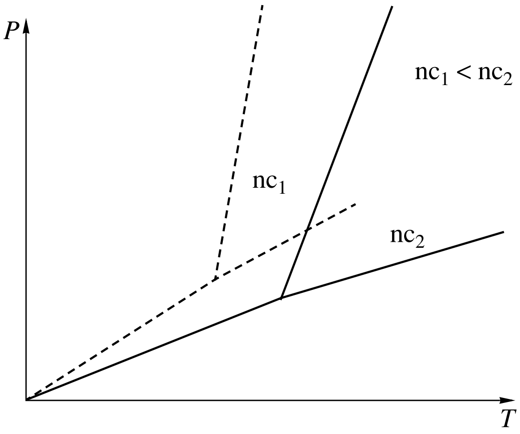

Fig. 10. Schematic diagram illustrating the evolution of the *P–T* phase diagram for the fullerite with a variation in the number of carbon atoms in the C_{nc} fullerene. As the number nc increases, the temperature at the triple and critical points increases and the pressure either decreases or (in the range 50 ≤ nc ≤ 85; see Fig. 8) remains unchanged; i.e., the slope of the phase transition lines decreases with an increase in the molecular mass of the fullerene.

ACKNOWLEDGMENTS

The author would like to thank V.I. Zubov, Wensheng Cai, A.D. Filenko, K.N. Magomedov, and Z.M. Surkhaeva for their participation in helpful discussions of the results and for their assistance in performing this study.

This work was supported by the Russian Foundation for Basic Research, project no. 02-03-33301.

REFERENCES

1. A. V. Eletskiĭ and B. M. Smirnov, Usp. Fiz. Nauk **165** (9), 977 (1995) [Phys. Usp. **38**, 935 (1995)].
2. B. V. Lebedev, Zh. Fiz. Khim. **75** (5), 775 (2001).
3. A. N. Aleksandrovskii, A. S. Bakai, A. V. Dollin, V. B. Esel'son, G. E. Gadd, V. G. Gavrilko, V. G. Mangelii, S. Moricca, B. Sundgvist, and B. G. Udovidchenko, Fiz. Nizk. Temp. **29** (4), 432 (2003) [Low Temp. Phys. **29**, 324 (2003)].
4. L. A. Girifalco, Phys. Rev. B **52** (14), 9910 (1995).

5. M. V. Korobov, E. V. Skokan, D. B. Borisova, and L. M. Khomich, Zh. Fiz. Khim. **70** (6), 999 (1996).
6. N. P. Kobelev, R. K. Nikolaev, N. S. Sidorov, and Ya. M. Soĭfer, Fiz. Tverd. Tela (St. Petersburg) **43** (12), 2262 (2001) [Phys. Solid State **43**, 2344 (2001)].
7. M. C. Abramo and C. Caccamo, J. Phys. Chem. Solids **57** (11), 1751 (1996).
8. E. A. Moelwyn-Hyghes, *Physical Chemistry* (Pergamon, London, 1961; Inostrannaya Literatura, Moscow, 1962).
9. M. N. Magomedov, Zh. Fiz. Khim. **63** (11), 2943 (1989).
10. L. N. Yakub, Fiz. Nizk. Temp. **19** (6), 726 (1993) [Low Temp. Phys. **19**, 522 (1993)].
11. V. I. Zubov, N. P. Tretiakov, J. F. Sanchez, and A. A. Caparica, Phys. Rev. B **53** (18), 12 080 (1996).
12. V. I. Zubov, N. P. Tretiakov, and J. N. Teixeira Rabelo, Mol. Mater. **13** (3), 349 (2000).
13. V. I. Zubov and I. V. Zubov, Fiz. Tverd. Tela (St. Petersburg) **44** (7), 1155 (2002) [Phys. Solid State **44**, 1205 (2002)].
14. V. V. Pokropivny and A. V. Pokropivny, Fiz. Tverd. Tela (St. Petersburg) **46** (2), 380 (2004) [Phys. Solid State **46**, 392 (2004)].
15. Y. Saito, T. Yoshikawa, and N. Fujimoto, Phys. Rev. B **48** (12), 9182 (1993).
16. M. Picholz and Z. Gamba, Phys. Rev. B **53** (5), 2159 (1996).
17. M. C. Valsakumar, N. Subramanian, M. Yousuf, P. Sahu, Y. Hariharan, A. Bharathi, V. S. Sastry, J. Janaki, G. Rao, T. Radhakrishnan, and C. Sundar, Phys. Rev. B **48** (12), 9080 (1993).
18. H. Kawada, Y. Fujii, H. Nakao, Y. Murakami, T. Watanuki, H. Suematsu, K. Kikuchi, Y. Achiba, and I. Ikemoto, Phys. Rev. B **51** (14), 8723 (1995).
19. V. N. Bezmen'nitsyn, A. V. Eletskiĭ, and M. V. Okun', Usp. Fiz. Nauk **168** (11), 1195 (1998) [Phys. Usp. **41**, 1091 (1998)].
20. M. N. Magomedov, Fiz. Tverd. Tela (St. Petersburg) **45** (1), 33 (2003) [Phys. Solid State **45**, 32 (2003)].
21. M. N. Magomedov, Zh. Fiz. Khim. **58** (7), 1804 (1984).
22. S. I. Novikova, *Thermal Expansion of Solids* (Nauka, Moscow, 1974) [in Russian].
23. M. I. Alam, M. S. Ali, and M. M. Hasan, Indian J. Pure Appl. Phys. **30** (5), 221 (1992).
24. M. N. Magomedov, Pis'ma Zh. Tekh. Fiz. **28** (10), 64 (2002) [Tech. Phys. Lett. **28**, 430 (2002)].
25. M. N. Magomedov, Metally, No. 6, 27 (2001).
26. M. N. Magomedov, Fiz. Tverd. Tela (St. Petersburg) **46** (5), 924 (2004) [Phys. Solid State **46**, 954 (2004)].
27. E. V. Manzheliĭ, Fiz. Nizk. Temp. **29** (4), 443 (2003) [Low Temp. Phys. **29**, 333 (2003)].
28. *Cryocrystals*, Ed. by B. I. Verkin and A. F. Prikhod'ko (Naukova Dumka, Kiev, 1983) [in Russian].
29. L. D. Landau and E. M. Lifshitz, *Course of Theoretical Physics*, Vol. 7: *Theory of Elasticity*, 4th ed. (Nauka, Moscow, 1987; Pergamon, New York, 1986).
30. B. M. Smirnov, Usp. Fiz. Nauk **171**, 1291 (2001) [Phys. Usp. **44**, 1229 (2001)].
31. O. Umiguchi and T. Inaoka, J. Phys. Soc. Jpn. **68** (2), 508 (1999).
32. M. N. Magomedov, Izv. Ross. Akad. Nauk, Met., No. 5, 73 (1992).
33. M. N. Magomedov, Teplofiz. Vys. Temp. **31** (5), 731 (1993).
34. V. D. Blank, V. M. Levin, V. M. Prokhorov, S. G. Buga, G. A. Dubitskiĭ, and N. R. Serebryanaya, Zh. Éksp. Teor. Fiz. **114**, 1365 (1998) [JETP **87**, 741 (1998)].
35. V. V. Brazhkin, A. G. Lyapin, S. V. Popova, S. K. Beĭliss, T. D. Varfolomeeva, R. N. Voloshin, A. G. Gavrilyuk, M. V. Kondrin, V. V. Mukhamad'yarov, I. A. Troyan, S. V. Demishev, A. A. Pronin, and N. E. Sluchanko, Pis'ma Zh. Éksp. Teor. Fiz. **76** (11), 805 (2002) [JETP Lett. **76**, 681 (2002)].
36. R. C. Reid, J. M. Prausnitz, and T. K. Sherwood, *The Properties of Gases and Liquids*, 3rd ed. (McGraw-Hill, New York, 1977).
37. W. Cai, N. Shao, X. Shao, and Z. Pan, J. Mol. Struct. **678** (3), 113 (2004).
38. M. N. Magomedov, Zh. Fiz. Khim. **62** (8), 2103 (1988).
39. M. M. Martynyuk, Zh. Fiz. Khim. **57** (4), 810 (1983).

Translated by O. Borovik-Romanova

Physics of the Solid State, Vol. 47, No. 4, 2005, p. 795.
Original Russian Text Copyright © 2005.

ERRATA

Erratum: “Martensitic Transformation and Electrical Properties of a $Ni_{2.14}Mn_{0.81}Fe_{0.05}Ga$ Alloy in Its Different Structural States” [*Phys. Solid State* 47, 556 (2005)]

R. N. Imashev, Kh. Ya. Mulyukov, I. Z. Sharipov, V. G. Shavrov, and V. V. Koledov

The scales in Figures 2 and 3 on pp. 557 and 558 should read nm instead of mm.

1063-7834/05/4704-0795$26.00 © 2005 Pleiades Publishing, Inc.